IRAS FAINT SOURCE SURVEY

EXPLANATORY SUPPLEMENT VERSION 2

D-10015

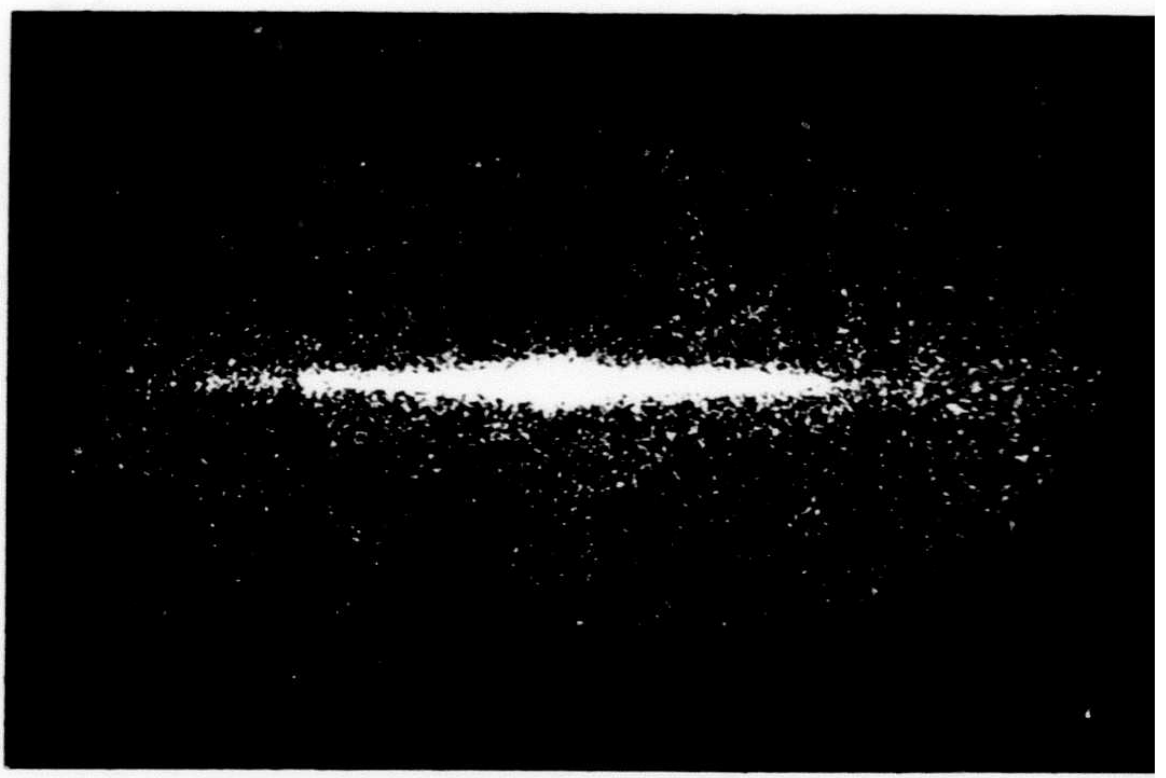

pg 1 of 439

INFRARED PROCESSING AND ANALYSIS CENTER

JULY 1988

D 10015

This document is to be referenced as:
Moshir, M. et al. 1992, Explanatory Supplement to the
IRAS Faint Source Survey, Version 2, JPL D-10015 8/92
(Pasadena: JPL)

2

D 10015

IRAS FAINT SOURCE SURVEY

EXPLANATORY SUPPLEMENT VERSION 2

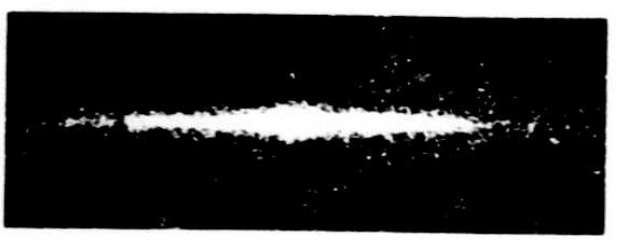

M. Moshir

G. Kopan

T. Conrow

H. McCallon

P. Hacking

D. Gregorich

G. Rohrbach

M. Melnyk

W. Rice

L. Fullmer

J. White

T. Chester

July 1992

The Infrared Astronomical Satellite (IRAS) was a joint project of NASA (U.S.), NIVR (The Netherlands) and SERC (U.K.).

INFRARED PROCESSING AND ANALYSIS CENTER
California Institute of Technology
Pasadena, California 91125

[redacted]

3

D 10015

PREFACE

This Explanatory Supplement accompanies the final release of the data products from the *IRAS* Faint Source Survey. This release includes the Faint Source Catalog for the *unconfused* $|b| \geq 10°$ sky (FSC v.2), the point-source filtered coadded images for the entire sky, and the reject file for the whole sky.

The current release of the Faint Source Catalog supersedes and replaces the version 1 of the FSC which was first released in 1989. Version 2 of the Faint Source Catalog for $|b| \geq 50°$ displays marked improvements relative to version 1 and has lower SNR thresholds as well. The point-source filtered images did not change.

The data described in this Supplement are available at the National Space Science Data Center (NSSDC) at the Goddard Space Flight Center; the interested reader is referred to the NSSDC for access to the *IRAS* Faint Source Survey data.

M. Moshir, T. Chester
Pasadena
July 1992

H

D 10015

Table of Contents

5

D 10015

III. ANALYSIS OF THE FAINT SOURCE SURVEY

6

D 10015

7

D 10015

8

D 10015

Index of Tables

I. INTRODUCTION

II. FAINT SOURCE SURVEY PROCESSING

III. ANALYSIS OF THE FAINT SOURCE SURVEY

D 10015

10

D 10015

Index of Figures

I. INTRODUCTION

II. FAINT SOURCE SURVEY DATA PROCESSING

D 10015

III. ANALYSIS OF THE FAINT SOURCE SURVEY

12

D 10015

13

D 10015

14

D 10015

15

D 10015

10

D 10015

IV. COMPARISON OF THE FAINT SOURCE CATALOG TO OTHER IRAS PRODUCTS

D 10015

I. INTRODUCTION

A. General Overview

The *Infrared Astronomical Satellite (IRAS)* conducted a survey of 98% of the sky from January to November, 1983 in four wavelength bands centered at 12, 25, 60, and 100 μm. It spent approximately two-thirds of the 300-day mission performing an unbiased survey of the sky, leading to the release in 1984 of the *IRAS Point Source Catalog* (PSC) containing some 250,000 sources. The PSC and aspects of the *IRAS* mission are explained in detail in the *Explanatory Supplement to IRAS Catalogs and Atlases* (1988), henceforth referred to as the *Main Supplement*.

The *IRAS* survey was designed to produce an extremely reliable catalog. The sky was scanned repeatedly by multiple detectors, and over half of the sky was covered by more than 12 individual detector scans per wavelength band. The PSC was produced by detecting sources in each of the individual detector scans, and then applying a series of stringent confirmation criteria to establish the reliability of those sources. This led to a reliability of the PSC which exceeded 99.997% over most of the sky, excluding cirrus sources, but at the cost of not reaching the full sensitivity attainable with the *IRAS* data.

The *IRAS Faint Source Survey* (FSS) described here has achieved roughly a one-magnitude increase in sensitivity (a factor of ~2.5) relative to the PSC by coadding the data before extracting sources. The FSS was produced by *point-source filtering* the individual detector data streams, and then *coadding* those data streams using a trimmed-average algorithm. Thus, confirmation is still applied to the data but in a much less stringent manner than was applied for the PSC. Three major data products were produced: images, a catalog (FSC), and its associated reject file. Figures I.A.1 and 2 show a comparison of the PSC, the FSS, and the FSC for one area. The reliability of the entire *Faint Source Catalog* (FSC) is high (> 94%).

This document explains in detail the products of the FSS, the processing methods used to produce them, and gives results of analysis of these products. Version 1 of this document accompanied the release of version 1 of the FSC and the plates (point-source-filtered, coadded images) for $|b| > 50°$; version 1 products were released in December of 1988. Following the release of FSC version 1, software improvements were made to compute noise more accurately. The improvements resulted in producing a more complete catalog of higher reliability at a give SNR. The resulting catalog is named FSC version 2. The current version of this document accompanies the release of all the products of the FSS. Although the plates were produced for the whole sky, we have analyzed and report

18

D 10015

B1 > B2

1110 = ✕ 1111 = ✳

B1 < B2

1110 = ▲ 1111 = ⊕

OTHER

0110 = ⌑ 0111 = ○

1010 = ↕ 1011 = Y

0010 = 3 0011 = ●

1100 = ☆ 1101 = △

0100 = 2 0101 = ↑

1000 = 1 1001 = ∞

0000 = + 0001 = 4

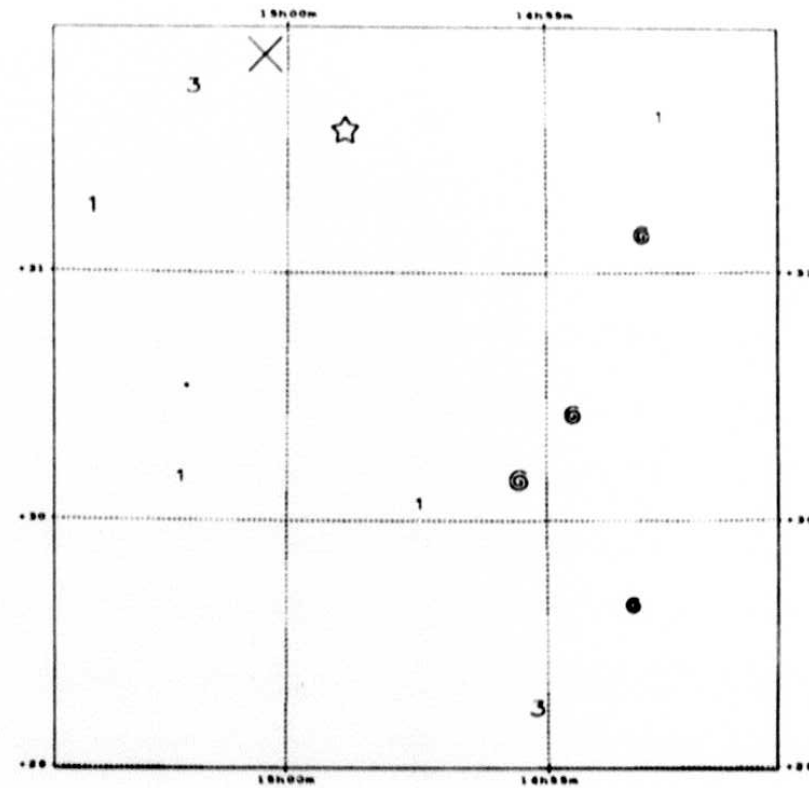

Figure I.A.1 A 3° × 3° area from the PSC in plate 1285. As an example of the color legend, 1100 signifies a source detected at 12 and 25 μm (usually a stellar object), 0011 signifies a sou ce detected at 60 and 100 μm (often an extragalactic object at high galactic latitudes). RA ranges from 14^h50^m to 15^h5^m and DEC from 29° to 32°. B1 refers to band 1 (12 μm), B2 refers to band 2 (25 μm).

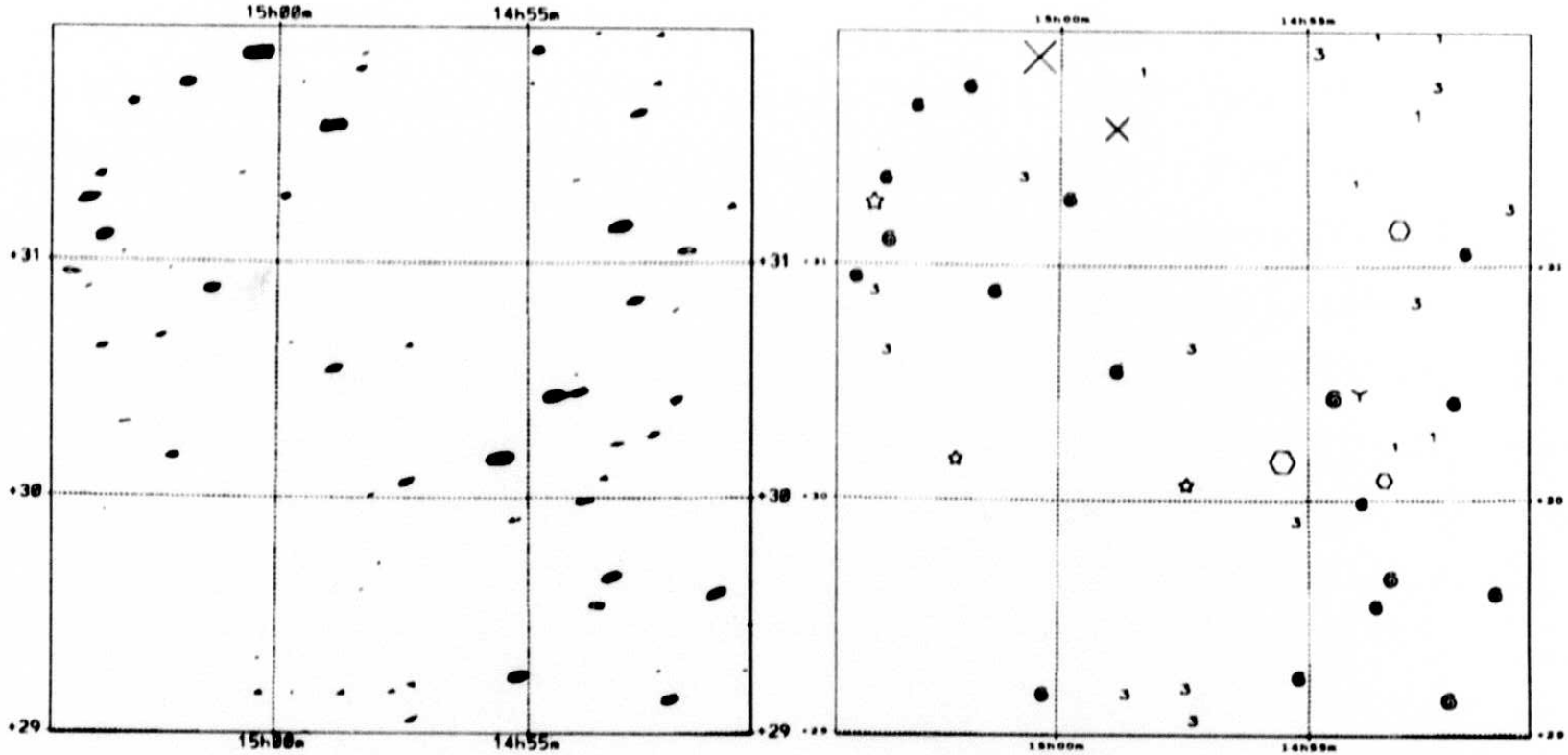

Figure I.A.2 Same area as in Figure I.A.1, but as seen on FSS plate (left figure), FSC (right figure). In the left figure the contour levels at 12 and 60 μm have been superimposed. Lowest contour at 12 μm is 75 mJy, and 120 mJy at 60 μm.

here on only the *unconfused* parts of the sky with $|b| \gtrsim 10°$, representing about 80% of the sky.

Due to avoidance of confused regions, the FSC has different spatial coverages at different spectral bands. Excluding confused regions, at 12 and 25 μm, the FSC extends down to an absolute galactic latitude of 10°, and at 60 μm down to a latitude of 20°. Figures I.A.3 and 4 show the spatial coverage of the FSC at 12 and 60 μm. Due to prevalence of the infrared cirrus at 100 μm, this spectral band was not considered for catalog qualification. Sources with 100 μm detections are present in the FSC only if they have been bandmerged with catalog quality detections at other bands. This is a change from version 1 of the FSC which included $\sim$ 200 sources detected only at 100 μm.

The scientific motivation for the FSS is to extract the maximum information on faint sources of small angular size from the *IRAS* survey data. The FSS is thus intended to be the final word from the *IRAS* survey data for faint point sources. (Exception: see caveat j in Section I.C.1, on variable sources.) The FSS also contains small extended sources with in-scan spatial extent less than $3' - 9'$, although we have not investigated whether it is possible to *identify* such sources using *only* the FSS. Other algorithms should be used to derive better positions and flux densities for these objects, since the FSS algorithm will produce erroneous estimates (see Section III.A.5). Larger sources have been suppressed by the point source filtering algorithm (their reported flux densities have been attenuated).

For faint *point* sources, the FSS produces results that are more accurate than the one-dimensional ADDSCAN/SCANPI processing at IPAC. The FSS was optimized to detect faint *point* sources, whereas ADDSCAN was designed to preserve the optimal resolution of the *IRAS* detectors and to obtain accurate flux density estimates for bright sources. Thus in general the signal-to-noise ratio is better for faint point sources in the FSS. Most users will no longer need to request ADDSCAN processing. ADDSCAN/SCANPI processing will still be valuable for users who require more accurate flux densities for bright sources, who suspect that their source is extended, or who suspect confusion with a nearby source and need higher in-scan resolution (see Section III.G.6).

Three major products, all of which are released to the astronomical community, have been obtained from the FSS (see Tables I.A.1 and 2). The point-source-filtered, coadded maps, called the FSS plates, represent the most fundamental product. These plates are in the form of images, and give the basic data from which the other two products are derived. These plates give the best estimate from the *IRAS* survey data of the point source flux density at every surveyed point of the sky. Typically, at a signal-to-noise ratio (SNR) of 3, the *plates* reach a factor of 3.5 times fainter than the PSC, except at 100 μm, and in

21

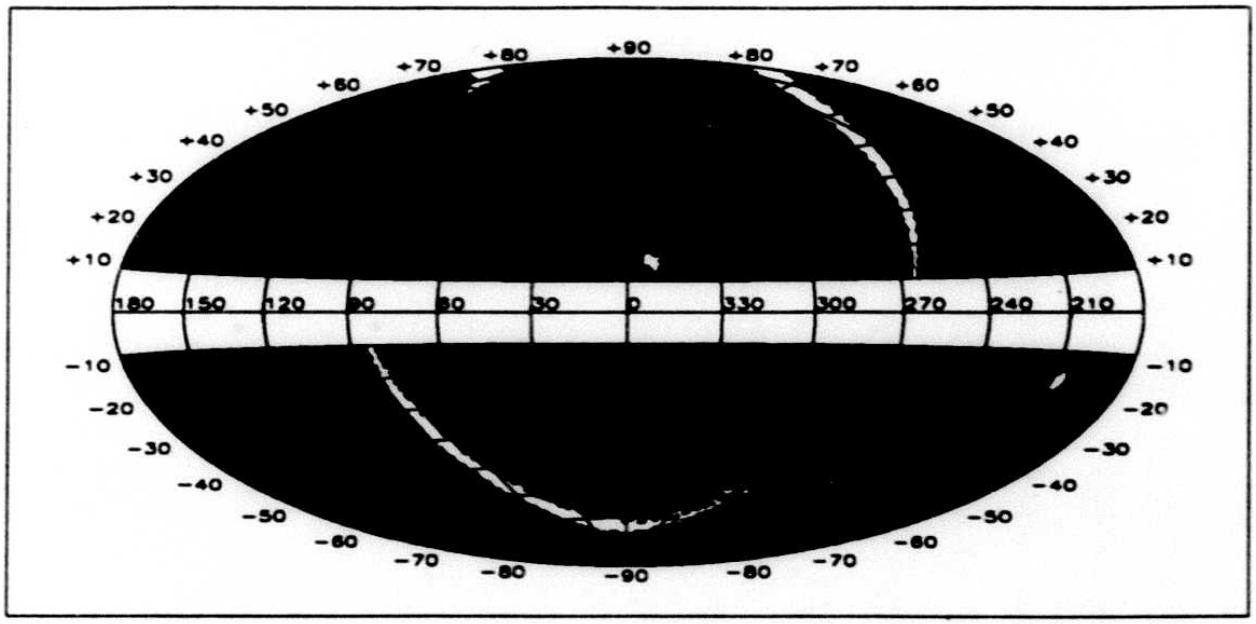

Figure I.A.3 Spatial coverage of the FSC at 12 μm

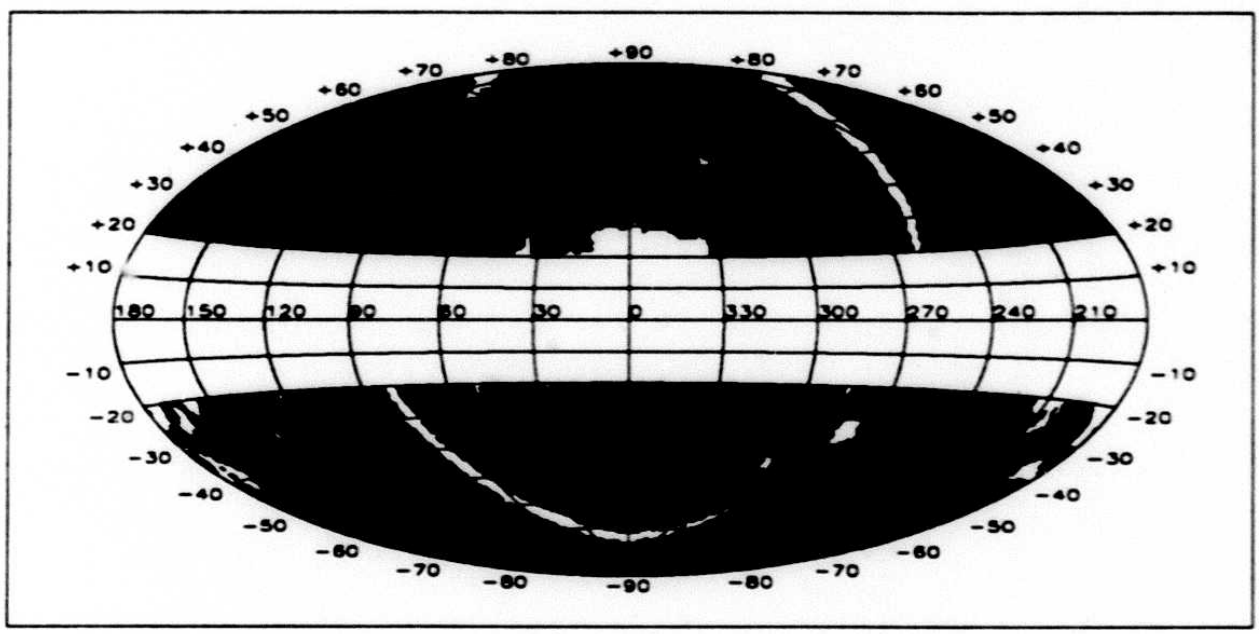

Figure I.A.4 Spatial coverage of the FSC at 60 μm

TABLE I.A.1 Products Released from the FSS

Product	Description	Medium	Date
Plates, $\|b\| > 50°$	495 6.6° × 6.6° fields (see Table I.A.2 for data parameters)	141 6250-bpi tapes	Dec. 1988
Plates, all sky	1,716 6.6° × 6.6° fields (see Table I.A.2 for data parameters)	40 8-mm tapes	Sept. 1990
Catalog V.1.0	27,827 point sources, $\|b\| > 50°$	1 6250-bpi tape†	Dec. 1988
Catalog V.1.2	27,827 point sources, $\|b\| > 50°$	1 6250-bpi tape†	Aug. 1989
Catalog V.2.0	173,044 point sources, *unconfused* sky, $\|b\| \gtrsim 10°$	1 6250-bpi tape‡	Sept. 1990
Catalog V.2.0 long form	173,044 point sources, *unconfused* sky, $\|b\| \gtrsim 10°$	1 8-mm tape	June 1992
Reject File	593,516 extractions rejected from the Catalog	1 8-mm tape§	June 1992

† The catalog is available in short form, giving essential information about each object.
‡ The catalog is available in short form, and in long form, which adds detailed and specialized information about each object.
§ The reject file is available only in long form.

TABLE I.A.2 Parameters of FSS Plates

Pixel Size	0.25′ × 0.25′ at 12 and 25 μm 0.50′ × 0.50′ at 60 and 100 μm
Data Contents	Separate grids at each wavelength for - point source flux density - its 1-σ scatter (in that pixel) - the number of observations

some plates at 60 μm. The plates are not as sensitive in areas with high cirrus content(see below). There are a number of caveats on the use of the plates, which are given below (see Section I.C). The plate data for the whole sky occupy 40 8-mm tapes, and data volume amounts to approximately 73 Gbytes.

The most useful product for most astronomers will undoubtedly be the FSC. This catalog is a compilation of the sources extracted from the FSS plates that have met reasonable reliability requirements. For the *faintest* sources in the FSC, the reliability is estimated to exceed roughly 90% at 12 and 25 μm and 80% at 60 μm. The "false" 20% at 60 μm

23

TABLE I.A.3 Catalog Thresholds for Version 2

Reliability Thresholds† Wavelength (μm)			LOCSNR Thresholds‡ Wavelength (μm)		
12	25	60	12	25	60
$\geq$ 90%	$\geq$ 90%	$\geq$ 80%	3.5	4.5	3.5

† In addition, all catalog quality sources are required to have at least 6 individual detector coverages at the peak flux pixel.

‡ LOCSNR is the ratio of the signal to data dispersion at a given *pixel*.

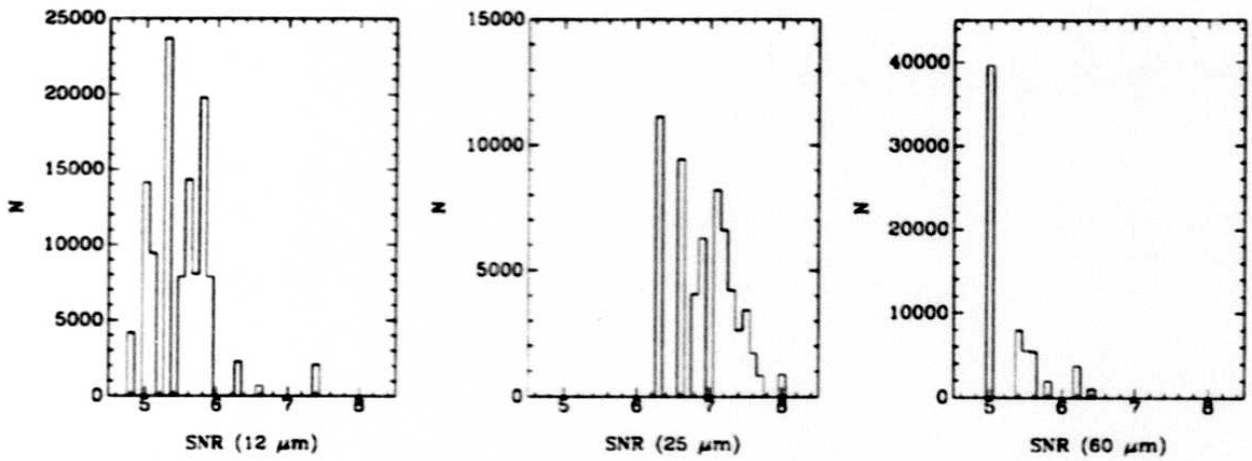

Figure I.A.5 Distribution of SNR thresholds for catalog sources. N gives the number of sources having the denoted SNR threshold.

result primarily from the *infrared cirrus*. Integrated over all SNRs, the catalog as a whole is at least 98.5% reliable at 12 and 25 μm, and ~94% at 60 μm (see Section III.D for further information). Although the reliability of the FSC cannot be as high as that of the PSC, which was > 99.997% at 12, 25 and 60 μm and ~93% at 100 μm (due also to cirrus) overall, the FSC is still a highly reliable catalog, and it can be used by astronomers with a high degree of confidence.

Because of the reliability requirement, the FSC does not achieve the full sensitivity of the FSS plates. Typically, only sources with SNR $\gtrsim$ 5-6 in the plates are contained in the FSC. (See Figure I.A.5 for the distribution of SNR thresholds, and Table I.A.3 for the exact catalog criteria. LOCSNR is the ratio of the signal to noise at a given *pixel*, whereas the SNR uses the noise calculated over a larger *area*.) The FSC is a factor of 2-2.5 times more sensitive than the PSC. The FSC typically contains sources with flux

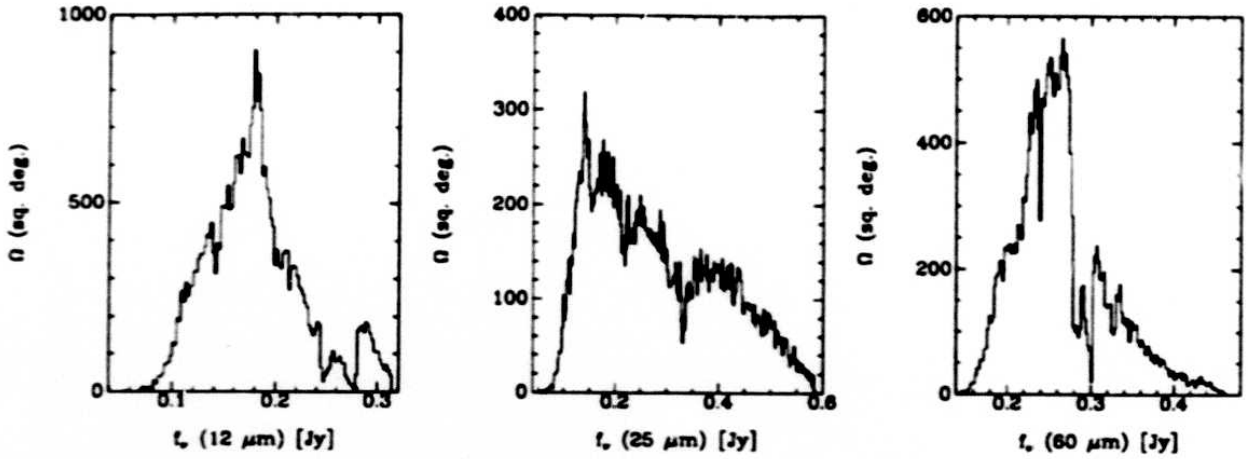

Figure I.A.6 Distribution of flux density 90% completeness levels in the FSC. These figures are histograms of completeness levels from Figures III.C.5–7. The bimodal behavior is due to enhanced noise near the ecliptic plane and confused regions.

densities above 0.2 Jy at 12, 25, and 60 μm, and above 1.0 Jy at 100 μm, although this latter number varies by as much as a factor of two, depending on the amount of infrared cirrus present in a given area of the sky. (See Figure I.A.6 for the distribution of FSC flux density completeness levels.) The large number of multiband sources in the catalog allows the users to perform significantly enhanced analysis on multiband sources. The number of sources with detections at 12, 25, and 60 μm is over 11,000, and sources with detections at 25, 60, and 100 μm number over 9,000. (See Figure I.A.7 for a color-color distribution of multiband sources in the catalog.)

The third product of the FSS is the *Faint Source Reject File* (FSR). The word *Reject* appears in the title to emphasize that the reliability of this database is significantly lower than that of the FSC. The FSR consists of extractions with SNR above 3.0 in the coadd plates that do *not* appear in the FSC, and thus gives a sensitivity gain of a factor of 3.5 as compared to the PSC.

We envision that these three products will be used in the following ways. The FSC can be used to find new sources and new information on previously known sources. The FSR can be easily used for the same purposes, but each user must calculate, using the information supplied herein, the statistical reliability of the sources in each use of the FSR. For example, if one searches the FSR for a tight positional match for a previously-known astronomical object with a good position, the statistical reliability of the set of objects found in the FSR for this search is usually extremely high, typically > 99%. However,

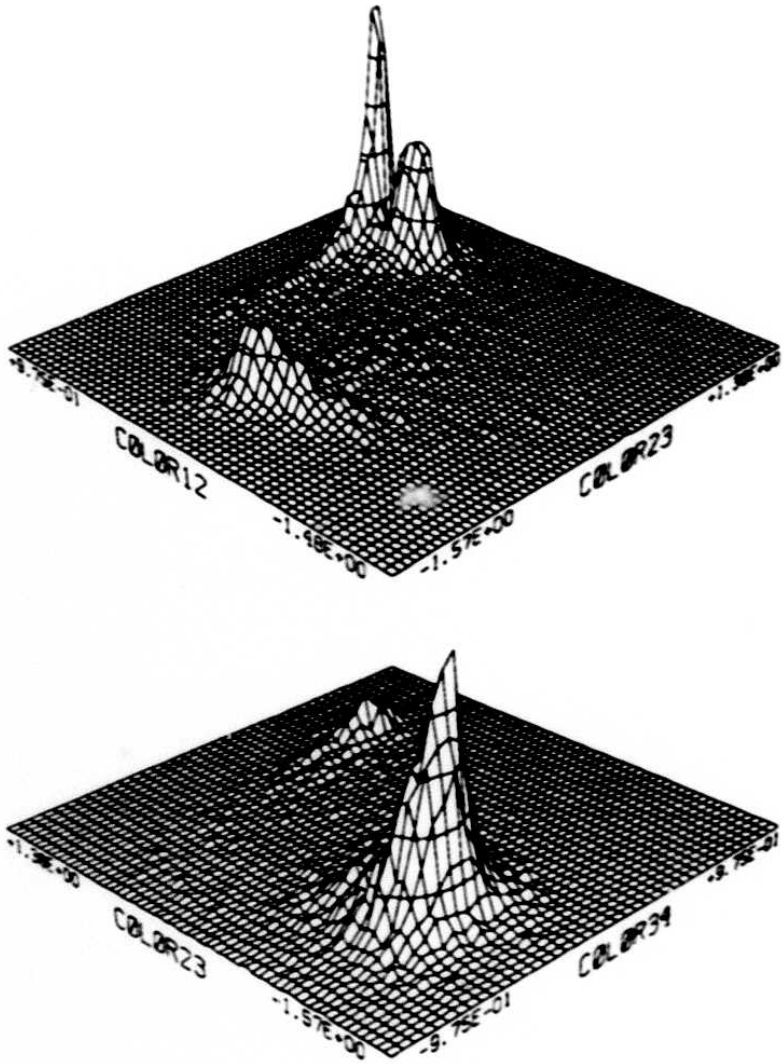

Figure I.A.7 Color-Color distribution of sources with flux density detections in at least three spectral bands. These plots show the relative numbers of sources in different color-color groups (scatter plots are given in Section III.B). Upper figure is a map of colors for sources with detections at 12, 25, and 60 μm. The lower figure is for sources with detections at 25, 60, and 100 μm. COLOR12 is log (f_ν(12 μm)/ f_ν(25 μm)), COLOR23 is log (f_ν(25 μm)/f_ν(60 μm)), and COLOR34 is log (f_ν(60 μm)/f_ν(100 μm)). Flux densities have not been color corrected in these figures.

if one searches the FSR for previously unknown sources in a large area, the statistical reliability of the objects found in the FSR can be quite low, sometimes as low as 10%.

The FSS plates require more care and sophistication in their use since they are much more voluminous than either the FSC or FSR, and contain artifacts that have been removed

D 10015

from, or flagged, in the FSC and FSR. The plates can be used to go even lower in SNR than the FSR, but with even lower reliability. They can also be used to go beyond the information presented in the FSC and FSR. Examples include using the plates as the raw material for more sophisticated analyses of confused areas or searching for small extended sources. They can be used to check the neighborhood of a given FSC or FSR source for possible problems, such as establishing which objects are likely to be pieces of larger structures rather than true point sources.

This ***Explanatory Supplement*** is intended to be a complete and self-contained description of the FSS itself. It does not contain the background information about the ***IRAS*** satellite, telescope, detectors, mission, etc., that can be found in the ***Main Supplement***. The textual part of this ***Explanatory Supplement*** is available in machine-readable form as well as in printed form.

The remainder of this introduction gives an overview of the FSS and its products. It presents important cautionary notes which apply to the use of the FSS. Chapter II begins with an overview of the processing involved in the FSS and then gives detailed information on all processing. Analysis of some of the properties of the FSS products is given in Chapter III. General properties of the plates are given first, since these apply as well to the FSC and FSR derived from the plates. The general statistics of the FSC are given, as well as detailed information about the completeness and reliability of the FSS and its products. The positional and photometric accuracies of the FSS are given, followed by a discussion of several known effects which appear in the data. Chapter IV compares the FSC version 2 to the PSC and also version 1.2 of the FSC to guide the users of these two catalogs in resolving discrepancies. The formats of the released data products are given in Chapter V. Chapter VI contains all references for this Supplement. Chapter VII acknowledges all the people and institutions involved in producing the FSS. Finally, Chapter VIII is a glossary of abbreviations and terms used in this document.

27

B. Summary Description of Products

B.1 Faint Source Plates

The FSS plates are 1,716 images that cover the entire sky and are available in FITS format. The plate centers and sizes are identical to the scheme used by the ESO/SERC and second Palomar sky surveys. The plates use equatorial coordinates with an orthographic projection based on 5° center separations in declination with an overlap of 1.6° at the equator.

For each plate, there are three separate grids of information for each band. For each pixel within a plate, the three grids give estimates of the point source flux density, the *instrumental* 1-σ uncertainty in the point source flux density, and the number of independent observations (counts).

The plates for $|b| > 50°$ were not reprocessed as part of the second release of the FSS.

B.2 Faint Source Catalog Version 2

The FSC version 2 contains 173,044 sources for $|b| \gtrsim 10°$. Version 2 is available only in machine-readable form in FITS table format.

The machine readable form of the FSC version 2 is available in two formats. The short format contains positions, flux densities, uncertainties, associations with known astronomical objects, and various cautionary flags. The long format contains more detailed and specialized information about the characteristics and processing history of each source. For example, various flux density correction factors and parameters of template fits are given in the long version.

In order to qualify for the FSC, a source had to have at least one spectral band whose differential reliability exceeded 90% at 12 and 25 μm, and 80% at 60 μm. Because of the infrared cirrus, the 100 μm band was not considered for reliability criteria and was treated differently in the FSC from the other bands. Sources with detections at 100 μm appear in the FSC only if they are bandmerged with catalog quality detections at other wavelengths.

Tables I.B.1-3 compare the characteristics and source content of the FSC and PSC. In Table I.B.3,

- 'stars' are defined as sources detected with a high flux density quality at 12 μm with $f_\nu(12\ \mu\text{m}) > f_\nu(60\ \mu\text{m})$
- 'galaxies' are defined as sources detected with a high flux density quality at 60 μm with $f_\nu(12\ \mu\text{m}) < f_\nu(60\ \mu\text{m})$
- 'other' are defined as the sources not falling in the above categories.

TABLE I.B.1 Comparison of Faint and Point Source Catalog Characteristics for $|b| \gtrsim 10°$

Characteristic	PSC	FSC
Sky coverage		
12 μm	96%	96%
60 μm	96%	94%
Relative sensitivity	1	2 - 2.5
Number of sources	95,274	173,044
Reliability *at lowest flux densities*		
12, 25 μm	>.998	$\gtrsim$.90
60 μm	>.998	$\gtrsim$.80
1-σ errors *for sources at completeness limit:*		
Position		
12 μm	3″ × 16″	4″ × 27″
60 μm	4″ × 15″	7″ × 25″
Photometry	10%	20%

TABLE I.B.2 Completeness Limits of Faint and Point Source Catalogs for $|b| \gtrsim 10°$

Wavelength (μm)	90% Completeness Limit (Jy) 2-HCON Sky (N~8)* PSC	FSC	3-HCON Sky (N~12)* PSC	FSC
12	0.45	0.18	0.38	0.15
25	~0.50	0.21	~0.42	0.17
60	0.64	0.28	0.56	0.23

* An HCON is a unit of sky coverage representing at least two confirming scans occurring within 36 hours (see *Main Supplement*). N is the number of individual detector coverages in a given band.

where $f_\nu(12\ \mu m)$ is the noncolor-corrected flux density at 12 μm and $f_\nu(60\ \mu m)$ is the noncolor-corrected flux density at 60 μm (see the *Main Supplement*).

Of the FSC sources, 42% are also PSC sources. Of these sources, the FSC has resulted in added detections for 45%, leaving 51% with unchanged band structure, 2% lost one or more bands and 2% both lost and gained bands. Of the 58% of the FSC sources which are totally new sources, 11% have measured flux densities at 60 and 100 μm, 21% have flux density measured only at 60 μm, and 30% have flux density measured only at 12 μm.

The major change for version 2 is the method of noise computation. This change and

D 10015

TABLE I.B.3 Number of Sources in Catalog Version 2

Source Type	FSC	PSC	New in FSC§	PSC with New Band(s)
'stars'	108,042	40,214†	57,392	20,837
'galaxies'	61,188	16,714‡	41,863	11,439
'other'	3,814	38,346†	718	534
TOTAL	173,044	95,274	99,973	32,811

§ Not all PSC sources are in the FSC so this column does not exactly equal the number of new sources in the FSC, although it closely approximates it (see Chapter IV).

† $|b| > 10°$.

‡ $|b| > 20°$.

other minor changes are discussed in Section II.H. This change has allowed us to create a much more complete catalog of higher reliability at a given SNR, which has allowed us to lower catalog thresholds. For example, we have been able to lower the SNR threshold at 60 μm from ~6 to ~5, which roughly doubles the number of new extragalactic sources present in the FSC as compared to the PSC.

Because of this improvement, we have *reprocessed the catalog for* $|b| > 50°$. This reprocessing *has not significantly changed positions or flux densities* of the sources in the version 1.2 catalog. Because we set the catalog requirements conservatively for version 1.2, the major effect has been *the addition of more sources to the FSC*, although a small fraction of sources from version 1.2 have been removed for version 2. For more details see Section IV.B.

B.3 Faint Source Reject File

The FSR contains extracted sources that are not in the FSC because the sources did not meet the reliability requirements of the catalog. The entries in the FSR consist mostly of sources in confused regions, in areas with $|b| \lesssim 10° - 20°$, and single-band objects with an SNR between 3 and 5–6. The FSR also includes sources from areas of the sky covered by fewer than six detector passes, and sources contaminated by or caused by cometary debris trails. By design, *this product does not meet the reliability standards of other IRAS products!*

The FSR has the same format as the long form catalog.

30

C. Cautionary Notes on the Use of the FSS

C.1 Cautionary Notes for the Entire FSS

All users of the FSS should note the following:

a) The FSS is primarily a *point* source survey. However, small extended sources will also be present in the FSS, but *their flux densities will, in general, be incorrect*. Small hot spots in extended sources will also be present with erroneous flux density values. See Section III.A.5 for further information.

b) Asteroids and comets may be present in the FSS because the data were confirmed only by a trimmed-average filter and a local SNR threshold. In areas covered by three or more HCONs, this effectively eliminates asteroids and comets. (An HCON is a unit of sky coverage representing at least two confirming scans occurring within 36 hours; see the ***Main Supplement***.) Also, data containing predicted positions of comets and asteroids known as of 1987 have been discarded. However, in areas covered by fewer HCONs, previously unknown asteroids and comets will appear in the FSS plates. Generally, in two-HCON areas the local SNR will be low enough to eliminate these sources from the FSC. It is theoretically possible, although improbable, that these sources may appear in the FSC in one-HCON areas. A brief search of the FSC for sources peaking at 25 μm with $f_\nu(12\ \mu\text{m}) > 0.5$ Jy did not reveal any obvious asteroids.

Cometary debris trails are also present in the plates in areas covered by fewer than three HCONs (see Figure III.C.9 for various HCON boundaries). Sources falling within these trails were not permitted in the FSC.

See Sections II.C.3, III.A, III.C.3, III.D, and III.G.2 for further information.

c) Significant variations in the coverage exist across the sky globally and locally which affect the depth of the FSS. Global variation resulted in 72% of the sky being covered by three or more HCONs, 24% of the sky being covered only by two HCONs, and 2% of the sky being covered only by one HCON. Areas covered by fewer than four detector passes, henceforth referred to as counts, are present in the plates, but will have no corresponding noise estimate available. Sources extracted from areas covered by fewer than six counts are not in the FSC, but can be found in the FSR.

The FSS also shows a local coverage variation caused by the extremely regular way that the survey scans were taken coupled with the planned "safety overlap" of survey scans. This results in a quasi-periodic coverage variation with a period near $\frac{1}{4}^\circ$. The FSS hence goes 10-20% deeper in small strips separated by that period. This results in "stripes" in

the FSS images and the FSC at low flux density levels which are *not* due to processing problems!

See Sections III.A.2 and III.C.2 for further information.

d) The Zodiacal light background causes the noise in the FSS to vary with ecliptic latitude by 20% at 12 μm and a factor of 2 at 25 μm. Virtually no effect is noticeable at 60 and 100 μm. See Sections III.A.3 and III.C.3 for further information.

e) The infrared cirrus and other galactic sources cause the noise in the FSS to vary by as much as a factor of 10 at 100 μm and significantly at 60 μm. See Sections III.A, III.C, and III.D for further information.

f) The infrared cirrus dominates the sky at 60 and 100 μm and in rare cases affects the sky at 12 and 25 μm. Many of the sources at 100 μm in the FSDB are actually pieces of degree-size structures rather than isolated discrete objects. The infrared cirrus can also corrupt 100 μm – and occasionally 60 μm – measurements of true point sources. See Sections III.A–D, G for further information.

g) The noise in the FSS plates *is not Gaussian*. Above roughly SNR=3 for 12 and 25 μm, there is a significant non-Gaussian tail that makes it much more likely to have a high SNR excursion by chance than in the Gaussian case. Users who naively use Gaussian statistics to calculate the probability of a given excursion due to chance *will get the wrong answer*.

Below roughly SNR~8 for 60 μm, the flux densities reported in the FSS plates are dominated by infrared cirrus, and thus Gaussian statistics are also inappropriate.

The trimmed mean algorithm was employed to minimize the non-Gaussian tail. See Sections III.A, III.C, and III.D for further information.

h) To account for the effects of background confusion, especially due to infrared cirrus, the thresholding noise for source extraction has been computed by measuring the 68% quantile of the positive flux densities. *However, only the instrumental noise is quoted in the plates.* See Section III.C.4 for further information.

i) A small flux density-dependent correction to flux densities due to the non-linear load resistor has not been incorporated into the plates. This correction *has* been applied in the FSC and FSR. Users who extract sources from the plates must apply the correction described in Section II.G.5 in order to obtain exact agreement with the FSC and FSR.

j) *IRAS* variable sources frequently have a flux density variation sufficient to cause a low local SNR. The flux density reported for these sources will be a trimmed average of the flux densities observed on each individual scan over the source. This variation may

D 10015

even cause their local SNR to fall below the catalog or extraction thresholds and exclude the sources from the FSC or FSR. For more details consult Section III.G.3.

k) The processing algorithms used in this release of the FSS have been tuned to the *unconfused* $|b| \gtrsim 10° - 20°$ sky. Users of the FSS inside the confused regions $|b| \lesssim 10° - 20°$ should perform their own analyses to obtain completeness and reliability estimates.

l) As for the PSC, a color correction must, in general, be applied to the quoted flux densities because of the wide spectral bandwidths of the *IRAS* detectors (see the *Main Supplement*, Section VI.C.3 for details). Color correction tables can be found in the end tables.

m) Following the passage of the spacecraft over the Galactic Plane, there was an enhancement in detector responsivity at 60 and 100 μm. This enhancement has been partially corrected for in the final calibration of IRAS data which became available after the production of the FSS. Thus, the data used for the FSS production did not correct the effects of passage across the Galactic Plane.

By not correcting for this effect we expect to see *at most* $\sim 10\%$ responsivity enhancement at 60 μm, which decays to 0 within $10° - 15°$ following Galactic Plane crossing. At 100 μm we expect to see *at most* $\sim 25\%$ enhancement in responsivity following Galactic Plane crossing, which decays to 0 within $25° - 40°$ following the passage through the Galactic Plane. The 12 and 25 μm spectral bands do not exhibit problems caused by the passage across the Galactic Plane.

C.2 Cautionary Notes for FSC and FSR

Users of the FSC and FSR must also be aware of the following:

a) The FSC is not a 100% reliable catalog. The reliability is a function of SNR and is estimated statistically on that basis for each source. The lowest reliability is 90%, 90%, and 80% at 12, 25, and 60 μm. Cirrus contamination of the sky at 100 μm prevented us from deriving meaningful reliability values at this band; consequently no reliability figures are quoted at 100 μm. The reliability of the FSR is much lower. The lowest reliability of the FSR ranges from 10% to 30% in each band. See Section III.D for further information.

b) Sky coverage of the FSC is not a straightforward cut in galactic latitude. The catalog is confined to the *unconfused* $|b| \geq 10°$ sky at 12 and 25 μm, and *unconfused* $|b| \geq 20°$ sky at 60 μm. The solid angle covered by the FSC is approximately 32,800 square degrees at 12 μm and approximately 25,400 square degrees at 60 μm. (Consult Figures I.A.3 and 4 for the spatial coverage of the FSC.)

c) Almost all quantities in the FSC are also functions of SNR. These include reliability,

33

completeness, positional accuracy, photometric accuracy, and source parameters such as correlation coefficients, etc. See Chapter III for further information.

d) The catalog was made from overlapping plates. Duplicates of sources were removed by picking the "best" representation from the different renditions from overlapping plates. The variation between different renditions is caused by differences in thresholding noise from overlapping plates, since the noise in the neighborhood of each source comes from slightly different areas. Near the edge of each plate, the noise was effectively estimated from different areas of the sky for each plate. The "best" source was picked to come from the plate where the source was farthest from a plate boundary. See Section II.G.2 for further information.

This method differs from the one employed for version 1 of the FSC. In version 1 the "best" source was picked to be *either* the one coming from the plate where the source was farthest from a plate boundary *or*, in some infrequent cases, the source which had the higher quality flux density. This caused the FSC version 1 to be slightly deeper in the overlapping regions since in those areas a given source had more chances to exceed the catalog thresholds due to statistical variations.

e) The catalog *flux density* thresholds vary with sky position and coverage, as discussed above in paragraphs c-f, h, and k. Upper limit flux densities are infrequently given as 0 in areas of very low coverage, when no meaningful upper limits could have been derived.

f) Some flux densities quoted for FSC sources may only be of moderate quality. Moderate-quality flux densities are given only for FSC sources that had a high-quality flux density in at least one band. Moderate-quality flux densities do *not* meet the reliability criteria of the FSC and are not as trustworthy. Their reliability may at times be quite low. In particular, all 100 μm detections have been given moderate-quality status. Users should be aware that the use of moderate-quality flux densities will bias samples of sources toward flatter unusual spectra, such as stars with excess flux density at longer wavelengths.

See Sections II.F and III.D for further information.

g) Due to the way in which the data were filtered and mapped, in a handful of cases nearby sources which were resolved by the PSC have coalesced into a single source. In these cases, the quoted flux densities and positions are suspect. See Sections III.A.5, IV.D for further information.

h) Because the reliability of the FSR is so low, sources in the FSR are, in general, *not* bandmerged. See Section II.F.2 for further information.

i) The noise used for the SNR quoted in the FSC and FSR was estimated by taking the 68% quantile of positive flux densities over an area of 79.25′ × 79.25′ at 12 and 25 μm and 99.5′ × 99.5′ at 60 and 100 μm. At 12 and 25 μm that noise was corrected by a scan density correction. The local SNR (LOCSNR) used the individual pixel noise value without correction. See Sections II.A and E for further information.

j) As for the PSC, the associations with other astronomical catalogs are *not* identifications. They represent purely positional coincidences provided as a service for the user. Each user must decide whether any association qualifies as an identification.

k) Flux density upper limits quoted in version 2 are 90% confidence upper limits. See Section II.F.2.e for further information.

l) As in most SNR-limited catalogs, the faintest sources in the FSR are expected to have flux densities which are overestimated. Noise fluctuations will push more fainter sources up in flux than brighter sources are pushed down in flux. As a result the fainter sources are expected to have a *lower intrinsic* flux density than the *observed* value. To correct for this effect a description of $\log N - \log S$ for underlying sources at each band and the parameterization of noise fluctuations may be used to correct for flux density overestimation for sources near the threshold.

No such correction has been applied to the flux densities in the FSC or FSR. For more details regarding the magnitude of flux density overestimation see Section III.G.8.

D. Overview of FSS Infrared Sky

The general distribution of sources in the FSC is shown in Figures I.D.1 to 3. Three classes of sources covering almost all objects in the FSC can be defined according to spectral energy distribution: most of the 108,042 sources that are brighter at 12 μm than at 60 μm are stars (Figure I.D.1), and most of the 61,188 sources that are brighter at 60 μm than 12 μm are external galaxies (Figure I.D.2). Finally, Figure I.D.3 shows the remaining 3,814 sources which do not fall into either of the above categories.

In Figures I.D.4 - 6, magnified portions of the sky centered on the North and South Galactic Poles are seen. Each figure depicts the contents of a spherical cap of area $\sim$ 313 deg^2 centered on the two poles. There are 255 'stars' in the North Cap, and 276 in the South Galactic Cap. In the North Cap there are 792 'galaxies', and the South Cap contains 628 such sources. Finally, there are 5 sources of type 'other' in the North Cap, and 4 in the South Cap. The North/South asymmetry of the *extragalactic* sky (Rowan-Robinson *et al.* 1986) is clearly seen from the number of 'galaxies' in Figures I.D.5a-b.

30

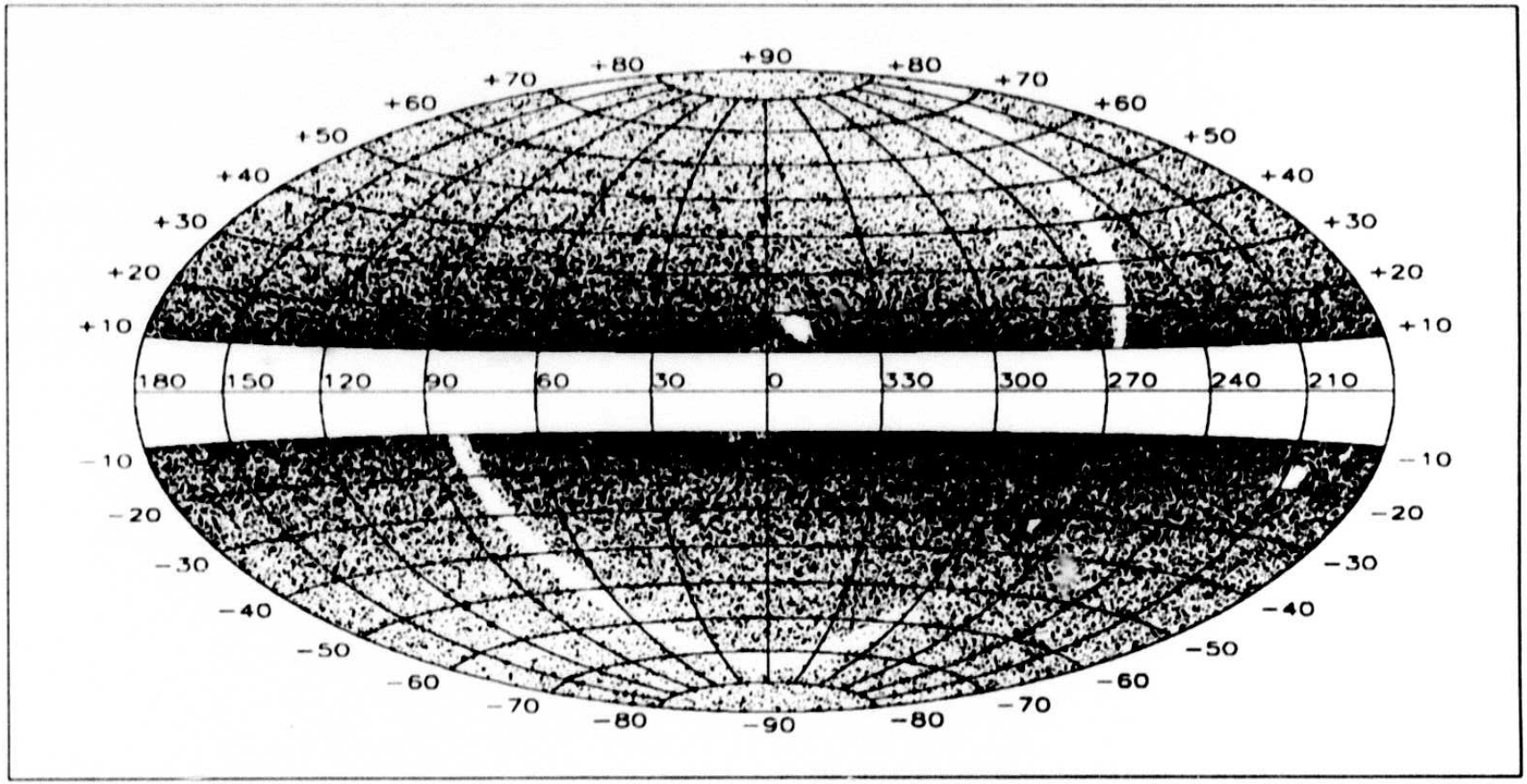

Figure I.D.1 **Aitoff projection map of 'stars', the FSC sources with f_ν (12 μm) > f_ν (60 μm) for |b| > 10°.**

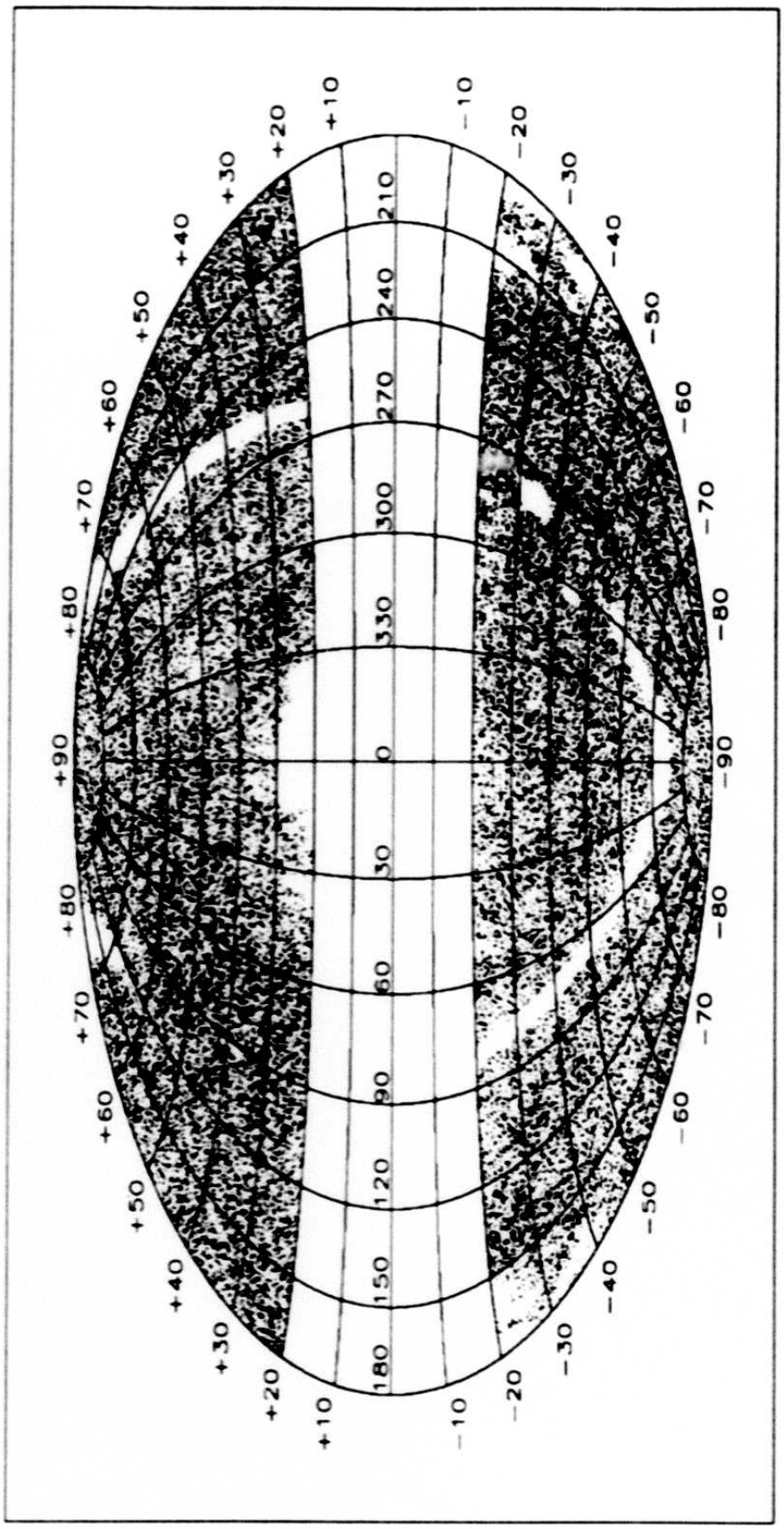

Figure I.D.2 Aitoff projection map of 'galaxies', the FSC sources with f_ν (60 μm) > f_ν (12 μm) for $|b| > 20°$.

D 10015

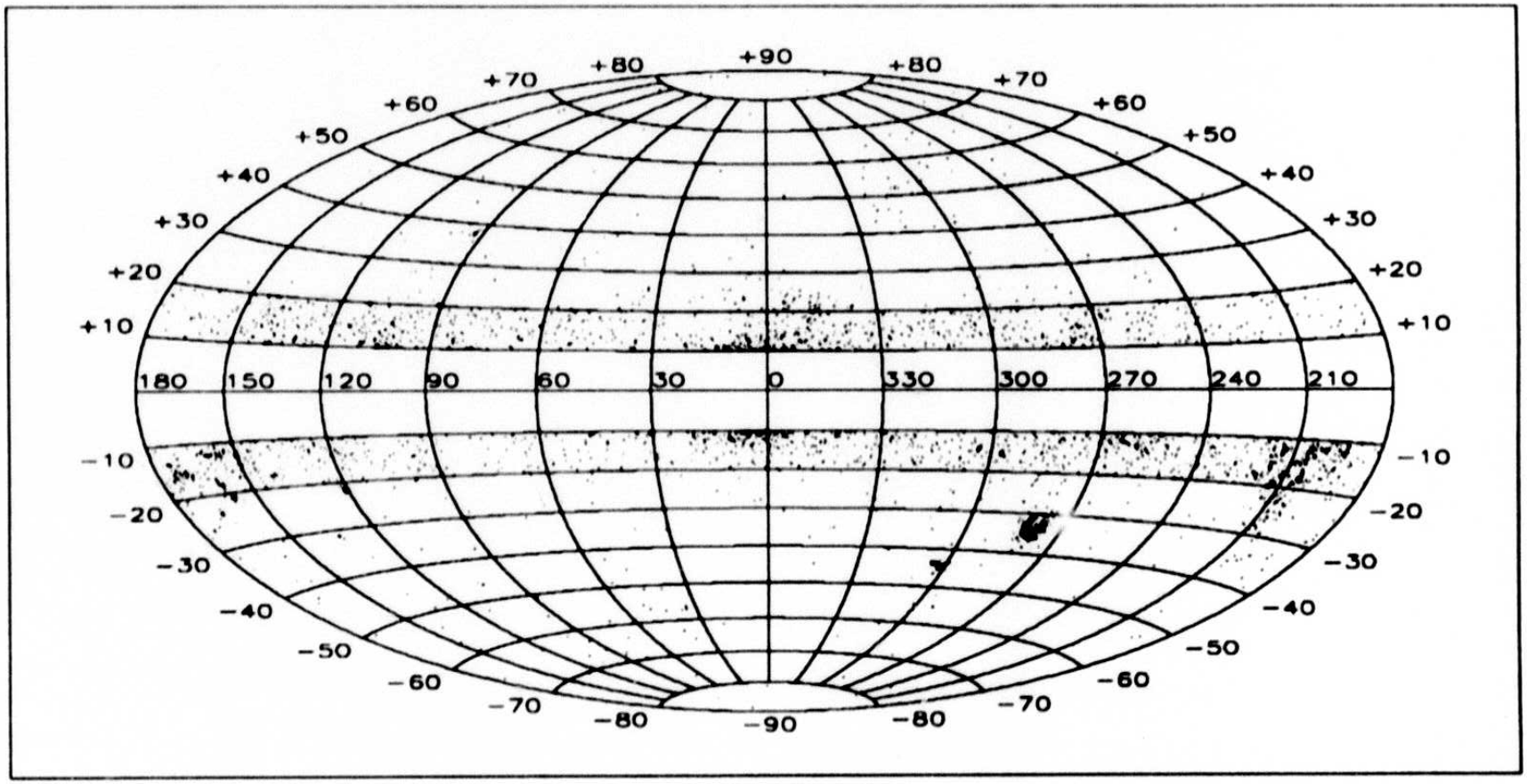

Figure I.D.3 Aitoff projection map of 'other', sources which are not 'stars' or 'galaxies'.

D 10015

D 10015

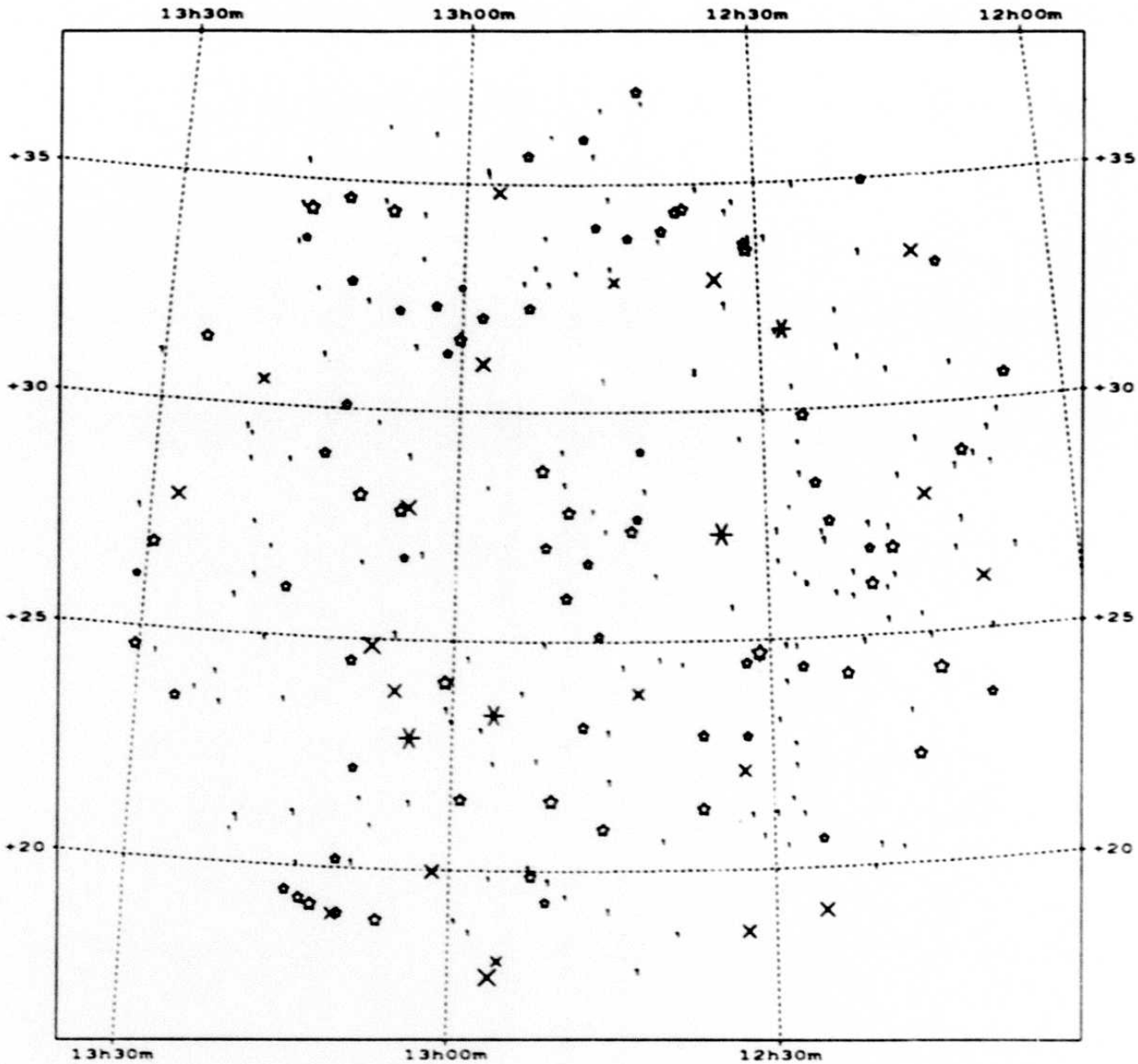

Figure I.D.4a Distribution of 'stars' within a cap of radius 10° centered on the North Galactic Pole. The color legend used here is the same as in Figure I.A.1.

40

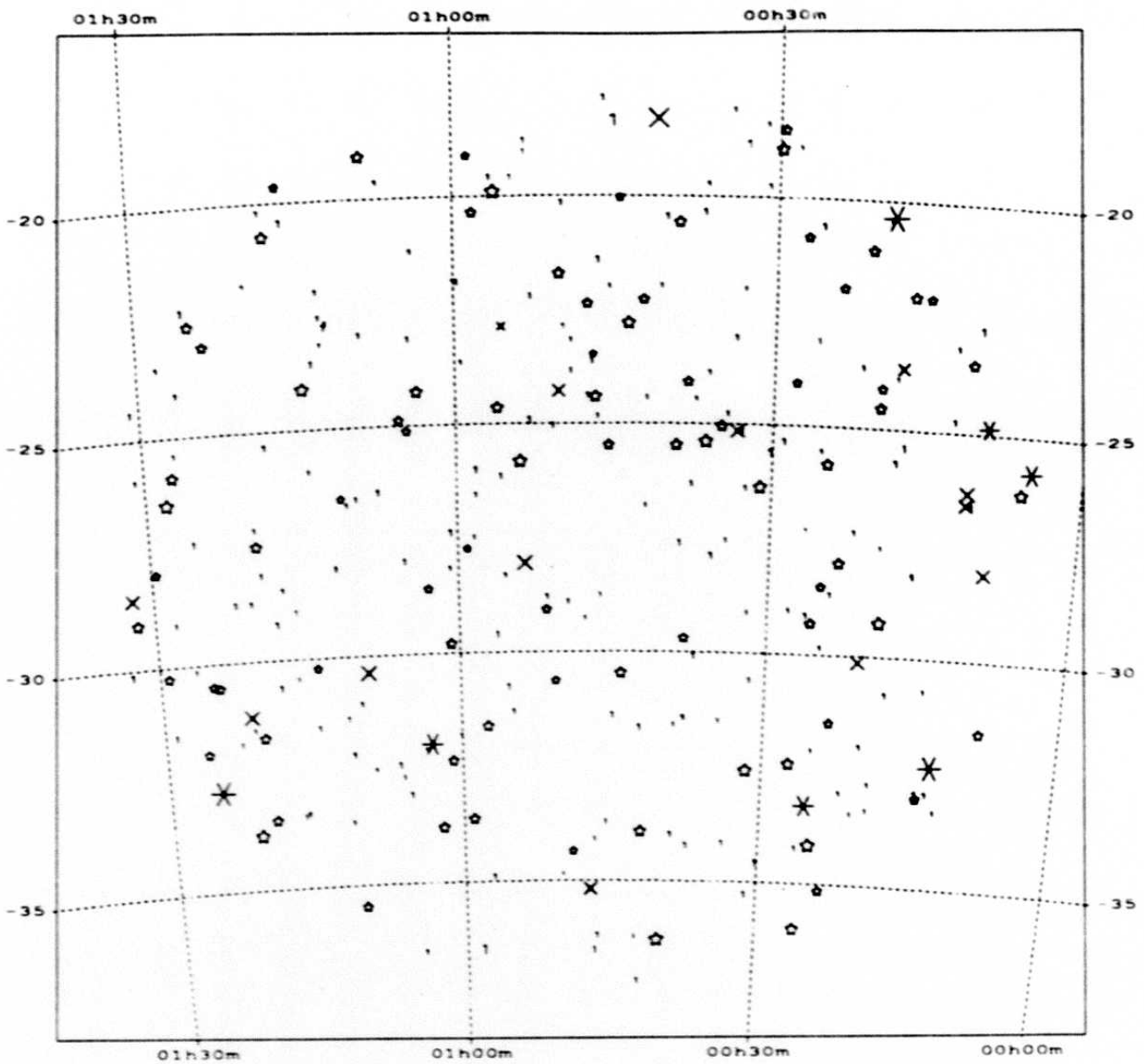

Figure I.D.4b Distribution of 'stars' in the South Galactic Cap. The color legend used here is the same as in Figure I.A.1.

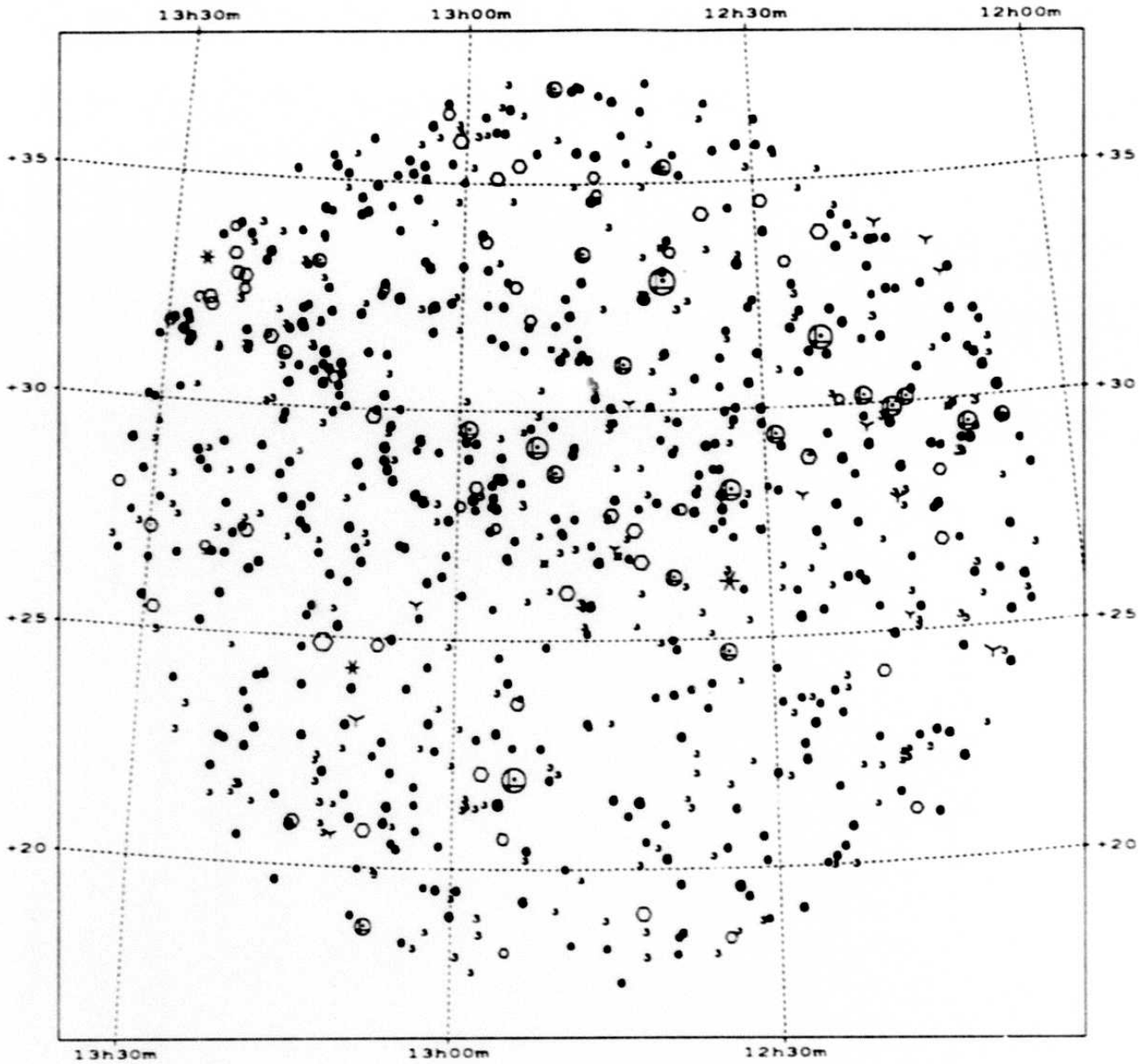

Figure I.D.5a Distribution of 'galaxies' in the North Galactic Cap. The color legend used here is the same as in Figure I.A.1.

42

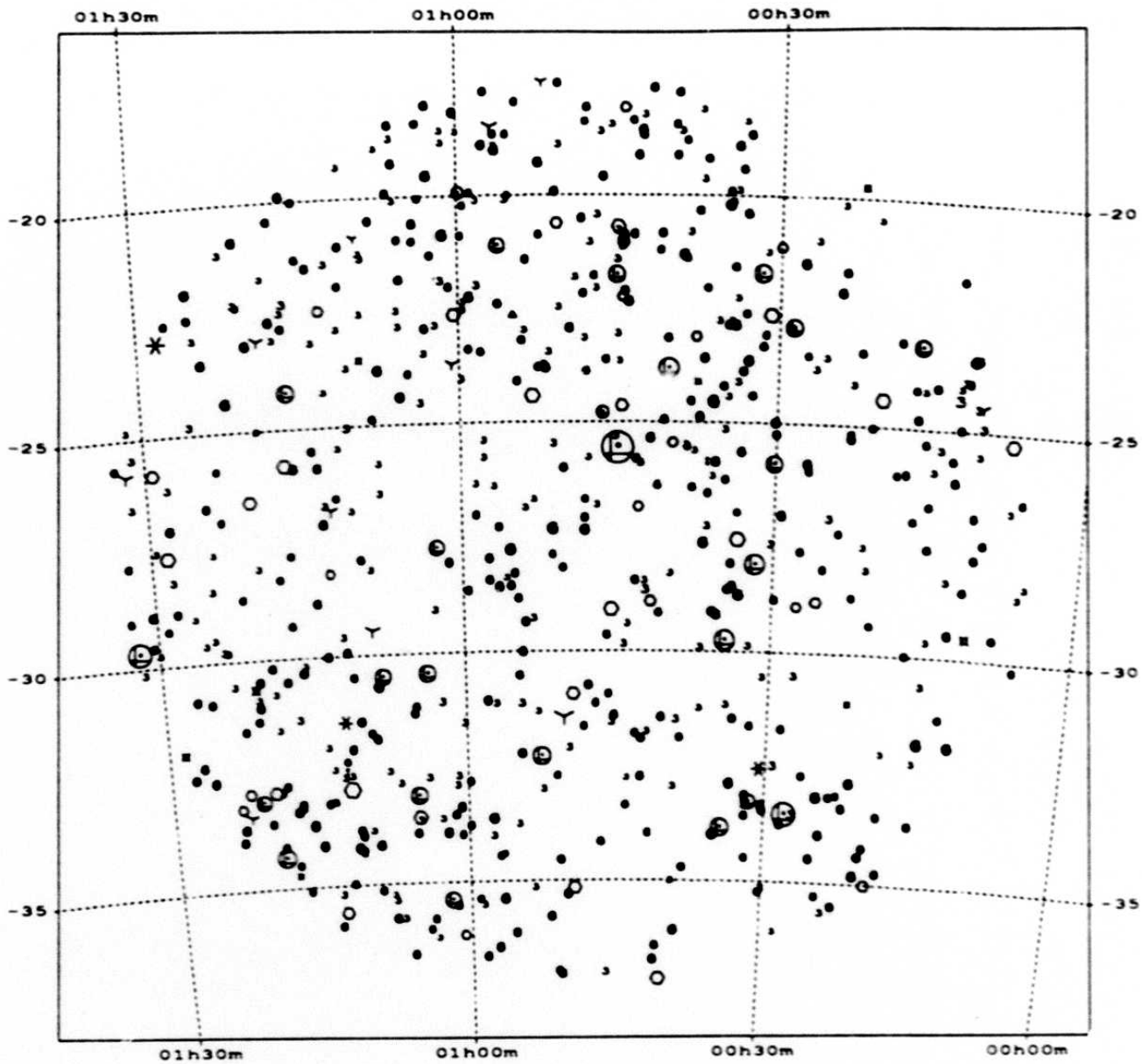

Figure I.D.5b Distribution of 'galaxies' in the South Galactic Cap. The color legend used here is the same as in Figure I.A.1.

43

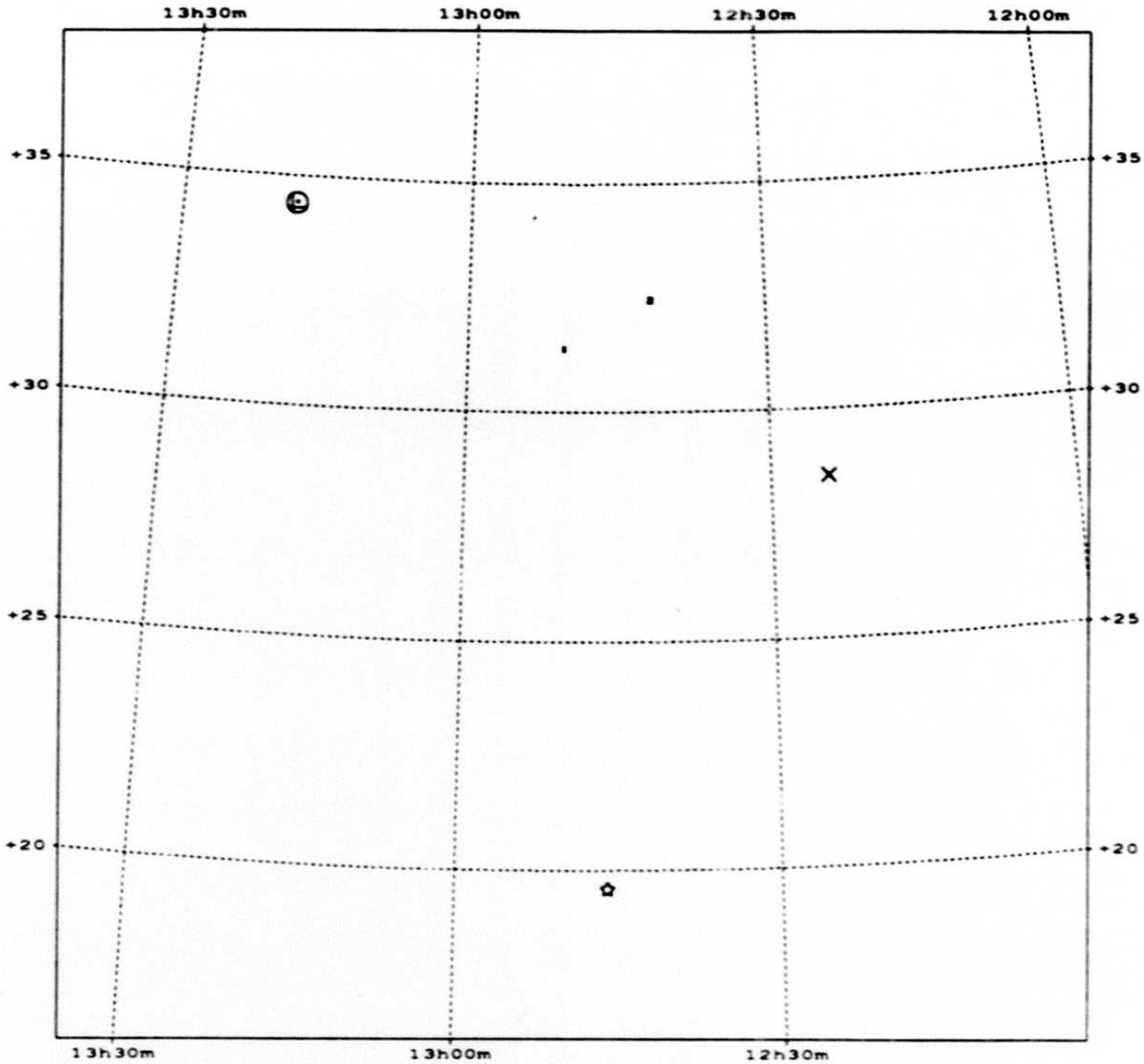

Figure I.D.6a Distribution of 'other' sources in the North Galactic Cap. The color legend used here is the same as in Figure I.A.1.

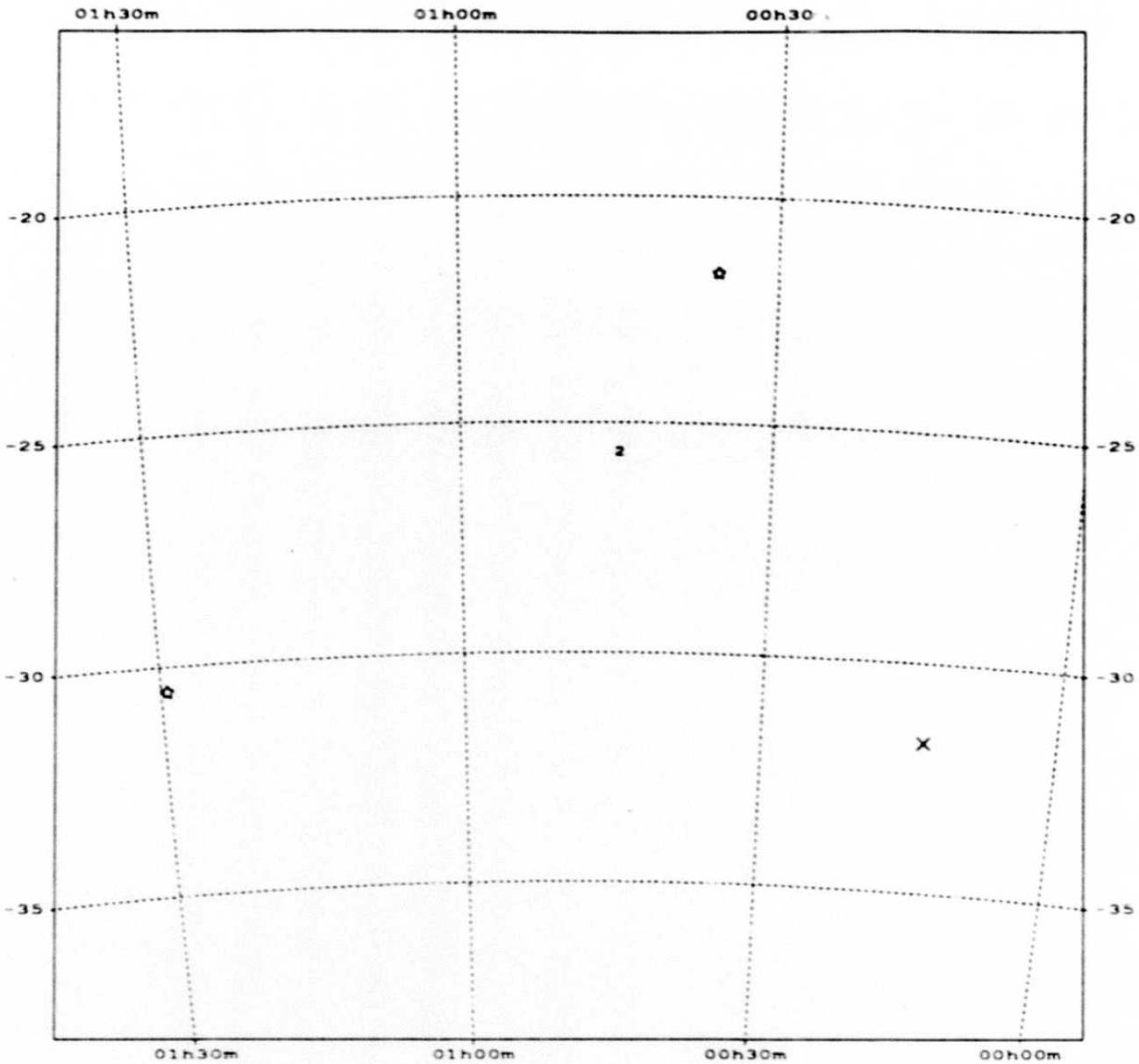

Figure I.D.6b Distribution of 'other' sources in the South Galactic Cap. The color legend used here is the same as in Figure I.A.1.

75

E. Terminology of FSS Processing and Graphical Index

Several terms such as 'SNR' or 'confusion', frequently encountered in the following chapters, may mean different concepts to different readers. To lessen the possibility of any misunderstanding, they will be described briefly.

Sources enter the FSDB by virtue of exceeding several thresholds. Foremost is the *signal-to-noise ratio* **SNR** ($=f_\nu/s_\nu$). The concept of signal f_ν is unambiguous, whereas s_ν, the noise, may be defined in many ways. The noise used for the computation of the **SNR** is the 68% quantile of all *positive* f_ν values from the **signal** grid, measured over **areas** ranging in size from $\sim (79')^2$ to $\sim (100')^2$ (12 to 100 μm bands). This 68% quantile is also referred to as the *thresholding noise*. In addition to the **SNR**, another secondary threshold is also encountered, the *signal-to-local-pixel noise ratio* **LOCSNR** ($=f_\nu/\sigma(f_\nu)$). The local-pixel noise $\sigma(f_\nu)$ comes from the **noise** grid and is the dispersion of the corresponding flux value in that **pixel** in the **signal** grid. The term *local SNR* is also frequently used as an abbreviation for the longer *signal-to-local-pixel noise ratio*.

The shortened term *local SNR* should therefore not be confused with the **SNR** which is the primary threshold for source extraction.

The term *confusion* is used on many occasions to describe the effects of background within a beam centered on an extracted source. Confusion may refer to true point source confusion (the presence of unresolved point sources within the beam, in which case measurements no longer apply to an individual source), or the presence of extended structures which have an appreciable power with a point source spatial frequency. The terms *confusion*, or *confused*, when used in reference to the 60 and 100 μm spectral bands, indicate the presence of pieces of extended structures within the beam. At low galactic latitudes the term *confusion*, when applied to the 12 and 25 μm spectral bands, implies the presence of both true point source confusion and the effects of extended background structures.

Proliferation of acronyms in a project of this scope is unavoidable. To clarify the meaning of acronyms, Chapter VIII is devoted to the definition of abbreviations and terms encountered in this work.

Many users may be interested in only some specific aspects of data processing. A 'graphical index' has been produced to aid the users find sections of interest. The graphical summary of the steps which lead from the raw detector data to the FSDB and FSC can be seen in Figure I.E.1. References to appropriate sections are placed next to each cartoon. These figures are an artist's view of various data processing steps, so curves or grids in these figures should not be treated as exact replicas of true data!

HU

1- Original data from the detectors in the focal plane Data conditioning (see Section II.C.2)

2- Median filtering and smoothing of the data (see Section II.C.3)

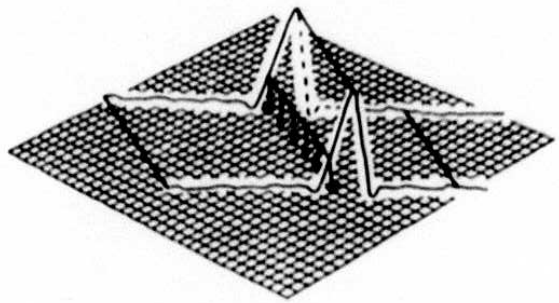

3- Binning of the filtered data (see Section II.C.4)

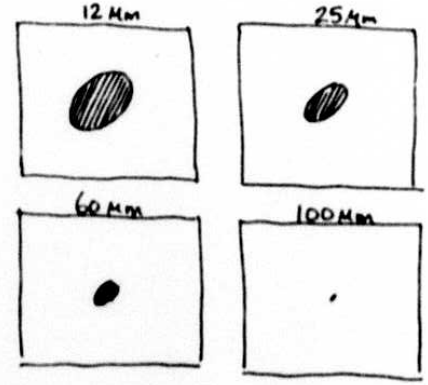

7- Bandmerging of sources (see Section II.F.2)

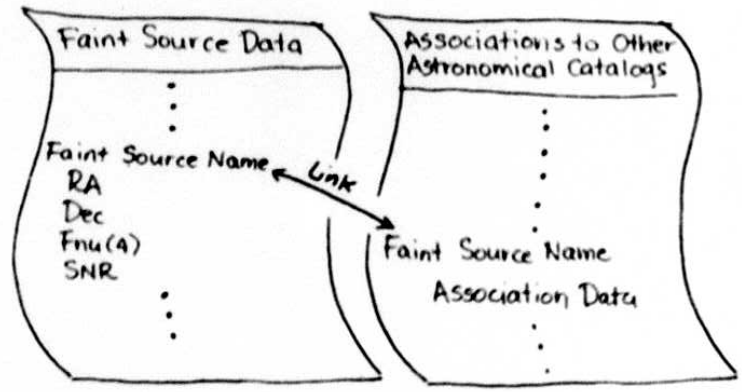

8- Creation of the Faint Source Data Base (FSDB) and association to other catalogs (see Sections II.G.2-3)

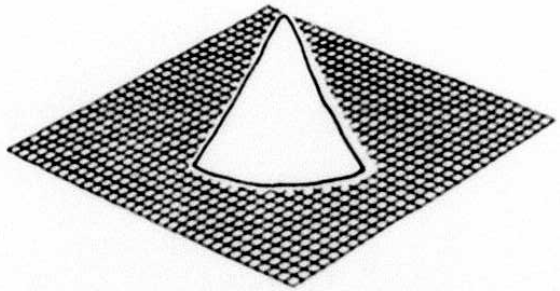

4- Conaddition of the data (see Section II.C.4)

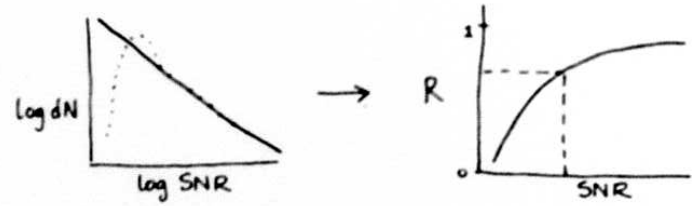

9- Determination of the reliability of the database (see Section III.D.3)

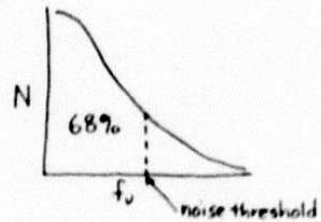

5- Threshold noise determination (see Section II.E.2)

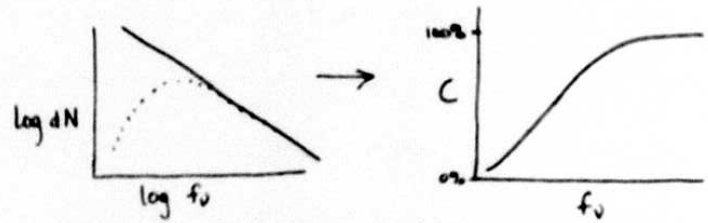

10- Determination of the database completeness limits (see Section III.C.6)

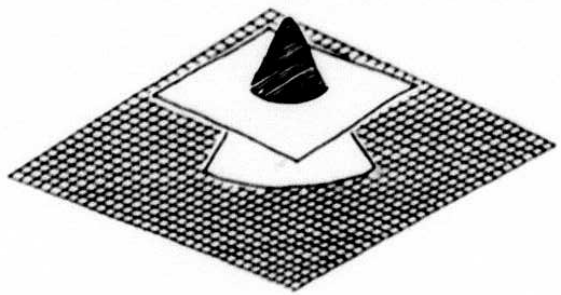

6- Sources detected above threshold (see Section II.E.3)

11- Placement of sources into the Faint Source Catalog (FSC) (see Section III.G.6)

Figure I.E.1 Steps leading from individual detector data to the final products, FSDB and FSC.

Illustration by Carol Oken

D 10015

Authors:

T. Chester and M. Moshir

H9

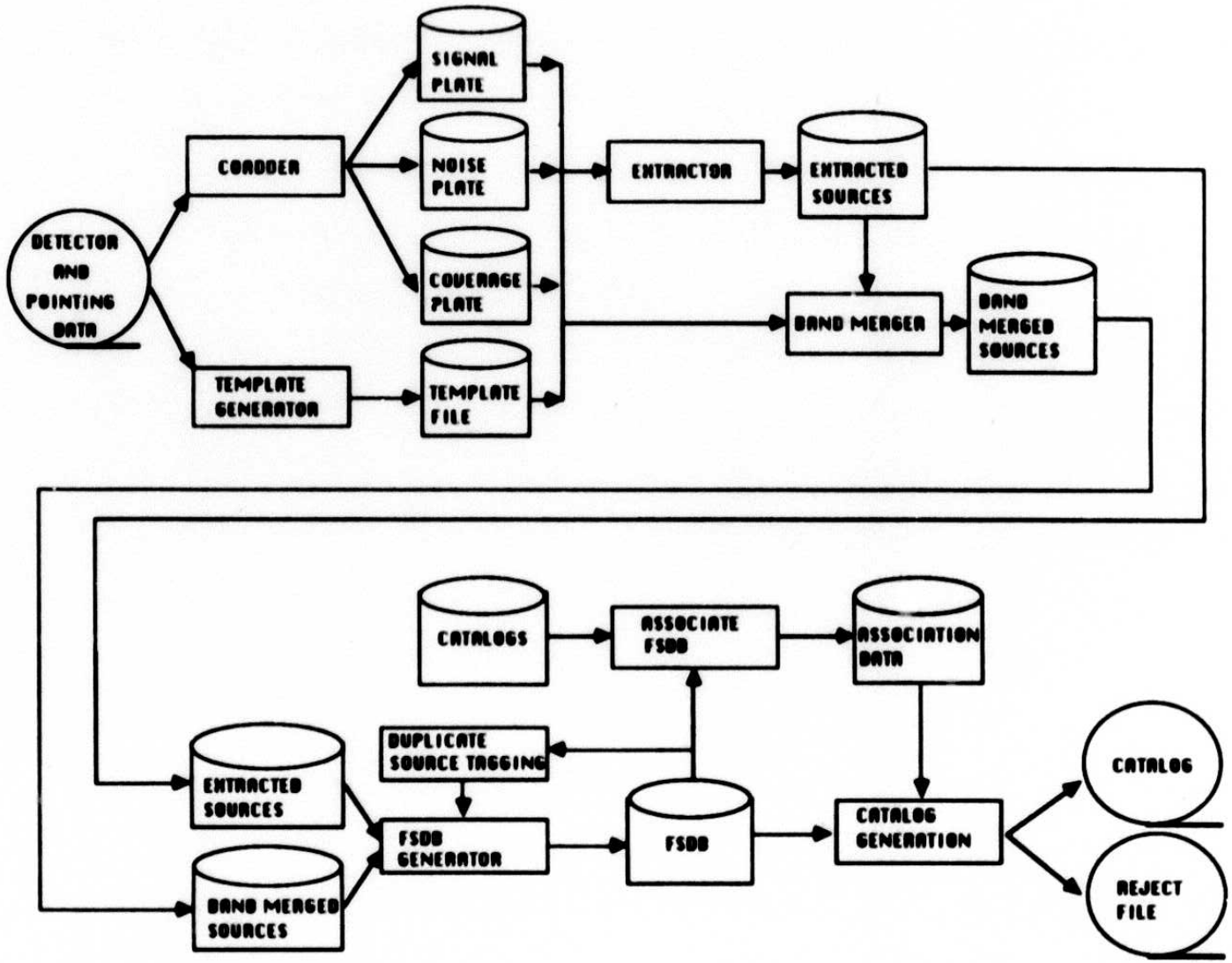

Figure II.A.1 The processing steps of the FSS.

D 10015

II. FAINT SOURCE SURVEY DATA PROCESSING

A. Overview

A.1 Summary of FSS Processing

Figure II.A.1 gives an overview of all the processing steps of the FSS. Each of these steps is described briefly in this overview section and in more detail in subsequent sections.

The input detector data for the FSS were exactly the same data used to produce the PSC and used the calibration discussed in Chapter VI of the ***Main Supplement***. However, to obtain maximal sensitivity for the FSS, the associated pointing information was reprocessed to provide significantly better pointing accuracies. In general, in-scan 1-σ uncertainties improved from 3.0″ to 1.5″, and cross-scan 1-σ uncertainties improved from 4.5″ to 3.0″. In addition, many scans that had anomalous pointing were improved to the standard of the others.

The detector data were conditioned by removing radiation hits (particle events), known asteroids, and known artifacts such as dust particles. The data were "point-source filtered" and base-line removed by smoothing with a three-point filter and by applying a median filter to groups of 23, 19, 17, and 15 data samples, excluding the middle 5 points, at 12, 25, 60, and 100 μm, respectively. These filter lengths correspond to in-scan angular sizes of 5.5′, 4.6′, 8.2′, and 7.2′, respectively. Thus any source component with larger sizes was suppressed from the resulting data.

The point-source-filtered data were binned into images using pixel sizes of $0.25' \times 0.25'$ at 12 and 25 μm and $0.50' \times 0.50'$ at 60 and 100 μm. The detector data were placed into all pixels which were covered by a cross-scan mask approximately equal to the cross-scan detector size. For each of those pixels, the data were resampled to pixel centers using linear interpolation in-scan.

Flux density and noise estimates for each pixel were computed using a trimmed-average estimator. Approximately 10% of the data in each pixel at both the highest and lowest flux density values were discarded, which removed artifacts such as weak radiation hits that were not removed in the previous conditioning step. The flux density for each pixel was estimated by the mean of the remaining data. The pixel noise was estimated by the rms noise of the remaining data, corrected for the effect of trimming, assuming Gaussian statistics. The noise of the data after trimming is too small because the outliers have been tossed out. This correction restores the noise estimate to what would have been

52

estimated from all samples (without trimming), if only Gaussian noise were present. The number of detector samples in each pixel was retained.

The FSS plates contain the number of detector samples, an estimate of the point source flux density, and an estimate of the 1-σ point source flux density noise at every pixel covered by the *IRAS* survey, with the following exception. No noise estimate was made for pixels covered by fewer than four detector samples, although flux density estimates are given whenever at least one measurement was made.

The plate centers and sizes are identical to the scheme used by the ESO/SERC Survey and new Palomar sky surveys. The plates are 6.6° × 6.6°, have 5° center separations in declination with an overlap of 1.6° at the equator, and total 1716 plates to cover the entire sky.

The Faint Source Data Base (FSDB) was produced plate-by-plate using an extractor, a bandmerger, and a database processor. The extractor computed a "local" thresholding noise array by computing the 68% quantile of the *positive* signal values for a set of non-intersecting cells of 317 × 317 pixels at 12 and 25 μm, and cells of 199 × 199 pixels at 60 and 100 μm, covering each plate. The noise cells correspond to 79.25′ × 79.25′ at 12 and 25 μm and 99.5′ × 99.5′ at 60 and 100 μm. The local noise array was interpolated to estimate the local thresholding noise at each pixel in the grid. The 1-σ uncertainty in this estimate of the local noise is ~2% for areas of the sky covered by 3 HCONs. The extractor thresholded the entire plate, selecting all sets of contiguous pixels having SNR $\geq$ 3. Those regions larger than a predetermined area were re-thresholded to isolate sources that may be confused.

Contiguous regions that satisfied two constraints were saved for further processing, and will be referred to as extractions. For $|b| \gtrsim 5°$ these constraints are 1) at least 6 pixels at 12, 25, and 60 μm and 12 pixels at 100 μm with SNR $\geq$ 3, and 2) at the peak flux pixel the ratio of signal-to-local-pixel noise (LOCSNR) greater than 3.5. (At approximately $|b| \sim 5°$ the area thresholds were raised to 12 pixels at 12, 25, and 60 μm, and 24 pixels at 100 μm. Furthermore the threshold for signal-to-local-pixel noise (LOCSNR) was raised to 4.5 at all bands.) The 6-pixel constraint, coupled with typical point source profiles, implies the peak pixel SNR must typically exceed 3.5 for any extraction. The signal-to-local-pixel noise criterion eliminated some aliased radiation hits and asteroids. For all extractions, the flux density was determined from the peak pixel value, and a position was determined from the flux-weighted centroid position. In addition, theoretical point source templates were generated for each plate by averaging a set of 16 templates computed within each plate. The best-fitting amplitude and correlation coefficient were derived for

53

each extraction through a fit to the average template. The full width at half maximum (FWHM) of templates is used in assigning positional uncertainties. None of the template fit quantities were used to derive final positions or flux densities, but the template amplitude and correlation coefficient are given for each source in the long form of the catalog.

To account for the local (*i.e.* point-source scale) variations in coverage, the SNR at 12 and 25 μm was further modified by an ***island correction factor*** to compensate for the local variations in the $1/\sqrt{n}$ behavior of noise. The SNR (at 12 and 25 μm) quoted for each source in the FSC and FSR includes the island correction factor.

The bandmerger used the positional uncertainties of extractions from each band to merge the detections of a given source into a single source and produce a final refined source position along with its uncertainties. It also determined flux density upper limits and uncertainties. The bandmerger used a 3-σ positional threshold to produce better than 99% completeness in merging true sources.

Extractions were treated differently depending on whether they exceeded the following SNR thresholds: 5.0, 5.5, 5.0, and 8.0 at 12, 25, 60, and 100 μm. (Note that these values are *not* identical to the FSC SNR thresholds. The FSC has a variable SNR threshold as depicted in Figure I.A.5.) Flux densities with SNRs above these thresholds were defined to be high quality flux densities *at the bandmerger level* and served as seeds for the bandmerging process. Flux densities for other extractions were defined to be moderate quality. They could merge with another seed, but could not themselves initiate the bandmerging process. Positions were refined only by high quality extractions. If no merger for a qualifying source in band A was found in another band B, a 90% confidence level upper-limit to flux density was computed for band B.

The bandmerged sources, along with the moderate quality extractions that did not bandmerge with a high quality extraction, were associated with other astronomical catalogs and placed in the FSDB.

The duplicate source processor marked the duplicate sources created by the overlap of the plates. Neighbor counts, a cirrus flag, and ancillary information were added to the database. A small flux density correction was applied to each source. A small number of sources were marked as being contaminated or caused by nearby bright sources or by cometary debris trails.

The FSC sources were selected through the reliability thresholds given previously in Table I.A.3. Sources were selected only from areas which were deemed not to be confused.

54

with at least six detector coverages in at least one band, and that were not marked as being contaminated by nearby bright sources or cometary debris trails.

A.2 Differences from Point Source Catalog Processing

The PSC was produced by detecting sources in each of the individual detector scans, and then applying a series of stringent confirmation criteria for reliability. The major differences from the FSC processing are as follows:

- Improved Pointing Reconstruction Data were used for the FSC.
- Sources were extracted from individual detector scans for the PSC, but were extracted from coadded scans for the FSC. The scans were median filtered before coaddition for the FSC.
- The individual detector data streams were filtered for radiation hits, asteroids and anomalies for the FSC, but were not filtered for the PSC. In addition, the trimmed-average procedure for the FSC filtered out weaker radiation hits and anomalies. The PSC relied on a rigorous confirmation strategy to filter out these events.
- Positions and flux densities were derived through combining detections from each of the individual detector scans for the PSC, whereas they were derived from the coadded data for the FSC.
- Sources had to be extracted and confirmed from at least three detector scans per HCON for at least two HCONs in order to appear in the PSC. Sources had to be extracted from coadded data which resulted from at least six detector scans and then satisfy reliability and local noise thresholds to appear in the FSC.
- Sources contaminated by cometary debris trails were eliminated from the FSC through visual inspection of the FSS plate, but were eliminated from the PSC by requiring confirmation from at least two HCONs.
- By measuring the 68% quantile of the flux densities over $\sim 1^\circ$ scales, the effects of source confusion were corrected for in the FSC. In the PSC, a separate high source density processor was used whenever the source density in a $\sim$1 square degree bin exceeded a band-dependent threshold. Basically, the high source density processor simply raised the threshold for entry into the PSC uniformly for those bins.
- Confirmation between HCONs was purely positional for the PSC, allowing variable sources to be properly treated. Variability resulted in lower local SNRs for the FSC, with no other indication that the source was variable. However in some cases it may be possible to recognize a variable source by examining its signal-to-noise ratio at the peak flux pixel, for details see Section III.G.3.

B. Improvements to Pointing Reconstruction

B.1 Introduction

This section addresses refinements to the original *IRAS* pointing reconstruction. The term "pointing reconstruction" is used here to indicate a reconstruction of the time history of the pointing direction of a fiducial point at the center of the focal plane, referred to as the boresight. The term "position reconstruction" will be reserved to indicate the reconstructed sky positions of the IR sources detected. Although the *pointing* reconstruction is an integral input to the *position* reconstruction, the associated accuracies can be quite different. For a discussion of position reconstruction accuracies see Section III.E.

To obtain the maximum sensitivity improvement for the FSS, the associated pointing information was reprocessed to provide significantly improved accuracy. In general, in-scan 1-σ errors improved from 3.0″ to 1.5″, and cross-scan 1-σ errors improved from 4.5″ to 3.0″. In addition, many scans that had anomalously bad pointing were improved to bring them to the same accuracies as the other scans.

The original pointing reconstruction used information only from on-board gyros and star and sun sensors (see *Main Supplement* Section V.B). The improvements derive from the use of positional differences between seconds-confirmed *IRAS* sources and matching sources in other catalogs. Since stars provide the largest set of matchable sources with accurately known positions, the pointing reconstruction refinement is tied to the 12 μm detectors.

B.1.a Overview of Original Pointing Reconstruction

The original pointing reconstruction was accomplished by first integrating the gyro outputs to provide a rough estimate of the attitude history, then refining that estimate with an extended Kalman filter (Kalman 1960) using measurements from the fine attitude sensors. Frequent fine-sun-sensor measurements and relatively infrequent fine-attitude calibrations (FACs) performed with visual star sensors, located in the *IRAS* focal plane, were processed by the filter to provide refined estimates for the set of model parameters used in the integration. Improved model parameters, of course, resulted in improved attitude histories. Estimated model parameters included initial spacecraft attitude errors and spacecraft-telescope alignment errors, as well as gyro drift errors, gyro scale-factor errors, and gyro axis alignment errors. The recursive Kalman filter was run first forward and then backward, working with one observation's worth of data at a time. The forward solution was then combined with the backward solution to provide a smoothed estimate using all available past and future information in the observation. The filter was re-initialized with

the updated model parameters and the process repeated for the next observation. Provision was made in the filter design to allow for parameter drift due to thermal stresses and aging effects. Although its implementation became rather involved, the Kalman filter approach worked extremely well, resulting in pointing reconstruction accuracies far better than the original requirements (see ***Main Supplement*** Section VII.C.2).

Prior to the mission a set of sources expected to be visible by ***IRAS*** was developed to help monitor performance. These will be referred to as the known infrared (KIR) sources. Differences between the known positions of the KIR sources and the corresponding ***IRAS*** positions at seconds-confirmation were broken down into components along the scan direction (in-scan) and perpendicular to the scan direction (cross-scan). These differences were plotted as a function of time over each of the approximately 5800 survey observations. The resulting plots, along with the associated statistics, served as the principal method of monitoring pointing reconstruction performance, but they were not used at the time to further refine the pointing.

B.1.b Pointing Requirements for FSS

The original pointing reconstruction done for the Point Source Catalog (PSC) was believed to be inadequate for the FSS due to large errors remaining in a small percentage of the data. The PSC position refinement algorithm used uncertainty weighting when combining the positional information from various scans, whereas the FSS algorithm does not. If several scans went into a PSC source position and one of them had bad pointing, the bad scan would do little to degrade the resulting positional accuracy as long as a correspondingly high uncertainty was attached. A bad scan used in the FSS, on the other hand, would be weighted the same as any other and might result in a serious degradation. Based on this reasoning, as well as pixel and detector sizes, absolute upper bound pointing error requirements of 7.5″ in-scan and 45″ cross-scan were imposed. The in-scan upper bound was simply set at half the pixel size. The cross-scan upper bound was not only based on pixel size, but also on considerations of average detector width and scan-to-scan overlap. Only those time periods where the after-refinement pointing errors could be demonstrated to be within these bounds would be accepted for the FSS.

The increased susceptibility of the FSS to bad pointing was somewhat mitigated by the trimmed-averaging technique applied to the flux densities. This technique, which was incorporated as a method to screen out radiation hits, discards a percentage of the highest and lowest flux densities in each pixel. Very bad pointing is likely to result in discrepant flux densities, the worst of which will subsequently be discarded by trimmed-averaging. This provides a safety net for the pointing. It is therefore unnecessary to guarantee that

57

all errors remain less than the requirements; a 3-σ (99.74%) confidence is enough. For cross-scan this means almost all the survey data can be accepted rather than just 95% of the data, as will be explained in Section II.B.5.d.

B.1.c Pointing Refinement Approach

The FSS refinement of the original pointing reconstruction uses the KIR position differences to modify the pointing rather than simply monitor it. Position difference histories based on KIR sources with accurately known positions closely approximate true pointing reconstruction error histories and will be referred to as "error histories". The in-scan and cross-scan errors were fitted independently using totally different schemes individually tailored to match the form of the observed error histories. The resulting fits for all 5800 survey observations were plotted against the fitted errors, hand checked and adjusted as necessary. Each of these steps will be described in detail.

B.2 Residual Pointing Error Data

B.2.a Source of Residual Error Data

In preparation for fitting, the KIR position error histories for the entire mission were placed in a file referred to as the Measured InfraRed Error (MIRE) file. Careful examination of this file indicated that in places more KIR measurements were needed to be able to fit the errors with confidence. Since many of the SAO stars detected by *IRAS* were not included in the original KIR source file, the most straightforward solution would have been to enlarge the KIR source file to include all SAO stars detected and then regenerate the error histories. This would have been very expensive, however, because it would have meant repeating most of the original processing for the entire mission.

The time-tagged positions of *all* seconds-confirmed *IRAS* sources from the original processing were saved in a series of files known as the Thirty-Six Hour (36HR) files. It was possible to obtain additional positional error measurements without rerunning by matching the correct *IRAS* sources from the 36HR files with SAO stars. However, there were many false *IRAS* sources at the seconds-confirmation level and many SAO stars were not bright enough in the IR to be detected. The *IRAS*/SAO matching difficulty could be greatly reduced by first matching the seconds-confirmed *IRAS* sources to hours-confirmed sources. The Working Survey Data Base (WSDB) file contained all hours-confirmed *IRAS* sources and positions of the seconds-confirmed sources associated with each hours-confirmed source. Unfortunately, in order to save file space, only one (usually the first) of the associated seconds-confirmed sources was time tagged in the WSDB. The

subset of the time-tagged IR sources associated with SAO stars in the WSDB provided the raw material for the first MIRE expansion.

After the first MIRE expansion the KIR measurement counts were much improved but still marginal in places. A second effort was mounted to pick up more *IRAS*/SAO matches. Fortunately, a large database of position-to-time matches had been generated previously, with a sizable investment of computer time, for another reason. This database contained approximately 60,000 *IRAS* sources located away from the galactic plane, a significant fraction of which turned out to be SAO stars. These sources provided the raw material for the second MIRE expansion. In order to make it into the MIRE file on either expansion the *IRAS* source in the WSDB was required to be less than 45″ from the associated SAO star. Furthermore, in order to avoid confusion, it was required that the associated SAO star itself be separated from all other SAO stars by at least 180″. Also, the associated SAO star was not allowed to be of spectral type O,B,A or "unspecified", inasmuch as these types were believed less likely to be detected by *IRAS*. Note that the requirement that the position difference be less than 45″ in the WSDB does not preclude measuring much larger differences at seconds-confirmation.

B.2.b Pre-fit Rejection Criteria

In-scan error histograms broken down by KIR type (see Section II.B.2.c) revealed that the points added in the two MIRE expansions had higher dispersions than the original KIR types matched to SAO stars. Apparently, more bad matches were getting through, implying the need for additional pre-fit rejection criteria. Detailed examination of a randomly chosen selection of points from the tails of the in-scan error dispersions confirmed this assumption. Many different rejection criteria were tried and checked by regenerating the histograms. As a result of this analysis the following rejection criteria were added:

1) Lack of seconds confirmation in bands 1, 2, or 3

$$[FSTAT(1) < 5 \ \ and \ \ FSTAT(2) < 5 \ \ and \ \ FSTAT(3) < 5]$$

2) Confusion in any band at seconds confirmation

$$[(CSTAT(1,i) = T \ \ and \ \ CSTAT(2,i) = F) \ for \ i = 1,2,3,4]$$

3) Confusion in any band at band merging or confusion correction in any band at hours confirmation

$$[(CSTAT(4,i) = T \ \ or \ \ CSTAT(7,i) = T) \ for \ i = 1,2,3,4]$$

59

4) SNR in band 1 less than 3

5) Detection template correlation coefficient in band 1 less than 0.85

6) Positional cross-covariance less than 500,000 (probability mass per steradian)

Any of these conditions were sufficient for rejection. For more information on the flux status (FSTAT) and the confusion status (CSTAT) variables, see the *Main Supplement* Section V.D.

Table II.B.1 Evaluation of Gaussian-Gaussian/CGU-Gaussian Cross-Covariance

$$P_y = \frac{exp\left(-\Delta_y^2/2\left(\sigma_{y_1}^2 + \sigma_{y_2}^2\right)\right)}{\sqrt{2\pi\left(\sigma_{y_1}^2 + \sigma_{y_2}^2\right)}}$$

$$P_z = \frac{1}{4L_z}\left\{erf\left[\frac{\Delta_z + L_z}{\sqrt{2\left(\sigma_{z_1}^2 + \sigma_{z_2}^2\right)}}\right] - erf\left[\frac{\Delta_z - L_z}{\sqrt{2\left(\sigma_{z_1}^2 + \sigma_{z_2}^2\right)}}\right]\right\}$$

$$P = P_y P_z$$

where:

P ≡ cross-covariance
1 ≡ CGU-Gaussian density function
2 ≡ Gaussian-Gaussian density function
z ≡ axis along which CGU is oriented
y ≡ axis perpendicular to "z"
Δ_i ≡ separation between the two probability density functions along axis "i"
L_z ≡ half width of uniform component of CGU
σ_{ij}^2 ≡ Gaussian variance along axis "i" of density function "j"
erf ≡ error function

The last of these rejection criteria, which turns out to be a very powerful discriminator against bad matches, requires further explanation. It is the cross-covariance of the pair of two-dimensional probability density functions which describe our position information on the two sources to be matched. Each of these density functions is expressed in units of probability mass per steradian. The cross-covariance is evaluated at the observed separation of the two sources. The positional probability density function for the SAO star is a simple two-dimensional Gaussian with major and minor axes of equal length.

The density function of the *IRAS* source, on the other hand, is best represented with the Convolved-Gaussian-Uniform (CGU) distribution described by Fowler & Rolfe (1982). It is a CGU in cross-scan and Gaussian in-scan. Expressions for the cross-covariance of these two density functions are shown in Table II.B.1. Fortunately these expressions are relatively simple to compute and were used to verify all *IRAS*/SAO matches. The threshold was selected to provide the same completeness and reliability as the processor which made the original KIR matches. The one remaining concern on this point is that we may have mistakenly thrown away good matches in cases where the uncertainties on the original pointing reconstruction were quoted too low. This is a concern we were highly sensitive to in the original reconstruction; therefore, we tended toward a modest overestimation of the pointing reconstruction uncertainties.

Table II.B.2 Breakdown of KIR Measurements Available for Fits

Type	Description	Before Pre-Fit Reject	After Pre-Fit Reject In-scan	After Pre-Fit Reject X-scan	Weight
1	SAO but not Two Micron	86,931	75,069	74,268	1.0000
2	Two Micron but not SAO	19,073	8,551	0	0.0514
3	AFGL	3,556	1,519	0	0.0600
4	Asteroids (better photometry)	1,577	1,289	1,241	1.1840
5	Asteroids	7,073	5,425	5,097	0.6190
8	Dutch LRS	3,342	1,573	0	0.1240
9	SAO and Two Micron	14,645	13,312	13,281	2.9510
10	SAO 1st MIRE Exp. (Final Cat.)	52,620	39,302	38,943	0.7280
12	SAO 1st MIRE Exp. (HCON Only)	3,541	1,881	0	0.4350
13	SAO 1st MIRE Exp. (T1/9 Dups)*	38,176	1,957	1,955	1.3070
14	SAO 2nd MIRE Exp. (Final Cat.)	72,310	50,080	49,866	0.6580
17	SAO 2nd MIRE Exp. (T1/9 Dups)*	56,457	2,671	2,670	0.9910

* Type 1 or 9 duplicate used only when corresponding type 1 or 9 measurement missing.

B.2.c Quantity and Quality of Measurements

The two MIRE expansions followed by the pre-fit selection process almost doubled the number of residual error measurements available for fitting. Table II.B.2 breaks these measurements down by KIR type. The source for each measurement type is described and the number of measurements available for both in-scan and cross-scan fits, after application

of the pre-fit rejection criteria, are listed. In each case the number available for cross-scan is slightly less than for in-scan because of extra rejection criteria placed on the cross-scan measurements. Measurements with out-of-range uniform uncertainties were rejected for cross-scan but not necessarily for in-scan. Because the cross-scan-fit algorithm does not provide measurement weighting based on catalog accuracy, measurement types with inherently higher uncertainties were not used at all for cross-scan fitting. Also, for reasons which will be described later, any measurement rejected during the in-scan fit process was discarded before starting the cross-scan fit. The in-scan-fit algorithm does provide for measurement weighting and the table lists the weights used for each measurement type. These weights were intended to be inversely proportional to the inherent variance of each measurement type. The needed variances were obtained by removing the preliminary estimates of the contributions which were due to pointing reconstruction from the in-scan error variances observed for each type. The inverse-variance weights were then normalized to equal 1.0 for the most abundant type.

B.3 In-scan Residual Error Fit

B.3.a Connected Polynomial Segment Fit

The original pointing reconstruction quality was monitored with time history plots of KIR error residuals types 1 and 9. From these plots it was obvious that for the vast majority of observations the residual errors are a minimum at the fine attitude calibrations (FACs) and vary as a low-order polynomial over time between and outside the FACs. This is a natural consequence of the way the original reconstruction was done (see Section II.B.1.a). The errors are a minimum at a FAC because it provided the highest quality pointing information; the errors increase with time past the FAC because of the build-up of gyro drift, etc. Residual error histories between FACs came out generally symmetric because the forward and backward solutions were combined. As illustrated in the upper half of Figure II.B.1, the in-scan error histories generally appear quadratic over time between FACs, continuous in value but not in slope at each FAC, and linear outside the FACs. Since there are never more than three FACs in an observation, no more than four connected segments should be needed for a fit. Based on these observations a customized in-scan-fit algorithm was devised. This algorithm will be referred to as the connected-polynomial-segment (CPS) fit. As implemented for this application there are assumed to be four (or lower) connected segments to be fit simultaneously, with each segment modeled as a second order (or lower) polynomial. The fits are constrained to match at the segment boundaries. In Table II.B.3 this problem is setup as a weighted least-squares fit subject to the stated constraints. The segment boundary constraints provide three equations,

62

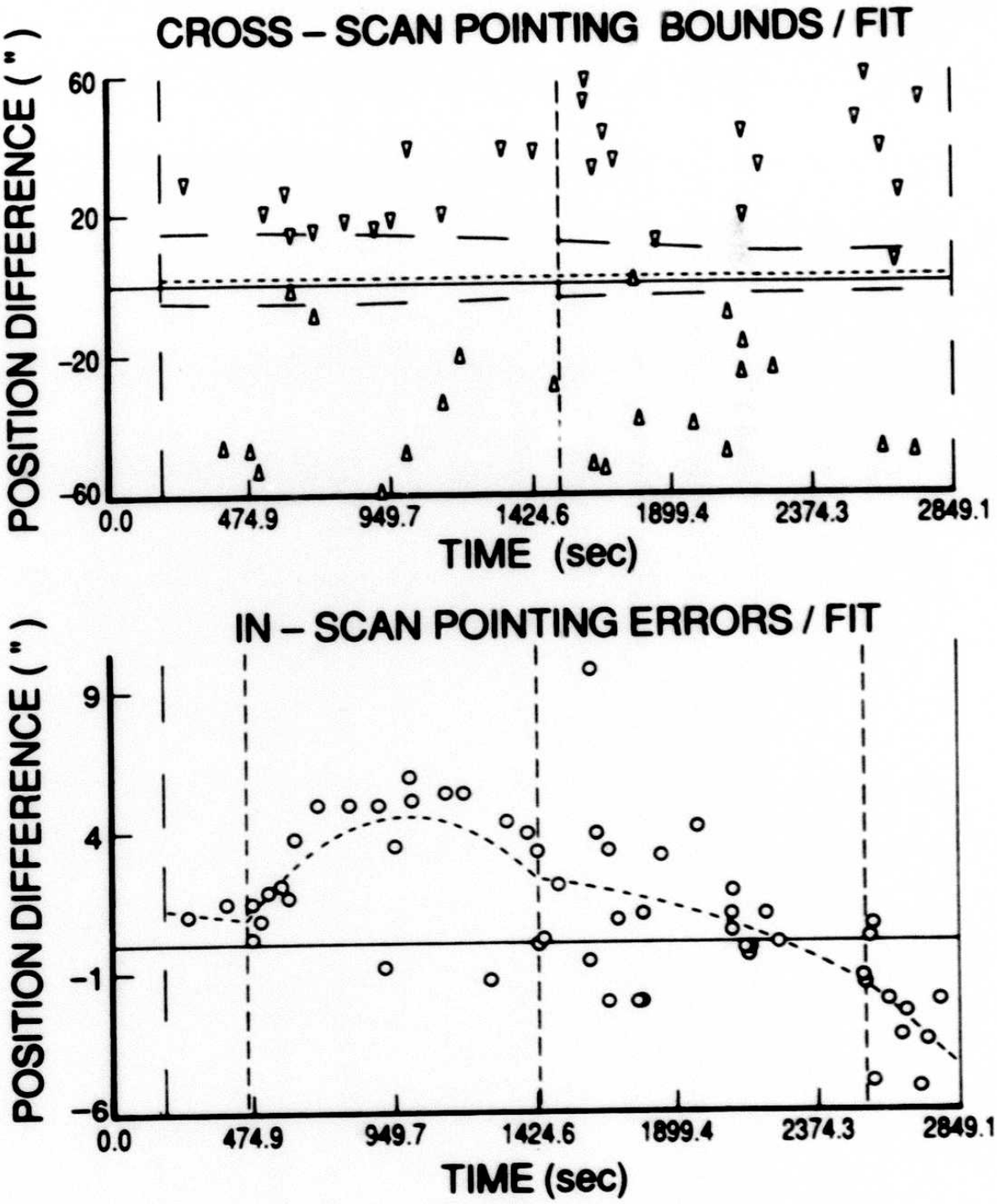

Figure II.B.1 An example of how SAO positions were used to improve the *IRAS* pointing. The old pointing is represented by the 0 difference line. The new pointing is represented by the dashed line. The circles represent the in-scan position errors of individual 'known infrared sources'. The triangles represent bounds on the cross-scan position errors.

and the requirement that "S" be a minimum provides nine more, giving the total needed to solve for the twelve unknown polynomial coefficients. Although straightforward in concept, expanding the partial derivatives of "S" leads to lengthy algebraic expressions which will not be presented here. Once obtained these expressions can be quickly evaluated by computer, thus setting up a matrix equation which can be readily solved. It is a simple matter to reduce the number of segments and/or the order of fit in a given segment by zeroing out rows and columns in this matrix.

B.3.b Implementation of In-scan Fit

Although the CPS algorithm provided the basic tool for the in-scan fitting, before it could be used each observation had to be preprocessed. First, any large data gap during an observation usually resulted in a discontinuity in the error residuals because the original pointing reconstruction could not carry the sensor information across these gaps. If, for instance, a large data gap occurred between FACs 1 and 2 of a three-FAC observation, that observation had to be treated as having five segments, i.e. two connected segments followed by three connected segments. In this case the CPS algorithm would be used twice in the same observation. To allow for the rare occurrence of two large data gaps in one observation the code was set up to provide up to six in-scan segments with never more than four of them connected.

Second, the preprocessor also had to provide the CPS algorithm with the order of the polynomial to use in each segment. This was decided by the number, the quality and the placement of the measurements in each segment. Because the connected segments were fitted as a whole, it was possible to bridge short internal segments having no measurements using a first-order polynomial and outside segments using a zeroth order.

Very short observations with only a couple of measurements presented special problems since it was not possible to do consistency checking. What if one of the measurements were way out in the tail of its uncertainty distribution or based on a bad source match? In general these were handled by picking a solution between the original reconstruction and the residual error fit, with the relative weighting depending on the circumstances.

During the course of working with this algorithm it became apparent that there were advantages to treating the FACs as pseudo error measurements. These were weighted less heavily than the KIR measurements and had little effect on the fit except in cases where there were few KIRs in the vicinity of a FAC. In these cases the pseudo measurements had the beneficial effect of pulling the fit closer to the original solution near the FACs.

Table II.B.3 Connected Polynomial Segment Fit

$$S = \sum_{j=i}^{4} \sum_{i=1}^{n_j} w_{ji}(F_{ji} - M_{ji})^2$$

where:

$$F_{ji} = c_{j1} + c_{j2}t_{ji} + c_{j3}t_{ji}^2$$

subject to constraints:

$$c_{22} = \frac{c_{11}}{T_{12}} + c_{13}T_{12} - \frac{c_{21}}{T_{12}} - c_{23}T_{12} + c_{12}$$

$$c_{32} = \frac{c_{21}}{T_{23}} + c_{23}T_{23} - \frac{c_{31}}{T_{23}} - c_{33}T_{23} + c_{22}$$

$$c_{42} = \frac{c_{31}}{T_{34}} + c_{33}T_{34} - \frac{c_{41}}{T_{34}} - c_{43}T_{34} + c_{32}$$

In order for S to be a minimum:

$$\frac{\partial S}{\partial c_{11}} = 0 \quad \frac{\partial S}{\partial c_{21}} = 0 \quad \frac{\partial S}{\partial c_{33}} = 0$$

$$\frac{\partial S}{\partial c_{12}} = 0 \quad \frac{\partial S}{\partial c_{23}} = 0 \quad \frac{\partial S}{\partial c_{41}} = 0$$

$$\frac{\partial S}{\partial c_{13}} = 0 \quad \frac{\partial S}{\partial c_{31}} = 0 \quad \frac{\partial S}{\partial c_{43}} = 0$$

where:

S = Weighted sum of squares of differences between the measurement and the fit at each point.
n_i = Number of measurements in segment i
$w_{i,j}$ = Weight of measurement j in segment i
$F_{i,j}$ = Value of fit of measurement j in segment i
$M_{i,j}$ = Value of measurement j in segment i
$c_{i,j}$ = Polynomial fit coefficients for segment i
$t_{i,j}$ = Time of measurement j in segment i
$T_{i,j}$ = Time at boundary between segments i and j

B.3.c In-scan Fit Consistency Rejection Criteria

As a last line of defense against bad measurements, the in-scan fitting algorithm checked each measurement for consistency with the fit. After fitting an observation the algorithm went back and computed the weighted square of the difference between fit and measurement at each point. Any point having a weighted residual greater than 7", while the magnitude of the difference itself was greater than 7", was flagged as "suspect". The "suspect" points were compared and the one with the largest weighted residual was marked "rejected". All "suspect" flags were removed and the whole process was then repeated without the rejected point. This process was continued until no further "suspect" points were found or a maximum of five iterations was reached. In-scan-fit-consistency rejections were rather rare (0.6%) and were monitored very carefully, as will be described in the next section.

B.3.d In-scan Fit Performance Monitoring/Tweaking

Although the CPS fitting was automated, the results were monitored for all observations via manual inspection of the polynomial fits plotted over the measurement histories of KIR types with high inherent accuracy. Points rejected at the time of fit due to inconsistency were tagged with a special symbol and visually verified on the plots. The plots were also checked to see whether the order of the polynomial fit had been selected properly; segments with few KIRs were given special attention. The weighting of each FAC as a pseudo error measurement was verified. Manual overrides on all these parameters were available and used as needed.

B.4 Cross-scan Residual Error Fit

B.4.a Bounding the Cross-Scan Error

Before discussing how the cross-scan fit was accomplished, consider the nature of the cross-scan measurements. Remember that the focal plane is made up of an array of rectangular detectors, narrow in the in-scan direction but wide in cross-scan. Knowing when a specific KIR source was seen on a specific detector tells much less about the cross-scan pointing error than the in-scan error. The situation is improved somewhat by the fact that the detectors are positioned on the focal plane in an overlapping pattern. Thus, knowing the focal plane geometry and the combination of detectors (from all bands) on which the KIR source was seen, one can use detector overlap to reduce the cross-scan measurement uncertainty. The basic nature of the problem, however, remains unchanged. The overlap region can be considered a pseudo-detector with a width equal to the amount of overlap. The cross-scan error is measured as the difference between cross-scan position of the center

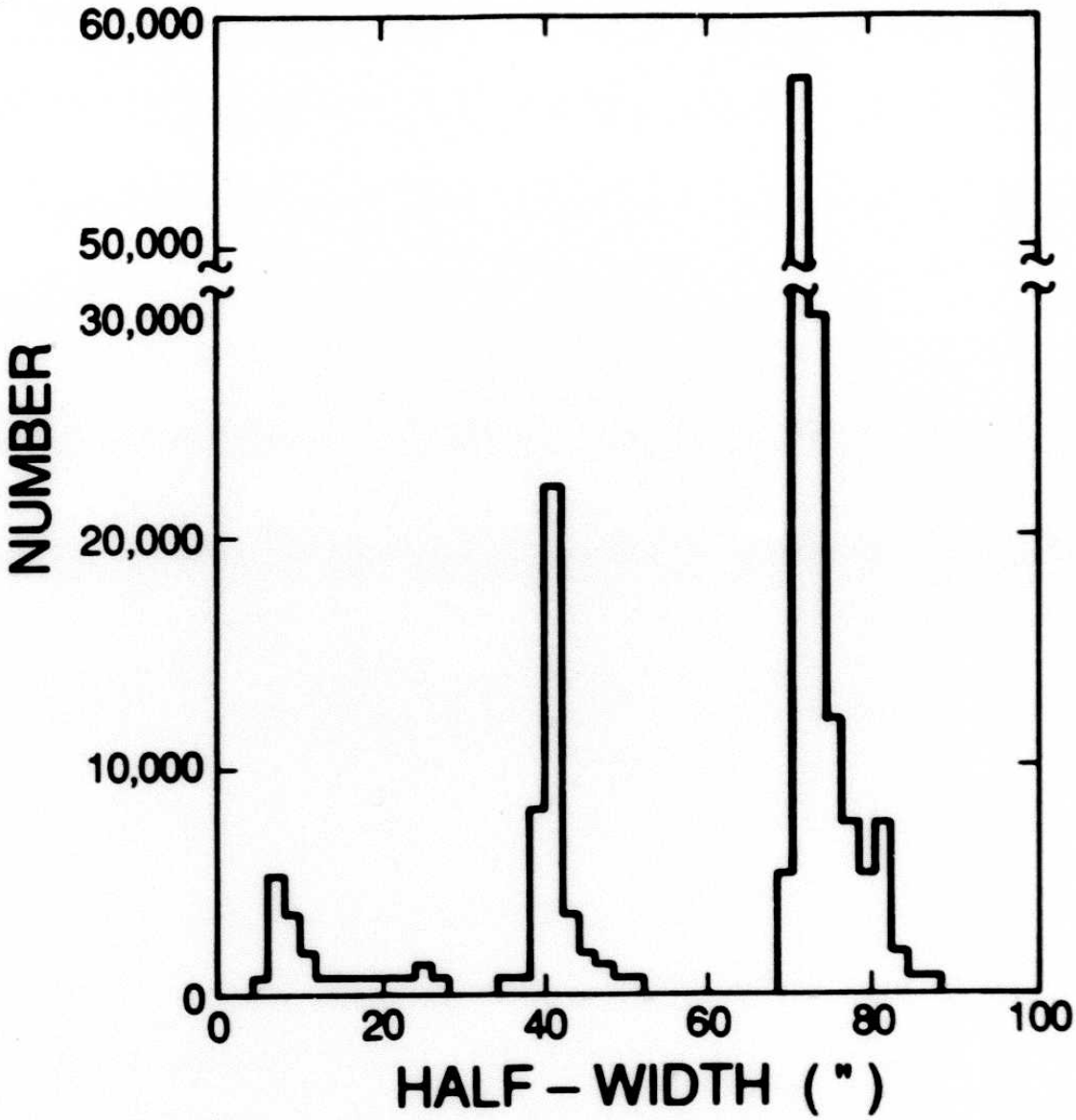

Figure II.B.2 Histogram of pseudo-detector half widths.

of the pseudo-detector (as determined from the original pointing reconstruction) and the known position of the KIR. Note that even in the presence of perfect pointing reconstruction this measurement can show an error up to half the width of the pseudo-detector. Given that the KIR sources are randomly distributed, and ignoring some subtleties which will be addressed later on, the errors should be uniformly distributed. Figure II.B.2 presents a histogram of pseudo-detector half-widths for the KIR measurements used in the cross-scan reconstruction.

The residual cross-scan errors from the original pointing reconstruction are Gaussian,

67

whereas the KIR measurements have a uniform uncertainty. One could assume the error is constant or linear, then perform an inverse-variance least squares fit with the width of the uniform uncertainty associated with each measurement reflected in its variance. Although this method works fine where the measurement density is very high and/or the uniform measurement uncertainties are low, it becomes much less effective at lower densities and higher uncertainties. The basic problem is that this scheme does not take full advantage of the information content of the uniform measurements. A uniform distribution has no points beyond 1.7321 σ, whereas a Gaussian distribution has over 8.3% of its points beyond this uniform cutoff value and is itself unbounded. Thus, although the uniform gives less information about where a point is most likely to be, it gives more information about where it is not. The cross-scan fit scheme devised for the pointing refinement makes use of this fact.

For purposes of cross-scan fitting each observation was divided into segments and the residual cross-scan error was assumed (as a first approximation) to be constant over a segment. This assumption implies that all cross-scan measurements within a single segment are measurements of the same error. Since each cross-scan measurement sets its own upper and lower bounds on that error, it follows that the maximum of the individual minima sets the lower bound for the segment and the minimum of the individual maxima sets the upper bound. Although the bounds will generally be reduced as the number of measurements increases, their values are not specifically predetermined by that number as they would be in the case of repeated independent Gaussian measurements. More important is the cross-scan spacing of the KIR sources encountered in a given time segment as is illustrated in Figure II.B.3 (divided into seven parts). In this simplified example a single detector detects a half dozen KIR sources during one cross-scan time segment. Part 1 shows the cross-scan placement of the detector on the sky based on the original pointing reconstruction, and part 2 shows the known cross-scan positions of the KIR sources encountered. Parts 3 and 4 show, respectively, the minimum and maximum cross-scan detector placements consistent with the KIR positions. Note that the bounds shown in part 5 are set by only the two KIR sources at the ends; the other KIR sources have no effect. It is theoretically possible to get arbitrarily tight bounds with only two fortuitously placed KIR sources. The best-estimate fit of the residual cross-scan error is taken as the centroid of probability mass for that portion of the Gaussian contained within the bounds (parts 6 and 7).

In between segment centers, the values of the bounds and of the fit are found by linear interpolation, and outside segment centers they are taken to be constant. Choosing the number of segments per observation involved trading off conflicting requirements. Long

68

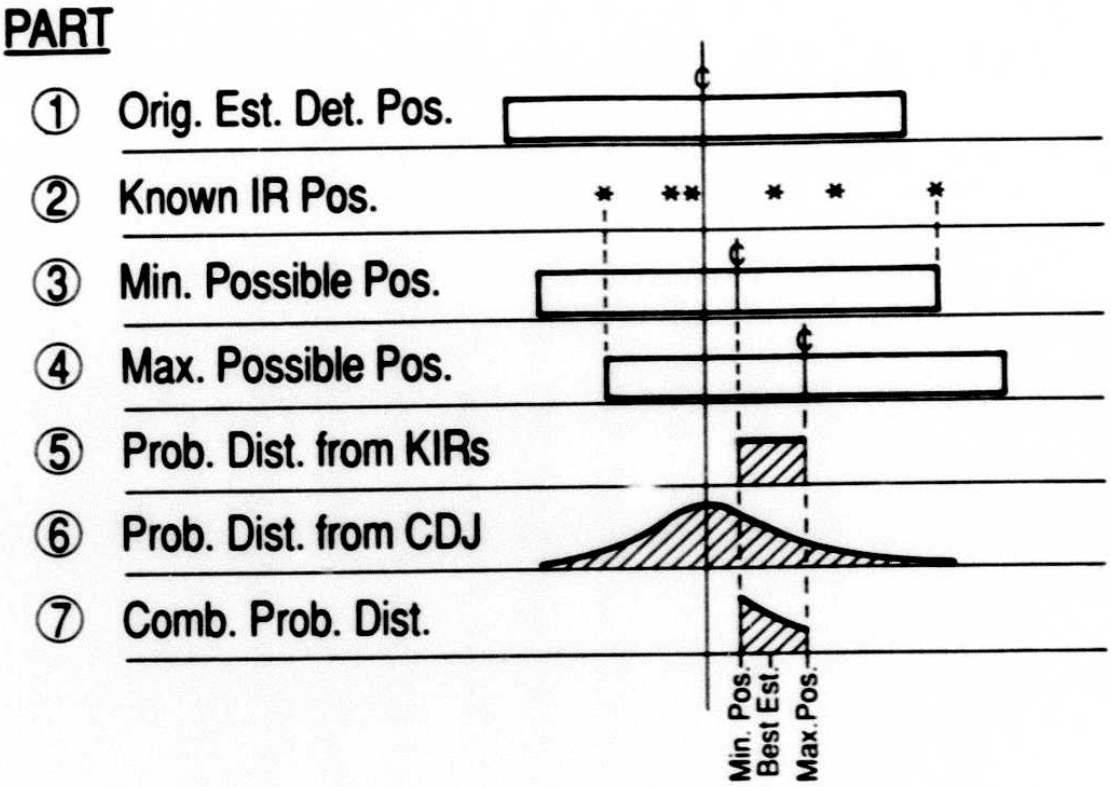

Figure II.B.3 Simplified illustration of cross-scan refinement.

segments are more likely to violate the "constant error" assumption, whereas short segments are less likely to have enough measurements to expect tight bounds. Based on a visual inspection of the cross-scan error-bound plots for many observations, it appeared that two or three cross-scan segments per observation would be about right. There were operational reasons for preferring two segments over three, and prototype code showed it to work well, provided the time of the segment boundary could be manually overridden.

B.4.b Cross-scan Fit Consistency Rejection Criteria

One problem which surfaces immediately concerns how to handle bad measurements. Although consistency checking is still possible, it is a far less powerful discriminator than it was for the in-scan fit. For this reason, any measurement rejected during the in-scan fit was dropped before starting the cross-scan fit. Several additional steps were taken to guard against bad cross-scan measurements. If the maximum of the minima for a segment should turn out greater than the minimum of the maxima, something is obviously wrong. It could be the result of a bad measurement or the assumption that the error is constant

over the segment. For the moment assume the former; the latter case will be discussed further on. One of the two extreme points is bad, but which one? Define the "isolation" of an extreme point to be the magnitude of the difference between the extreme point itself and the average of the closest two points from the same set. The more isolated of the two extreme points is more likely to be a bad measurement. Even if both points were equally likely to be bad, discarding the more isolated one minimizes the damage resulting from an incorrect choice. Less than 0.6% of the cross-scan measurements had to be rejected as "impossible" situations.

Since there is no guarantee that the correct choice has been made, and because some bad measurements may not be bad enough to show up as "impossible" situations, another line of defense is needed. To this end, rather than using the extreme point alone to define the bound, the algorithm uses the average of the two most extreme points on each side. This considerably reduces the potential for damage from a single bad measurement.

B.4.c Cross-scan Fit Performance Monitoring/Tweaking

The performance of the cross-scan fit algorithm was monitored through visual inspection of the cross-scan-error-bound plots for all observations. The lower portion of Figure II.B.1 is a typical example of such a plot. Lower bounds from individual KIR measurements are plotted as up arrows and upper bounds as down arrows; only individual bounds within ±60″ are plotted. The cross-scan fit history is marked by a line of short dashes and the associated upper and lower bounds with lines of long dashes. The vertical dashed line near the middle of the observation marks the boundary between the two cross-scan segments. Although Figure II.B.1 does not include an example of such a point, the plot symbols for measurements rejected on the basis of fit consistency were enclosed in small squares.

These plots were very useful in checking the reasonableness of the fit. Measurements rejected on the basis of the cross-scan consistency check were examined carefully. In cases where the rejection appeared to result from a violation of the "constant error" assumption it was usually possible to avoid the inconsistency by manually shifting the time of the cross-scan segment boundary. It was also possible to manually reject measurements if they appeared suspect. Remember that rejecting a cross-scan measurement which forms an extreme point will enlarge the associated bound, generally moving the refined fit closer to the original reconstruction. Solutions calling for large changes in the cross-scan fit were rare and were examined even more carefully. In extreme cases data associated with the original reconstruction were also reviewed. As can be seen in the time-weighted histogram

MO

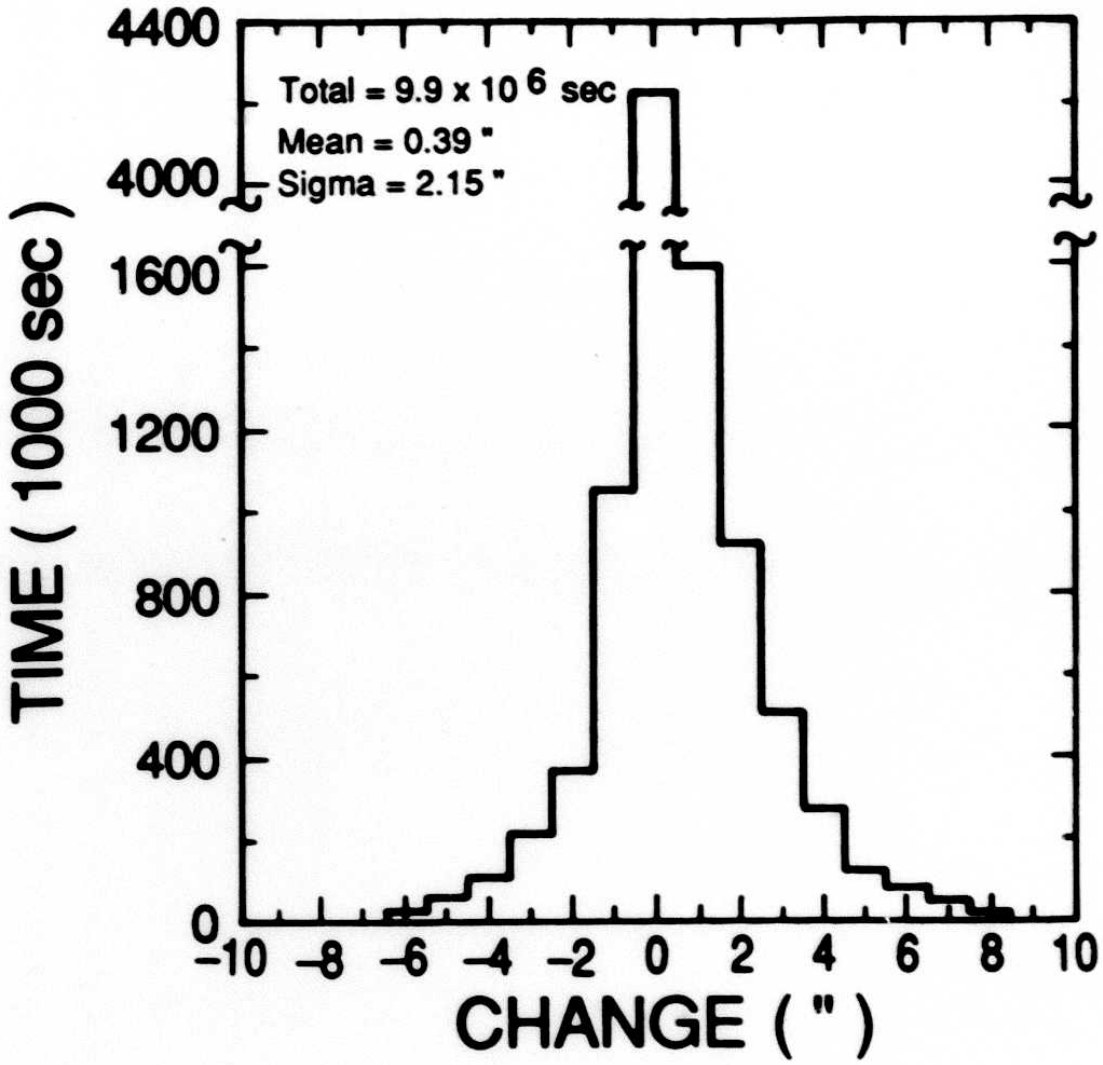

Figure II.B.4 Histogram of cross-scan changes.

of cross-scan changes presented in Figure II.B.4, the number of segments with large cross-scan corrections is relatively small.

B.5 Evaluation of Results

B.5.a In-scan Fit Statistics

A summary of in-scan fit statistics, broken down by KIR type, is presented in Table II.B.4. For each type the number of measurements rejected during the in-scan fit process and the number actually used are listed. The means and standard deviations of the in-scan difference measurements both before and after the fit are also given, and the weighting factors from Table II.B.2 are repeated for quick reference. When interpreting this table it is important to keep several points in mind. At first thought one might expect the change

D 10015

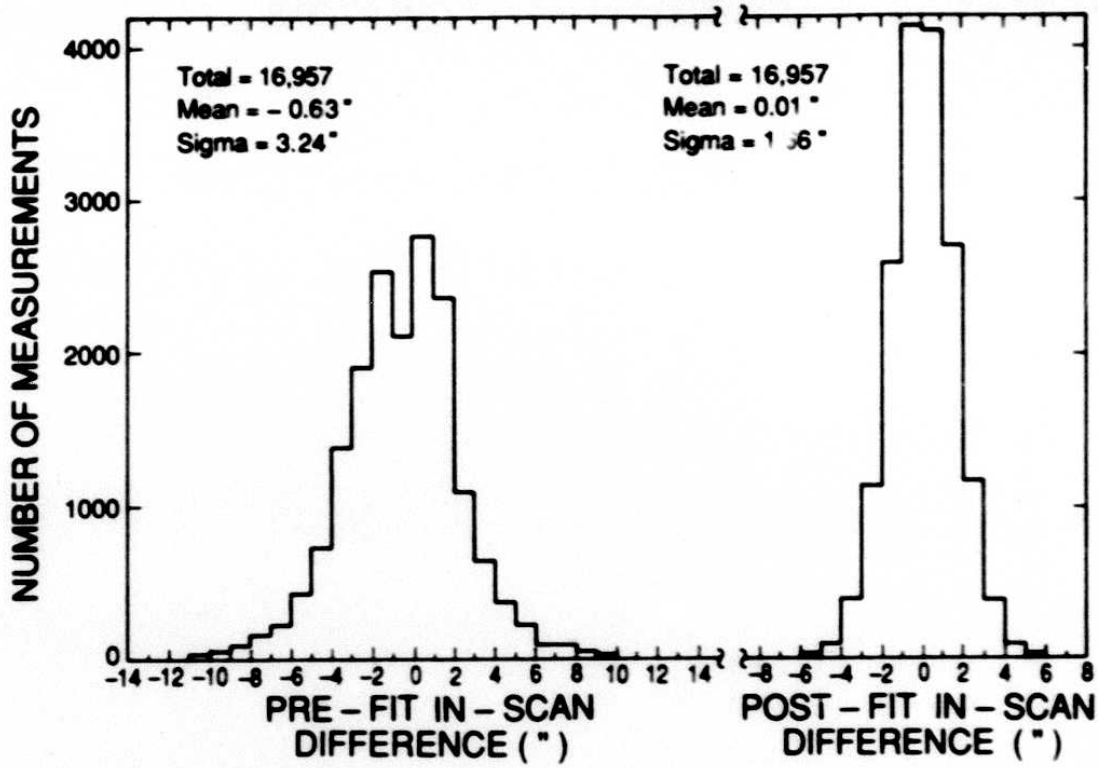

Figure II.B.5 In-scan position difference histogram a) pre-fit, b) post-fit. Only types 10, 13, 14, and 17 with SNR_1 >25 were used.

in variance to be the same for each measurement type. This expectation assumes that the various measurement types were mutually independent both before and after the fit. Since the measurements themselves were used for the fit, however, the change in error is correlated between measurements and this affects the change in variance. The situation is further complicated by the fact that the measurements were not equally weighted during the fit. Given that the most accurate measurement types were weighted most heavily, the fit was naturally biased toward these measurements. Use of these heavily weighted measurement types as unbiased estimators of the pointing reconstruction improvement is therefore misleading.

The principal characteristic that distinguishes type 9 from type 1 measurements is that the associated SAO stars are bright in the infrared wavelengths. This is a selection effect dictated by the fact that the type 9 stars showed up in the Two Micron Survey and the type 1 stars did not. Because they are brighter in the IR, the type 9 stars end up with more accurately determined seconds-confirmed positions. There is less contribution from error sources not associated with the pointing reconstruction; i.e. detection timing, etc. This makes the type 9 stars better indicators of the pre-fit pointing reconstruction

M2

Table II.B.4. In-Scan Fit Statistics

KIR Type	Measurements Rejected	Used	Pre-Fit Stats Mean(")	σ(")	Post-Fit Stats Mean(")	σ(")	Weight
1	684	74,385	-0.70	3.66	-0.05	2.10	1.00
2	0	8,551	-0.31	12.82	0.30	12.76	0.05
3	0	1,519	-0.38	11.99	0.37	11.99	0.06
4	25	1,264	-0.12	3.14	0.43	1.85	1.18
5	84	5,341	-0.25	3.90	0.25	2.91	0.62
8	1	1,572	-0.03	8.27	0.63	7.83	0.12
9	25	13,287	-0.64	2.98	0.03	1.23	2.95
10	262	39,040	-0.68	3.86	0.01	2.65	0.73
12	8	1,873	-0.36	4.86	0.35	4.08	0.44
13	1	1,956	-0.54	2.49	0.14	1.41	1.31
14	181	49,899	-0.69	3.99	-0.05	2.57	0.66
17	1	2,670	-0.68	2.70	-0.05	1.43	0.99

accuracy. Since they were heavily weighted in the fit they are not as reliable as post-fit indicators.

Most of the measurements added during the two MIRE expansions had slightly larger dispersions and were therefore weighted less heavily than the original measurements. Stars bright in the IR were not separated out prior to the fit and assigned higher weights. For this reason they can be used as unbiased estimators of the post-fit accuracy. Figure II.B.5 presents pre-fit and post-fit in-scan difference histograms for the most accurate measurements from the MIRE expansions. Only measurements of types 10, 13, 14 and 17 with SNR in band 1 greater than 25 were used. Note that the standard deviation was cut in half and a small but significant mean error was removed. Improvement is particularly noteworthy in the tails of the distribution. The post-fit histogram shows negligible errors greater than the 7.5" pixel half-width. Small adjustments can be made to account for the increased inherent uncertainties associated with the MIRE expansions and the uncertainties associated with the SAO catalog itself. After making these adjustments it appears that the post-fit in-scan pointing reconstruction is good to about 1.5" (1 σ).

B.5.b Cross-scan Fit Statistics

The cross-scan pointing reconstruction improvement is more difficult to quantify than the in-scan. This is because the reconstructed cross-scan position of a seconds-confirmed KIR source generally reflects a large uncertainty associated with the overlap region for

M3

Table II.B.5. Cross-Scan Fit Statistics

KIR Type	All Measurements Number Rejected	Number Used	Narrow Edge Detections (Half Width < 7″) Number Used	Pre-Fit Stats Mean(″)	σ(″)	Post-Fit Stats Mean(″)	σ(″)
1	340	73,928	2,010	1.50	5.14	0.82	3.81
4	14	1,227	33	2.36	5.66	1.70	4.39
5	133	4,964	77	2.08	6.43	1.47	5.21
9	86	13,195	509	1.80	4.35	0.96	3.13
10	182	38,761	727	1.26	5.34	0.68	3.78
13	9	1,946	63	1.58	3.59	0.87	2.53
14	264	49,602	1,112	1.73	5.26	0.93	3.84
17	20	2,650	109	1.40	4.13	0.64	3.16

the detector combination involved. If the probability-of-detection distribution across the overlap region were truly uniform it would be a simple matter to subtract its effect from the measurement difference statistics to obtain the cross-scan pointing reconstruction accuracy. Unfortunately, the probability-of-detection distribution appears more like a CGU. The reasons for this are not fully understood, but include among other things the effects of optical blur and KIR position errors. When analyzing the cross-scan difference measurements, it is very difficult to separate the Gaussian component of this CGU distribution from the Gaussian contribution of the pointing reconstruction itself.

Table II.B.5 presents a summary of cross-scan fit statistics, broken down by KIR type. For each type the total number of measurements rejected during the cross-scan fit process and the total number actually used are listed. In order to minimize the contribution of the detectors, the difference statistics presented in the table are based on the subset of measurements where the overlap region is very small (half-width <7″). Means and standard deviations both before and after the fit are tabulated. The pre-fit standard deviations are smaller than the values previously published in Table VII.C.2 of the *Main Supplement* primarily because of a more stringent cutoff on detector overlap size allowed. Comments made previously concerning the fact that the post-fit in-scan measurements are correlated also apply to the cross-scan.

Figure II.B.6 gives cross-scan measurement difference histograms before and after fitting. They use the same measurement set used for the in-scan histograms, with the additional constraint that the detector overlaps are required to have a half-width less than

74

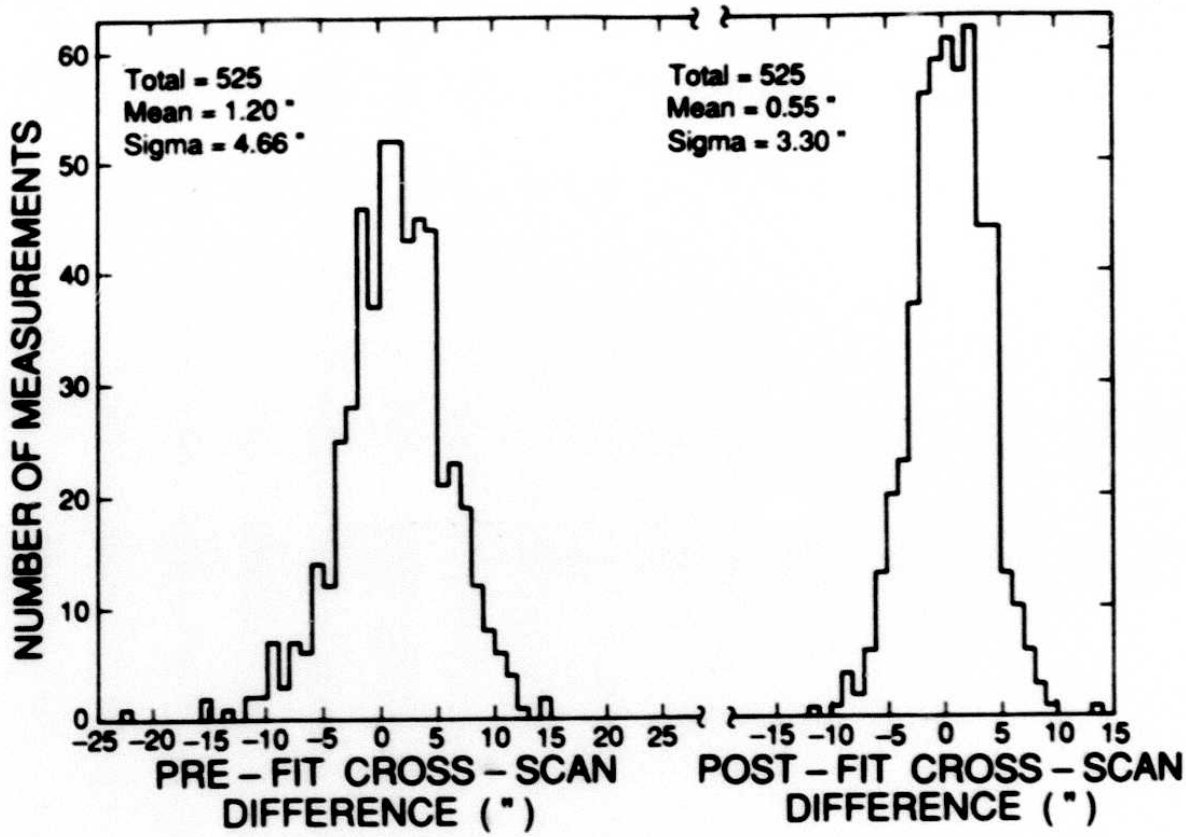

Figure II.B.6 Cross-scan difference histogram. a) pre-fit, b) post-fit.

7″. These histograms show significant cross-scan improvement; both the mean and variance of the measurement differences have been halved. For reasons discussed previously we are unable to remove the contribution of the detector overlap to the standard deviation of the differences. Depending on what one assumes about the contribution of the detector overlap, the cross-scan pointing reconstruction accuracy probably lies somewhere between 2.5 and 3.0″ (1 σ).

B.5.c Pointing Refinements Not Used by FSS

As the final step in validating the refined pointing reconstruction, it was fed back through the algorithm which generated the KIR error histories for the original pointing reconstruction to verify that the corrections had been made properly. All survey observations were run through this procedure to be sure that the tapes containing the original pointing reconstruction histories had been properly matched with those containing the original *IRAS*/SAO difference measurements. This was a matter of some concern because the original processor frequently required several passes but provided no unequivocal identifiers

D 10015

Table II.B.6 In-Scan Fit Adjustments Not Used by FSS

SOP	OBS	MAX DIF (″)	Duration of DIF >3.0″ (sec)	Duration of DIF >7.5″ (sec)
79	34	8.5	155	33
103	19	5.0	122	0
123	41	3.5	31	0
126	23	5.0	75	0
139	40	4.5	68	0
157	8	12.0	122	83
206	10	7.0	24	0
269	36	5.0	67	0
327	29	4.5	111	0
401	49	11.0	150	150
424	36	5.5	82	0
455	20	12.0	152	40
472	36	6.0	38	0
506	26	6.0	394	0
515	47	10.0	109	109
535	16	4.0	122	0
568	6	8.5	60	21
Overall		12.0	1882	436

on the tapes to match up those generated on the same pass. This final check occasionally resulted in new *IRAS*/SAO matches and provided another opportunity to review the fits.

As a result of this final review, the fits for a small number of observations were adjusted, and these adjustments are reflected in the overall pointing reconstruction statistics already presented. Unfortunately the FSS task was too far along at this point to easily incorporate these changes. A total of 17 observations had in-scan fit adjustments that at some point of time exceeded the 2-σ in-scan uncertainty (3″). These observations are listed in Table II.B.6 along with the magnitude of the maximum in-scan difference, as well as the approximate time intervals spent above the 3.0″ 2-σ uncertainty and the 7.5″ half-pixel width. Note that only in a half dozen instances is the half-pixel width exceeded and then only over brief periods of time. No cross-scan adjustments greater than the 2-σ cross-scan uncertainty (6″) were made. Since it was felt that the magnitude and duration of the pointing adjustments indicated a very minor effect, the adjustments were not incorporated into the FSS.

Table II.B.7 Observations Discarded Due to Pointing Uncertainties

Category	SOP	OBS	FAC	FIT	Duration (sec)
1	59	3	No	No	83
	59	7	No	No	74
	59	12	No	No	675
	59	19	No	No	762
	339	13	No	No	92
	401	22	No	No	123
	433	23	No	No	130
	433	29	No	No	131
	523	8	No	No	82
2	298	7	Yes	No	204
	443	9	Yes	No	238
	448	40	Yes	No	581
	457	2	Yes	No	280
	590	14	Yes	No	200
Total					3,655

B.5.d Observations Discarded Due to Pointing Uncertainties

As mentioned in Section B.1.b, the original plan was to use only those time intervals for FSS that could be demonstrated using KIR matches to fall within the stated requirements of 7.5″ in-scan and 45″ cross-scan. Strict adherence to this plan would have resulted in discarding slightly over 5% of the data based on violations of the cross-scan requirement. It was not that the cross-scan pointing errors exceeded 45″ during 5% of the time, but rather that there were insufficient KIR matches to prove otherwise. While it is impossible to prove that there are no cross-scan errors greater than 45″, it can be shown to be highly unlikely. The original reconstruction was better in cross-scan than previously thought. As already shown in Figure II.B.7, pre-fit statistics on narrow edge detections of IR-bright SAO stars indicate a 45″ cross-scan error to be almost a 10-σ point. One might still argue the case based on an excess in the tails of the distribution, but no corrections of even half this magnitude were encountered during the cross-scan fit process. In the unlikely event that such a large error should be encountered in the 5% of the data which cannot be adequately bounded, the trimmed averaging technique discussed previously would in all probability discard it.

In the final analysis, less than 0.04% of the potentially usable survey time was dis-

M7

carded because of our inability to adequately reconstruct the pointing. The discarded observations can be broken into two categories as indicated in Table II.B.7. The first category includes those observations which had no successful FACs and no KIR matches which could be used for a fit. Observations without FACs had the potential for very large in-scan errors in the original reconstruction because FACs provided the only absolute in-scan position reference. It is interesting to note that fits were obtained for another 66 no-FAC observations, totaling 65,754 seconds. The second category in Table II.B.7 lists observations over 200 seconds long with one or more FACs, but insufficient KIR matches to allow a fit. These were considered suspect because of the lack of KIR matches. Another 172 similar observations less than 200 seconds long were accepted. As can be seen from the table most of the discarded observations are quite short and total only 3,655 seconds out of almost 9.7 million seconds of potentially usable survey time.

D 10015

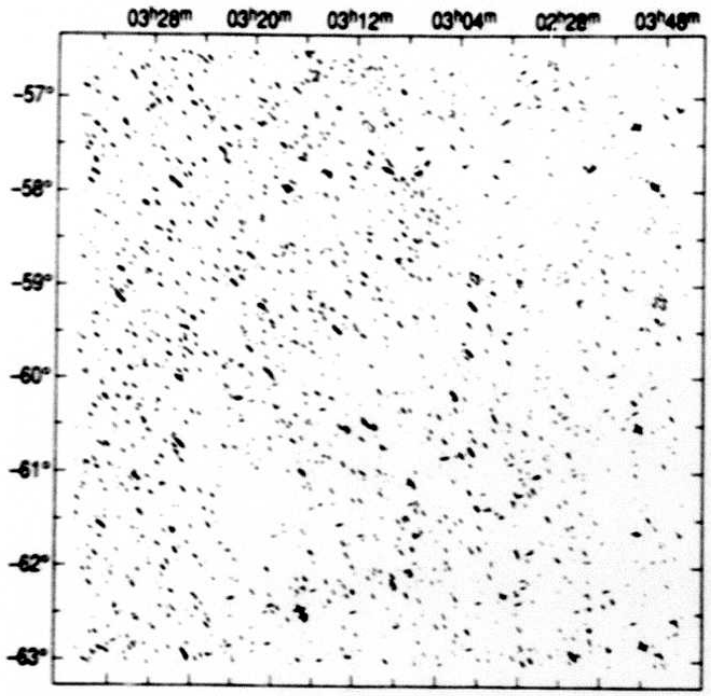

Figure II.C.1.a Plate 116 coadded without deglitching or trimming.

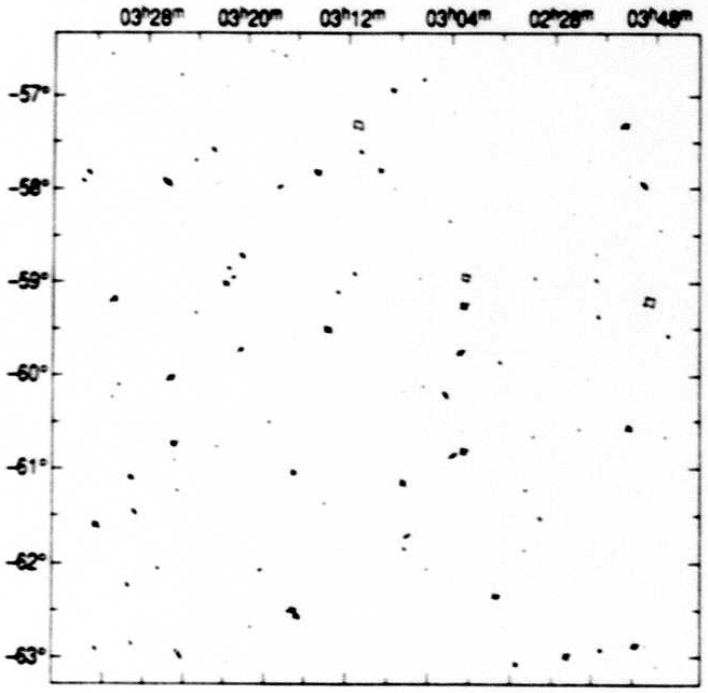

Figure II.C.1.b Plate 116 coadded with deglitching and trimming.

19

C. The Coadding Algorithm for the Plates

C.1 Overview

The Faint Source Survey catalog sources were extracted from point-source filtered images of *IRAS* survey data. Faint Source Survey images were produced by filtering and spatially coadding the *IRAS* survey data using the improved pointing data described in Section II.B.

The following major steps were performed in order to produce the FSS plates:

- The data were conditioned by removing radiation hits, known asteroids, and other artifacts
- The data were smoothed and the baseline was removed with a median filter
- The filtered data were spatially binned, and the flux density and noise were estimated for each bin

These steps are discussed in detail in the following.

Figure II.C.1.a shows a contour map of the 12 μm band for plate 116 coadded without deglitching and data trimming. Figure II.C.1.b shows the same plate coadded with deglitching and data trimming as described below. In both cases the lowest contour is at SNR = 5.

C.2 Data Conditioning

The *IRAS* detector data contained artifacts due to radiation hits, spacecraft electrical anomalies, asteroids and orbital debris, dust particles reflecting light into the telescope field of view, and internal reflections due to bright off-axis bodies such as the moon and planets. The major sources of non-Gaussian noise were radiation hits and 1 Hz electrical crosstalk at 12 and 25 μm from temperature sensors in the focal plane. Radiation hits and electrical glitches were removed with a combination of in-line deglitching and robust estimation with a trimmed average. Known asteroids and other anomalies were removed by clipping affected time ranges from the data.

C.2.a Deglitching

Even though the *IRAS* survey strategy was to avoid the South Atlantic Anomaly (a high radiation area, see the ***Main Supplement***) and an on-board deglitcher was incorporated into the satellite, many artifacts with amplitudes less than 100 times the sample noise were present in the data due to charged particles impacting the detectors (radiation hits). Three levels of protection were incorporated in the Faint Source processing to eliminate the effects of residual radiation hits. First, an in-line deglitcher was implemented to detect and remove high frequency artifacts over 5 times the detector noise. Second, a trimmed-average flux

density-estimation technique was used. Third, a local noise was estimated based on the dispersion in each pixel to allow discovery of surviving artifacts.

The in-line deglitching algorithm capitalized on the modest in-scan oversampling provided by the data. The point source signature has a full-width at half-maximum of three samples, while the typical radiation event affects primarily one sample with a small tail. The deglitching algorithm monitored the output of a high pass filter for events over a SNR threshold (as measured on a single detector scan) as compared to an in-line noise estimator. If an event was detected with SNR > 5, the instantaneous power out of the high pass filter was compared to the smoothed power out of a band pass filter tuned to the point source frequency. If the ratio of power through the point source filter to that through the high pass filter was less than a threshold, a glitch was identified and removed from the data. The power ratio thresholds used were 1.0 for positive glitches and 0.4 for negative glitches. The thresholds were set conservatively to preclude deglitching true structure in complex areas. This filter removed more than 95% of the radiation hits with SNR > 5 in addition to artifacts due to magnetic pickup from the spacecraft momentum coils.

Figure II.C.2 shows data for the 12 μm detectors before and after deglitching. True sources appear on at least two adjacent detectors with a three- to five-second time difference. Some obvious artifacts are left in the data because their signatures are too wide to be reliably differentiated from point sources in a single detector data stream. These remaining artifacts are dealt with by the data trimming described below.

C.2.b Asteroids and Anomalies

Known asteroids were removed from the data using sighting predictions provided by the *IRAS* asteroid and comet survey system (see *IRAS* Asteroid and Comet Survey 1986). For each predicted coverage of an asteroid by the *IRAS* focal plane, a section of data was removed from each affected detector centered on the predicted detection time. The times removed were 1.0, 1.0, 1.6, and 2.8 seconds at 12, 25, 60, and 100 μm, respectively. These times included allowances for the asteroid orbit determination uncertainties, pointing uncertainties, and the duration of the detector transit. For each interval clipped, an additional filter length (see below) was not used due to filter initialization. For the most part, the asteroid sightings were within 10° of the ecliptic plane. For a typical plate near the ecliptic, 0.3% of the data were clipped at 12 and 25 μm, 0.5% at 60 μm, and 0.8% at 100 μm.

Data were also clipped corresponding to a list of anomalies discovered during the original processing of the *IRAS* data. These anomalies included massive proton hits, off-axis artifacts from bright objects, artifacts due to reflections from dust particles, paint

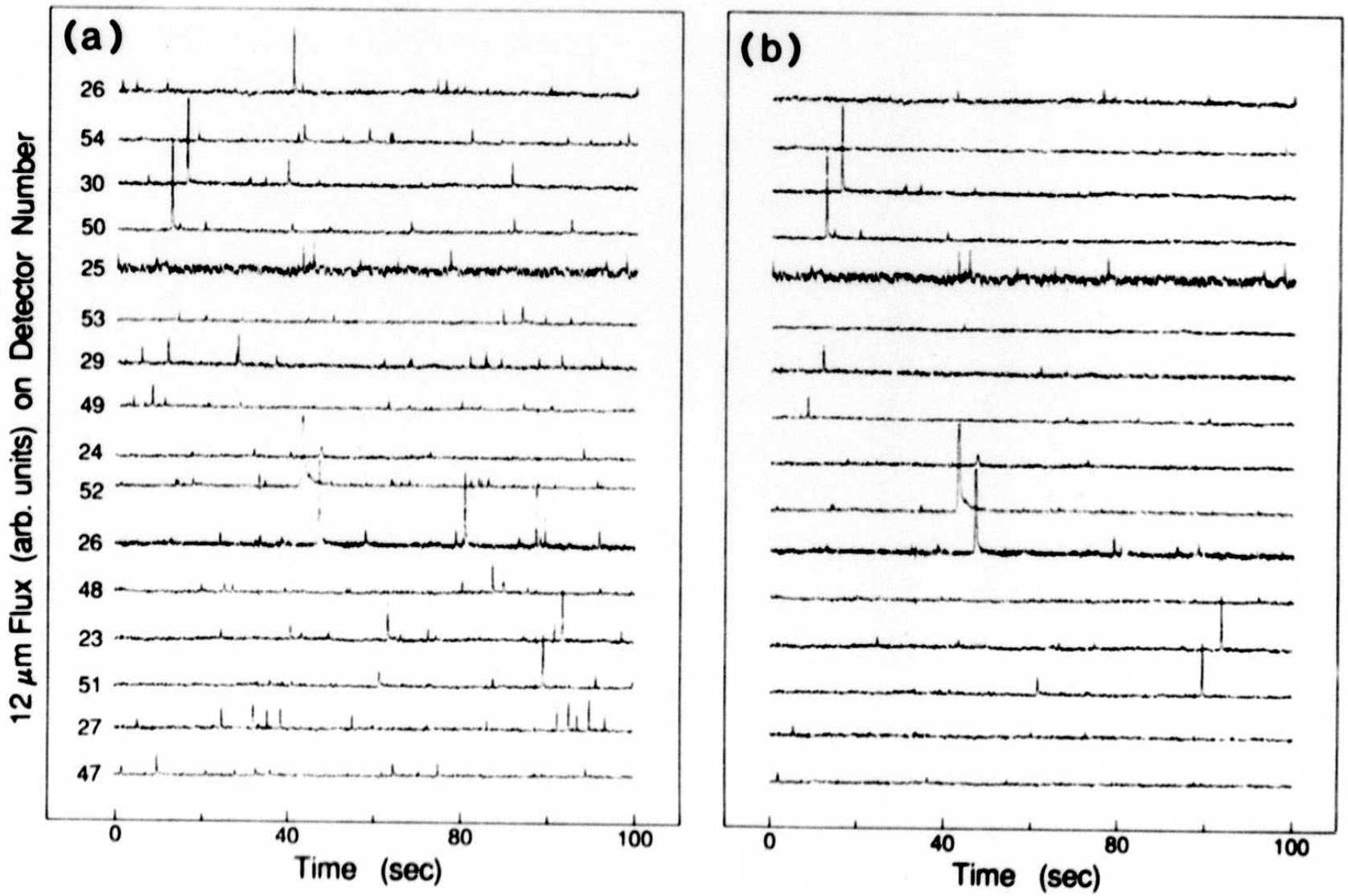

Figure II.C.2 Detector data at 12 μm a) before and b) after deglitching.

flakes, and orbiting debris, data with uncorrectable pointing errors, and other peculiarities. The anomalies list was compiled from various sources and is known to be incomplete. The list of anomalies removed is given in Appendix II.1.

C.3 Median Filtering and Smoothing

Baseline offsets, background, and low frequency noise were removed from the data using a median filter. The filter lengths, optimized for signal-to-noise performance as described below, were 23, 19, 17, and 15 samples at 12, 25, 60, and 100 μm, respectively. The baseline removed was the median of the points in the filter centered on the point in question. The filter excluded the central five points to avoid biasing the baseline when a source was centered in the filter. This filter was found to provide optimum signal-to-noise performance when combined with a smoothing filter to roll off the high frequency noise. The median filter was therefore preceded by a three-point smoothing filter which attenuated noise at frequencies above the point source bandwidth, and simultaneously reduced the effects of the data quantization (which was at a level of approximately 1 σ per data number in the original data streams) on baseline. The smoothing filter was a simple three-point convolutional filter with coefficients of 0.3, 0.4, 0.3 for all four wavelength bands. This filter combination was compared to the simple linear zero-sum filter used in Pointed Observation processing (see *IRAS* Pointed Observation Guide 1985). Signal-to-noise performance was improved by up to 20% over the linear filter (depending on the band), at a cost of occasionally curious behavior in confused areas (see Section III.A).

The median filter lengths were tuned to maximize sensitivity to point sources. The main criterion used to maximize sensitivity was maximizing reliability (while maintaining completeness) at absolute flux density levels. An indirect criterion used was maximizing the ratio of signal-to-median noise. Signal-to-noise is not necessarily a sufficient criterion by itself as the source extraction process may be affected by the two-dimensional spatial frequency content of the noise. Reliability by itself was not sufficient, due to uncertainties in its determination. Somewhat different techniques were used for tuning each wavelength band, as each band is unique in both source flux density distribution and noise, and each band is discussed separately.

Four plates were selected for the tuning process that were representative of the types of sky to be encountered in the processing. These plates cover various galactic latitudes and levels of cirrus contamination and are summarized in Table II.C.1.

Reliability at 12 μm was evaluated by measuring the fraction of sources associated with stars in the SAO catalog. Figure II.C.3a shows the association rates for plate 1280 as a function of filter length for minimum absolute flux density levels from 0.11 to 0.20 Jy.

83

TABLE II.C.1 Plates Used for Median Filter Tuning

Plate	Galactic Longitude	Galactic Latitude	Cirrus	Comments
1280	76.1	86.1	low	
1407	63.4	43.5	moderate	
50	309.1	-46.8	moderate	contains part of LMC
432	253.6	8.9	high	

Figure II.C.3b displays the median noise for each of the four test plates as a function of filter length. The median noise shows a consistent decrease with longer filters. Since the reliability usually is maximized at a filter length of 23 points, and the noise is within 2% of the minimum, a 23-point filter was chosen for 12 μm.

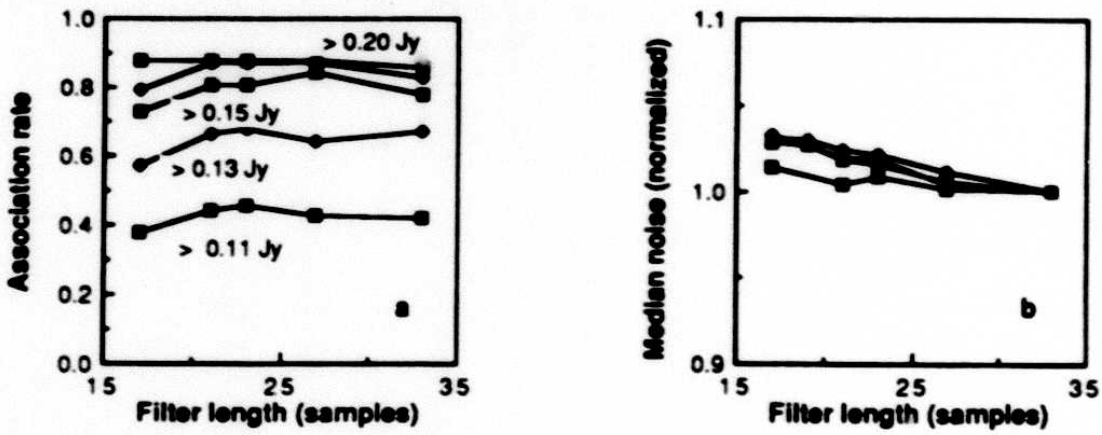

Figure II.C.3 The effect of filter length at 12 μm on a) association rate to SAO catalog, and b) median noise for 5 FSS plates. The median noise is normalized to the noise at a filter length of 33 points.

Reliability at 25 μm was more easily maximized by minimizing extractions having flux density only at 25 μm. Since stars are brighter at 12 μm and galaxies are brighter at 60 μm, essentially all extractions at 25 μm with no confirming flux density in an adjacent band are false. Figure II.C.4a displays the fraction of 25 μm-*only* extractions (with respect to total number of 25 μm extractions) above SNR ~5 as a function of filter length for plates 432 and 1280. Figure II.C.4b displays the median noise for all four plates as a function of filter

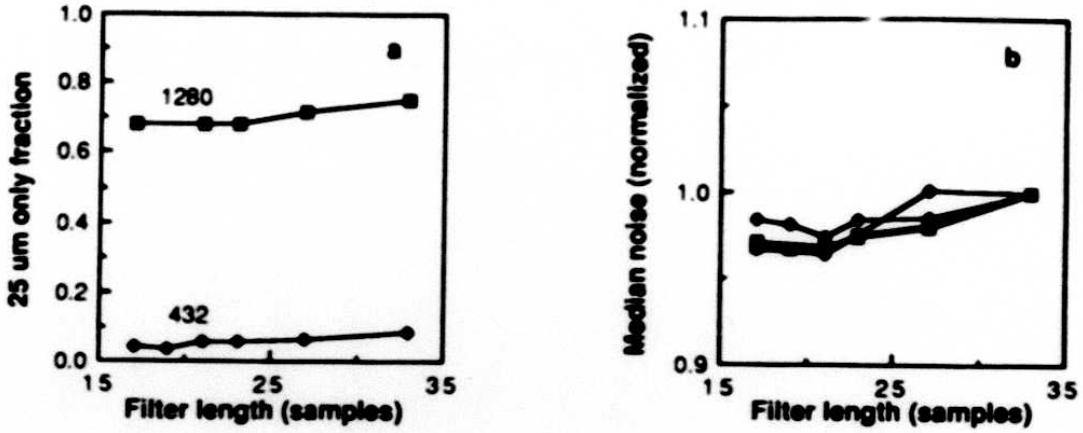

Figure II.C.4 The effect of filter length at 25 μm on a) reliability and b) median noise.

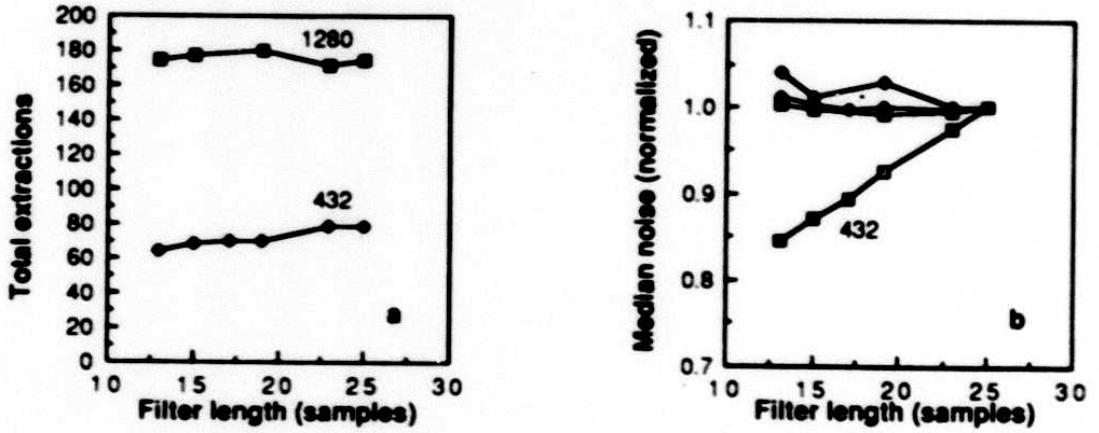

Figure II.C.5 The effect of filter length at 60 μm on a) reliability and b) median noise.

length. A filter length of 19 points was chosen at 25 μm, as the noise and unreliability are both minimized near this length.

Reliability at 60 μm was evaluated by measuring the total number of extractions over a given absolute flux density level as a function of filter length. If the flux density of true sources remains constant, an excess of extractions over a given absolute level will reflect an increase in false sources. Figure II.C.5a shows the total extractions vs filter length for an absolute flux density level near SNR = 5. This curve is shown for a low cirrus plate

(1280) and a high cirrus plate (432). For the low cirrus plate no obvious correlation with filter length exists, but for the plate contaminated with cirrus, contamination increases rapidly with filter length. Figure II.C.5b shows the noise as a function of filter length for all four test plates. The noise is a weak function of filter length and is minimized at a length of 17 points, except for the cirrus-infested plate 432, for which the cirrus is filtered out at shorter filter lengths. A 60 μm filter length of 17 points was chosen as the best noise compromise, due to exaggerated filter sidelobes for shorter filters.

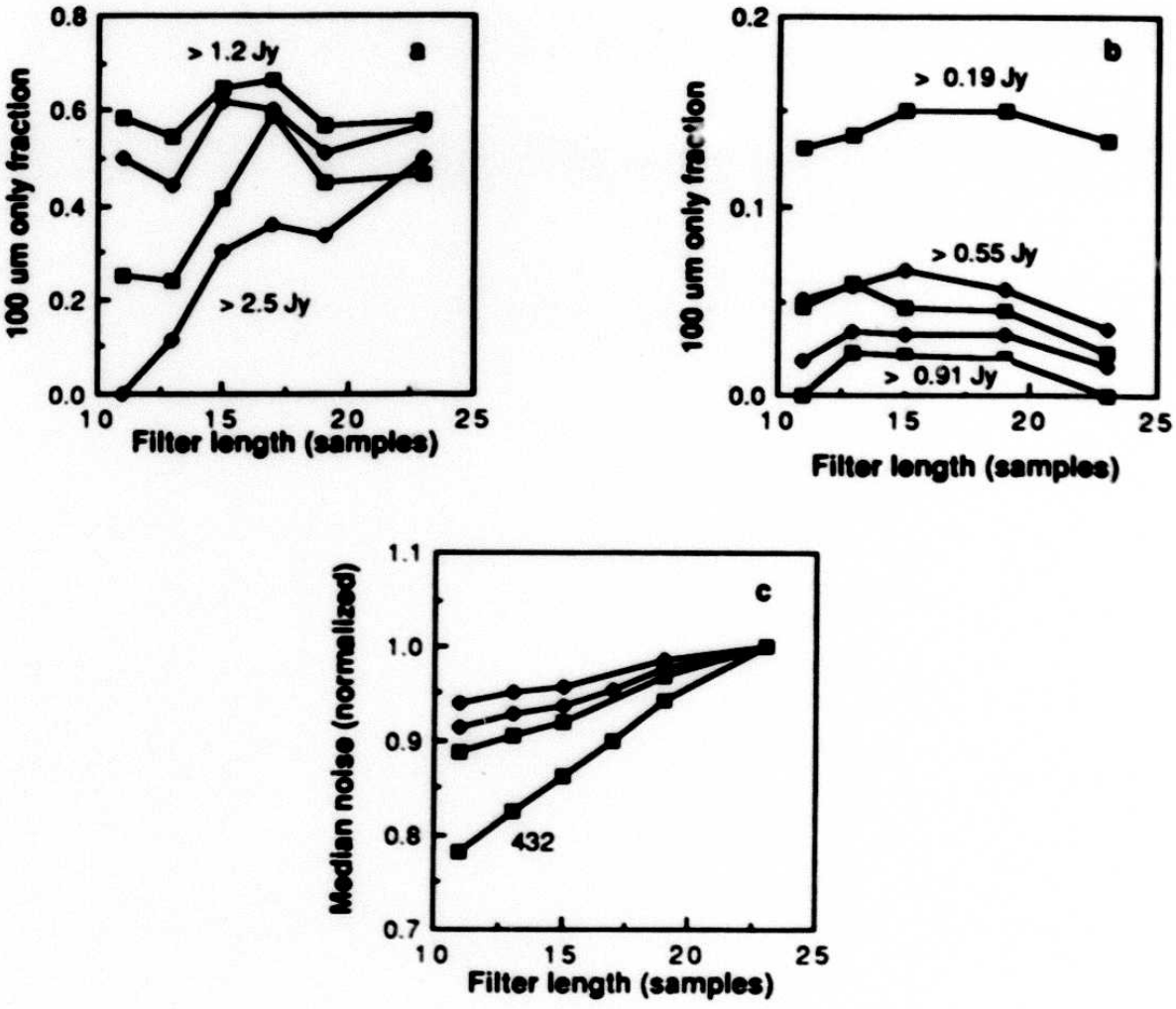

Figure II.C.6 The effect of filter length at 100 μm on a) reliability in plate 432, b) reliability in plate 1280; and c) noise for all four test plates.

The effects of infrared cirrus dominate at 100 μm, often manifested as sources detected at only 100 μm. The reliability at 100 μm was evaluated by examining the fraction of

86

Table II.C.2 Correction Factors for the Trimmed Noise Estimate

Total Samples	Samples Trimmed from Each End	Fraction Trimmed from Each End	Increase in Noise Due to Trimming	Trimmed Noise Estimate Correction Factor
4	0	.00	1.00	1.00
5	1*	.20	1.07	1.07*
6	1	.17	1.05	2.02
7	1	.14	1.04	1.86
8	1	.13	1.04	1.71
9	1	.11	1.03	1.62
10	1	.10	1.03	1.56
11	1	.09	1.03	1.50
12	1	.08	1.02	1.45
13	1	.08	1.02	1.41
14	1	.07	1.02	1.39
15	2	.13	1.04	1.77
16	2	.13	1.04	1.71
17	2	.12	1.04	1.66
18	2	.11	1.03	1.62
19	2	.11	1.03	1.58
20	2	.10	1.03	1.56

*All five samples were used for the noise estimate for this case.

extractions at 100 μm only exceeding a given absolute flux density level as a function of filter length. An excess of these extractions at a given flux density represents an increase in the number of spurious sources. Figure II.C.6a displays this fraction as a function of filter length for plate 432 for minimum flux density levels from 1.2 to 2.5 Jy. Figure II.C.6b shows the same quantity for plate 1280 for minimum flux density levels from 0.19 to 0.91 Jy. The fraction of 100 μm only extractions increases with filter length in both plates but less so in 1280, the plate with less cirrus. The number of extractions at 100 μm only in plate 1280 decreases at the longest filter lengths due to increased bandmerging of cirrus, which is in turn caused by the larger extent passed by the longer filter. Figure II.C.6c displays the noise for all four plates as a function of filter length. The noise is strongly correlated to filter length, regardless of the extent of cirrus contamination. The reliability and noise criteria suggest that the shortest filter is optimal at 100 μm. A 15-point filter was chosen over longer filters for these reasons, but was chosen over an even shorter filter to attenuate sidelobes and to include more points for a more robust baseline estimate.

C.4 Binning and Estimation of Flux and Noise

The conditioned and filtered data were mapped t plate coordinates using a focal plane geometry model (see Appendix II.2) and the boresight pointing data. Detector center positions were computed in pixel coordinates at one-second boresight samples and linearly interpolated. The detector data were binned into pixels under a cross-scan mask equal to 96% of the cross-scan detector aperture. The data were resampled in-scan to pixel centers using linear interpolation. The pixel sizes are 0.25′ square at 12 and 25 μm, and 0.50′ square at 60 and 100 μm. These pixel sizes are approximately equal to the in-scan detector sample spacing, except at 100 μm, where the pixel size is smaller by a factor of two to maintain sufficient sampling in cross-scan. Only 57 of the 62 detectors in the focal plane were used in the FSS processing, as three were dead on arrival in orbit (detectors 17 and 20 in band 2, and 36 in band 3), and two were excessively noisy (detector 25 in band 1 and 42 in band 2).

Once all the survey data for the band were binned, flux density and noise estimates were computed for each pixel using a trimmed average estimator (Tukey 1962). The fraction of data trimmed was optimized in conjunction with the other data filtering and conditioning. The data were trimmed by discarding approximately 10% of the samples at each of the highest and lowest extremes. The flux density was estimated by the mean of the remaining central samples. The noise was estimated from the trimmed samples and corrected for the increase in noise in the estimate due to trimming the flux density estimate (Wright 1984) and for the effect of truncating the distribution during the computation of the sample variance (Melnyk 1986).

The flux density and noise estimates, $\hat{f}$ and $\hat{n}$, are computed as follows:

$$\hat{f} = \frac{1}{N}\left(\sum_{1}^{M} f_i - \sum_{1}^{K}(f_i + f_{M+1-i})\right) \qquad (II.C.1)$$

$$\hat{n}^2 = C^2(M)\frac{S - \hat{f}^2 N_s}{M(N_s - 1)} \qquad (II.C.2)$$

where M is the total number of samples, K is the number of samples trimmed from each end for the flux density estimate, f_i is the filtered sample i, and $C(M)$ is the trimmed noise estimate correction factor given in Table II.C.2. N is the number of samples averaged, N_s is the number of samples used in the noise estimate, and S is the sum-squared of the trimmed samples:

$$N = M - 2K \qquad (II.C.3)$$

$$N_s = M - 2L \qquad (II.C.4)$$

$$S = \sum_{1}^{M} f_i^2 - \sum_{1}^{L} (f_i^2 + f_{M+1-} \qquad (III.C.5)$$

where L is the number of samples trimmed for the noise estimate and is not equal to K when $M = 5$ (see Table II.C.2).

The noise corrections were made based on the actual quantized trim fraction for each pixel given the number of measurements for that pixel. Noise corrections were made under the assumption that the trimmed distribution is equivalent to the distribution remaining if the untrimmed distribution had been Gaussian. This assumption was verified by measuring the width of the flux density distributions for high galactic latitude plates, where the distribution was dominated by noise. The theoretical effect of the trimmed average on the dispersion in the estimate as a function of percent trimmed on each end is shown in Figure II.C.7 for several distributions. The increase in standard deviation in the estimate is on the order of 3% for a Gaussian distribution when 10% is trimmed from each end. For the *IRAS* data the effective noise was minimized at that fraction trimmed. At smaller trim fractions, undeglitched radiation hits increase the fraction of false sources; whereas at higher fractions trimmed, the Gaussian noise dominates. The measured noise vs. fraction trimmed is shown in Figure II.C.8 for a high galactic latitude plate. The noise shows a clear minimum at 12 to 60 μm. The dispersion at 100 μm continues to fall somewhat due to a component coming from the correlated structure of the infrared cirrus in the field. The fraction trimmed was optimized by minimizing the noise and by minimizing the fraction of false sources as a function of absolute flux density level at representative areas of the sky.

The noise estimation strategy was modified for low counts to improve the stability of the noise estimate by including some of the trimmed samples in computing the local noise. At the trim fraction used (10%), this affected only pixels with exactly five measurements. For those pixels, the highest and lowest samples were trimmed from the flux density estimate, but were included in the noise estimate. This necessitated using separate factors to correct the computed noise for the effect of trimming the mean and for the effect of trimming the population standard deviation. The number of samples used in the flux density and noise estimates and the total noise correction factor as a function of total number of samples are shown in Table II.C.2. Although a flux density estimate is given for all pixels with one or more counts, no noise estimate is given for pixels with fewer than four counts. The algorithm accumulated the sum and sum squared for each pixel, and maintained the extrema, which were backed out of the sums in the estimation step. An approximation to the trimming was used at high counts, as it was impractical to store more than six ex-

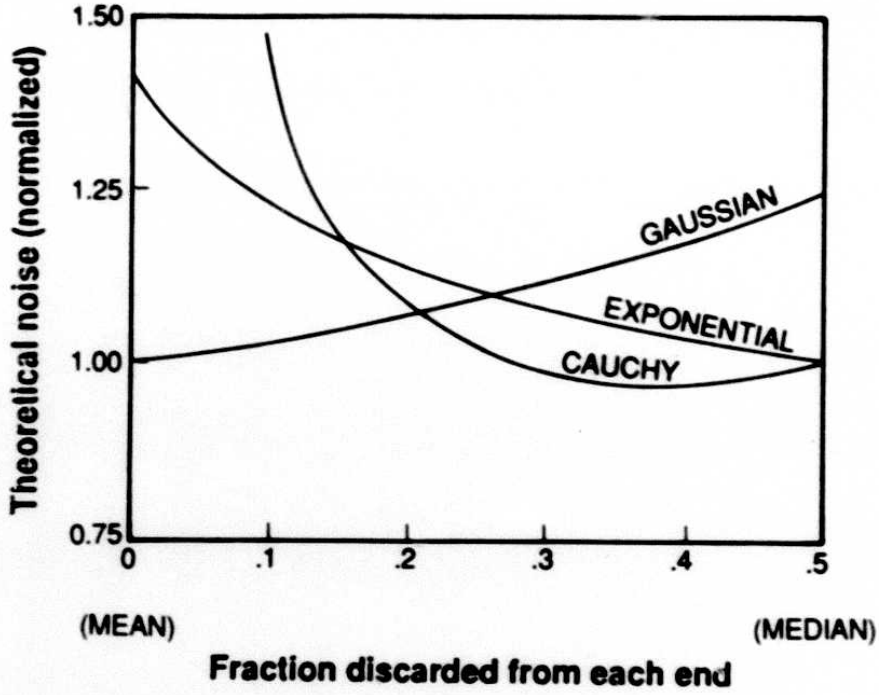

Figure II.C.7 Theoretical dispersion vs trim fraction.

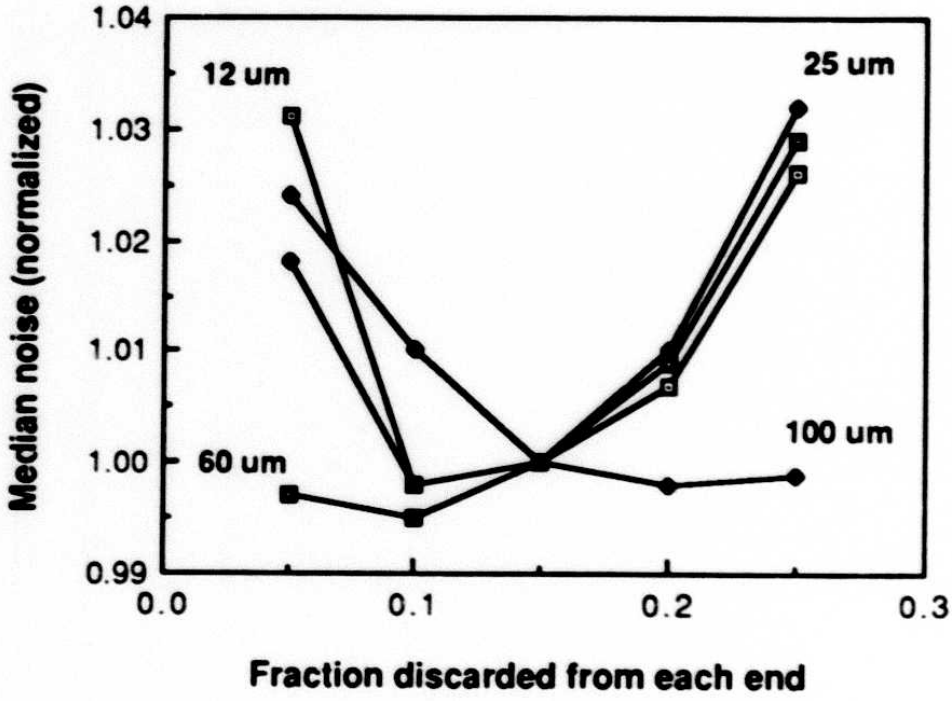

Figure II.C.8 Measured noise vs. trim fraction.

trema per pixel. When the number of counts exceeded 30, more than six samples needed to be trimmed. Since only six buffers were available the two most extreme samples were periodically backed out and the six extreme values of the remaining set were maintained. This modified strategy was found to increase the noise by less than 1% in the worst case (areas with very high coverage), and thus may be neglected.

C.5 Point Spread Function

The point spread function for the Faint Source Survey plates is complex due to the rectangular shape of the detectors and the variation in scanning angles during the *IRAS* survey. In addition, the point-spread function may not be used in the traditional linear sense since the non-linear median filter invalidates the superposition principle. The image of an isolated point source (the point spread function) varies from nearly rectangular at the ecliptic plane to an X-shape near the ecliptic poles. The point spread function also varies on the scale of arc minutes due to the overlap pattern of the detectors which covered the point. Figure II.C.9 shows a point spread function at low ecliptic latitude and a point spread function near the north ecliptic pole for each of the four wavelength bands.

To understand the point spread function, it is necessary to understand the *IRAS* focal plane and the *IRAS* survey coverage. The focal plane array of survey detector apertures is shown in Figure II.C.10. Because the detector apertures are rectangular, they result in a basically rectangular response function. The aspect ratio varies from approximately 6 at 12 μm to 1.7 at 100 μm. Each wavelength band has two modules of detectors which provide redundant coverage as the sky is scanned (see also Section II.D.2). The two modules are offset by half a detector in the cross-scan direction. This configuration produces the cross-scan point spread function shown in Figure II.C.11 from a single focal plane scan, assuming all detectors traversed are operational. Four full size detector apertures from each module are shown above, and the cross-scan point spread function resulting from the illustrated point source passage is shown below. The coadded signal in each overlap zone is the average of the contributing detector signals. Note that a single scan will produce essentially the same point spread function for a source anywhere within a given 2′ cross-scan detector overlap zone. The point spread function within a plate is due to a combination of single scan profiles from separate scans.

The *IRAS* spacecraft scanned the sky with the solar elongation held constant, and thus always crossed the ecliptic with the scan direction oriented perpendicular to the plane. This caused the detectors, and thus the point spread function, to be oriented with their long axis parallel to the plane when near the ecliptic. The situation becomes more complicated as the ecliptic poles are approached. In most areas of the sky, the coverage is dominated

91

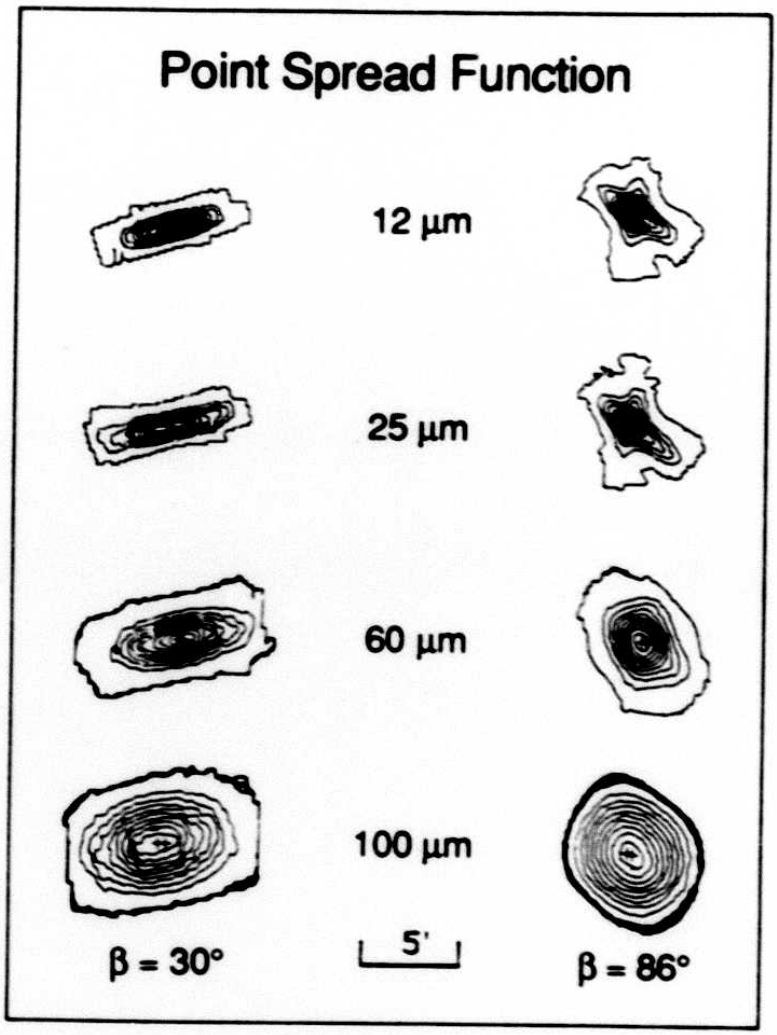

Figure II.C.9 Point spread function vs. ecliptic latitude.

by two basic focal plane orientations, resulting in an X-shaped point spread function. In some areas, such as at the ecliptic poles, many focal plane orientations contribute, tending to circularize the point spread function. Due to the foregoing complications, the source extraction for the Faint Source Survey used a variable template as described in Section II.D. The flux densities estimated from the template fit were not used for the FSC. See Section II.D for uses of the templates.

The positional uncertainty for high SNR sources in the Faint Source Survey is dominated by the effect of the sampling on the point spread function. As noted above, the position of a single band source is localized to 2′ by a single focal plane passage. This position is further localized by successive scans of the focal plane. Modeling the offset be-

12

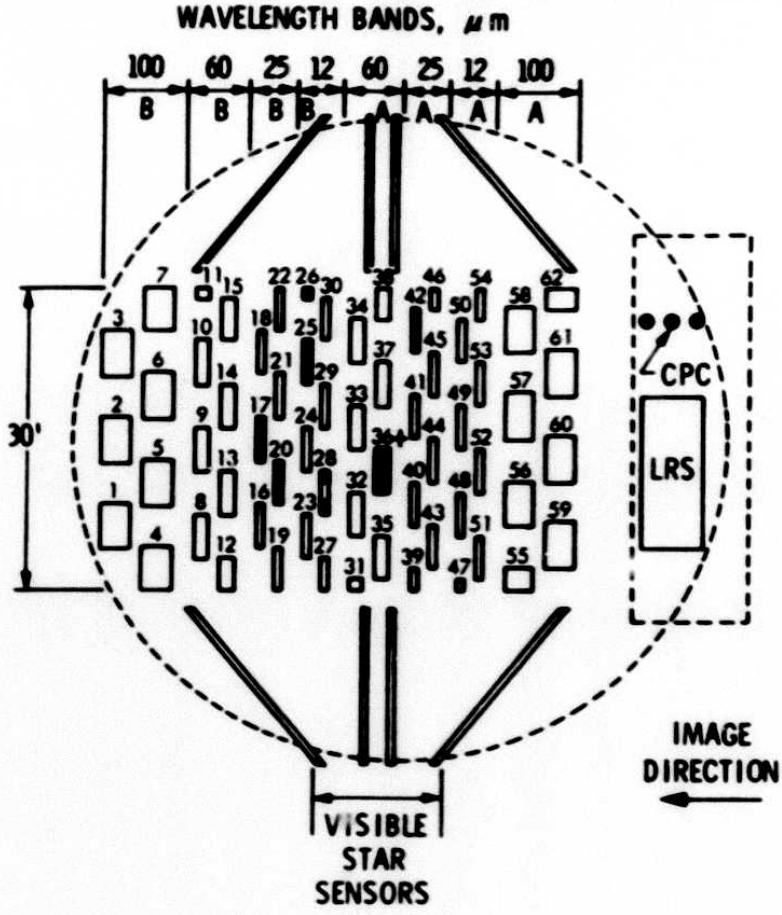

Figure II.C.10 A schematic drawing of the *IRAS* focal plane. The numbered rectangles in the central portion each represent the field of view of a detector, filter and field lens combination. The image of a source crossed the focal plane in the direction indicated. The filled-in detectors were inoperative while the cross-hatched detectors showed degraded performance during the mission.

tween successive scans as a uniformly distributed random variable, one would expect the position uncertainty to reduce as the square of the number of scans. This simple model is reasonably accurate for the position estimation technique used for the FSC. For the *IRAS* Point Source Catalog (PSC), elaborate modeling of the probability density functions and the measured overlap of the detections was used to compute positions and uncertainties in an optimum manner (see the *Main Supplement*). Since the individual detections are not available when coadding the data, the Faint Source Survey relies on the centroid of the composite point spread function to provide position information. Sampling effects analogous to the stochastic model described above cause the cross-scan point spread function, and thus the computed positions, to vary. At low signal-to-noise, position information

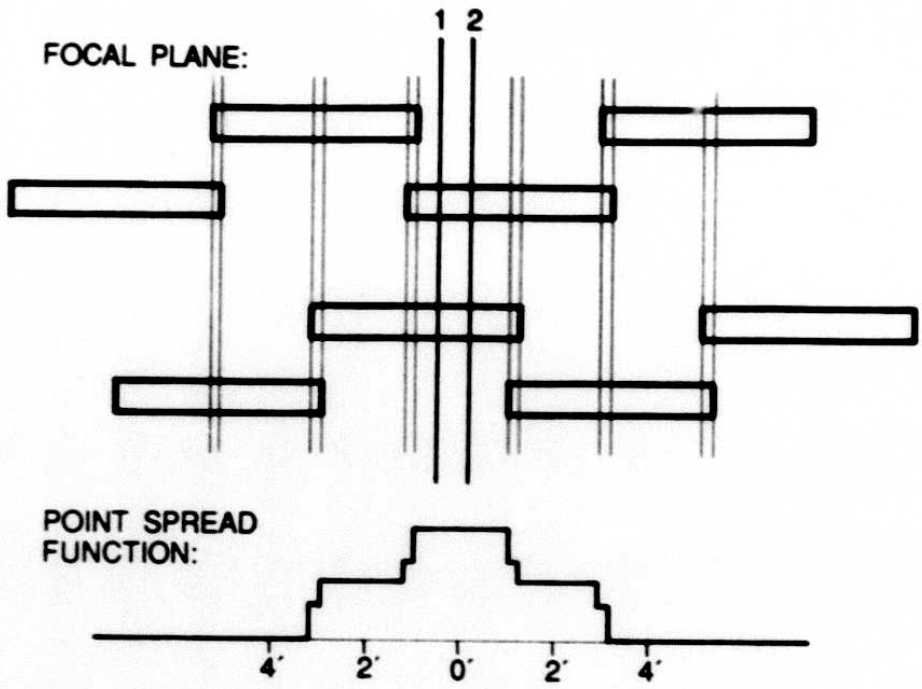

Figure II.C.11 Cross-scan point spread function resulting from a single focal plane scan. Point source tracks at 1 and 2 result in the same cross-scan signature.

is dominated by detector noise. The FSC position accuracies compare favorably with the more complex technique used in the PSC at low signal-to-noise and are discussed in Section III.E.

C.6 The Focal Plane Model

The focal plane model used in the coadd processor is given in Appendix II.2. The center positions relative to the telescope boresight and the cross-scan mask used for coaddition are given for each of the 62 detectors. Appendix II.2 also gives the timing offset used for the first sample in the frame for each of the 62 detectors. These timing offsets compensate for the commutation delay, the time delay induced by the on-board electronics, and a small additional offset introduced in each band to compensate for an experimentally-determined mean position offset. The experimentally-determined offsets were based on position error statistics from pre-production tuning runs for 13 FSS plates. The focal plane model used for the FSS was optimized to give best position estimates for extracted sources (using flux-weighted centroids as position estimators, see Section II.E.3 for details). This focal plane slightly differs from the one used by the PSC which used another estimator for position (based on *single-scan* position estimators).

D 10015

D. Template Generation and *IRAS* Focal Plane Characteristics

D.1 Introduction

As part of the FSS processing, templates were generated for the expected point spread function for every plate. Knowing the point spread function at a point, it was possible to fit the ***observed*** data to the template and compute the correlation coefficient of the fit (see Section II.E.4). The template width along its major and minor axes gave the beam size which was used to estimate positional uncertainties for sources (see Section II.F.3).

Because the template profiles contained high frequency variations along their major axes over a single plate (see Section II.D.4), more stable averaged templates were used for the computation of the correlation coefficients for each detection in the database. A lower than expected value of correlation coefficient could be used to recognize extended or unresolved sources.

To make these templates, the characteristics of the *IRAS* focal plane needed to be assessed accurately, and we needed to synthesize the coadded image of an arbitrarily located point source. To synthesize the image, detector response functions were needed. Sections IV.A.1-4 of the *Main Supplement* qualitatively discuss the profiles of focal plane detectors. For FSS processing, a more accurate and detailed map of the focal plane was constructed.

The data from a set of 32 ***Additional Observations*** (AOs) of the infrared-bright planetary nebula, NGC 6543, were analyzed and a set of 59 ***detector response functions*** were derived (Moshir 1986). Unfortunately, in the infrared NGC 6543 may be slightly extended and thus may not be an ideal point source with which to construct the detector response functions. Also, the AOs were done at one half of the survey rate, which introduced a slight flattening of the top of detector responses compared to survey scans. Because the various levels of smoothing applied during coaddition (see Section II.C.3) attenuated these differences, for the purposes of FSS processing these issues were ignored (also see the example of Arp 220 in Section II.D.4). These issues must be considered in any other use of these detector response functions.

The resulting functions allowed us to reconstruct the point spread function for any arbitrarily located point source. Furthermore, analysis of these functions indicates that the non-uniformity of focal plane detectors results in a predictable photometric uncertainty. Thus the manner of scanning a point source across the focal plane determines how well the position and flux density of the coadded source could be reconstructed.

One of the steps of FSS processing created a set of synthesized point spread functions for each plate. To do this, a set of 16 positions, covering the plate uniformly, were

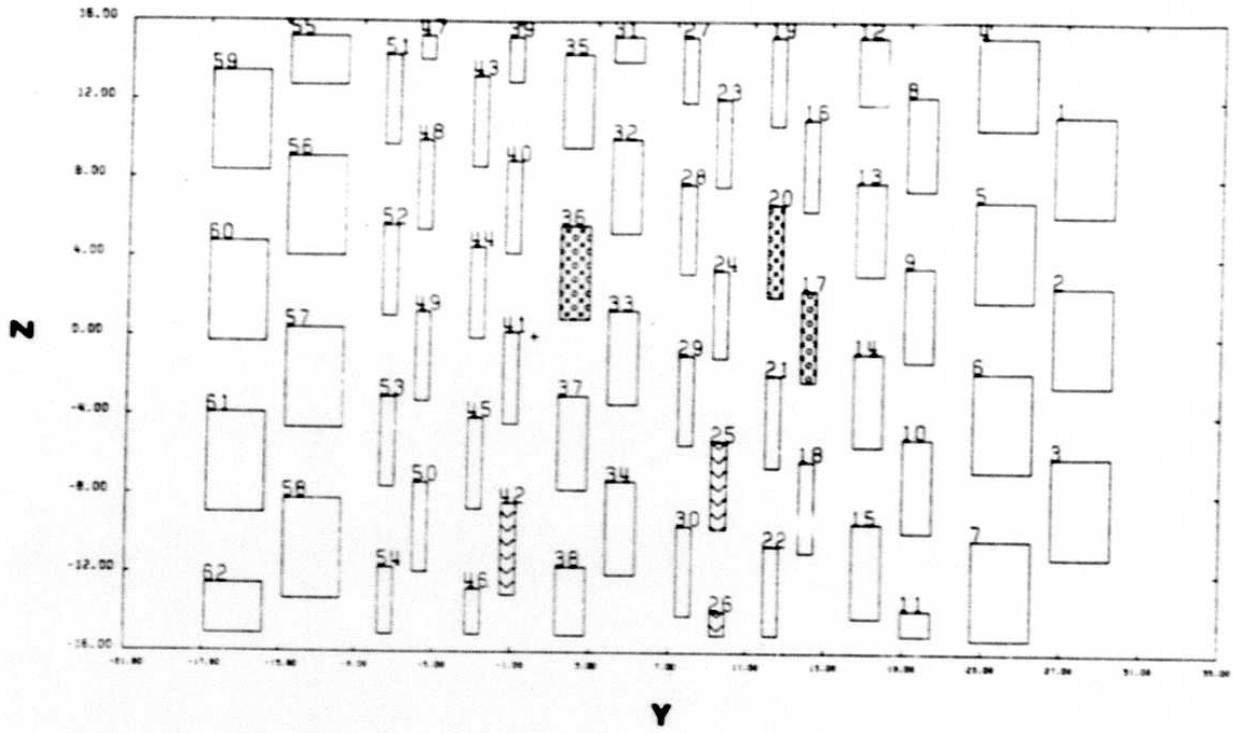

Figure II.D.1 ***IRAS*** **focal plane, geometric view, scale in arcminutes.**

chosen and the point spread functions were synthesized at each of those points. These synthesized point spread functions are referred to as templates and were used both by the source extractor and the bandmerger. The source extractor used the templates to compute the two-dimensional correlation coefficients. The bandmerger used the effective template extent to compute positional uncertainties; the orientation and size of templates dictate the region within which a given *seed* in one band searched for *mergers* in other bands.

In Section II.D.2 the most recent results on detector response functions are presented; in Section II.D.3 it is shown how the nonuniformity in detector cross-scan response affects photometric uncertainties; the method of template creation, their general properties, and their eventual use by the extractor is discussed in Section II.D.4; and template use by the bandmerger is discussed in Section II.D.5.

D.2 Detector Response Functions

The *IRAS* focal plane consisted of 8 modules (each consisting of 7 or 8 detectors), two modules per spectral band, labeled A and B. As a point source image entered the focal plane, in each spectral band it was first seen by the A module and seconds later by the B module; more information on these modules can be found in Section II.C.4 of

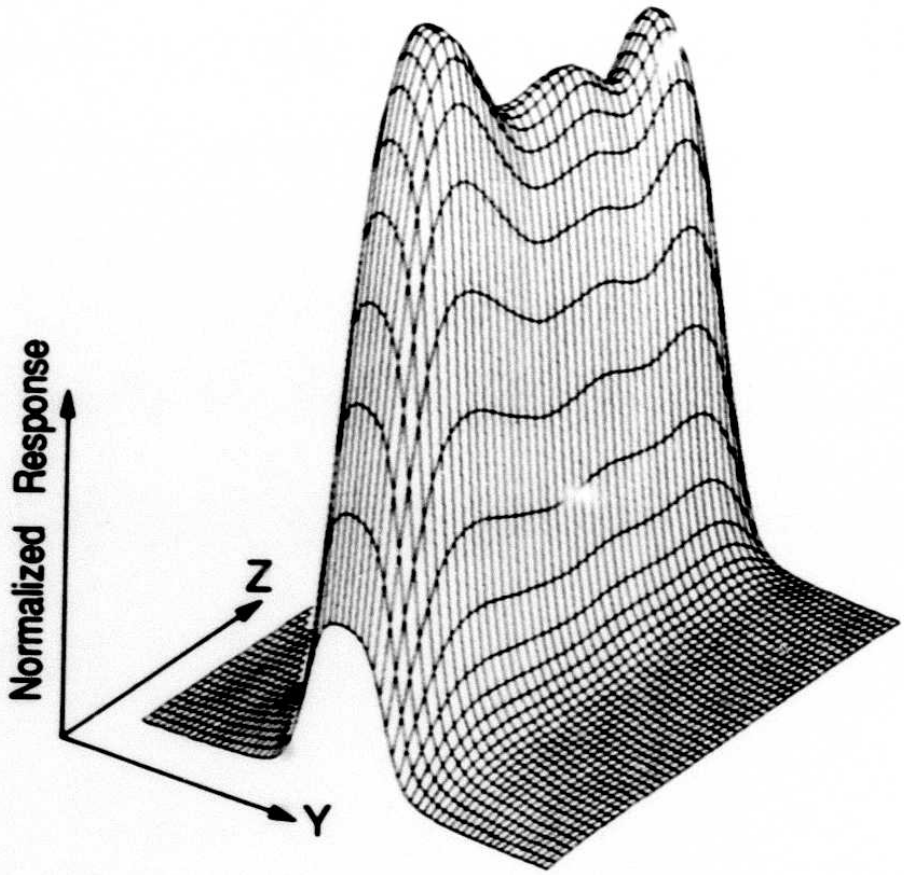

Figure II.D.2 Detector response function, detector 23.

the *Main Supplement*. Figure II.D.1 gives the physical set up of the *IRAS* focal plane in which several anomalous detectors have been marked. Detectors 17 and 20 at 25 μm and detector 36 at 60 μm were dead. Compared to other detectors at 12 μm, detector 25 was approximately two to three times noisier, and detector 26 displayed two to three times more noise than normal during the periods February 2-10, 1983 and March 16-June 6, 1983 for unknown reasons; detector 42 was generally two to three times noisier than other detectors at 25 μm. Detector 28 at 12 μm showed severe response attenuation over half of its cross-scan extent.

For each of the 59 active detectors within the focal plane a two-dimensional map of detector responsivity has been derived. With these maps it is possible to simulate the *Calibrated Raw Detector Data* (CRDD) stream from each individual detector as a point source is scanned by the focal plane. A sample of these two dimensional detector response

D 10015

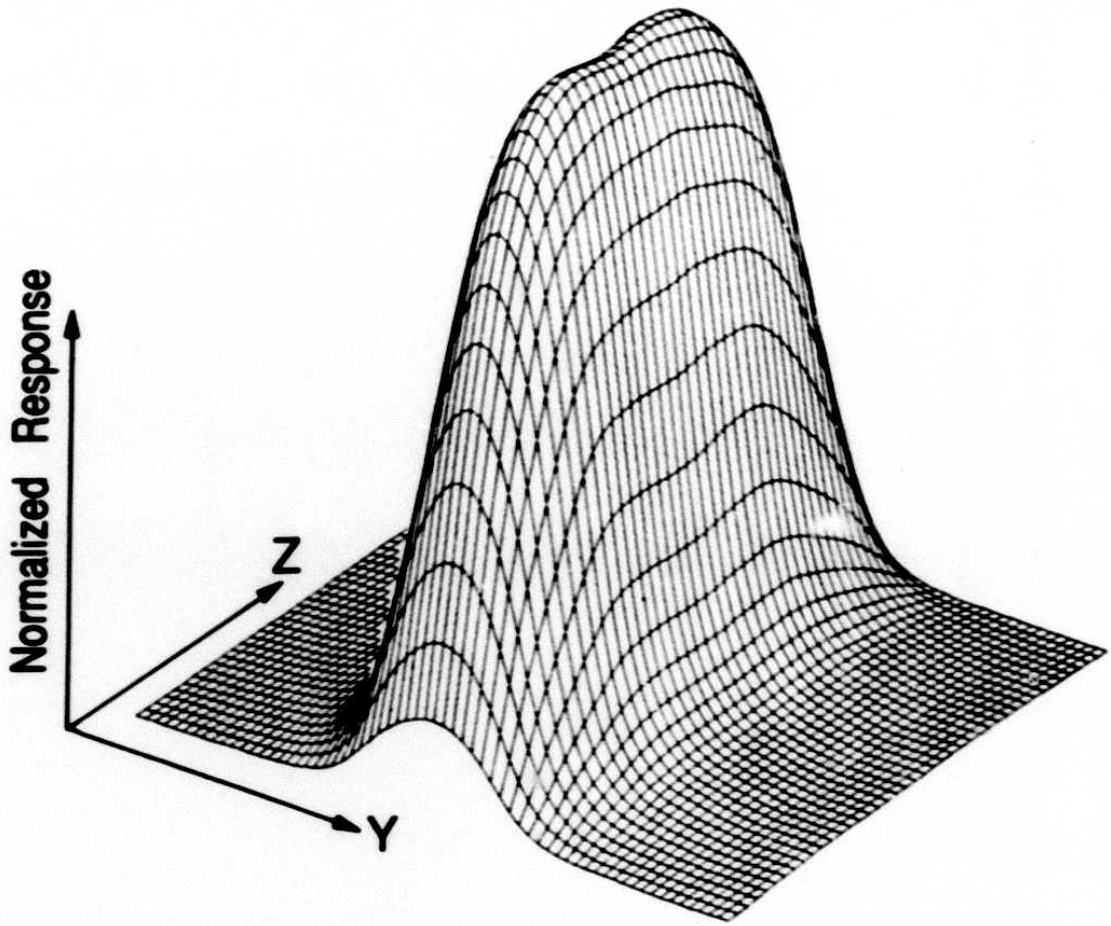

Figure II.D.3 Detector response function, detector 37.

functions is seen in Figure II.D.2 for detector 23 at 12 μm and in Figure II.D.3 for detector 37 at 60 μm (notice differences from the same profiles in Figures IV.A.3.2 and IV.A.3.3 in the *Main Supplement*). The responsivity of the focal plane as a whole is displayed in Figure II.D.4. Note that in this image the quarter-size detectors are effectively round.

New solid angles subtended by each detector have been calculated based on these 59 detector response functions and the logic involved in flux density calibration. These refined solid angles differ from those quoted in Table IV.A.1 of the *Main Supplement*. Compared to the *Main Supplement*, the average of new effective solid angles for *full-size* detectors has increased by 14%, 8%, and 6% at 12, 25, and 100 μm, and decreased by 3% at 60 μm. The complete list of updated effective solid angles is displayed in Table II.D.1. These refinements in our knowledge of detector responsivity have been applied to the latest calibration of *IRAS* data. Although these refinements have no impact on FSS

98

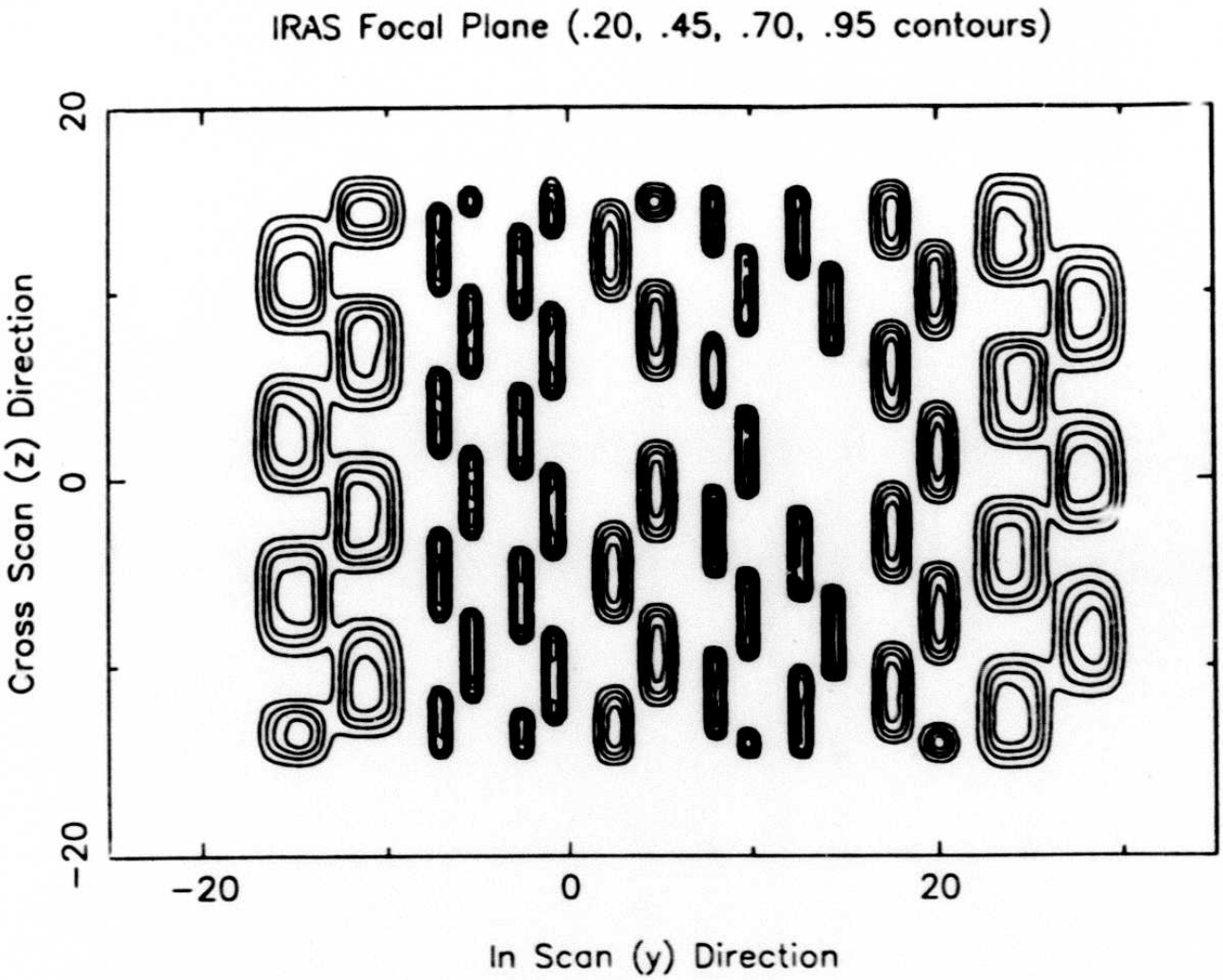

Figure II.D.4 ***IRAS*** **focal plane, detector response view, scale in arcminutes. (Figure provided by K. Young.)**

flux density calibration because FSS processing is not concerned with the absolute sky brightness, they are given here for the sake of completeness. These changes have produced noticeable improvements in images which retain the absolute sky brightness.

To complete the discussion of detector response functions we consider the cross-scan responsivity of the 8 modules comprising the focal plane. Detectors in each module had a slight overlap in the cross-scan direction. Proceeding from a detector center towards its edge, the responsivity begins to fall and soon an overlapping detector's output begins to rise. This mechanism caused a nonuniform cross-scan response for each module in the focal plane. In Figure II.D.5 this cross-scan response variation is seen for modules A and B at 12 and 25 μm, and Figure II.D.6 displays the 60 and 100 μm cross-scan responsivities for

99

Table II.D.1 Updated Effective Detector Solid Angles

Band	Detector No.	Ω [10^{-7} sr]	Detector No.	Ω [10^{-7} sr]
100 μm	1	14.1	55	7.9
	2	13.7	56	13.3
	3	12.9	57	14.0
	4	13.1	58	12.9
	5	13.2	59	14.0
	6	13.2	60	13.8
	7	13.6	61	14.2
			62	6.8
60 μm	8	6.10	31	1.97
	9	6.04	32	6.40
	10	6.07	33	6.32
	11	1.92	34	6.25
	12	4.85	35	6.36
	13	6.10	36	-
	14	6.19	37	6.37
	15	6.56	38	4.84
25 μm	16	3.39	39	1.82
	17	-	40	3.50
	18	3.46	41	3.44
	19	3.40	42	3.48
	20	-	43	3.50
	21	3.48	44	3.45
	22	3.38	45	3.46
			46	1.78
12 μm	23	3.21	47	0.89
	24	3.22	48	3.31
	25	3.17	49	3.22
	26	0.92	50	3.29
	27	2.41	51	3.25
	28	2.95	52	3.19
	29	3.25	53	3.24
	30	3.25	54	2.45

modules A and B. There is a gap in cross-scan responsivity of module B at 25 μm due to dead detectors 17 and 20, and a gap in module A at 60 μm due to dead detector 36. The large variation seen at cross-scan location 5.5′ in module B at 12 μm is due to detector

100

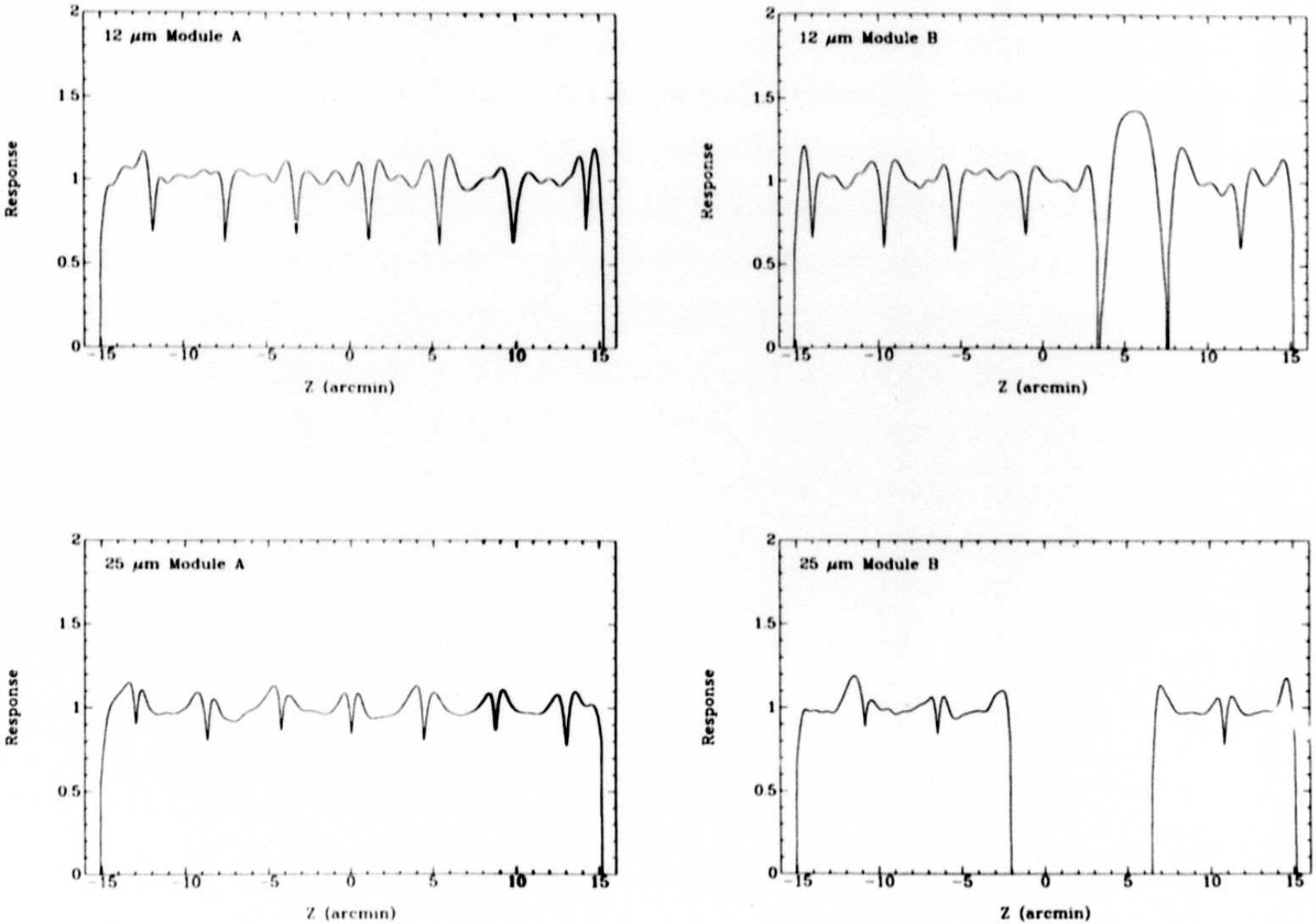

Figure II.D.5 Normalized cross-scan responsivity of modules A and B, at 12 and 25 μm.

28 which had a degraded cross-scan response. In these figures the normalization of each detector is such that a source of flux density of unity will give the indicated response. This normalization corresponds to the method of point source flux density estimation employed by the *IRAS* Point Source Catalog (PSC) processing.

D.3 Detector Responsivity and Photometric Uncertainties

Figures II.D.5 and II.D.6 indicate the inherent flux density uncertainty associated with an infinitely bright source detected only a finite number of times. If a given source were scanned N times, it would be observed N times by module A and N times by module B, resulting in flux density measurements f_i^A, and f_i^B, $i = 1, \ldots, N$ ($f^{A,B}$ being samples taken from cross-scan responsivity curves of Figures II.D.5 and II.D.6). The quoted flux density would then be $f = 1/(2N) \sum_{i=1}^{N} (f_i^A + f_i^B)$. The variable f could be considered as a random deviate with a specific distribution function $\phi(f/f_0)$ which in the limit of N tending to infinity would approach a delta function $\delta(f/f_0 - 1)$ with f_0 being the actual flux density of the source. For typical values of N ($\approx 4 - 8$) encountered during the *IRAS* mission, a Monte Carlo simulation of the above measurement process yields flux density dispersions of typically 4%. These dispersions for the case N=6 are given in Table II.D.2. The distribution function $\phi(f/f_0)$ has been computed through numerical simulation for the N=6 case, and can be seen in Figure II.D.7. In practice this responsivity dispersion effect is combined with the noise in the detectors (both temporal and spatial noises, see Section III.A.2) given by a distribution function $P(\xi)$. As a consequence the *experimentally observed* flux density distribution function is the convolution of the two distributions, $\int \phi(f/f_0 - \xi) P(\xi) \, d\xi$. For bright sources the ϕ distribution dominates the flux density uncertainties; for fainter sources the ϕ distribution ceases to matter.

Table II.D.2 Bright Source Photometric Dispersions, N=6 Scans

	12 μm	25 μm	60 μm	100 μm
$\sigma(\phi)$	4%	2.7%	4.5%	4.3%

D.4 Template Generation

To synthesize the predicted point spread function at any point, the hypothetical point was scanned across the focal plane using the telescope pointing history. In Figures II.D.8 and II.D.9 the focal plane crossings of two arbitrarily chosen points are shown, one at the North Galactic Pole (ecliptic latitude of 30°) and another at the North Ecliptic Pole. In the first case there are only a handful of scans, whereas in the second case the focal plane

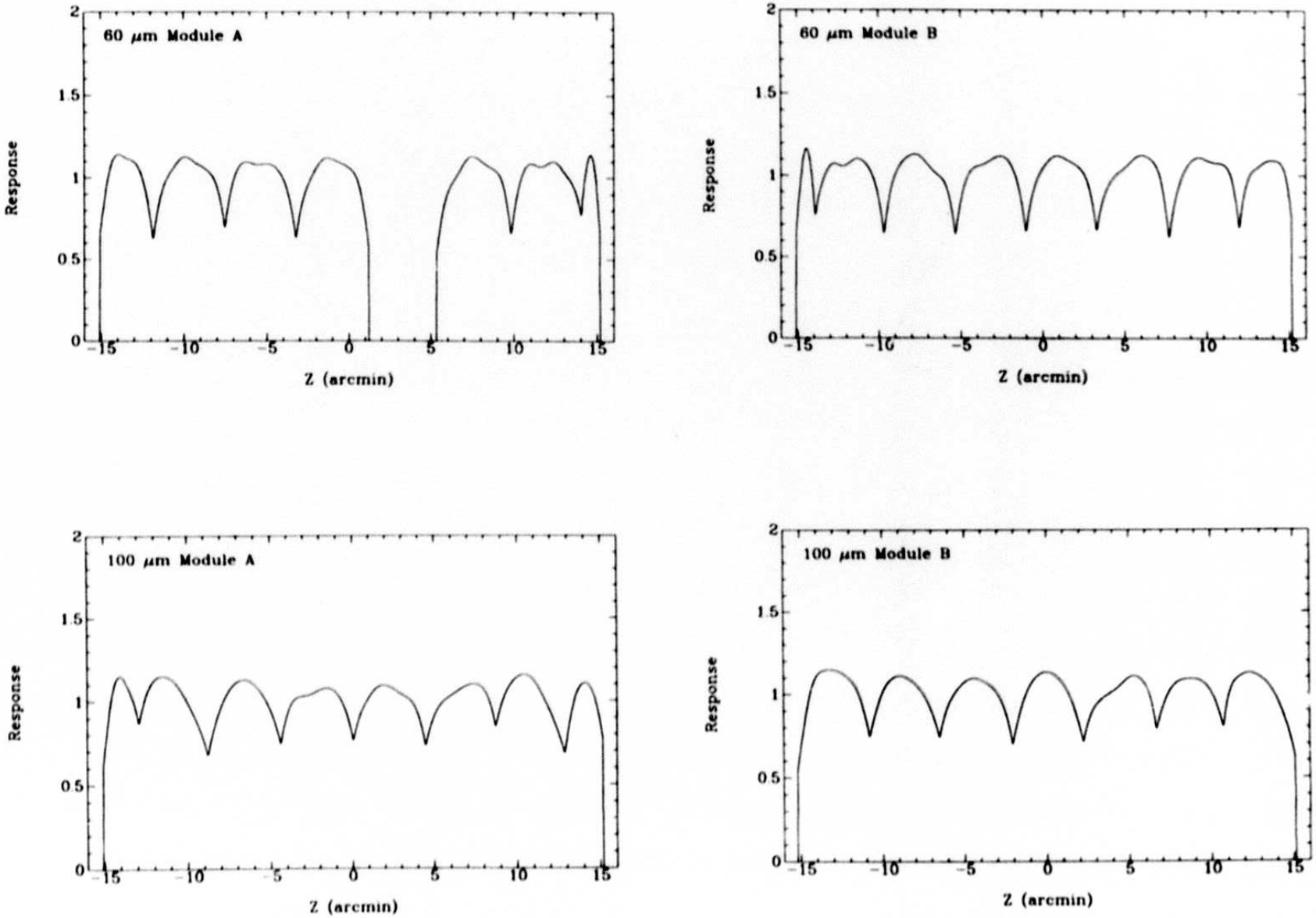

Figure II.D.6 Normalized cross-scan responsivity of modules A and B, at 60 and 100 μm.

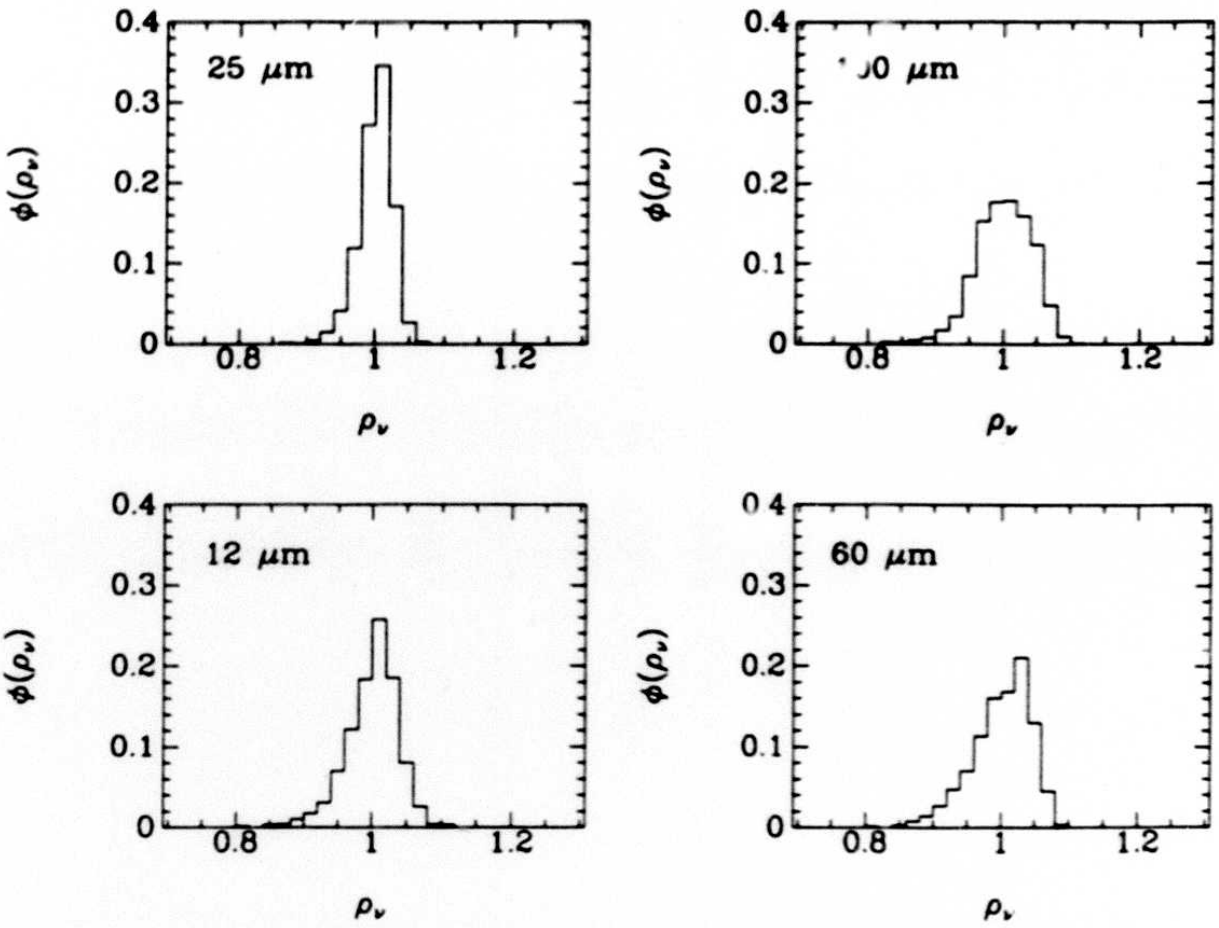

Figure II.D.7 Photometric distribution function $\phi(\rho_\nu)$, where $\rho_\nu = f_\nu/f_0$, N=6 scans.

is densely covered (due to convergence of spacecraft orbits at ecliptic poles, see Section III.B of the *Main Supplement*).

The information from pointing history and response functions was used to synthesize a set of CRDD streams. The synthesized data were processed by the coaddition software and a synthesized point spread function generated.

Comparisons have been made between the synthesized point spread functions and the actual *observed* point spread functions. They show close agreement between the synthetic and observed point spread functions. As one example the point spread functions for Arp 220 were computed using the actual data taken during the mission and also using the simulated data. The results at 60 μm are shown in Figure II.D.10. The in-scan and cross-scan profiles show impressive agreement between the observed and synthetic data.

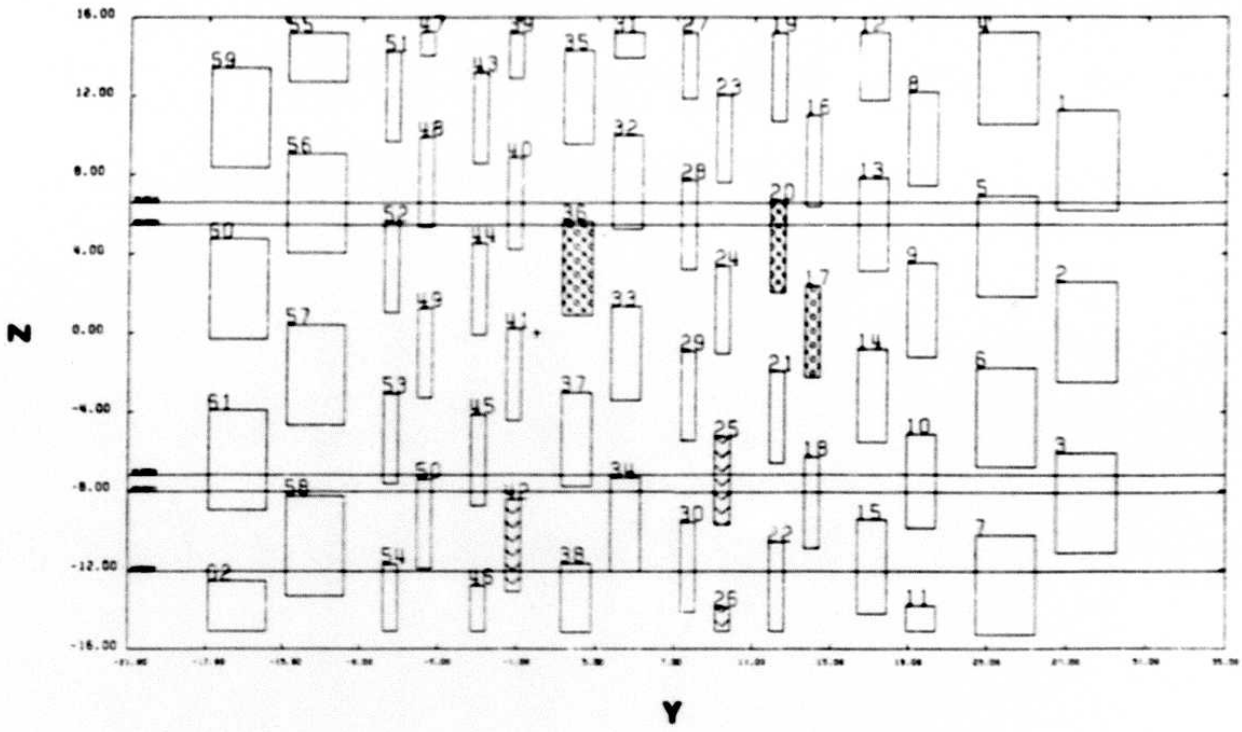

Figure II.D.8 Focal plane crossings at the North Galactic Pole, $\beta \approx 30°$, scale in arcminutes.

Furthermore, the widths of profiles (a measure of the physical extent of a source) are within 1-2% of each other.

Sixteen templates were generated for each plate. Due to the high frequency variations along the template major axis (caused by variations in focal plane cross-scan nonuniformity and the finite number of scans available), the average of the sixteen templates was also computed. The average templates did not show high frequency variations along the major axis.

Over most of the sky, templates in a single plate do not vary appreciably in the in-scan direction. However, at higher ecliptic latitudes where the density of scans increases and the scans have common convergence points, there are observable changes in the in-scan profile of templates over the scale of a plate. In fact, since scans intersect at greater angles for higher latitudes, the distinction between in-scan and cross-scan directions is lost. We shall use "in-scan" to refer to the direction of the smaller axis of the point spread function, and "cross-scan" to refer to the orthogonal direction.

The variations in the shape and extent of templates influenced band merging and

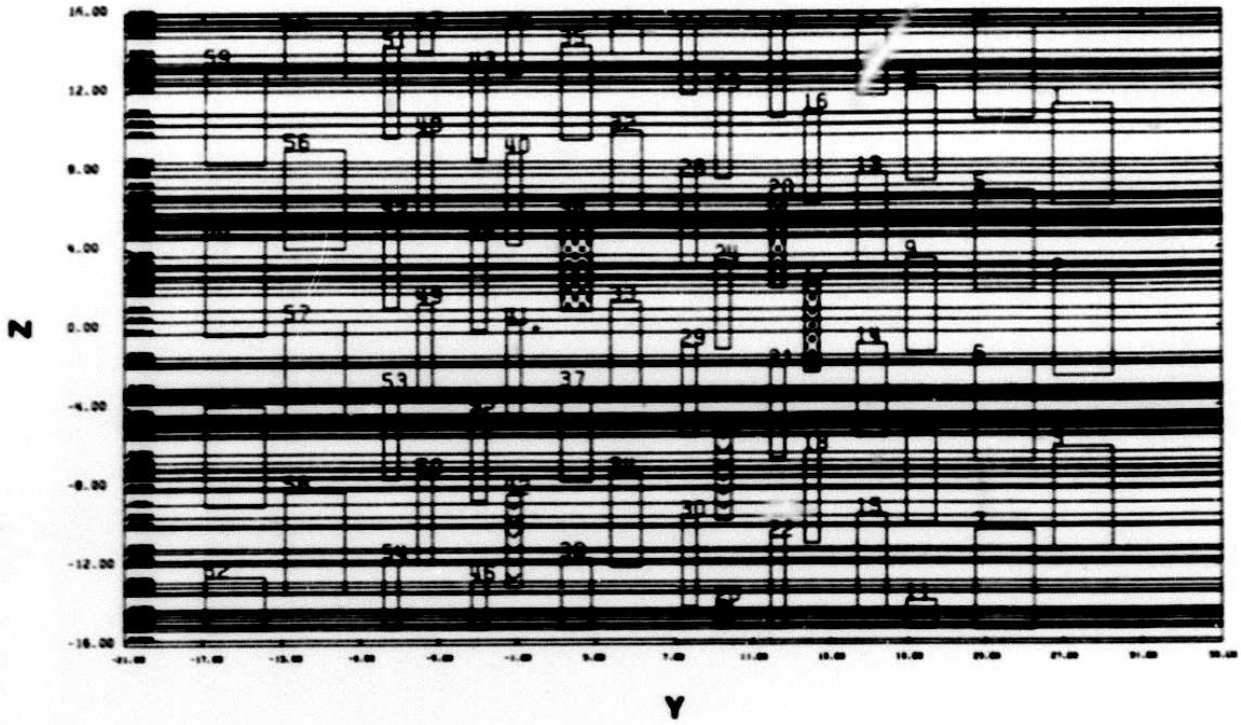

Figure II.D.9 Focal plane crossings at the North Ecliptic Pole, scale in arcminutes.

detection of same-band confusion (see Section II.F.2). To illustrate these variations, templates from two areas of the sky will be seen. Slices in the in-scan and cross-scan directions through three templates from plate 1632 (containing the North Ecliptic Pole) are shown in Figure II.D.11. The following points should be noted:

a) Beam orientation varies by almost 70° across the plate. The bandmerging algorithm oriented a search ellipse along the beam orientation to look for mergers. In extreme cases, some bands may not have been properly merged if the beam orientation varied rapidly over a scale of several beams.

b) The in-scan full width at half maximum (FWHM) varies from a low of 1.07′ to a high of 1.56′ at 12 μm, and from a low of 2.1′ to a high of 2.6′ at 60 μm. As the ecliptic pole is approached (sequence a through c in Figure II.D.11) the distinction between in-scan and cross-scan is lost.

In plates where scans are homogeneously oriented, the in-scan profiles change little from location to location and the beam orientation does not vary by more than a few

106

D 10015

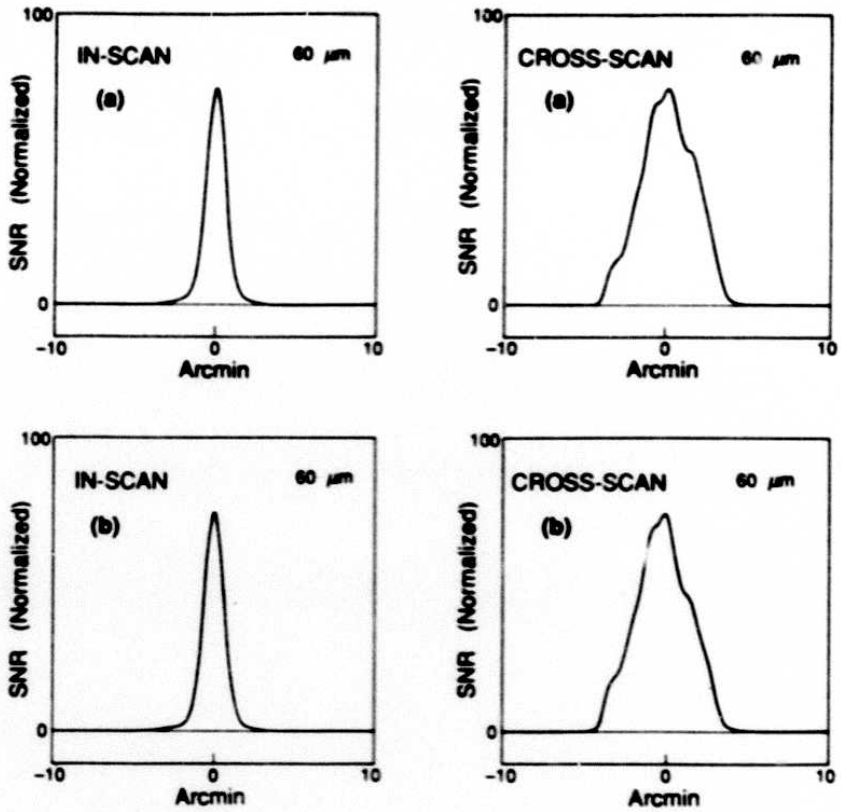

Figure II.D.10 Arp 220; slices along the major and minor axes of the point spread functions at 60 μm. Simulated (a), and the observed data (b).

degrees. Slices through three templates from plate 1215 (containing the North Galactic Pole, $\beta \approx 30°$) are shown in Figure II.D.12. In this plate the beam orientation does not vary by more than 7° over the plate, therefore caveat a) referring to missed mergers does not apply. Also the figures show that the distinction between in-scan and cross-scan profiles remains unambiguous. The high frequency variations in the cross-scan direction are easily seen in (a) and (b). The average template (c) is the one used to compute the two-dimensional correlation coefficients (see Section II.E) and is smooth in the cross-scan direction.

D.5 Template Use in Bandmerger

The information about the extent and orientation of synthesized point source profiles was used extensively by the bandmerger. As is described in greater detail in Section II.F, the search for mergers proceeded by inspecting sources within an elliptical region oriented according to the beam direction. The size of the search region was determined by a multiple of an error ellipse. The formulae used to estimate the positional uncertainties (see Equations II.F.5 and 6) involved the FWHM of the beam in the in- and cross-scan

107

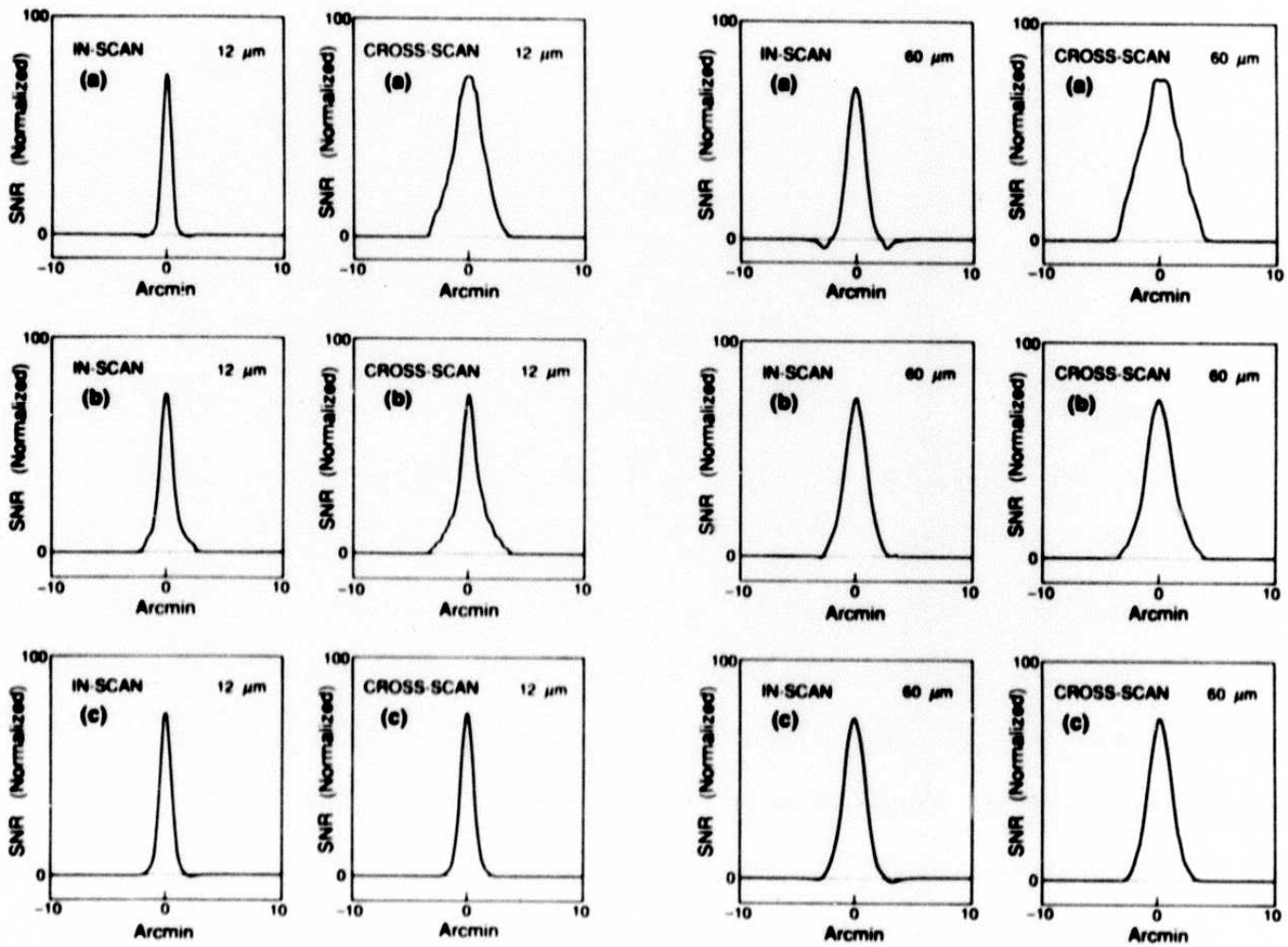

Figure II.D.11 In-scan and cross-scan profiles at 12 and 60 μm for three points located near the North Ecliptic Pole; (a) $\beta \approx 84°$, (b) $\beta \approx 87°$, (c) $\beta \approx 89°$. Notice the sequential widening of in-scan profiles while the cross-scan profiles narrow. In (c) the distinction between in-scan and cross-scan directions is lost.

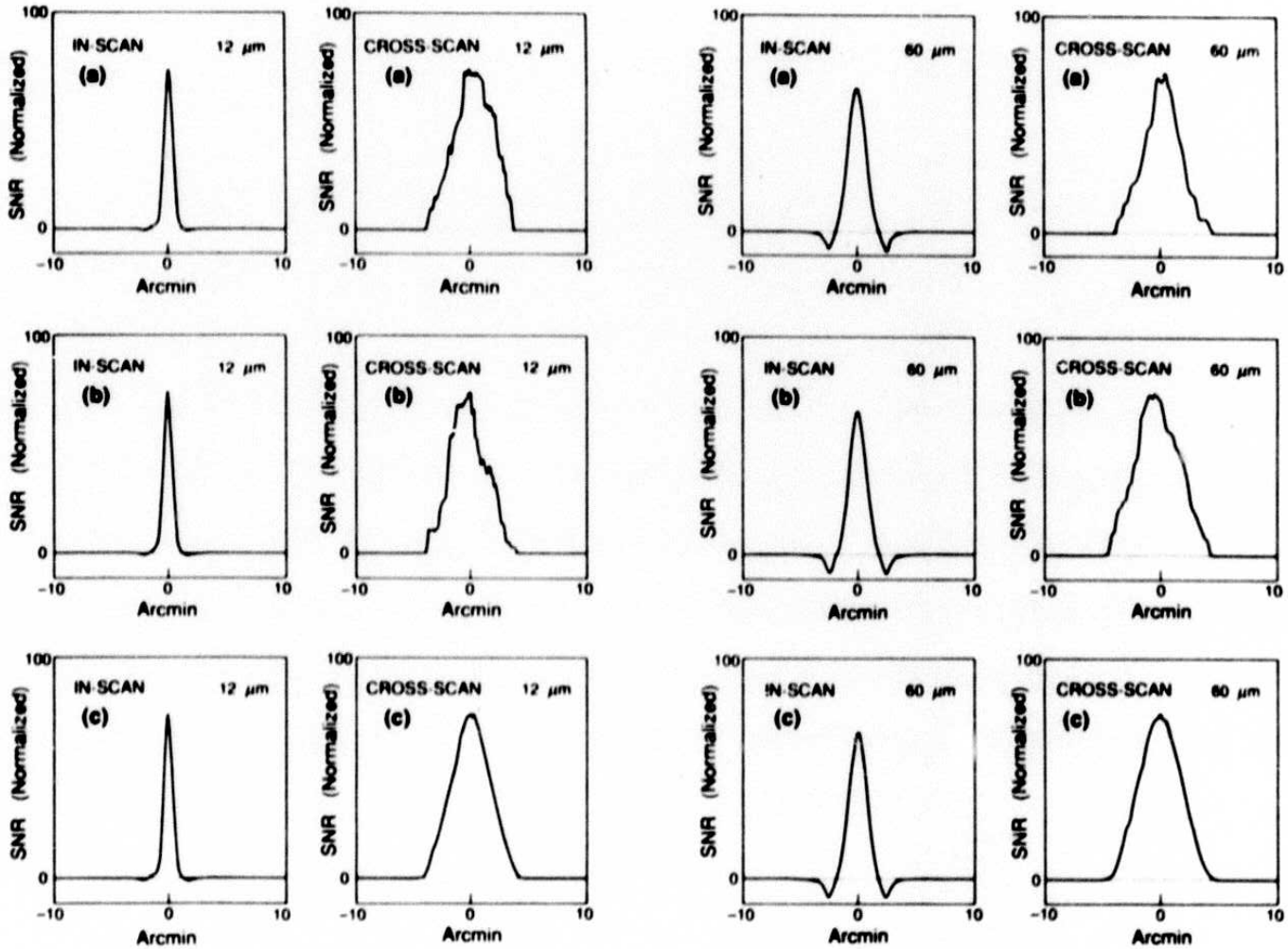

Figure II.D.12 In-scan and cross-scan profiles at 12 and 60 μm for two points located near the North Galactic Pole, at (a) $\beta \approx 27°$, (b) $\beta \approx 29°$. (c) is the average template used for this plate. Notice the in-scan profiles do not change from (a) to (b) in contrast to Figure II.D.11. Also note the cross-scan profiles show high frequency wiggles in (a) and (b). The in-scan behavior of (c) the average template is similar to (a) and (b), whereas, it is very smooth cross-scan.

D 10015

Table II.D.3 Synthesized In-scan and Cross-scan Beam Statistics

Area	Band(μm)	In-Scan(′)	Cross-Scan(′)
$\|b\| \geq 50°$	12	1.10 ± 0.11	4.40 ± 0.76
	25	1.14 ± 0.12	4.34 ± 0.87
	60	2.03 ± 0.10	4.57 ± 0.57
	100	4.01 ± 0.10	5.78 ± 0.34
$\|b\| \geq 75°$	12	1.06 ± 0.02	4.76 ± 0.35
	60	1.99 ± 0.03	4.82 ± 0.39
$\|\beta\| \geq 75°$	12	1.22 ± 0.16	2.95 ± 0.68
	60	2.15 ± 0.18	3.66 ± 0.59

directions. In each plate a 4 × 4 grid of FWHMs was computed from the available grid of templates. For algorithmic simplicity the values for FWHMs were obtained from the second moments of the template shape matrices (and appropriately scaled to agree within 10% with *direct* width measurements from templates).

The FWHMs quoted here are not the same as the *temporal* FWHMs which are equal to detector widths. The difference occurs because in FSS processing temporal data have been smoothed, filtered, and projected onto sky using scans with varying orientations. Thus the FWHMs here will be larger than nominal detector sizes.

The observed FWHMs varied from place to place as illustrated in previous figures. Figure II.D.13 shows the variation of in-scan beam size at 12 μm as a function of galactic coordinates; the in-scan beam size increases at higher ecliptic latitudes. Figure II.D.14 shows the variation of cross-scan beam size at 12 μm with galactic coordinates. The cross-scan beam size decreases at higher ecliptic latitudes. As Figure II.D.11 shows, in-scan and cross-scan FWHMs are much more similar at extremely high ecliptic latitudes. This reflects the loss of distinction between "in-scan" and "cross-scan" at high ecliptic latitudes. Table II.D.3 gives the statistics for the beam-sizes and their dispersions at 12, 25, 60, and 100 μm for different parts of sky.

The same point in the sky was passed over by the spacecraft on several occasions, each passage having been at a different orientation. As a result the effective beam had an orientation which might vary on scales of a few degrees depending on the sky location. This abrupt variation is most visible near the ecliptic poles. Figure III.D.15 shows variations of the beam position angle across the sky.

110

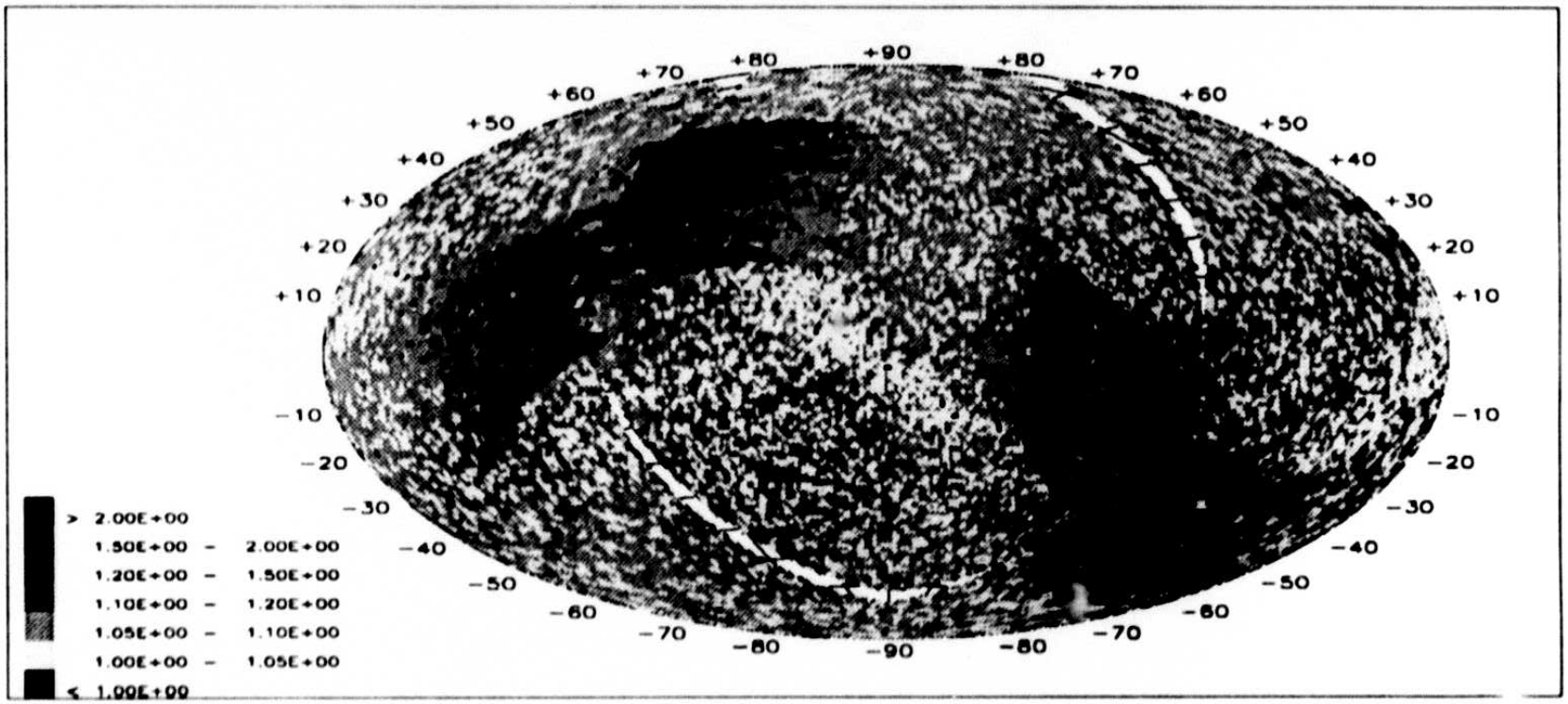

Figure II.D.13 **In-scan beam-size (in arc minutes) variation at 12 μm, the Aitoff map is in galactic coordinates.**

D 10015

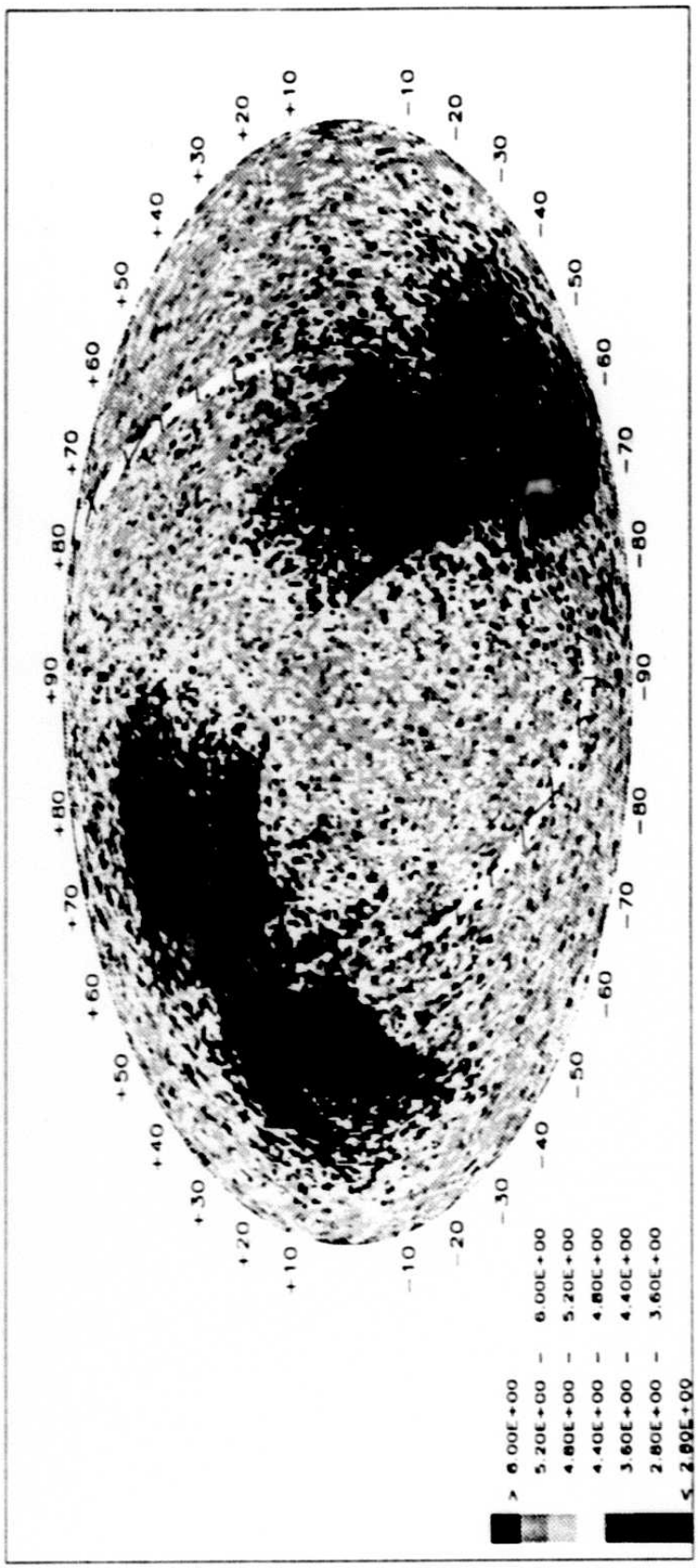

Figure II.D.14 Cross-scan beam-size (in arc minutes) variation at 12 μm, the Aitoff map is in galactic coordinates.

112

D 10015

113/114

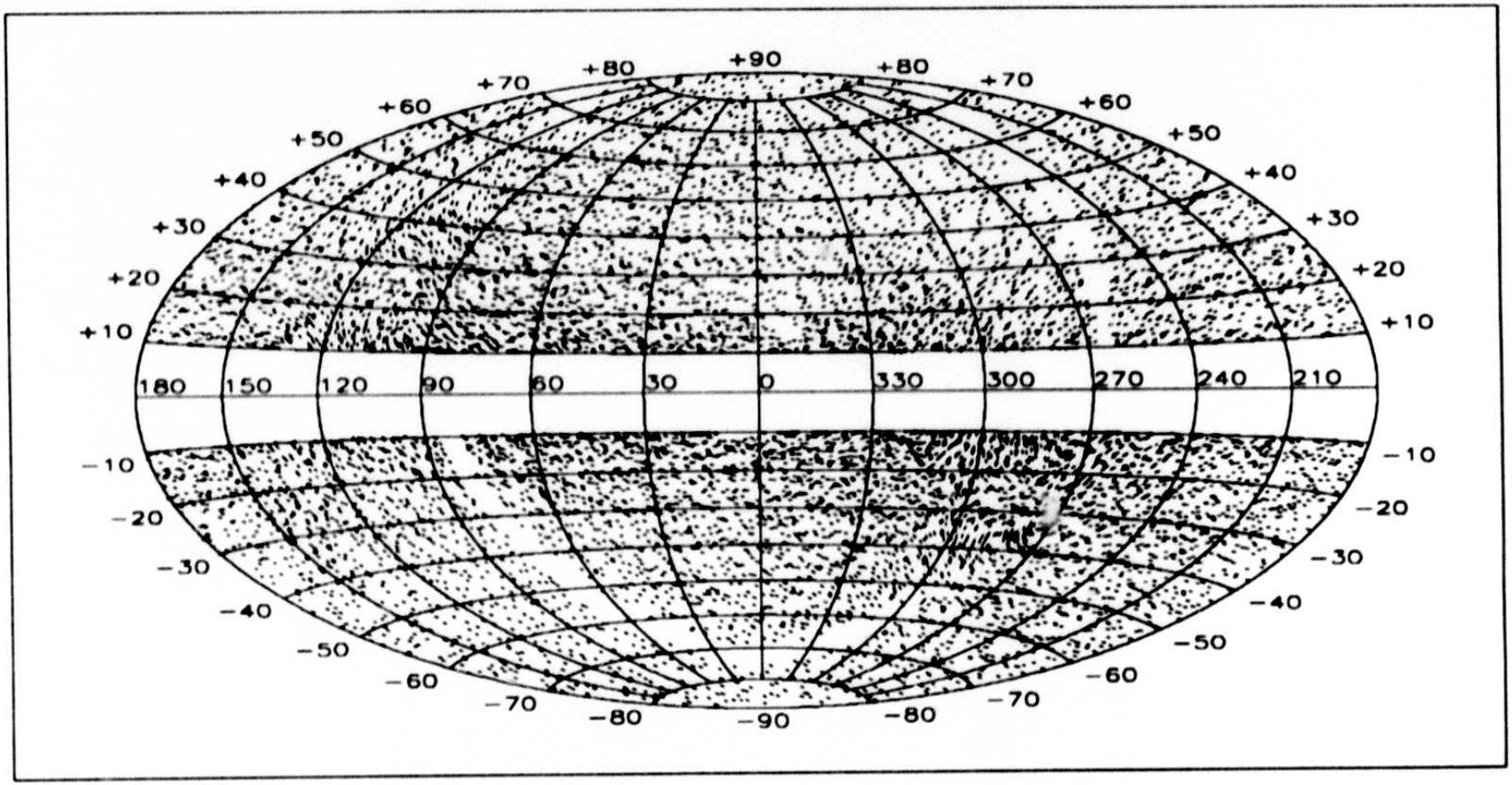

Figure II.D.15 **Beam position angle. The Aitoff projection is in galactic coordinates. In this map the orientation of each line segment with respect to the plot vertical direction (measured counter-clockwise, ranging from 0° to 180°) is equal to the angle between the major axis of the beam and the North Equatorial Pole (measured east of north).**

D 10015

E. The Extractor

E.1 Introduction

The FSS source extractor detects potential sources from FSS plates using standard image segmentation techniques. Signal-to-noise thresholding is used for initial segmentation, and rethresholding is used to break up regions above a preset area. The SNR is calculated using a noise value obtained from the width of the histogram of the signal pixels over a local area. A least squares fit is done to a two-dimensional externally-generated template (described in Section II.D), and a correlation coefficient is reported for this fit. Also provided are a large number of quantities relating to the region shape and position.

E.2 Signal-to-Noise Computation

In order to estimate the SNR for thresholding we need to consider potential errors in both the flux and the noise. The flux density data are filtered with a median filter N samples in length with the central 5 samples deleted so that

$$f_i \rightarrow f_i - median\{f_{i-k}, f_{i+k}; k = 3 \ldots [N/2]\} \qquad (II.E.1)$$

(see Section II.C.3). This filter distorts point source data if there are multiple sources or a background which varies rapidly within the N sample filter length. No attempt has been made to correct for the flux density bias in these cases.

Since we are attempting to extract point sources from the data, we should estimate the noise in a given region by removing every resolvable point source from the data and using the flux density distribution of the remainder to determine the "noise". This distribution will contain the effects of electronic noise, radiation hits, non-inertial IR sources, source confusion and extended structure. Since we lack *a priori* knowledge of the point sources, we approximate this distribution by including the resolved sources and measuring the width of the flux density distribution. This noise (σ^T) is used for thresholding and is estimated in the following way. A noise array is computed by histogramming the plate signal values over a 317×317 pixel cell at 12 and 25 μm and a 199×199 pixel cell at 60 and 100 μm. The noise value for this array is taken to be the 68% quantile ("1σ") of the positive part of the histogram. We also calculate the "skewness" of the distribution by computing its 87% quantile ("1.5σ"). The cell size is chosen to be $(79.25')^2$ at 12 and 25 μm, and $(99.5')^2$ at 60 and 100 μm. With this choice of cell sizes, noise variations on scales of $\lesssim 1°$ can not be faithfully rendered (also see Sections III.A.1 - 4, and III.C.1). The SNR at a pixel is calculated by dividing the flux density at the pixel by the noise value obtained from a bivariate linear interpolation in the noise array.

115

We calculate and report for each source a noise correction factor (NOISCOR) which is the ratio of the noise obtained above to the median noise for the plate. This median noise is obtained by finding the median over the entire plate of all of the pixel-noise values which are the standard deviations of the flux density produced by the median filter (see Section II.C.4). If the NOISCOR is not near unity, it is an indication that the noise contains a substantial component of the noise effects described above. We also report a noise correction factor ratio (NOISRAT) which is the ratio of the "1.5σ" to "1σ" points of the histogram. NOISCOR is a holdover from the version 1 processing; it is reported only for the sake of continuity.

A scan density or *island effect* correction to the SNR due to the effects of inhomogeneous data coverage is also made (see Section III.C.2). The average of the number of scans for each pixel is obtained using the same cell size and position as the noise to provide an average scan density array. The correction is given by

$$I_i = \sqrt{n_i}\langle 1/\sqrt{n}\rangle \qquad (II.E.2)$$

where n_i is the number of scans at pixel i, and $\langle n\rangle$ is the average scan density obtained by interpolation in the average scan density array. This correction is applied only to the 12 and 25 μm data. However at approximately $|b| \sim 5°$ the application of this correction at 12 and 25 μm was stopped. This was due to the increasing contribution of background to the noise, and the noise would have no longer followed the simple scaling law discussed in Section III.A.2. FPFLAG_D in the long form of the catalog is set to zero when the island correction has been applied at 12 and 25 μm.

E.3 Thresholding

A standard image segmentation technique known as thresholding is used to separate the image into regions. The image is scanned a line at a time for pixels above a fixed signal-to-noise threshold. The SNR of the i-th pixel (SNR_i) is computed from

$$SNR_i = \frac{f_i}{\sigma_i^T} \qquad (II.E.4)$$

where f_i is the signal (flux density) at pixel i, σ_i^T is the interpolated noise at i. The noise is obtained by a four-point bivariate linear interpolation in the array described in the previous section. Adjacent pixels are assigned an identification number and connected regions are merged. Whenever a region terminates (no further adjacent pixels), two characteristics of the region are tested against criteria to aid in selection of regions to be saved. First, the area of a potential source must be greater than 6 pixels at 12, 25, or 60 μm or 12 pixels

at 100 μm. This value was selected to attempt to minimize acceptance of noise spikes as potential sources and corresponds to increasing the effective SNR threshold by about 20%. Next, the peak pixel of the region must have the ratio of signal-to-local pixel noise (LOCSNR) greater than 3.5. Regions that pass these criteria are processed further. For plates, with centers beginning at approximately $|b| \sim 5°$, the area thresholds were raised to 12 pixels at 12, 25, and 60 μm, and 24 pixels at 100 μm. Furthermore, the threshold for signal-to-local pixel noise was raised to 4.5 at all bands. These changes became necessary due to the large number of extractions that would have otherwise resulted. This change in thresholding occurred on a platewide basis, and therefore the region boundaries in galactic coordinates are jagged. Because of the yet higher latitude thresholds for the FSC, it was not affected by this change. FPFLAG_E in the long form of the *reject* file has been set to 1 to indicate that the source was extracted under new thresholds.

After a section of the plate has been thresholded, regions that exceed a 50-pixel area (100 pixels at 100 μm) are "rethresholded". This technique consists of computing an average SNR over the pixels in the selected region. This value is assumed to be the new "background" for the region and is added to the original threshold value (3.0) to form a new threshold, and the above-described thresholding technique is applied again. If there are new regions from this first rethresholding step that exceed a smaller 30-pixel area (50 pixels at 100 μm), they are subjected to a second rethresholding. Any new regions obtained from these two rethresholding steps are again tested against the selection criteria and are saved if they pass.

The flux density reported for each potential source is the *peak* flux density in the region, which corresponds to the actual point source flux density as reconstructed by the filter algorithm. The SNR reported is given by

$$SNR = SNR_i \times I_i \qquad (II.E.5)$$

where SNR_i is the signal-to noise (see Eq. II.E.4) at the pixel where the flux density is measured and I_i is the *island effect* correction (equal to 1.0 for the 60 and 100 μm data). Positional information reported for each potential source includes the coordinates of the peak flux density pixel and the position of the flux density-weighted centroid of the area. Positional uncertainties are computed in a later step of the processing (see Section II.F.3).

E.4 Template Fits

Each region that has been saved is fit to an average template that has been previously generated for the plate (see Section II.D.4). A single parameter linear regression using the form $y = ax$ is used to fit only the amplitude of the template. Uniform weighting is used.

This fit is done at the pixel nearest the flux density-weighted centroid and that pixel's four nearest neighbors (or third nearest for the 100 μm band). A correlation coefficient R is calculated for each source from

$$R = \frac{\sum x_i y_i}{\sqrt{\sum x_i^2 \sum y_i^2}}. \qquad (II.E.6)$$

(where y_i refers to observed data and x_i refers to template data). The correlation coefficient at the center pixel and the maximum correlation coefficient and its position relative to the center are reported for each region. A flux density value obtained from the resulting template amplitude is also reported. The region over which the template is fit is computed directly from the second moment of the *shape* distribution of the template.

D 10015

F. The Bandmerger

F.1 Introduction

Approximately one-half of sources in the FSC were detected in more than one wavelength band. The procedure used to merge these detections into a single source is called "bandmerging" and is the subject of this chapter.

The objective of a bandmerging algorithm is to merge all detections of a given source into a single source and make use of the partially independent position measurements to refine the position of the source. It must also minimize random positional associations, and discriminate between distinct, but nearby, sources. The bandmerging process may result in new positions and positional uncertainties for a source. In fact, the bandmerging for the FSC determines positions, positional uncertainties, flux density uncertainties, and flux density upper limits for every source in the FSC. It also warns the user through a number of flags about potential problems in determining these quantities.

There is a trade-off between reliability and completeness. If the search window for counterparts at another wavelength is too big, then too many random mergers will be made, and if it is too small, then not enough mergers will be made. This bandmerging algorithm stresses completeness at the expense of reliability.

The clear-cut example of a point source detected at more than one wavelength versus the random association of two sources at different wavelengths is an oversimplification. For example, most of the sources at 60 and 100 μm are external galaxies $\sim 30''$ in diameter. It is conceivable that the positions at 12 and 60 μm of such a galaxy could differ by a statistically significant amount, because the radiation at 12 μm may be coming from different environments than the radiation at 60 μm. The positional agreement (or disagreement) in this case would not be random, and some astronomers could argue against calling both detections the same source.

The situation is simplified in the present case because we do not wish to include any *a priori* information that would bias an otherwise flux density-limited survey. For example, infrared colors would help the merging process and improve the reliability of the entire catalog, but would introduce a bias that would limit its use in statistical studies. Thus, *the bandmerging algorithm uses no color information* in choosing match candidates. It determines matches based only on positional agreement.

Producing an unbiased catalog of bandmerged sources from a multiwavelength survey requires separate and independent SNR thresholds to be set at each wavelength that meet

119

their respective reliability requirements (Section III.D). These thresholds are called "high-quality" thresholds.

Next, one needs to decide on a search window size that satisfies the bandmerging completeness requirements. This algorithm strives for better than 99% (*i.e.* 3 σ) completeness. An important trade-off in picking a window size is discrimination of distinct but nearby sources. If the windows are too large, the ability to resolve close doubles will be lost. An example might be a star detected at 12 μm that lies very close to a galaxy detected at 60 μm. Fortunately, the distribution of positions of detections about a source is nearly Gaussian, and little is gained in completeness past the 3-σ contour. Inside the 3-σ contour, little is gained in discrimination of close double sources (due to the small probability of two resolvable sources lying so close to each other), while the loss in completeness of bandmerging is great. Since the FSC is not confusion-limited for high latitude sky, the reliability of the bandmergers above the "high-quality" thresholds will be great (>99%), and will probably exceed the bandmerging reliability requirements.

Next, "moderate quality" bandmerging SNRs can be set to meet the bandmerging reliability requirements. The idea is to set low SNR thresholds to "saturate" the bandmerging windows that were selected. The "moderate-quality" SNR thresholds are essentially set at the confusion limit. If the surveys are not confusion-limited at the "high-quality" thresholds described above, then these fainter, "moderate-quality" detections will be preserved as mergers to the bright, "high-quality" detections. Such "moderate-quality" detections are tagged.

This way, a positional coincidence between a bright detection and a faint detection will allow the faint detection to be included without degrading the flux density-limited survey that satisfies the completeness and reliability requirements. However, the survey below this limit will be biased towards sources with flat flux density distributions.

The "moderate-quality" SNR thresholds are set at 3 times the width of the confusion (error) distribution (see Section II.E), which is 3 σ for a Gaussian distribution with no sources. This threshold corresponds to the confusion limit for instrumental noise and confusion-limited surveys. At this threshold, most of the "detections" are due to random instrumental noise fluctuations or background structure (faint point sources and/or extended emission) and do not represent real, single point sources. Studies of the source and count distribution for a wide class of models have shown that a catalog should not include sources below 5 times the width of the error distribution, however. (Murdoch, Crawford and Jauncey 1973; Condon 1974.)

The FSC bandmerging algorithm uses two search radii. For a high quality detection in

search of a moderate-quality merger, it uses a 3-σ window (see Sections II.F.2 and II.F.3). For a high-quality merger candidate, the 3-σ ellipse is not allowed to become smaller than 10″ × 30″. The reason for this is the search window for high-quality mergers is a smaller area than that of a moderate-quality window (see Section II.F.2). Thus, it is possible to obtain slightly higher completeness with little cost to resolving close pairs. These radii correspond (approximately) to the point at which the probability for a random match equals the probability of finding a legitimate merger.

Moderate-quality mergers do not contribute to position or positional uncertainty refinement of the source due to their low reliability.

F.2 The Bandmerging Algorithm

This section gives a brief description of the FSC bandmerging algorithm. Details concerning how it determines positions, flux densities, their uncertainties, and warning flags appear in Sections II.F.3-5.

The FSC bandmerging algorithm first searches each band to identify sources for same-band-confusion. For unconfused sources, it then combines all detections from all wavelength bands and segregates them into high and moderate quality detections. Only high quality detections search for mergers at other wavelengths. After all matches are made, the positions and position uncertainties are refined for sources that are composed of multiple high-quality detections. Finally, at wavelengths where no moderate or high quality flux density is quoted, upper limits are determined (see Section II.F.4).

F.2.a Same-Band Confusion

When two or more detections in a given band are "too close" to each other, then these detections should be tagged for recognition by other modules down the line. A scale for confusion distance is needed to perform this confusion recognition. The most natural parameter to set the scale is the beam size. Figures II.D.13 and 14 display the variation in the beam size at 12 μm. A rectangle of size $dY \times dZ$, oriented according to the beam orientation, is centered on every detection and is used to define the scale of same band confusion. The extent of this rectangle depends on the spectral band, and also the actual point source beam size (see Section II.D.5). Since the same band confusion processor is a broad filter, in every plate a *single* rectangle is used per band for the *whole* plate, and the reference point from which the window is selected is taken to be the plate center. To illustrate the adaptive nature of the same band confusion windows, Table II.F.1 displays the window sizes for several areas of the sky. When a source is flagged as same band

for mergers out of all of the detections on the list below it, including detections already selected as mergers. This process repeats until all of the high quality detections have been chosen as a seed or a merger.

F.2.d Multiple Matches and Confusion

If a seed finds more than one (usually two) potential mergers at a particular band, it uses a two-step process to select the best one. First, it checks whether one of the mergers is a high quality detection. If it is, then the high quality one is chosen as the best candidate. If both are high quality or moderate quality detections, then it selects the best one based on the probability of obtaining the observed positional discrepancy between the seed and merger candidate (*i.e.* it picks the one with the lowest value in the left hand side of the equation above). The rejected merger candidate cannot be included in the catalog unless it is the best choice for another seed, which rarely occurs.

Occasionally more than one (usually two) seeds will select the same merger. The merger probably has a flux density contribution from more than one source, *i.e.* it is a confused detection. In this case, the merger is used in *both* sources as an *upper limit*, a flag is set to denote this condition. See Section II.F.4.C for a description of warning flags.

F.2.e Upper Limits

After all bandmerging and position refinement has been performed (see Section II.F.3), the signal and noise maps are checked at the position of each source at wavelengths where no detections are found.

The peak flux density and a median noise are calculated from a 5 × 5 pixel box centered on the source. In version 1, the maximum of the peak flux density and 3 times the median noise from the box was used as the estimate of the upper limit. However, this method does not provide a confidence level for upper limits. For version 2, we have computed a new flux density upper limit at a later stage which corresponds to a 90% confidence estimate. Briefly, if $P(x)$ denotes the cumulative distribution of flux density in the presence of noise, then the upper limit is computed according to $P(f_\nu^{true} \leq f_\nu^{upper\ limit}) = 0.90$; $P(x)$ satisfies $P(0) = 0$, $P(\infty) = 1$ (flux densities are always positive!). From the measured peak flux density f_0, and the noise σ (this noise is turned into a Gaussian equivalent at the 87% quantile level by using the NOISRAT value at the source location; NOISRAT is described in Section III.A.1), and *assuming* a Gaussian form for P, the flux density upper limit is computed (Review of Particle Properties, 1990). In the short-form version of the catalog, in the absence of a detection, the field for flux density is replaced by an upper limit which is either:

- the merger detection, when quality index is 3 (in Section II.F.4.c the meaning of each quality index in fully described).
- the 90% confidence upper limit as described above, when quality index is 1.
- three times the median noise, when quality index is 0.

The long-form version gives the 90% confidence upper limit, the peak flux density, the median noise, and the quality index for all four bands at every source position.

F.3 Positions and Their Uncertainties

The positions of the individual detections are the flux density-weighted centroid positions above a given threshold (usually SNR = 3) unless they have been re-thresholded (see Section II.E.3).

The final position of a source with high-quality detections in more than one wavelength is given by:

$$\vec{r}_{final} = \vec{r}_{seed} + \Delta_{min}\hat{i}_{min} + \Delta_{maj}\hat{i}_{maj} \qquad (II.F.2)$$

where $\vec{r}_{seed}$ is the position of the seed, $\hat{i}$ is the unit vector in the direction of the minor or major axis of the position uncertainty ellipse, and Δ_{min} and Δ_{maj} are given by:

$$\Delta_{min} = \frac{\sum_j \frac{(\vec{r}_j - \vec{r}_{seed})\cdot\hat{i}_{min}}{\sigma^2_{j,min}}}{\sum_j \frac{1}{\sigma^2_{j,min}}} \qquad (II.F.3)$$

and

$$\Delta_{maj} = \frac{\sum_j \frac{(\vec{r}_j - \vec{r}_{seed})\cdot\hat{i}_{maj}}{\sigma^2_{j,maj}}}{\sum_j \frac{1}{\sigma^2_{j,maj}}} \qquad (II.F.4)$$

where the sums include only high quality detections, and $\sigma_{j,min}$ and $\sigma_{j,maj}$ are the semi-minor and semi-major axis relative position uncertainties of the detection in wavelength band j, and in all cases the 100 μm band has *not* been used in position refinement.

F.3.a Positional Uncertainties

The positional uncertainties are the combination of the relative positional uncertainty of detections from different bands and the absolute pointing uncertainty of the source on the sky.

The relative positional uncertainty of a detection in band j is given by

$$\sigma^2_{j,min} = \left(\frac{\alpha_{1,min}\ \mathrm{FWHM}_{j,min}}{2\ \mathrm{SNR}}\right)^2 + \beta^2_{j,min} \qquad (II.F.5)$$

D 10015

Table II.F.2 Derived Positional Uncertainty Constants

Wavelength	Minor Axis α	Minor Axis β (″)	Major Axis α	Major Axis β
12 μm	0.85	1.25	1.00	0.90
25 μm	0.80	1.45	1.00	0.95
60 μm	0.75	4.00	1.00	0.75
100 μm	0.75	4.50	0.85	0.50

and

$$\sigma^2_{j,maj} = \left(\frac{\alpha_{j,maj}\,\mathrm{FWHM}_{j,maj}}{2\,\mathrm{SNR}}\right)^2 + \frac{(\beta_{j,maj}\,\mathrm{FWHM}_{j,maj})^2}{24\,\mathrm{N}} \qquad (II.F.6)$$

where α and β are constants, FWHM is the full width at half-maximum of the appropriate templates used for that region of the plate, SNR is the signal-to-noise ratio (corrected for local counts), and N is the number of counts after data trimming has taken place (see Eq. II.C.3). These are the positional uncertainties used to determine mergers. The FWHM values derive from the *second moment* of the template and are accurate to about 10% (see Section II.D.5). The first term in both of the positional uncertainties is that due to a Gaussian beam. This is a good approximation along the minor axis of the source and requires only an additional small "fudge-factor" to account for the rest of the non-Gaussian and systematic components in the positional uncertainty. The major axis positional uncertainty requires an additional term that accounts for the uniform part of the uncertainty distribution, and any additional small term can be neglected.

The values of α and β are determined from the dispersion of interband positional discrepancies of sources associated with known objects. Table II.F.2 lists the values for α and β from this comparison.

If a source is detected in more than one wavelength band, the detections are merged and the resulting positions are refined separately along the minor and major axes of the position uncertainty ellipse according to

$$\sigma^2_{merged} = \frac{1}{\sum \frac{1}{\sigma_j^2}} \qquad (II.F.7)$$

where the sum is over high quality detections, σ_{merged} is the resulting relative positional uncertainty in the given direction, and σ_j is the relative positional uncertainty for the detection in band j in the same direction (given in Eqs. II.F.5 and 6).

125

The absolute positional uncertainty is then obtained from the merged relative uncertainty using

$$\sigma^2_{final} = \sigma^2_{merged} + \sigma^2_0 \qquad (II.F.8)$$

where σ_0 = 1″ and 3″ along the minor and major axes, respectively. The σ_0 terms represent the overall *IRAS* pointing reconstruction, binning errors, and source extraction errors. The values for σ_0 are determined from the dispersion of the final FSC positions of known sources about their optical and radio positions. Only sources above galactic latitudes of 50° were used for tuning of parameters. The uncertainty of the positional uncertainties is 10-15% based on the observed plate-to-plate variation.

F.4 Fluxes, Their Uncertainties, and Upper Limits

The flux densities quoted for detections in the FSC are the value of the peak flux density pixel (see Section II.E.3).

F.4.a Flux Uncertainties

The fractional uncertainty of a flux density measurement in band j, $\sigma_{f,j}$, is derived from the maximum of:

$$\frac{1}{\mathrm{SNR}_{local}} \qquad (II.F.9)$$

and

$$\left(\frac{1}{\mathrm{SNR}^2} + \frac{\gamma_j^2}{\frac{N}{12}}\right)^{1/2} \qquad (II.F.10)$$

where SNR_{local} is the peak flux density divided by the noise in the same pixel (also called LOCSNR), SNR is the signal-to-noise ratio (corrected for local coverage described in Section II.E.3), N is the number of counts, and γ_j is a constant equal to the photometric uncertainty of an infinitely bright source sampled 12 times (see Section II.D.3). The value of γ at 12 μm has been experimentally determined to be 0.05 (based on a comparison with *The Bright Star Catalog*) and agrees with simulations based on exact cross-scan responsivity of detectors (see Section II.D.3). The same value has been assumed for the other bands.

F.4.b Flux Density Upper Limits

In bands with no detections, the upper limit is derived in one of three ways:

(a) the peak flux density of a confused *merger* (See flag 3 in Section II.F.5.)

(b) the 90% confidence upper limit when quality index is 1 (See Section II.F.2.)

(c) three times the median noise (excluding blank pixels) in a 5 × 5 pixel box centered on the source.

All of these quantities are present in the long form of the catalog. The Quality Index indicates which type of upper limit was used and flags difficulti with flux density upper limits. It is described below. The short form includes an upper limit only if the Quality Index is > 0.

F.4.c The Quality Index

This index indicates how the quoted flux density or upper limit was derived. A larger number for the quality index means a more reliable flux density or upper limit estimate. A value less than zero means that at least half of the data were missing from the 5 × 5 pixel box used to determine the upper limit and should be treated cautiously. The meanings of quality index values are described below, in order of decreasing reliability.

If a flux density is quoted for a source, whether it is of high or moderate quality (see flag 4 in Section II.F.5), the quality index is set to ten times the flux density divided by the median noise from the 5 × 5 pixel box centered at the position of the source. Quoted flux densities should result in quality indices of ≥ 30.

A value of 3 for the quality index indicates that the upper limit is derived from a merger detection that was a candidate for more than one seed (case (a) above, see flag 3 in Section II.F.5).

Values of 1 and 0 are normal upper limits and correspond to cases (b) and (c) above.

Values of -1 and -2 both indicate that > 50% of the data are missing from the 5 × 5 pixel box. Three times the peak noise in the box is used in place of the median noise in (c) in the comparison above. The upper limit is probably an accurate one, but caution should be exercised.

If the quality index is -3 or -4, then no noise data were available, although there are flux density measurements in the box. This occurs if there are less than four measurements per pixel everywhere in the box. If the peak flux density is > 0, it is used as an upper limit and the quality index is set to -3; if the peak flux density is < 0, then 3 times the plate median noise is used as an upper limit and the index is set to -4. The quality of these upper limits is marginal. Careful interpretation of upper limits with a quality index of -3 or -4 is urged.

A value of -5 for the quality index signifies that a detection is quoted, but there is no noise data from which to determine a quality index. Such a detection is of very low reliability and should be treated with extreme caution.

A quality index of -6 indicates that there is no flux density or noise data in the 5 × 5 pixel box at this wavelength. In this case the upper limit is three times the plate median

D 10015

Table II.F.3 Bandmerging Warning Flags

Flag	Warning	Value
1	Same-band confusion	Number of sources in the same band within a beam (full width). Always ≥ 1.
2	>1 merger	0 if 0 or 1 merger found, else number of merger candidates (usually 2).
3	>1 seed	0 if 0 or 1 seed detection has selected this detection, else number of potential seeds (usually 2).
4	Moderate quality merger	Number of seeds that could have selected this detection (usually 1).
5	Plate edge	0 = detection is > 30′ from plate edge 1 = detection is < 30′ from edge 2 = detection touches plate edge
6	Unused merger	Number of seeds that selected this detection (usually 1).

noise. This number is of dubious value and should not be used without extreme caution. Remember, there are no data from which to derive a detection or an upper limit. The quoted value is illustrative only.

F.5 Warning Flags

The merging process alerts the user to potential problem via six flags in each wavelength band. Table II.F.3 summarizes the six flags, which are described in detail below.

F.5.a Same-Band Confusion Flag

This flag gives the number of detections of similar or greater flux density within a window whose dimensions are approximately equal to the beam size (full width) centered on the position of a given detection (see Section II.F.2.a). This number is given for all of the high and moderate quality detections that comprise the source. The window is centered on the position of the original detection, not the final position of the merged source. It is ≥ 1 for all detections. If two detections at the same wavelength differ in flux density by more than a factor of 1.5, then this flag will equal 1 for the brighter source (because the brighter source is probably not affected by the fainter one), but the flag for the fainter detection will equal 2 (warning the user that another bright source is nearby). Detections with same-band confusion flags > 1 cannot be seeds, regardless of their SNR.

128

F.5.b > 1 Merger Flag

This flag indicates that the seed detection found more than one merger candidate at this wavelength. The flag equals the number of merger candidates (usually 2). The best merger is chosen based on the relative positions of the seed and mergers and their position uncertainties, but the merger does not contribute to position or position uncertainty refinement of the source (see Section II.F.2). This flag equals 0 if the seed finds 0 or 1 mergers.

F.5.c > 1 Seed Flag

This flag indicates that a given merger was a candidate for more than one seed detection. The flag equals the number of seeds that could have selected this detection, and the merger flux density becomes an upper limit for all of the seed detections unless either of two conditions are met:

(1) the seed detection had more than one merger choice, and it selected another merger, or

(2) the peak flux density at the final position of the source exceeds the merger flux density (see Section II.F.4).

F.5.d Moderate Quality Merger Flag

This flag indicates that the reliability of the detection at this wavelength does not meet reasonable reliability requirements (see also II.F.2.b). A flux density is quoted only because of the positional coincidence that this detection has with a seed (which has a more reasonable reliability). A moderate quality detection does not contribute to position or position uncertainty refinement of the source (see Sections II.F.2 and II.F.3). This flag is equal to the number of seeds that could have selected this detection (usually 1). This flag equals -1 if the moderate quality detection was not a candidate for merging from any seed.

F.5.e Plate Edge Flag

If a detection falls within 30′ of a plate edge, this flag equals 1. If the detection touches the edge of a plate, the flag equals 2 and the detection is not used to refine the position or position uncertainty of the source. If the detection is more than 30′ from the plate edge, the flag equals 0.

F.5.f Unused Merger Flag

This flag is nonzero if the detection was a potential merger that was not selected (*i.e.* the seed detection chose a better candidate). The flag equals the number of possible seeds (usually one). There should be a corresponding seed nearby with flag #2 set (see above).

G. Data Base Generation

G.1 Introduction

The Faint Source Data Base (FSDB) generator receives all extractions (see Section II.E) after they have passed through the bandmerger (Section II.F) on a plate-by-plate basis. It operates on these extractions and places them, along with the information produced by the other FSS processors, into the FSDB. All sources in the FSDB are then placed in the FSC or the Faint Source Reject File (FSR) according to the criteria given below.

The FSDB generator performs the following tasks:

- Receives the source lists produced by the bandmerger
- Tags duplicate sources and selects a source representative from among them
- Associates all sources with other astronomical catalogs
- Counts the number of neighbors for each source, and produces a cirrus flag for each source
- Applies final flux density calibration adjustments
- Rejects sources which touch a FSS plate edge
- Tags sources contaminated by cometary debris trails (see Section III.G.1) or by nearby bright sources (see Section III.G.3)
- Applies the Final Catalog Criteria to place all FSDB sources into either the FSC or FSR.
- Computes a 90% confidence estimate for flux density upper limits at wavelengths where no detections are found.

Each of these steps is described in more detail below or elsewhere in this supplement.

The FSDB generator receives the file of bandmerged sources after each plate is bandmerged. Information in this file allows the generator to look up the component extractions that were merged to make each source. These records, in turn, contain some needed information from the plate generator. Once all the information is gathered, it is organized into a single record and stored in the FSDB. Since the processing is plate oriented, and some information affects the entire plate in question, the FSDB is organized by plate.

Information provided by the bandmerger includes refined positions, simple upper limit flux densities, flux-density and positional uncertainties, cross-band and same-band confusion indicators, as well as which bands were merged and a preliminary evaluation of the flux density qualities. Information provided by the source extractor includes, for each band, flux densities, positions, correlation coefficients, source shape information, various

D 10015

TABLE II.G.1. Overlap Plate Coverage of the Entire Sky

# Plates	% of Sky
1	39.13
2	39.38
3	13.71
4	7.47
5	0.31

TABLE II.G.2. Overlap Plate Coverage for $|b| > 50°$

# Plates	% of Sky
1	43.07
2	39.56
3	11.75
4	5.61
5	trace

noise estimates and detection counts, and other statistical information relating to the local coverage.

The generator also rejects a small number of sources from each plate from the FSDB. Sources are not thresholded on any parameters by the generator, but are only rejected if any of the extracted pixels of all merged bands (including single-band sources, i.e. no mergers) touch a plate edge. Such sources are irretrievably corrupted by the plate edge and will be better represented on another plate due to the overlap provided by the plate structure.

G.2 Duplicate Source Tagging

Tables II.G.1 and 2 show the relative fractions of the sky covered by one, two or more plates due to the plate overlap inherent in the plate coverage strategy. The FSDB generator must find the duplicate representations of sources in the FSDB located in the areas of overlap. Once identified, all duplicates (henceforth called dups) are flagged such that each dup points to all others. From among these dups one is chosen to represent the source in the database; this source is called the 'rep'. The dup chosen to be the rep is always the one farthest from its plate's edge. With one class of exceptions (discussed later), only reps can be selected as catalog sources. This method differs from the one employed for version 1 of the FSC. In version 1 the "best" source was picked to be *either* the one coming from the plate where the source was farthest from a plate boundary *or* in some

131

D 10015

infrequent cases the source which had the higher quality flux density. This caused the FSC version 1 to be slightly deeper in the overlapping regions since in those areas a given source had more chances to exceed the catalog thresholds due to statistical variations.

A dup of a given source is recognized only by its proximity; any two sources within 45″ of each other are flagged as dups. A pointer is added to the FSDB record of both sources that points to the other. Care is taken to keep all the dup lists of a single source identical, so that each source always has a complete list of its dups. Thus, in addition to adding the most current dup to the list, each source must search the other's dup list for entries it does not possess. This will occur, for example, when two sources are within 45″ of one another, and a third source is close enough for dup status to only one of these sources. Only the first two will find each other during the primary positional search; the latter must be added as part of the symmetrization process that keeps all lists identical. This is called chaining. *Two sources well over 45″ apart could end up in each other's dup lists through a process of fortuitous chaining.* Table II.G.3 gives an egregious example of this effect. Note that some dups are chained in from over 1.5′ away, more than twice the dup search radius.

Table II.G.3 also demonstrates a result of dup processing contrary to the intuitive idea of a dup; some of the dups are on the same plate. This situation arises (as a result of the symmetrization process) when two sources close together on the same plate both fall within the dup radius of a source on another plate. It can also happen directly when two sources on the same plate are within the dup radius of one another. This is usually a result of confusion among separate objects or the result of resolved objects being split into several closely related point sources by the point source filter and the extractor. (The example in Table II.G.3 is an extended source).

(The example given in Table II.G.3 in version 1 of this supplement, NGC 3726, is no longer an example of the chaining described above. Due to small position shifts of its component IR detections, what was one extended dup chain in version 1 of the database has broken into two separate dup lists in version 2. Thus NGC 3726 has two separate reps in the new database due to its extended nature. However, only one of these met the catalog criteria - the same component present in version 1.)

To mitigate against the possibility that such a chaining process will eliminate close distinct objects properly separated by the extractor and bandmerger, dups which are on the same plate as the rep were tested against the catalog acceptance criteria. Thus, in the example, components 1 and 2 are dups of the rep, source 3, but are on the same plate as the rep. They were thus both tested for inclusion in the catalog. (Both failed, but the rep

132

TABLE II.G.3 An Example of Duplicate Coverage in the FSDB§

#	Plate	RA h	RA m	RA s	DEC d	DEC m	DEC s	Flux Density Quality†	Distance to Other Dups (″) 1	2	3	4	5	6	7	8	9	Distance to Nearest Plate Edge(′)
1	56	05	27	48.8	−67	29	04	1 1 2 1	-	49.1	37.3	4.9	36.5	57.7	53.5	3.6	37.4	49.9
2	56	05	27	56.1	−67	28	38	1 1 1 2	49.1	-	85.0	44.9	84.1	10.4	6.1	45.9	85.0	49.5
3	56‡	05	27	44.9	−67	29	33	1 3 1 1	37.3	85.0	-	40.6	0.9	94.3	89.9	39.8	0.8	50.4
4	85	05	27	49.7	−67	29	04	1 1 2 1	4.9	44.9	40.6	-	39.8	53.8	49.5	1.3	40.7	44.6
5	85	05	27	45.0	−67	29	33	1 3 1 1	36.5	84.1	0.9	39.8	-	93.4	89.1	39.1	0.9	44.2
6	85	05	27	56.8	−67	28	28	1 1 1 2	57.7	10.4	94.3	53.8	93.4	-	4.5	54.7	94.3	45.2
7	86	05	27	56.3	−67	28	32	1 1 1 2	53.5	6.1	89.9	49.5	89.1	4.5	-	50.4	89.9	43.1
8	86	05	27	49.5	−67	29	03	1 1 2 1	3.6	45.9	39.8	1.3	39.1	54.7	50.4	-	40.0	42.5
9	86	05	27	45.0	−67	29	34	1 3 1 1	37.4	85.0	0.8	40.7	0.9	94.3	89.9	40.0	-	41.9

§ Source is MC 50 (McGee, *et al.*, Aust. J. Phys., 25, 581-613 (1972), an LMC radio object.)

† 3 = High quality; 2 = Moderate quality; 1 = Upper limit (Given in order: 12, 25, 60, and 100 μm).

‡ Representative in the catalog.

D 10015

passed and is in the catalog.) There are 391 dups included in the catalog for this reason. Dups on plates other than that of the rep are not considered for the catalog.

The dup search radius of 45″ was picked somewhat arbitrarily; it is a compromise between identifying all dups and falsely flagging sources as dups. As a check on how many true dup sources may be farther away than 45″, each source in the FSC was searched for FSC neighbors within 90″ (twice the dup search radius). If any sources found a) came from different plates, b) had a detection in at least one common band, and c) the common flux densities were within 30%, then they were counted as possible missed (unflagged) dups. There were <200 such possible missed dups. Thus, at most, about 200 FSC sources may be duplicate representations of sources already present in the FSC.

G.3 Associating Other Catalogs to the FSDB

After a plate has been added to the FSDB, its sources are positionally associated to a large number of astronomical catalogs. These associations are *not* identifications; the user must decide whether to accept any of the associations as identifications. We provide the positional associations as an aid to users for such determinations.

The associations were carried out in a manner nearly identical to that employed in the production of the PSC (see the ***Main Supplement***, Section V.H). The only differences are related to the plate nature of the data, an extension in the number of available catalogs and a minor difference in the way unused fields are handled. The most important difference is the change in the search windows employed in performing the positional matches. Table II.G.4 gives a list of the catalogs used for associations and the match window used, as well as a summary of the contents of the catalog and the number assigned to the catalog. The catalog numbering scheme has gaps in the sequence for historical reasons.

The positions given in each catalog are precessed to equinox 1950 (the equinox of all *IRAS* data) and any known proper motions are applied to produce epoch 1983.5. Since the FSS data are plate oriented, the catalogs are then "snipped" into plates so that processing sources in any given plate would not require searching the whole catalog. A suitable additional area around the geometric boundaries of each plate is included in the snipped area, so that sources near plate boundaries will associate with all available cataloged sources.

As the catalogs are associated to the FSDB sources, the various data available in each catalog are refined and reduced to a few fields, as was done for the PSC. Table II.G.5 gives a description of the contents of the fields as they are used for each of the catalogs. When one of the available three fields has no information (i.e. is blank), a value of −999

134

D 10015

is given, except for historical reasons FIELD3 is frequently set to zero when blank rather than −999. When a field contains a number over 9999, the value saturates at 9999.

The associations of the FSDB to each catalog are done using a rectangular window of half widths 26″ by 165″ or greater. These values are roughly the 3-σ in-scan and cross-scan uncertainties, respectively, for the weakest 12 μm FSC sources, as estimated from the FSC v.1.2. (See Sections II.F.3 and III.E for a description of the FSC v.2 positional uncertainties). The window is oriented such that the short dimension of the box is lined up with the minor axis of the source's error ellipse and centered on the FSDB source. This default window size is used when the positional uncertainty of the catalog is small compared to that of the FSC. If this is not so, the dimensions of the window are expanded until the box completely contains the nominal uncertainty measure assigned to the catalog. The windows employed in the positional matches to each catalog are given in Table II.G.4. If a given catalog contains a source size, this size, if larger than either dimension of the match window, is also used to expand the search window.

When associating the FSDB to other *IRAS* products (the PSC and especially the SSC), the slightly (PSC) or very (SSC) different sets of scans used to make the *IRAS* measurement could result in very different estimations of the meaning of "in-scan" and "cross-scan" from that made by the FSS processing, especially near the ecliptic poles. Because the search window is dependent on the scan direction, this could result in missed associations to these catalogs, particularly near the ecliptic poles. In practice, probably very few are missed for this reason.

Each FSDB source, including dups, is in turn associated to each catalog. A single FSDB source can match multiple entries in a given catalog, and a single object on the sky may appear in many catalogs (especially extragalactic catalogs). All these associations are recorded. No attempt is made to resolve multiple associations or redundancies. Associations are listed in catalog number order (arbitrarily chosen) and, within a catalog, in RA order. If a catalog contains multiple references to a single position, only the first reference is used.

Once an association is made, the catalog information is copied into the FSDB association file, along with the radius vector from the FSDB source to the catalog position and the distances to the catalog position along the major and minor axes of the error ellipse. Also, the type of objects contained in the catalog is summarized in a flag, and a cumulative object-type flag is kept for all catalog associations to a given FSDB source. These flags are reported in Table II.G.4 and are described in Table II.G.6.

35

TABLE II.G.4 Catalogs Used for Associations with FSS Sources

Catalog No.	Catalog Type*	Catalog Name	Search Box (")	Source Size Used in Association
1	S	General Catalogue of Variable Stars, Kukarkin, *et al.*	26 × 165	
2	S	Dearborn Observatory Catalogue of Faint Red Stars, Lee, *et al.*	180 × 180	
3	SGO	Revised Air Force Geophysical Laboratory Four-Color Survey, Price & Murdoch	26 × 165	
4	S	Two Micron Sky Survey Neugebauer and Leighton	26 × 165	
5	O	Globule List Wesselius	90 × 165	X
6	G	Second Reference Catalogue of Bright Galaxies, de Vaucouleurs, *et al.*	26 × 165	
7	S	Early Type Stars with Emission Lines, Wackerling	26 × 165	
8	SGO	Equatorial Infrared Catalogue Sweeney	26 × 165	
9	G	Uppsala General Catalogue of Galaxies, Nilson	26 × 165	
10	G	Morphological Catalog of Galaxies, Vorontsov-Velyaminov, *et al.*	180 × 180	
11	O	Strasbourg Planetary Nebulae	26 × 165	
12	G	Catalogue of Galaxies and Clusters of Galaxies, Zwicky, *et al.*	26 × 165	
13	S	Smithsonian Astrophysical Observatory Star Catalog	26 × 165	
14	GO	ESO/Uppsala Survey of the ESO (B) Atlas, Lauberts	90 × 165	X
15	S	Bright Star Catalogue - 4th Edition, Hoffleit	26 × 165	

* See Table II.G.6 for meaning of catalog type symbols.

TABLE II.G.4 Catalogs Used for Associations with FSS Sources (cont.)

Catalog No.	Catalog Type*	Catalog Name	Search Box (″)	Source Size Used in Association
16	S	New Catalog of Suspected Variable Stars, Kukarkin, *et al.*	90 × 165	
17	S	General Catalogue of Cool Carbon Stars	26 × 165	
18	S	Catalog of Nearby Stars Gliese	26 × 165	
19	S	General Catalog of S Stars Stephenson	90 × 165	
20	O	Parkes HII Region Survey Haynes, *et al.*	120 × 165	X
21	O	Bonn HII Region Survey Altenhoff, *et al.*	80 × 165	
22	O	Catalog of CO Radial Velocities Toward Galactic HII Regions, Blitz, *et al.*	80 × 165	X
23	O	Catalogue of Dark Nebulae Lynds	90 × 165	X
		Comparison Catalog of HII Regions Marsalkova		
		Catalog of Star Clusters and Associations, Alter, *et al.*		
		Catalog of Bright Diffuse Galactic Nebulae, Cederblad		
		Untersuchungen über Reflexionsnebel am Palomar Sky Survey, Dorshner and Gürtler		
		A Study of Reflection Nebulae van den Bergh		
		Catalog of Southern Stars Embedded in in Nebulosity, van den Bergh and Herbst		
24	S	Two Micron Sky Survey with Improved Positions, Kleinmann and Joyce	26 × 165	

* See Table II.G.6 for meaning of catalog type symbols.

TABLE II.G.4 Catalogs Used for Associations with FSS Sources (cont.)

Catalog No.	Catalog Type*	Catalog Name	Search Box (")	Source Size Used in Association
25	G	Catalog of Dwarf Galaxies van den Bergh	90 × 165	
26	G	Atlas of Peculiar Galaxies Arp	120 × 165	
27	G	Galaxies with an Ultraviolet Continuum, Markarian, *et al.*	90 × 165	
28	G	Catalog of Extragalactic Radio Sources Having Flux Densities Greater than 1 Jy at 5 GHZ Kuhr, *et al.*	60 × 165	
29	G	Catalogue of Quasars and Active Nuclei, Véron-Cetty and Véron	90 × 165	
30	G	Lists of Galaxies Zwicky	90 × 165	
31	G	Atlas and Catalog of Interacting Galaxies, Vorontsov-Velyaminov	120 × 165	
32	GOI	*IRAS* Small Scale Structure Catalog	120 × 165	X
33-38	GI	(Internal Use)	26 × 165	
39	O	Ohio State University Radio Catalog	120 × 165	
40	S	University of Michigan Spectral Atlas Vol. 1 Vol. 2 and 3	 60 × 132 26 × 165	
41	SGOI	*IRAS* Serendipitous Survey Catalog	60 × 165	
42	SGOI	*IRAS* Point Source Catalog Version 2	26 × 165	
48	G	Virgo Cluster Catalog Bingelli, *et al.*	26 × 165	
49	G	Dressel and Condon	26 × 165	
50	O	*IRAS* Crossings of Numbered Asteroids	180 × 180	

* See Table II.G.6 for meaning of catalog type symbols.

TABLE II.G.5 Meaning of the Source Association Fields

Catalog	Field and Meaning	
1 GCVS	Type	Blank
	Field1	Code gives meaning for Fields 2-3
	if Field1 = 1	Field2 and Field3 are B mag [decimag] at max, min
	if Field1 = 2	Field2 and Field3 are V mag [decimag] at max, min
	if Field1 = 3	Field2 and Field3 are photographic mag [decimag] at max,min
	if Field1 = 4	Field2 and Field3 are estimated V mag [decimag] at max,min
	if Field1 = 5	Field2 is -999 and Field3 is 0
2 Dearborn Obs.	Type	Blank
	Field1	Code for Field2 (1,2)
	Field2	if Field1 is 1, Field2 is red magnitude [decimag] if Field1 is 2, Field2 is -999
	Field3	0
3 Revised AFGL	Type	Blank
	Field1	Magnitude at 4.2 μm [decimag]
	Field2	Magnitude at 11 μm [decimag]
	Field3	Magnitude at 27 μm [decimag]
4 2-μm Sky Survey	Type	Blank
	Field1	K magnitude [decimag]
	Field2	I magnitude [decimag]
	Field3	0
5 Globules (Wesselius)	Type	Blank
	Field1	-999
	Field2	Minimum diameter ["]
	Field3	Maximum diameter ["]

TABLE II.G.5 Meaning of the Source Association Fields (cont.)

Catalog	Field and Meaning	
6 R C 2	Type	Blank
	Field1	Harvard V magnitude [decimag]
	Field2	B_T [decimag]
	Field3	D_o ["]
7 Stars with em. lines	Type	Blank
	Field1	V magnitude [decimag]
	Field2	-999
	Field3	0
8 Equatorial IR Cat.	Type	Blank
	Field1	Flux density [10^{-16} W cm$^{-2}\mu$m] at 2.7 μm
	Field2	-999
	Field3	0
9 UGC	Type	Blank
	Field1	Zwicky magnitude [decimag]
	Field2	Minimum diameter ["] in B
	Field3	Maximum diameter ["] in B
10 MCG	Type	Blank
	Field1	-999
	Field2	Minimum diameter ["] in B
	Field3	Maximum diameter ["] in B
11 Strasbourg Planetary Nebulae	Type	Blank
	Field1	V magnitude of Nebula [decimag]
	Field2	B magnitude of Central Star [decimag]
	Field3	Minimum diameter of Nebula ["]
12 Zwicky	Type	Blank
	Field1	Zwicky magnitude [decimag]
	Field2	-999
	Field3	0

140

TABLE II.G.5 Meaning of the Source Association Fields (cont.)

Catalog	Field and Meaning	
13 SAO	Type	Spectral Type
	Field1	V magnitude [decimag]
	Field2	p_g magnitude [decimag]
	Field3	0
14 ESO/ UPPSALA	Type	First 3 characters of object type
	Field1	B magnitude [decimag]
	Field2	Maximum diameter ["]
	Field3	Minimum diameter ["]
15 Bright Stars	Type	Spectral Type
	Field1	V magnitude [decimag]
	Field2	B-V [centimag]
	Field3	U-B [centimag]
16 Suspected Var.	Type	Spectral Information
	Field1	V magnitude at maximum [decimag]
	Field2	-999
	Field3	0
17 Carbon Stars	Type	Spectral Type (may be truncated)
	Field1	p_g magnitude [decimag]
	Field2	V magnitude [decimag]
	Field3	I magnitude [decimag]
18 Gliese	Type	Spectral Type (may be truncated)
	Field1	V magnitude [decimag]
	Field2	B-V magnitude [millimag]
	Field3	U-B magnitude [millimag]
19 S Stars	Type	Blank
	Field1	p_g magnitude [decimag]
	Field2	V magnitude [decimag]
	Field3	I magnitude [decimag]

TABLE II.G.5 Meaning of the Source Association Fields (cont.)

Catalog	Field and Meaning	
20 Parkes HII Survey	Type	Blank
	Field1	-999
	Field2	Minimum diameter ["]
	Field3	Maximum diameter ["]
21 Bonn HII Survey	Type	Blank
	Field1	Flux density at 4.875 GHz (Jy)
	Field2	Diameter ["]
	Field3	0
22 Blitz	Type	Blank
	Field1	Diameter [arcsec]
	Field2	V_{CO} [km/s]
	Field3	Peak T_A [°K]
23 OSU	Type	Blank
	Field1	-999
	Field2	-999
	Field3	Diameter ["]
24 IRC w/good pos.	Type	C if 2.2-μm sources are possibly confused, blank otherwise
	Field1	Right ascension difference (IRC-*IRAS*) [deciseconds of time]
	Field2	Declination difference (IRC-*IRAS*) ["]
	Field3	0
25 DDO	Type	Blank
	Field1	-999
	Field2	-999
	Field3	0
26 Arp	Type	Blank
	Field1	-999
	Field2	-999
	Field3	0

TABLE II.G.5 Meaning of the Source Association Fields (cont.)

Catalog	Field and Meaning	
27 Markarian	Type	Blank
	Field1	-999
	Field2	-999
	Field3	0
28 Strong 5 GHz	Type	Object type (GAL or QSO)
	Field1	V magnitude [decimag]
	Field2	5 GHz flux density [deciJy]
	Field3	0
29 Véron-Cetty Véron	Type	Object classification
	Field1	V magnitude [decimag]
	Field2	Redshift × 1000
	Field3	0
30 Zwicky 8 Lists	Type	Blank
	Field1	-999
	Field2	-999
	Field3	0
31 VV	Type	Blank
	Field1	Special flag (see below)
	Field2	-999
	Field3	0
32 *IRAS* Small-Scale Structure	Type	Blank
	Field1	Hex-coded bands
	Field2	-999
	Field3	-999

143

D 10015

TABLE II.G.5 Meaning of the Source Association Fields (cont.)

Catalog	Field and Meaning	
39§ OSU Radio	Type	Blank
	Field1	Frequency
	Field2	Flux [deciJy]
	Field3	0
40 Michigan Spectral	Type	Class†
	Field1	Mag [decimag]
	Field2	HD number [low byte]
	Field3	HD number [high byte]
41 Serendipitous Survey	Type	Blank
	Field1	Hex-coded SSC bands
	Field2	First SSC flux density [mJy]‡
	Field3	Second SSC flux density
42 PSC II	Type	Blank
	Field1	Hex-coded PSC bands
	Field2	First PSC flux density [mJy]‡
	Field3	Second PSC flux density [mJy]
48 Virgo Cluster Catalog	Type	Class†
	Field1	B_T magnitude [decimag]
	Field2	Heliocentric velocity [km/s] (-999 when not available)
	Field3	Source size 100 × $log\ D_{est}(.1')$

§ Catalog numbers 33-38 reserved for internal use.

† Source name and type fields were combined to hold spectral type and class (Catalog 40), or object classification (Catalog 48).

‡ Flux densities given are the first two measurements in order from 12 to 100 μm.

TABLE II.G.5 Meaning of the Source Association Fields (cont.)

Catalog	Field and Meaning	
49 Dressel and Condon	Type	Blank
	Field1	-999
	Field2	-999
	Field3	-999
50 Asteroids	Type	Blank
	Field1	-999
	Field2	First four digits of crossing time [seconds, since 1980.0]
	Field3	Last four digits of crossing time

VV Catalog Flags (Catalog 31)

Field1	Explanation
10	VV 10 has the same coordinates as VV29 in the VV Atlas. The UGC was used to confirm that the coordinate is correct for VV 29 and erroneous for VV 10. The UGC position for VV 10 = UGC 10814 was adopted.
11	The VV position is substantially different (> 400″) from positions for the object in other catalogs. The VV position has been assumed to be in error because two or more other catalogs agree on a different position. The UGC position has been adopted.
12	Same as for 11, but the OSU position has been adopted.
13	The position in the VV Atlas, and the position listed for the VV object in the OSU are in disagreement. The true position has been established to be close to that of the OSU by the use of overlay transparencies on the POSS. The OSU position has been adopted.
14	Same as for 13, but the OSU position is not very good either, so a new position has been measured (accurate to about 1′.)
-999	No information given

+5

D 10015

TABLE II.G.6 Meaning of Catalog Type Field

Symbol	Meaning
S	Catalog contains stellar sources
G	Catalog contains extragalactic sources
O	Catalog contains nonstellar or extragalactic objects, such as planetary nebulae, HII regions, dark clouds or (in the case of catalog 50 only) asteroids
I	The catalog is derived all or in part from *IRAS* data

G.4 Neighbor Counts and Cirrus Flag

The FSDB was compared against itself to produce counts of FSS neighbors for each source. Neighbors were counted for one or more of three circular radii – 6′, 15′ and 30′ – and in each of seven categories: final catalog neighbors, data base neighbors, cold 60-100 μm or 100 μm-only neighbors, and counts of neighboring 12, 25, 60, and 100 μm extracted flux densities. These counts are written into the FSDB. Only six of these are reported in the short catalog: the 6′ catalog neighbor count, the 6′ extraction counts (one for each band), and the 30′ cold 60-100 μm or 100 μm-only count (the cirrus flag).

The "cirrus flag" is the number of 100 μm-only neighbors plus the number of 60 and 100 μm sources with $\log [f_\nu(60\ \mu\text{m})/f_\nu(100\ \mu\text{m})] < -0.75$. It is used as a tracer of local cirrus contamination (see Section III.G.6). Such a source is not necessarily cirrus. However, since the background density of galaxies varies slowly across the sky, a rapid increase in cold 100 μm counts indicates an increase in the contribution from the only other large population of cold IR sources: cirrus.

G.5 Non-Linear Flux Density Correction

As was done for the *IRAS* Pointed Observation Products (see IPAC Report "A User's Guide to *IRAS* Pointed Observation Products," E.T. Young, *et al.*), the FSS incorporates a non-linear correction to the flux density of each source. This correction accounts for the differences between a two- and three-parameter fit to the performance of a load resistor in the satellite electronics. In the original *IRAS* processing, a two-parameter fit to the load resistor was used; later work showed that a three-parameter fit was more appropriate. The difference between these two fits is now applied as a flux density correction indexed by the brightness of the source and the background surface brightness. The magnitude of the correction varies from < 5% for faint sources to ≈ 10% for some of the brightest sources (> 1000 Jy). Thus, the non-linear flux density correction for most FSS flux densities is small. This non-linear correction is the same as the one applied to PSC V.2.

1146

A table of the actual correction factors used – by band, source brightness, and background brightness – appears in Table 4 of "A User's Guide to the *IRAS* Pointed Observation Products" (see reference above). Correction factors for the FSS were calculated from linear interpolation in that table. The correction factor used for each FSS flux density is stored as a part of its record in the Faint Source Database.

The flux density correction is incorporated in the final reported flux density for sources in the FSDB (FSC and FSR). It has not been applied to the flux densities in the FSS plates. Hence, users of the plates must apply this correction themselves.

G.6 Catalog Criteria

The FSC is a reliability-driven survey of the unconfused sky for $|b| > 10°$ at 12, 25 μm and for $|b| > 20°$ at 60 μm with flux densities at 100 μm carried along as appropriate. Sources with a flux density detection only at 100 μm were not admitted to the catalog. In the range $|b| = 10°-20°$, 60 μm-only sources (as well as 60 and 100 μm sources) were excluded. Only sources with at least one high-quality flux density – those passing the reliability constraints given in Section III.D.3 – are included in the catalog. The minimum reliability requirement for a catalog source is 90% at 12 and 25 μm and 80% at 60 μm. Detections failing to achieve high quality are designated moderate quality and can enter the catalog only when bandmerged with a high-quality detection.

Catalog selection in each band was based on three parameters: the local SNR (LOCSNR, the peak flux density divided by the instrumental noise in the pixel containing the peak flux density), the number of detections contributing to the peak flux density, and the estimated reliability.

The test on LOCSNR is a last filter to remove sources caused by radiation glitches, known and unknown asteroids, and other transitory phenomena. The thresholds were the same as the source extractor (3.5) at all bands except at 25 μm where it was set to 4.5. In addition, each high-quality band was required to have at least 6 detector samples (before trimming) contributing to the peak flux density measurement.

By far the most restrictive test was on the estimated reliability. The SNR, the local sky noise, and the galactic latitude (at 12 and 25 μm) or the NOISRAT (at 60 μm) were used to produce an estimate of the reliability in each band with a detection for each source. See Section III.D.3 for a complete discussion of the method used to estimate a source's reliability.

In some regions of sky, the sky noise or the NOISRAT (at 60 μm) exceeded the maximum sky noise or NOISRAT which was considered for reliability analysis. In these

D 100 15
cases, no estimate of the reliability could be given in the affected band. In such a case the flux density at that band was tagged as moderate quality; i.e. to get into the catalog that detection must accompany another band's high quality detection. Thus, in addition to the regions of sky excluded from the catalog based on galactic latitude (mentioned in the first paragraph), other regions of the sky more difficult to define geometrically were excluded in various bands. See Figures IV.A.5 and 6 for one means of delineating these regions.

Cirrus contamination at 100 μm is so pervasive that to delineate unacceptable regions of sky and estimate the reliability in this wavelength region was judged to be of token value. Such a large undertaking would likely have resulted in only a few additional catalog sources, since few reliable (non-cirrus) objects will have a lone 100 μm detection. For this reason detections at 100 μm are all declared by fiat to be moderate quality. They therefore require a bandmerged high quality detection to enter the catalog.

178/179

D 10015

H. Processing Changes for Version 2 of the FSC

The discussions in the version 1 FSS Explanatory Supplement expounded the merits of making software changes in order to improve the sensitivity of the catalog while retaining the same reliability, especially at longer wavelengths. This section discusses those changes.

The most significant change for version 2 involved the method of noise computation. Although the method employed in version 2 is computationally more intensive, its superiority to the version 1 method justified the change. As a result we have been able to lower the 60 μm catalog SNR threshold from ~ 6 to ~ 5 (see Figure I.A.5). Consequently, version 2 contains an increased number of galaxies compared to version 1. Changes in processing software were made to the Extractor, Bandmerger and portions of the Data Base Generator. Furthermore a new algorithm was used to estimate 90% confidence level flux density upper limits. The criterion for entry into the version 2 catalog was based on the source reliability exceeding 90% at 12 and 25 μm and 80% at 60 μm. This differs from the version 1 criterion which was based on the SNR exceeding 6.0, 6.5, 6.0, 8.9† at 12 through 100 μm. Another difference is the prohibition imposed on the entry of 100 μm-*only* sources into the version 2 catalog, regardless of their SNRs. This decision was due to the prevalence of the infrared cirrus which made a thorough analysis of reliability impossible during the allotted time. However our experience from the version 1 catalog indicates that probably only a *few hundred* 100 μm-only sources were excluded from the catalog of over 173,000 sources. The software which produced the FSS *plates* did not undergo any changes, resulting in no version 2 of the plates.

H.1 Changes to the Extractor

The method of noise computation is the most significant change. In version 1, the noise was derived by taking the median pixel noise over a region of $(15')^2$ - $(30')^2$ and then correcting that noise for background structure through a noise correction factor derived over an *entire* FSS plate of 6.6° square. Because the cirrus has significant structure within a FSS plate, the noise correction factor should have been computed over a significantly smaller area. Or better still, the noise should have been computed directly from the signal grid.

For version 2, the noise computation comes entirely from the pixel (signal) histogram by taking the 68% quantile of the *positive* flux density values for each of a set of non-intersecting cells of 317 × 317 pixels at 12 and 25 μm, and cells of 199 × 199 pixels at 60

† Sources with high-quality flux density only at 100 μm were placed in the version 1 catalog only if the cirrus flag was less than 3.

150

and 100 μm, covering each plate. The noise cells correspond to regions of size $79.25' \times 79.25'$ at 12 and 25 μm and $99.5' \times 99.5'$ at 60 and 100 μm. The resulting noise array was then interpolated to estimate the local thresholding noise at each pixel in the plate. The pixel noises given in the plates are now ignored. The extractor also calculates the equivalent '1.5-σ' point at the 87% quantile in order to retain some information about the shape of the noise distribution.

This change has resulted in quoting more correct SNR values that are higher for true isolated sources and lower for cirrus sources or sources in confused areas.

The "island correction" is calculated exactly in version 2 by calculating directly the mean of $\frac{1}{\sqrt{N}}$. (It was approximated in version 1.) The island correction is applied only to sources at 12 and 25 μm for plates with centers within $|b| \gtrsim 5°$, and is no longer applied to sources at 60 and 100 μm.

The extractor in version 1 required the ratio of flux density to the standard deviation in that pixel (LOCSNR) to exceed 4.5 for *at least* one of the contiguous pixels which were above a fixed signal-to-noise-ratio (SNR) threshold of 3. The extractor for the version 2 processing did not have this requirement. This criterion was a holdover from the code that processed the Additional Observations, and is not useful for the FSS. In version 2 it is necessary for the *peak-flux* pixel to have a LOCSNR which exceeds 3.5 - in addition to the usual threshold of 3 on SNR. However below $|b| \sim 5°$ the threshold on LOCSNR was raised to 4.5 in order to reduce the extracted source density.

H.2 Changes to the Bandmerger

The bandmerger SNR thresholds for seeds were changed to 5, 5.5, 5, and 8 for 12, 25, 60, and 100 μm, respectively. This was necessary so that all sources in a deeper catalog would be bandmerged.

Sources which bandmerge with extractions at 100 μm did not have their positions refined by the position of the 100 μm extraction.

Minimum convolved positional uncertainties of $10'' \times 30''$ have been assigned to every extraction pair only for the purposes of bandmerging, which results in mandatory bandmerging for all extractions within an ellipse of axes $30'' \times 90''$. This change has cleaned up the few percent of bright sources that did not band merge in version 1.

H.3 Changes to the Database Generator

The duplicate source processing was changed to eliminate duplicate sources solely on the basis of distance from a plate edge. This removed the small bias toward accepting more sources in the overlap areas. In addition sources from different bands which were not

51

bandmerged but still fell within dup processing window were now allowed to be considered for the catalog.

A larger minimum window for the associations has been used. The new size is 26″ × 165″, as compared to the old size of 24″ × 135″. This larger size was necessary to prevent missing some true associations for the weaker sources.

D 10015

Authors:

Section A	T. Chester and M. Moshir
Section B	H. McCallon
Section C	G. Kopan and M. Melnyk
Section D	M. Moshir
Section E	D. Gregorich and M. Moshir
Section F	P. Hacking and M. Moshir
Section G	T. Conrow
Section H	T. Chester and M. Moshir

153

APPENDIX II.1 ANOMALOUS DATA REMOVED FROM FAINT SOURCE PROCESSING

SOP	OBS	Start Time (UTCS)	Duration (sec)	Anomaly Type
43	11	67077764	254	particle interference
45	21	67175904	52	particle interference
47	25	67265372	60	particle interference
51	28	67444515	416	particle interference
57	22	67695428	114	particle interference
59	3	67754511	389	no s/c attitude calibration
59	7	67756784	2869	no s/c attitude calibration
59	12	67763679	849	no s/c attitude calibration
59	19	67769822	1021	no s/c attitude calibration
63	26	67949390	255	particle interference
71	29	68307421	347	particle interference
72	10	68337805	212	particle interference
74	19	68439651	249	particle interference
91	32	69171731	717	particle interference
116	15	70238726	255	detector calibration problems
117	5	70268789	22	charged particle hit
117	22	70292554	21	particle interference
117	28	70300602	303	detector calibration problems
119	8	70352660	122	detector calibration problems
119	11	70355951	22	particle interference
120	30	70426888	122	detector calibration problems
121	9	70439258	122	detector calibration problems
122	34	70513485	122	detector calibration problems
125	7	70606198	181	detector calibration problems
126	31	70686612	181	detector calibration problems
132	8	70922460	485	particle interference
132	19	70933610	20	charged particle hit
133	23	70975534	230	particle interference
139	24	71243310	205	detector calibration problems
139	31	71249496	205	detector calibration problems
139	40	71255665	205	detector calibration problems
140	5	71261848	205	detector calibration problems
140	14	71268035	205	detector calibration problems
140	22	71274220	205	detector calibration problems
145	28	71503454	249	particle interference
147	1	71556002	488	particle interference

APPENDIX II.1 ANOMALOUS DATA REMOVED FROM FAINT SOURCE PROCESSING (continued)

SOP	OBS	Start Time (UTCS)	Duration (sec)	Anomaly Type
149	5	71646624	100	detector calibration problems
149	16	71658996	100	detector calibration problems
150	3	71695330	20	charged particle hit
150	8	71702080	20	charged particle hit
150	8	71702250	20	charged particle hit
152	29	71813308	100	detector calibration problems
154	32	71899898	100	detector calibration problems
155	14	71914570	22	particle interference
157	6	71993015	100	detector calibration problems
158	33	72073200	100	detector calibration problems
160	24	72147027	138	detector calibration problems
161	19	72184603	138	detector calibration problems
161	32	72196687	138	detector calibration problems
161	40	72202872	138	detector calibration problems
164	12	72308417	138	detector calibration problems
167	55	72461994	28	particle interference
168	23	72487631	34	particle interference
171	43	72629728	80	unidentified anomaly
171	47	72635450	300	unidentified anomaly
176	14	72827699	732	particle interference
178	17	72919776	38	charged particle hit
180	18	73009174	32	particle interference
187	51	73328076	46	particle interference
203	5	73980690	20	charged particle hit
203	35	74015400	20	particle interference
217	44	74617083	20	charged particle hit
217	50	74627805	20	charged particle hit
217	50	74628086	286	particle interference
223	43	74886805	262	particle interference
227	38	75040901	23	particle interference
232	16	75246111	24	particle interference
232	23	75251212	37	particle interference
235	26	75394474	521	particle interference
236	1	75403271	180	detector calibration problems
236	9	75409388	180	detector calibration problems

APPENDIX II.1 ANOMALOUS DATA REMOVED FROM FAINT SOURCE PROCESSING (continued)

SOP	OBS	Start Time (UTCS)	Duration (sec)	Anomaly Type
236	26	75427930	221	charged particle hit
237	28	75480733	35	particle interference
239	27	75567231	327	particle interference
241	16	75637966	52	particle interference
243	28	75739323	183	particle interference
244	11	75757976	42	particle interference
245	26	75820201	28	particle interference
267	28	76769324	578	particle interference
268	4	76792072	279	particle interference
278	20	77243560	20	charged particle hit
279	19	77273751	2763	bias boost problem
279	20	77276514	1847	bias boost problem
279	21	77278361	715	bias boost problem
279	22	77279076	825	bias boost problem
279	23	77279901	763	bias boost problem
297	15	78050150	55	particle interference
298	7	78094661	520	pointing error
298	24	78117904	24	particle interference
306	22	78448378	116	particle interference
306	23	78452064	213	charged particle hit
306	25	78455298	78	charged particle hit
306	25	78456082	208	particle interference
333	33	79620862	20	charged particle hit
335	15	79689852	284	particle interference
337	43	79797790	270	particle interference
339	13	79858597	202	no s/c attitude calibration
356	9	80601599	22	particle interference
357	27	80647429	23	particle interference
357	41	80662356	40	particle interference
359	23	80735751	21	particle interference
360	5	80769094	176	particle interference
360	24	80786252	24	particle interference
361	31	80834374	38	particle interference
365	2	80975645	27	particle interference
365	2	80975770	28	particle interference

APPENDIX II.1 ANOMALOUS DATA REMOVED FROM FAINT SOURCE PROCESSING (continued)

SOP	OBS	Start Time (UTCS)	Duration (sec)	Anomaly Type
367	32	81095272	26	particle interference
369	14	81161485	35	particle interference
377	45	81525279	469	particle interference
381	40	81702948	149	particle interference
392	10	82153450	20	charged particle hit
393	37	82215859	271	particle interference
397	37	82385774	503	particle interference
399	25	82459724	253	particle interference
400	12	82499613	256	particle interference
401	22	82542310	147	no s/c attitude calibration
415	60	83180200	59	particle interference
418	30	83293709	21	particle interference
423	41	83520265	55	particle interference
433	23	83926933	577	no s/c attitude calibration
433	29	83933172	523	no s/c attitude calibration
443	9	84353823	958	pointing error
445	40	84460268	20	particle interference
448	40	84594749	1034	pointing error
457	2	84950476	609	pointing error
462	5	85171387	252	particle interference
473	31	85664175	21	particle interference
476	10	85783270	24	particle interference
491	25	86436552	269	particle interference
495	43	86633120	20	charged particle hit
512	26	87359240	25	particle interference
518	12	87601786	251	particle interference
521	48	87749404	22	particle interference
523	8	87804322	209	no s/c attitude calibration
525	14	87895705	248	unidentified anomaly
533	40	88268814	26	particle interference
534	13	88288035	22	particle interference
564	6	89580595	20	particle interference
566	22	89677671	30	particle interference
577	41	90163301	227	particle interference
582	24	90378132	76	particle interference
582	31	90384248	60	particle interference
590	14	90713166	378	pointing error

APPENDIX II.2 FOCAL PLANE MODEL FOR FSS

Detector	Wavelength (μm)	Mask Location(′) In-Scan	Cross-Scan	Width (′)	Time Offset (sec)
1	100	28.00	8.71	5.05	-.106
2	100	28.01	.04	5.05	-.046
3	100	28.01	-8.62	5.05	-.044
4	100	23.97	12.86	4.68	.017
5	100	23.97	4.37	5.05	.019
6	100	23.98	-4.29	5.05	.079
7	100	23.98	-12.77	4.70	.081
8	60	19.66	9.80	4.75	-.048
9	60	19.67	1.14	4.76	-.046
10	60	19.67	-7.53	4.76	-.044
11	60	19.67	-14.46	1.30	-.042
12	60	17.14	13.49	3.45	.015
13	60	17.15	5.47	4.76	.017
14	60	17.15	-3.20	4.75	.019
15	60	17.15	-11.86	4.75	.021
16	25	14.03	8.71	4.65	-.031
17	25	14.03	.04	4.65	-.029
18	25	14.03	-8.62	4.65	-.027
19	25	12.26	12.96	4.48	-.025
20	25	12.26	4.37	4.65	-.023
21	25	12.27	-4.29	4.65	-.021
22	25	12.27	-12.88	4.49	-.019
23	12	9.47	9.81	4.55	-.020
24	12	9.48	1.14	4.55	-.018
25	12	9.49	-7.52	4.54	-.016
26	12	9.49	-14.50	1.20	-.014
27	12	7.71	13.55	3.33	-.012
28	12	7.71	5.47	4.54	-.010
29	12	7.72	-3.19	4.54	-.008
30	12	7.72	-11.86	4.54	-.006
31	60	4.54	14.55	1.28	-.049
32	60	4.53	7.61	4.75	-.047
33	60	4.53	-1.06	4.75	-.045
34	60	4.53	-9.73	4.75	-.043

APPENDIX II.2 FOCAL PLANE MODEL FOR FSS (continued)

Detector	Wavelength (μm)	Mask Location(′) In-Scan	Cross-Scan	Width (′)	Time Offset (sec)
35	60	2.02	11.94	4.75	.014
36	60	2.01	3.27	4.76	.016
37	60	2.01	-5.40	4.75	.018
38	60	2.01	-13.41	3.47	.020
39	25	-1.17	14.05	2.33	-.032
40	25	-1.17	6.55	4.65	-.030
41	25	-1.17	-2.12	4.65	-.028
42	25	-1.17	-10.78	4.65	-.026
43	25	-2.93	10.88	4.65	-.024
44	25	-2.93	2.22	4.65	-.022
45	25	-2.93	-6.45	4.65	-.020
46	25	-2.93	-13.95	2.33	-.018
47	12	-5.68	14.64	1.18	-.021
48	12	-5.68	7.65	4.55	-.019
49	12	-5.67	-1.02	4.55	-.017
50	12	-5.67	-9.68	4.55	-.015
51	12	-7.44	11.98	4.55	-.013
52	12	-7.44	3.32	4.55	-.011
53	12	-7.43	-5.35	4.55	-.009
54	12	-7.43	-13.41	3.36	-.007
55	100	-11.33	13.95	2.52	-.107
56	100	-11.33	6.55	5.05	-.105
57	100	-11.33	-2.12	5.05	-.045
58	100	-11.32	-10.79	5.05	-.043
59	100	-15.36	10.88	5.06	.018
60	100	-15.36	2.21	5.05	.020
61	100	-15.36	-6.46	5.05	.080
62	100	-15.36	-13.85	2.53	.082

D 10015

III. ANALYSIS OF THE FAINT SOURCE SURVEY

A. Plate Properties

A.1 Overview

Plate properties are of interest because all FSS data products are derived from the plates. The FSS plates measure 6.6° × 6.6° and are based on equatorial coordinates with centers separated by 5° in declination, and overlap by 1.6° at the equator. An orthographic projection scheme is used. The plates have 1584 × 1584 pixels of size 0.25′ × 0.25′ at 12 and 25 μm, and 792 × 792 pixels of size 0.50′ × 0.50′ at 60 and 100 μm. In each band the data have been coadded and result in three grids containing the point-source-filtered flux density at every point, the estimate of flux density uncertainty at every point, and the number of times a given pixel received a data sample.

In the following sections we describe the attributes of the plates which bear on the proper use and interpretation of the FSS data. In the rest of this section we briefly describe some of these features.

Because of the survey strategy of the *IRAS* telescope and the earlier than expected exhaustion of the telescope coolant, the sky was not scanned with uniform coverage. Two regions in the sky, each roughly 5° wide and 60° long, were not covered by the telescope during the survey part of the *IRAS* mission. For these regions the *IRAS* Serendipitous Survey Catalog (SSC) should be consulted for possible coverage. Outside of the no-coverage zones the amount of coverage per pixel varied from 1 to over 200 counts. The non-uniformity of coverage appears on all angular scales. In particular, the regular pattern of survey scans coupled with the overlap scheme leads to the presence of strips separated by approximately $\frac{1}{4}^\circ$ in which the coverage is deeper than the surrounding neighborhood. This leads to low level coverage stripes in the flux density grids and in all FSS products. In Section III.A.2 the extent of sky coverage and the scaling of noise with respect to coverage will be described in detail.

Areas of sky suitable for the study of faintest IR objects can be found by locating regions where the FSS noise estimate reaches its lowest values. Variations in coverage, electronic noise, and background structure all contribute to FSS noise estimation. These variations should be taken into account when a search for clear and deep windows into the IR sky is made.

The FSS noise estimate varies to first order as $\sigma_0/\sqrt{N}$ at shorter wavelengths, where N is the number of times a pixel is covered. In the remainder of this section σ_0 stands for the average single scan detector noise. To first order, highest sensitivity of the survey is

160

D 10015

III. ANALYSIS OF THE FAINT SOURCE SURVEY

A. Plate Properties

A.1 Overview

Plate properties are of interest because all FSS data products are derived from the plates. The FSS plates measure 6.6° × 6.6° and are based on equatorial coordinates with centers separated by 5° in declination, and overlap by 1.6° at the equator. An orthographic projection scheme is used. The plates have 1584 × 1584 pixels of size 0.25′ × 0.25′ at 12 and 25 μm, and 792 × 792 pixels of size 0.50′ × 0.50′ at 60 and 100 μm. In each band the data have been coadded and result in three grids containing the point-source-filtered flux density at every point, the estimate of flux density uncertainty at every point, and the number of times a given pixel received a data sample.

In the following sections we describe the attributes of the plates which bear on the proper use and interpretation of the FSS data. In the rest of this section we briefly describe some of these features.

Because of the survey strategy of the *IRAS* telescope and the earlier than expected exhaustion of the telescope coolant, the sky was not scanned with uniform coverage. Two regions in the sky, each roughly 5° wide and 60° long, were not covered by the telescope during the survey part of the *IRAS* mission. For these regions the *IRAS* Serendipitous Survey Catalog (SSC) should be consulted for possible coverage. Outside of the no-coverage zones the amount of coverage per pixel varied from 1 to over 200 counts. The non-uniformity of coverage appears on all angular scales. In particular, the regular pattern of survey scans coupled with the overlap scheme leads to the presence of strips separated by approximately $\frac{1}{4}^\circ$ in which the coverage is deeper than the surrounding neighborhood. This leads to low level coverage stripes in the flux density grids and in all FSS products. In Section III.A.2 the extent of sky coverage and the scaling of noise with respect to coverage will be described in detail.

Areas of sky suitable for the study of faintest IR objects can be found by locating regions where the FSS noise estimate reaches its lowest values. Variations in coverage, electronic noise, and background structure all contribute to FSS noise estimation. These variations should be taken into account when a search for clear and deep windows into the IR sky is made.

The FSS noise estimate varies to first order as $\sigma_0/\sqrt{N}$ at shorter wavelengths, where N is the number of times a pixel is covered. In the remainder of this section σ_0 stands for the average single scan detector noise. To first order, highest sensitivity of the survey is

160

attained when maximal coverage is reached. In addition to the variation of N as discussed above, σ_0 also varies slowly over angles of several degrees due to detector noise variation with background. The noise, σ_0, increases by approximately 20% at 12 μm and by almost 100% at 25 μm between the ecliptic poles and the ecliptic plane. No similar dependence on ecliptic coordinates is observed at 60 and 100 μm. Noise dependence on ecliptic coordinates is discussed in Section III.A.3.

During source extraction, a thresholding noise is computed at every point from the flux density grid. This thresholding noise has an uncertainty, due to finite sample size, of approximately 2–3% for an area with three HCON coverage. Section III.A.4 treats this issue.

The source extractor computes two types of noise at each point. One comes directly from the 68% quantile of the positive values from the flux density grid, and the other from the median of the noise grid (see Section II.E.2). The data in the noise grid reflect the instrumental noise, and in the limit of infinite coverage tend to 0, as is seen from equation II.C.2. The ratio of 68% quantile noise to the median of the noise grid is called the *noise correction factor* (NOISCOR). In the absence of correlated noise (due to structured background, etc.) and for N large enough ($\gtrsim$10), these two estimates of noise will agree, and both will tend to zero, while the NOISCOR approaches 1. NOISCOR can become different from unity when there is either low coverage (even when noise is Gaussian, see Figure III.A.1) or when noise is correlated. In practice, due to background and coverage variations, the two estimates of noise differ. If the sky coverage were uniform, this parameter could in principle be used to estimate the contribution of background to the overall sky noise. Since the NOISCOR combines the effects of coverage and background, a second parameter is computed which is independent of coverage. This latter parameter comes from the ratio of the 87% quantile of the positive flux density grid to the 68% quantile. This ratio is called the *noise ratio* (NOISRAT). If the noise in the sky were purely Gaussian, and 0% of the data were trimmed, NOISRAT would be equal to 1.5. Departure of this ratio from 1.5 indicates the presence of structured noise. The statistical uncertainty in individual values of this ratio is 2–3%. The noise used in the estimation of the SNR is the 68% quantile of flux density grid computed on grids of 317 × 317 pixels at 12 and 25 μm and 199 × 199 pixels at 60 and 100 μm.

The use of a median filter to *point-source filter* the data occasionally results in unexpected behavior. The filters result in complete suppression of structures larger than 5.5′, 4.6′, 8.2′, and 7.2′ in extent for the 12 through 100 μm bands, respectively. The effects of the median filter on extended objects are treated in Section III.A.5.

161

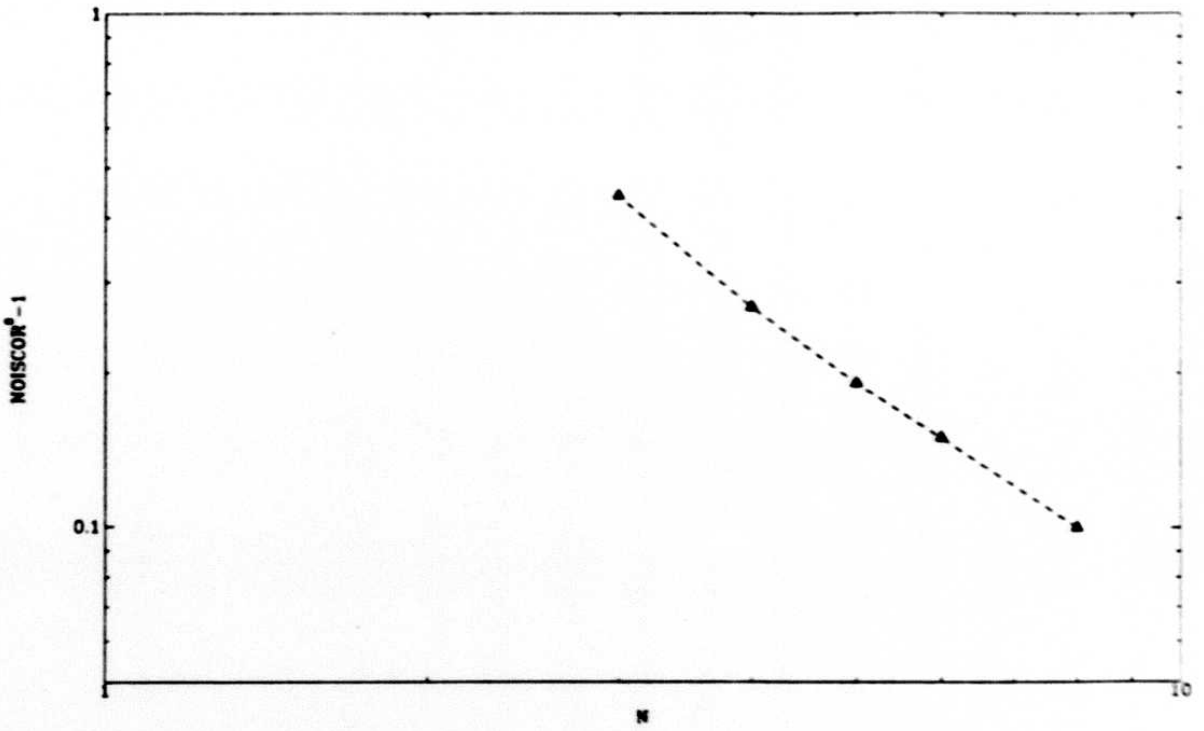

Figure III.A.1 Variation of NOISCOR with the number of data samples N, for a Gaussian distribution with no trimming. Notice that even for a Gaussian distribution NOISCOR is not unity when N is small.

The nuclear radiation hits in the detector data have been deglitched according to the algorithm described in Section II.C.2.a. The statistics for the number of deglitched radiation events show a clear dependence on geographic latitude, thus displaying the residual effects of the increased radiation environment at the *South Atlantic Anomaly* (SAA) and the polar horns (see Sections III.B and III.D of the *Main Supplement*). We have relied on the trimmed-average filter to remove the weaker radiation hits. The trimmed-average method discards approximately 20% of the data, which is suitable for low to medium radiation environments. A higher trimming fraction, perhaps as high as 50%, would have been preferred in areas with enhanced radiation events. However, the high radiation zones are higher coverage zones and the 1/N attenuation due to coaddition compensates. Section III.A.6 gives the deglitcher statistics. Section III.A.7 treats the issue of high source density regions.

A.2 Sky Coverage and Scaling of Noise

During the *IRAS* mission 98% of the sky was surveyed to varying depths: 72% of the sky was covered by three or more HCONs, 24% of the sky was covered by only two HCONs, and 2% of the sky received only one HCON coverage. The FSS plates report a

162

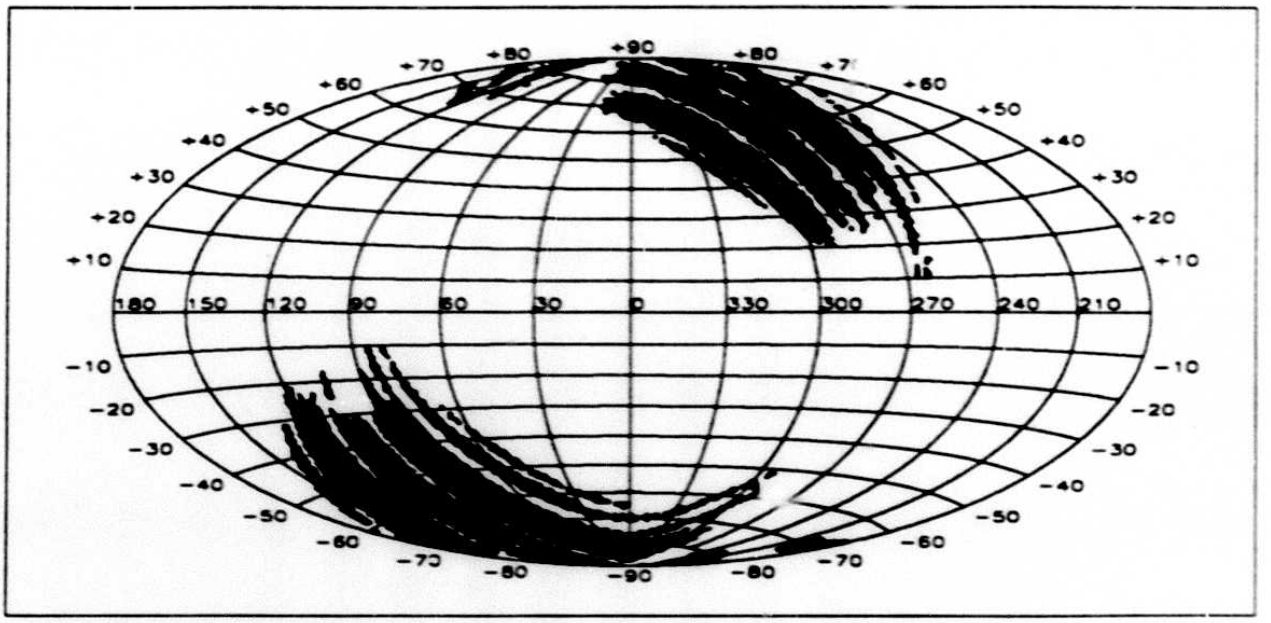

Figure III.A.2 Areas with $|b| \geq 10°$ covered by an average of 5.5 – 8.5 detector passes at 12 μm.

flux density value at any pixel with at least one data sample. A value for the pixel noise is reported only for those pixels with at least four data samples. The users of FSS plates should keep this in mind while reading flux densities and noises directly from the plates.

The following figures display the depth of coverage in galactic coordinates for $|b| \geq 10°$. The 12 μm band is chosen for display of coverage. Figures III.A.2 - 4 show those areas where the average number of counts per pixel falls within the ranges 5.5 - 8.5, 8.5 - 12.5, and more than 12.5 counts, respectively.

Noise estimation is an essential part of source selection. A brief parameterization of sky noise will be given, and each contribution will be discussed.

Noise in the data consists of two parts, one which scales with coverage and a fixed pattern noise which does not. The first component scales in amplitude as $1/\sqrt{N}$ with the number of samples N. The fixed pattern component of noise is due to the finite size of the detectors and the presence of a fixed pattern of background point sources plus extended structures. This fixed pattern noise is not reduced in amplitude with increasing coverage.

Denote the probability distribution for a fluctuation $\mathcal{A}$ due to background by $P_c(\mathcal{A})$. This expression is a convolution of the underlying source counts, the detector cross-scan profiles (see Section II.D.2), and the median-filtered detector in-scan profiles. We will

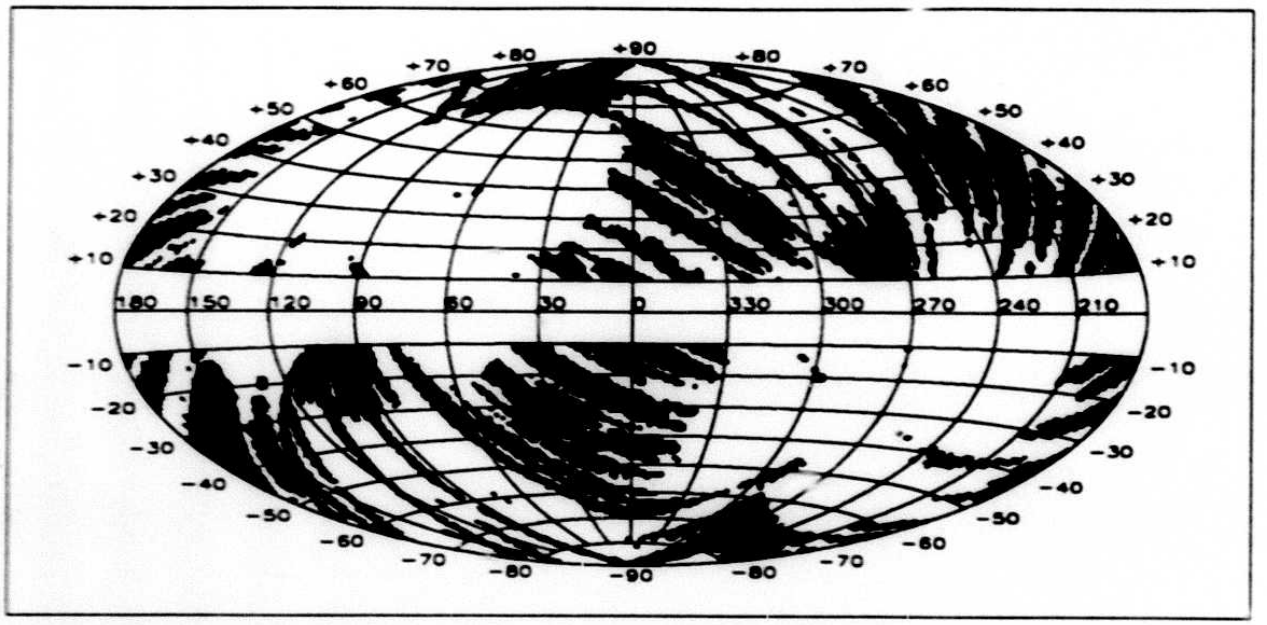

Figure III.A.3 Areas with $|b| \geq 10°$ covered by an average of 8.5 – 12.5 detector passes at 12 μm.

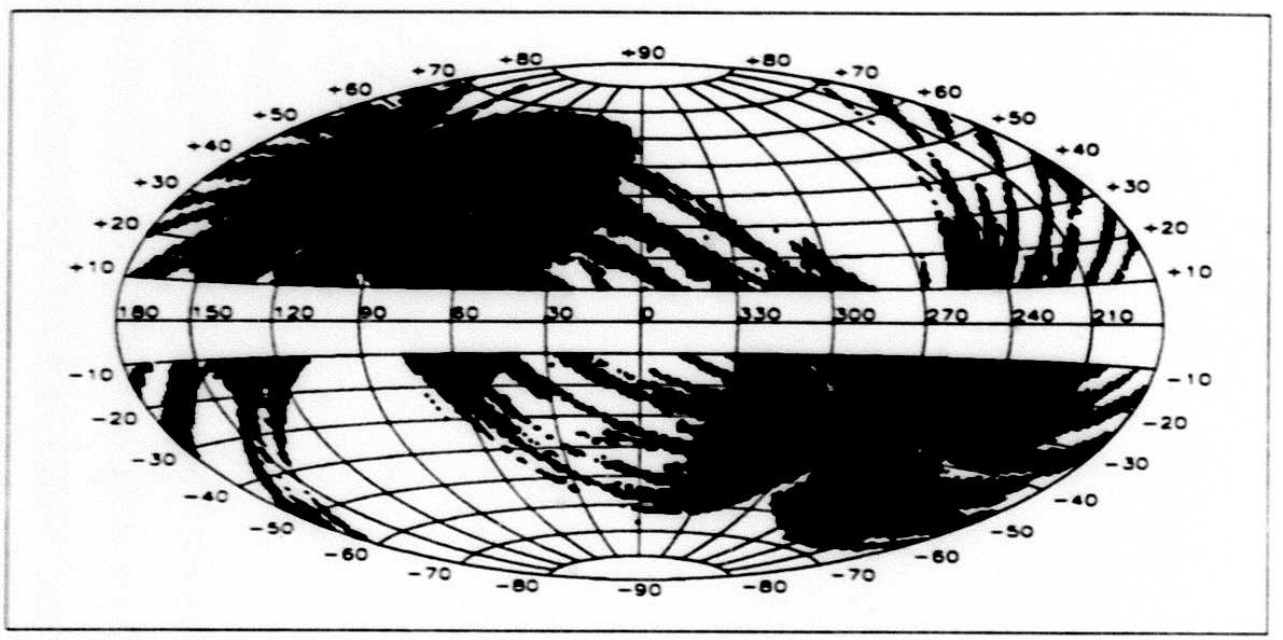

Figure III.A.4 Areas with $|b| \geq 10°$ covered by an average of more than 12.5 detector passes at 12 μm.

164

not use a theoretical model to compute the confusion noise. Instead, we will estimate the width of the distribution $P_c(\mathcal{A})$ from the available data. Denoting the distribution of the temporal noise (the part scaling with coverage) by $P_t(\epsilon)$, the distribution of the total noise $\xi = \epsilon + \mathcal{A}$ (this last quantity ξ yields what we call "noise") is given by $P(\xi) = \int \delta(\xi - \epsilon - \mathcal{A})\, P_t(\epsilon)\, P_c(\mathcal{A})\, d\epsilon\, d\mathcal{A}$. If the width of the temporal noise is given as $\sigma_0/\sqrt{N}$ (recalling the scaling with coverage) and the width of the spatial noise is given by a, then σ, the width of *total noise*, is

$$\sigma^2 = \frac{\sigma_0^2}{N} + a^2 \qquad (III.A.1)$$

The parameter σ_0 appearing in equation III.A.1 is not in general a constant. At 12 and 25 μm, it decreases with increasing ecliptic latitude. At 60 and 100 μm, no such dependence on ecliptic latitude is observed ($\sigma_0 \sim 100$ mJy at 60 μm, and ~ 300 mJy at 100 μm). The parameter a in equation III.A.1 is a non-trivial function of galactic coordinates since it represents the effects of background sources and extended structures. The data for high galactic latitude ($|b| \gtrsim 50°$) indicate that at 12 and 25 μm a is a negligible quantity typically of the order of 1 mJy. Thus the scaling of noise with coverage at 12 and 25 μm is well represented by

$$\sigma^2 = \frac{\sigma_0^2}{N} \qquad (III.A.2)$$

At 60 and 100 μm, no such general statements can be made regarding a, and thus the application of equation III.A.2 to these two bands would be erroneous. For high galactic latitudes ($|b| \gtrsim 50°$), a varies from 10 to 40 mJy at 60 μm, and from ~30 to ~320 mJy at 100 μm. Special runs were made on several plates, where the number of data samples, N, were kept fixed at values of 6, 8, 10, and 12 counts. Then the noise on cells of size $\sim 1.6° \times 1.6°$ were computed. For each cell, the data were fitted to equation III.A.1, and the parameters a were obtained. A sample for plate 868 can be seen in Figure III.A.5.

The width of the distribution, $P(\xi)$, is defined by the FSS as the point ξ_0 where $\int_0^{\xi_0} P(\xi)\, d\xi = .683 \times \int_0^{\infty} P(\xi)\, d\xi$. *Notice that this definition departs from the conventional one where the width is taken to be the square root of the second moment of the distribution.* When the distribution $P(\xi)$ is Gaussian the two definitions give identical values. We define σ in this way because *the histogram of flux density values is asymmetrical due to the presence of sources and because extractions are made only from pixels with positive flux densities.*

A.3 Noise Variation with Ecliptic Latitude

The zodiacal emission dramatically affects the detector noise. The degree of this noise variation depends on the spectral band considered. The data indicate that detector noise

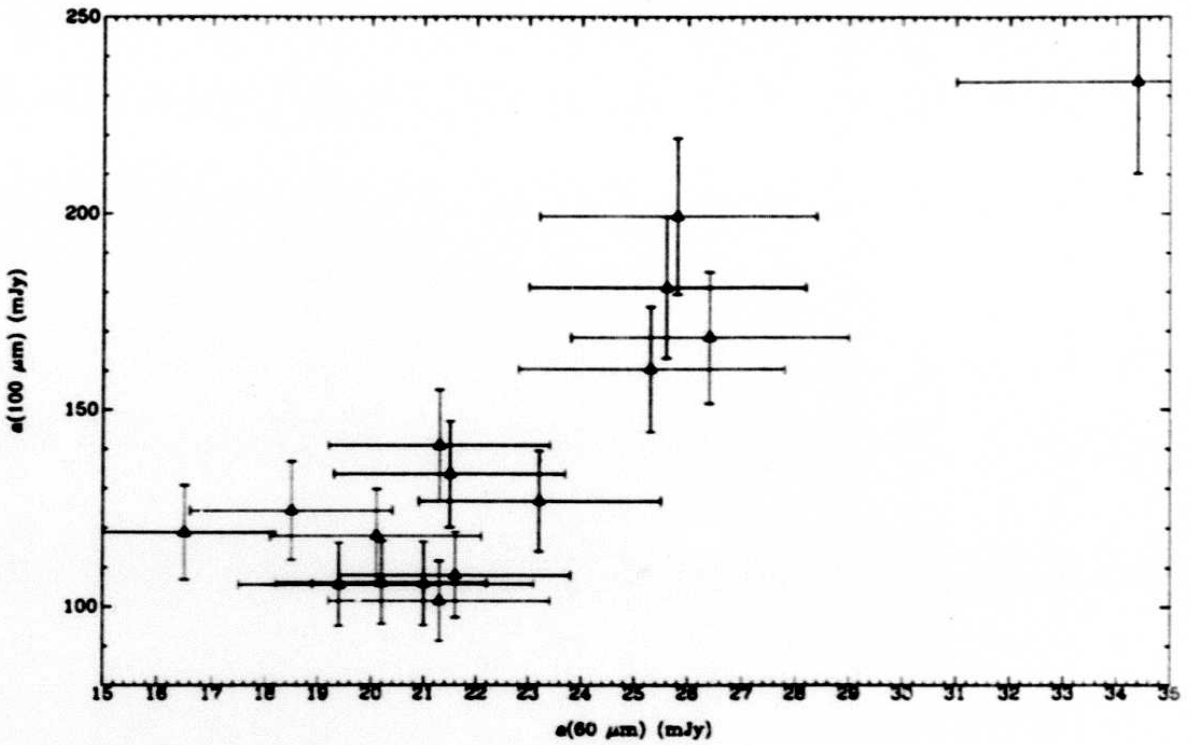

Figure III.A.5 Scatter plot of a (from equation III.A.1) at 60 and 100 μm, computed on a scale of $\sim 1.6°$, for FSS plate 868 ($l \sim 357°$ and $b \sim 48°$).

due to the photons from the extended emission from the solar neighborhood attains its smallest value at the ecliptic poles, and its largest values at the ecliptic plane. This variation is 20% at 12 μm. The noise variation is the most dramatic at 25 μm, corresponding to a 100% increase. The variation at 60 μm is less than 5%, and there is little evidence of any variation at 100 μm.

The coverage also varies with ecliptic latitude and causes a variation in thresholding noise (through equations III.A.1 and 2). Due to convergence of satellite orbits at the ecliptic poles, the higher coverage zones occur at high *ecliptic* latitudes, which translate into mid-*galactic* latitudes (see Figure III.A.4).

Thus both effects reinforce each other and plate noise at 12 and 25 μm attains its lowest value at high ecliptic latitudes. Correspondingly, near the ecliptic plane plate noise at 12 and 25 μm reaches its highest value. As a consequence, the flux density at which a given level of completeness is reached varies across the sky. Section III.C.3 discusses this variation.

A.4 Error of Noise Estimates

The FSDB contains an estimate of noise for every extraction in the database. Details

1606

of the algorithm are presented in Section II.E. In the present section we estimate the uncertainty of the thresholding noise.

The quoted noise is basically a statistic coming from a subregion Γ of a plate. (Γ is $\sim 79.25' \times 79.25'$ at 12 and 25 μm and $\sim 99.5' \times 99.25'$ at 60 and 100 μm.) From equation III.A.1 it is seen that the estimate of the noise depends on coverage N, temporal noise σ_0, and spatial noise a. So long as the underlying parameters σ_0 and a do not vary appreciably on a scale given by Γ (a valid assumption in all but the most confused regions of sky), the uncertainty in noise comes from the finite sample size and coverage N. Very roughly, $\sigma_\sigma^2 \propto 1/N$. For a region with a mean coverage of approximately 12 counts per pixel, the uncertainty on σ over the region Γ is approximately 3–4% for 12 to 100 μm bands. For other values of coverage, the scaling law $\sigma_\sigma \propto 1/\sqrt{N}$ may be used to estimate the noise uncertainties.

A.5 Median Filter Response to Extended Structure

This section discusses the effects of the in-scan median filter on extended structure. The median filter is used to remove background and DC offsets prior to coadding the data as described in Section II.C. The filter completely removes structures larger than the length of the filter, and severely attenuates structures larger than half the filter length.

The filter is non-linear and an exhaustive discussion of its behavior is outside the scope of this document; however, the general characteristics may be inferred from a few simple cases. We consider separately the response of the filter to each of the following cases: isolated point sources, two nearby point sources, compact extended sources, and complex extended structure. The amplitude response of the filter to Gaussian extended sources as a function of size is also presented.

The local background is computed as the median of n points centered on the sample point in question, excluding the central five points. This background is subtracted from the sample point. The central five points were excluded from the baseline computation to avoid underestimating the flux density of faint sources due to the bias in the median induced by the presence of the source (this bias is on the order of one standard deviation of the data). The filter lengths were 23, 19, 17 and 15 samples for 12, 25, 60, and 100 μm as described in Section II.C.

The point source signature and the resulting filter response are shown in Figure III.A.6 for each of the four wavelength bands. The point source response half-width is approximately three samples for all four wavelength bands in the detector data stream. Note the negative sidelobes, caused by the source flooding one side of the filter. The sidelobe

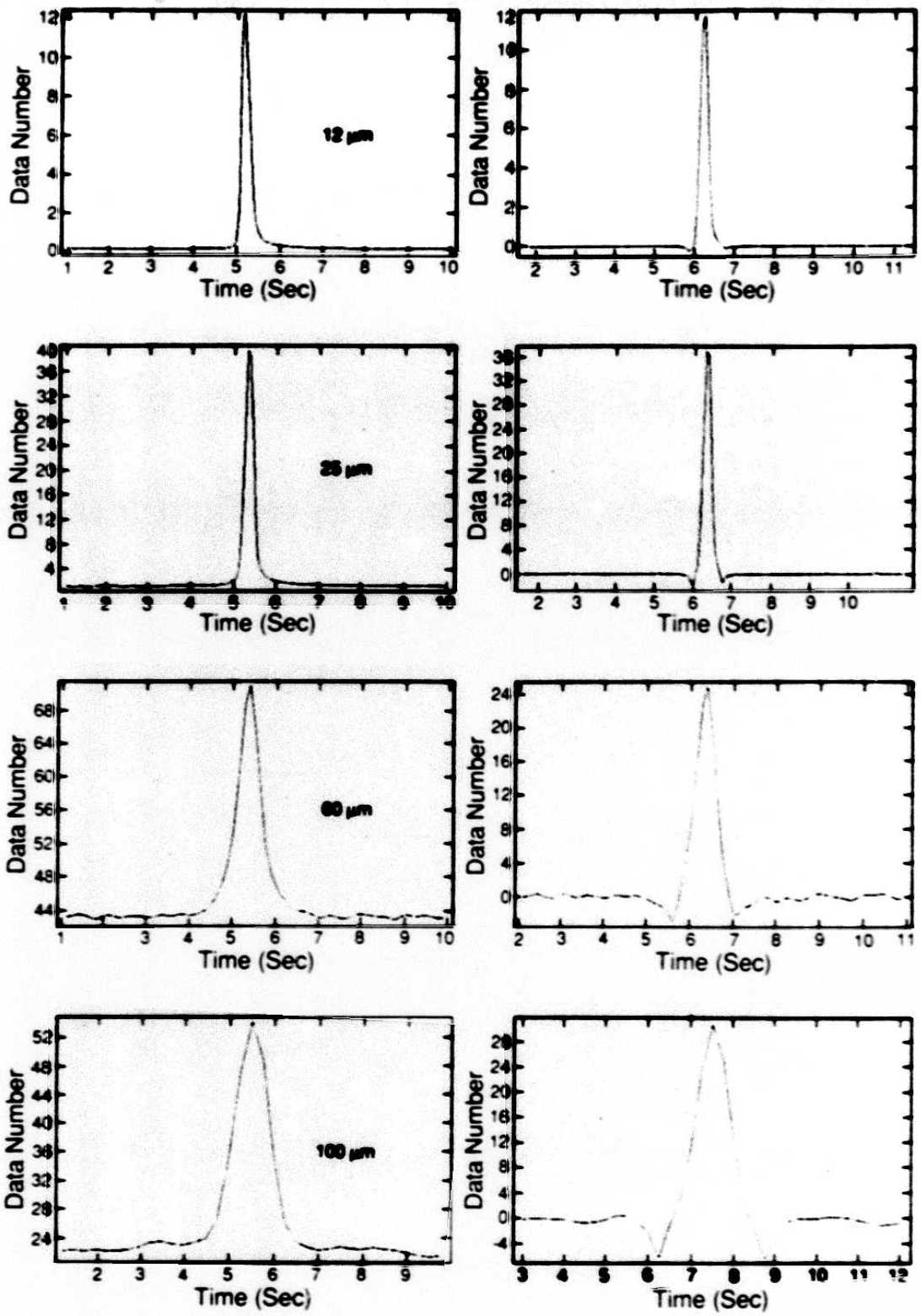

Figure III.A.6 Detector signature and median filter response to a point source in each wavelength band.

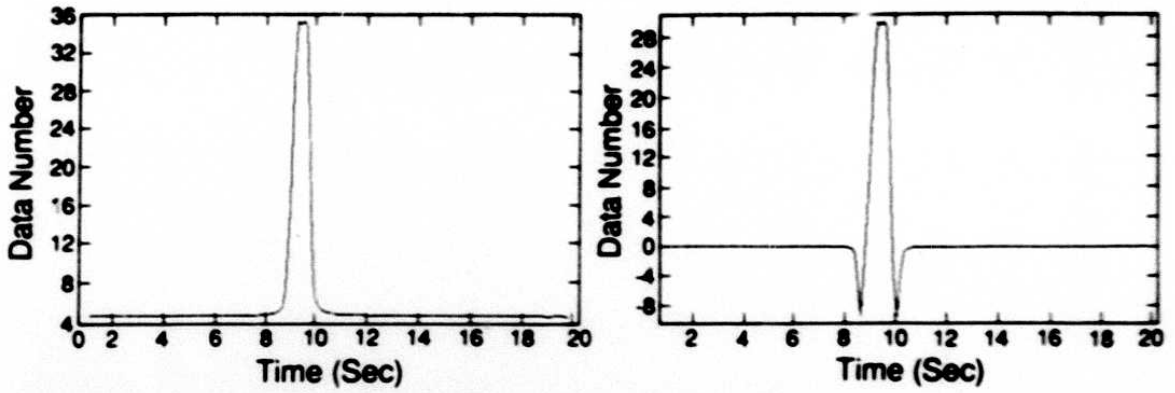

Figure III.A.7 Detector signature and median filter response to two point sources separated by 1 FWHM.

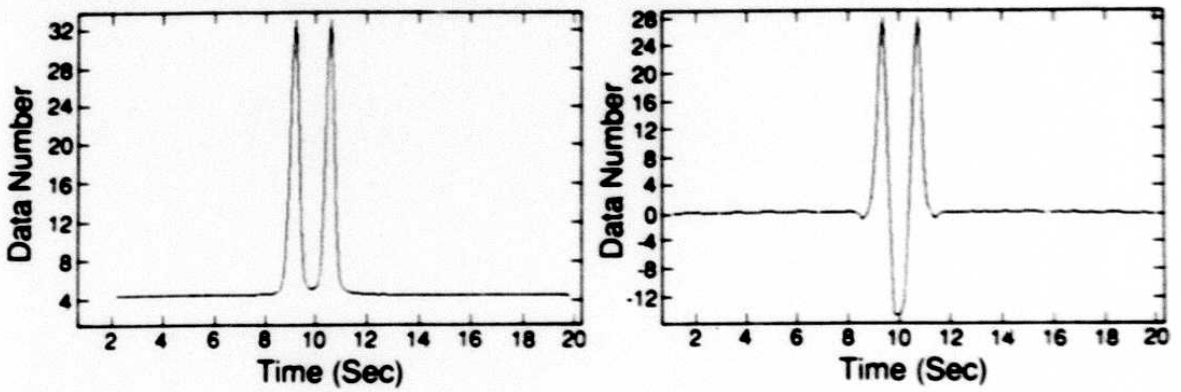

Figure III.A.8 Detector signature and median filter response to two point sources separated by 4 FWHM.

amplitude increases from 12 to 100 μm as the filter becomes shorter with respect to the point source width. These negative sidelobes are apparent in the in-scan direction in the coadded plates.

Figure III.A.7 shows the detector signature and the resulting filter response to two point sources separated by one full-width at half-max at 60 μm. Negative sidelobes of 0.3 times the peak value have developed. As the source separation is increased, a negative depression develops between the sources and the sidelobes diminish. Figure III.A.8 shows the detector signature and the resulting filter response at a separation equal to four times the full-width half-max of the detector point source signature. A negative depression of over one-half the peak value has developed. The depression decreases as the separation is increased, until one source has exited the filter before the second enters. Since the filter is

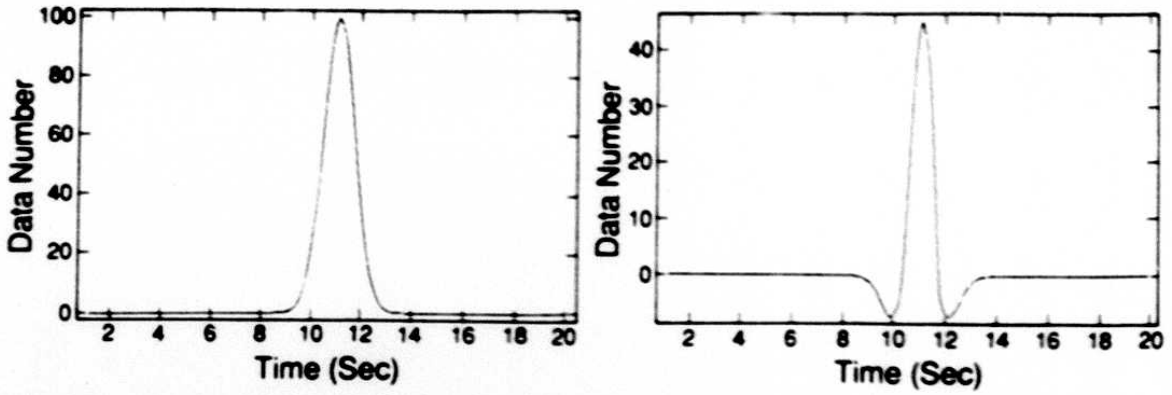

Figure III.A.9 Detector and median filter responses to a Gaussian extended source.

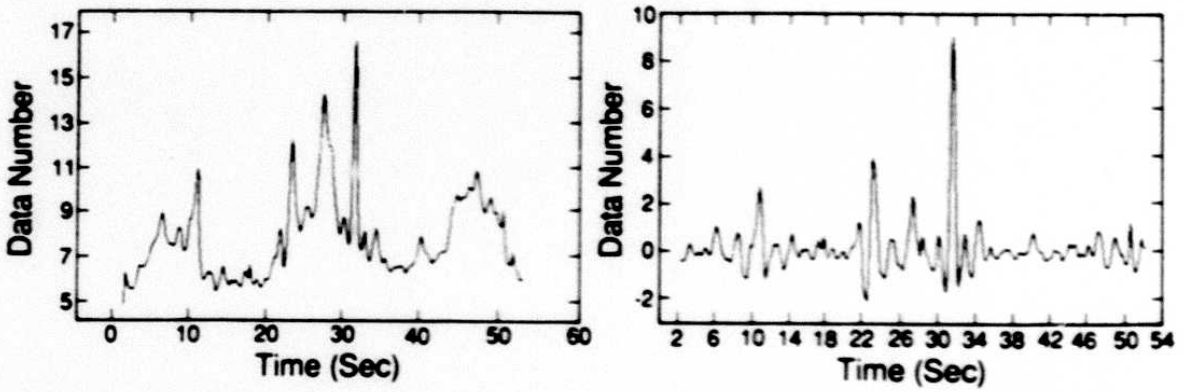

Figure III.A.10 Detector and median filter response to extended structure in LMC.

non-linear, the superposition principle does not apply and this behavior is also dependent on the relative amplitude of the sources. The filter has a tendency to suppress faint sources adjacent to brighter ones.

Figure III.A.9 shows the detector signature and the resulting filter response to a Gaussian extended source with a full-width at half-max of approximately three times that of the point-spread function. Significant side-lobes have developed, and the peak response is reduced by more than 50%.

Figure III.A.10 shows detector data from a scan through the LMC at 60 μm before and after filtering. A considerable fraction of the filtered data has negative flux density.

Figure III.A.11 shows the peak filter response in each of the four bands to a Gaussian source of unit flux density as a function of full-width at half-maximum of the source. This

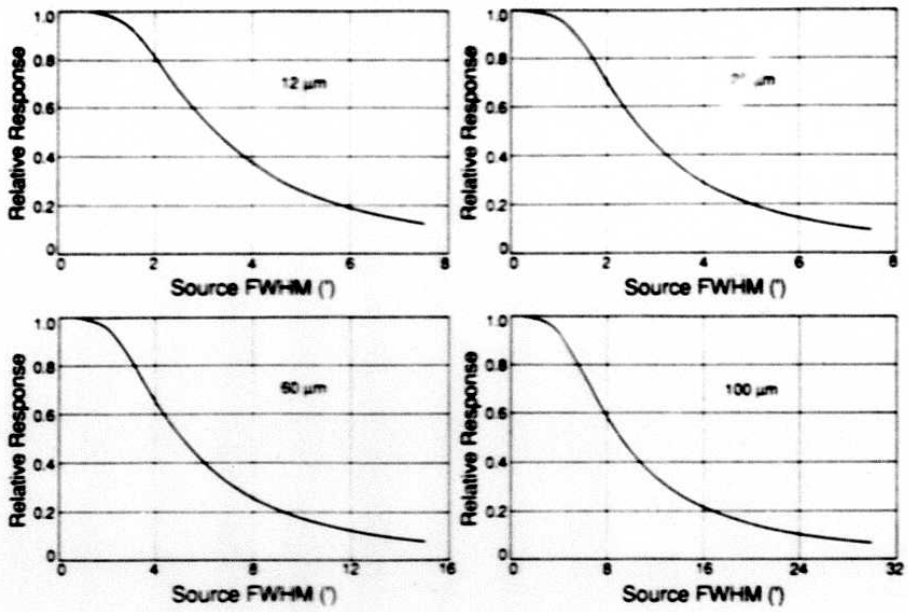

Figure III.A.11 Peak response of median filter to Gaussian extended sources normalized to peak (before filtering) of the extended source. A point source has zero width on this figure.

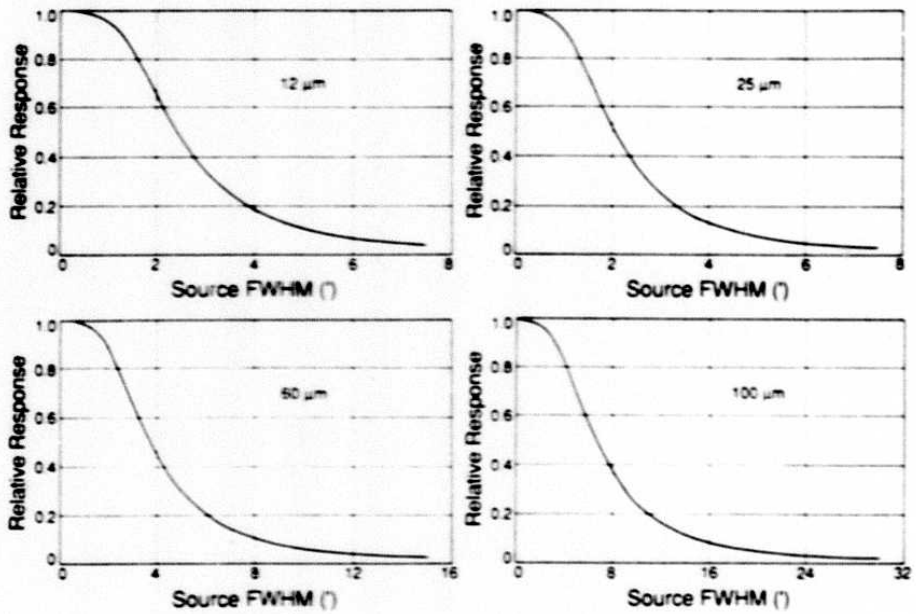

Figure III.A.12 Integrated response of median filter to Gaussian extended sources normalized to peak (before filtering) of the extended source. A point source has zero width on this figure.

171

width does not include the response of the telescope which is convolved with the filter response, and thus a point source has a width of zero on this scale. Figure III.A.12 shows the integral of the median filtered response between zero crossings in the in-scan direction. Both curves are relative to the convolved peak of the extended source.

A.6 Radiation Hit Rate Variation with Geographic Latitude

Nuclear radiation hits exceeding a single-scan signal-to-noise ratio threshold of 5 have been removed (with a 95% efficiency) from the data stream according to the algorithm described in Section II.C.2.a. Any radiation hits below the threshold will contribute to the coadded images, unless they are removed by a secondary filter. This secondary line of defense is the trimmed-mean algorithm described in Section II.C.4. The fraction of data which is trimmed at each extremum is 10% (see Section II.C.5) regardless of the location in the sky. It will be seen that the distribution of radiation hit rates shows a distinct dependence on geographic latitude (resulting from the Earth's radiation belts). Thus it is possible that some of the coadded images may contain residual radiation hits. The contribution of radiation hits to the overall noise in the plates is relatively small.

Even if radiation hits were not removed below the SNR threshold of 5, the effect on the plate noise would be minimal since it can be shown that the contribution of radiation hits to thresholding noise σ may be reduced to the following simple form (if we let $\sigma^2 = \sigma^2_{nom-radhit} + \sigma^2_{radhit}$)

$$\frac{\sigma^2_{rad}}{\sigma^2} = c\delta \qquad (III.A.3)$$

where $\delta \sim 0.03 - 0.13$ (the δ term arises from the different sampling rates at different bands), and $c \sim 1$ (the c term contains the information on the radiation hit count rates and the deglitcher threshold). Those radiation hits which do survive the trimmed-mean filter (survival due to trimming only 10% of extrema) manifest themselves in the form of single-band false sources in the FSDB. However, practically all such cases have a low SNR and thus their entry into the FSC is highly suppressed.

At 60 and 100 μm, the nuclear radiation hits result in the enhancement of intrinsic detector electronic noise (see the *Main Supplement*). The higher radiation zones are at lower galactic latitudes where the effects of extended structures are more pronounced. For these two bands the electronic noise is complemented by the fixed pattern noise (see Equation III.A.1). We have not investigated the effects of this enhanced electronic noise responsivity on reliability of sources.

Because the statistics for the number of radiation hits removed by the deglitcher are retained during coaddition, it is possible to compute the rate of radiation hits per unit

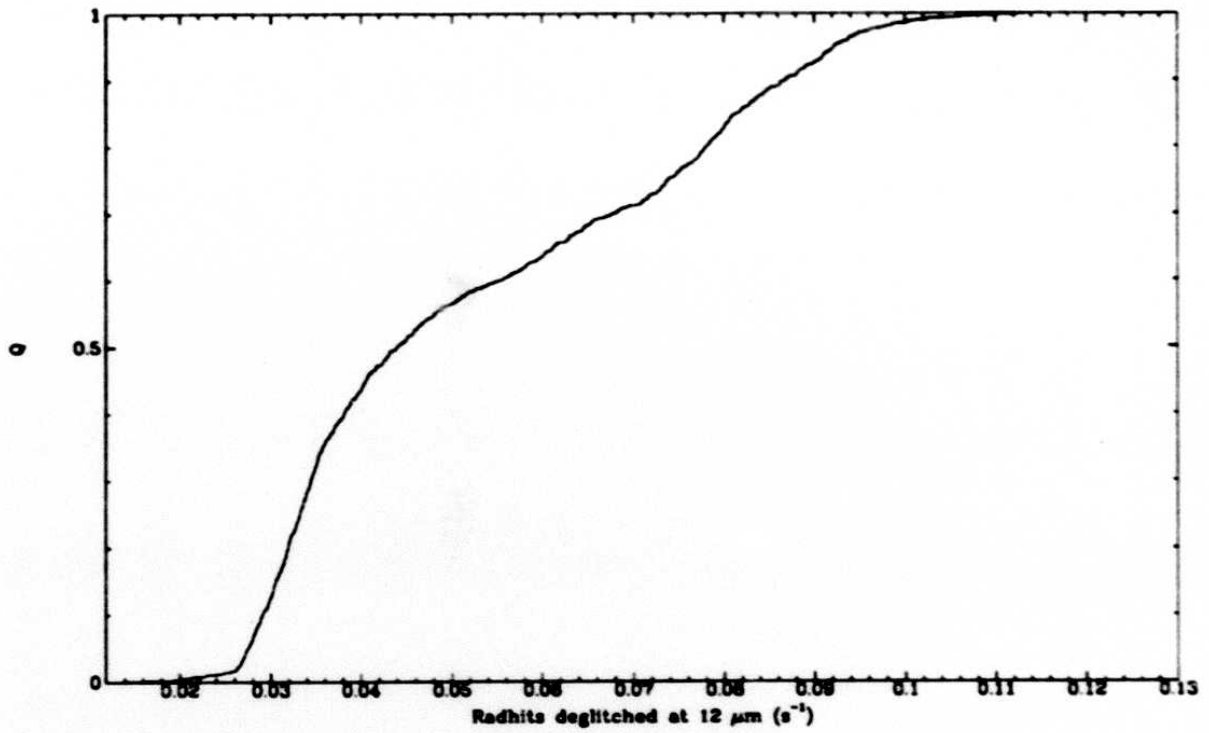

Figure III.A.13 Cumulative distribution of deglitched radiation hits at 12 μm; the median of the distribution is $\sim 0.044\ s^{-1}$.

time as a function of position. Figure III.A.13 shows the cumulative distribution function of radiation hits removed per second per detector at 12 μm. Figure III.A.14 displays the Aitoff projection of deglitched radiation hits at 12 μm.

The two regions of enhanced radiation hit rate in Figure III.A.14 correspond to the polar horns of the Van Allen belt. The radiation hit rate in these regions is typically 3 - 6 times greater than at latitudes near the equator. It was noted in section III.A.3 that the single sample noise at 12 μm increases by ~20% from the ecliptic pole to the plane. As a result, even if the radiation environment were uniform, we would have expected to see only ~55% more deglitched data at high ecliptic latitudes compared to the ecliptic plane (also note the proximity of equatorial and ecliptic poles). Thus almost all of the 3 - 6 fold enhancement in deglitched data near the equatorial poles is due to the radiation environment and not instrumental effects.

Asymmetries in the hit rate between the northern and southern equatorial hemispheres are attributable to residual effects of the South Atlantic Anomaly (see *Main Supplement* Section III.B.6), which increased radiation hit rates across significant portions of the Southern Hemisphere. Direct effects of the South Atlantic Anomaly do not show up since no data were taken within it. Under the assumption that radiation hits of all intensities

D 10015

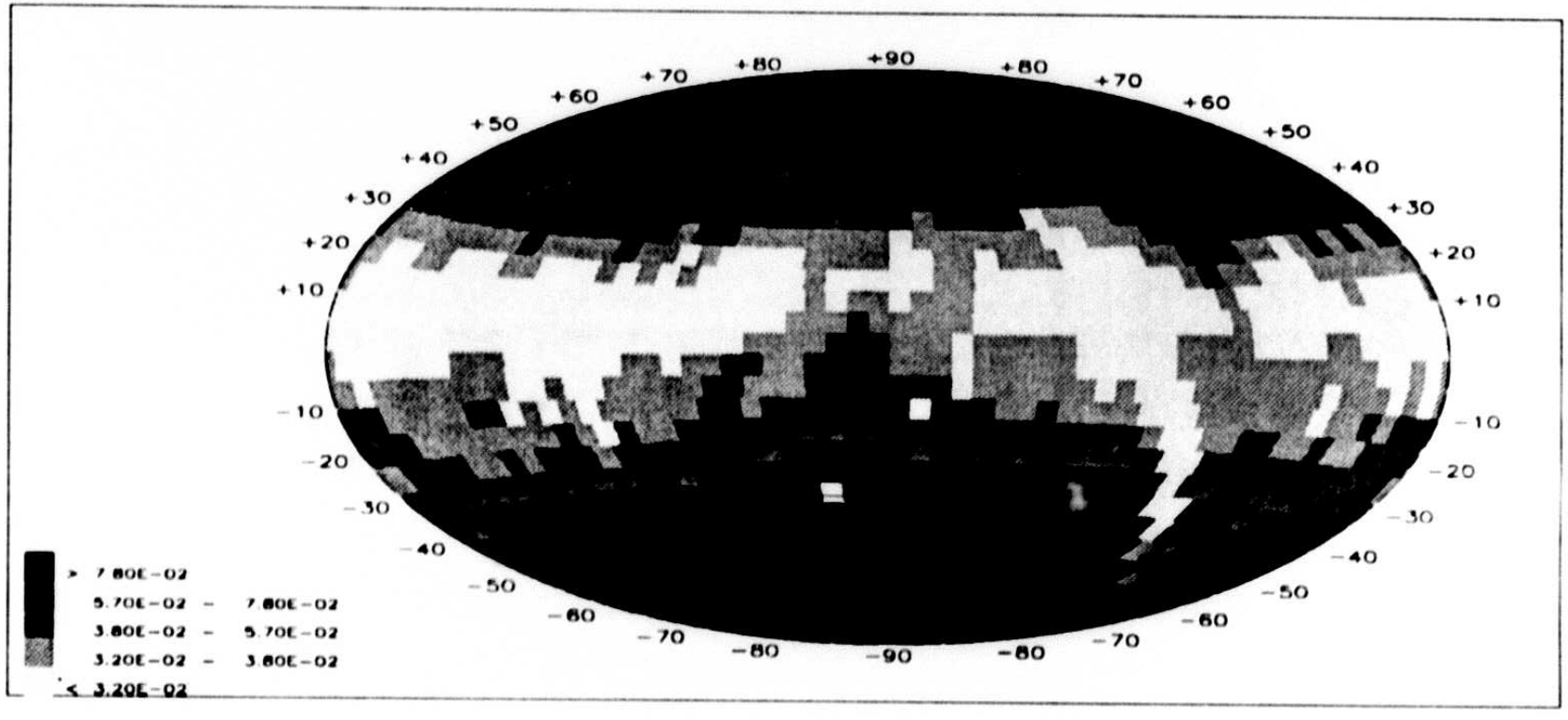

Figure III.A.14 Number of radiation hits removed per second per detector by the FSS deglitcher at 12 μm. The Aitoff projection is in equatorial coordinates.

have the same equatorial latitude dependency, the ***undeglitched***, single scan signal-to-noise ratio < 5 radiation hit rates should follow the distribution in Figure III.A.14. Thus, undeglitched single scan signal-to-noise ratio < 5 radiation hits are expected to be 3–6 times more numerous near the polar horns than at lower latitudes.

A.7 High Source Density

In regions of high source density, multiple sources can fall within a single effective beam. The resulting source confusion lowers completeness and causes photometric and positional errors in extracted sources. For the ***IRAS*** PSC, complex algorithms were implemented to alleviate confusion problems in the final catalog processing (see the ***Main Supplement***). For the FSC, the source extraction was done relative to a noise, which was computed from a histogram of the flux densities in all the pixels in a nearby area. The noise is thus dependent on both the instrumental noise and the radiant flux in the surrounding area (see Section III.A.2). This technique elevates the extraction threshold in areas of high source density and/or containing complex background structure (such as cirrus). Due to this technique, areas of high source density are largely absent from the FSDB and the FSC.

As is customary (Condon 1974), we have made a direct measurement of the flux-density error distribution, including confusion noise. The noise has been estimated by the flux density value corresponding to the 68% quantile of the positive flux density values in the surrounding area. The area used is $(79.25')^2$ for the 12 and 25 μm bands, and $(99.5')^2$ for the 60 and 100 μm bands. Histograms of the number of FSDB sources per square degree with SNR > 5 are presented in Figures III.A.15 – 18. Comparing to the PSC high source density limits of 45, 45, 16, and 6 sources per square degree in the 12, 25, 60 and 100 μm bands, respectively, only the 60 and 100 μm bands contain areas exceeding those limits. However, the limits used in the PSC are not strictly applicable, as confusion limits are a function of the background considered. In cases where the confusion is caused by the cirrus background, the use of a straight number-flux-density relationship applicable to *point* sources is erroneous. Furthermore, derivations from the theory of confusion error assume a linear system whereas the FSS processing includes a non-linear baseline filter. However, these histograms demonstrate that the source density in the FSDB has been limited to levels near those one would impose because of confusion errors. The areas of high source density are further limited in the FSC by the catalog selection thresholds, primarily by the exclusion of the $|b| \leq 20°$ sky for the 60 μm band, the NOISRAT thresholds and the sky noise limits (see Section III.D.3). Aitoff projections of the catalog sources (Figures I.D.1

and 2) show areas of source exclusion in the FSC. Areas such as Ophiuchus, Orion, and the Large Magellanic Cloud are largely excluded by the catalog selection criteria.

Histograms of the number of FSC sources per square degree are presented in Figures III.A.19 - 22. The 12, 25 and 60 μm bands have no areas over the PSC high source density limits, and the 100 μm band has 38 square degrees with source densities one count over the PSC limit, 13 square degrees with two counts over the PSC limit, and 4 square degrees with three sources over the limit.

Although the classical confusion problem is reduced to low levels, the FSDB and FSC still contain confused sources, extended sources, and sources coming from the infrared cirrus.

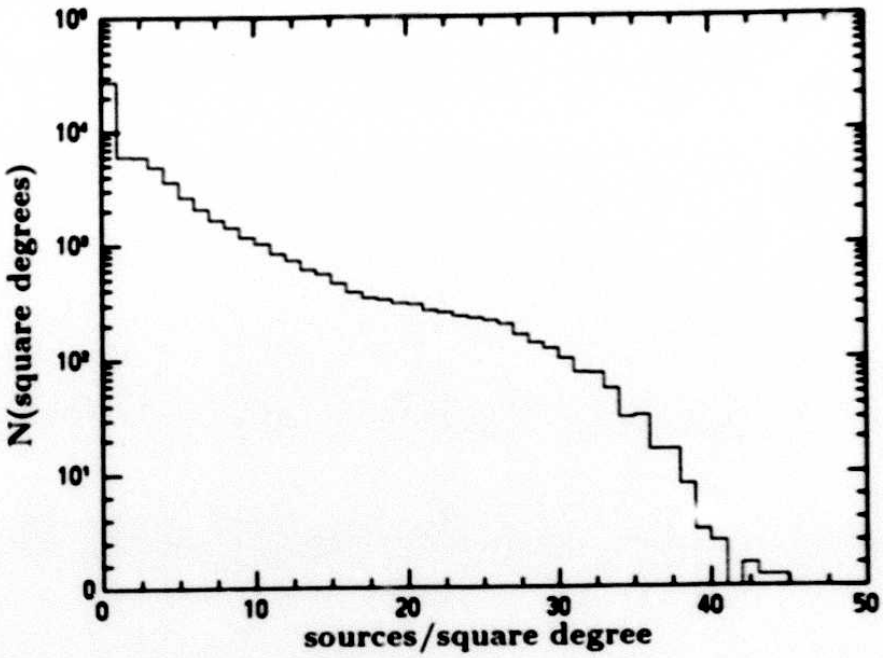

Figure III.A.15 Number of square degrees with a given source density, in the FSDB, at 12 μm for sources with SNR > 5.

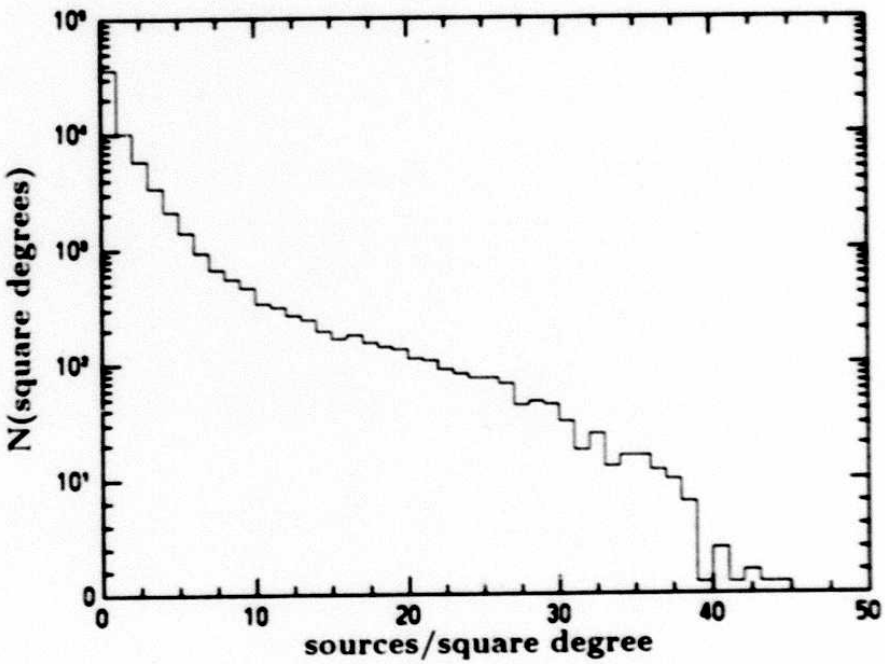

Figure III.A.16 Number of square degrees with a given source density, in the FSDB, at 25 μm for sources with SNR > 5.

177

D 10015

D 10015

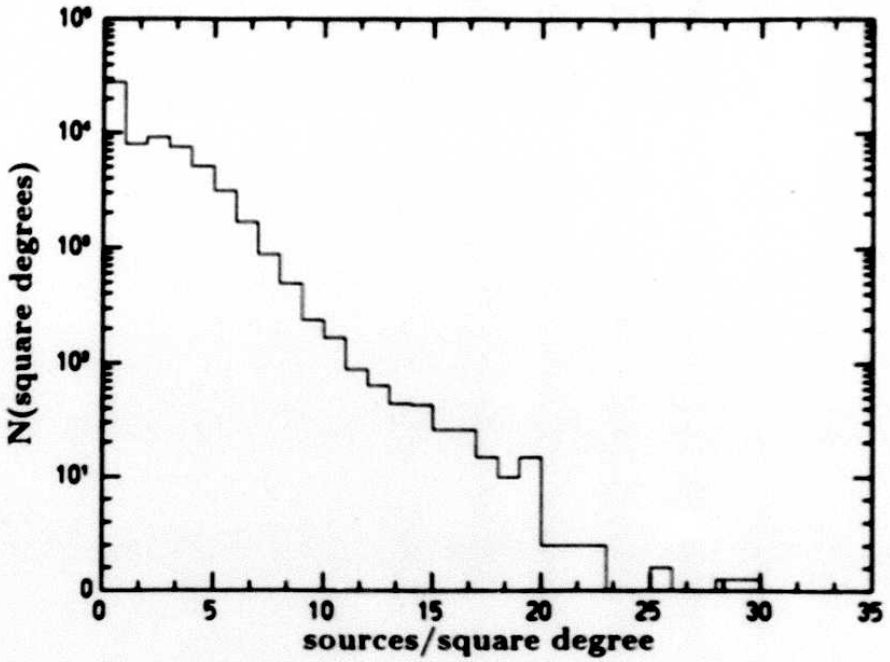

Figure III.A.17 Number of square degrees with a given source density, in the FSDB, at 60 μm for sources with SNR > 5.

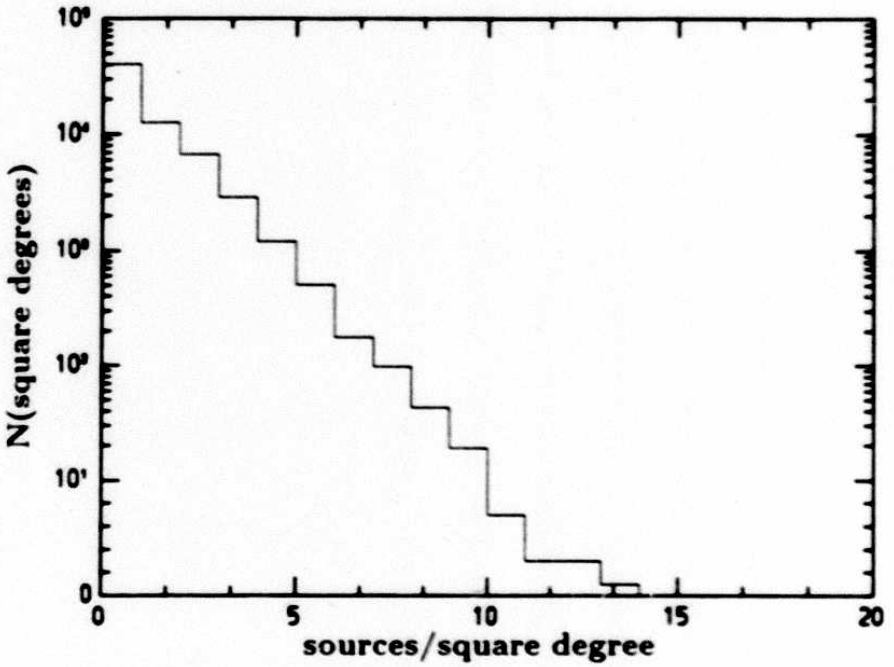

Figure III.A.18 Number of square degrees with a given source density, in the FSDB, at 100 μm for sources with SNR > 5.

178

D 10015

D 10015

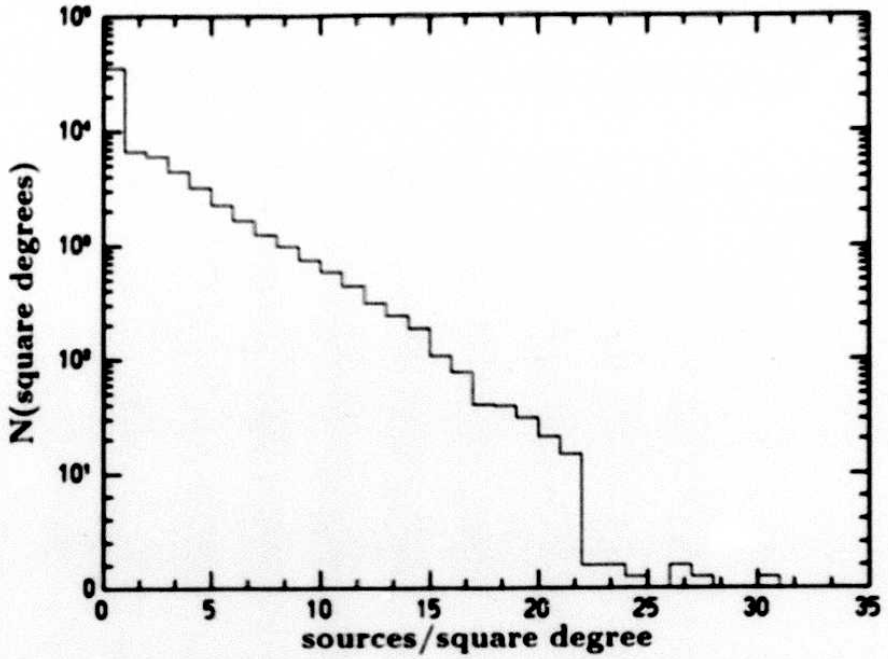

Figure III.A.19 Number of square degrees with a given source density in the FSC at 12 μm.

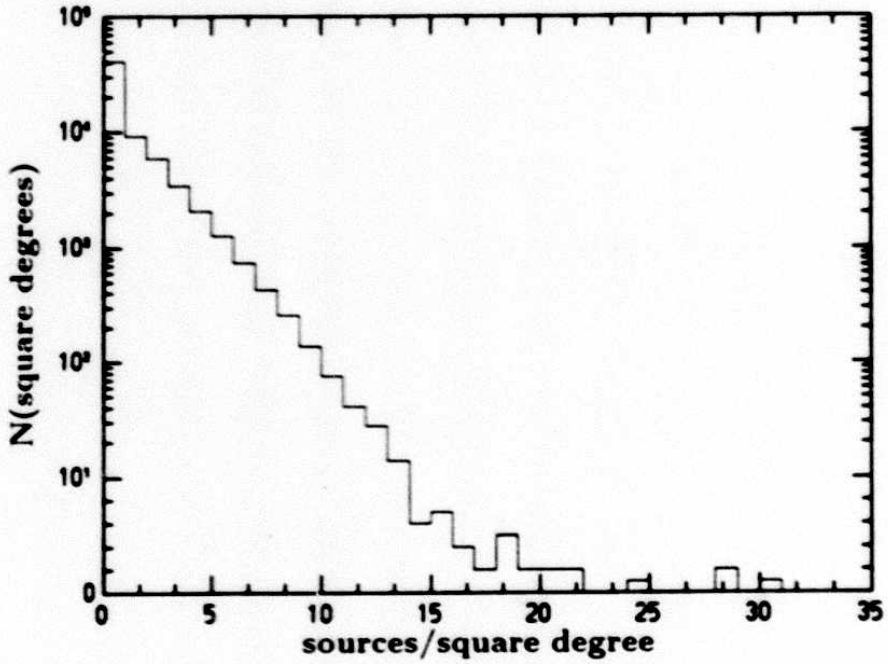

Figure III.A.20 Number of square degrees with a given source density in the FSC at 25 μm.

179

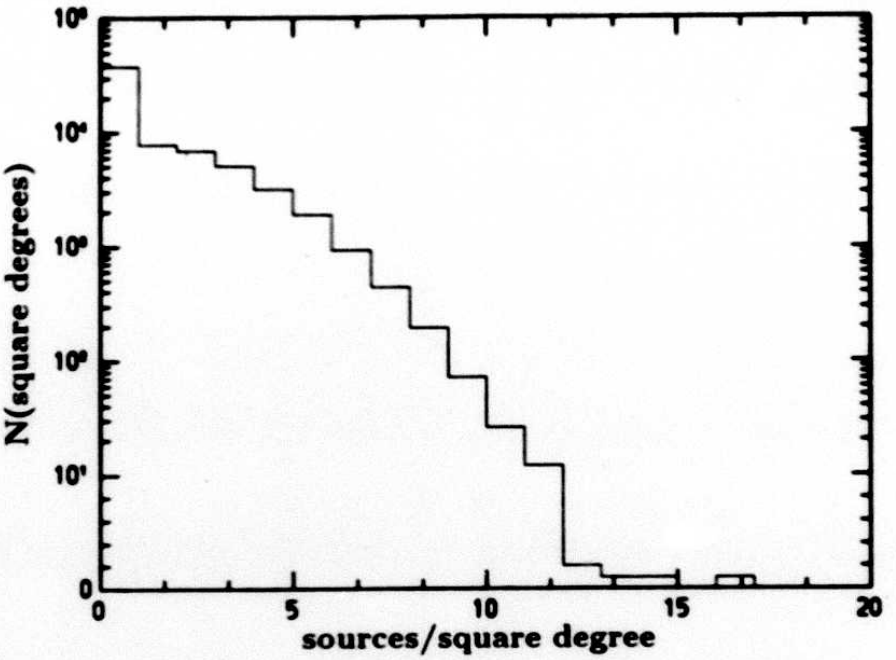

Figure III.A.21 Number of square degrees with a given source density in the FSC at 60 μm.

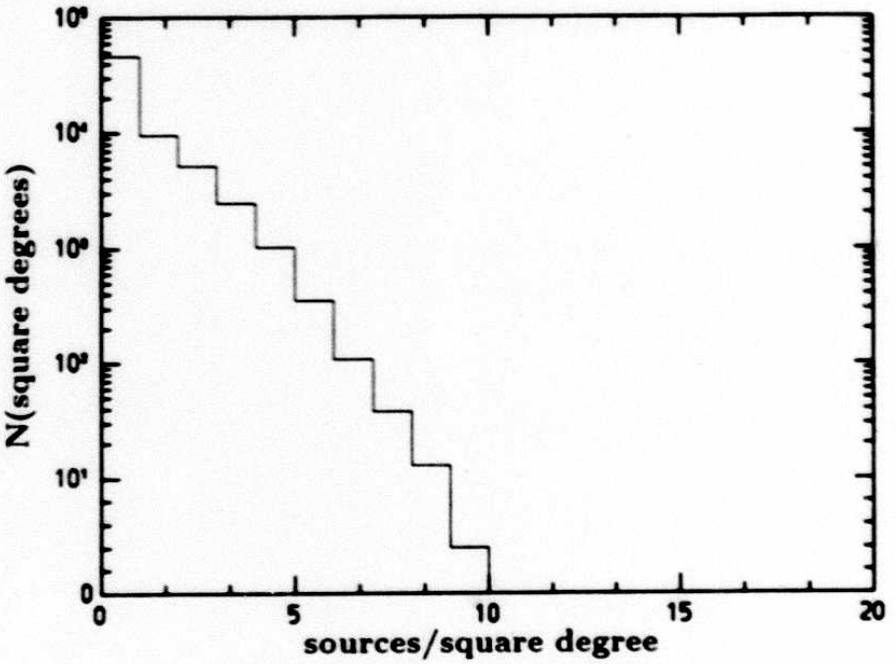

Figure III.A.22 Number of square degrees with a given source density in the FSC at 100 μm.

180 1181

B. FSC Content Summary

B.1 Spectral Classification of FSC Sources

The Faint Source Catalog contains 173,044 sources. Table III.B.1 gives the total number of sources of each *IRAS* spectral type, considering both high- and moderate-quality flux densities. The first column lists the various band combinations, encoded in the following fashion: The presence or absence of a measured flux density in a given band is denoted by "1" or "0". Measurements at 12, 25, 60, and 100 μm are encoded, respectively, from the most to the least significant bit of a four-bit number. Thus, a source measured only at 12 μm is represented as "1000", while one measured at 12 and 60 μm is denoted by "1010".

In summary, 51% of catalog sources are detected in only one *IRAS* spectral band, 39% have two band detections, 7% are detected in three bands, and approximately 3% of catalog sources are detected in all four bands.

Table III.B.1 Spectral Classification of FSC Sources for Version 2

Band Combination[1]	# of Sources	% of Total FSC
1000	61,232	35
1100	40,339	23
1110	6,907	4
1111	4,671	3
0100	367	–[2]
0110	2,382	1
0111	4,621	3
0010	26,913	16
0011	23,556	14
0001	0	0
1101	103	–
1010	715	–
1011	1,017	–
1001	215	–
0101	6	–

[1] In order of 12, 25, 60, 100 μm
1 = high- or moderate-quality flux density
0 = upper limit

[2] Less than 1%

TABLE III.B.2 Number of 'Stars' and 'Galaxies' in the FSC

Source Classification	Number	% of Total FSC
'stars'	108,042	63
'galaxies'	61,188	35
'other'	3,814	2
all	173,044	100

TABLE III.B.3 Number of Sources in Color-Color and Color-Flux Density Plots

Figure Number III.B.	Number of Sources: High Quality	Number of Sources: High and Moderate Quality
1	3,744	11,578
2	3,050	9,292
3	28,400	52,020
4	4,326	13,310
5	5,466	18,581
6	32,258	33,865

B.2 Number of 'Stars' and 'Galaxies'

Three classes of objects may be defined in the FSC according to the spectral energy distribution of the sources. Sources brighter at 12 μm than at 60 μm and with a high-quality 12 μm flux density are mostly stars; sources brighter at 60 μm than at 12 μm and with a high-quality 60 μm flux density are mostly galaxies, the remainder are mostly sources which did not have a ***high*** quality detection at either 12 or 60 μm and failed to fall into either category. Table III.B.2 gives the number of sources in the FSC in each class.

B.3 Color-Color and Color-Flux Density Plots

Figures III.B.1-6 present color-color and color-flux density plots of FSC sources in various ***IRAS*** spectral bands. Color_{ij} is defined as $\log((f_\nu(\text{band } i))/(f_\nu(\text{band } j)))$. In each case, two plots were produced: one containing only high-quality flux densities, the other including high- and moderate-quality flux densities. ***No upper limit flux densities were included in any plot; no color correction was applied to the flux densities in these plots***. Table III.B.3 gives the number of sources included in each plot, by Figure number.

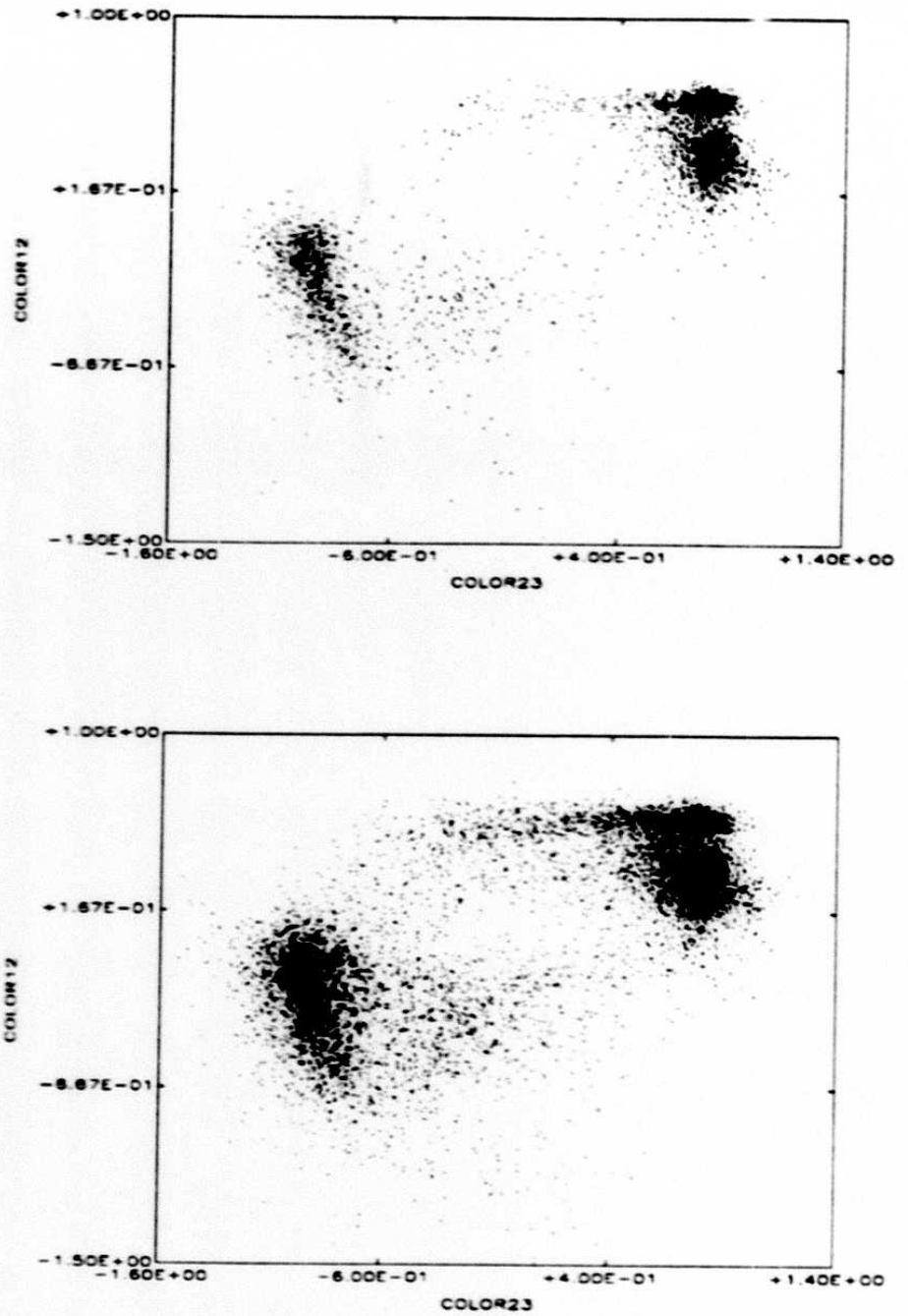

Figure III.B.1 Color at 12-25 μm vs. color at 25-60 μm for all catalog sources with high-quality (upper figure) and high- or moderate-quality (lower figure) flux densities in the indicated bands. In Figures III.B.1–6 color$_{ij}$ is defined as log (f_ν(band i)/f_ν(band j)).

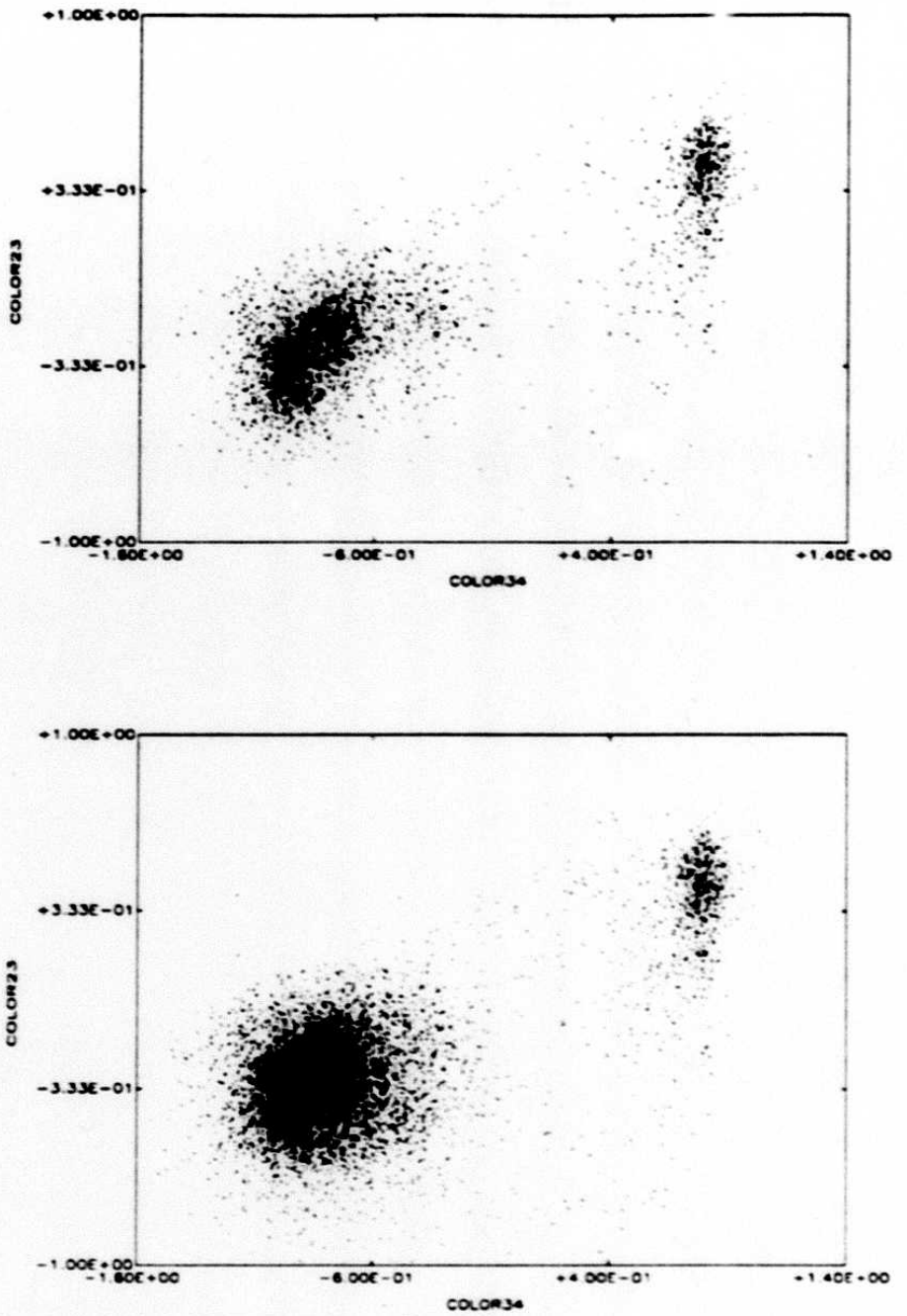

Figure III.B.2 Color at 25-60 μm vs. color at 60-100 μm for all catalog sources with high-quality (upper figure) and high- or moderate-quality (lower figure) flux densities in the indicated bands.

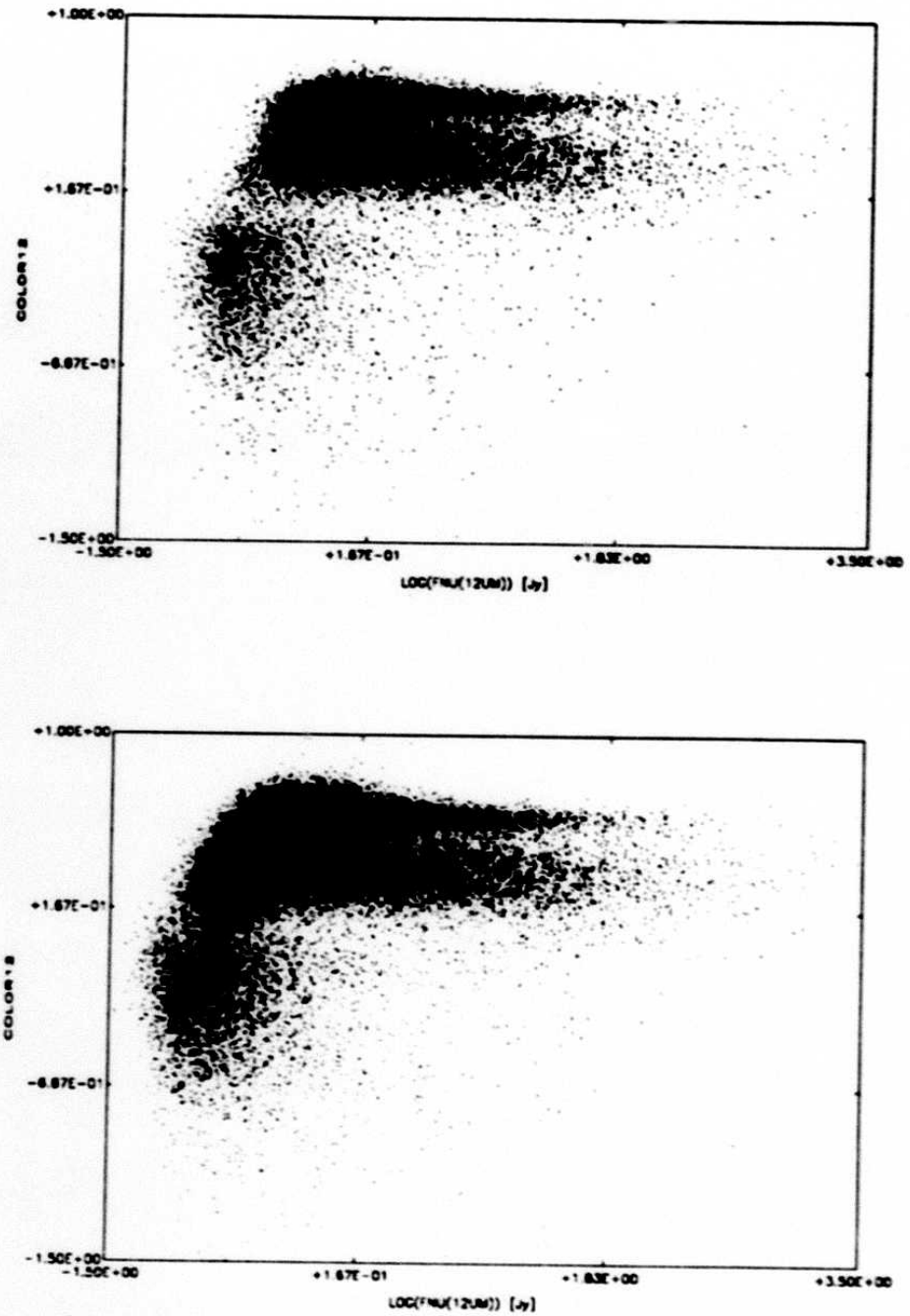

Figure III.B.3 Color at 12-25 μm vs. $f_\nu(12\ \mu\text{m})$ for all catalog sources with high-quality (upper figure) and high- or moderate-quality (lower figure) flux densities in the indicated bands.

D 10015

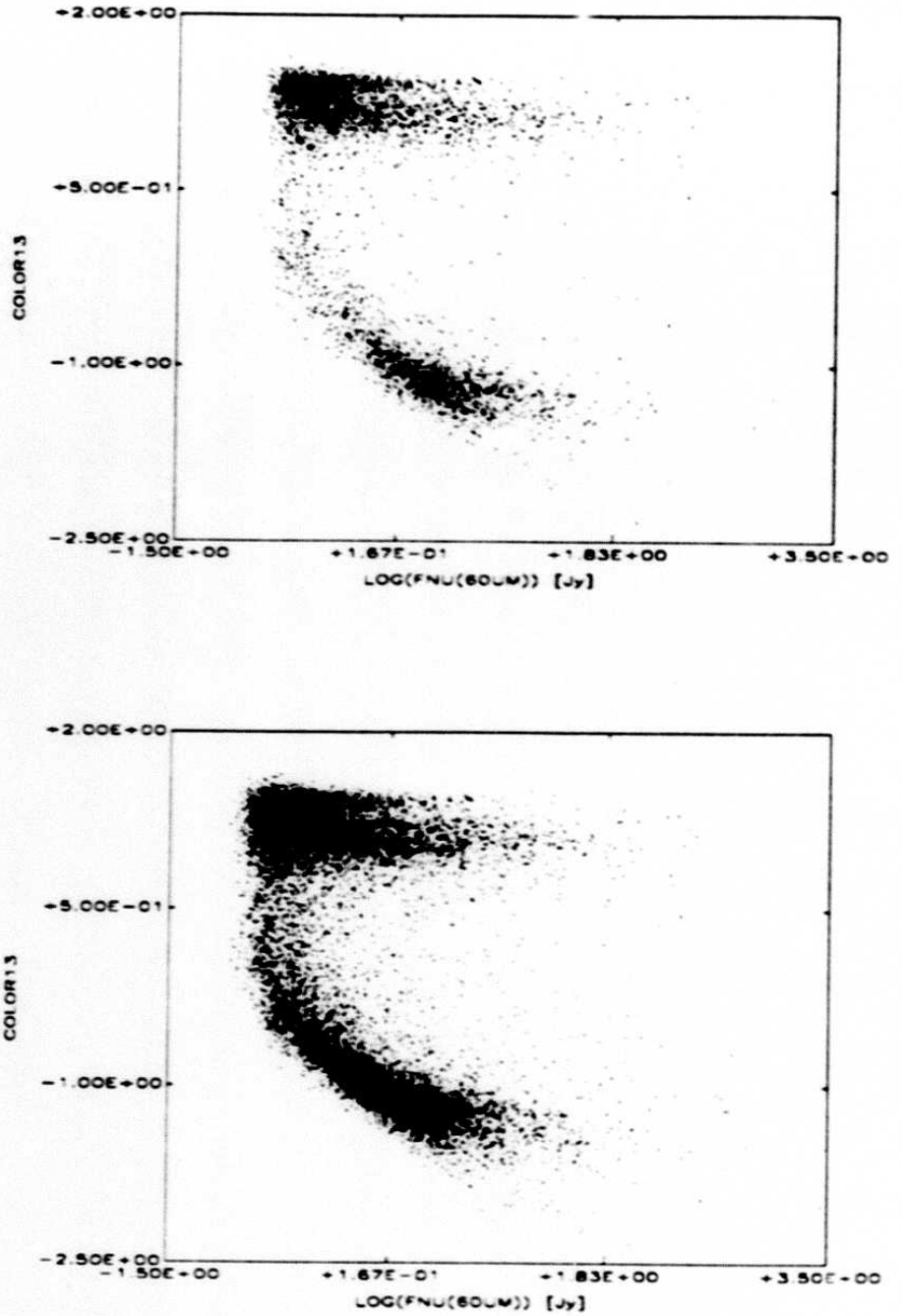

Figure III.B.4 Color at 12-60 μm vs. $f_\nu(60\ \mu m)$ for all catalog sources with high-quality (upper figure) and high- or moderate-quality (lower figure) flux densities in the indicated bands.

87

D 10015

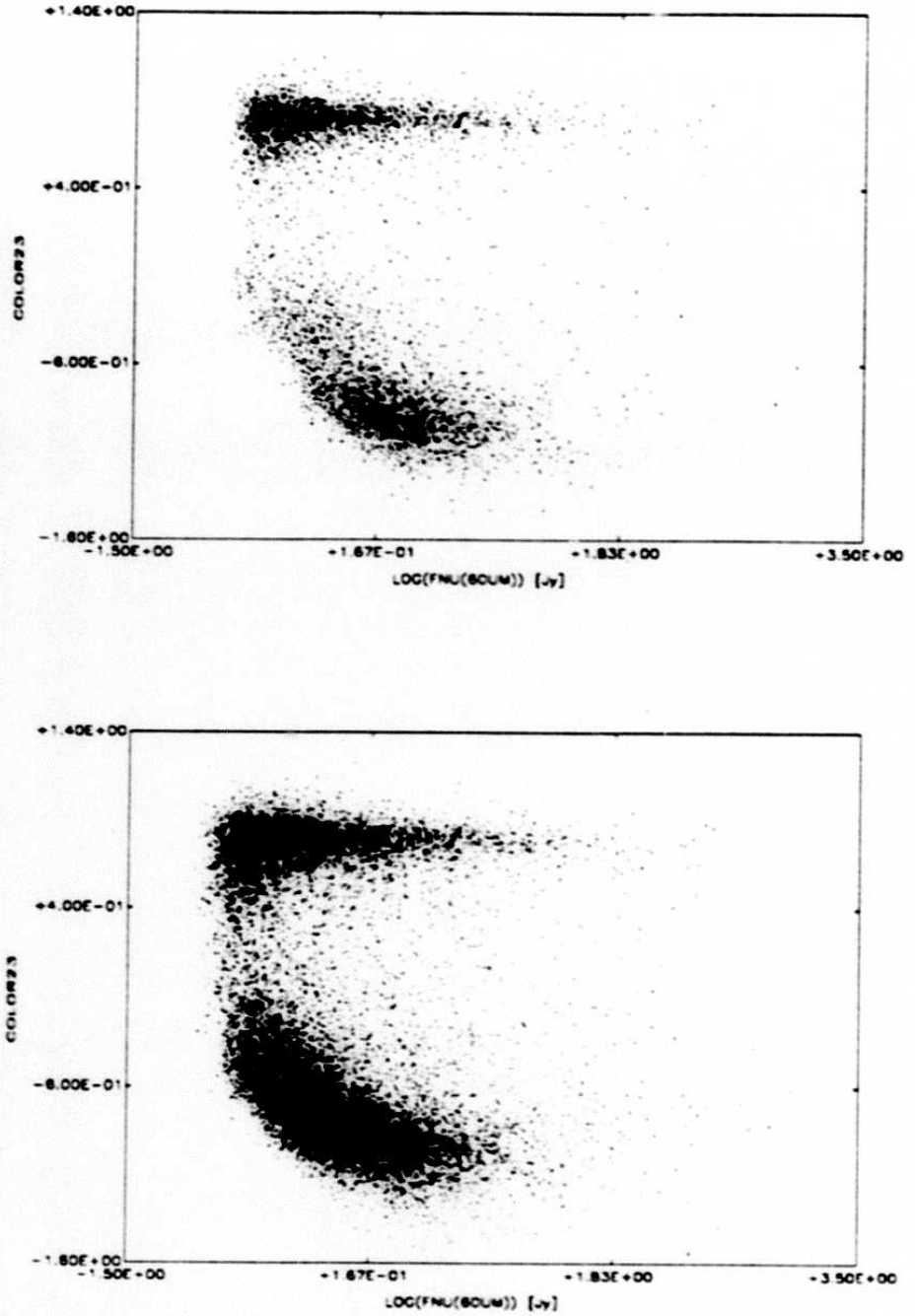

Figure III.B.5 Color at 25-60 μm vs. $f_\nu(60\ \mu\text{m})$ for all catalog sources with high-quality (upper figure) and high- or moderate-quality (lower figure) flux densities in the indicated bands.

188

D 10015

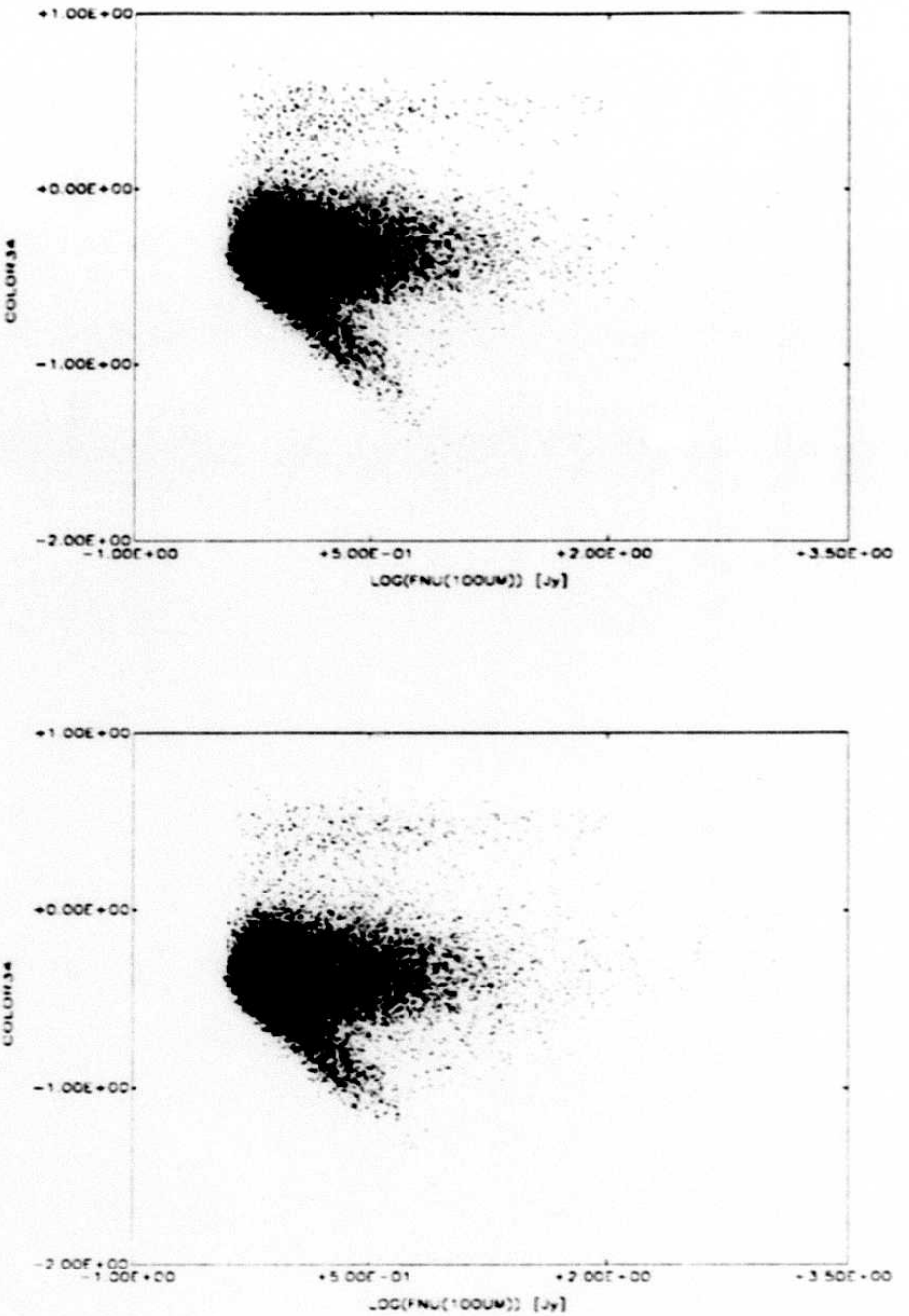

Figure III.B.6 Color at 60-100 μm vs. $f_\nu(100\ \mu\text{m})$ for all catalog sources with high-quality (upper figure) and high- or moderate-quality (lower figure) flux densities in the indicated bands.

89

D 10015

C. Completeness

C.1 Overview

Variations in coverage, noise, and extended sky brightness structures, cause the completeness of the Faint Source Catalog (FSC) to vary with sky position (see Section III.A). For those readers not interested in pursuing the details given in this section, Figures III.C.1–4 give curves displaying the fraction of the covered sky for which the FSC is at least 90% complete above a given flux density at each wavelength band (Figure III.C.4 applies to the completeness level of the ***Database*** and not the ***Catalog*** since the 100 μm band was not treated for catalog qualification). Those readers are warned that these plots are only correct as averages over areas of at least $1° \times 1°$. Small-scale variations exist over smaller areas caused by differences in the sensitivity of individual detectors coupled with the regular survey scan strategy. These variations have not been incorporated into Figures III.C.1–4.

These figures can be summarized by saying that, for half of the sky with $|b| \geq 10°$ (for 12 and 25 μm bands) and $\geq 20°$ (for 60 μm), the 90% completeness level of the FSC is *at most* 180, 290, 260 mJy at 12, 25, and 60 μm. At 100 μm for the FSDB for $|b| \geq 10°$ sky, the corresponding figure is 0.95 Jy. The previously mentioned figures for the FSC were derived from statistical arguments (Eq. III.C.2). For the FSDB, methods based on source count analysis also yield independent completeness estimates for the database. Specifically:

- At 12 μm, the FSDB for $|b| \geq 10°$ is 90% complete to 140 mJy for areas with a threshold noise of 32–36 mJy and to 80 mJy for areas with a threshold noise of less than 16 mJy.
- At 25 μm, the FSDB for $|b| \geq 10°$ is 90% complete to 200 mJy for areas with threshold noise in the range 48–65 mJy, and to 77 mJy for areas with threshold noise less than 18 mJy.
- At 60 μm, the 90% completeness level of the FSDB for $|b| \geq 20°$ is determined to be *at most* in the range of 260 to 300 mJy.

Figures III.C.5–7 show the spatial distribution of the FSC 90% completeness levels at 12, 25, and 60 μm. Figure III.C.8 depicts the spatial distribution of the FSDB 90% completeness levels at 100 μm (because the 100 μm band was not treated as a catalog quality band the completeness levels refer to the FSDB).

These completeness numbers have been derived through source count analysis and comparison with the *Serendipitous Survey Catalog* (SSC), and the sky maps have been derived based on the spatial variations of *Catalog SNR thresholds* and sky noise values.

90

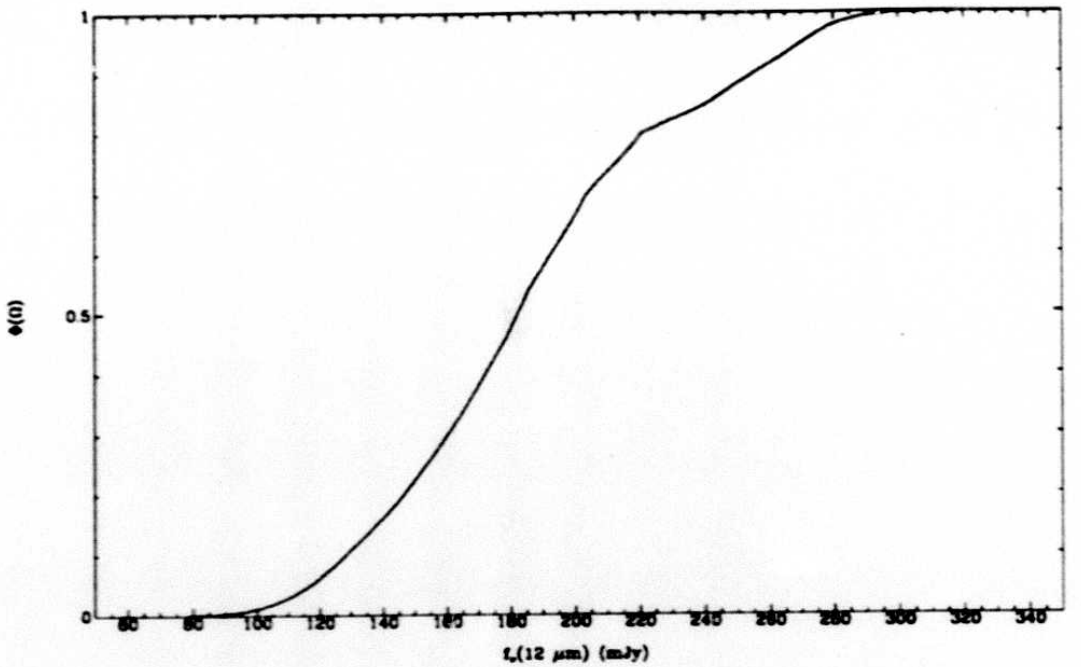

Figure III.C.1 Cumulative fraction of the covered $|b| \geq 10°$ sky for which the FSC is at least 90% complete above a given flux density at 12 μm.

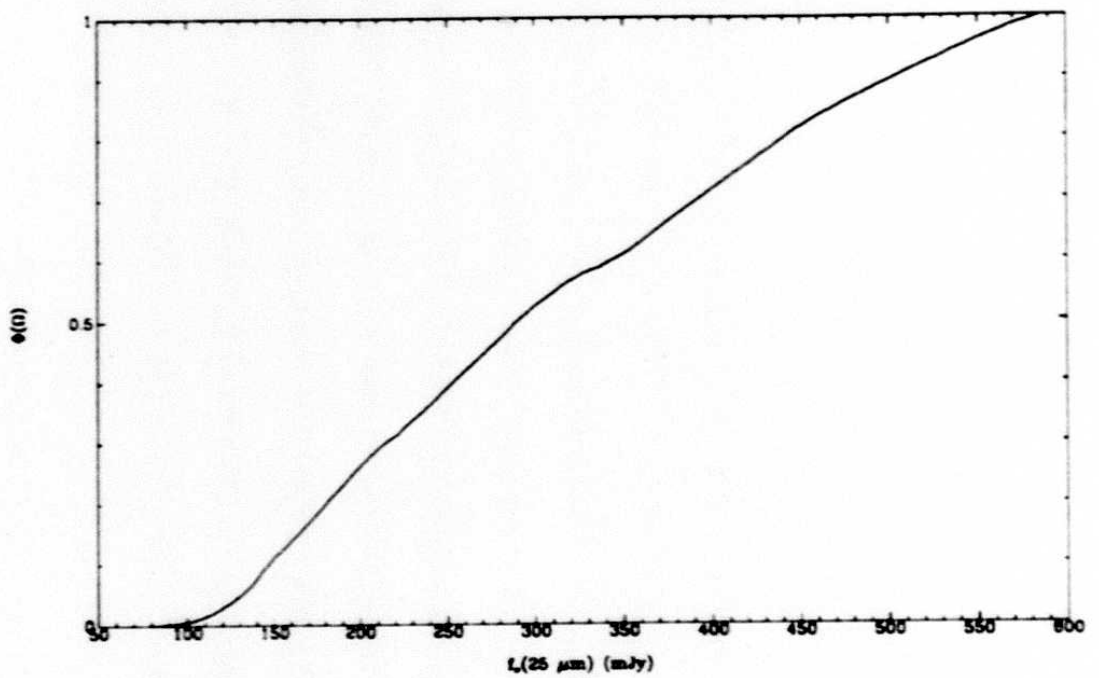

Figure III.C.2 Cumulative fraction of the covered $|b| \geq 10°$ sky for which the FSC is at least 90% complete above a given flux density at 25 μm.

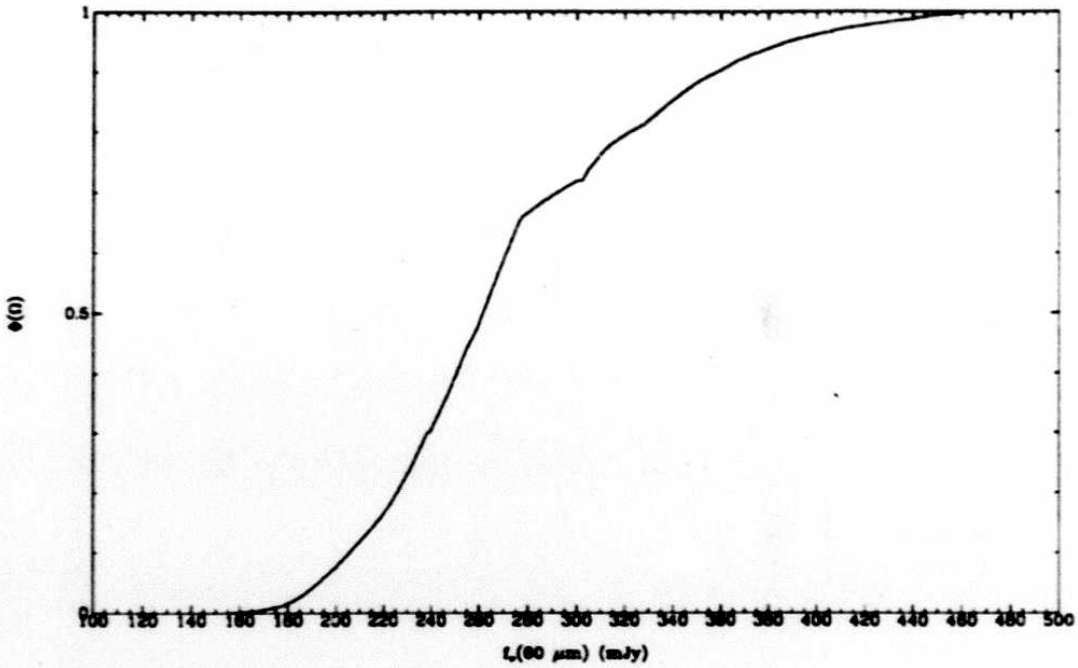

Figure III.C.3 Cumulative fraction of the covered $|b| \geq 20°$ sky for which the FSC is at least 90% complete above a given flux density at 60 μm.

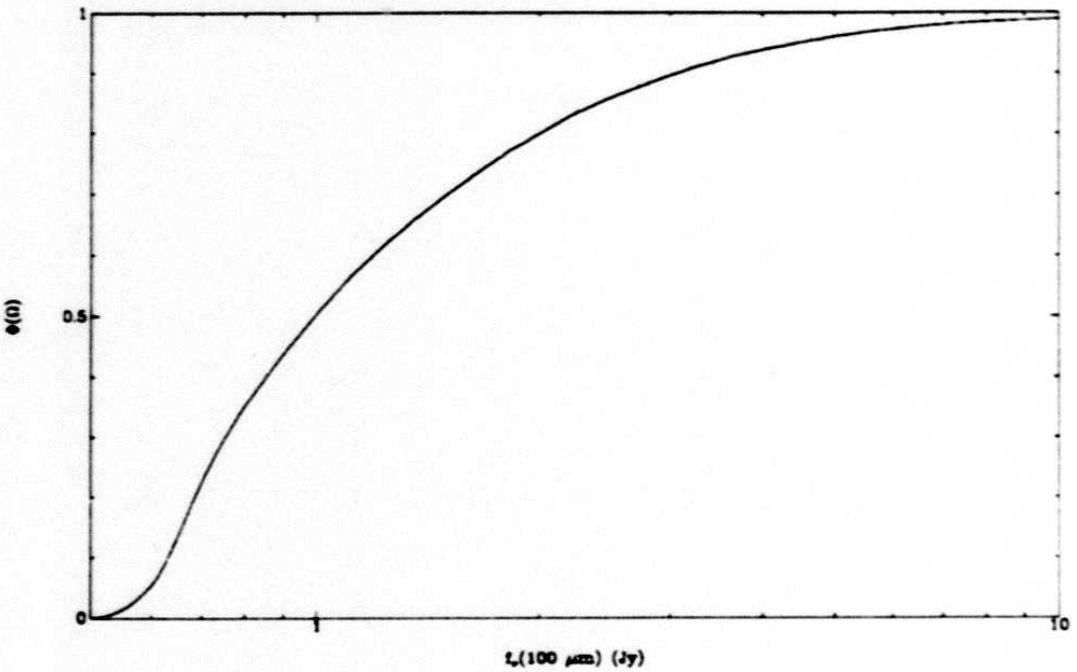

Figure III.C.4 Cumulative fraction of the $|b| \geq 10°$ sky for which the FSDB is at least 90% complete above a given flux density at 100 μm. (Notice that this figure refers to the FSDB.)

193

D 10015

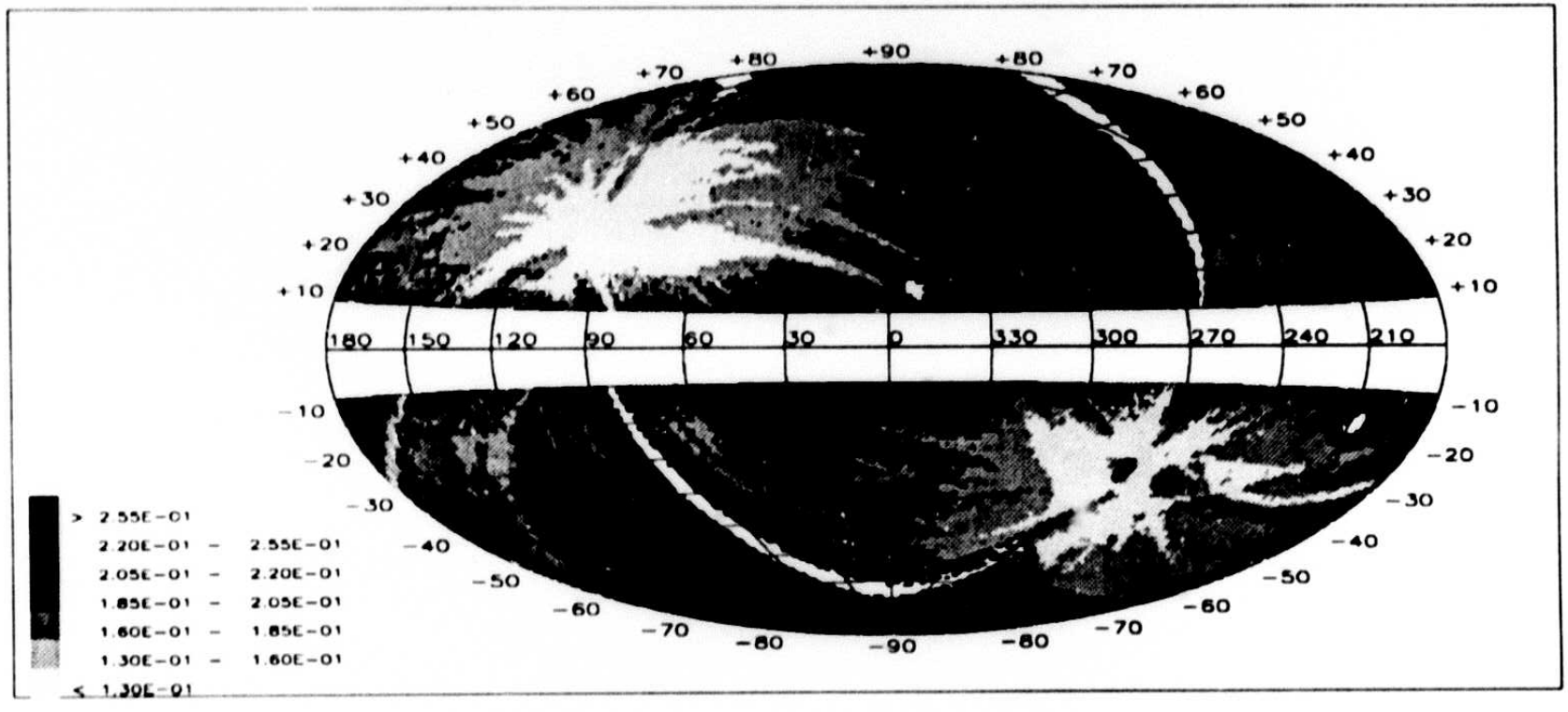

Figure III.C.5 Spatial distribution of the 90% completeness levels of the FSC at 12 μm, in galactic coordinates. Units are Janskys. (Small holes in the figure occur when there are no sources in a 1° x 1° area of sky.)

D 10015

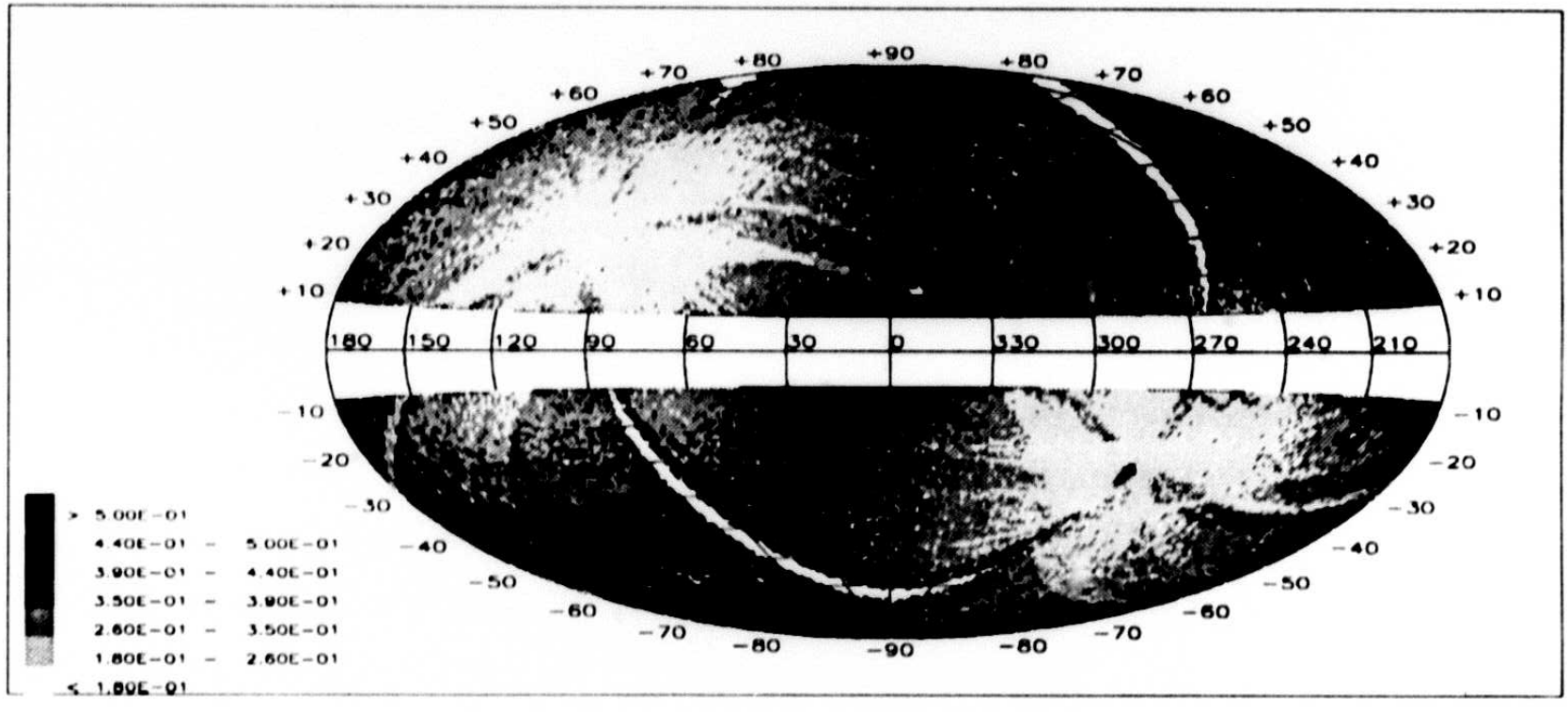

Figure III.C.6 Spatial distribution of the 90% completeness levels of the FSC at 25 μm, in galactic coordinates. Units are Janskys.

195

D 10015

Figure III.C.7 Spatial distribution of the 90% completeness levels of the FSC at 60 μm, in galactic coordinates. Units are Janskys.

196

D 10015

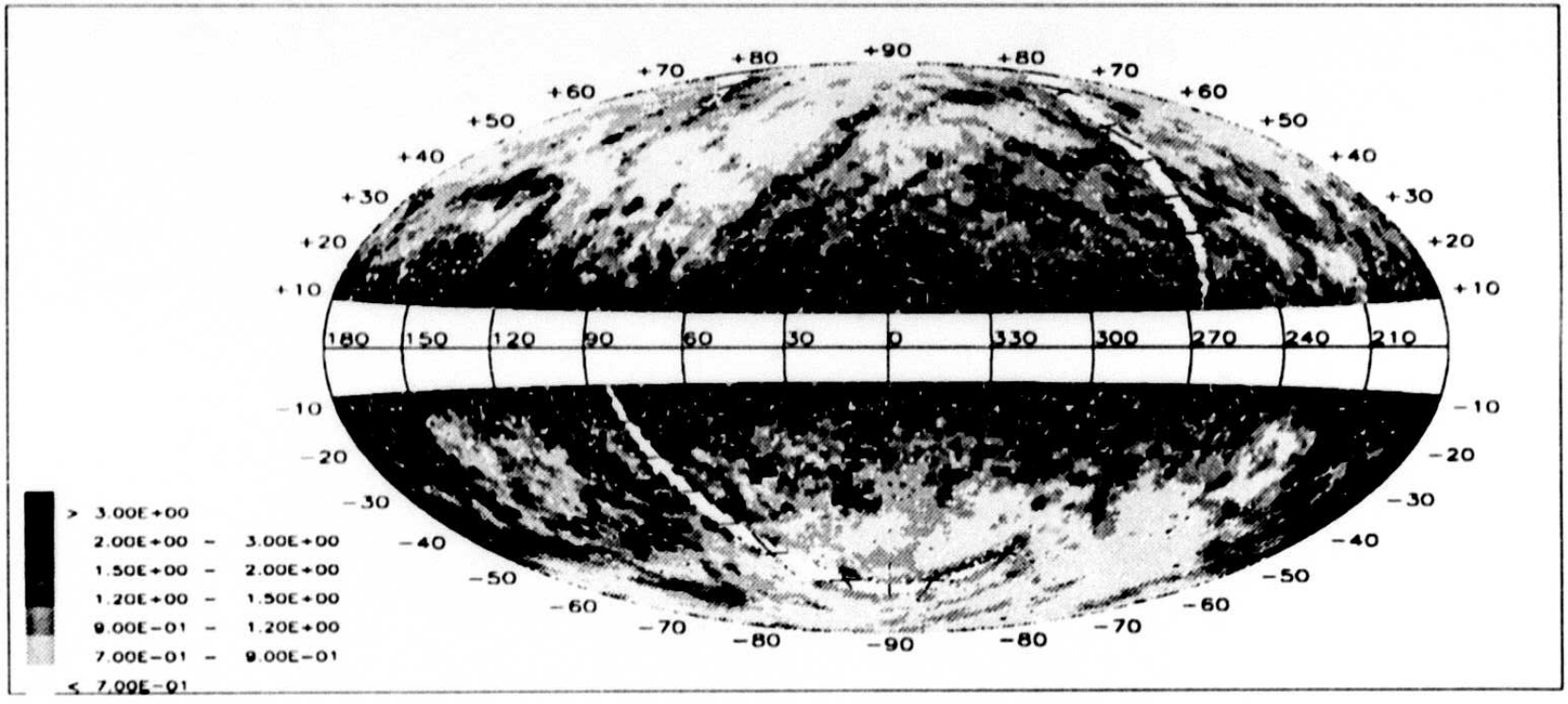

Figure III.C.8 Spatial distribution of the 90% completeness levels of the FSDB at 100 μm, in galactic coordinates. Units are Janskys. (Notice that this figure refers to the *Data Base* and not the *Catalog*.)

- $\sigma_\nu(l,b)$ is the *total* noise (see Section III.A.2), which is a strong function of the ecliptic latitude β at 12 and 25 μm, and at 60 and 100 μm is influenced by galactic longitude and latitude. This noise includes all effects of large scale structure and confusion. (For more discussion of noise and the relationship between σ_ν and $\sigma_{0,\nu}$ see Section III.A.)

The preceding formulation is only a general indicator of the completeness levels of the FSC and should be treated with caution for at least two reasons:

1) We have implicitly assumed a Gaussian profile for the noise distribution. However, the discussions in Section III.A indicate that this assumption is accurate only at high galactic latitudes and only in extremely clean parts of sky. A more acceptable description of the noise distribution would be needed to properly compute its 90% quantile. The two quantiles at 68% and 87% can be used to estimate another measure of the 'noise', however the use of only two points to extrapolate to the 90% point might introduce other non-quantifiable uncertainties. For the sake of simplicity we have avoided such an approach and for the remainder of this section we treat the noise at 68% as the Gaussian equivalent.

2) The noise $\sigma_\nu(l,b)$ is computed over an area Γ of $\sim 1.32° \times 1.32°$ at 12 and 25 μm and an area of $\sim 1.66° \times 1.66°$ at 60 and 100 μm, and consequently its variations on smaller scales would not be observable. However, the large scale filamentary structure has scales of variation from a fraction of a degree to many degrees. As a result, when a filamentary structure occupies only a portion of a noise cell Γ, the noise will underestimate the true background noise in the *cirrus*-contaminated part of the cell, while overestimating the noise in the clean portion of the cell (see also Section III.D). Thus in such a scenario the completeness is dominated by the *cirrus* content of the region. Consequently in areas with a large gradient in $\sigma_\nu(l,b)$ the above formulation will give inaccurate completeness limits. Furthermore, the noise estimate has a 1σ error of 2-3% in its estimation at any point.

In the following sections a more detailed discussion of the variables affecting completeness will be presented. In Section III.C.2 we discuss the effects of sky coverage, in Section III.C.3 we consider the variation of noise as a function of ecliptic latitude, and in Section III.C.4 the issue of cirrus will be discussed. In Section III.C.5 the effects of local SNR thresholds on completeness will be detailed, in Section III.C.6 the estimates of completeness of the survey using source counts will be described, and Section III.C.7 discusses the comparison of the FSS against the Serendipitous Survey Catalog.

C.2 Sky Coverage

The discussions in Section III.A indicate that at 12 and 25 μm the noise scales according to Eq. III.A.2, and thus the completeness formulation can be based on Eq. III.C.1. Due to the *IRAS* survey coverage strategy, the coverage varies on both small and large

198

scales. Therefore N_ν, the number of detector passes, which enters Eq. III.C.1 cannot be considered a constant.

C.2.a Large-Scale Variations

The *Main Supplement* describes fully the large-scale variations in sky coverage. Figure III.C.9 is reproduced from the *Main Supplement* , and shows the large-scale depths of coverage. The clear areas in the middle plot were covered with at least two sets of confirming scans (two HCONs), while the clear areas in the bottom plot were covered with three or more HCONs. The two-HCON areas resulted in an average number of data samples per pixel of 8, and the three-HCON areas resulted in an average number of 12. However, as discussed below, in the two-HCON areas, N_ν can vary from 4 to 12. Similarly, in the three-HCON areas, N_ν can vary from 6 to 18.

The shaded areas in the top part of Figure III.C.9 show the areas that received zero-HCON coverage and thus were excluded from the Point Source Catalog. However, half of that area was covered by at least one scan and is therefore present in the FSS. Roughly 15% of the sky received more than three-HCON coverages. See also Figures III.A.2–4 which display the average of pixel coverage on cells of $1° \times 1°$ for the 12 μm band.

C.2.b Small-Scale Variations

There are several effects which cause significant small-scale variations in coverage. They are:

- The boundaries of the areas of large-scale coverage variation produce pronounced edge effects.
- There exists a quasi-periodic variation with period near 15′ caused by the regular manner in which the survey scans were overlapped. This produces "stripes" of higher coverage in a sea of lower coverage. Figures III.C.10A and B show a vivid example of this coverage variation for a plate at the North Galactic Cap. This effect is discussed further in Section III.A.
- Failed detectors produce stripes of low coverage in a sea of high coverage. These stripes are also quasi-periodic with period near 15′.
- Data outages caused by the clipping of radiation hits and known asteroids produce islands of low coverage in a sea of higher coverage. Outages due to radiation hits peak near geographic latitudes of 60° (see Section III.A.6), and outages due to known asteroids peak in the ecliptic plane (notice the dark patches in Figure III.C.10B).

The "island effect" correction is discussed in Section II.E, which attempts to correct sources in the FSDB for small-scale variations in coverage.

199

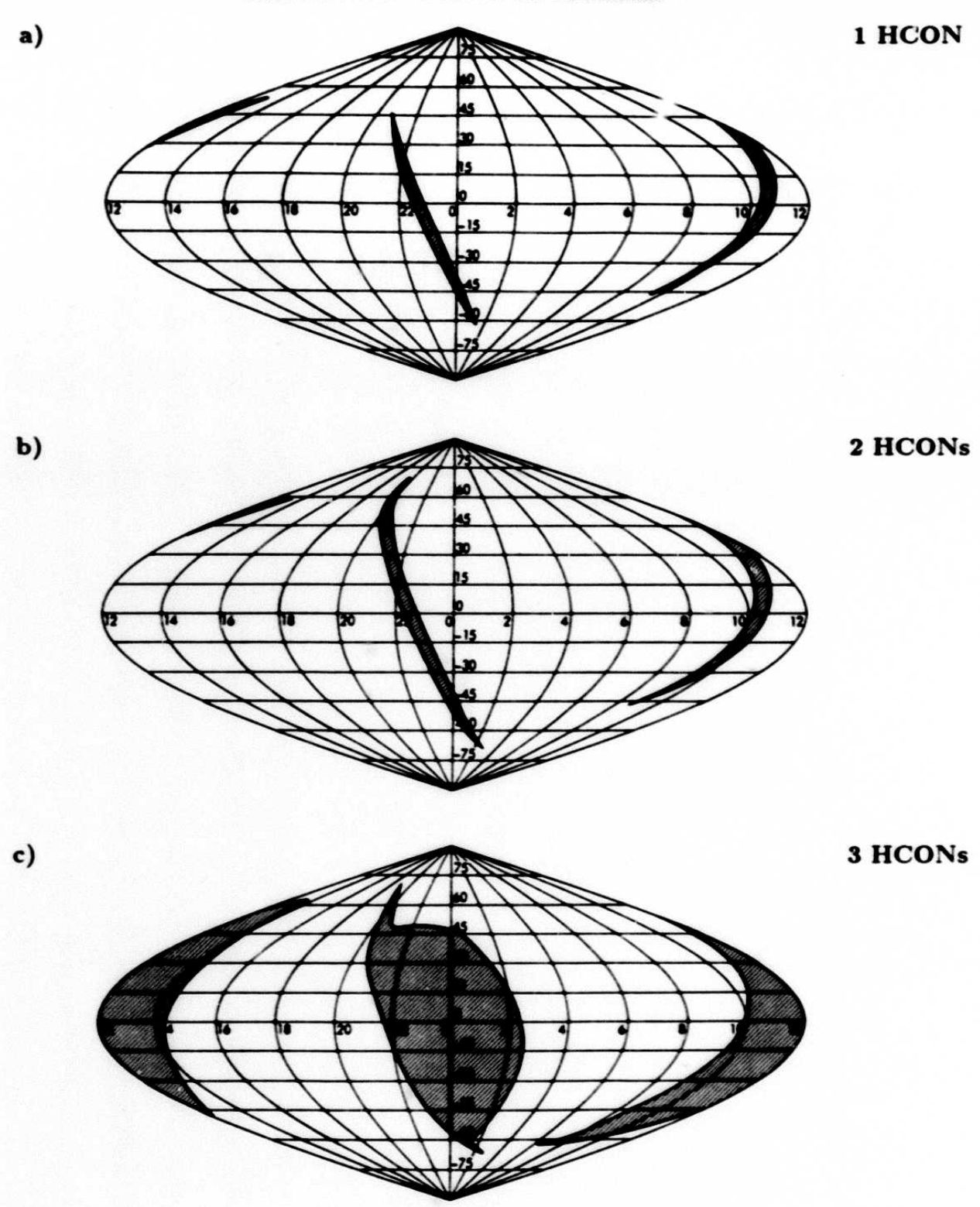

Figure III.C.9 Large-scale depth of coverage. Clear areas in a) received coverage by at least one HCON, in b) by at least two HCONs, and in c) by at least three HCONs. The maps are in equatorial coordinates.

200

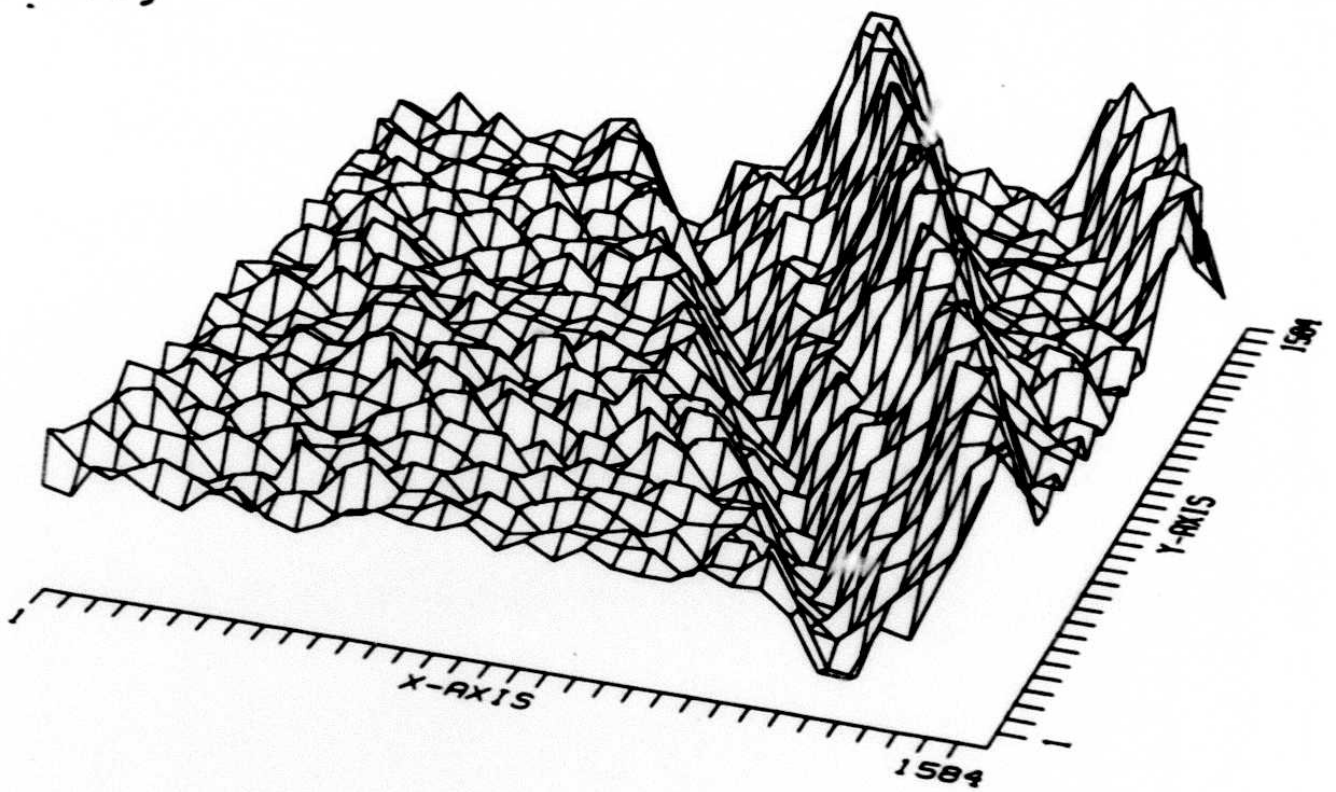

Figure III.C.10A Medium-scale coverage variation across plate 1213 (North Galactic Cap). The plateau corresponds to a pixel average of 8 counts, the high ridges correspond to a pixel average of 10 counts, and the valley corresponds to a pixel average of 7 counts. The axes refer to positions in the plate in pixel units.

One way to quantify the small-scale variation will now be described. A useful parameter describing the small-scale/large-scale variations of data coverage is

$$\zeta = \frac{< N_\nu >_\Gamma - < N_\nu >_\Delta}{< N_\nu >_\Gamma} \qquad (III.C.3)$$

In the preceding formula Δ is a region the size of a point source (roughly 10 pixels), and Γ is the region used for the computation of thresholding noise. The closer ζ is to 0, the more uniform is the coverage over the region Γ and the more consistent the completeness estimate. ζ has a standard deviation of 0.14 at 12 μm and 0.16 at 25 μm, which gives an estimate for the standard deviation of $F_\nu^{90\%}$ of 7% and 8% at 12 and 25 μm, respectively, as estimated from Eq. III.C.2. In Figure III.C.11 the distribution function P(ζ) of the observed values for ζ at 12, 25, 60, and 100 μm is seen.

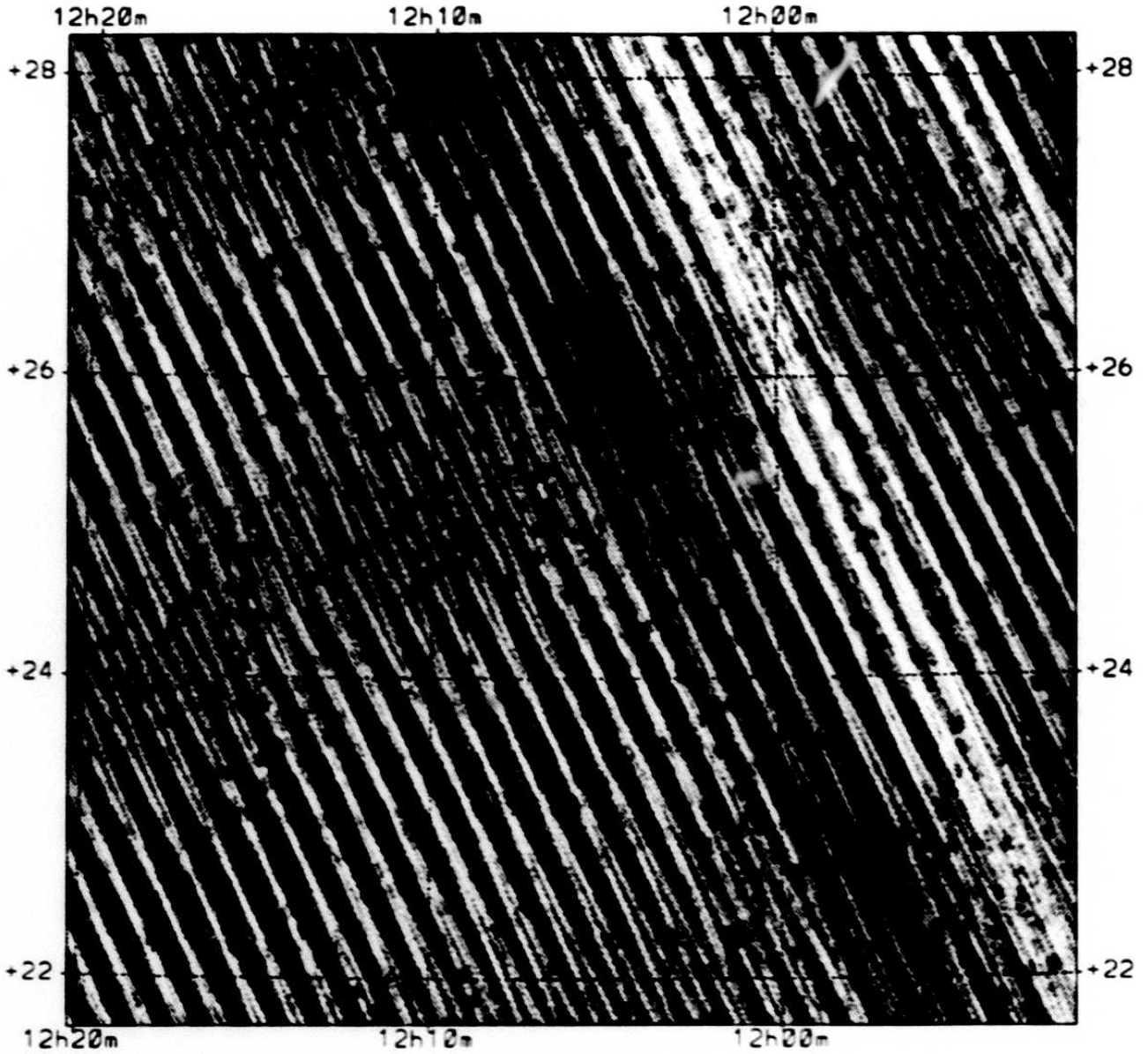

Figure III.C.10B Small-scale coverage variation across plate 1213 (North Galactic Cap). In this map the quasi-periodic variations in coverage can be clearly seen. Small dark rectangular patches scattered uniformly in the figure are caused by clipping of radiation hits.

C.3 Variation With Ecliptic Latitude

At 12 and 25 μm. noise is a strong function of the ecliptic latitude. Let $< \sigma >$ denote the average noise. Within a region approximately 30° on each side of the ecliptic plane.

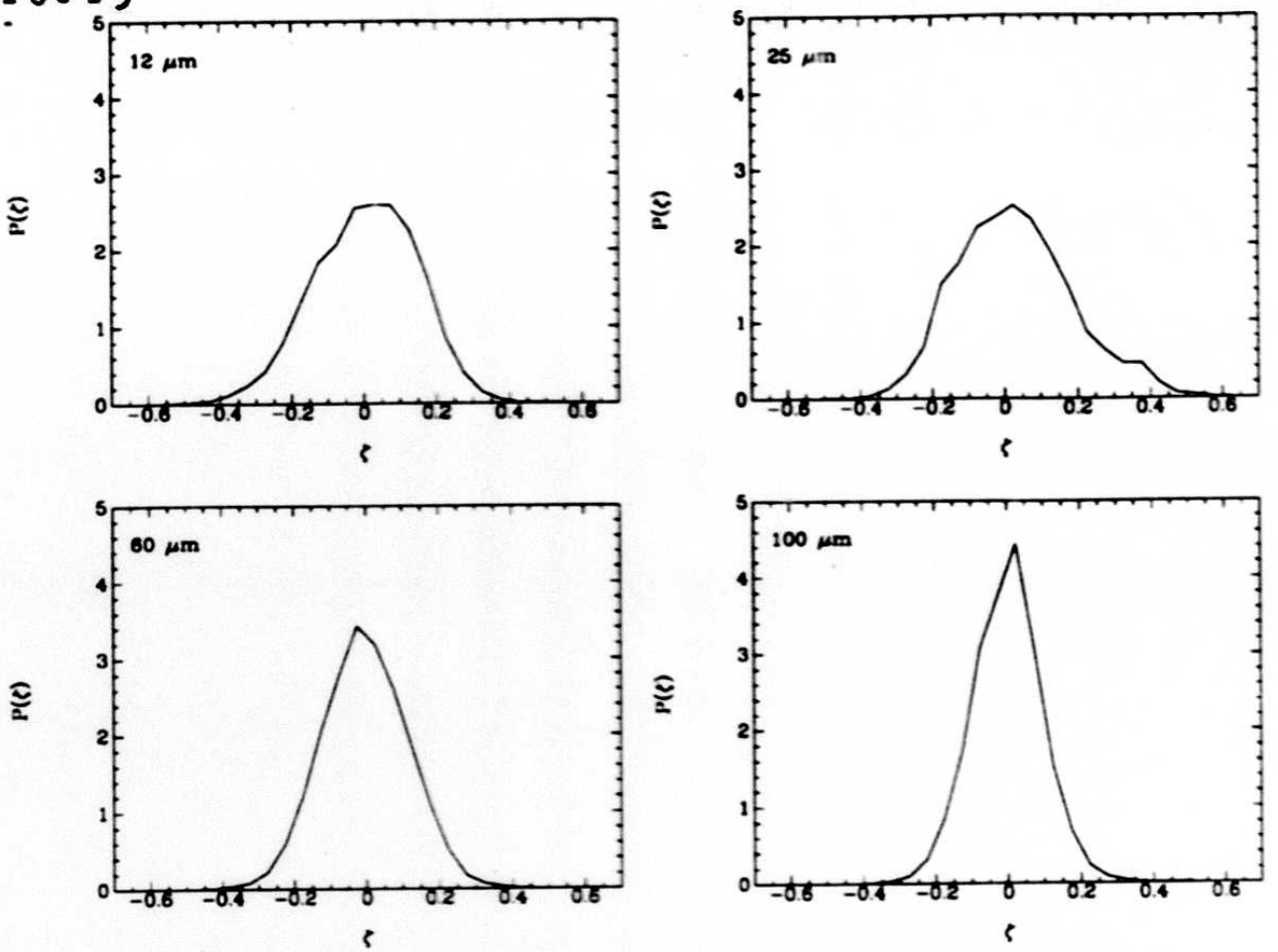

Figure III.C.11 Distribution function of ζ (Eq. III.C.3) at 12, 25, 60, and 100 μm.

$< \sigma >$ shows a definite increase as a result of background photons. A fit of the noise data at 12 and 25 μm separately to the zodiacal background results in a simple parameterization of the detector output noise as a function of the number of background photons

$$< \sigma(n_\gamma) >^2 = \sigma_1^2 + \sigma_2^2 \left(\frac{n_\gamma}{n_0}\right) \qquad (III.C.4)$$

The behavior of $< \sigma(\beta) >$ at 12 and 25 μm as a function of ecliptic latitude, β, is seen in Figures III.C.12 and III.C.13. In the preceding formula n_0 is the number of background photons at the ecliptic plane, and n_γ is the number of photons at the observation point. Table III.C.1 displays the values for σ_1 and σ_2 occurring in Eq. III.C.4 at 12 and 25 μm.

With this simple parameterization of the detector noise at 12 and 25 μm, and the fact that the catalog criteria avoid regions with extended structures, it is possible to use Eq. III.C.1 in the form

$$F_\nu^{90\%} = (\mathrm{SNR}_\nu^T + 1.3) \times < \sigma(\beta) > / \sqrt{N_\nu} \qquad (III.C.5)$$

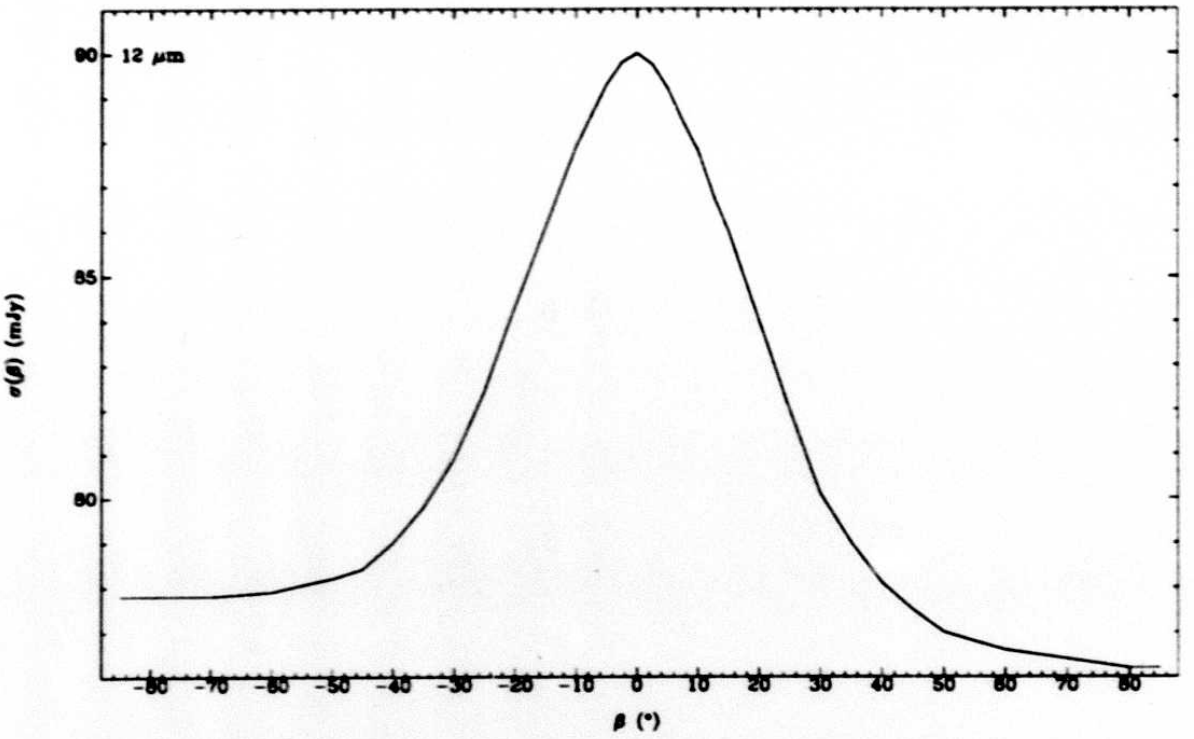

Figure III.C.12 Noise at 12 μm as a function of ecliptic latitude.

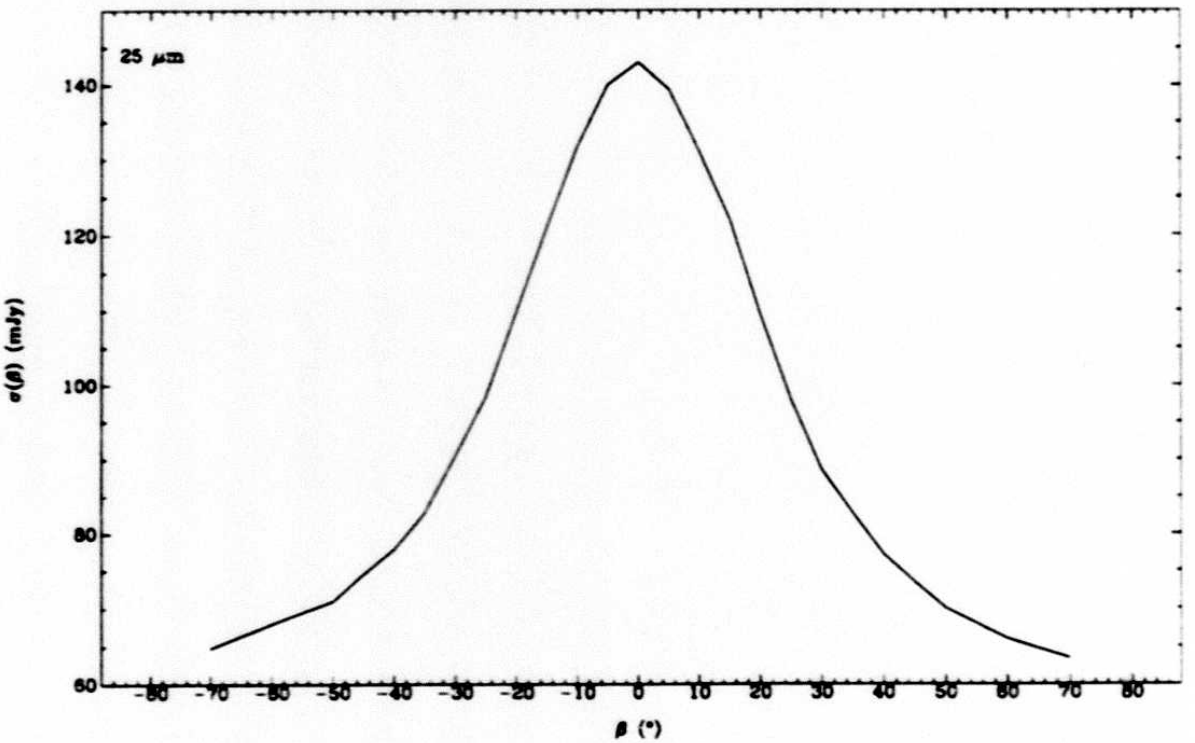

Figure III.C.13 Noise at 25 μm as a function of ecliptic latitude.

Table III.C.1 Detector Noise Parameters

12 μm		25 μm	
σ_1 (mJy)	σ_2 (mJy)	σ_1 (mJy)	σ_2 (mJy)
76	49	53	134

Recall SNR^T stands for the signal-to-noise cutoff which is discussed in detail in Section III.D.3.

The value of SNR_ν^T in equation III.C.5 varies with location in the sky (a histogram of SNR_ν^T values for the catalog can be seen in Figure I.A.5), depending on parameters which are discussed in detail in Section III.D.3. The other parameters in this equation, namely N_ν and $< \sigma(\beta) >$, also vary with sky position. At any given depth of coverage (fixed N_ν), the 90% completeness level of the FSC rises as the ecliptic plane is approached, reflecting the increase in noise shown in Figures III.C.12 and III.C.13. This rise in the 90% completeness level is approximately 20% at 12 μm, and a factor of *two* at 25 μm. In Figures III.C.5 and III.C.6, which are in *galactic* coordinates, the dark belt running diagonally across the figures shows the regions around the ecliptic plane and the ensuing rise in completeness levels.

C.4 Effects of the Infrared Cirrus

The major cause of variation in completeness at 60 and 100 μm is attributed to the extended structure in the sky, the *infrared cirrus*. For most of the sky at these two bands, the instrumental noise is significantly lower than the sky noise due to the observed filamentary structure. The extended background manifests itself by raising the total noise relative to the instrumental noise as described in Section III.A. Since the coverage at 100 μm has a smaller range of variation than other bands (due to lack of dead detectors), the effects of coverage on variations of NOISCOR would be subordinate to the effects of background (see Section III.A.1), therefore the distribution of NOISCOR at 100 μm follows the cirrus contamination at this band. As expected, this parameter varies by a factor of over 20 across the sky. Because the method of source extraction uses the noise coming from the 68% quantile of the flux distributions (see Section II.E), the effects of cirrus contamination are automatically included by effectively raising the source extraction threshold in units of flux density. As a result, the completeness levels in cirrus contaminated regions will be raised. In Figure III.C.14 the histogram of NOISCOR at 100 μm is displayed. Note that in the absence of structured background and with a high enough coverage this parameter should be ~ 1 (see Figure III.A.1). In Figure III.C.15.a the spatial distribution of NOISCOR at 100 μm can be seen. This plot indicates that the 100 μm band is almost always

205

plagued by *cirrus*; and that there are few areas that could be called *cirrus*-free ($|b| \gtrsim 60°$ is such a cirrus-free area). Further evidence that NOISCOR at 100 μm follows the cirrus contamination is provided by a map of the large-scale emission from interstellar dust at 100 μm, seen in Figure III.C.15.b (prepared by M. Jones, Queen Mary and Westfield College, London, from the maps of 100 μm interstellar dust emission by Rowan-Robinson *et al.* 1991).

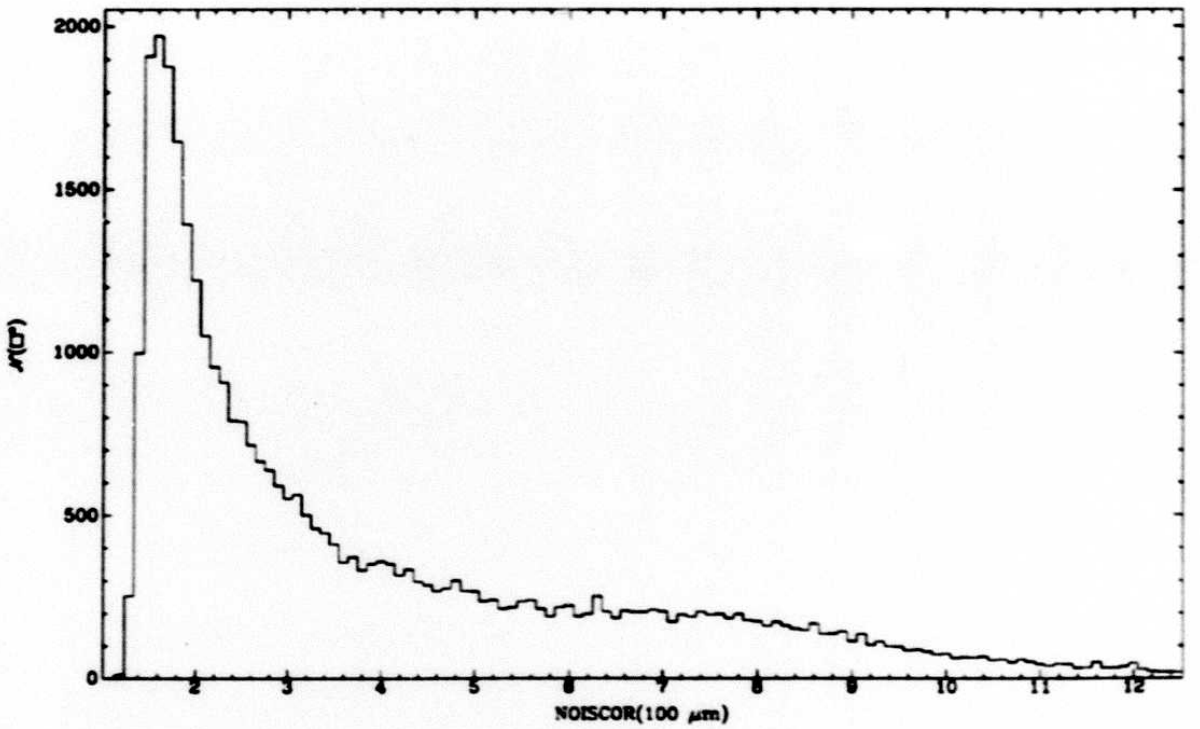

Figure III.C.14 Distribution of NOISCOR at 100 μm across the whole sky. An unconfused background would result in NOISCOR ~ 1.

C.5 Effect of Cuts in LOCSNR

During the source extraction process, a cut is imposed on the signal-to-local-pixel noise ratio (LOCSNR) of sources in each band. This cut is set at a level to ensure that transient events such as asteroids or aliased radiation hits do not enter the FSC. A computation of the probability distribution of LOCSNR as a function of the true SNR of the source and the amount of data coverage yields Tables III.C.2 through III.C.4 (the computations were based on assuming Gaussian noise, and used the trimmed-mean algorithm to compute SNR and LOCSNR, Eq. II.C.1-5). These tables show the fraction of sources with LOCSNR exceeding a given value at a given observed SNR. The tables thus give the effects of cuts in LOCSNR on completeness at any SNR. These tables apply to all bands uniformly, since

207

D 10015

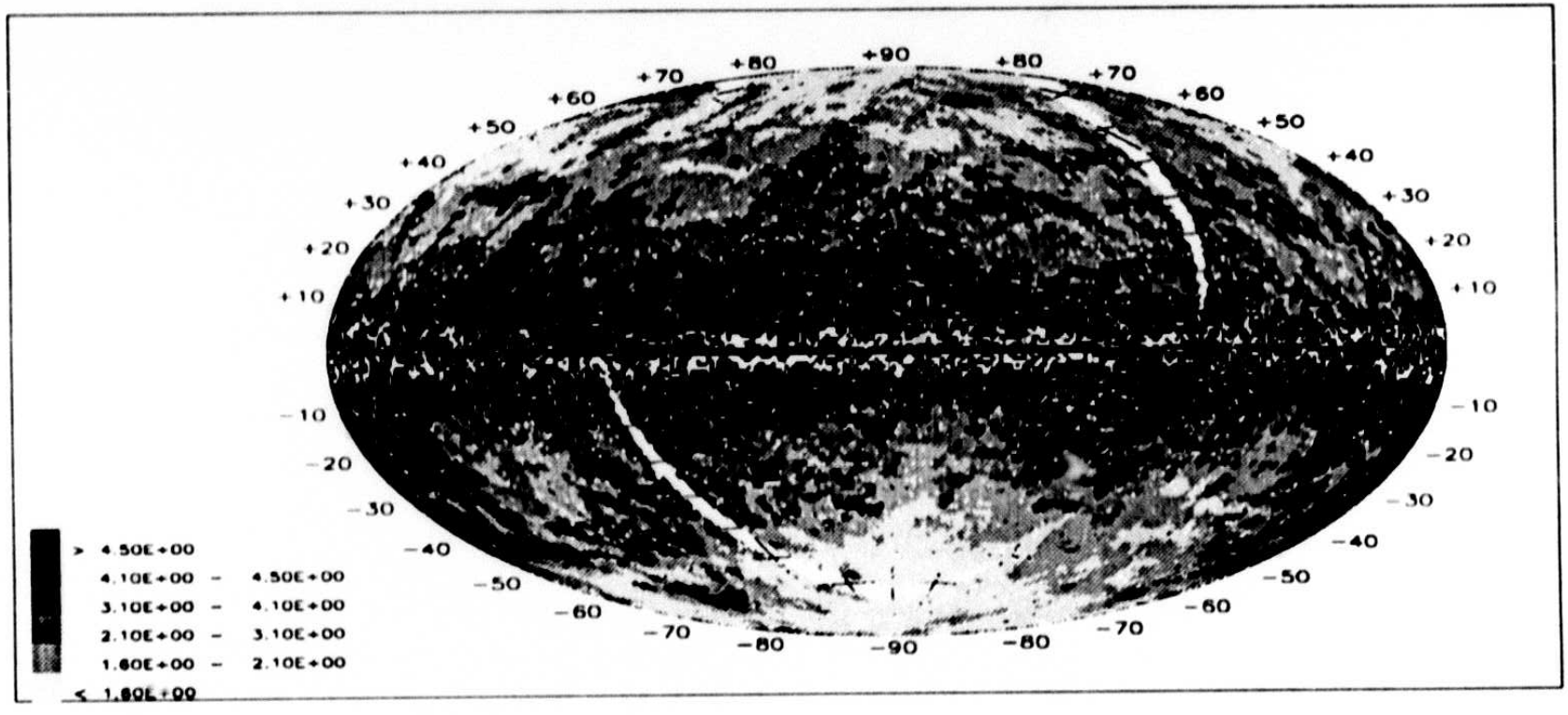

Figure III.C.15.a Spatial distribution of the NOISCOR at 100 μm, in galactic coordinates. Darkness of regions depicts progressive increase of the infrared cirrus. When NOISCOR $\gtrsim 3$ the gain in sensitivity due to coaddition is lost. Blank regions in the map occur when there are no 100 μm detections.

D 10015

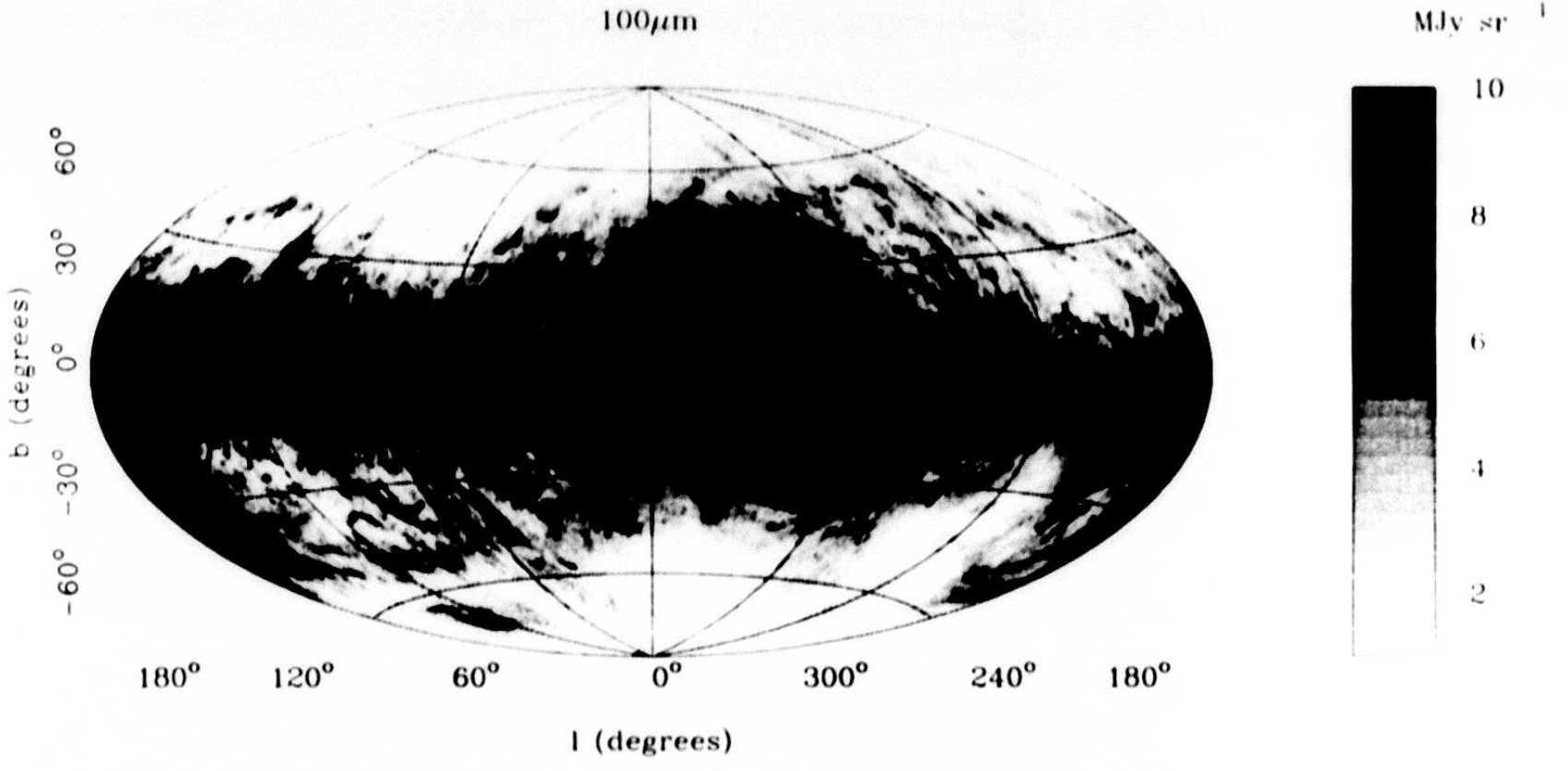

Figure III.C.15.b Spatial distribution of large scale emission from interstellar dust at 100 μm. (Figure prepared by M. Jones, Queen Mary and Westfield College, London, from the maps of 100 μm interstellar dust emission by Rowan-Robinson *et al.* 1991.)

they derive solely from statistics. The effects of cuts in LOCSNR have been included in the rest of this chapter.

As an example, with the LOCSNR cut set at 3.5 (as is done for the PSC at 12, 60, and 100 μm), 11.1% of the sources with SNR = 6 and N_ν = 6 (Table III.C.3) will be excluded from the catalog. Figure III.C.16 shows the fraction of sources which will be present at any given SNR, when the number of data counts is equal to 8.

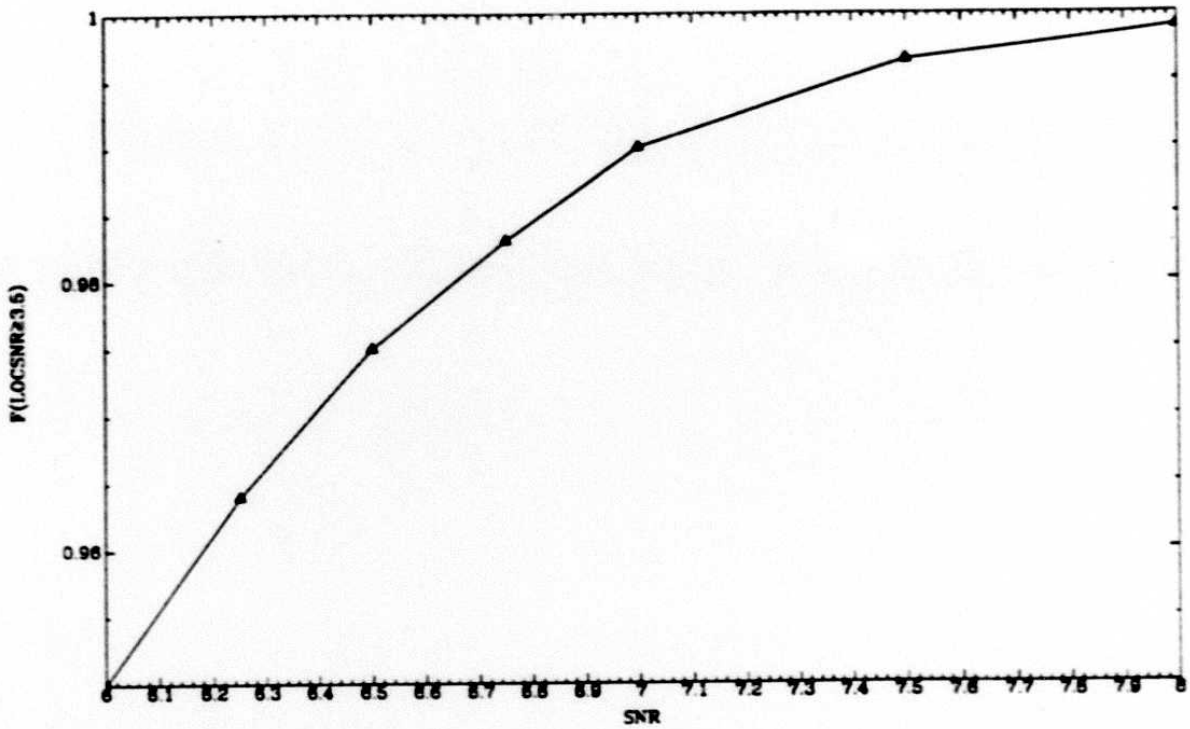

Figure III.C.16 Fraction of sources with eight data counts at given SNR, with LOCSNR exceeding 3.50.

C.6 Completeness from Analysis of Source Counts

If we are dealing with a constant population of sources in a given band, source count analysis would give good results for completeness and reliability. Unfortunately, *this is probably not the case*. At 12 μm at high galactic latitudes and at low flux levels we start to see the reduction in the volume density of stellar sources as we see through several scale heights of the galactic plane for many source types (Chester 1986). At 25 μm, again at high galactic latitudes, we see the reduction in volume density of stellar sources. At 60 μm, the galaxies that we observe show clustering on various angular scales, the IR galaxies might be undergoing significant evolution as the look-back time increases, and, above all, the number counts are certainly affected by cirrus.

209

TABLE III.C.2 Fraction of Sources with LOCSNR Exceeding Given Values at SNR=5

LOCSNR	No. of Data Counts 6	7	8	9
2.0	.991	.997	.999	.999
2.5	.952	.975	.987	.994
3.0	.877	.914	.939	.959
3.5	.780	.817	.847	.875
4.0	.678	.704	.727	.751

TABLE III.C.3 Fraction of Sources with LOCSNR Exceeding Given Values at SNR=6

LOCSNR	No. of Data Counts 6	7	8	9
2.0	.999	.9999	.9999	.9999
2.5	.987	.996	.999	.9999
3.0	.952	.975	.987	.994
3.5	.889	.926	.950	.967
4.0	.811	.850	.880	.907
4.5	.725	.756	.785	.813

TABLE III.C.4 Fraction of Sources with LOCSNR Exceeding Given Values at SNR=6.5

LOCSNR	No. of Data Counts 6	7	8	9
2.0	.9997	.9999	1.0	1.0
2.5	.994	.998	.9998	1.0
3.0	.972	.988	.995	.998
3.5	.925	.956	.975	.985
4.0	.860	.899	.926	.949
4.5	.783	.821	.852	.880

Nonetheless, it still is of interest to conduct the analysis. If we consider only narrow ranges of fluxes and certain types of sources, we can mitigate source density and evolution effects. However, any conclusions we draw from the analysis can only corroborate de-

ductions derived from other analyses. ***Claims for completeness or reliability derived from source count analysis alone are made only with significant reservations.***

C.6.a 12 μm

In order to compute the completeness of the Faint Source Data Base (FSDB), we separate the sources into five distinct classes based on the noise as computed in Section II.E. These classes are also used for the reliability computations in Section III.D. The classes include sources with noise levels in the range of <16, 16–22, 22–28, 28–32, and 32–36 mJy. In this section we use the data, based on the observed versus predicted source counts, to obtain completeness figures. The method assumes a population of IR sources having a number distribution

$$N(>s) = \frac{\mathcal{N}_0}{s^{\alpha}} \qquad (III.C.6)$$

over a small range of s. At 12 and 25 μm, the set of sources from the SAO catalog are chosen which are of spectral types G and earlier. This criterion ensures that fluxes at 12 μm will be traced down to a flux density of 80 mJy without appreciable loss due to completeness fall-off of the SAO catalog. (This conclusion is based on the $V - [\ 12\ \mu m\ ]$ distributions of observed SAO stars of different spectral types.) A maximum likelihood method is used for the *differential* source counts. The method is fully described in Section III.D.3 and is used to estimate, from the observed source counts at a high enough flux density, the appropriate values for $\mathcal{N}_0$ and α, from which the predictions for source counts are made at lower flux values. The ratio of *observed* counts to *predicted* counts yields the completeness estimates C

$$C(s) = \frac{dN_{observed}(s)}{dN_{predicted}(s)} \qquad (III.C.7)$$

For illustration, plots of dN versus s for all noise classes and the maximum likelihood fits are shown in Figure III.C.17. The results for the behavior of C as a function of flux density are presented in Figure III.C.18 for the previously mentioned noise ranges. From these plots, 90% values for C are tabulated in Table III.C.5. ***At 12 μm the Faint Source Data Base is 90% complete to 80 mJy for areas with a noise range of <16 mJy and to 140 mJy for areas with a noise range of 32–36 mJy.***

C.6.b 25 μm

Completeness at 25 μm is affected by the variation of detector noise by a factor of two due to background photons as the ecliptic plane is approached (notice the implications of Eq. III.C.4 and III.C.5). Thus, for a constant number of data counts at a given SNR, the completeness levels at 25 μm will vary by a factor of two (note that the FSDB has an SNR threshold of 3.0). As at 12 μm, Eq. III.C.7 is used to estimate completeness for five classes

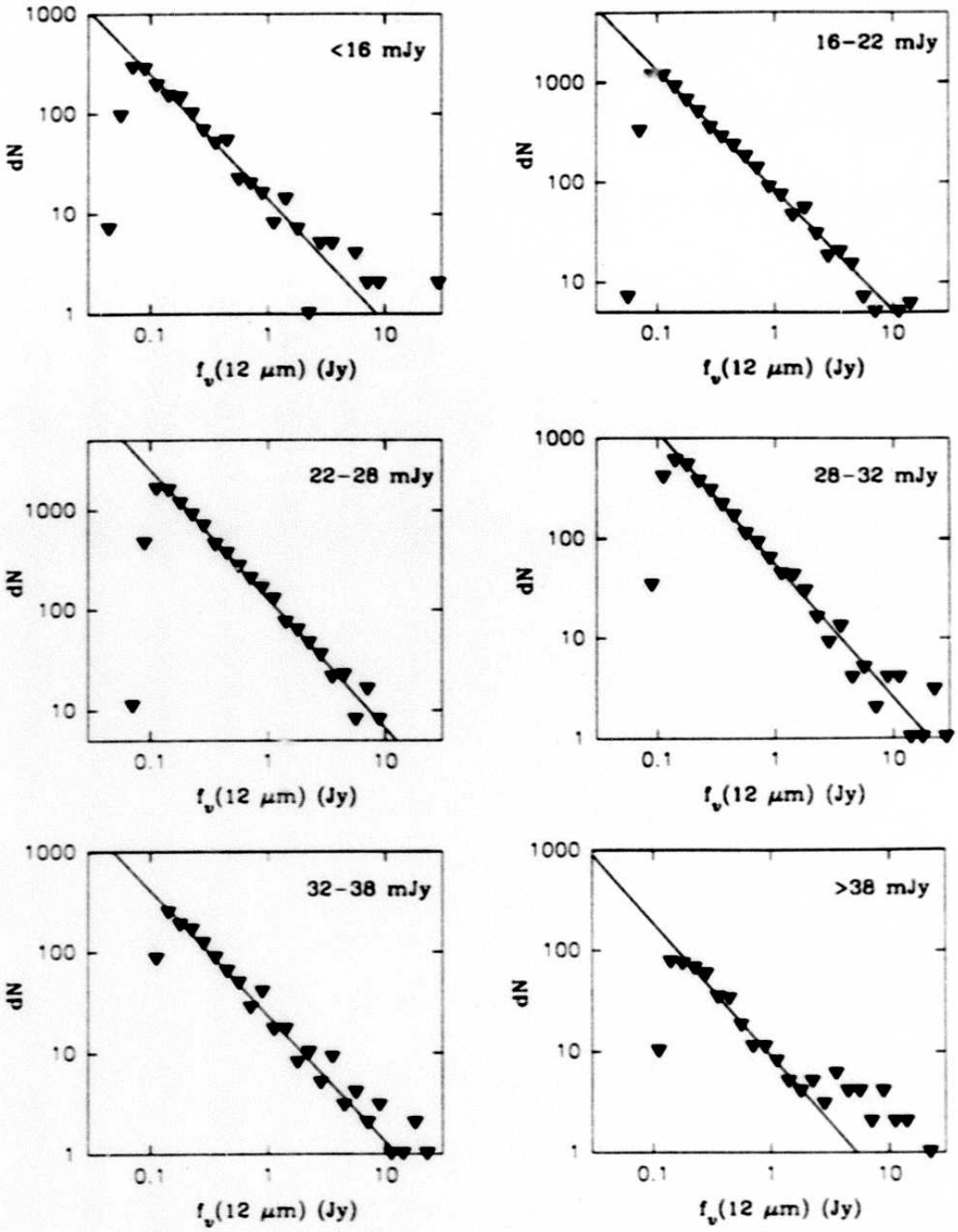

Figure III.C.17 Source counts for SAO sources of spectral types G and earlier and detected at 12 μm for each noise range. The solid line is the maximum likelihood fit.

of noise level. These classes have noise levels of <18, 18–28, 28–38, 38–48, and 48–65 mJy. Plots of dN versus s are shown in Figure III.C.19 and the results of the computation for

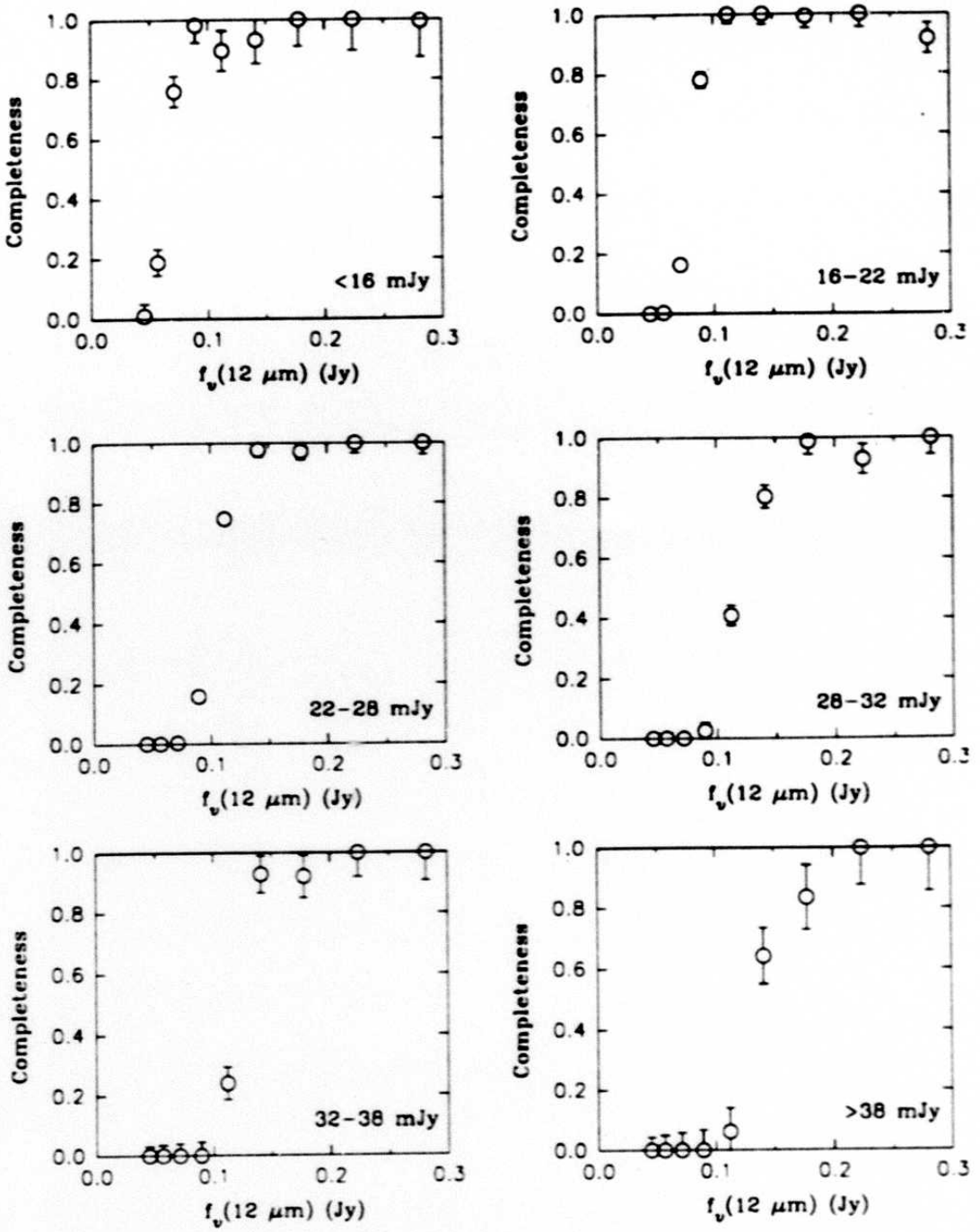

Figure III.C.18 Completeness for each noise range, as noted in the lower right corner of each plot, versus flux density at 12 μm.

C are displayed in Figure III.C.20. A hand-drawn curve through the data points gives a 90% completeness value which is reproduced in Table III.C.6. The conclusion is that *at*

Table III.C.5 12 μm 90% Completeness Levels

$\sigma(12\ \mu m)$ (mJy)	$F_\nu^{90\%}$ (mJy)
<16	80^{+10}_{-10}
16 - 22	95^{+6}_{-6}
22 - 28	122^{+4}_{-4}
28 - 32	153^{+12}_{-12}
32 - 36	140^{+72}_{-13}

Table III.C.6 25 μm 90% Completeness Levels

$\sigma(25\ \mu m)$ (mJy)	$F_\nu^{90\%}$ (mJy)
<18	77^{+10}_{-9}
18 - 28	100^{+8}_{-7}
28 - 38	159^{+30}_{-10}
38 - 48	168^{+12}_{-10}
48 - 65	$200^{+\infty}_{-11}$

25 μm the FSDB is 90% complete to 77 mJy at the lowest noise level and to 200 mJy at the highest noise level.

C.6.c 60 μm

The estimation of completeness at 60 and 100 μm is hampered by the absence of a catalog of extragalactic sources complete beyond the limiting flux densities of the FSS. While it was feasible to use the SAO catalog for the early type stars to estimate the completeness levels at 12 and 25 μm, a similar effort can not be easily undertaken for sources at 60 μm. A catalog of sources at 60 μm which is complete down to levels lower than the FSDB is the *IRAS Serendipitous Survey Catalog* (SSC 1986). The only shortcoming of the SSC for this purpose is that it covers only a small fraction of the sky, with most of the coverage at lower galactic latitudes. Thus not all combinations of FSDB attributes such as the effects of depth of coverage or the cirrus background could be tested. The results of comparisons of the FSDB versus SSC give an indication of completeness. The results of this analysis will be seen in Section III.C.7.

However, with great caution we will quote a rough estimate on completeness levels at 60 μm using source counts (for cautionary notes on the use of the source count method at 60 μm see Section III.D.3.c). As a catalog to trace the extragalactic sources we employ

214

D 10015

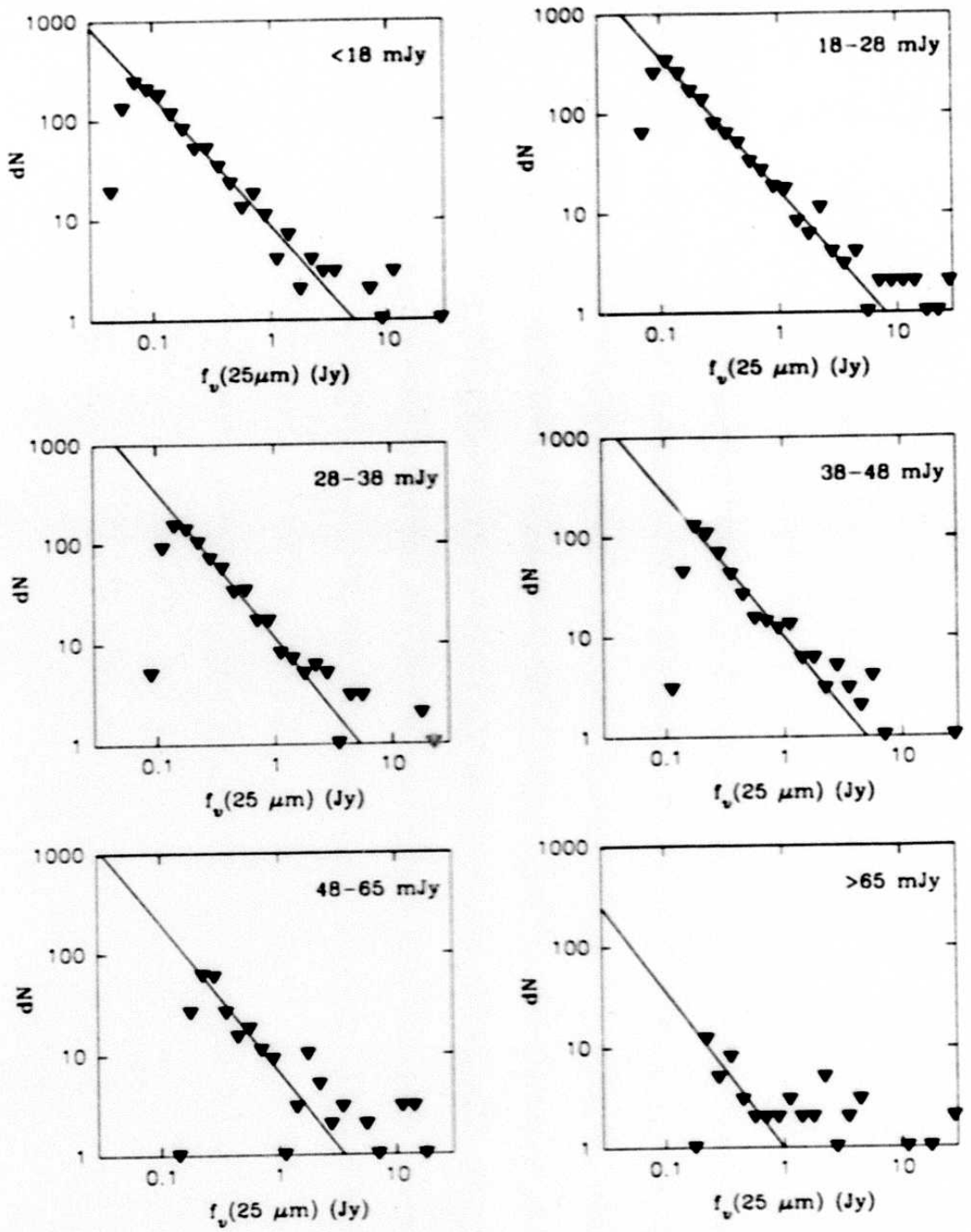

Figure III.C.19 Source counts for SAO sources of spectral types G and earlier and detected at 25 μm for each noise range. The solid line is the maximum likelihood fit.

the Zwicky Catalog of galaxies. *It is known that an optical catalog of galaxies can not be treated as a good tracer of IR galaxies. Redshift surveys have shown that the IRAS*

215

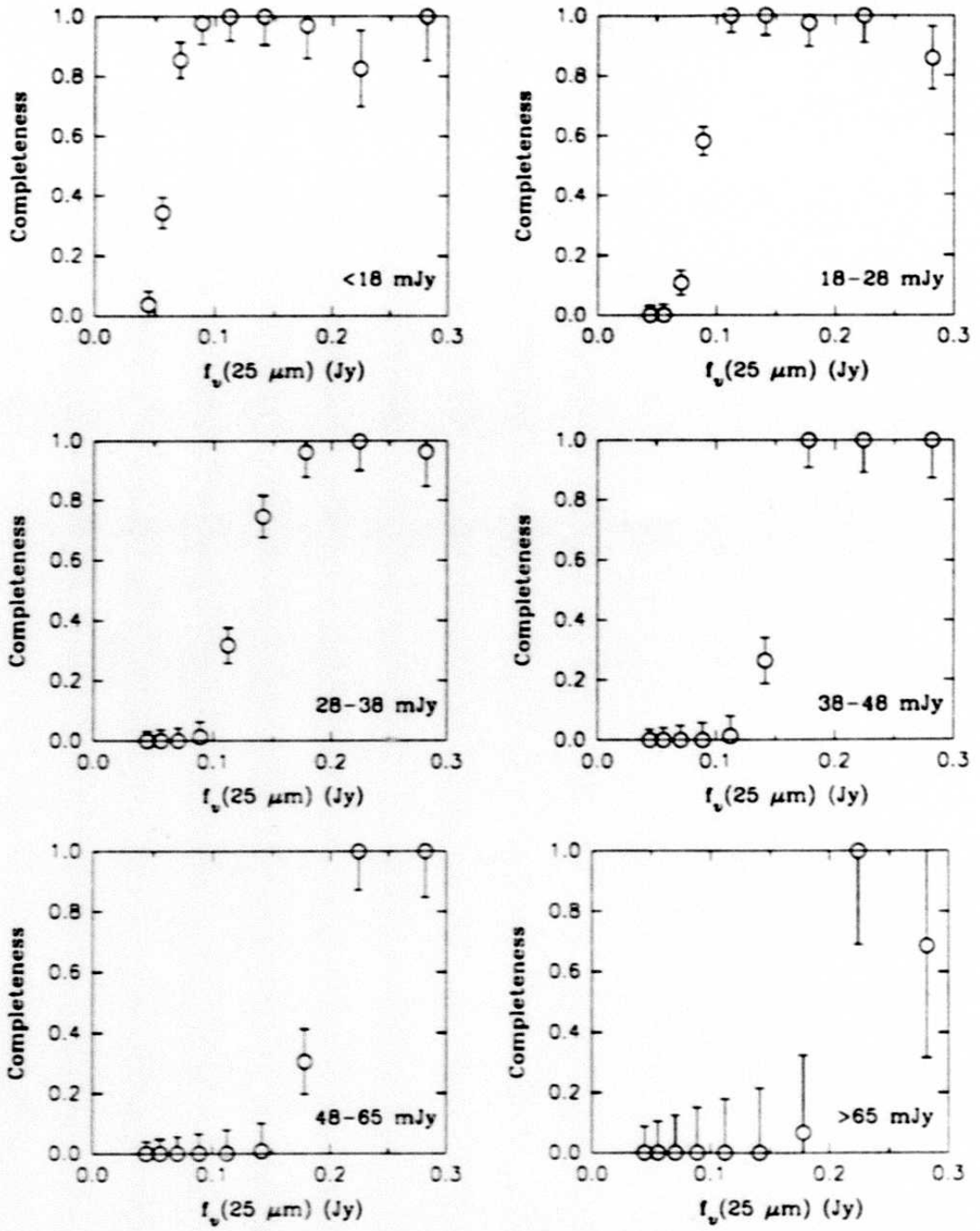

Figure III.C.20 Completeness for each noise range, noted in the lower right corner of each plot, versus flux density at 25 μm.

PSC *is deeper than the Zwicky Catalog. Since the* FSS *is even deeper than the* PSC, *the proportion of galaxies from the* FSDB *in the Zwicky Catalog is likely to be smaller still.* Thus an incompleteness found from the 60 μm counts of Zwicky galaxies will be in part

216

- The SSC is based on the ***Additional Observations*** (AOs), which raster-scanned the sky at ***one-half*** the rate of the survey.

Although comparison of the SSC and PSC fluxes show agreement to ~ 5% for 12, 25, and 60 μm and 10% for 100 μm at high flux levels, the agreement of SSC and FSS flux densities at fainter levels imposes an overall uncertainty in our results.

More specifically, let us go back to Eq. III.C.7 which states

$$C(s) = \frac{dN_{observed}(s)}{dN_{predicted}(s)}. \qquad (III.C.7)$$

Notice that in the previous section ***both*** $dN_{observed}$ and $dN_{predicted}$ were based on the ***same*** flux density scale s, whereas in this section we will be considering the estimate C where

$$C(s) = \frac{dN_{observed}(s')}{dN_{predicted}(s)}. \qquad (III.C.8)$$

This equation involves ***both*** s' ***and*** s, where s (flux density from the SSC) is chosen to set the standard and s' (flux from the FSS) is assumed to be on the same scale as s; in other words $s' = s + \epsilon\, g(s)$, where both ϵ and g are assumed to be small perturbations.

For the comparisons in this section we take the SSC sources which fall on regions also covered by the FSS. Regions below 30° galactic latitude, within 5° of the center of the LMC or the SMC, or within areas not covered by the *IRAS* survey, are eliminated. The bulk of the SSC cirrus sources are removed by rejecting sources with a 60 to 100 μm flux ratio of less than 0.3. For each SSC source, the closest FSDB source with an SSC association is checked. For each band of the SSC source with a high quality flux, the associated FSDB source is required to have a consistent flux. The data are then binned in units of SSC flux density. In each bin there are I SSC sources and J FSS matches to those sources. Completeness C is computed from

$$C = \frac{J}{I}. \qquad (III.C.9)$$

Incompleteness at flux densities ≥ 1 Jy has been analyzed for all sources with $b \geq 50°$. Of the 27 sources with problems, 14 SSC sources had one or more bands which had been split off into another source in the FSDB, 10 sources had not been associated to the SSC because the in-scan positional separations were beyond the FSDB association box, 2 sources were portions of extended objects that had been treated differently by the two processing methods, and 1 SSC source was due to cross-talk.

C.7.a 12 and 25 μm

Figure III.C.21 shows the FSDB completeness vs. the SSC at 12 μm. *At 12 μm, the 90% completeness level of the FSDB for $|b| \geq 30°$ occurs in the range of 140 to 180 mJy.*

218

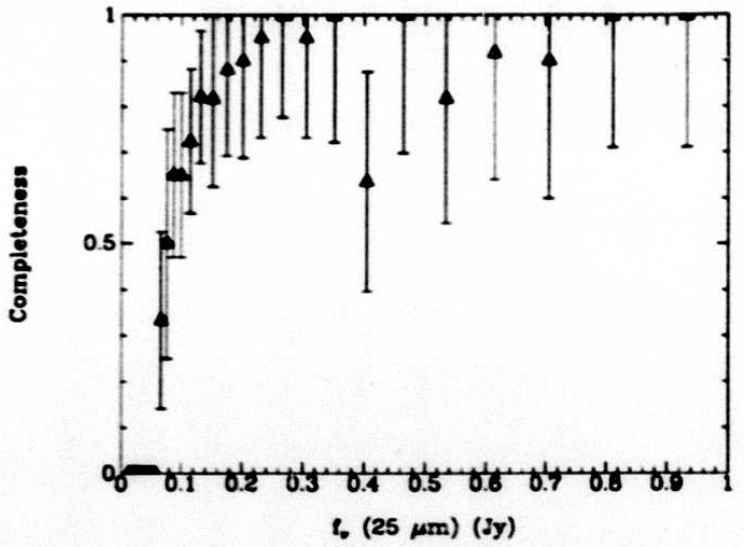

Figure III.C.22 Completeness of the FSDB at 25 μm relative to the SSC for the $|b| \geq 30°$ sky.

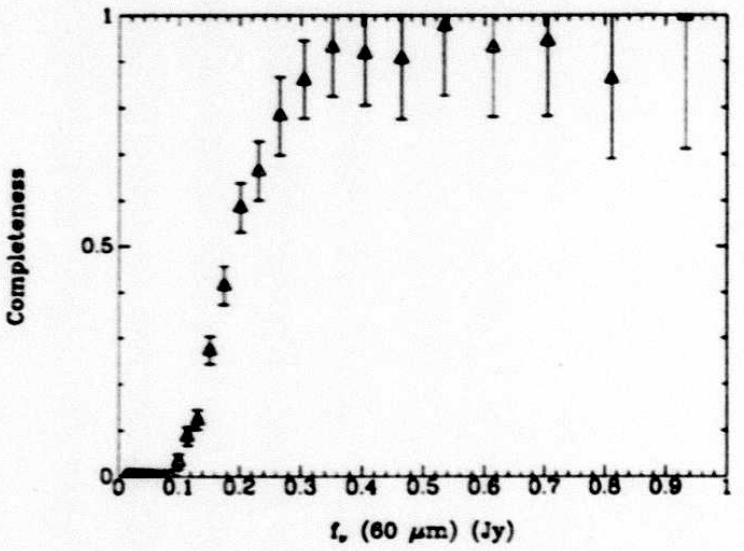

Figure III.C.23 Completeness of the FSDB at 60 μm relative to the SSC for the $|b| \geq 30°$ sky.

from this section are to be used while remembering that the extraction threshold varies as a function of position, as this will strongly affect local completeness. The completeness levels shown will be deeper than our quoted values for areas painted lighter in Figure III.C.15.a and less deep for areas painted darker in Figure III.C.15.a. In addition, the completeness of the FSC is limited by the decision to exclude sources detected at 100 μm only. *At 100 μm, the 90% completeness level of the FSDB for $|b| \geq 30°$ is 1.0 - 1.2 Jy.*

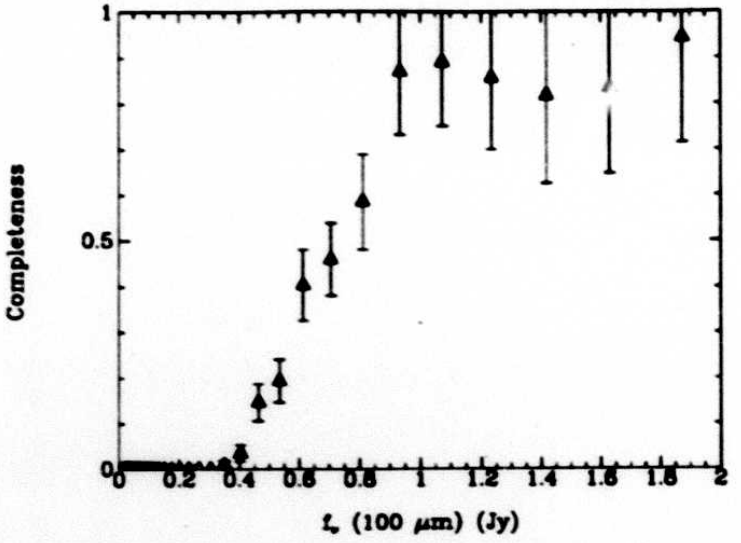

Figure III.C.24 Completeness of the FSDB at 100 μm relative to the SSC for the $|b| \geq 30°$ sky.

reliability estimates which agree within their uncertainties. The reliability of a source with high-quality flux density at 12 or 25 μm is better than 90% at th *lowest* flux-density levels, and essentially 99% for the catalog considered as a whole. The few spurious sources derive from radiation hits or moving sources. The reliability of a source with high-quality flux density at 60 μm is better than 80% at the *lowest* flux-density levels, and 94% for the catalog as a whole. The spurious sources derive almost entirely from structures in the infrared cirrus that look like a point source to *IRAS* in the in-scan direction although they may be far from point-like in the cross-scan direction.

D.2 Definitions, Assumptions and Limitations

The reliability, R, of a point source extraction with flux density in a given band is defined as the probability that the extraction corresponds to a true, celestially-fixed point source of radiation in that given band. Extended sources such as infrared cirrus are thus considered to be *false* sources unless most of the radiation emanates from a region small enough to be considered as a point source to *IRAS* ($< 1' - 4'$, depending on wavelength). Explicitly,

$$R = \frac{Total\ no.\ true\ sources}{Total\ no.\ true + false\ sources}. \qquad (III.D.1)$$

Note that this definition of reliability is wavelength dependent. This usage will be retained throughout this section. We note that the term reliability refers to the likelihood of source existence and *not* to the accuracy of flux density measurement. The estimate given for R is a *minimum reliability* estimate (discussed in Section III.D.1). For each source, a single parameter MINREL (*min*imum *rel*iability) is defined which is the *maximum* of the minimum reliability estimates for each band. Thus MINREL gives a lower limit to the *source* reliability, and is not to be confused with the reliability of individual flux-density measurements for that source. (Of course, MINREL will exactly equal the reliability of *one* of the flux-density measurements for that source.) In particular, moderate-quality flux densities quoted for such a source may have drastically lower reliability. This is a consequence of our desire to provide flux-density measurements down to SNR $\sim$ 3 in as many bands as possible for sources with at least one high-quality flux-density measurement.

To clarify the interpretation of MINREL, consider the example of a source with detections at 12 and 25 μm. It has a high-quality flux density at 12 μm, with SNR=16 and R=99%, and a moderate-quality flux density at 25 μm with SNR=4 and R=20%. This source will have MINREL=99. Because the source at 25 μm was found within a small area surrounding the 12 μm source, the true reliability of the flux-density measurement

223

at 25 μm is actually closer to 90% than the nominal value of 20%. The probability of a random match within a small area between a high-quality source at 12 μm and some source at 25 μm is small. (Note that significant numbers of random 25 μm matches occur only when the search area is large — one of those sources with SNR=4 selected *at random* would have R=20%.)

Source confusion may produce positions and flux-density measurements which do not correspond to sky truth. However, we do not consider the results as unreliable measurements since they are expected consequences of the ***IRAS*** resolution.

R is a function of several variables, the most important of which is the SNR. Often, SNR is treated as a convenient and equivalent way of labeling confidence levels which refer to a Gaussian distribution. However, for non-Gaussian distributions, parameters other than SNR are needed to completely determine the confidence levels. For this reason R also depends on the number of data points coadded and the amount of *cirrus* present.

We emphasize that R cannot be computed using Gaussian statistics. As mentioned above, radiation hits, moving sources, and cirrus produce false sources at a much higher rate than would be expected from Gaussian statistics. (See Figures III.D.2 and 3 for a vivid illustration of this point.)

D.3 Estimates from Source Count Slope Comparisons

The usual source count analysis depends on observing a homogeneous population of sources that satisfy a power law distribution

$$N_0(> s) = \frac{N_0}{s^\alpha} \qquad (III.D.2)$$

over some range of flux density. (In this section N will refer to source counts rather than the number of data samples.)

Normally, one observes at what flux density the source counts fall away from the power law fit to derive where the catalog becomes *incomplete*. However, in this section we use the source counts of the entire extraction database (not just the FSC) to derive ***reliability*** information. We observe that the number counts *steepen* at low flux-density levels, and that more sources are present in the database than are expected for the power law fit at higher flux-density levels. (However, at 60 μm the steepening of source counts may be partially due to the effects of evolution.) For illustration, Figure III.D.1 displays the actual differential source counts for a narrow range of control parameters (which are

224

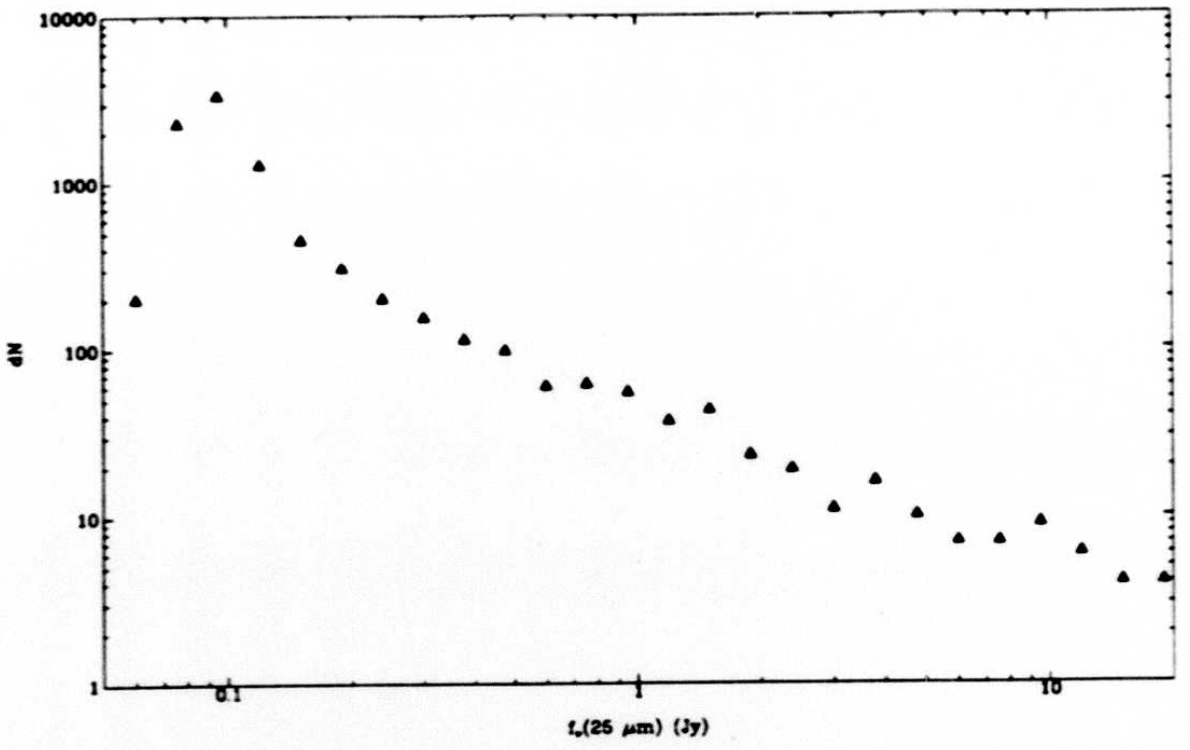

Figure III.D.1 Differential source counts at 25 μm for the entire *database* but subject to a narrow range of control parameters (described in Section D.3.b).

fully discussed in D.3.b) at 25 μm. This figure illustrates the steepening of the source counts at low SNRs followed by a roll-off due to the fall in completeness. Figure III.D.1 was chosen as an extreme example to clearly show the steepening of source counts.

Another mechanism also contributes to the steepening of the source counts. Suppose that the underlying source counts in the absence of measurement uncertainties follow Eq. III.D.2; the addition of measurement errors causes faint sources to be pushed up and bright sources pushed down in flux. However, there are more faint sources than bright ones and, as a result, the net effect is to inflate the source counts relative to the underlying counts. The inflation factor drops to unity at high SNRs where the noise becomes unimportant. However, the inflation factor can become noticeable at lower SNRs. (See Figure III.D.2, where the dashed curve c denotes the inverse of inflation factor.)

Because the false source density depends on SNR, not flux density, we perform the source count analysis versus SNR. (Although the infrared cirrus source count distribution depends on flux density, because of the use of the 68% quantile of flux densities as the 'noise', it is better characterized via SNR.) Sources selected for analysis of source counts

225

must have similar depths of coverage, thresholding noise, cirrus background, etc. With this in mind, the true sources will also satisfy a power law distribution in SNR

$$N_0(>\mathrm{SNR}) = \frac{\mathcal{M}_0}{\mathrm{SNR}^\alpha} \qquad (III.D.3)$$

where SNR = s/σ (the thresholding noise being σ). The number of false sources due to noise follows a distribution

$$N_{false}(>\mathrm{SNR}) = A \times P(\mathrm{SNR}) \qquad (III.D.4)$$

We do not need to know the functional form of this distribution for this analysis. Therefore at any given SNR the *total* observed source count satisfies

$$N_{obs}(>\mathrm{SNR}) = N_0(>\mathrm{SNR}) + N_{false}(>\mathrm{SNR}) \qquad (III.D.5)$$

Due to the rapid fall-off of the false source distribution with SNR we have

$$N_{obs}(>\mathrm{SNR}) \overset{SNR\gg 1}{\longrightarrow} N_0(>\mathrm{SNR}) \qquad (III.D.6)$$

It is hence possible to find the most likely values for the power law distribution from the observed counts at high SNR. We then use this power law to predict the expected number of sources at lower SNR. We apply this method to the *differential* source counts dN_{obs} and dN_0 since it is well known that analysis of integral source counts can give erroneous results. Within a small SNR range [SNR - Δ, SNR + Δ], the differential reliability is defined by

$$R(\mathrm{SNR}) = \frac{dN_0(\mathrm{SNR})}{dN_0(\mathrm{SNR}) + dN_{false}(\mathrm{SNR})}. \qquad (III.D.7)$$

It has already been emphasized that the use of Gaussian statistics in estimating reliability is grossly erroneous. To illustrate this point we have modeled the noise and the source counts for stars and galaxies to derive the expected reliabilities in the presence of non-Gaussian noise.

To model the noise, the 68% and 87% quantiles of flux distributions are used in a log-linear extrapolation to obtain other quantiles. This phenomenological approximation appears to be a reasonable estimator for most of the unconfused $|b| \gtrsim 20°$ sky. Furthermore the beam size is required to complete the computation of $dN_{false}(\mathrm{SNR})$. For this exercise the beam size has been approximated by $\sim 4\ \Omega^{geom}$ where autocorrelation of detectors due

126

to coaddition has been taken into account. (Ω^{geom} is the *geometric* solid angle of a typical detector in a given band). This results in a density of $\sim$ 100–200 beams/square degree. For computation of $dN_0(\mathrm{SNR})$, source counts of the form $N(>s) \sim \mathcal{N}_0/s^\alpha$ have been used, with $\mathcal{N}_0$ and α derived from actual maximum likelihood fits of stellar and extragalactic data over some representative parts of sky.

Earlier in this section it was mentioned that the presence of measurement errors causes a steepening of the source counts at the faint end. To demonstrate this effect we have used a Gaussian noise model with the variance of the flux density *fractional* error given by $\sigma^2 = 1/\mathrm{SNR}^2 + (0.05)^2$; this noise model is used to generate apparent source counts from the underlying distribution given by Eq. III.D.2 (with $\alpha \sim 0.9$) for the 12 μm band. The ratio of the true source count to the apparent count is shown by the dashed curve c in Figure III.D.2. When the effects of source count inflation are taken into account, the reliability figures given by Eq. III.D.7 are modified and the results are displayed by the filled circles in Figure III.D.2. The inclusion of source count inflation results in a slight increase in the reliability estimate. We have not pursued the question of source count inflation at 60 μm due to measurement errors because, for this band at faint levels, most of the sky becomes cirrus dominated within a beam. The result of this modeling for the 60 μm band (without any source count inflation factors) is seen in Figure III.D.3. It is observed that below SNR $\sim$ 10, the use of Gaussian statistics will lead to a grossly optimistic estimate for reliability.

D.3.a 12 μm

Because the source surface density $\mathcal{N}_0$ appearing in Eq. III.D.2 plays a significant role in the formalism, areas of sky with different underlying source densities should be treated separately. Due to the increase in source density at the galactic plane, we have binned the galactic latitude $|b|$ into the bands 10°–20°, 20°–30°, 30°–50°, and > 50°. Furthermore, for the transformation in Eq. III.D.3 to be meaningful we have binned the thresholding noise into the narrow ranges of < 16 mJy, 16–22 mJy, 22–28 mJy, 28–32 mJy, and 32–36 mJy. At any part of sky where the noise exceeds 36 mJy, we refrained from computing reliability and assigned a reliability value of 0 to a detection regardless of its SNR. (The regions where noise exceeds the threshold are in Orion and Ophiuchus, the large holes in Figure I.A.3.) It is emphasized that a reliability value of zero does *not* imply that the source is declared to be definitely false - the value zero is only a flag indicating lack of information. In such instances the flux quality flag has been set to the moderate quality value. Other than $|b|$ and noise, significant parameters affecting R at 12 μm are the SNR and the number of

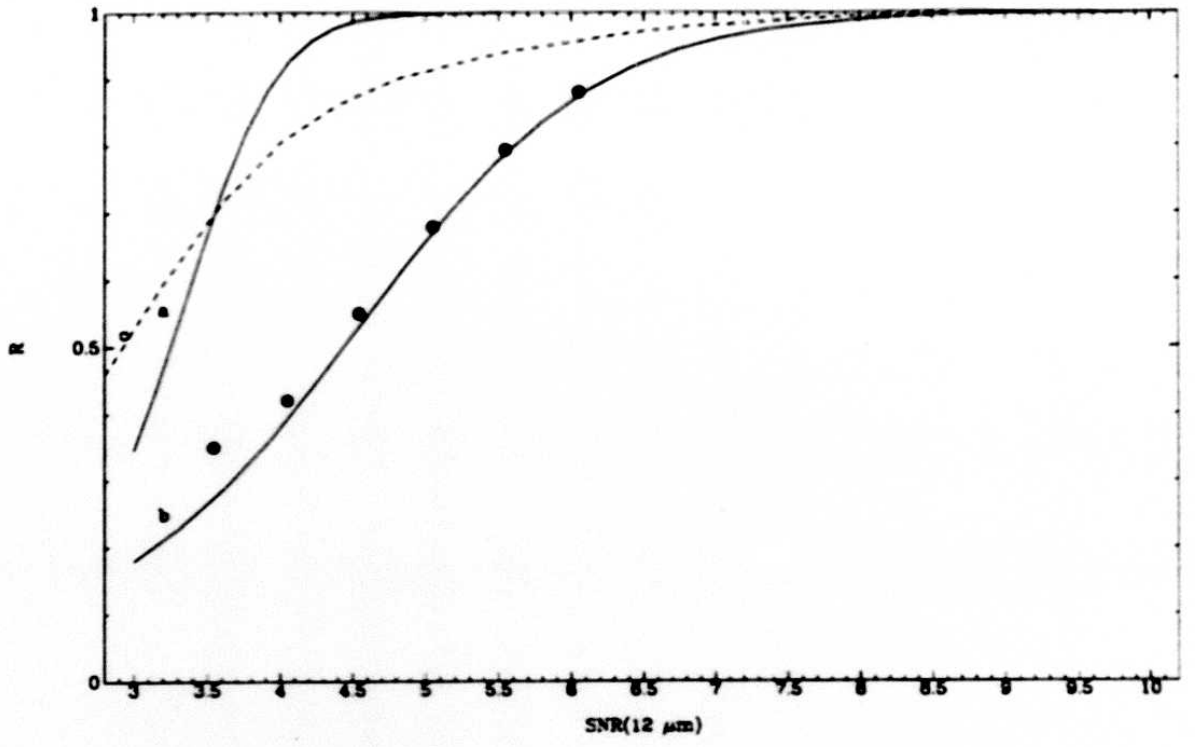

Figure III.D.2 Comparison of reliability at 12 μm for a) Gaussian noise, b) non-Gaussian modeling of noise. This plot assumes a noise of 30 mJy, a density of 150 beams/square degree, a NOISRAT of 1.55, and a surface density of $N(> s\ (Jy)) \sim .5 / (s/.5)^{.9}$ sources/square degree, applicable to high galactic latitude sky. The dashed curve c shows the ratio of underlying source count to the apparent source count in the presence of measurement errors. The solid circles are the reliability estimates, corrected for the source count inflation effect.

points coadded (this latter parameter has already been factored in through the binning in noise; consult Eq. III.A.2). No sources are allowed to enter the catalog if the coverage in the peak-flux pixel is less than 6 counts. To discriminate against bright moving sources we also put a constraint on the per-pixel SNR (local SNR) of the source by demanding this ratio to be greater than 3.5.

For each entry in this two-dimensional table of $|b|$ and noise, maximum likelihood estimates for the parameters of expected source counts are derived*.

* The likelihood function is

$$\mathcal{L} = \prod_{i=1}^{J} P_{m_i}(\lambda_i)$$

226

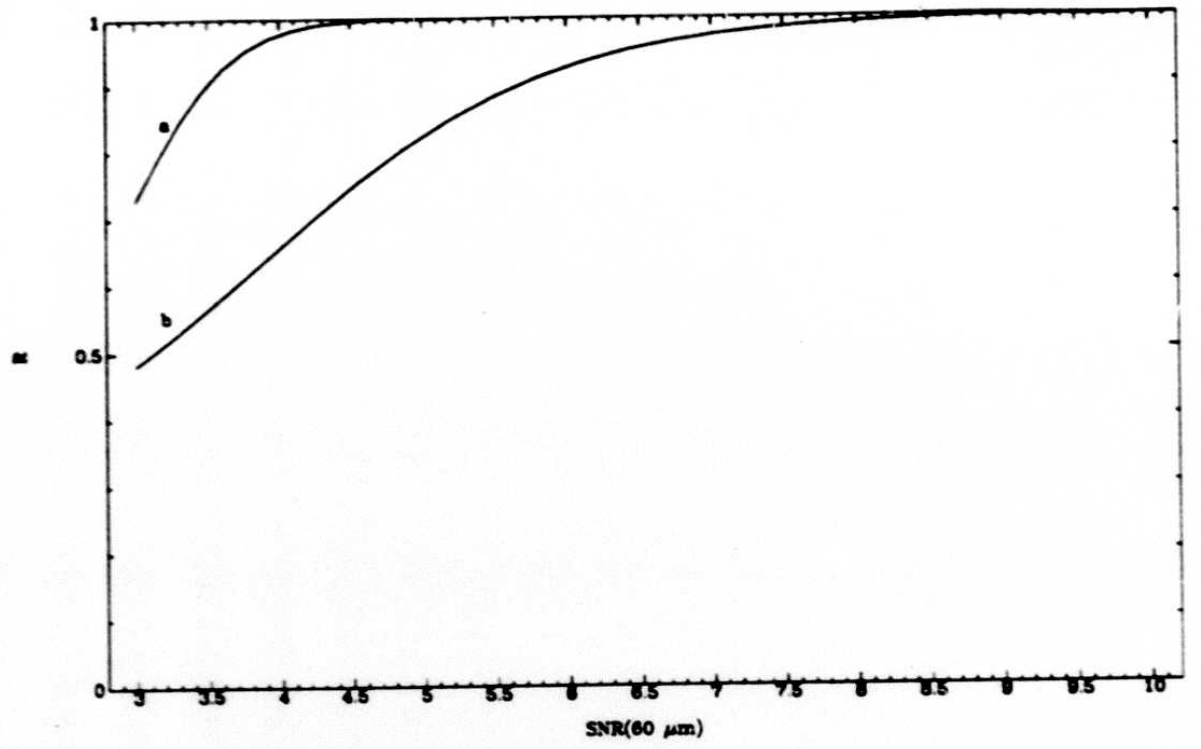

Figure III.D.3 Comparison of reliability at 60 μm for a) Gaussian noise, b) non-Gaussian modeling of noise. This plot assumes a noise of 42 mJy, a density of 100 beams/square degree, a NOISRAT of 1.6, and a surface density of N(> s (Jy)) $\sim$ .6 / (s/.5)$^{1.5}$ sources/square degree, applicable to some moderately cirrus-free high galactic latitude sky.

---

where $P_{m_i}(\lambda_i)$ is the probability of observing m_i counts in the i^{th} bin when the expected value for that bin is λ_i, namely

$$P_{m_i} = \frac{\lambda_i^{m_i}}{m_i!} e^{-\lambda_i}$$

The differential source counts are taken to follow a power law $dN(s)/ds = K/s^{\alpha+1}$, the *expected* number within a given bin $[s - \Delta, s + \Delta]$ is therefore

$$\Delta N = \int_{s-\Delta}^{s+\Delta} \frac{K}{s^{\alpha+1}} ds$$

The parameters K and α are to be determined from

$$\frac{\partial \ln \mathcal{L}}{\partial \alpha} = 0 , \quad \frac{\partial \ln \mathcal{L}}{\partial K} = 0$$

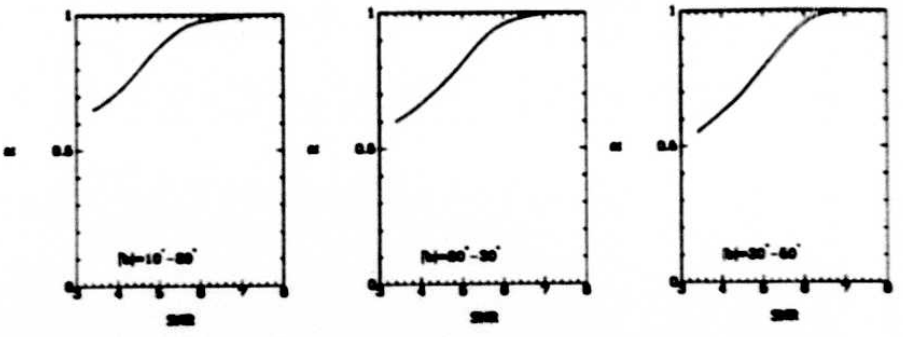

Figure III.D.4 Reliability from source counts at 12 μm for areas of sky where noise is less than 16 mJy.

Once the *expected* numbers are determined a reliability figure is computed. It is emphasized that in this method *no assumptions or modeling of noise* are used, the reliability is derived strictly on the basis of the contents of the FSDB.

Every entry in the $|b|$ and noise table yields a table of reliabilities as a function of SNR. At 12 μm this corresponds to *eighteen* distinct tables. To conserve space, the tables have been rendered in graphical form. Figures III.D.4 – 8 display reliability as a function of SNR for each noise range as a function of galactic latitude band.

Due to the interplay of ambient source surface density and effects of non-Gaussian noise, it is not easy to give specific patterns to the behavior of reliability. At high galactic latitudes it is seen that at a *fixed* low SNR the reliability increases as the noise goes down (reduction in noise being due to an increase in coverage, Eq. III.A.2). For two reasons the reliability at a given SNR rises as the number of coadded points is increased. First, as coverage gets deeper the thresholding noise is lowered (see Eq. III.A.2) and consequently source density increases. Second, the probability distribution for false sources (Eq. III.D.4) should become more Gaussian as coverage is increased (Central Limit Theorem). It is also observed that for a *fixed* noise range, the reliability at a given SNR increases as the galactic latitude is lowered, due to the actual physical increase in the source surface density.

For every 12 μm detection in the FSDB with $|b| \geq 10°$ and thresholding noise less than 36 mJy, a value for source reliability has been computed. For all other 12 μm detections, the value of reliability has been set to zero. It is emphasized once more that a value of zero for reliability is a flag indicating lack of sufficient information for assigning reliability, and *not* a statement of our lack of confidence in its reality. We selected a threshold of R=90% as the requirement for inclusion in the FSC, in addition to the extraction requirement that

230

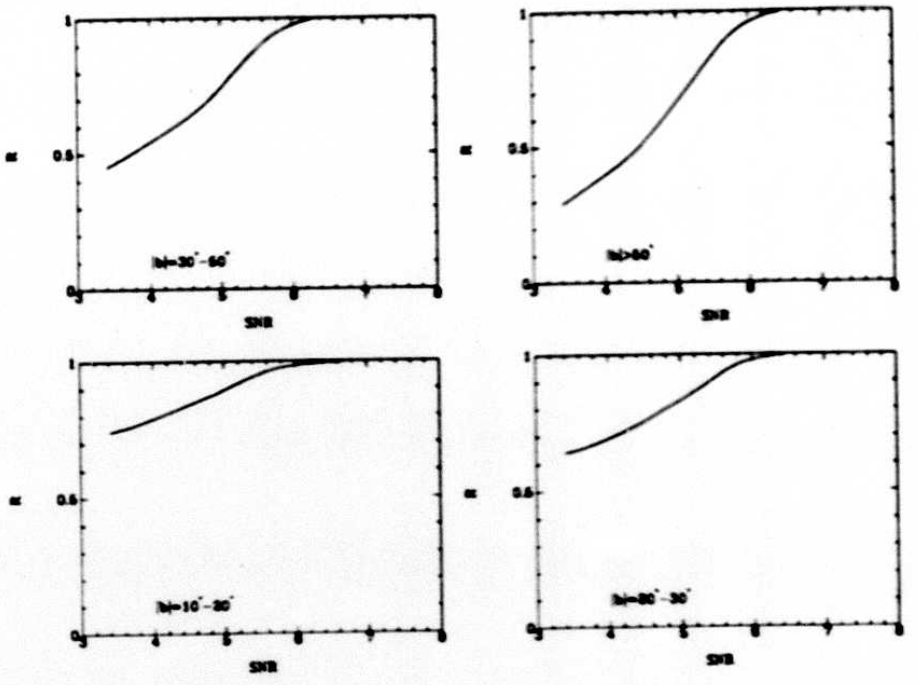

Figure III.D.5 Reliability from source counts at 12 μm for areas of sky where noise is within 16 – 22 mJy.

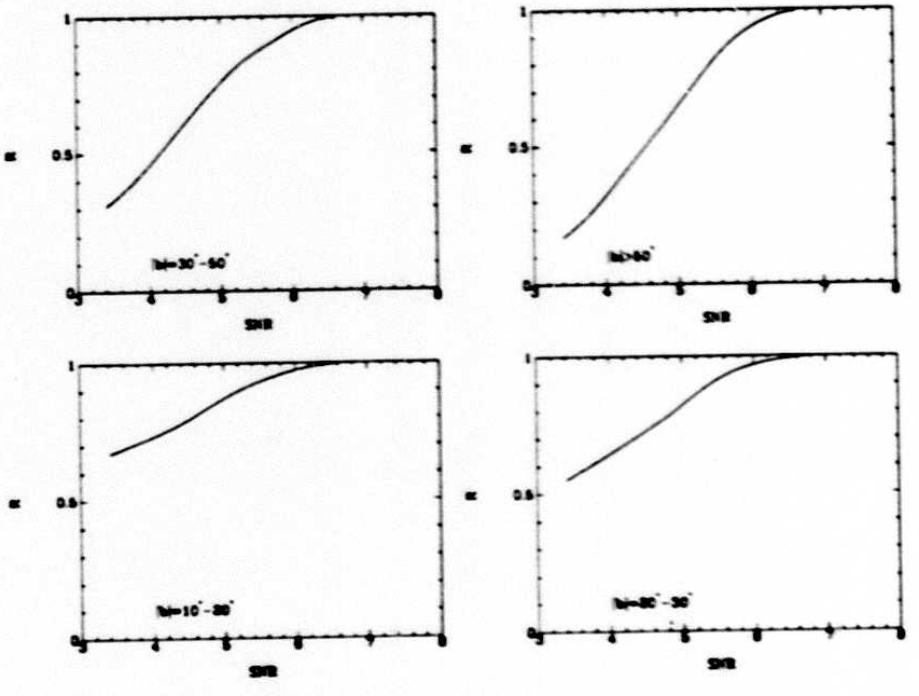

Figure III.D.6 Reliability from source counts at 12 μm for areas of sky where noise is within 22 – 28 mJy.

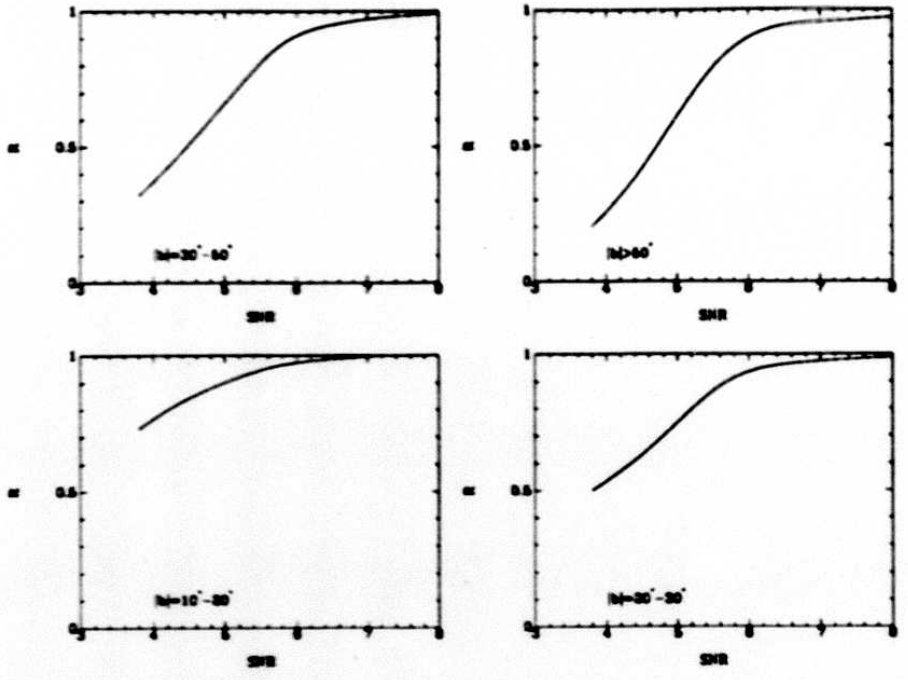

Figure III.D.7 Reliability from source counts at 12 μm for areas of sky where noise is within 28 – 32 mJy.

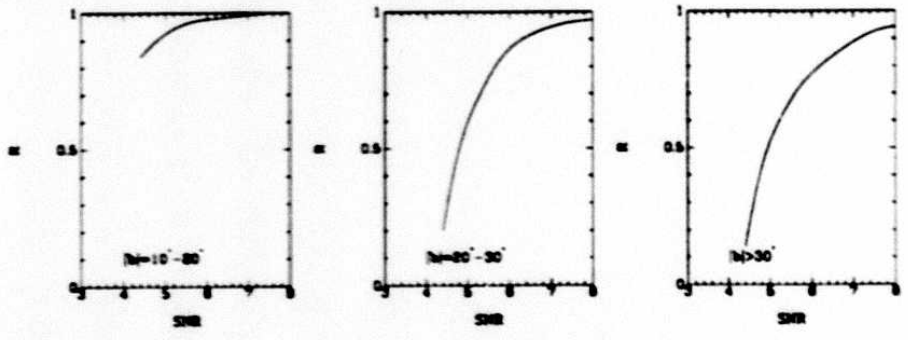

Figure III.D.8 Reliability from source counts at 12 μm for areas of sky where noise is within 32 – 36 mJy.

the peak-flux pixel have at least 6 data points, and the per pixel SNR at the peak-flux pixel should exceed 3.5.

D.3.b 25 μm

The behavior of reliability at 25 μm is similar to that at 12 μm. To discriminate against bright moving objects we put a constraint on the per-pixel SNR of the source to be greater than 4.5. We have grouped the galactic latitude $|b|$ into bands 10°– 20°, 20°– 30°,

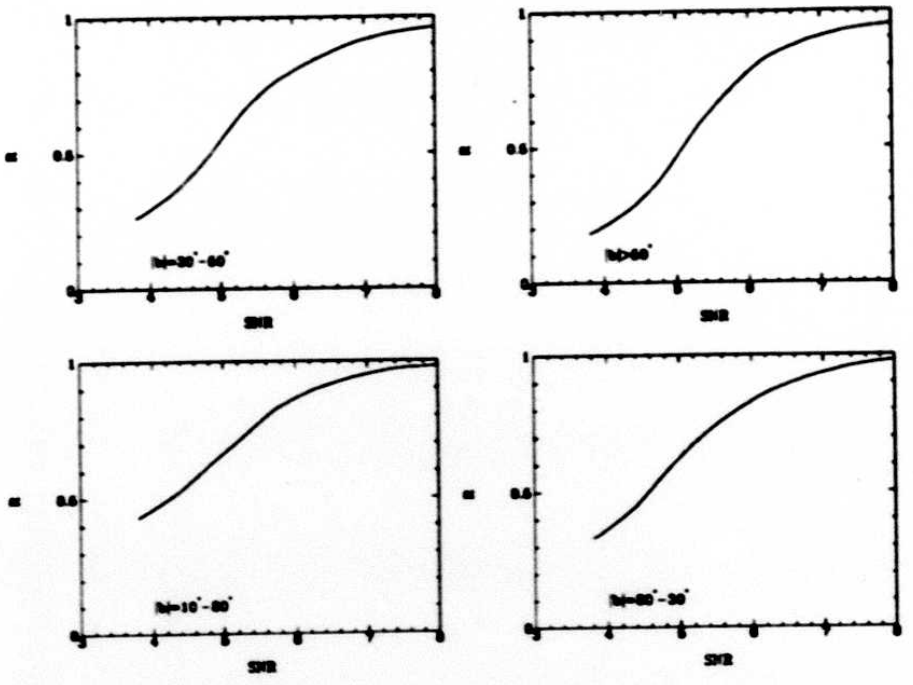

Figure III.D.9 Reliability from source counts at 25 μm for areas of sky where noise is less than 18 mJy.

30° – 50°, and > 50°. The thresholding noise has been binned into the ranges of < 18 mJy, 18 – 28 mJy, 28 – 38 mJy, 38 – 48 mJy, and 48 – 65 mJy. At any point where the noise exceeded 65 mJy, we did not compute a reliability and assigned it a value of zero. Again it is noted that a zero value for source reliability implies lack of sufficient information for its computation and not lack of source reality! In such instances the flux quality flag has been set to the moderate quality value. The computation of reliability follows the same maximum likelihood method as described for the 12 μm band. For each range of $|b|$ and noise, a table of reliability as a function of SNR is derived, resulting in *twenty* different tables which we have rendered in graphical form in figures III.D.9 – 13.

For every FSDB detection at 25 μm with $|b| \geq 10°$ with a threshold noise less than 65 mJy, a value for source reliability has been computed. All other 25 μm detections in the FSDB have been assigned a value of zero for their reliability. Note again that a zero value for R is only a flag denoting lack of sufficient information for its computation, and not a statement on lack of reality. We picked a threshold of R=90% as the requirement for inclusion in the FSC (subject to the extra constraint of peak-flux pixel receiving 6 or more data points, and the per pixel SNR at the peak-flux pixel exceeding 4.5).

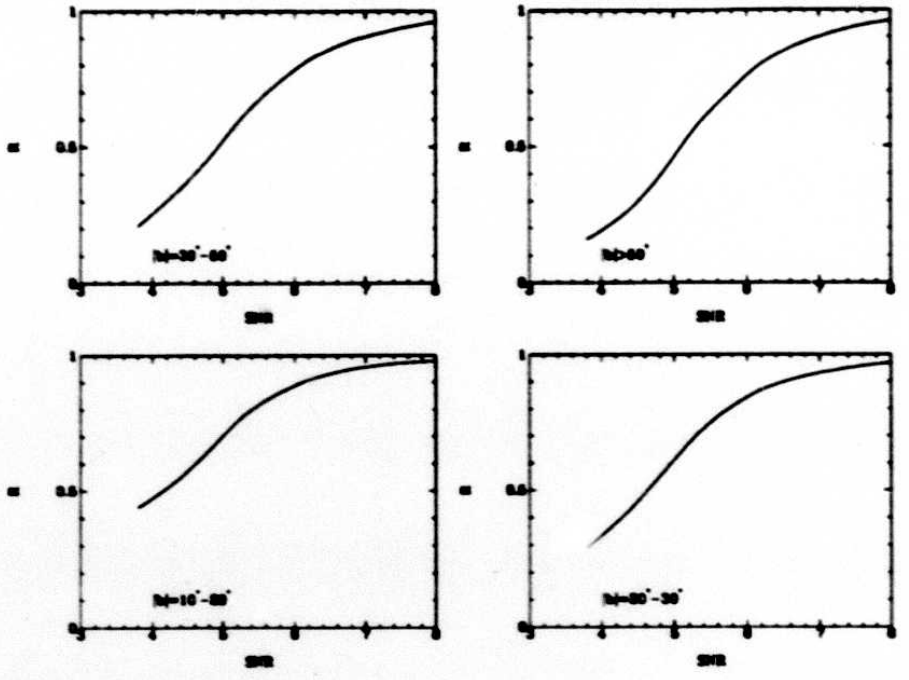

Figure III.D.10 Reliability from source counts at 25 μm for areas of sky where noise is within 18 – 28 mJy.

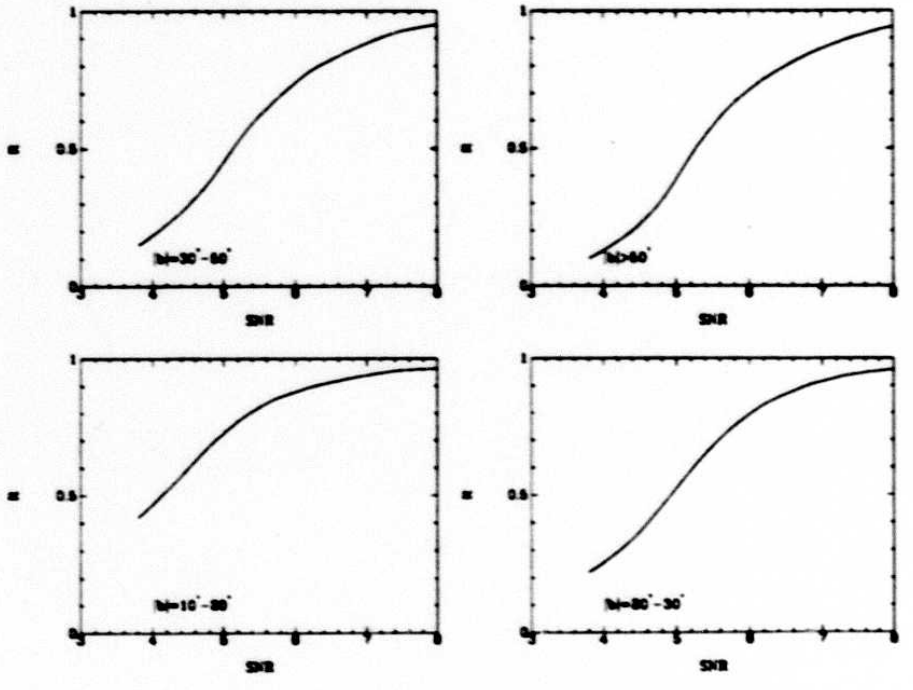

Figure III.D.11 Reliability from source counts at 25 μm for areas of sky where noise is within 28 – 38 mJy.

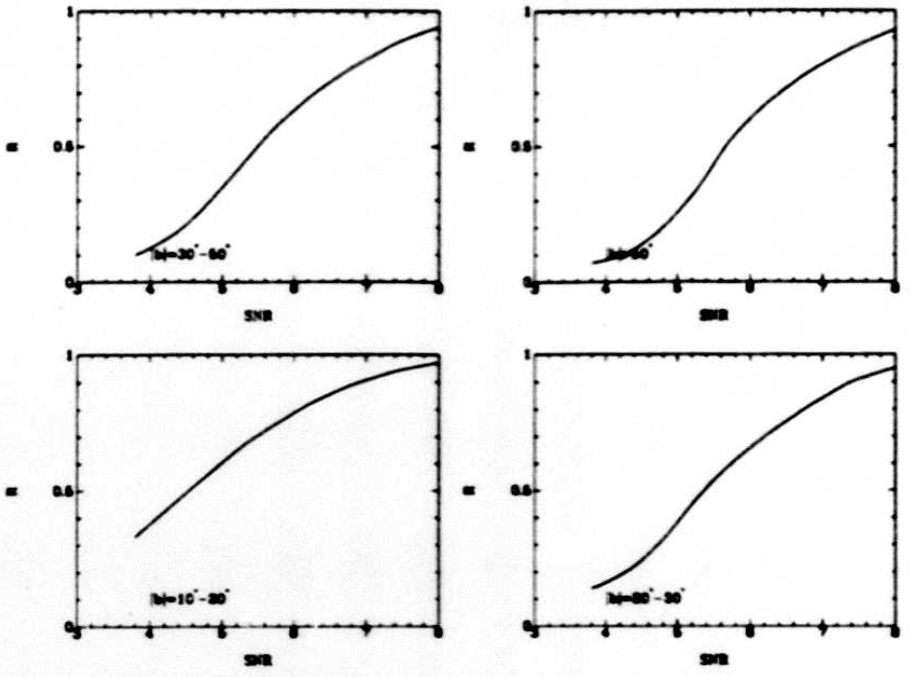

Figure III.D.12 Reliability from source counts at 25 μm for areas of sky where noise is within 38 – 48 mJy.

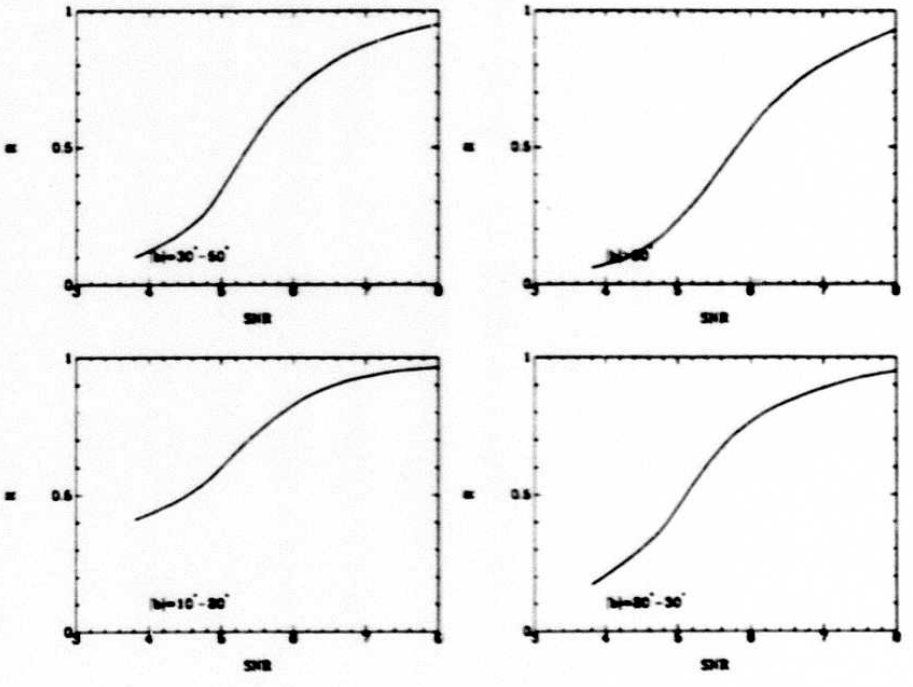

Figure III.D.13 Reliability from source counts at 25 μm for areas of sky where noise is within 48 – 65 mJy.

D 10015

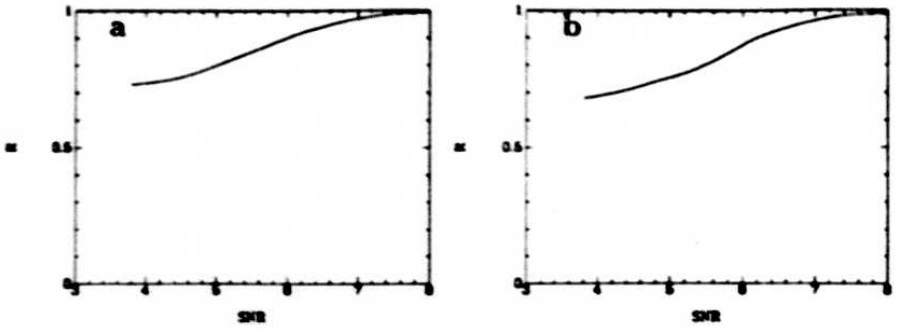

Figure III.D.14 Reliability from source counts at 60 μm for areas of sky where noise is within 30 – 38 mJy. a) NOISRAT < 1.6, b) NOISRAT = 1.6–1.66.

D.3.c 60 μm

At 60 μm the extragalactic sources which constitute the majority of observed sources are arranged in groups and clusters all over the sky, with no simple demarcation coordinates. Thus the control parameters have been chosen to be the threshold noise and the degree of cirrus contamination, as measured by NOISRAT (see Section III.A.1). (The stellar contribution to the 60 μm source population which shows a dependence on galactic latitude is small and thus not considered for this argument.) We therefore did not use the source surface density as one of our control parameters (this point will be addressed later in this section).

The noise has been grouped into the ranges 30 - 38 mJy, 38 - 44 mJy, and 44 - 60 mJy. The NOISRAT is binned into the ranges < 1.6, 1.6 - 1.66, and 1.66 - 1.72. We furthermore confined our attention to the $|b| \geq 20°$ sky. In addition, at any point where either the noise exceeded 60 mJy or the NOISRAT exceeded 1.72, no value for reliability was computed and R was set to zero. Finally the maximum likelihood method described earlier was employed to compute reliability. For each range of noise and NOISRAT a table of reliability as a function of SNR is derived, resulting in *eight* distinct tables shown graphically in Figures III.D.14 - 16.

Every 60 μm detection in the FSDB with $|b| \geq 20°$, with a threshold noise less than 60 mJy and NOISRAT less than 1.72 has been assigned a reliability figure. Any other 60 μm detection has been assigned a reliability of zero. It is noted that a value of zero for R is only a flag which indicates lack of sufficient information for computation of R, and definitely not an indication that the source is false. A threshold of R=80% was picked as the requirement for inclusion in the FSC (subject to the further constraint that the peak-flux pixel should have at least 6 data points and that the per pixel SNR at the peak-flux pixel should exceed 3.5).

237

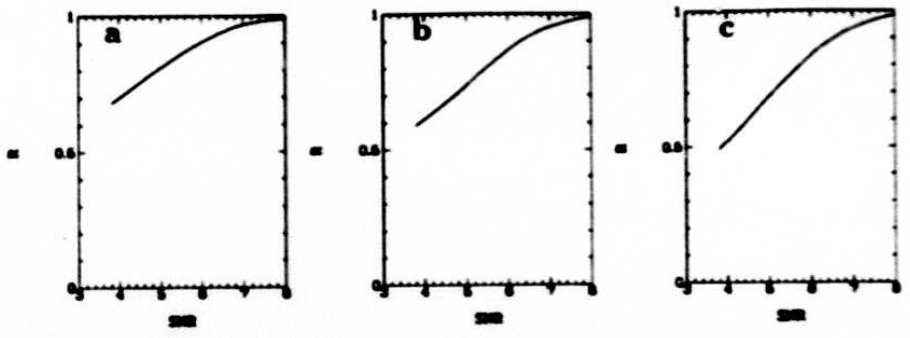

Figure III.D.15 Reliability from source counts at 60 μm for areas of sky where noise is within 38 – 44 mJy. a) NOISRAT < 1.6, b) NOISRAT = 1.6–1.66, c) NOISRAT = 1.66–1.72.

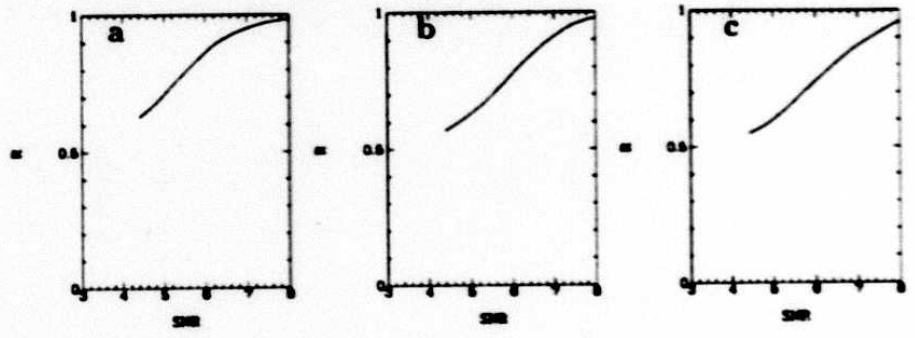

Figure III.D.16 Reliability from source counts at 60 μm for areas of sky where noise is within 44 – 60 mJy. a) NOISRAT < 1.6, b) NOISRAT = 1.6–1.66, c) NOISRAT = 1.66–1.72.

Use of the source counts method at 60 μm must be treated with caution. Differences between stellar and extragalactic statistics should be taken into account. Stars observed at 12 and 25 μm are smoothly distributed in the sky. Galaxies observed at 60 and 100 μm cluster on angular scales of many degrees which causes variations in the slope of source counts and in surface density. The surface density of extragalactic sources from the FSS at 60 μm shows appreciable variation across the sky on scales of larger than roughly 10° as indicated in Figure III.D.17 (Moshir 1989), including a distinct difference between the north and south galactic caps (Rowan-Robinson *et.al.* 1986, Lonsdale *et.al.* 1990). This variation in surface density has *not* been included in our estimation of 60 μm reliability figures.

It can be shown that approximately (if variations in functional form in Eq. III.D.4 are ignored) the *local* reliability, $\mathcal{R}$, is related to the average reliability R (the 60 μm

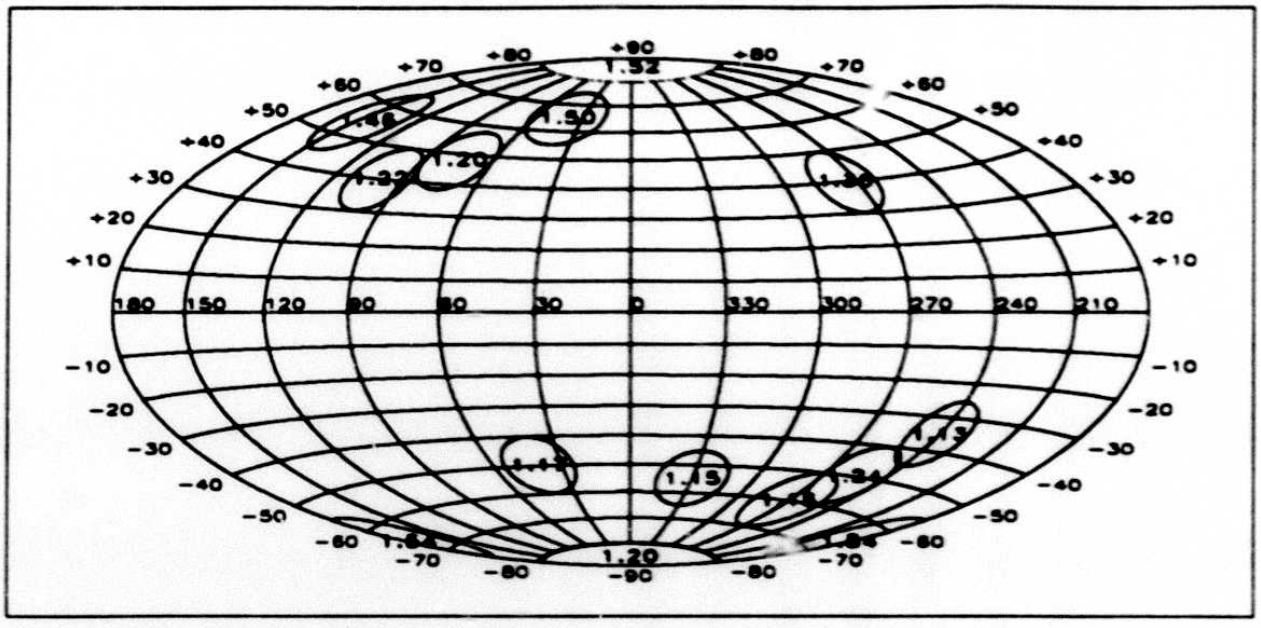

Figure III.D.17 Surface density of 60 μm extragalactic sources per square degree at 300 mJy for selected areas of sky (each region having $\Omega \sim 300$ deg^2), coordinate system is galactic.

reliability) as follows:

$$\mathcal{R} = \frac{r\,R}{1 + (r-1)\,R} \qquad (III.D.8)$$

where r denotes the ratio of local source surface density to the average source surface density for $|b| \gtrsim 20°$.

The ratio r depends on the definition of *local*. For example, in the direction of the Virgo Cluster, if local is taken as the core of the cluster (angular scale of $\sim 5°$), then $r \sim 1.9$, whereas if local is taken as an angular extent of $\sim 20°$, then $r \sim 1.3$. Using Eq. III.D.8 within the core of the Virgo Cluster, the lowest reliability of sources in the FSC would be 88% and not 80%. Figure III.D.17 may be used similarly to derive expected local reliability for the regions displayed.

Our imaging and spectroscopic follow-up of many 60 μm sources selected from the FSDB have so far indicated that in areas of sky where cirrus contamination is at a minimum, the reliabilities of 60 μm detections are at least as good as Figures III.D.14 - 16 report, and *in many instances even higher than the curves would indicate*. Since these follow-up programs are still in progress, the detailed results will appear elsewhere at later dates.

The decision to confine the FSC coverage to the $|b| \geq 20°$ sky can be justified by

D 10015

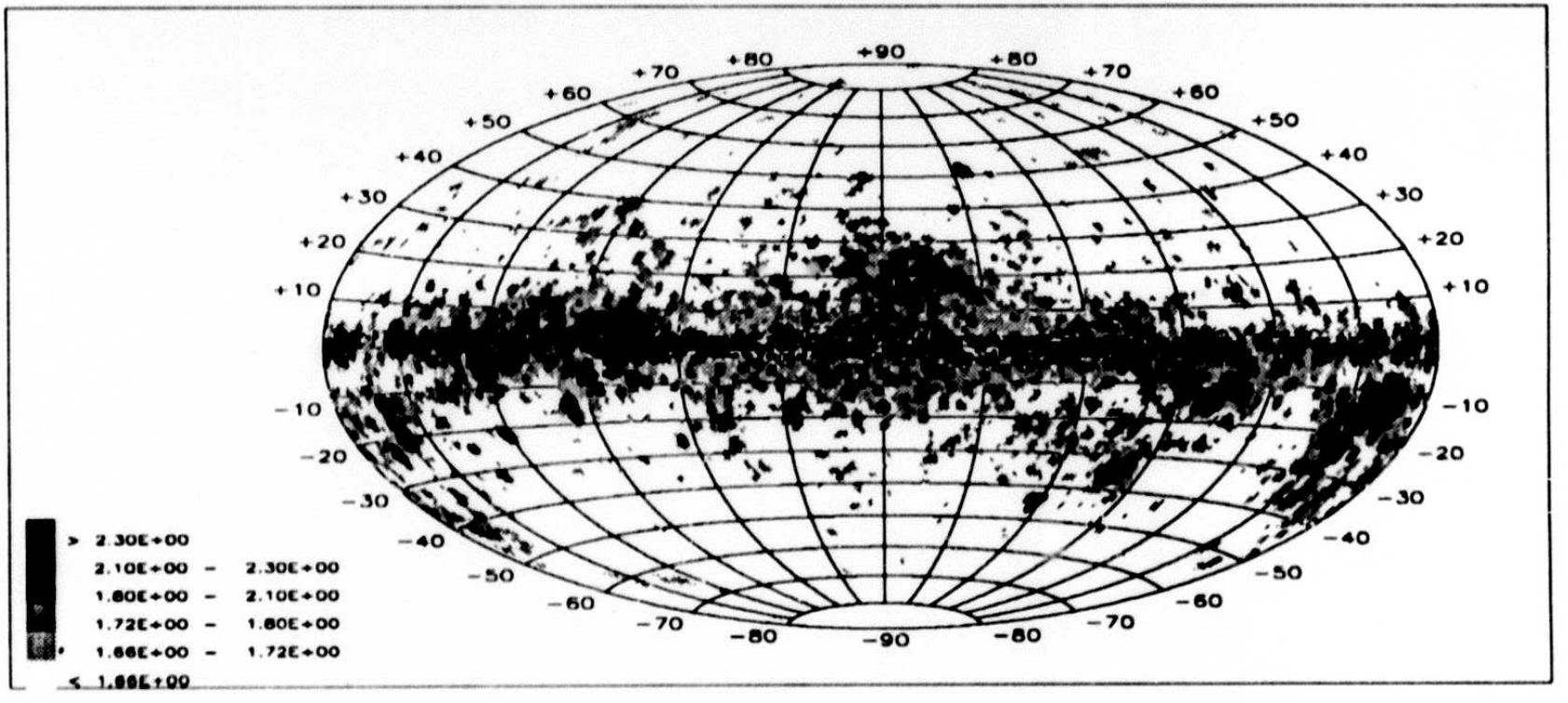

Figure III.D.18 Spatial distribution of the NOISRAT at 60 μm, in galactic coordinates. Areas with $|b| \geq 20°$ where NOISRAT exceeded 1.72 were not considered for entry into the FSC. The blank regions in the galactic plane occur when there are no 60 μm detections.

observing Figure III.D.18. This is a map of NOISRAT at 60 μm (R has been computed only for areas where NOISRAT is below 1.72 and noise is less than 60 mJy). This map shows that if we had selected a galactic latitude cut-off of $|b| \geq 30°$ we would have had a clean latitude cut-off with only the LMC and the SMC being excluded. However, in the interest of having a higher, although patchy, coverage we chose a latitude of 20°. This map shows that in certain parts of sky it is possible to penetrate to as low a latitude as 5° and still have some 'clean' windows. The users of the *reject* file may wish to pursue their search of extragalactic sources through the clean areas in Figure III.D.17. Section III.G.7 treats the issue of infrared cirrus in more detail.

D.3.d 100 μm

It was indicated in Section III.D.1 that at 100 μm we decided against performing any reliability computation. This was mainly due to the deleterious effects of the infrared cirrus. Only small regions at high galactic latitudes can be considered *relatively* cirrus-free, for example see the lightly shaded areas in Figure III.C.15. Consequently *every* 100 μm detection in the FSDB has been assigned an R value of zero, bearing in mind that the value zero is a flag indicating lack of sufficient information and not a statement on source falsehood. Although we have not computed a value for R, in the course of our analysis it was determined that for areas with $|b| > 70°$ an SNR >7 would normally yield a reliability of better than 90%. In the latitude band $|b|$=50°- 70°, it was found that selecting an SNR > 9 would generally yield a reliability of 90% or better. Users of the *reject* file may wish to use these thresholds for selection of 100 μm-only sources.

D.4 Estimates from Optical Counterpart Identification

Because of the uncertainties and problems involved in the source count analysis, we have also used optical counterpart identifications. Basically, a very high fraction of all *IRAS* sources have counterparts present on the optical sky survey photographs. Although the counterpart checking is tedious and therefore cannot be done for all sources in the catalog, by sampling different SNR ranges, we can confirm the conclusions reached by source count analysis.

To derive a reliability estimate, we correct the optical counterpart rate at any SNR by dividing by the optical counterpart rate at high SNRs. Again, this estimate gives a minimum reliability because, for various reasons, more of the low SNR sources without optical counterparts could be real. However, in this section we assume that any increase in the percentage of sources without optical counterparts are due to false sources.

At 12 μm, it is possible to check nearly every source in the high galactic latitude sky

Table III.D.1 Reliability Estimates from Optical Counterpart Identification at 60 μm

SNR	R(%)
6.0	85 ±4
8.5	93 ±3

because nearly 80% of all 12 μm FSC sources have *cataloged* optical counterparts. All of the remaining FSC sources within the north galactic cap ($b > 50°$) were checked on the Palomar Observatory Sky Survey (POSS) plates. The results are in general agreement with Figures III.D.5 and 6.

At 60 μm, two SNR ranges were checked on ESO/SERC and POSS plates. The sources were chosen from the SNR ranges [5.5, 6.5] and [8.0, 9.0]. Furthermore, the selection was done across the whole $|b| \geq 50°$ sky and not localized. In each range 100 sources were selected and checked for associations with other astronomical catalogs; the remainder which were unassociated were individually checked on the ESO/SERC or POSS plates as appropriate. Based on the number of extragalactic matches (taking into account the probability of random extragalactic matches which was also measured over $|b| \geq 50°$), a reliability figure for each of the two SNR ranges was computed. We stress again that this figure for R is a *minimum* reliability estimate. The result is displayed in Table III.D.1. It should be noted that this estimate agrees with the estimate based on source count analysis within the respective uncertainties.

D 100 15

E. Positional Accuracy

E.1 Introduction

The positional uncertainty of a FSS source is a strong function of the wavelength bands in which it was detected and the SNR of each of these detections. The positional uncertainty along the major axis of the positional uncertainty ellipse (this usually corresponds to the cross-scan direction) also depends on the number of samples comprising the detection. Section II.F describes the positional uncertainty estimation algorithm. In Section III.E.2 the accuracy of this estimator will be discussed.

Prior to the full production of the FSS, the focal plane model used for coaddition (see Section II.C.4) was adjusted to minimize the inter-band positional discrepancies, as well as discrepancies with respect to absolute sky standards (see Section II.C.6). This analysis was performed by comparing the mean positional discrepancies between the FSC sources and SAO stars, or galaxies with accurately measured positions (Dressel and Condon 1976) in regions of the sky where all of the satellite scans were in the same direction and nearly parallel. The resulting mean positional accuracy of the FSS is $\sim 0.3''$ in all four bands. Section III.E.3 considers the issue of overall positional bias of sources.

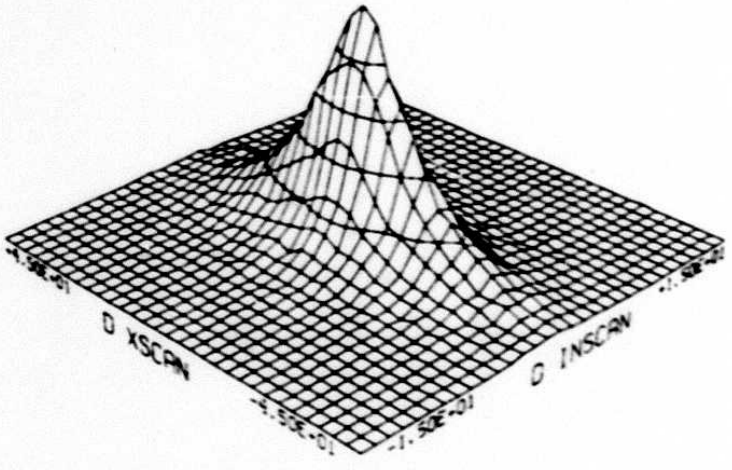

Figure III.E.1 Distribution of positional discrepancies for FSDB sources detected at 12 μm and associated to SAO stars. Units are seconds of arc.

E.2 Accuracy of Positional Uncertainties

Higher SNR sources have smaller positional uncertainties (see Section II.F.3). Distribution of positional discrepancies of FSS stellar sources relative to the SAO star catalog is very sharp; the full width at half maximum of the distribution along the minor axis is 4", and along the major axis it is 24" (see Figure III.E.1). The rms positional accuracy

243

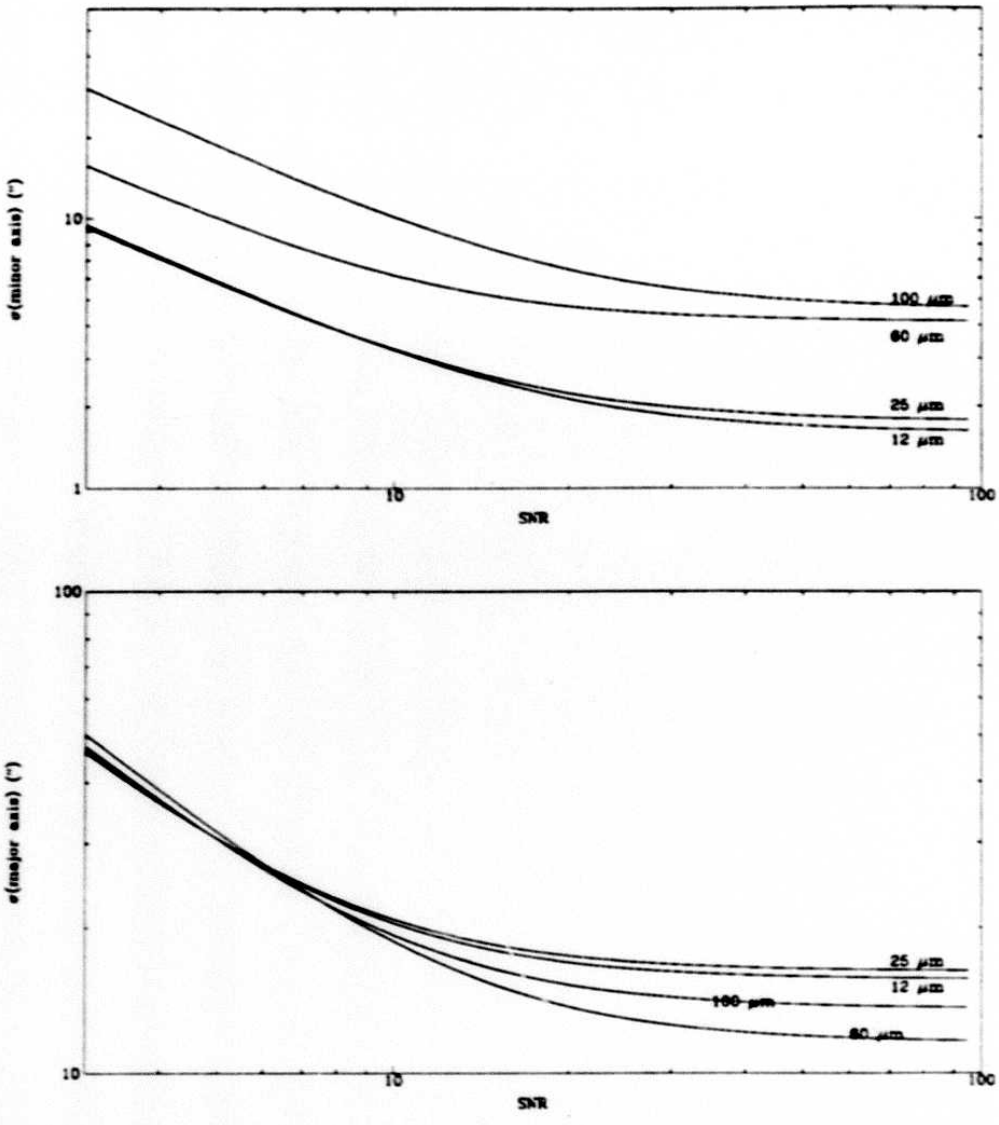

Figure III.E.2 Positional uncertainty of individual detections with 12 data counts along the minor axis (upper figure) and the major axis (lower figure) of the positional uncertainty ellipse (computed using Eqs. II.F.5 – 6, employing constants from Table II.F.2 and beam sizes from Table II.D.3, and Table II.C.2 was used to trim the counts.)

of sources at 60 μm associated with a catalog of galaxies with accurate positions (Dressel and Condon 1976) is 5″ and 16″ along the minor and major axes, respectively. The estimator for positional uncertainty of sources is derived from a phenomenological formulation discussed in Section II.F.3. Figure III.E.2 illustrates the positional uncertainty for *single-band* detections as a function of SNR for sources having received 12 data counts (which is trimmed to 10) and includes positional uncertainties of 1″ and 3″ along the minor and

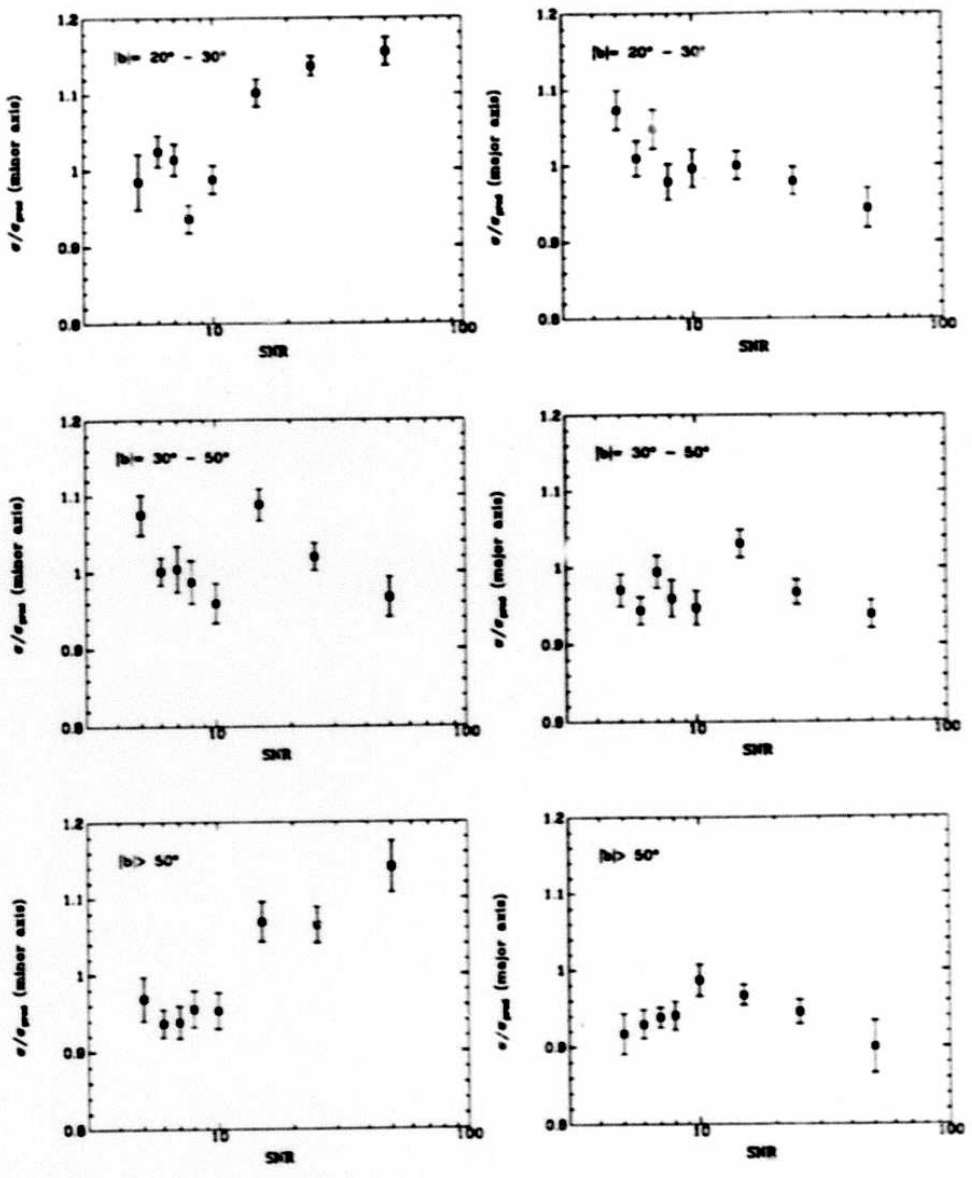

Figure III.E.3 Accuracy of the positional uncertainty estimator along the minor and major axes of the uncertainty ellipse for 12 μm sources identified with SAO stars in three galactic latitude bands.

major axes. It does not include sources detected at more than one wavelength. The figure does give representative positional accuracies for multiband sources with steep spectra (including most stars and galaxies.)

Figure III.E.3 shows the degree of accuracy of the positional error estimators for three galactic latitude bands. To prepare these figures the subset of 12 μm sources identified with stars from the SAO catalog was used. From this sample the distribution functions for positional dispersions $\hat{\Omega}_{SAO} - \hat{\Omega}_{FSS}$ were computed. ($\hat{\Omega}$ is the unit length vector pointing to

the source position.) The σs from these distributions were then compared with the quoted values from Eqs. II.F.5–6. This analysis indicates that the quoted values for positional uncertainties are accurate to within 10–15%. For an explanation of the in-scan trend with SNR also see next section regarding the residual in-scan positional bias at high SNR.

E.3 Positional Biases

Prior to the full FSS production the timing offsets necessary to remove positional biases were obtained by performing a comparison of FSS sources with SAO stars and galaxies with accurate positions for a sample of 13 FSS plates (see Section II.C.6). This process removed the gross biases due to commutation delay and on-board electronics. However since the FSS positions are derived from the ***flux weighted*** centroid positions of each constituent band, it is expected that for ***bright*** sources the asymmetry in point source profiles due to detector hysteresis (point source profiles show a slight, slowly decaying tail following the passage of a source across detectors, see Figures V.C.2.a–d of the ***Main Supplement***) would manifest itself in the form of a slight positional bias. The bias would be most pronounced when all scans are in the same direction and also parallel to each other. In cases where scans are at widely varying angles or involve opposing scan directions the effects of bright point source profile asymmetry would be washed out. The median of the $\hat{\Omega}_{SAO} - \hat{\Omega}_{FSS}$ distribution along the minor axis of the uncertainty ellipse has been computed on regions of size $\sim 6^\circ \times 6^\circ$ for sources having SNRs between 15 and 50. An Aitoff map of the result in ecliptic coordinates, for regions which had at least 5 SAO stars, can be seen in Figure III.E.4. The distribution of median values on these $6^\circ \times 6^\circ$ regions has a σ of $\sim 0.6''$, and the distribution itself can be seen in Figure III.E.5. In order to observe the behavior of the bias on finer SNR scales, the in-scan position bias has been computed as a function of SNR for several regions of sky. The results for an area defined by $35^\circ < \lambda < 59^\circ$ and $|\beta| < 60^\circ$ can be seen in Figure III.E.6, this part of sky was covered by three sets of ***ascending*** scans. Since the scans are all in the same direction the bias for the brighter end of the sample is clearly recognizable. Figure III.E.7 displays the variation of bias as a function of SNR for an area defined by $157^\circ < \lambda < 212^\circ$ and $|\beta| < 60^\circ$, this part of sky was covered by two sets of ***descending*** scans, and in this case the bias at the bright end has a value opposite in sign to the ascending set, as expected. It is noted that in both regions shown, for SNRs less than ~10 the position bias disappears, thus for the ***majority*** of FSS sources (which have low as opposed to high SNRs) the positional bias can be taken as zero within the observational uncertainties.

246

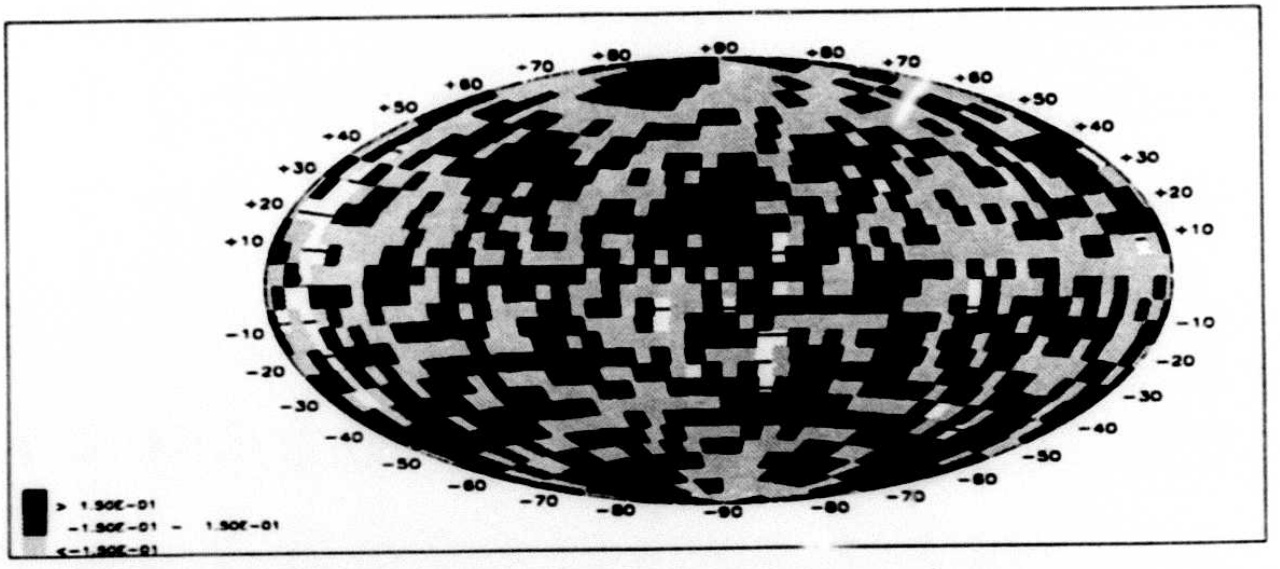

Figure III.E.4 Median positional bias along the minor axis of the uncertainty ellipse computed on regions $\sim 6° \times 6°$ in size, for 12 μm sources with SNR between 15 and 50 and identified with SAO stars. The Aitoff projection is in ecliptic coordinates. Only regions having at least 5 SAO stars have been plotted. Units are seconds of arc.

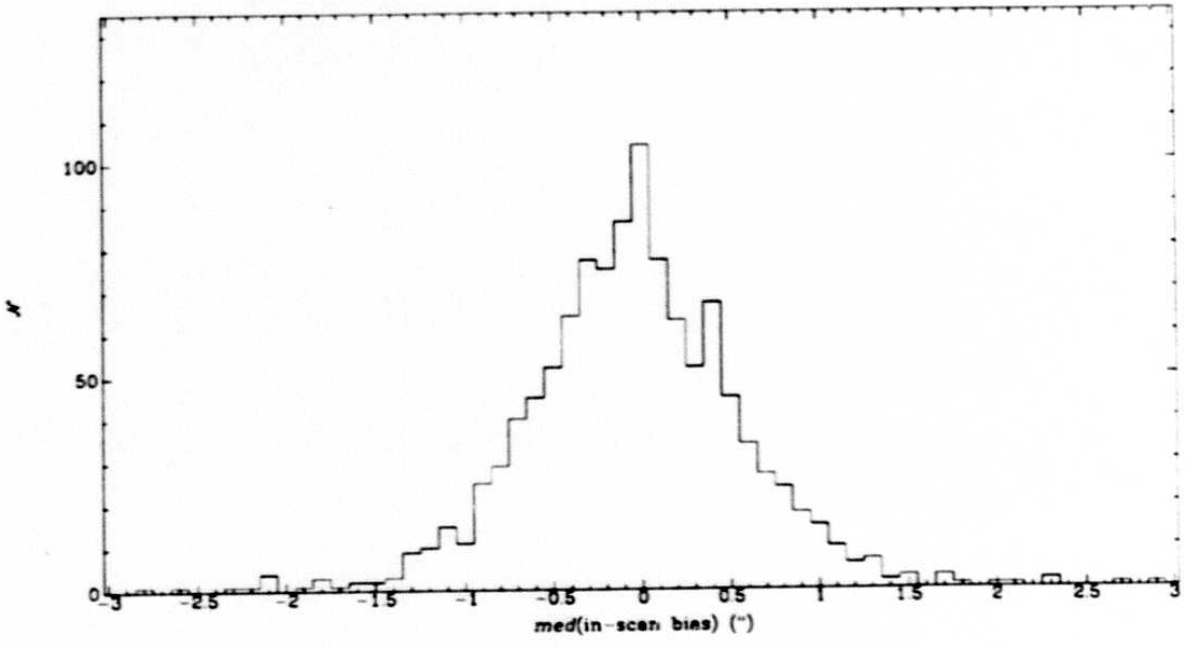

Figure III.E.5 Distribution of median positional biases along the minor axis of the uncertainty ellipse (data from Figure III.E.4), $\mathcal{N}$ denotes the number of *regions* having a given value. This distribution has a σ of $\sim$0.6".

247

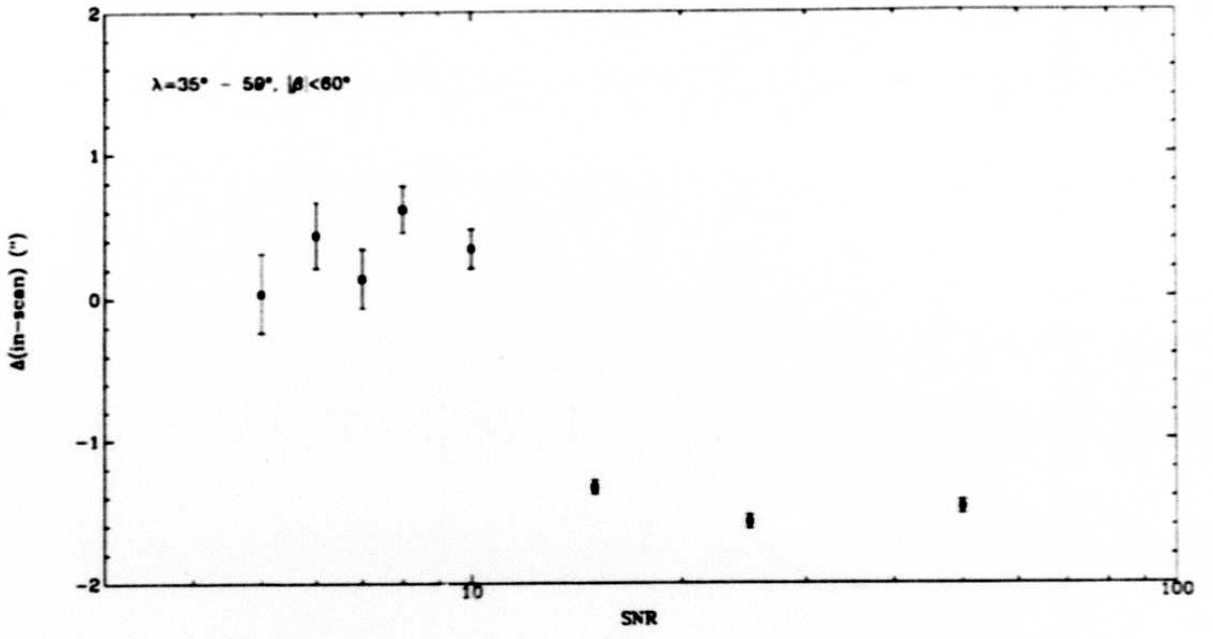

Figure III.E.6 Median positional bias along the minor axis of the uncertainty ellipse as a function of SNR, the region of sky used for this figure was covered by three sets of ascending scans.

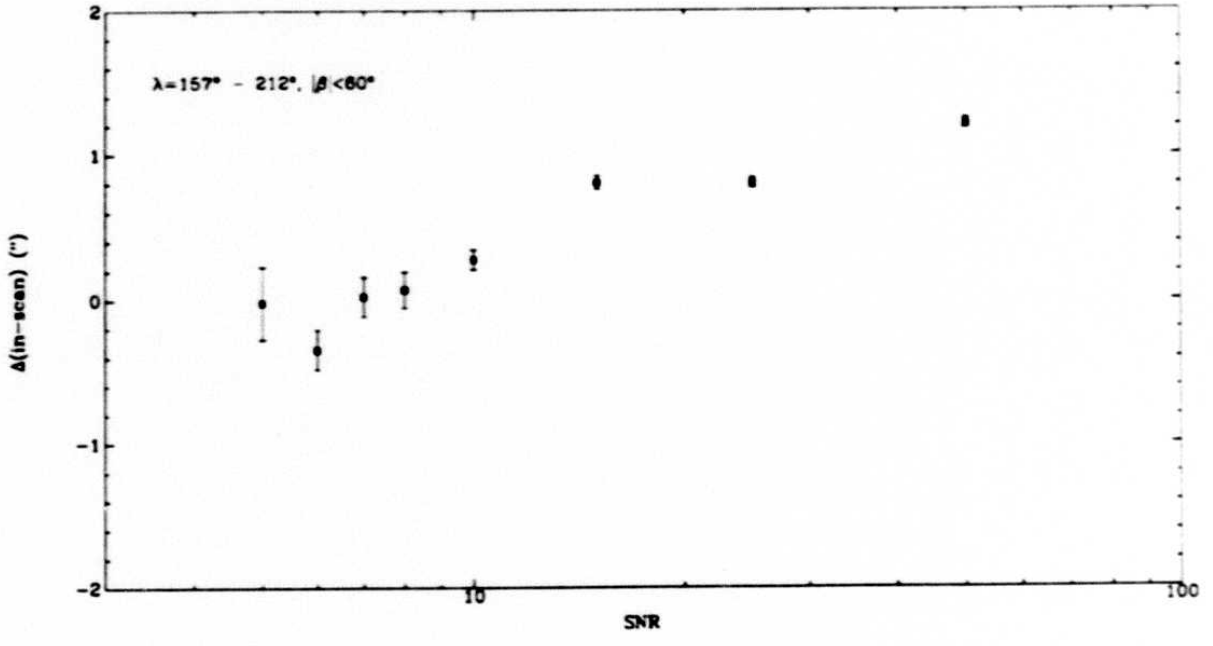

Figure III.E.7 Median positional bias along the minor axis of the uncertainty ellipse as a function of SNR, the region of sky used for this figure was covered by two sets of descending scans.

F. Calibration and Photometric Accuracy

F.1 FSS Calibration

The photometric calibration of the FSS is tied directly to the absolute calibration of the PSC described in detail in the *Main Supplement*. The FSS calibration was accomplished by intercomparing the measured flux-densities of 5,771 detections (for $|b| > 50°$) contained in both the PSC and the FSDB. As described below, this calibration was tested for the entire sky by separately intercomparing the PSC and "calibrated-FSDB" flux densities of associated sources located within broad galactic latitude bands covering the sky. Sections III.F.1 and III.F.2 are devoted to this issue. Section III.F.3 treats the effects of binning (during the coaddition process) on flux density errors.

After the FSS photometric calibration had been tied to the absolute calibration of the PSC, a comparison was made between the flux density scale of the FSS and the *Serendipitous Survey Catalog* (SSC) at 12 and 60 μm. This comparison showed that the FSS and the SSC were on a consistent flux density scale at 12 μm. However, at 60 μm it was found that the SSC consistently quoted *higher* flux density values than the FSS. It is our belief that the FSS flux densities are accurately tied to the absolute calibration of the PSC. We have not pursued the causes of this discrepancy between the SSC and PSC/FSC. More details may be found in Section III.F.4.

F.1.a $|b| > 50°$ Calibration

The $|b| > 50°$ PSC-FSDB associated sources used for calibration were restricted to those with PSC flux densities which fell within a limited flux-density range: 1–30 Jy at 12, 25, and 60 μm and 3–30 Jy at 100 μm. This was done to exclude (1) faint detections near the PSC threshold affected by the PSC "flux-density over-estimation" and (2) bright detections most affected by the background dependent, nonlinear response of the feedback resistors (as described in Section XII.A.1 and Sections II.C.5 and VI.A.5, respectively, of the *Main Supplement*). For the detections within these flux-density ranges a scale factor between the FSDB and PSC at each wavelength was computed as the mean of the f_ν(FSDB)/f_ν(PSC) ratios, with each ratio weighted by f_ν(FSDB). The flux-density weighting gave nearly equal weight to the relatively small number of bright sources and the larger number of faint sources in the flux-density limited ranges. The scale factors were used as a first adjustment to the FSDB, forcing the mean ratios to unity. The adjusted FSDB measurements were then corrected for the nonlinear feedback resistors response. The mean f_ν(FSDB)/f_ν(PSC) ratios were recomputed after applying two additional constraints. First, detections with FSDB-to-PSC flux-density ratios out-

D 10015

TABLE III.F.1 Associated PSC-FSDB Detections for $|b| > 50°$ Within the Calibration Window

Wavelength (μm)	f_ν(FSDB)/f_ν(PSC) Number	Population σ
12	2115	0.045
25	772	0.048
60	1882	0.060
100	1002	0.053

side the range $0.75 < f_\nu(\text{FSDB})/f_\nu(\text{PSC}) < 1.25$ were excluded. These discrepant measurements amounted to less than 3% of the total detections in any one of the latitude bands. Second, suspected "cirrus" sources were eliminated by excluding 100 μm-only FSDB sources and FSDB sources with $f_\nu(60)/f_\nu(100) < 0.25$ and $f_\nu(60) > f_\nu(12)$ (i.e. cold, non-stellar sources). Hereafter, the region defined by the PSC flux-density limits, the $f_\nu(\text{FSDB})/f_\nu(\text{PSC})$ ratio constraints, and the FSDB color restrictions used to exclude cirrus sources is called the "calibration window."

The final FSDB calibration was achieved by applying the recomputed scale factors to the adjusted FSDB measurements corrected for the feedback resistors response (with the mean ratios forced to unity). The same calibration corrections were also applied to the FSS plates, except for the feedback resistors response corrections, which are as large as 10% for sources brighter than 1,000 Jy (see Sections I.C.1 and II.G.5). Figure III.F.1 displays the distribution of the "calibrated FSDB"-to-PSC flux-density ratios vs. PSC-flux density at each wavelength for the $|b| > 50°$ detections in the calibration window. The number of detections and the population dispersion from unity are listed in Table III.F.1.

F.1.b Allsky Calibration Check

The calibration of the FSDB over the entire sky was checked by comparing the mean "calibrated FSDB"-to-PSC flux-density ratios of detections located in four broad galactic latitude bands. In each latitude band the wavelength band detections were restricted to lie within the calibration window described above. The latitude bands are listed in Table III.F.2 and include two separate bands for detections within 10° of the Galactic Plane. For each latitude band the number of detections at each wavelength, the average FSDB-to-PSC flux-density ratio, and the population dispersion from the average ratio are listed. The

250

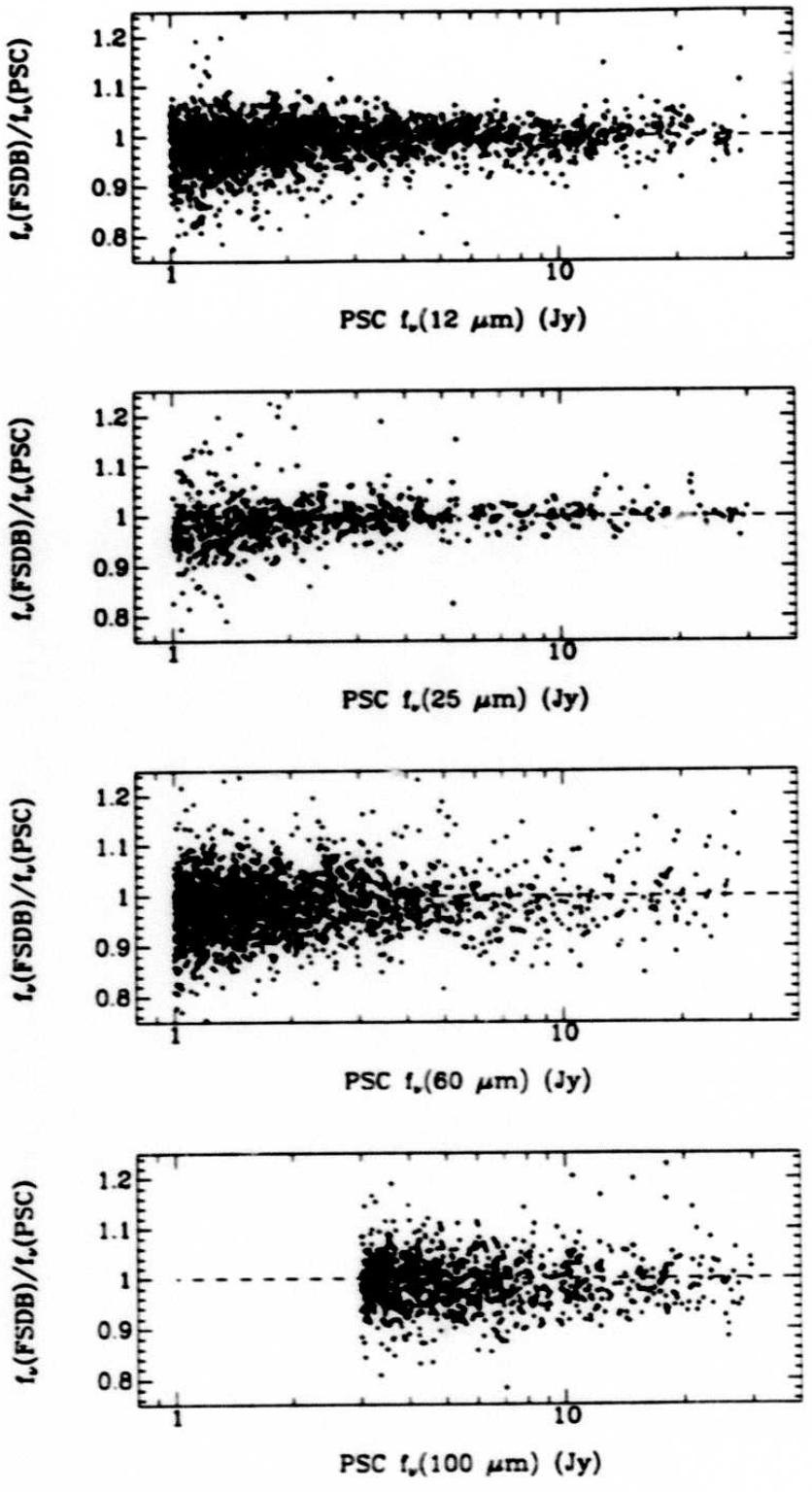

Figure III.F.1 f_ν(FSDB)/f_ν(PSC) ratios vs. f_ν(PSC) at 12, 25, 60, and 100 μm for $|b| > 50°$ detections within the calibration window.

251

TABLE III.F.2 Calibration Window FSDB-to-PSC Flux Density Comparison in Galactic Latitude Bands

Wavelength (μm)	Number	f_ν(FSDB)/f_ν(PSC) Average Ratio	Population σ
All-Sky			
12	56027	0.99	0.068
25	32054	0.99	0.070
60	14985	0.99	0.080
100	4372	0.98	0.069
$50° \geq \|b\| > 30°$			
12	3726	1.00	0.044
25	1396	1.00	0.050
60	2303	0.99	0.063
100	1082	0.99	0.058
$30° \geq \|b\| > 10°$			
12	11721	0.99	0.049
25	4861	0.99	0.049
60	4078	0.98	0.071
100	1568	0.98	0.072
$10° \geq b \geq 0°$			
12	18500	0.99	0.076
25	12161	0.99	0.075
60	3417	0.98	0.096
100	343	0.98	0.084
$0° > b \geq -10°$			
12	19965	0.99	0.074
25	12864	0.99	0.075
60	3305	0.99	0.094
100	377	0.98	0.092

mean ratios differ from unity by no more than 2% in any latitude band and the largest dispersion is less than 10%.

F.2 Relative Photometric Accuracy

F.2.a Comparison with PSC

Figures III.F.2 - 5 show the wavelength band distributions of the estimated photometric uncertainty of the FSDB relative to the PSC over the range of PSC detections from ~ 250 mJy to 1,000 Jy (750 mJy to 1,000 Jy at 100 μm) for the entire sky and

D 10015

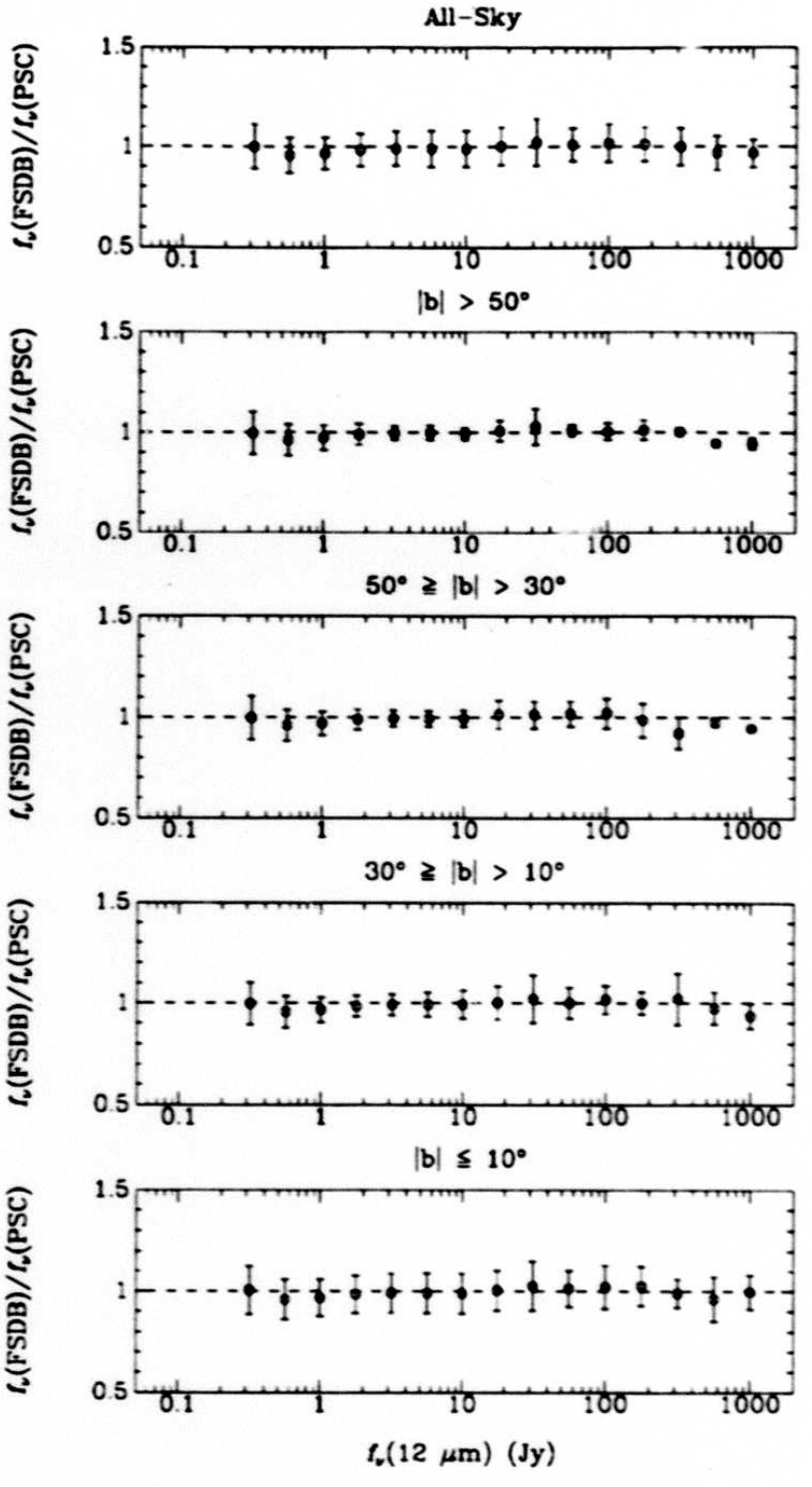

Figure III.F.2 Distribution of f_ν(FSDB)/f_ν(PSC) vs. f_ν(PSC) at 12 μm over the PSC range of 250 mJy $\leq f_\nu \leq$ 1,000 Jy. The f_ν(FSDB)/f_ν(PSC) ratios have been binned in equally spaced intervals of 0.25 in log f_ν(PSC). The error bars are at $\pm 1\ \sigma$ of the bin population dispersion.

253

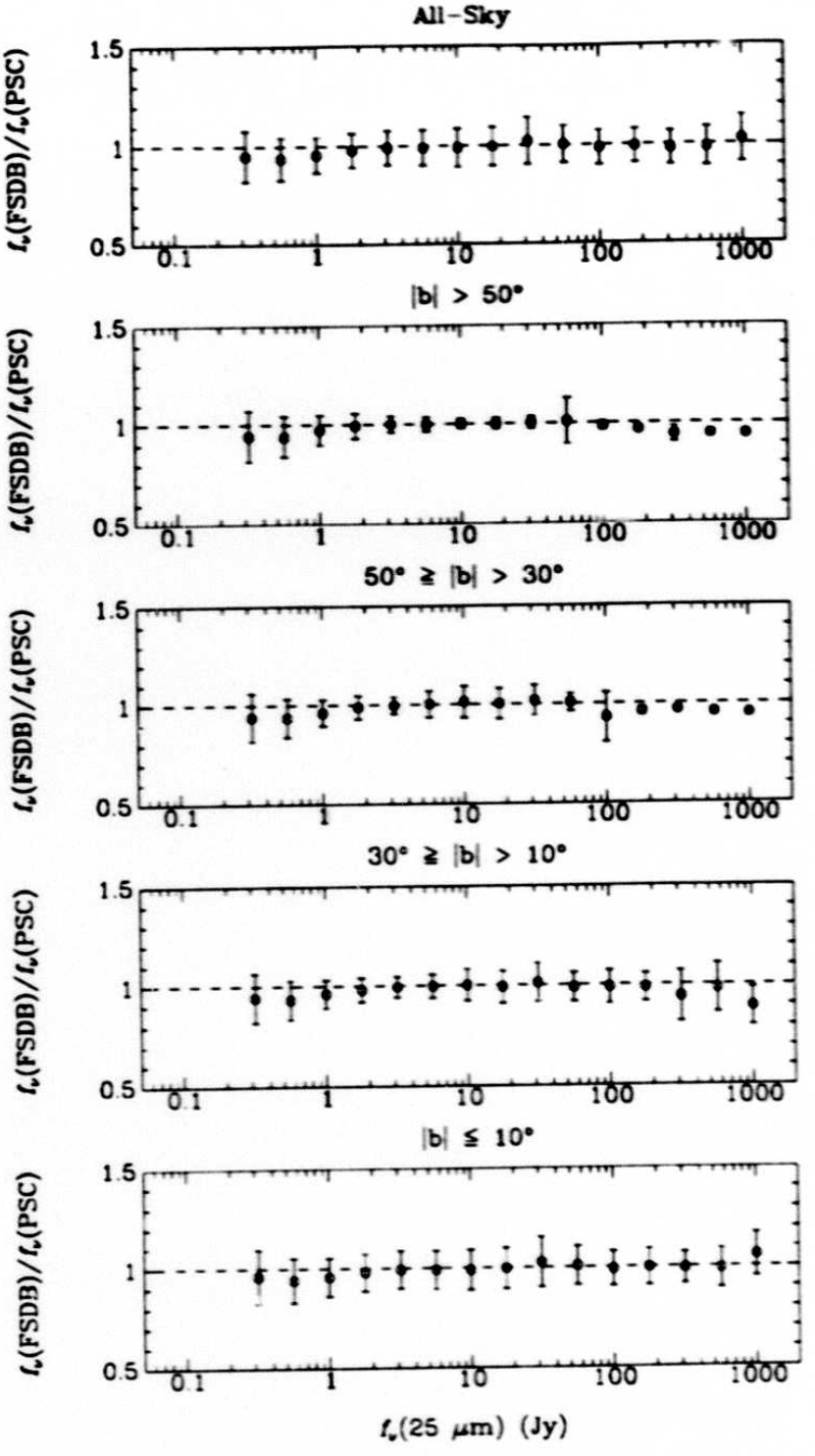

Figure III.F.3 Distribution of f_ν(FSDB)/f_ν(PSC) vs. f_ν(PSC) at 25 μm over the PSC range of 250 mJy $\leq f_\nu \leq$ 1,000 Jy. The f_ν(FSDB)/f_ν(PSC) ratios have been binned in equally spaced intervals of 0.25 in log f_ν(PSC). The error bars are at $\pm 1\ \sigma$ of the bin population dispersion.

D 10015

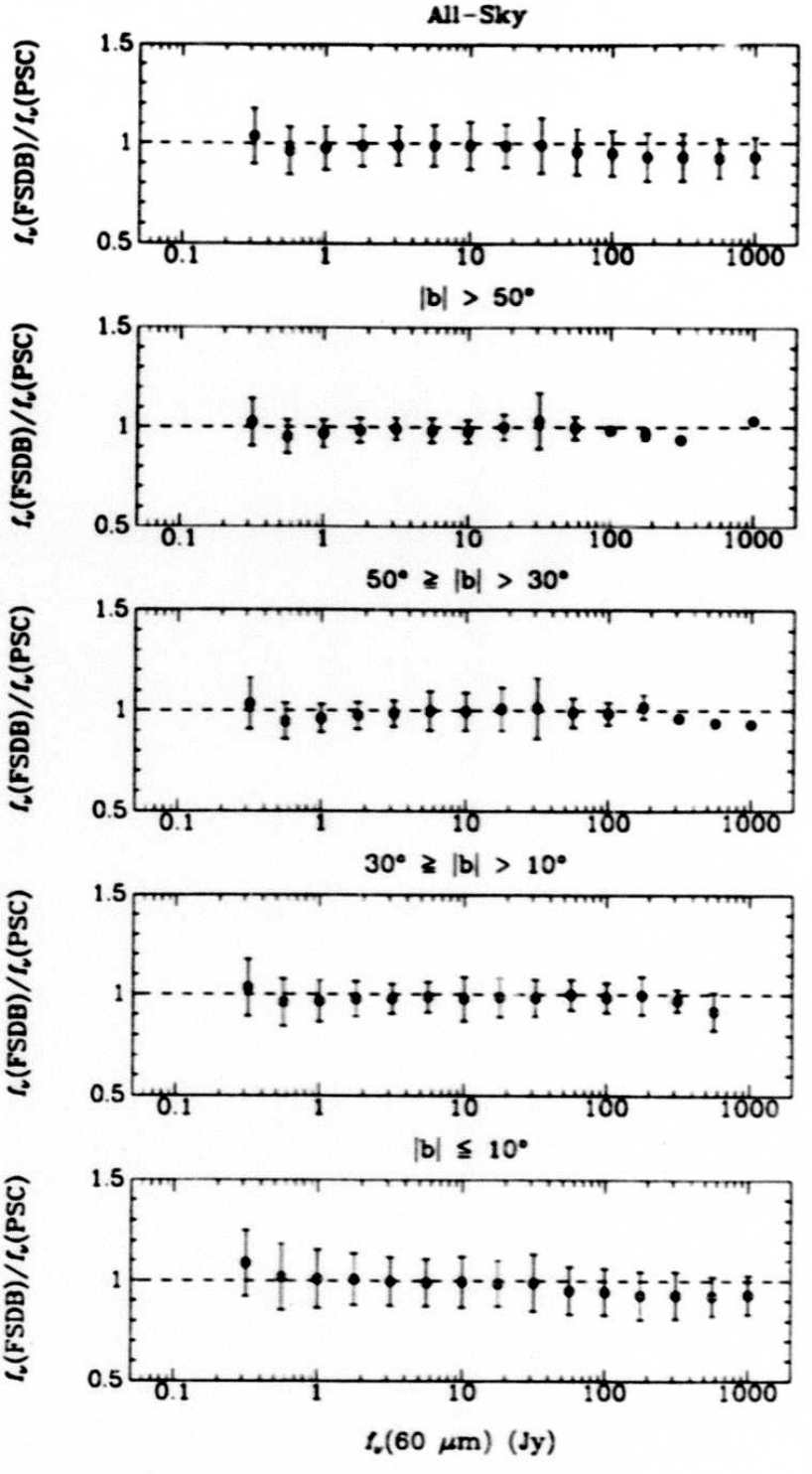

Figure III.F.4 Distribution of f_ν(FSDB)/f_ν(PSC) vs. f_ν(PSC) at 60 μm over the PSC range of 250 mJy $\leq f_\nu \leq$ 1,000 Jy. The f_ν(FSDB)/f_ν(PSC) ratios have been binned in equally spaced intervals of 0.25 in log f_ν(PSC). The error bars are at $\pm 1\ \sigma$ of the bin population dispersion.

255

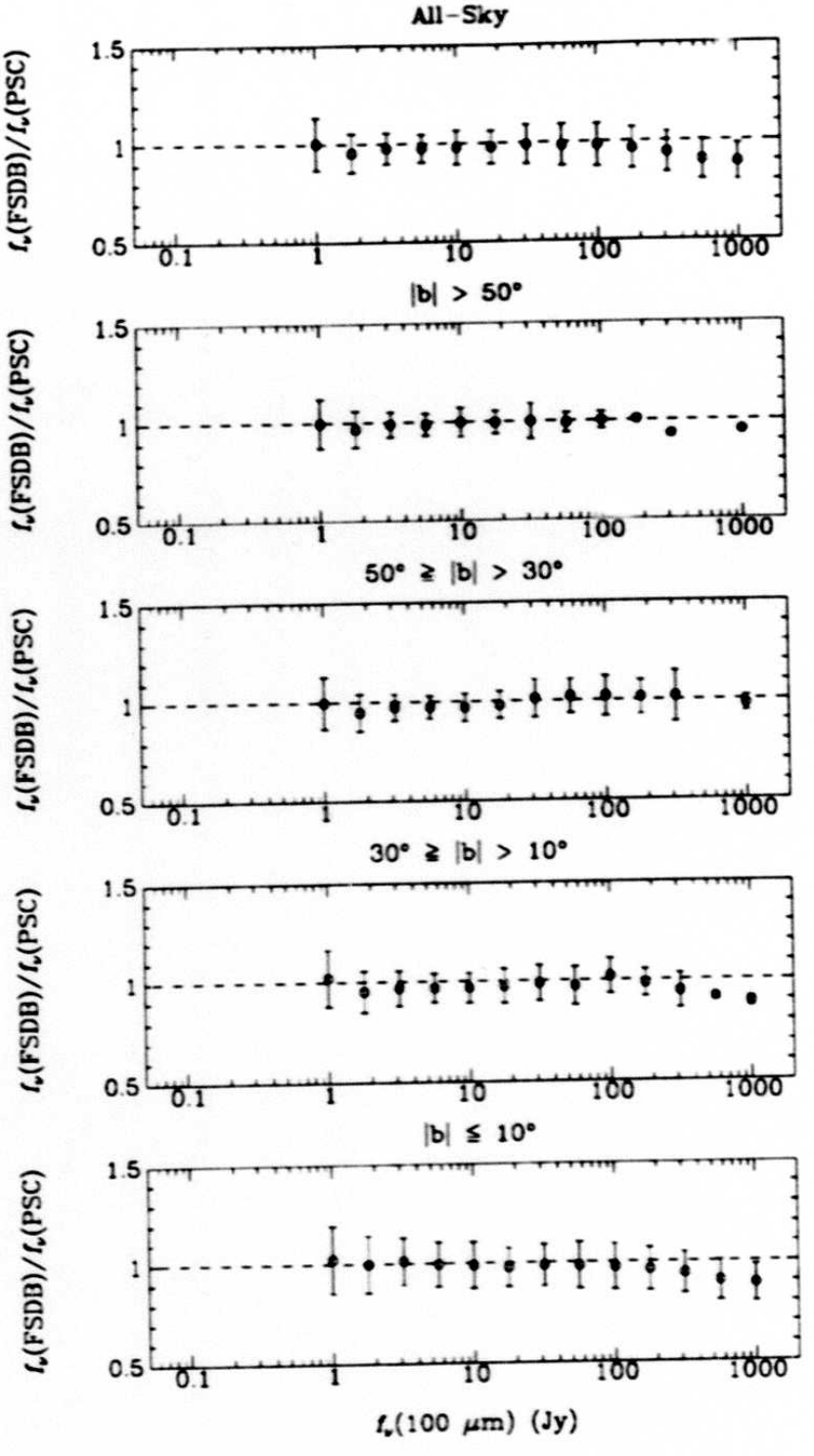

Figure III.F.5 Distribution of f_ν(FSDB)/f_ν(PSC) vs. f_ν(PSC) at 100 μm over the PSC range of 750 mJy $\leq f_\nu \leq$ 1,000 Jy. The f_ν(FSDB)/f_ν(PSC) ratios have been binned in equally spaced intervals of 0.25 in log f_ν(PSC). The error bars are at $\pm 1\ \sigma$ of the bin population dispersion.

within four Galactic latitude bands. Both "cirrus" sources and discrepant detections outside the range $0.50 < f_\nu(\mathrm{FSDB})/f_\nu(\mathrm{PSC}) < 1.50$ have been excluded. In the figures the $f_\nu(\mathrm{FSDB})/f_\nu(\mathrm{PSC})$ ratios have been binned in equally spaced intervals of 0.25 in $\log f_\nu(\mathrm{PSC})$. The error bars are at $\pm 1\ \sigma$ (population) from the mean ratios of the binned data.

For detections brighter than the mean PSC threshold ($\sim$ 0.5 Jy at 12, 25, and 60 μm; $\sim$ 1.5 Jy at 100 μm) the bin averages are within 5% of unity and the 1 σ bin uncertainties are typically $\leq$ 10%. For fainter detections the uncertainties are within 15%. Bright 60 and 100 μm sources ($f_\nu > 300$ Jy) near the Galactic Plane are systematically brighter by $\sim$ 10% in the PSC than in the FSDB. However, too few bright sources are available in the other latitude bands to determine whether this trend exists for the entire sky. (It is possible that the nonlinear response correction model as applied in FSS is inadequate for these sources, however in this work we have not pursued this matter further.)

F.2.b Comparison with Bright Stars

An estimate of the FSDB photometric uncertainty at flux-density levels fainter than the PSC was made by comparing the FSDB infrared detections of optically bright stars to the values predicted by an empirical stellar photospheric color-color relation derived by Waters *et al.* (1987). Figures III.F.6–8 show the distribution of the predicted-to-observed flux-density ratios at 12, 25, and 60 μm, respectively, for the subset of stars in the Bright Star Catalogue (Hoffleit and Jaschek 1982) detected in the FSS and meeting the $[B-V]$ color constraint of the model of Waters *et al.*. The predicted emission at 25 and 60 μm was derived from the V–[12 μm] relation reported by Waters *et al.* assuming [12 μm]–[25 μm] and [12 μm]–[60 μm] colors of $0^{\mathrm{m}}.0$.

In the flux-density range of 100 mJy to 10 Jy the mean ratios of the binned data are within 10% of unity and have 1 σ population dispersions of less than 20%.

F.2.c Comparison of Infrared Colors

Figures III.F.9 and 10 show the infrared color properties of faint and bright FSDB detections. The distribution of $f_\nu(12\ \mu\mathrm{m})/f_\nu(25\ \mu\mathrm{m})$ color vs. $f_\nu(25\ \mu\mathrm{m})$ (Figure III.F.9) is for a total of 5,278 stars in the Bright Star Catalog (Hoffleit and Jaschek 1982). No large systematic differences with source brightness are evident in these data; the mean flux-density color of the faint end ($f_\nu(25\ \mu\mathrm{m}) < 1$ Jy) is within 5% of the mean color of the brighter end.

In Figure III.F.10 the distribution of $f_\nu(60\ \mu\mathrm{m})/f_\nu(100\ \mu\mathrm{m})$ color vs. $f_\nu(100\ \mu\mathrm{m})$ is plotted for a total of 8,069 FSDB sources in the $|b| > 10°$ sky associated with cataloged

D 10015

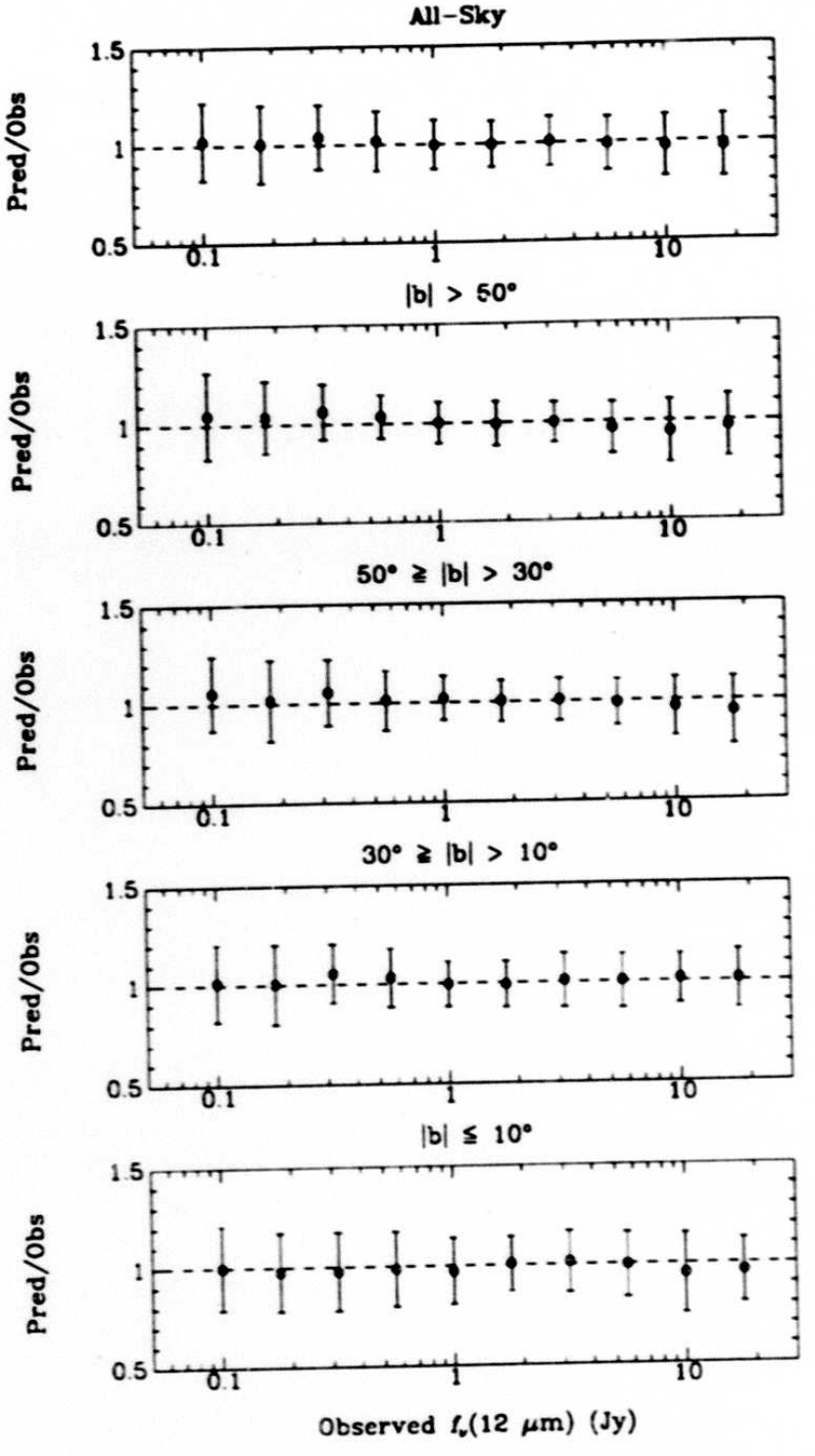

Figure III.F.6 Distribution of predicted-to-observed flux densities of bright stars at 12 μm. The predicted stellar photospheric emission was derived from the empirical relation of Waters *et al.* 1987 (See Section III.F.2.b).

258

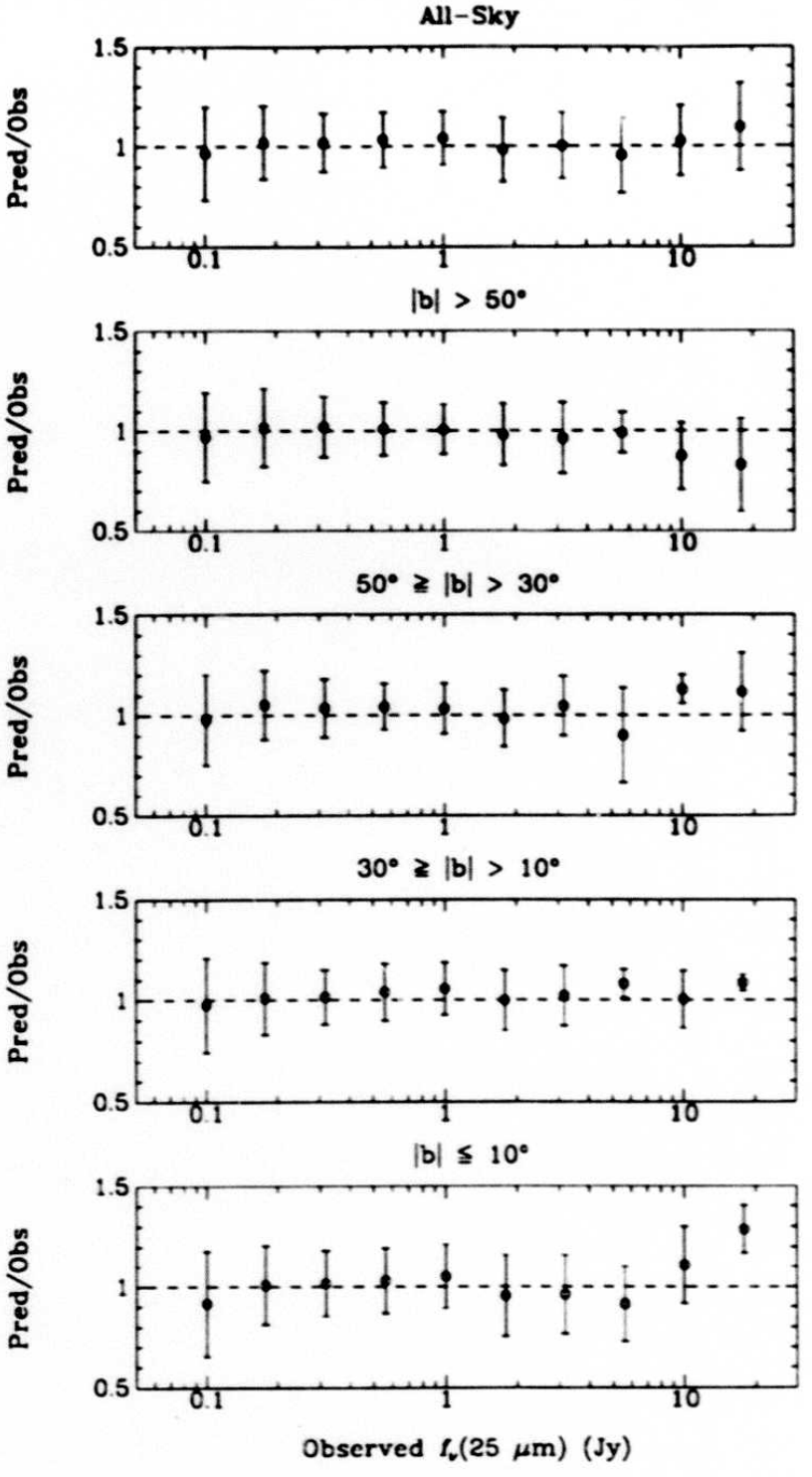

Figure III.F.7 Distribution of predicted-to-observed flux densities of bright stars at 25 μm. The predicted stellar photospheric emission was derived from the empirical relation of Waters *et al.* 1987 (See Section III.F.2.b).

D 10015

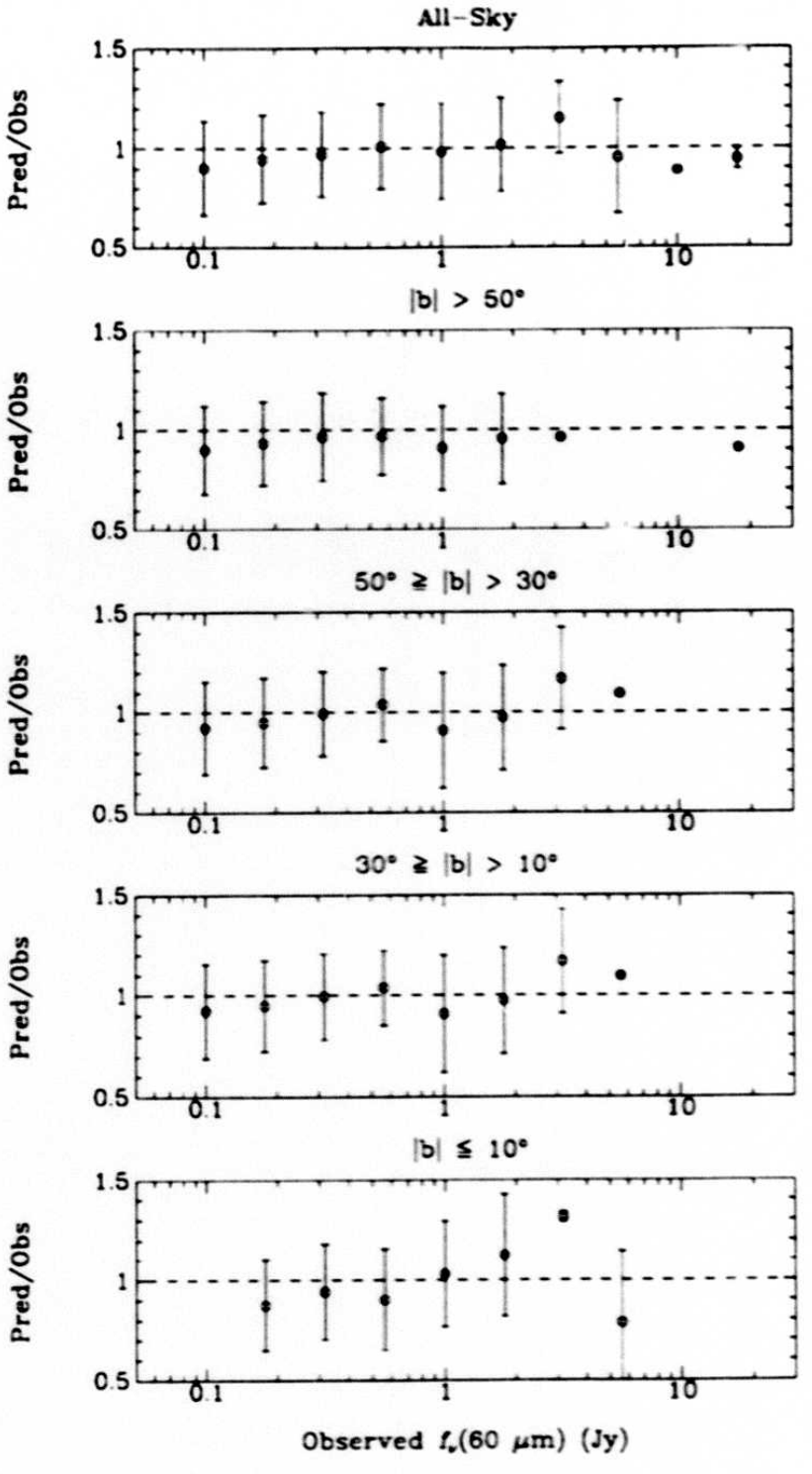

Figure III.F.8 Distribution of predicted-to-observed flux densities of bright stars at 60 μm. The predicted stellar photospheric emission was derived from the empirical relation of Waters *et al.* 1987 (See Section III.F.2.b).

260

D 10015

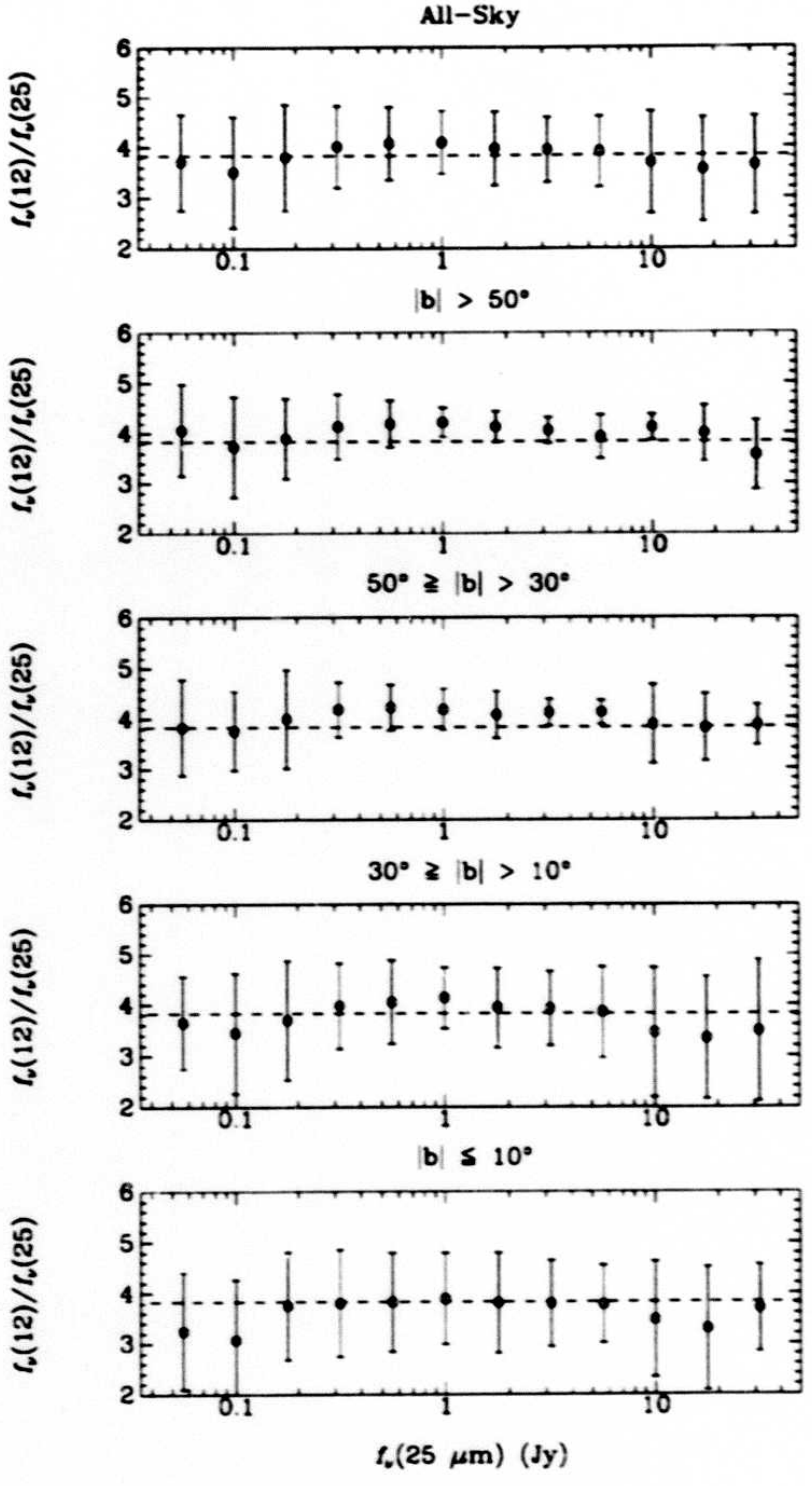

Figure III.F.9 Distribution of $f_\nu(12\ \mu m)/f_\nu(25\ \mu m)$ color vs. $f_\nu(25\ \mu m)$ for 5,278 bright stars. The dashed line is at $f_\nu(12\ \mu m)/f_\nu(25\ \mu m) = 3.83$, the mean color of these sources in the range 1 Jy < $f_\nu(25\ \mu m)$ < 30 Jy.

201

D 10015

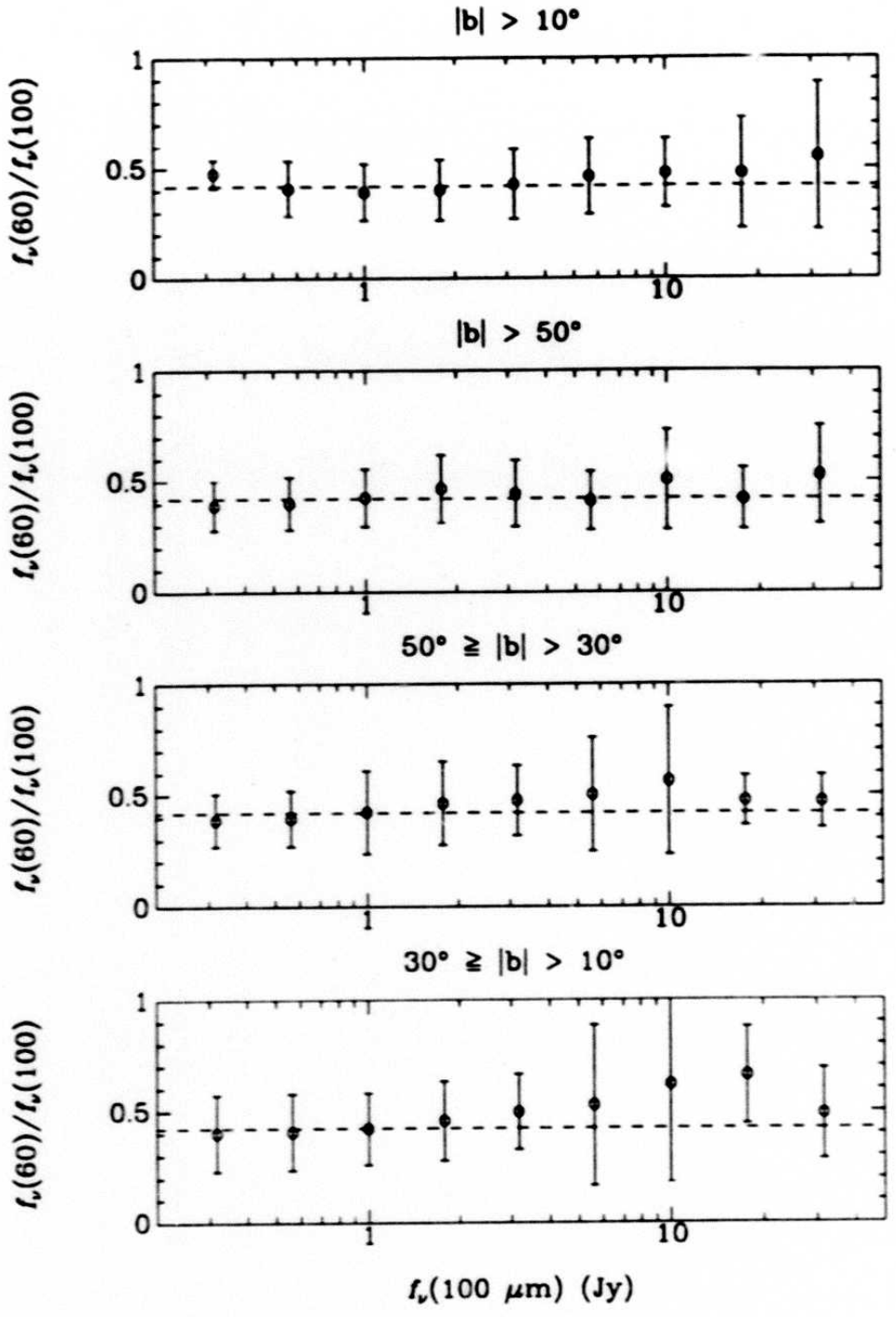

Figure III.F.10 Distribution of $f_\nu(60\ \mu m)/f_\nu(100\ \mu m)$ color vs. $f_\nu(100\ \mu m)$ for 8,069 associated FSDB extragalactic sources with $|b| > 10°$. The dashed line is at $f_\nu(60\ \mu m)/f_\nu(100\ \mu m) = 0.42$, the mean color of these sources in the range 3 Jy < $f_\nu(100\ \mu m)$ < 30 Jy.

262

extragalactic sources. The mean color of the fainter sources ($f_\nu(100\ \mu m) < 1$ Jy) is within 10% of the mean color of the brighter sources.

F.2.d Summary

The FSDB matches the PSC to within 5% over the range of the PSC threshold to ~ 1,000 Jy. Over this range the relative photometric uncertainty of the FSDB is within 10%. The infrared FSDB detections of bright stars at 12, 25, and 60 μm at flux-density levels fainter than the PSC threshold to ~ 100 mJy are in agreement with predicted values to within 10% with uncertainties of < 20%. The mean $f_\nu(12\ \mu m)/f_\nu(25\ \mu m)$ and $f_\nu(60\ \mu m)/f_\nu(100\ \mu m)$ flux-density colors of faint and bright FSDB detections show no large systematic differences and agree to within 10%.

F.3 Variation due to Binning

In regions of the sky covered by more than one plate, extracted sources will have multiple representations (dups), one of which is chosen for entry into the catalog (the rep) (see Section II.G.2). To estimate the uncertainty introduced into flux-density measurements from the process of binning the data (see Section II.C.4), this representative can be compared against the other representations of the source on overlapping plates (the dups). Tables III.F.3 and 4 show the results of such a comparison.

TABLE III.F.3 Percentage Binning Error in Flux Density Measurements for All Sources

Band	<X>*	σ_x	N*
12 μm	-1.1×10^{-4}	2.9×10^{-2}	87,805
25 μm	3.6×10^{-4}	3.2×10^{-2}	45,038
60 μm	-5.3×10^{-4}	3.8×10^{-2}	49,790
100 μm	4.9×10^{-4}	2.6×10^{-2}	23,633

*See text

For each rep/dup pair we calculate the following parameter:

$$X = \frac{f_\nu^{dup} - f_\nu^{rep}}{f_\nu^{rep}}$$

in each band for which the rep and dup both have an extracted flux density in common. Table III.F.3 shows $< X >$, σ_x, and N, the number of samples used in each statistic. The column labeled σ_x is an estimate of the variation in flux density introduced by binning. Table III.F.4 shows the same statistics calculated for sources near the reliability threshold used to determine catalog selection.

TABLE III.F.4 Percentage Binning Error in Flux Density Measurements for Sources Near Catalog Reliability Threshold

Band	<X>*	σ_x	N*
12 μm	-4.0×10^{-4}	3.9×10^{-2}	3,643
25 μm	-9.7×10^{-4}	3.0×10^{-2}	185
60 μm	-8.7×10^{-4}	4.5×10^{-2}	3,819

*See text

There is a slight increase in the width of the distribution near threshold due to noise and unreliability near the threshold. This comes about as follows. Since pixel sizes were optimized for point-source-width objects, and noise exists at shorter spatial scales, noise-generated binning errors can arise from the specific geometric differences in pixel placement and orientation between plates. This effect is greatest near the threshold. Unreliability causes apparent binning errors near threshold when extraction of noise excursions with random positions are flagged as dups.

F.4 Flux Density Scale of the FSS/PSC vs the SSC

Introduction

All of the *IRAS* point source products (PSC,SSC,FSC) have been designed to have a common flux density scale, with the PSC defined to be the primary flux density standard for *IRAS* point sources.

The description of the process of anchoring the FSS flux density scale to that of the PSC is given in Section III.F.1. After the FSS had been tied to the PSC, a comparison was made between the FSS and the *Serendipitous Survey Catalog* (SSC) for samples of 12 and 60 μm sources. This analysis showed that at 12 μm both the SSC and the FSC *are* in agreement, but at 60 μm the flux density scale for the SSC is *inflated* relative to the FSC from ~5% to ~16% (from brighter to fainter sources). This finding at 60 μm is indirectly confirmed in Section III.C.7 where other independent measures of flux density completeness are discussed. We have not pursued the causes of the discrepancy between the SSC and the PSC/FSC. We believe that the process described in Section III.F.1, tying the flux density scale of the FSS to the PSC, is based on a sound foundation. We have not made similar comparisons at 25 and 100 μm.

F.4.a FSS - SSC Comparison at 12 μm

For this comparison sources were chosen from the SSC by requiring good to moderate quality detections at 12 μm as well as requiring that the selected sources have a stellar

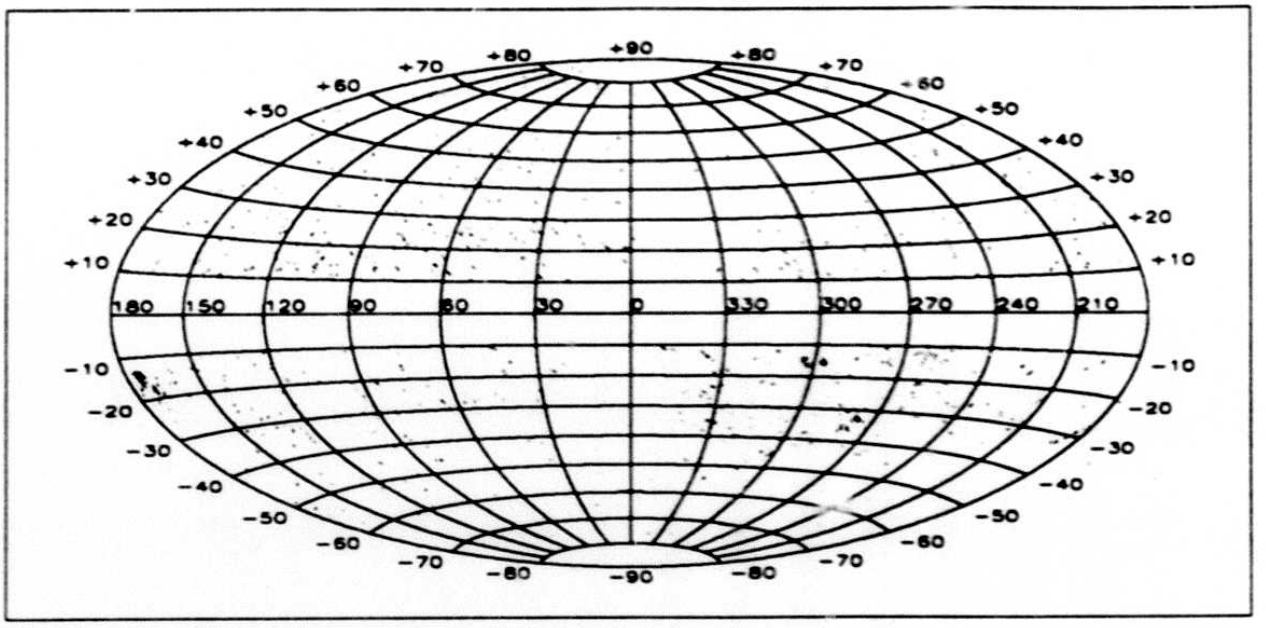

Figure III.F.11 Spatial distribution of 12 μm SSC sources identified with the FSS sources. This sample was used to compare the SSC and FSC flux density scales. The Aitoff projection is in galactic coordinates.

color (fqual(1)=2,3 and $f_\nu(12\ \mu m) > f_\nu(60\ \mu m)$). These sources were next matched to the FSS database and those SSC sources which had an FSS match with a thresholding noise <36 mJy were kept. Matches were confined to be within a radius of 90″. Once matches were found, they were further constrained by the condition:

$$\Delta_{in}^2/(\sigma_{in}^{FSS^2} + \sigma_{in}^{SSC^2}) + \Delta_z^2/(\sigma_z^{FSS^2} + \sigma_z^{SSC^2}) < 9 \qquad (III.F.1)$$

namely, matches had to be within a 3-σ error ellipse.

Sources selected according to these conditions are plotted in galactic coordinates in the Aitoff map in Figure III.F.11. The distribution of f_ν^{FSS}/f_ν^{SSC} for sources from Figure III.F.11 is seen in Figure III.F.12.

For narrow flux density ranges the median values of the scatter plot in Figure III.F.12 have been computed, they are seen in Figure III.F.13. This last figure demonstrates that for the 12 μm band, the SSC and FSS appear to be consistent within a couple of percent (a formal interpretation of the points and error bars indicates that the two sets are consistent within a 3-σ range). Notice that the point at 0.15 Jy in Figure III.F.13 is off the main trend. This can be ascribed to the incompleteness of the FSS at this low a flux density. At

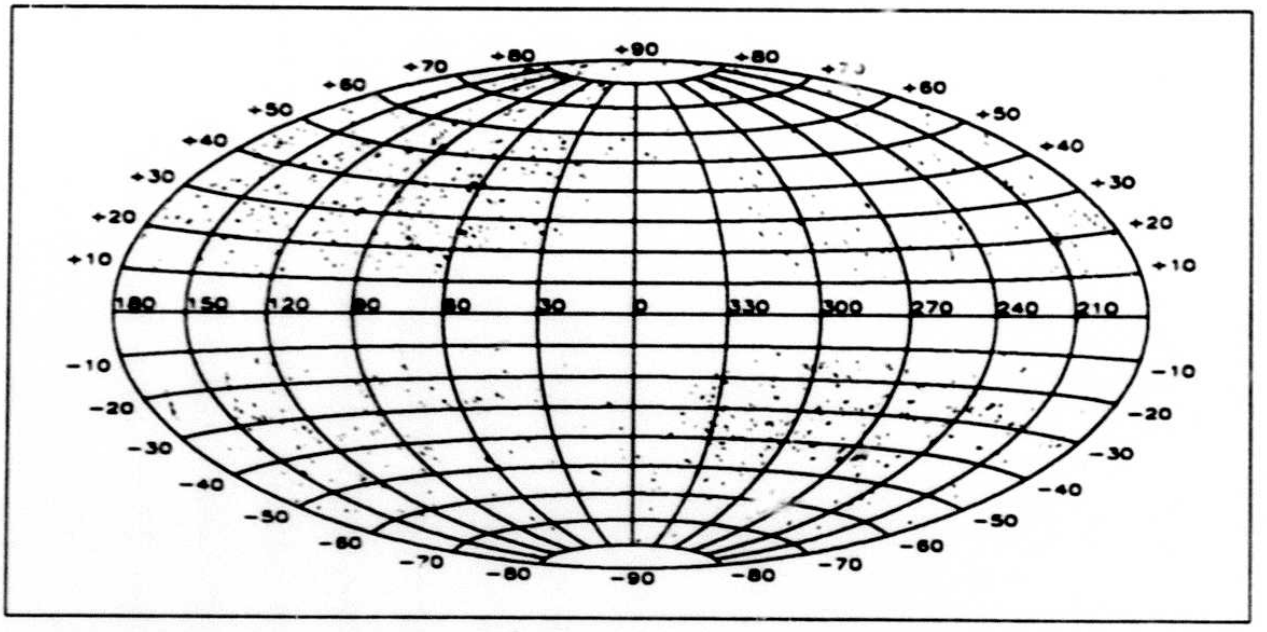

Figure III.F.14 Spatial distribution of 60 μm SSC sources identified with the FSS sources. This sample was used to compare the SSC and FSC flux density scales. The Aitoff projection is in galactic coordinates.

a non-stellar color (fqual(3)=2,3 and $f_\nu(60\ \mu m) > f_\nu(12\ \mu m)$). These candidates were matched to the FSS database. Those SSC sources which had FSS matches with NOISRAT(3) < 1.72, and thresholding noise < 60 mJy were kept (a source in FSC was required to satisfy these last two conditions). In addition, matches were confined to be within a radius of 90″; once matches were found, they were further constrained by Eq. III.F.1.

A map of the locations of the resulting sample can be seen in Figure III.F.14. The distribution of f_ν^{FSS}/f_ν^{SSC} for the sources from Figure III.F.14 is seen in Figure III.F.15. The median point of the scatter plot has been computed for several narrow flux density ranges, seen in Figure III.F.16. In this last figure a trend in the flux ratios is seen. At high flux densities (> 10 Jy) the SSC is inflated by ~5% relative to the FSS; the inflation factor increases to ~16% at a flux density of ~0.5 Jy. For example, Figure III.F.16 indicates that a quoted SSC flux density of 0.50 Jy corresponds to a flux density of 0.43 Jy in the FSS (also see Section III.C.7.b).

D 10015

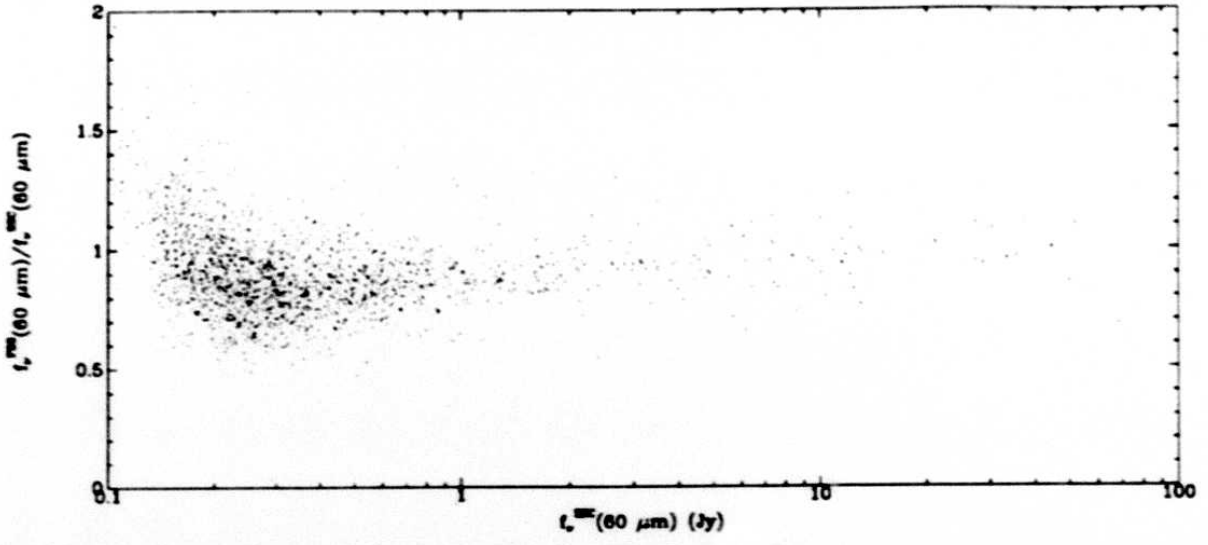

Figure III.F.15 Distribution of the ratio of flux densities from the FSDB relative to the SSC as a function of flux densities from the SSC at 60 μm.

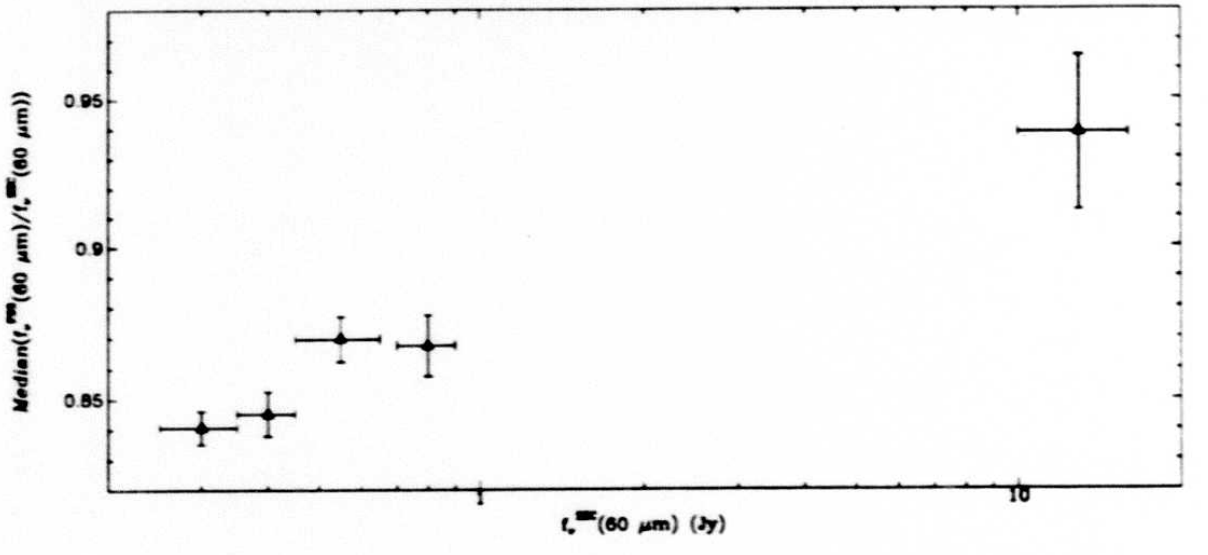

Figure III.F.16 Median value of the flux density ratios from the FSDB relative to the SSC as a function of flux densities from the SSC at 60 μm.

268

G. Known Problems

G.1 Overview

FSS processing has removed a large number of defects and artifacts from the data (see Section II.A for an overview). However, there are several limitations to the FSDB which the user should bear in mind. The FSS processing was designed to filter most of the transient effects such as radiation hits, moving objects in the field of view, known data anomalies, etc. This filtering was not perfect; for example, we were able to remove the signatures of asteroids when their existence was known to us, but the removal of any *unknown* asteroid would be left to the trimmed-mean algorithm. On the other hand, we decided not to use the then-available information on cometary debris trails, and decided to deal with the artifacts caused by comet trails after the processing had ended. Internal reflections of very bright sources were also another artifact that we decided to leave in the data, and allowed the trimmed-mean algorithm to filter them out as much as possible, with a final manual clean-up at the end of processing.

Another limitation would occur if a source had a drastic variation in brightness during the mission. Its photometric uncertainty might have become so large as to have caused the source extractor to filter it out completely at the extraction stage.

The median filtering scheme used for background removal was based on preserving fidelity of *single point* sources, it is expected that IR extended sources or barely resolvable doubles would yield flux densities and positions which should not be taken as the last word. Other types of processing would be more appropriate in such cases; one possibility is to line up all detector scans going over the source and coadd them along one direction. This preserves the full in-scan resolution of the *IRAS* data (this method forms the basis for ADDSCAN/SCANPI processing).

At longer wavelengths the background tends to cause an increase in clutter and photometric uncertainty as the Galactic Plane is approached. The severity of infrared cirrus at 100 μm was such that all of the 100 μm detections were given a moderate flux-quality index. Although it is possible to trace the areas infested with infrared cirrus, the methods employed to delineate such areas are statistical in nature. The proper use of data at low galactic latitudes in high background regions requires attention on an individual basis.

In any catalog of astronomical objects with flux measurement errors (with source counts which decrease with increasing flux density), flux densities of sources of the faint end are overestimated. Due to measurement errors, the number of sources moved up in flux exceeds the number of sources moved down in flux. As a result, for a given apparent flux

density interval, the mean of the *true* flux densities of the sources in that range is smaller than the *apparent* value. This translates into an overestimation in quoted flux densities. The effect depends on the underlying source counts and the behavior of measurement errors; overestimation becomes noticeable only at low SNRs and its magnitude can be estimated. No correction has been applied to the FSDB for this small effect.

In Section III.G.2 the effects of comet trails on the FSC are discussed, the question of variable sources is dealt with in Section III.G.3, the effects of optical cross-talk are discussed in Section III.G.4, questions related to asteroids and their removal are the subject of Section III.G.5, performance of the FSS processing in dealing with extended sources is addressed in Section III.G.6, the topic of infrared cirrus and its effects on the data forms the subject of Section III.G.7, and finally the question of a possible flux density overestimation for faint sources is addressed in Section III.G.8.

G.2 Cometary Debris Trails

Linear features are observed in the contour plots of the FSS plates. In most cases, these are "cometary debris trails" (Sykes *et al.* 1986); this term will be used interchangeably with "linear features". However, it is possible that some of these features are due to other causes.

Figure III.G.1 shows the debris trails visible on plate 754. The '*' symbols represent four extracted "sources" which passed the criteria for inclusion in the FSC. (See also Figures III.G.3 and 4.)

A visual check of contour plots for the ~1280 plates covering the $|b| > 15°$ sky revealed cometary debris trails in 36 plates. Contour plots for the latitude band from $+15°$ to $-15°$ were not available to be examined.

Table III.G.1 is a list of plates containing 'suspected' comet trails and the bands influenced. No trails were visible at 100 μm.

"Sources" passing the thresholds for the FSC are sometimes extracted from these linear features even though, in most cases, they are not true inertial point sources. Some "true" sources also fall on the trails. Although they can be associated with sources in other catalogs and/or appear on the Palomar Sky Survey plates, their *flux densities* may be affected to some extent by the dust trails. For these reasons, we have eliminated any source from the FSC which falls within the 2-σ contour centered on the linear feature.

The sources listed in Table III.G.2 have been removed from the FSC. They are available in the FSR. Nine of these were included in the FSC, version 1, and maintain their

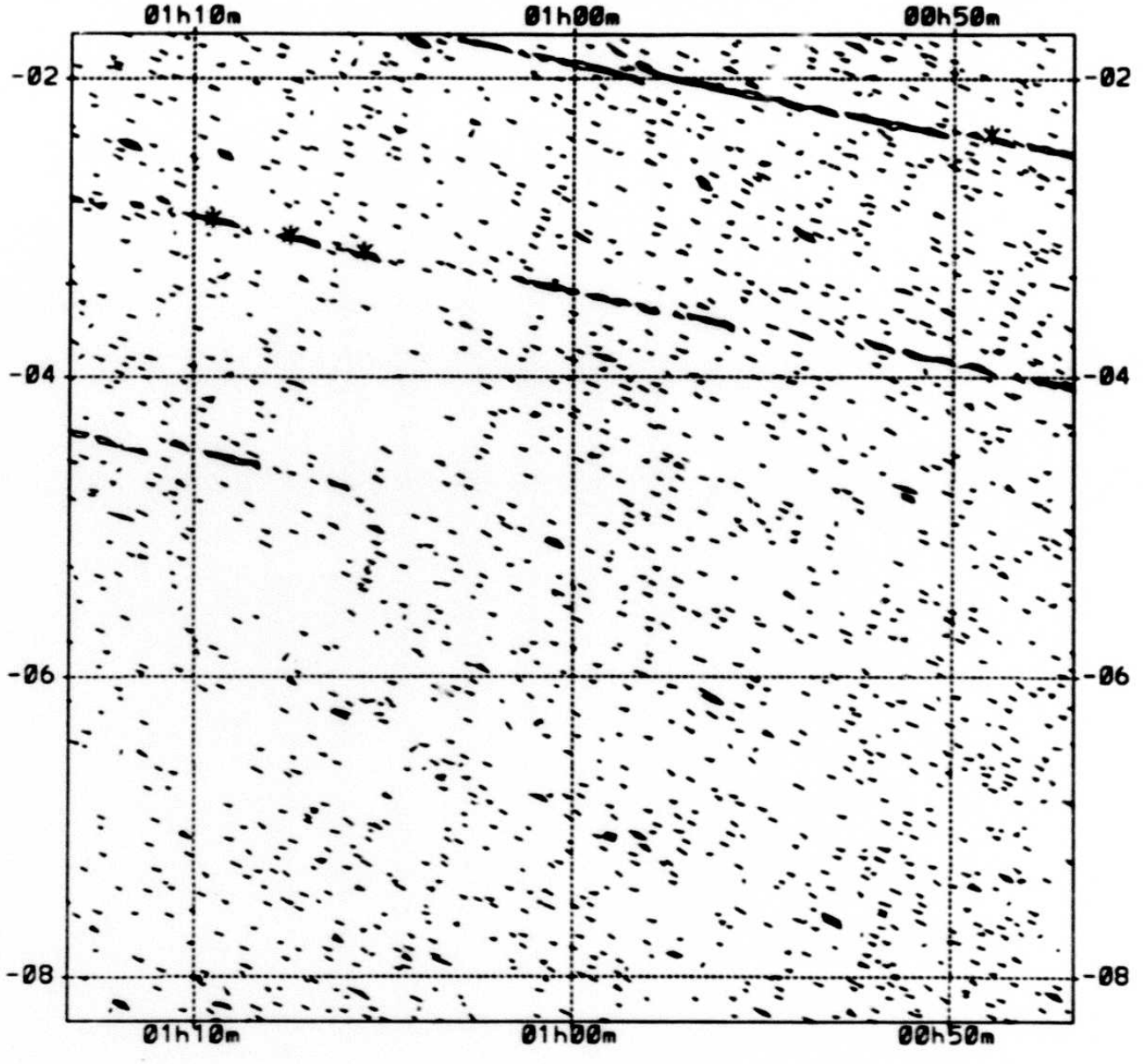

Figure III.G.1 Linear features on plate 754. The '*' represents four extracted sources passing catalog criteria. The contour map is at 12 μm.

names from that version. Position refinement and more precise trail definition resulted in the exclusion of these sources from the FSC, version 2.

G.3 Variable Sources

Variable sources may at times have a flux-density variation sufficient to cause a low local SNR, LOCSNR (ratio of peak flux to dispersion in peak-flux pixel). The flux density reported for these sources will be a trimmed-average of the flux densities observed on each

TABLE III.G.1 Plates Containing Extended Linear Features

Plate No.	12 μm	25 μm	60 μm
583		x	
603		x	x
635		x	
649	x	x	x
652	x	x	
653	x	x	
654		x	
719	x	x	
720	x	x	x
722		x	
723		x	
751	x	x	x
752	x	x	x
753	x	x	x
754	x	x	x
755	x	x	x
756	x	x	x
757	x	x	x
758	x	x	x
759	x	x	x
760	x	x	
761	x	x	
790	x	x	
791	x	x	x
821	x	x	x
822	x	x	x
824	x	x	x
825	x	x	x
826	x	x	x
827	x	x	x
828	x	x	x
829	x	x	x
830	x	x	x
831	x	x	x
861	x	x	x
862	x	x	x

D 10015

TABLE III.G.2 Sources Removed from the FSC in Cometary Dust Trail Areas

FSDB Name	α δ hhmmss.s:ddmmss	Plate	FSDB Name	α δ hhmmss.s:ddmmss	Plate
*F00001-0353	000010.7-035350	751	Z02085-0053	020832.2-005336	829
Z00165-0347	001634.9-034714	752	Z02139-0033	021356.1-003308	830
Z00229-0330	002255.4-033049	752	Z02162-0302	021614.2-030241	830
*F00351-0433	003506.6-043318	753	Z02200-0240	022005.9-024011	758
Z00355-0259	003531.9-025951	753	Z02211-0233	022111.2-023354	758
Z00450-0235	004504.7-023535	753	Z02298-0150	022950.1-015043	830
Z00489-0224	004854.8-022409	754	*F02326-0141	023235.1-014128	831
*F00529-0342	005255.4-034247	754	Z02359-0121	023558.0-012101	831
Z01054-0311	010526.3-031136	754	Z02362-0119	023613.1-011912	831
Z01073-0305	010723.7-030508	754	Z02368-0116	023648.0-011621	831
Z01093-0258	010923.9-025823	754	Z02389-0109	023855.2-010939	831
Z01140-0245	011405.1-024539	755	Z02438-0042	024353.0-004223	831
Z01202-0226	012013.4-022607	827	*F02460-0028	024604.2-002850	831
Z01222-0352	012212.2-035225	755	Z02550-0518	025505.5-051814	760
Z01236-0348	012337.7-034831	755	Z02555-0515	025533.8-051548	760
*F01251-0207	012510.7-020753	827	Z03059-0419	030558.5-041954	760
Z01269-0332	012658.8-033211	755	Z12315+0207	123130.7+020718	861
Z01353-0132	013522.3-013240	828	Z12403+0031	124018.9+003148	861
*F01387-0118	013847.5-011837	828	Z12554-0214	125529.0-021412	862
Z01389-0253	013859.7-025318	756	Z13500-1231	135003.9-123116	649
Z01394-0120	013925.4-012050	828	Z14012-1422	140116.9-142233	649
Z01398-0249	013953.2-024923	756	Z14025-1437	140231.1-143709	649
Z01409-0114	014057.7-011414	828	Z14162-0855	141617.6-085554	722
Z01432-0104	014317.8-010422	828	Z14284-1004	142829.9-100441	722
Z01454-0229	014530.0-022947	756	Z14397-1108	143945.9-110842	723
Z01457-0228	014542.0-022849	756	Z15000-1323	150002.8-132330	652
Z01473-0221	014720.0-022155	828	Z15229-1522	152254.9-152231	653
Z01481-0218	014806.0-021827	828	Z15254-1534	152528.6-153418	653
Z01516-0034	015137.2-003436	829	Z15416-1700	154136.5-170015	654
Z01520-0032	015200.8-003209	829	Z15446-1713	154440.5-171318	654
Z01532-0031	015317.9-003136	829	*F22448-1952	224453.3-195227	603
Z01536-0030	015338.5-003013	829	Z22469-1850	224654.8-185057	603
Z01543-0029	015422.4-002913	829	Z23160-0519	231603.2-051950	821
Z01584-0011	015828.5-001156	829	Z23423-0433	234220.9-043307	822
Z01599-0129	015958.9-012913	829	Z23432-0430	234313.1-043033	822
Z02054-0108	020524.9-010832	829	Z23518-0413	235150.5-041347	751
Z02074-0340	020724.9-034053	757	Z23536-0408	235336.5-040859	751
*F02080-0338	020804.2-033843	757	Z23587-0426	235842.5-042618	751

* These sources were included in FSC, version 1, and maintain their names from that version of the catalog. Position refinement and more precise trail definition resulted in the exclusion of these sources from FSC, version 2.

273

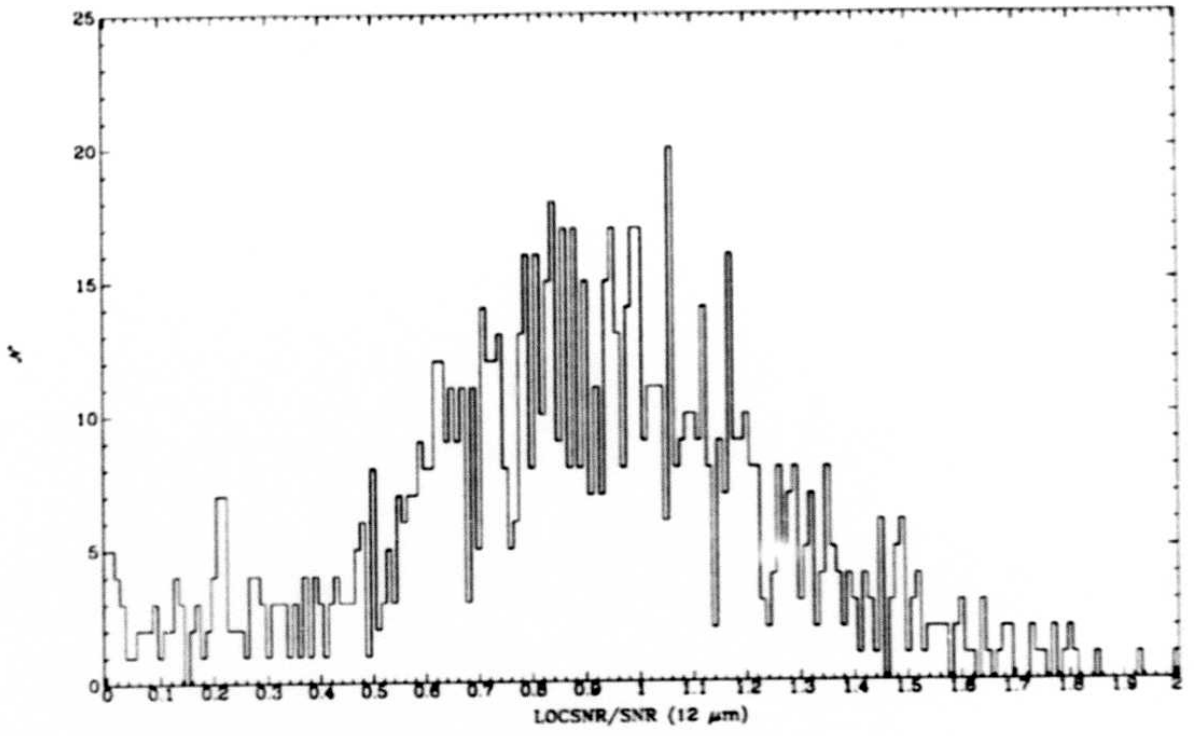

Figure III.G.2 Distribution of LOCSNR/SNR for 1,030 randomly selected 12 μm sources in the FSC.

individual scan over the source. This variation may even cause their local SNR to fall below the catalog or extraction thresholds and exclude the sources from the FSC or FSR. In general if the source is sufficiently variable during the ***IRAS*** mission, there is a possibility that such a variation may be detected in the FSS data. We have selected a random set of 1,030 12 μm sources from the FSC, and computed their distribution of $\frac{\text{LOCSNR}}{\text{SNR}}$. As expected, this distribution is centered near unity. This distribution, seen in Figure III.G.2, shows that 87% of the sources in the sample have $\frac{\text{LOCSNR}}{\text{SNR}}$ *greater* than 0.5. To compare against variable sources we have selected a set of 1,035 12 μm sources in the FSS identified with sources in the PSC having a probability of variability > 90% (see Section VII.D.3 of the *Main Supplement*). For this group the distribution of $\frac{\text{LOCSNR}}{\text{SNR}}$ shows a very different behavior as is seen in Figure III.G.3. In this distribution, 90% of the sources have $\frac{\text{LOCSNR}}{\text{SNR}}$ *less* than 0.5. The ratio $\frac{\text{LOCSNR}}{\text{SNR}}$ may be useful to identify variable sources. We made no attempt to identify and flag variable sources in the database using the aforementioned scheme. When there are associations with the PSC, the PSC variability index could be used to identify such sources.

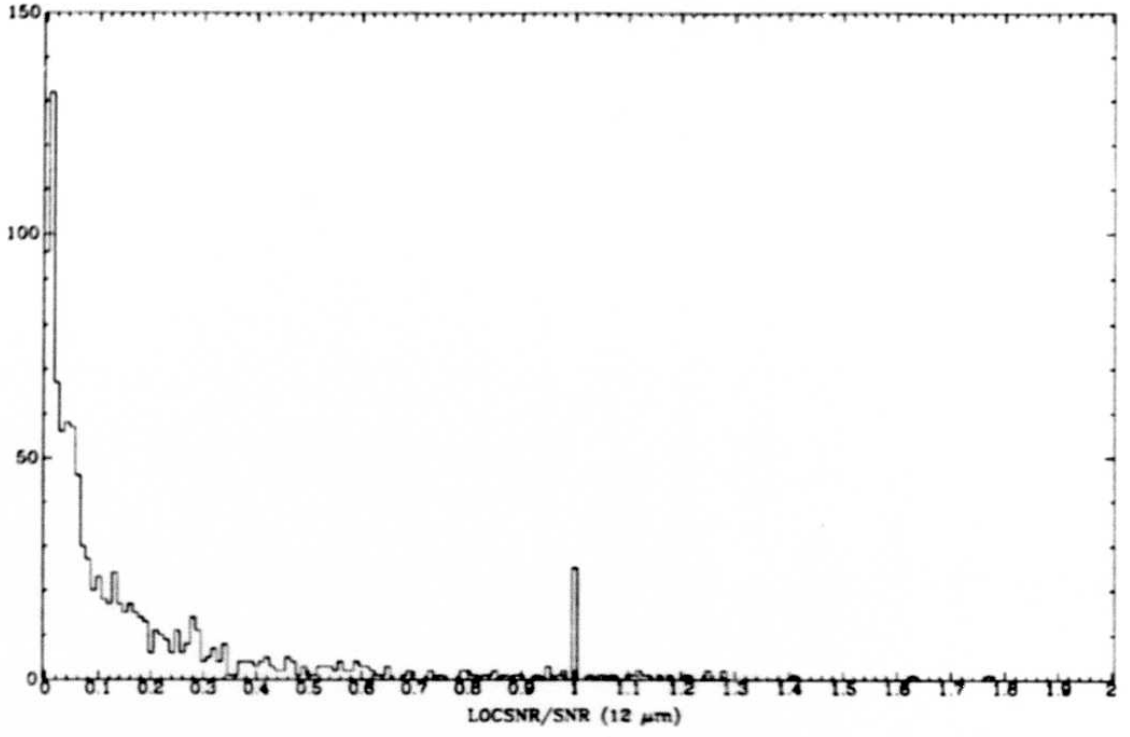

Figure III.G.3 Distribution of LOCSNR/SNR for 1,035 12 μm FSS sources also identified with PSC sources having a probability of variability >90%. This distribution has a mode at 0.01, and a median of 0.07.

G.4 Optical Cross Talk

G.4.a Problem Statement

The point-spread function of the telescope caused bright sources to illuminate more detectors in the focal plane than just those over which their image centers passed. The resulting spurious input to areas adjacent to the bright source's proper grid location was generally removed by the point-source filter and the trimmed-mean filter used in coaddition. One by-product of bright sources which often persisted in spite of such techniques was the optical cross-talk registration of the diffraction image of the telescope secondary support structure (spider). The spider produced a six arm cross-talk radiation pattern on the focal plane - two in the in-scan direction and four at angles of $\pm 60°$ and $\pm 120°$ with respect to the in-scan direction (see the ***Main Supplement*** Section VII.E.2 for further information). The brightest sources are represented on the plates as very broad sources (because three adjacent detectors were fully illuminated by each pass over the source, hence a 9′ wide registration). These bright sources can be accompanied by up to four lobes - the cross-talk "spider arms" - branching from the central peak. (The two in-scan lobes are suppressed

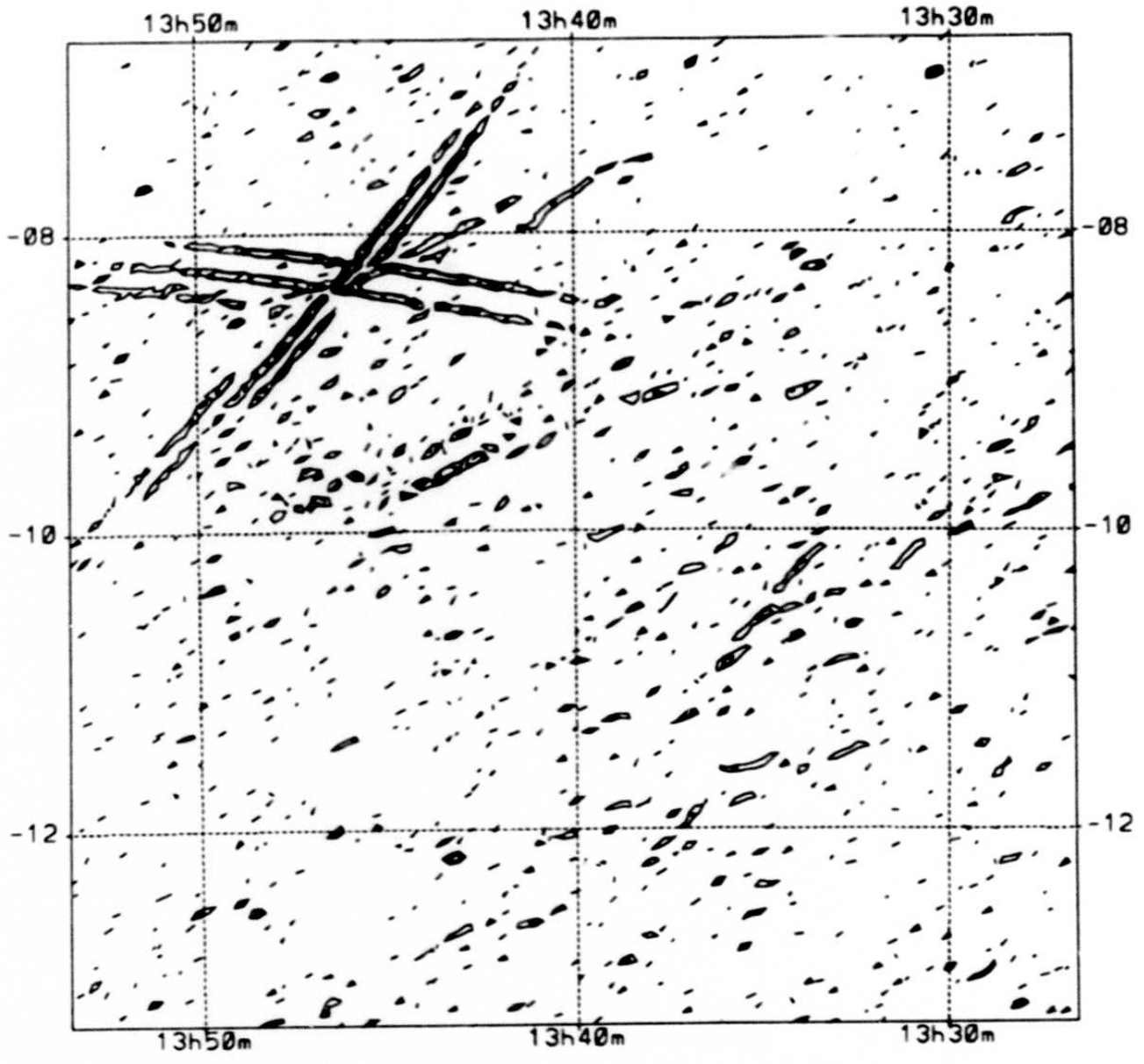

Figure III.G.4 A dramatic example of optical cross-talk at 60 μm for FSS plate 720. Saturn's motion between its first and second hours confirmations leave a double image of the planet and its attendant spider arms.

by the point-source filter.) Portions of the cross-scan lobes can be extracted as separate sources.

Figure III.G.4 shows a dramatic example of optical cross-talk on FSS Plate 720. Saturn at 60 μm shows on the plate as a pair of "x" patterns, one for each hours-confirming coverage. Part of a third "x" shows from the third HCON which began about $\frac{1}{2}^{\circ}$ to the

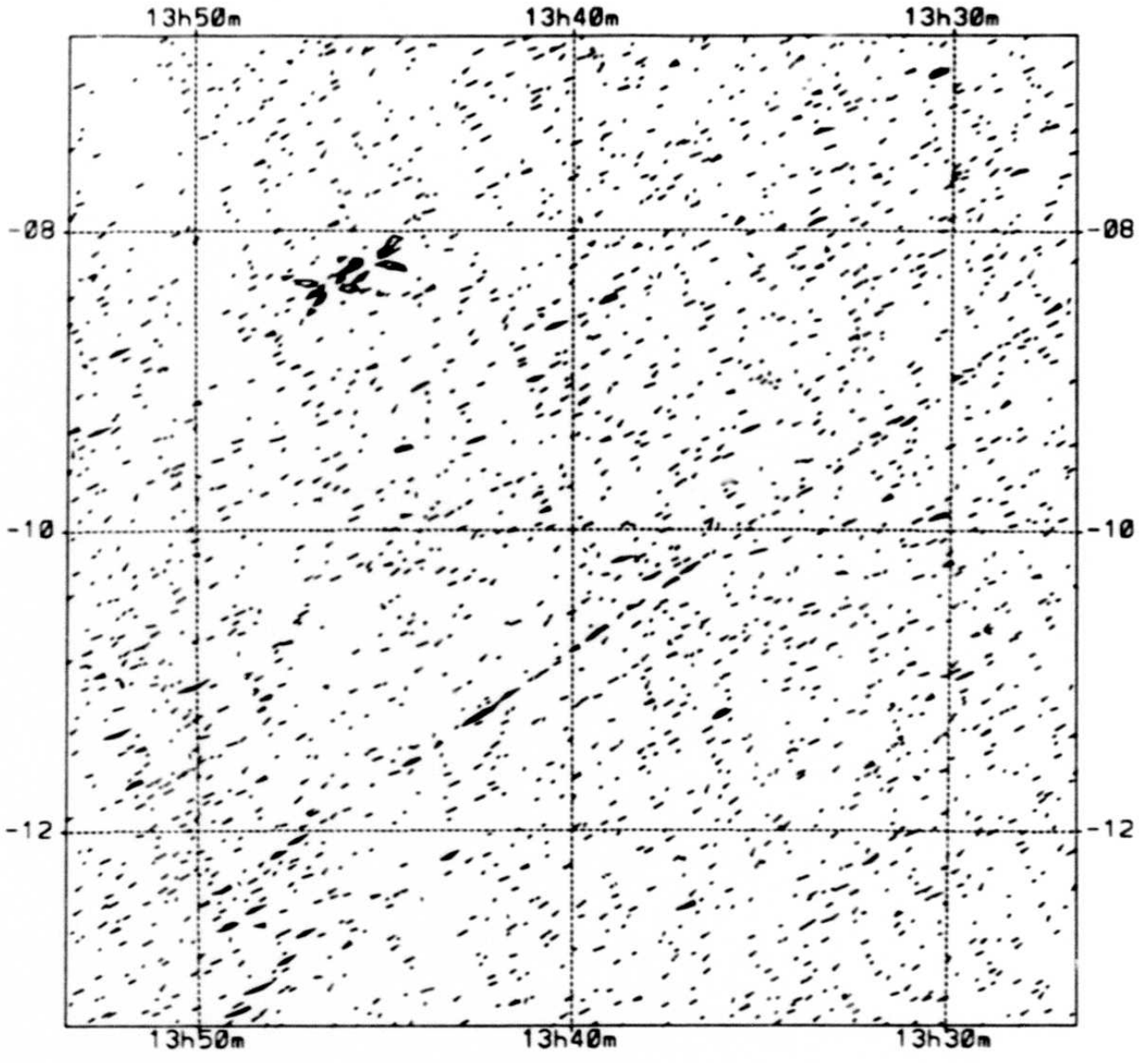

Figure III.G.5 Optical cross-talk at 25 μm for FSS plate 720. Note also the cometary debris trails of Tempel 1.

left of Saturn. Figure III.G.5 shows the same plate at 25 μm. Most of the extractions in the arms do not survive final catalog processing — most often they are below the local SNR (LOCSNR) threshold. Final catalog sources in or near the arms were checked for optical counterparts (via catalog association or POSS examination) to assure their reliability. Four uncataloged galaxies, including one pair of galaxies, were found in this check. It is

277

TABLE III.G.3 Bright Source Neighbors Suppressed as Cross-Talk

Name	Parent Flux Source	Parent Flux Density (Jy)	Problem Band (μm)	Flux Ratio	Distance (′)
Z00456−2534	NGC253	784	60	5×10^{-4}	8
Z09446+1340	IRC+10216	6582	25	1×10^{-4}	13
Z09448+1336	IRC+10216	6582	25	4×10^{-4}	8
Z09457+1331	IRC+10216	9941	12	2×10^{-4}	7
Z09462+1314	IRC+10216	9941	12	2×10^{-5}	22
Z09463+1312	IRC+10216	9941	12	2×10^{-5}	24
Z09465+1333	IRC+10216	9941	12	3×10^{-5}	19
"	"	4807	60	1×10^{-4}	"

noteworthy that optical cross-talk from Saturn appeared twice in the PSC. Both of these sources were rejected from the FSC due to low local SNR.

G.4.b Correction Method

The FSS plates were examined for evidence of "spider arms" radiating from the central position. Bright sources in the high-latitude plate contour plots were checked for wide "x" patterns around the central sources. Suspicious lobes appear above ~1000 Jy at 12 μm and at ~500 Jy in the other bands. Sources extracted from spider arms were found to accompany sources with flux densities of 1600 Jy at 12 μm, 1200 Jy at 25 μm, and 800 Jy at 60 μm. None were found at 100 μm.

All sources brighter than half the empirically-observed cross-talk thresholds, namely flux densities of 800, 600, 400, and 400 Jy at 12, 25, 60, and 100 μm, were checked by looking for them on the POSS or ESO/SERC plates; the absence of a corresponding source was taken as sufficient evidence that the FSDB source is in fact cross-talk. Almost all of these cross-talk sources are rejected from the final catalog by the catalog thresholds. Table III.G.3 lists the eight sources which had to be suppressed by hand.

G.5 Residual Asteroid Contamination

None of the 3500 known (as of June 1987) asteroids are present in the FSC. This is due to the three layers of protection applied during data processing: known asteroid removal (see Section II.C.2.b), data trimming (see Section II.C.4), and local SNR thresholding (see Sections II.E.3 and II.G.6). In this section we discuss the effects of asteroid removal on the plate images.

Although all data for all known asteroids should have been removed from the FSS

TABLE III.G.3 Bright Source Neighbors Suppressed as Cross-Talk

Name	Parent Flux Source	Parent Flux Density (Jy)	Problem Band (μm)	Flux Ratio	Distance (′)
Z00456−2534	NGC253	784	60	5×10^{-4}	8
Z09446+1340	IRC+10216	6582	25	1×10^{-4}	13
Z09448+1336	IRC+10216	6582	25	4×10^{-4}	8
Z09457+1331	IRC+10216	9941	12	2×10^{-4}	7
Z09462+1314	IRC+10216	9941	12	2×10^{-5}	22
Z09463+1312	IRC+10216	9941	12	2×10^{-5}	24
Z09465+1333	IRC+10216	9941	12	3×10^{-5}	19
"	"	4807	60	1×10^{-4}	"

noteworthy that optical cross-talk from Saturn appeared twice in the PSC. Both of these sources were rejected from the FSC due to low local SNR.

G.4.b Correction Method

The FSS plates were examined for evidence of "spider arms" radiating from the central position. Bright sources in the high-latitude plate contour plots were checked for wide "x" patterns around the central sources. Suspicious lobes appear above ~1000 Jy at 12 μm and at ~500 Jy in the other bands. Sources extracted from spider arms were found to accompany sources with flux densities of 1600 Jy at 12 μm, 1200 Jy at 25 μm, and 800 Jy at 60 μm. None were found at 100 μm.

All sources brighter than half the empirically-observed cross-talk thresholds, namely flux densities of 800, 600, 400, and 400 Jy at 12, 25, 60, and 100 μm, were checked by looking for them on the POSS or ESO/SERC plates; the absence of a corresponding source was taken as sufficient evidence that the FSDB source is in fact cross-talk. Almost all of these cross-talk sources are rejected from the final catalog by the catalog thresholds. Table III.G.3 lists the eight sources which had to be suppressed by hand.

G.5 Residual Asteroid Contamination

None of the 3500 known (as of June 1987) asteroids are present in the FSC. This is due to the three layers of protection applied during data processing: known asteroid removal (see Section II.C.2.b), data trimming (see Section II.C.4), and local SNR thresholding (see Sections II.E.3 and II.G.6). In this section we discuss the effects of asteroid removal on the plate images.

Although all data for all known asteroids should have been removed from the FSS

input data prior to coaddition, two sources of asteroid contamination remain: errors in removing data from known asteroids and optical cross-talk from bright known asteroids.

IRAS sightings of some known asteroids (very bright ones in a couple of identified examples) were not correctly predicted by the processing done preparatory to the release of the *IRAS* Asteroid and Comet Survey. Although these oversights had no significant affect on that product, they did allow some bright asteroid signals to pass onto the FSS plates. We do not know how many such cases exist, but they are certainly few and of little consequence. The trimmed-average algorithm and local SNR thresholds removed non-inertial data from the FSC, even without the added protection of asteroid data removal. These "un-removed" asteroid sightings leave their impressions on the plate images as normal-looking point sources of low local SNR, with one source per coverage HCON.

Optical cross-talk (see Section III.G.3) from very bright asteroids could cause some of their single-scan point-spread functions to extend beyond the area clipped from the input data. Occasionally, this "leakage" is sufficient to cause an extraction, but never a catalog source. For the most part, this cross-talk merely results in displeasing plate blemishes.

FSS plates are blemished by asteroid removal in another minor way. Because the regions of a plate from which asteroid data have been removed have fewer coverages than the surrounding area, these regions are noisier. Therefore, it is often possible to pick out areas on a plate where asteroid removal has taken place by noting a small rectangular region (the typical shape of the area over which data are removed) with large noise excursions. These excursions have very low local signal-to-noise ratios.

G.6 Extended Sources

The median filtering scheme (see Section II.C.3) was tuned to preserve point source structures and attenuate extended sources. In cases when there are compelling reasons to believe that a source is extended or resolvable at the spectral band of interest, it is advisable to use other processing methods such as HIRES or ADDSCAN/SCANPI processing. To illustrate the effects of extent on flux densities reported by the FSS, we have used the data for 62 sources in the Virgo Cluster known to be extended at 60 μm (G. Helou, private communication). The results of ADDSCAN flux densities show the expected underestimation of flux densities by the FSS due to the source extent. Figure III.G.6 displays the ratio of ADDSCAN flux densities to FSC flux densities as a function of ADDSCAN flux density.

If an object is known or suspected to be extended, then ADDSCAN would report a more accurate flux density than the FSS. It has not been firmly determined that ADDSCAN of sources fainter than ~ 0.4 Jy would in general yield any quantifiable improvements over

279

D 10015

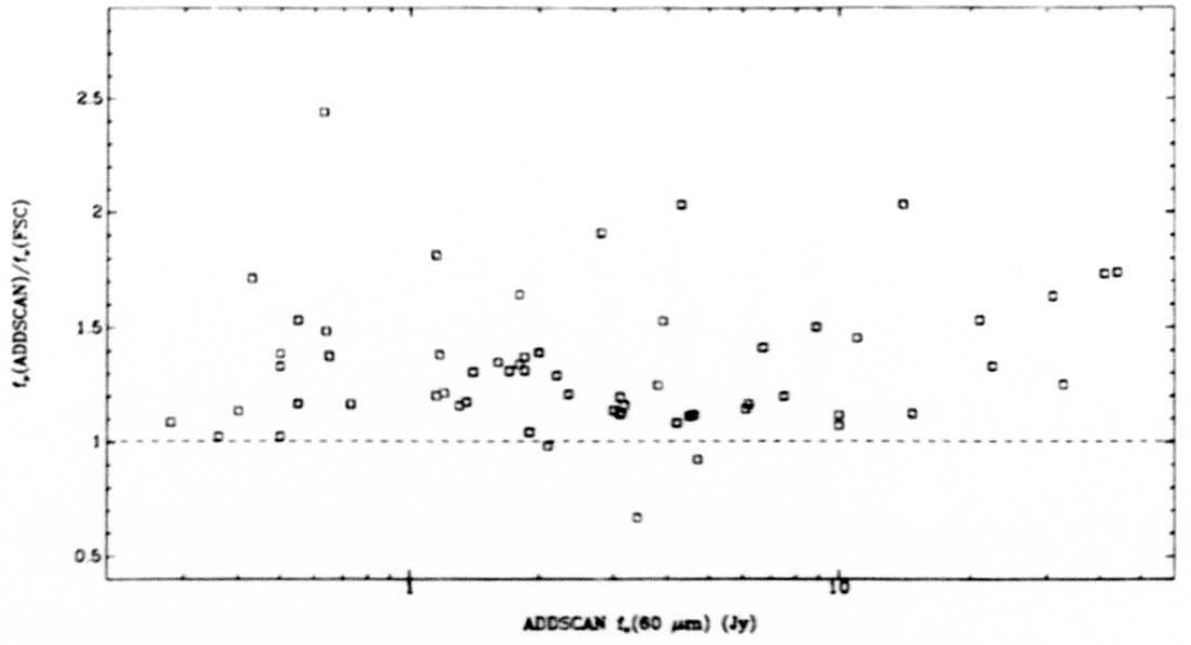

Figure III.G.6 Distribution of the ratio of ADDSCAN flux density to FSC flux density as a function of ADDSCAN flux density at 60 μm for a sample of 62 galaxies in the Virgo Cluster which are *unambiguously* extended.

the FSS. We expect that the *majority* of the sources in the FSS (which are faint sources) report an accurate flux density.

G.7 The Cirrus Flag and the Properties of Cirrus in the FSDB

G.7.a Introduction

One of the early discoveries of the *IRAS* mission was the ubiquitous presence of large scale, filamentary, interstellar structure, dubbed infrared cirrus (see *Main Supplement*, Section V.H.4). Cirrus is present in all areas of the sky without exception; only its density and brightness vary, both of which increase at lower galactic latitudes and in localized cirrus structures at high galactic latitudes. Some areas of the sky are, however, comparatively cirrus-free (or "clean"); in such regions the cirrus is either too faint or too sparse to contaminate the process of point-source extraction and flux-density estimation. In the FSS, cirrus usually appears one dimensional, resolvable only along its shorter dimension (see below). Cirrus is also "cold" and is thus detected most often at 100 μm, sometimes at 60 μm, and occasionally at shorter wavelengths.

Cirrus contamination occurs in the FSDB whenever an *IRAS* scan track crosses a cirrus filament which lies roughly orthogonal to the scan direction. Orthogonal to scan direction the cirrus has unresolved components. After filtering has removed the in-scan

280

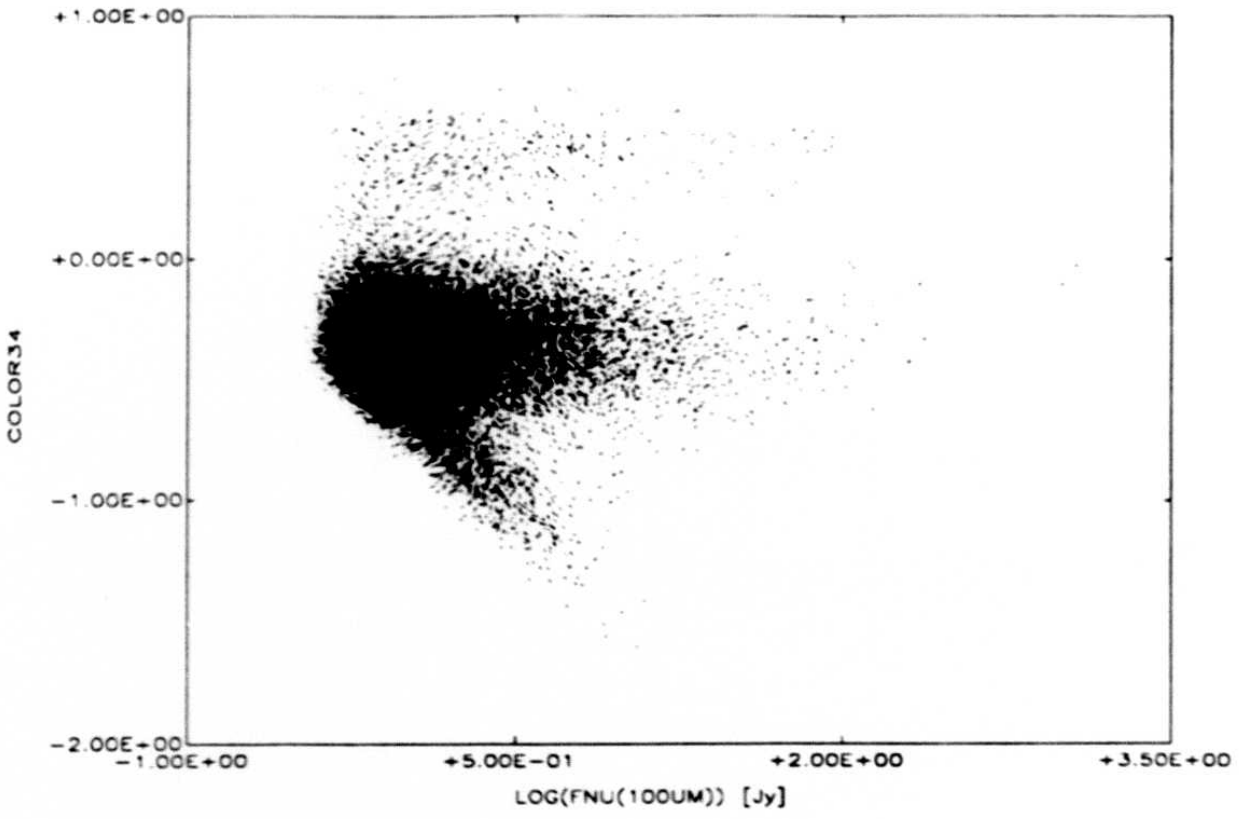

Figure III.G.7 $\log(f_\nu(60\ \mu m)/f_\nu(100\ \mu m))$ **(color34) vs.** $f_\nu(100\ \mu m)$ **for all catalog sources with high-quality flux densities in both bands. The lack of sources below the diagonal at lower left is due to the catalog threshold at 60** μ**m.**

low-frequency components and the resulting data are gridded, a filament of point-source-width signal may survive on the plate. This filament (even if degrees in extent in the cross-scan direction) may, after rethresholding, have one or more local maxima extracted, entering the FSDB as a single source or a chain of sources.

In order to reduce the contamination of the FSC by cirrus, reliability at 60 μm was made a function of background structure through the dependence of reliability on NOISRAT (see Section III.D.3.c for details), and furthermore no 100 μm-only sources were permitted into the FSC. However this is not to say that cirrus has been completely eliminated from the FSC. Scrutiny of Figure III.G.7 (which shows the ratio of $f_\nu(60\ \mu m)$ to $f_\nu(100\ \mu m)$ versus $f_\nu(100\ \mu m)$ for catalog sources having high quality fluxes at 60 μm and moderate quality fluxes at 100 μm) indicates that the catalog still contains "cold" (meaning $\log(f_\nu(60\ \mu m)/f_\nu(100\ \mu m)) \lesssim -0.75$) sources with detections at both long wavelengths. The surface density of such "cold" sources increases as the Galactic Plane is approached, indicating the galactic as opposed to *extra*galactic nature of these objects.

The rest of this section will provide the properties of cirrus in the FSDB. The methods used to delineate high cirrus regions will be discussed; the parameters which may be useful in discriminating against high cirrus regions will be indicated.

G.7.b Template Fit Indicators

The source extractor fits a point-source template to each detection and reports various degrees of fit for every source (see Section II.E). One of the fit parameters, FRATIO, measures the ratio of the peak flux density coming from the template to the actual observed peak flux density. Discussions in Section III.A.5 (see Figure III.A.9) indicate that the median filter used will result in the attenuation of source amplitude as size increases. For a point source this ratio is centered on 1, and as the source size increases FRATIO will increase. Analysis of this parameter has shown that it does indeed delineate areas of sky which are covered by extended structures. The sky has been binned into cells $\sim 1° \times 1°$ in size and the *median* value of FRATIO for all sources within the cell has been determined. Because *point* sources have a very tight distribution centered at a value of 1, regions which are devoid of extended structures would have a median very near 1. On the other hand, dominance of a cell by mostly extended structures increases the median value beyond 1. Figure III.G.8 gives the sky distribution of median FRATIO at 60 μm for $|b| \geq 10°$. A *cell*-median FRATIO of 1.13 will discriminate against most *areas* infested with non-point source detections. On a source-by-source basis, FRATIO $\gtrsim 1.2$ is most often indicative of source extent. In Figure III.G.9 the median of FRATIO at 100 μm for $|b| \geq 10°$ is seen. It is not surprising to observe that the contamination of sky by extended structures is more severe at 100 μm than at 60 μm.

G.7.c The Cirrus Flag

The use of noise on a localized basis (computed on $1.66° \times 1.66°$ sized cells at 60 and 100 μm, see Section II.E) allows the source extractor to keep track of background variations on scales $\gtrsim 1°$. Thus this scheme raises the extraction threshold in regions of high background confusion, resulting in fewer cirrus induced sources. However when the background changes on scales smaller than $\sim 1°$, the method of noise computation will smooth out the noise. As a result a rapidly changing cirrus background will encounter a *lower* thresholding noise and the outcome is an increase in the number of extracted sources. In such situations a "clustering" of sources at 100 μm will be observed. To identify those areas still contaminated by cirrus, the "cirrus flag" has been computed. The cirrus flag for each source is the number of "100 μm-only" sources (FSDB sources detected only at 100 μm) within a radius of 30′ of the source. The only known non-cirrus objects which may be detected as 100 μm-only sources are external galaxies, which, even though clustered, do

D 10015

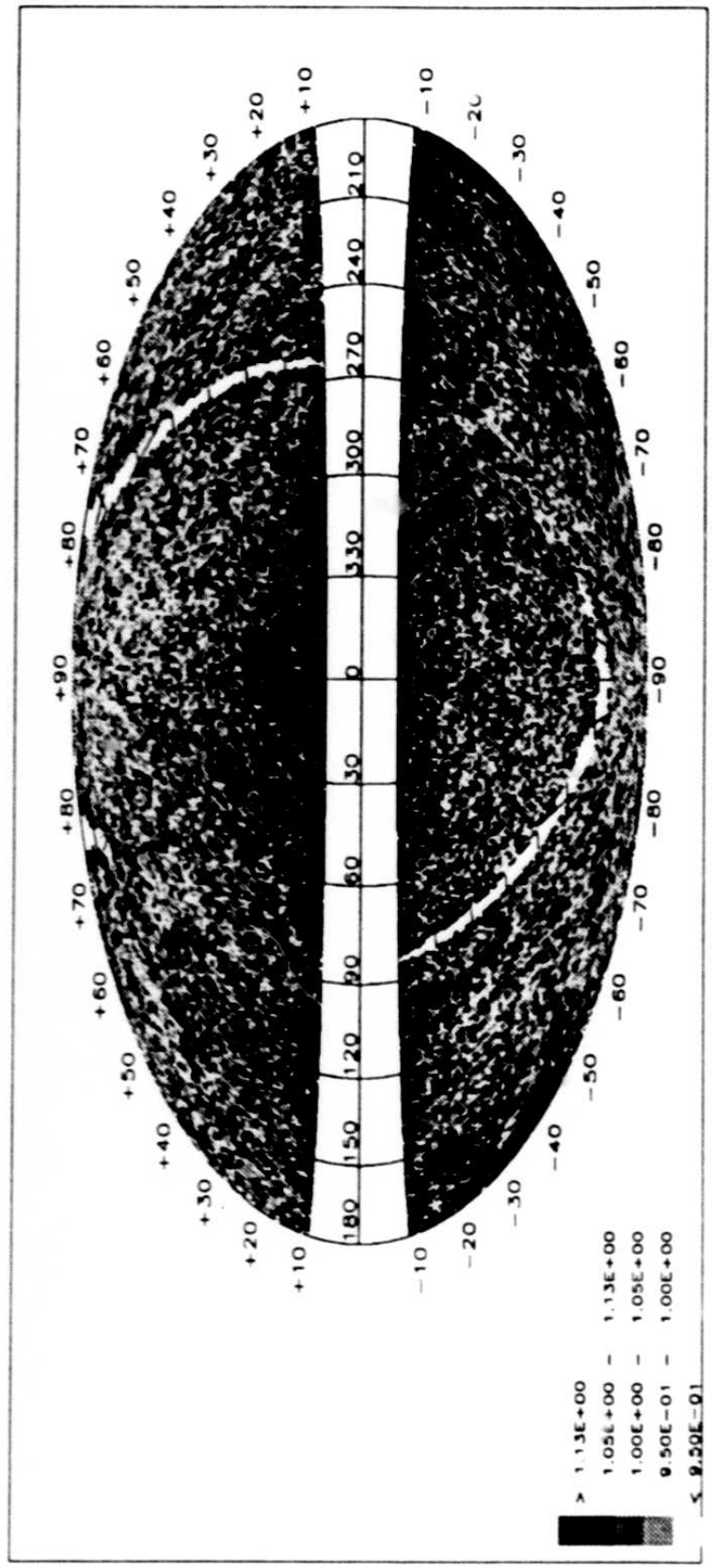

Figure III.G.8 Spatial distribution of the *median* value of FRATIO at 60 μm, in galactic coordinates. A value greater than 1 is indicative of presence of extended structures in the cell.

283

D 10015

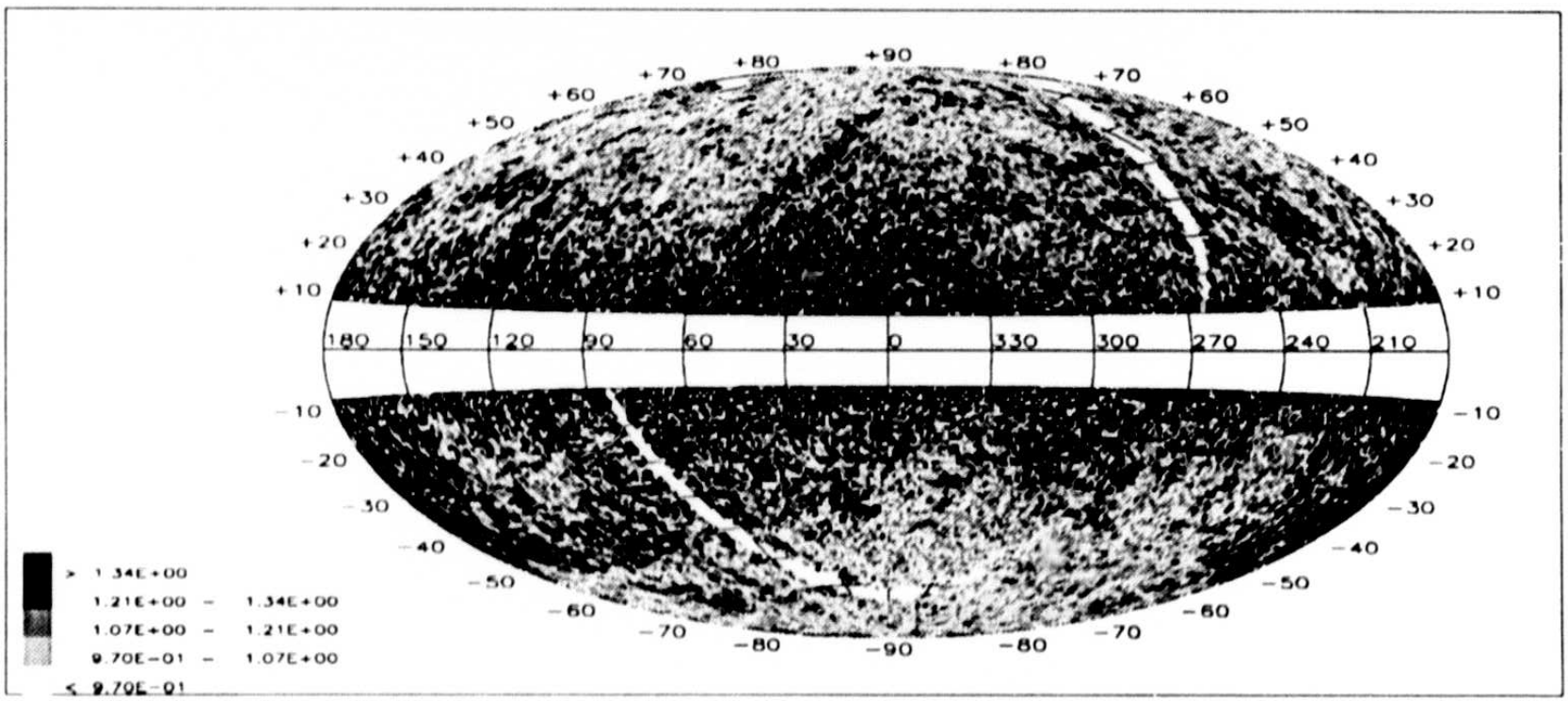

Figure III.G.9 Spatial distribution of the *median* value of FRATIO at 100 μm, in galactic coordinates. A value greater than 1 is indicative of presence of extended structures in the cell.

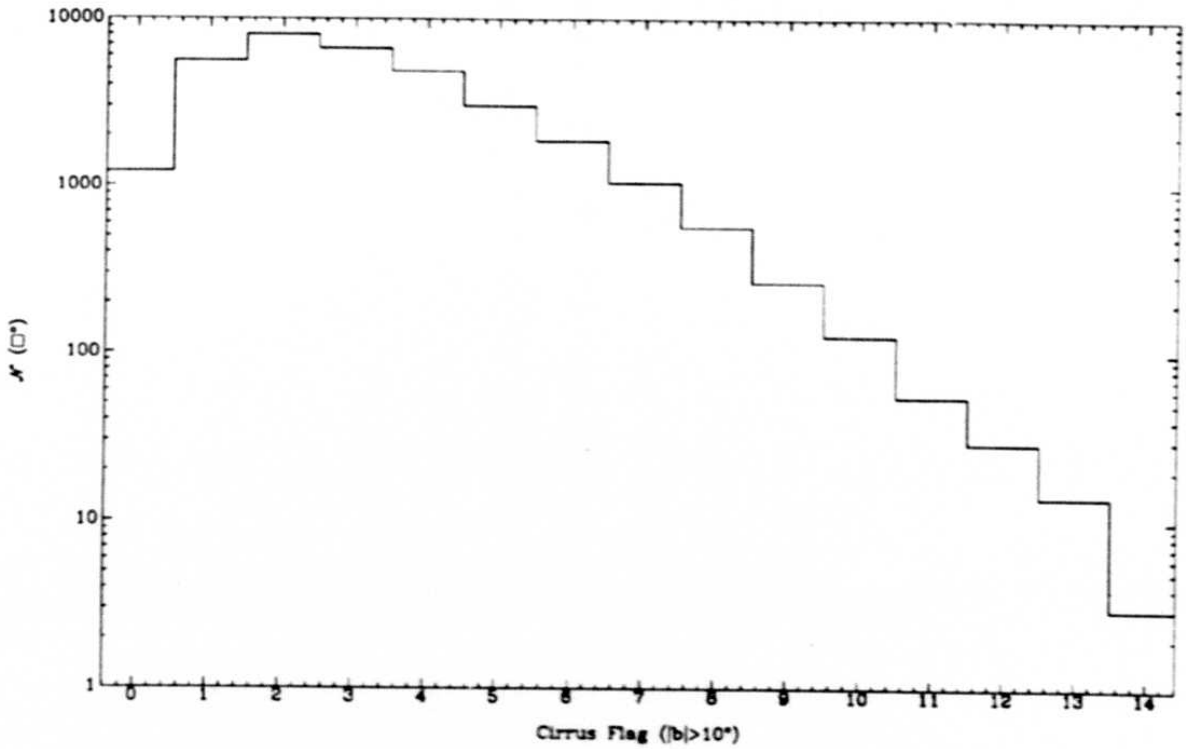

Figure III.G.10 Distribution of number of $\sim 1° \times 1°$ cells with a given cirrus flag for $|b| \geq 10°$.

not vary greatly in distribution at small angular scales. Thus, any rapid local increase in the number of 100 μm-only sources is attributable to cirrus, which, as mentioned, usually appears in the FSDB as chains or clusters of these objects.

The histogram of cirrus flag for $|b| \geq 10°$ can be seen in Figure III.G.10 and peaks at a cirrus flag of 2.

To illustrate the effectiveness of the cirrus flag as a tracer of local cirrus contamination, a plate which contains a respectable amount of filamentary structure has been selected (plate 968), and a grey scale plot of the FSS plate at 100 μm is seen in Figure III.G.11. In this figure the black contiguous regions are ridges from the cirrus structure; the dynamic range of this figure does not fully show the variations on small scales. In Figure III.G.12 all of the FSDB sources extracted within this plate are shown. The filled circles denote sources with a cirrus flag >2, while open circles denote sources with a cirrus flag $\leq$2. The high degree of correlation between cirrus structure in the sky and the cirrus flag is immediately seen.

The cirrus flag also can be used as another tracer of cirrus on scales larger than a plate. Figure III.G.13 shows the distribution of maximum observed cirrus flag on cells of

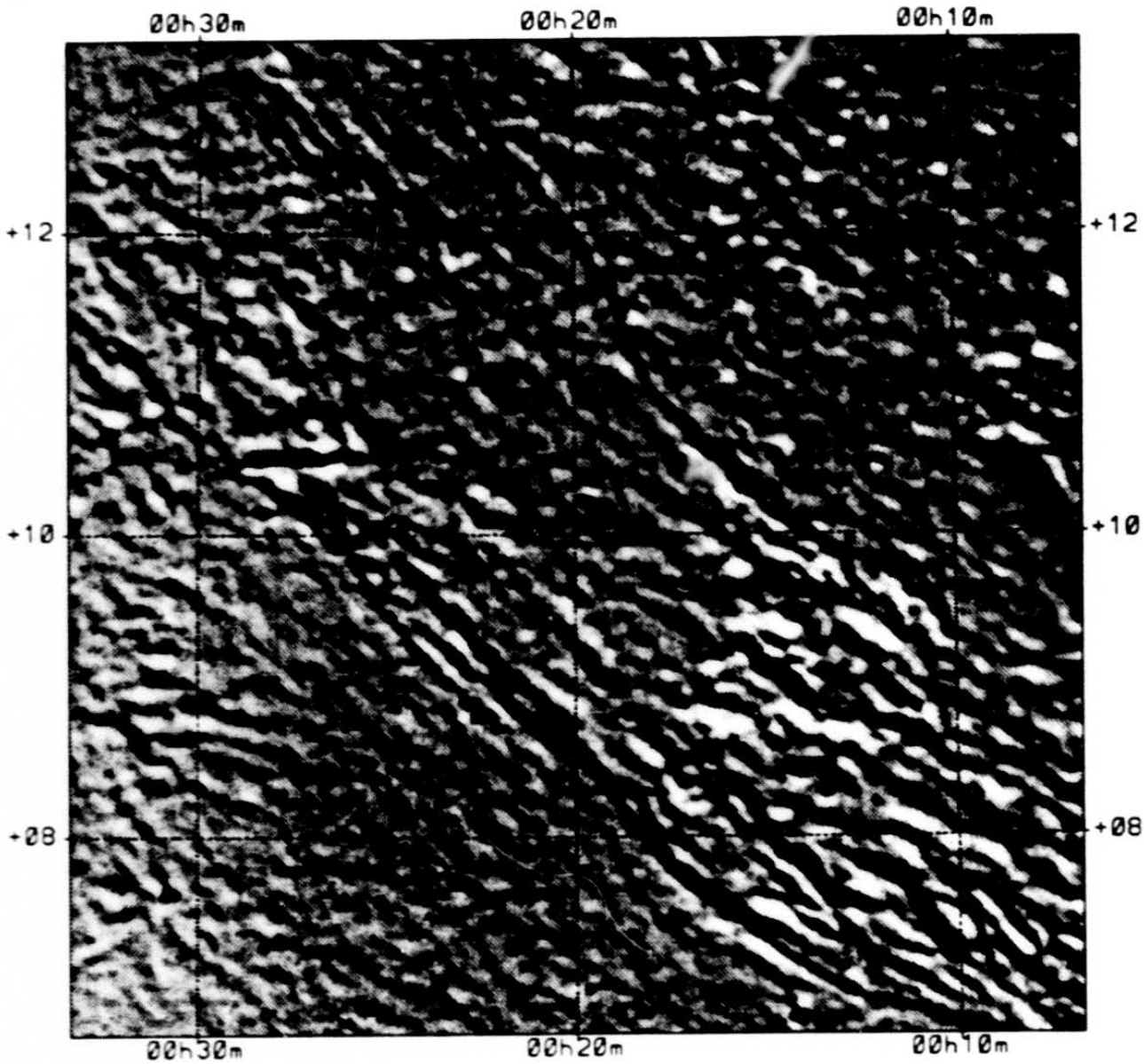

Figure III.G.11 Point source filtered image of FSS plate 968 at 100 μm.

size $\sim 1^\circ \times 1^\circ$ over the $|b| \geq 10^\circ$ sky. A comparison of this map with maps III.G.8 and 9 shows many similarities. However the map of cirrus flag shows more variation across the sky, the reason being that a high value of cirrus flag does *not* necessarily imply that a given source is a cirrus artifact, whereas a high value of FRATIO strongly indicates an extended source, which is most likely a piece of cirrus structure.

Despite these strong indications that the cirrus flag effectively maps cirrus on the sky, it does not perfectly discriminate against cirrus on a source-by-source basis. Reliable

D 10015

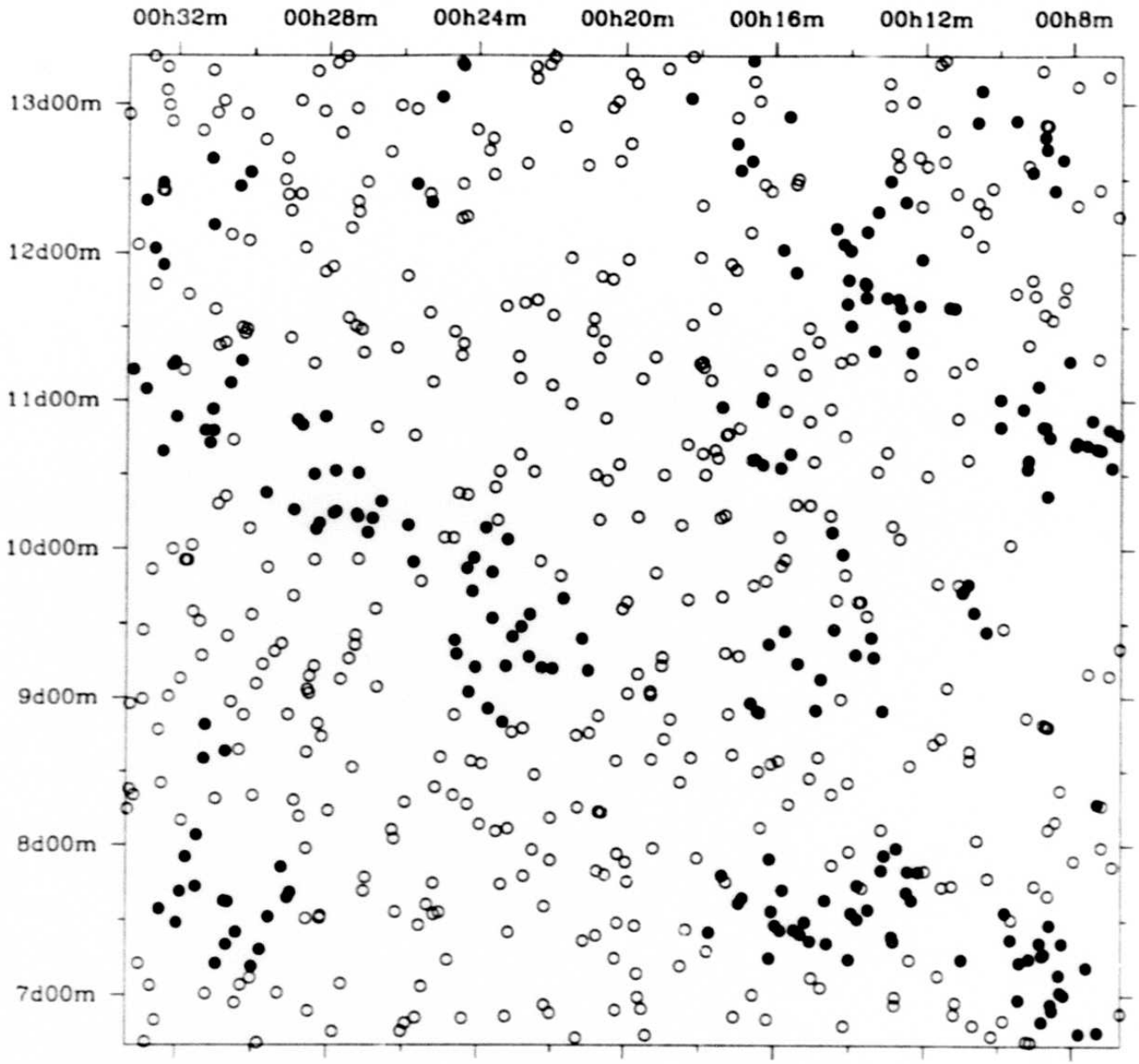

Figure III.G.12 Positions of all the FSDB sources in the area covered by Fig. III.G.11. Dark circles represent sources with high-cirrus-flag values (> 2), open circles denote sources with low values (≤ 2).

sources extracted in cirrus-contaminated regions can have high cirrus flags, even if they themselves are not cirrus contaminated. Furthermore, sources with high and low cirrus flags can mix together on very small angular scales (see Figure III.G.12); in these areas it is inevitable that some sources with low cirrus flags will be cirrus contaminated. Any segregation of sources based solely on the cirrus flag cannot separate cirrus from non-

287

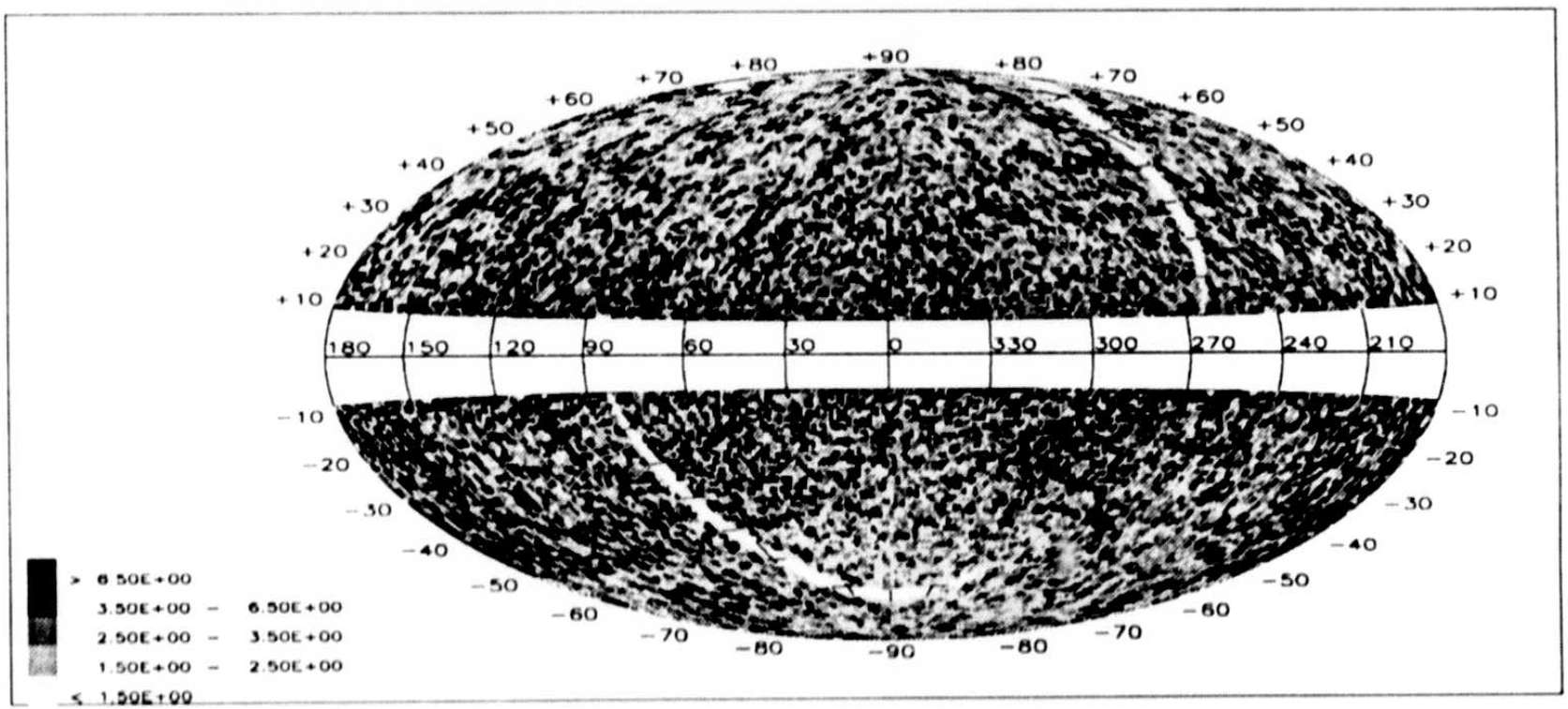

Figure III.G.13 Spatial distribution of the *maximum* value of cirrus flag on $\sim 1^\circ \times 1^\circ$ cells, in galactic coordinates. A value greater than 2 is usually indicative of presence of cirrus in the cell.

cirrus sources with complete accuracy. Nonetheless, we have concluded that the cirrus flag when used in conjunction with other parameters discussed in this section can be used to discriminate against cirrus.

To further illustrate the effects of selections based on cirrus flag, we consider the color temperature of sources of different cirrus flag values. For $|b| \geq 10°$ we selected all sources with detections at both 60 and 100 μm; furthermore to assure a reasonably complete sample we selected only sources with $f_\nu(60\ \mu m)$>0.35 Jy (see completeness maps in Section III.C). The distribution of color temperature, $\log(f_\nu(60\ \mu m)/f_\nu(100\ \mu m))$, was obtained for those sources with cirrus flag less than or equal to 2 and also those with cirrus flag greater than 2. The sample with cirrus flag ≤ 2 is seen in Figure III.G.14. This distribution has a median of -0.33, which is typical of extragalactic sources. In this distribution we can also see a warmer component due to stellar sources. We also observe a long tail into the very cold regions which indicate that some cirrus is still present in the sample. The distribution for sources with a cirrus flag greater than 2 seen in Figure III.G.15 shows two peaks; one can be identified with the external galaxies, and the second colder population as being due to cirrus artifacts. As was noted in the previous paragraph, the cirrus flag is not a perfect discriminant, and this fact shows up in Figures III.G.14 and 15. The low cirrus-flag sample is highly indicative of an extragalactic sample but with a hint of cirrus still present, and the high cirrus-flag sample shows the clear separation of external galaxies and cirrus. Thus selecting on cirrus flag alone will bring about a definite reduction in sample completeness with no guarantee that the resulting sample is completely cirrus-free. It is noted that in Figure III.G.15 the color temperature at which both cirrus and extragalactic populations are in equal proportion happens at $\log(f_\nu(60\ \mu m)/f_\nu(100\ \mu m)) \sim -0.75$; users of the *reject* file may wish to use this cut in color to make a *very* quick selection on sources.

The foregoing analyses have been based on a source-by-source study of structure in the sky. In what follows, the structure in the sky will be treated in a *global* sense.

G.7.d Noise Distribution Parameters

The source extractor computes two measures of noise on a localized basis (see Section II.E.2), the 68% and 87% quantiles of the flux density distribution. If the noise were Gaussian, the ratio of 87% quantile flux to 68% quantile flux would be 1.5 (see Section III.A.1). This ratio, called NOISRAT, has been found to trace the extended structures in the sky and has been used as a control parameter for determination of 60 μm reliabilities (see Section III.D.3.c for further details). NOISRAT denotes the deviation of the noise distribution from a Gaussian measured on a scale of $\sim 1.6° \times 1.6°$ (at 60 and 100 μm). Thus variations on smaller scales are smoothed and would not be reflected in this parameter.

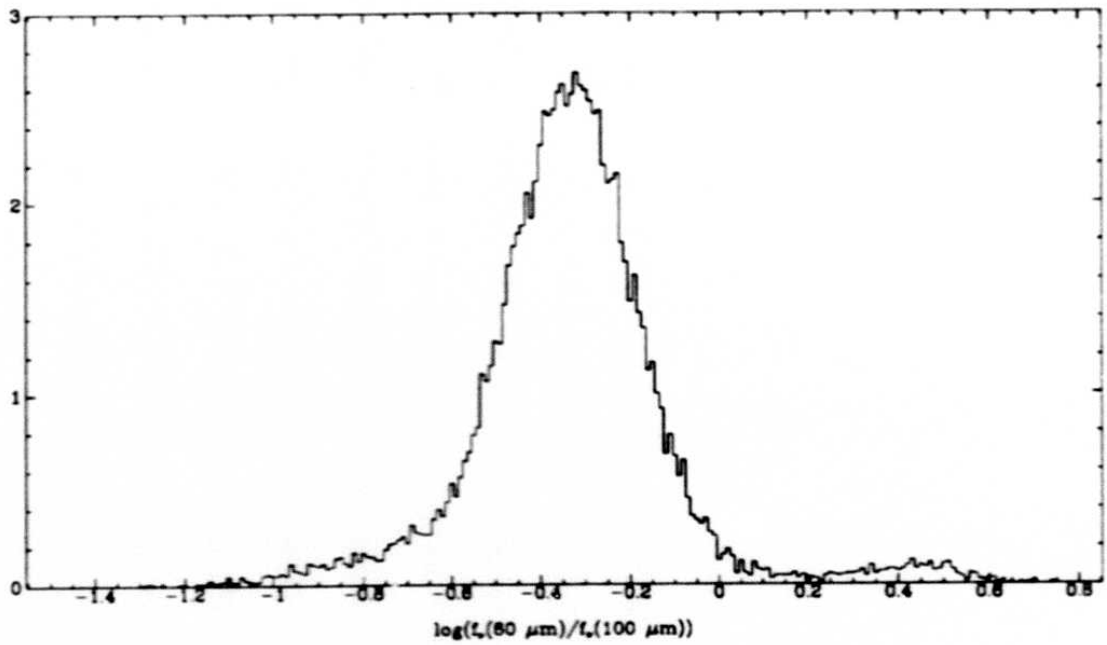

Figure III.G.14 Distribution function of $\log(f_\nu(60\ \mu m)/f_\nu(100\ \mu m))$ over the $|b| \geq 10°$ sky for 60-100 μm sources with $f_\nu(60\ \mu m)$>0.35 Jy, and cirrus flag≤2.

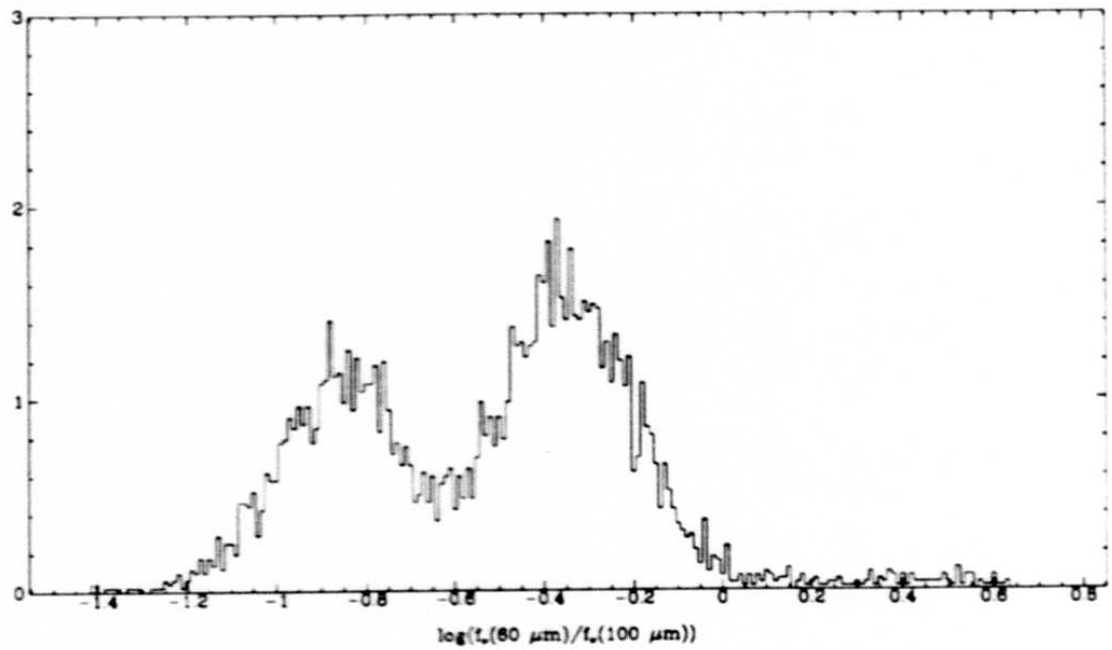

Figure III.G.15 Distribution function of $\log(f_\nu(60\ \mu m)/f_\nu(100\ \mu m))$ over the $|b| \geq 10°$ sky for 60-100 μm sources with $f_\nu(60\ \mu m)$>0.35 Jy, and cirrus flag>2.

It is however possible to combine the *point*-wise parameters FRATIO and cirrus flag with the NOISRAT maps to make masks for source selection purposes. In Figure III.G.16 the distribution of NOISRAT at 60 μm for $|b| \geq 10°$ can be seen. Empirically it is found that for NOISRAT $\gtrsim$ 1.7 the extragalactic source counts start to show noticeable deviations from the counts seen in areas of lower NOISRAT, and this observation has led to selecting a cut-off of NOISRAT=1.72 for allowing 60 μm detections to enter the FSC (also see Figure III.D.18 for a higher dynamic range of NOISRAT). In Figure III.G.17 magnified portions of Figure III.G.16 in the direction of Galactic Center and the Galactic anti-Center can be seen. These two maps show that the background can change rapidly over a scale of $\sim$1°. In Figure III.G.18 the distribution of NOISRAT at 100 μm can be seen. It is noted that all of the maps provided in this section show great consistency in delineating contaminated regions. A selection of sources based on a combination of the parameters discussed in this section would allow the user to obtain samples less tainted by cirrus. In summary, sources with FRATIO$\gtrsim$ 1.2 are usually extended, sources with cirrus flag > 2 are usually but not always cirrus contaminated, and sources lying in regions with NOISRAT$\gtrsim$ 1.7 are usually severely affected by the cirrus background.

G.8 Flux Density Overestimation

In any catalog of astronomical objects (for which the source counts at a given flux density decrease with increasing flux density) which is contaminated by noise, the flux densities of sources at the faint end are overestimated. When the source counts decrease with increasing flux density, the number of sources moved up in flux exceeds the number moved down. Consequently at a given apparent flux density f_0, the expectation value of the observed flux densities is higher than the *true* value f (which could have been obtained through an instrument with lower instrumental and confusion noise). The effect becomes appreciable at low SNRs (Murdoch, Crawford and Jauncey 1973) and becomes negligible with increasing SNR. The flux densities of sources in the FSDB are overestimated in this fashion at low SNRs (here referred to as a source-count-effect bias).

Furthermore, where a thresholding takes place (number of contiguous pixels, the LOC-SNR at the peak pixel, and the SNR, all exceeding set thresholds), noise fluctuations in the downward direction will take the candidates out of consideration. Upward fluctuations bring fainter sources above the threshold. As a result, just above the threshold the expectation value of the apparent flux densities is higher than the *true* value. The flux overestimation due to the thresholding effect operates at all SNRs (most of the overestimation is experienced within the range [$SNR_{threshold}$, $SNR_{threshold}+1$]): the previously

292

D 10013

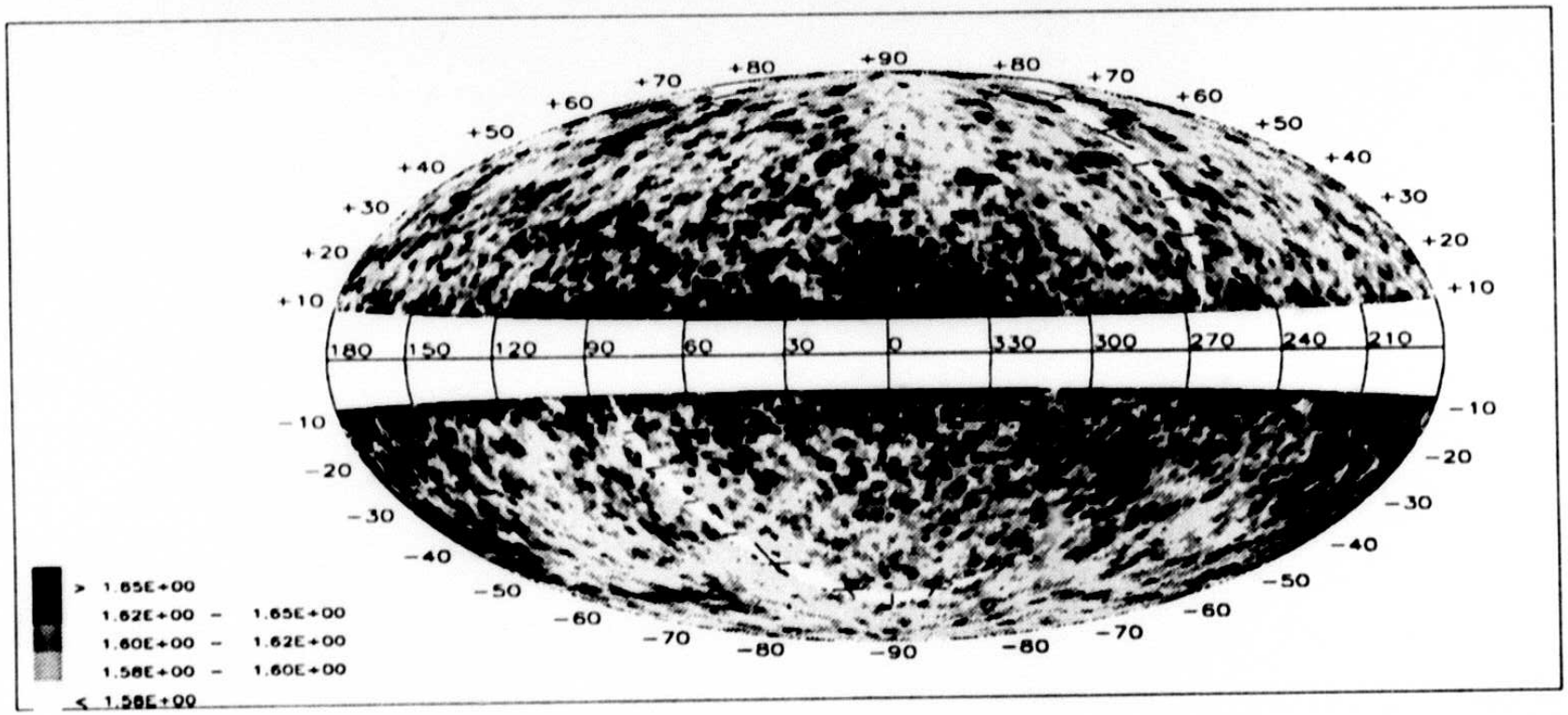

Figure III.G.16 Spatial distribution of the NOISRAT at 60 μm for $|b| \geq 10°$, the Aitoff projection is in galactic coordinates. See also Figure III.D.18 which displays the higher ranges of NOISRAT near the Galactic Plane.

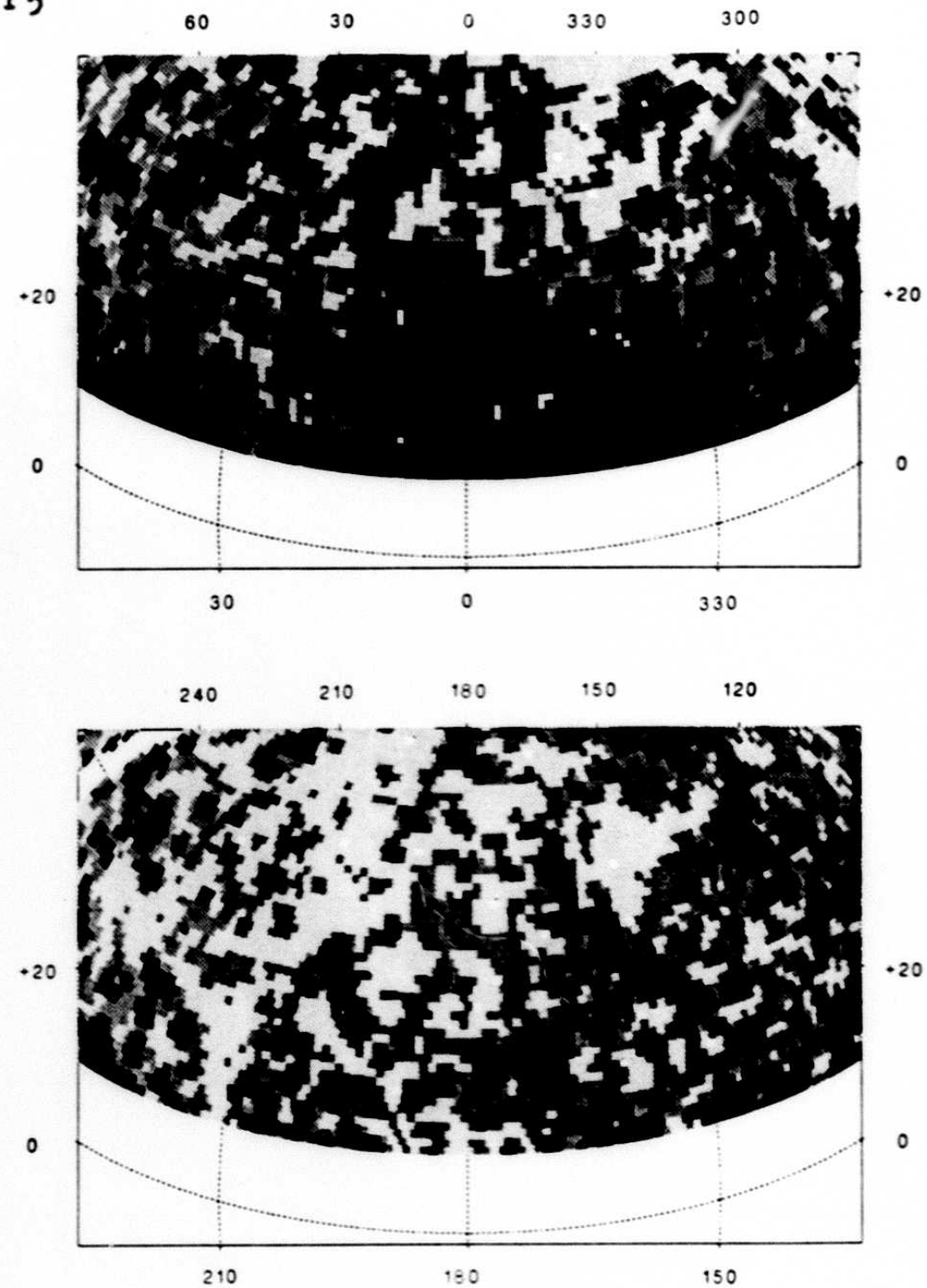

Figure III.G.17 Magnified portions from Figure III.G.16. The upper figure is in the direction of the Galactic Center (the dark region at the center is part of the Ophiuchus complex), and the lower figure is in the direction of the Galactic anti-Center. The rapid variation of NOISRAT on scales of ~1°should be noted. The orthographic projection is in *galactic* coordinates.

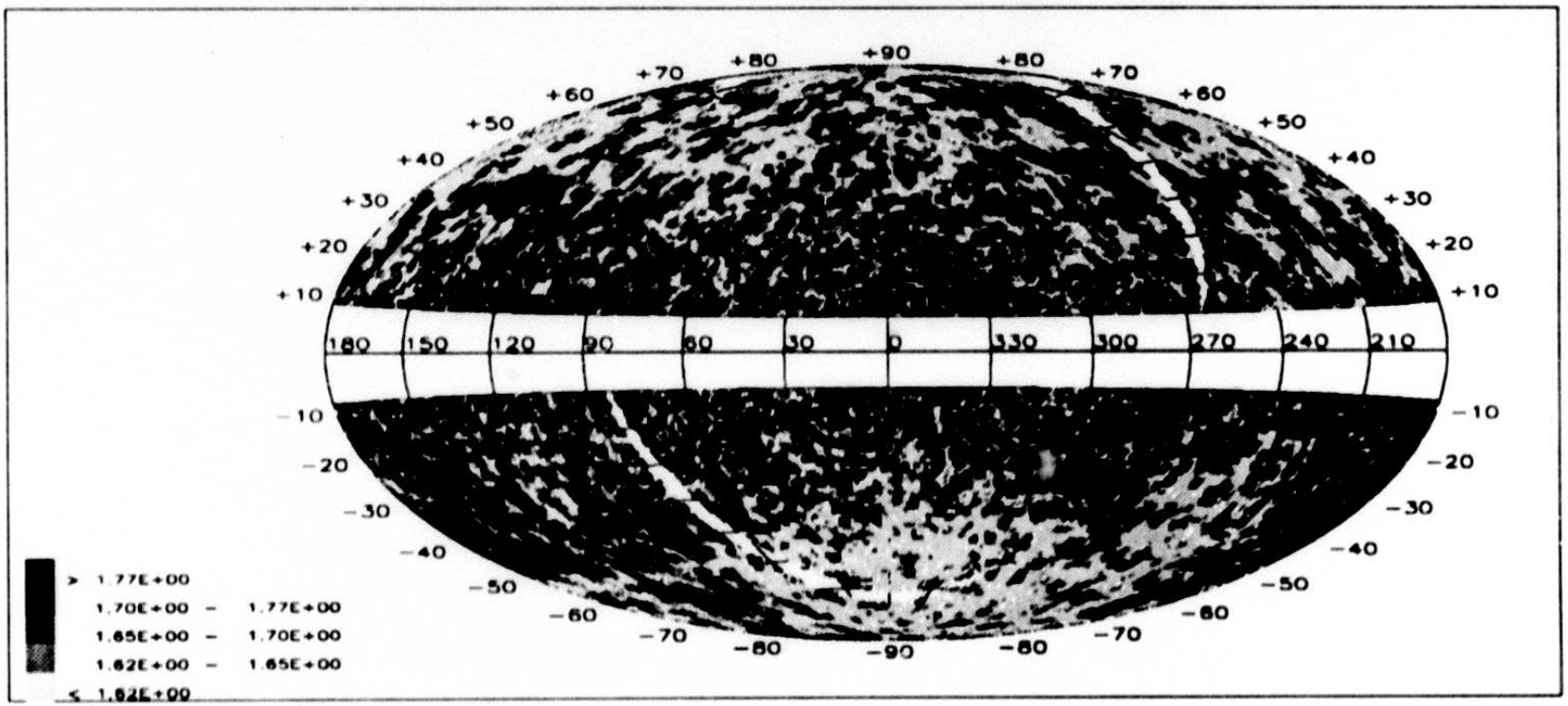

Figure III.G.18 Spatial distribution of the NOISRAT at 100 μm for $|b| \geq 10°$, the Aitoff projection is in galactic coordinates. A value $\gtrsim 1.7$ is usually indicative of presence of cirrus in the cell.

discussed source-count-effect bias is present at all SNRs, but becomes unimportant with increasing SNR.

In this section various estimates for the flux density overestimation are given. Users are also cautioned that the interpretation of the data at the faint end of the FSDB requires special attention to the manner in which sources are chosen for a given analysis. To illustrate the problem of source selection, stellar sources of the type K0 III, detected at both 12 and 25 μm will be considered in detail. It will be seen that the color-temperature derived from 12 and 25 μm detections decreases as the flux density at 25 μm is reduced. This behavior is attributable to a flux density overestimation at 25 μm.

To notice the effect it is important to treat one category of sources where a given astrophysical quantity (for example a temperature) is not expected to change as a function of apparent source brightness. It is feasible to use stellar data to study the problem at 25 μm, and to some extent at 60 μm. However, it is not possible to use the same method at 12 and 100 μm. We can only surmise that the behavior at 12 μm may be similar to 25 μm (the only similarity is that both spectral bands predominantly detect stellar sources with source counts of slope $\sim$1).

The analysis to follow indicates that the expected flux density overestimation at 25 μm is $\sim$2% at SNR$\sim$5. At 60 μm the overestimation is conjectured to be *at most* $\sim$6% at SNR$\sim$5. However we caution that the 60 μm data do not yield as convincing a result as at 25 μm.

G.8.a Overestimation at 25 μm

For this analysis, sources with detections at both 12 and 25 μm (which were located in areas of sky with 25 μm thresholding noise less than 30 mJy) were selected from the FSDB (*not* the FSC). Furthermore, the sample was confined to those which were associated to spectral types K0 (the majority of these sources are of luminosity class III) which show little evidence of true IR excess. The scatter plot of color at 12 and 25 μm as a function of brightness at 25 μm is seen in Figure III.G.19.

If the median 12 μm - 25 μm color of this scatter diagram is computed at various SNRs, a measure of flux density overestimation at 25 μm may be obtained, as displayed in Figure III.G.20. In this figure, the trend at high SNRs has been used to determine the expected trend at all SNRs. This figure indicates that at SNR$\sim$4 the overestimation may be as high as 15%.

The previous analysis suffers from one flaw. Thresholding at 25 μm leaves a partially complete sample at low values of SNR(25 μm). Figure III.G.21 shows the distribution

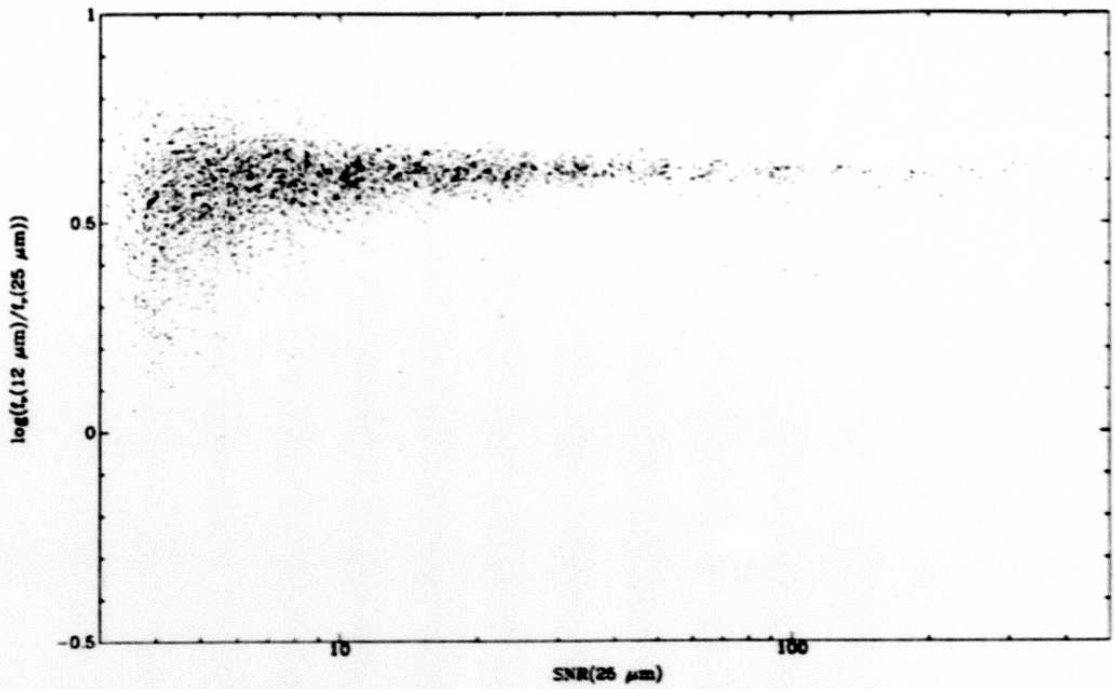

Figure III.G.19 Scatter plot of $\log((f_\nu(12\ \mu m)/(f_\nu(25\ \mu m))$ vs the SNR at 25 μm for a population of 12 and 25 μm sources which are associated with stellar sources of type K0 III.

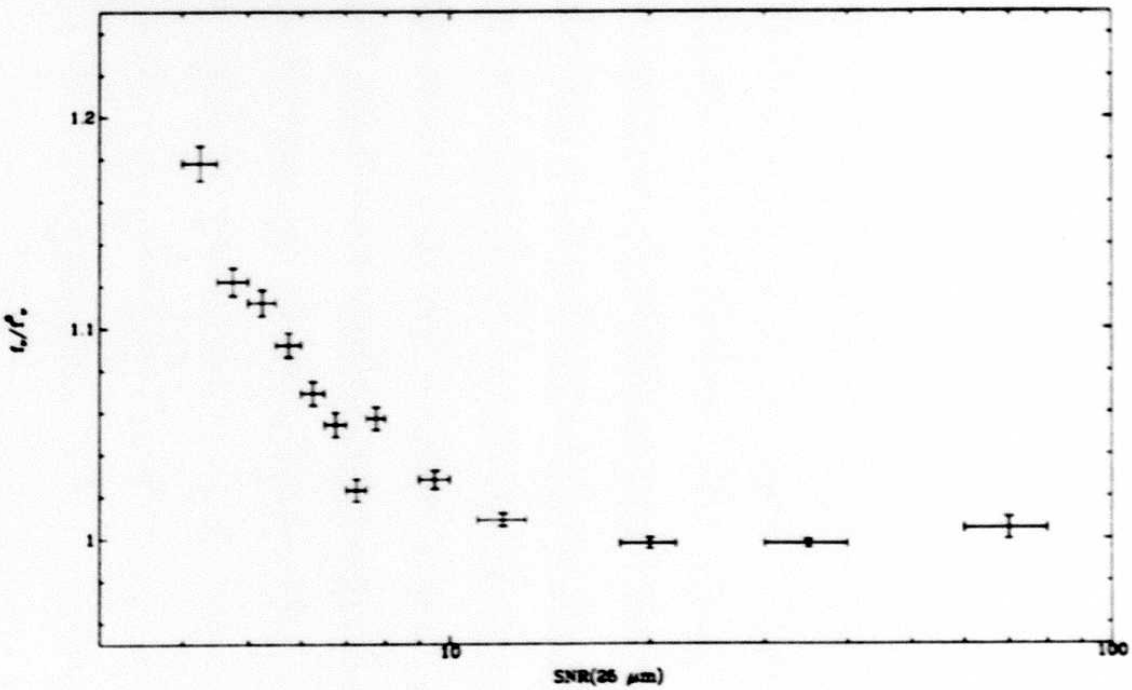

Figure III.G.20 Flux density overestimation (almost all due to thresholding effects, see the text) at 25 μm as a function of SNR at 25 μm, f_ν is the observed flux density and f_ν^0 is the expected flux density.

of 12 μm - 25 μm color as a function of SNR(12 μm). It is clearly seen that below SNR(12 μm)~15 the observed colors are mostly cold. The dispersion in color is expected to increase as sources become fainter (due to increased uncertainties at both 12 and 25 μm, in addition to an intrinsic spread in color). Below SNR(12 μm)~15, the effects of thresholding at 25 μm manifest themselves. Those sources which are pushed down in flux density at 25 μm fall below the extraction thresholds and thus the 'warm' population is severely depleted, whereas fainter sources pushed up in flux show up as an enhancement of the 'cold' population. For an unbiased analysis, those sources should be used which would still be present in the figure if their LOCSNR were as low as the selection threshold and still had a SNR above some fixed value (a value which would guarantee reasonable sample completeness, taken to be 4.0 for this analysis). Therefore, points in Figure III.G.21 are restricted by selecting sources such that $f_\nu(25\ \mu m) > f_\nu^{limit}(25\ \mu m)$, where for each source an effective "4 σ" limiting flux density $f_\nu^{limit}(25\ \mu m) \equiv \max(f_\nu(25\ \mu m)/SNR(25\ \mu m) \times 4.0, f_\nu(25\ \mu m)/LOCSNR(25\ \mu m) \times 4.0)$ is defined. In addition, at the limiting flux density $f_\nu^{limit}(25\ \mu m)$, the distribution of 12 μm - 25 μm color would be very wide; we require that for the source under consideration this limiting flux should be such that the resulting limiting 12 μm - 25 μm color would span the 'warm' population as well. This last condition can be satisfied by requiring that $\log(f_\nu(12\ \mu m)/f_\nu^{limit}(25\ \mu m)) \geq 0.75$. (The value 0.75 was selected from an inspection of Figure III.G.19, where several faint sources are seen to have a color even 'warmer' than 0.75.) As a result, the scatter diagram in Figure III.G.22 is obtained. We have removed the effects of thresholding from this figure, thus a trend to cooler temperatures in this figure would be indicative of flux overestimation.

Consequently, the flux density overestimation is measured for the sample defined in Figure III.G.22 as a function of SNR at 12 μm (eventually SNR(12 μm) is converted to an effective SNR at 25 μm). The variation of color as a function of SNR(12 μm) is seen in Figure III.G.23. The same figure is transformed into an overestimation plot as a function of SNR(25 μm), which is displayed in Figure III.G.24.

The previous two step process requires a transformation of SNR from 12 μm to an effective SNR at 25 μm. The 12 μm - 25 μm color for the brightest sources, along with the distribution of threshold noises at 12 and 25 μm (which is seen in Figure III.G.25) have been used for this purpose.

Finally, the expected flux density overestimation at 25 μm is found to be $\approx$2% at SNR~5. Since the effects of thresholding have been accounted for (almost completely, but we stipulate that our selection criteria may not have been 100% complete), the observed overestimation may be attributed to a source-count-effect bias.

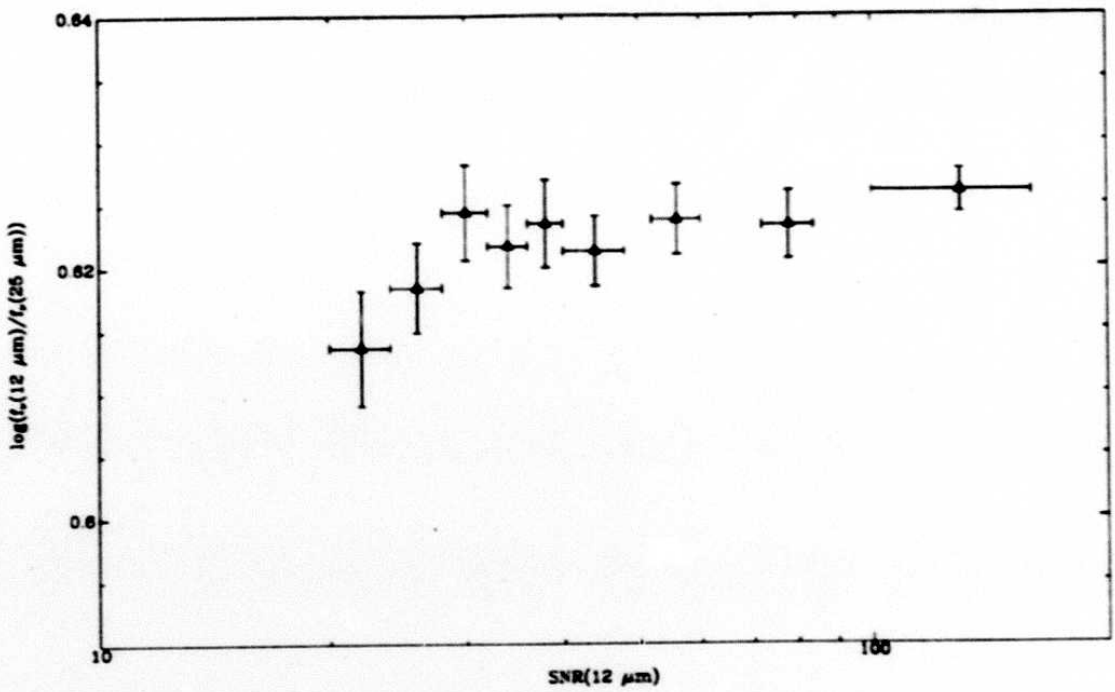

Figure III.G.23 Variation of $\log((f_\nu(12\ \mu m)/(f_\nu(25\ \mu m))$ with SNR at 12 μm for a population of K0 III sources detected at 12 and 25 μm.

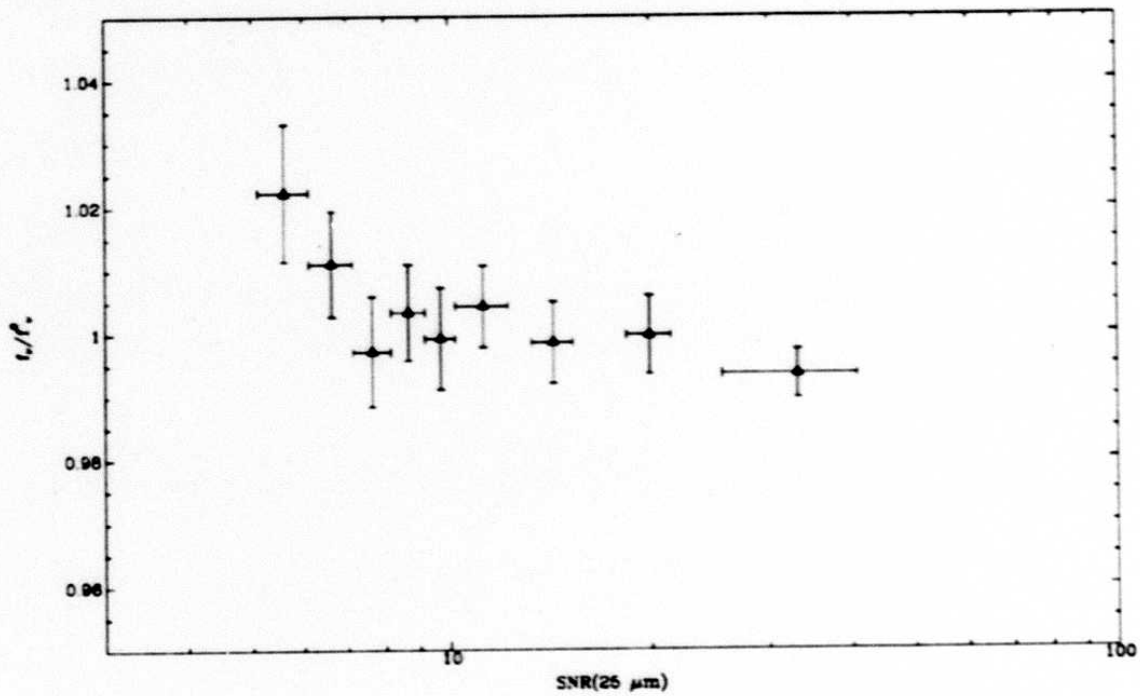

Figure III.G.24 Flux density overestimation (ratio of observed to predicted flux density) at 25 μm as a function of the SNR at 25 μm.

D 10015

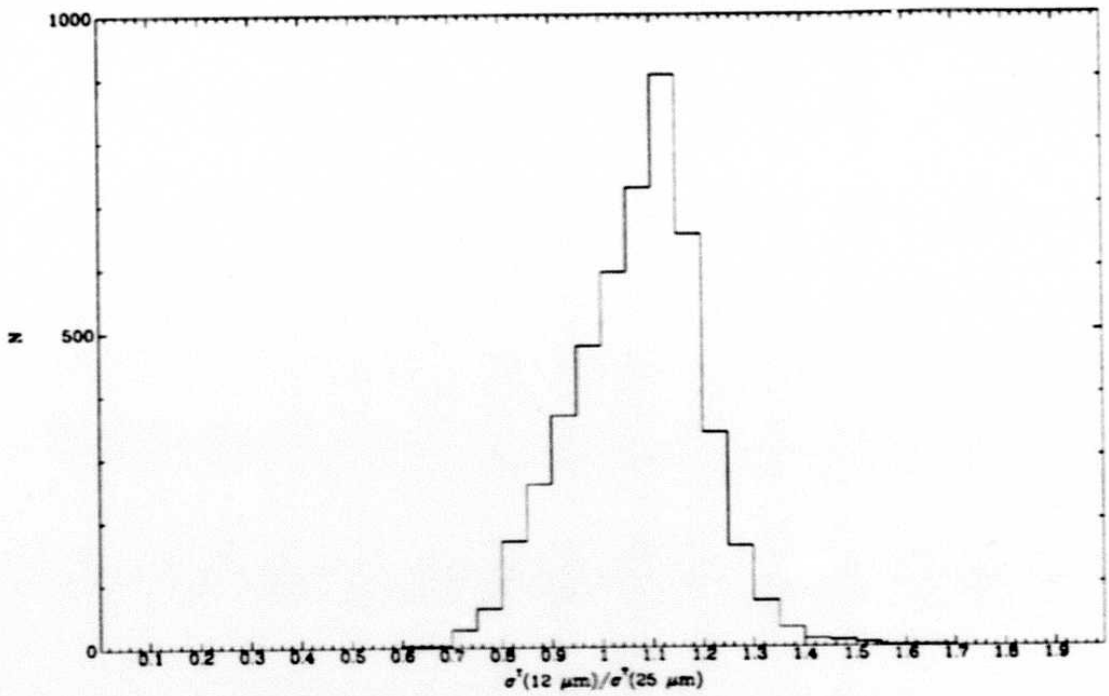

Figure III.G.25 Distribution of the ratio of threshold noises at 12 and 25 μm for the region containing selected K0 III sources.

G.8.b Overestimation at 60 μm

The 60 μm result is obtained similarly. Sources with detections at 12, 25, and 60 μm (within areas having 25 and 60 μm thresholding noises less than 30 and 60 mJy respectively, and the 60 μm NOISRAT less than 1.72) were selected from the FSDB, the sample was further confined to cases where the sources were of spectral type K0.

Employing the arguments presented in Section III.G.8.a, the sample was confined to those sources which would still be present in the plot if they were observed at the extraction thresholds. Analysis of 25 μm - 60 μm color variation was performed with respect to the SNR at 25 μm and then the effective SNR at 60 μm was computed. Variation of 25 μm - 60 μm color with SNR at 25 μm is seen in Figure III.G.26. From these data the flux density overestimation at 60 μm is computed, which is seen in Figure III.G.27.

The number of sources in the 12 and 25 μm sample was sufficiently large that the flux overestimation at 25 μm could be readily seen. On the other hand, the total number of sources in the 12, 25, and 60 μm sample was only 139. As a result, conclusions regarding the 60 μm flux overestimation are not as convincing. At low SNRs ($\lesssim$5), the effects due to sample incompleteness (at 60 μm) manifest themselves by the presence of more sources with cooler temperatures. Thus, the measured flux overestimation may still be influenced

300

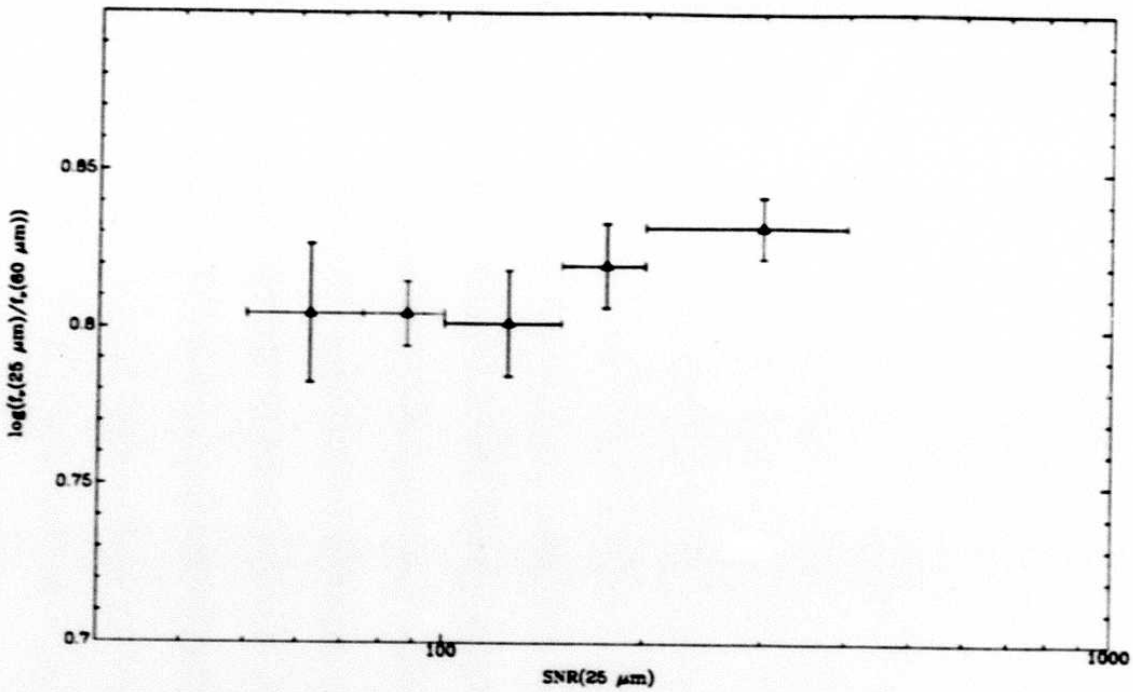

Figure III.G.26 Variation of $\log((f_\nu(25\ \mu m)/(f_\nu(60\ \mu m))$ with SNR at 25 μm for a population of K0 III sources detected at 12, 25, and 60 μm.

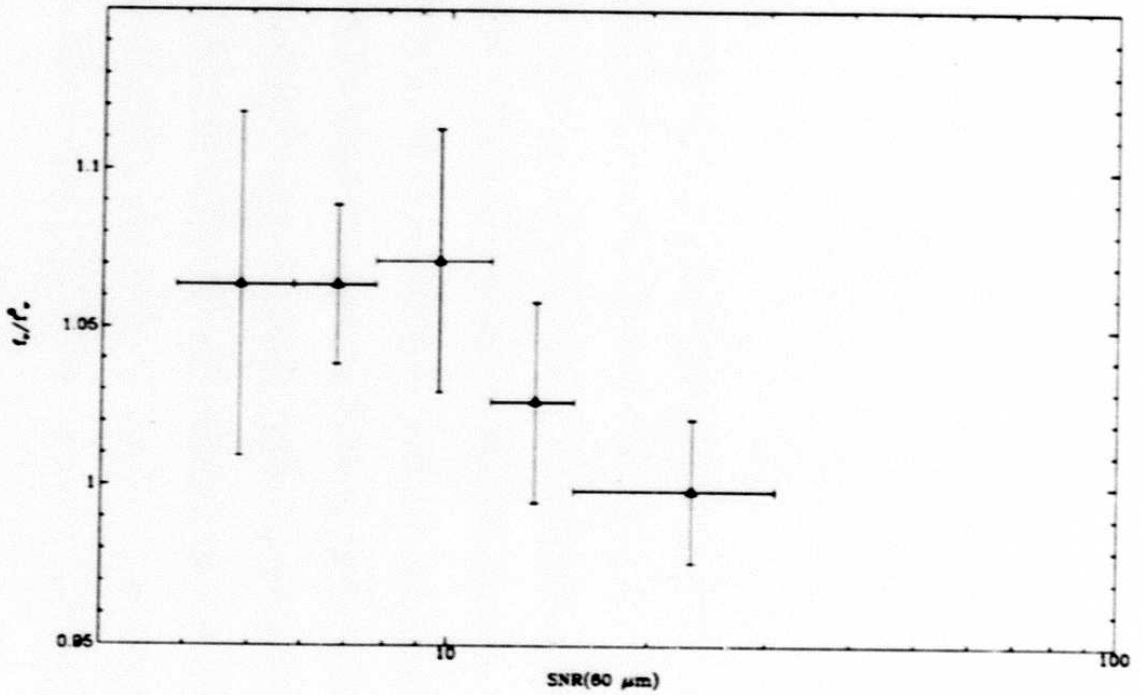

Figure III.G.27 Flux density overestimation (ratio of observed to predicted flux density) at 60 μm as a function of the SNR at 60 μm.

301

by thresholding effects. Even though Figure III.G.27 indicates a flux overestimation of ~6% at SNR~5, this value should be treated as *an upper limit to the true* 60 μm *flux density overestimation*.

D 10015

H. Ranges of Catalog Parameters

Tables III.H.1, 2, and 3 show the ranges of all parameters contained in the FSC. Table III.H.1 shows the ranges of FSC parameters not related to flux-density measurements in specific bands. Table III.H.2 shows the ranges of band-related parameters, sometimes broken down by flux-density quality. Table III.H.3 shows the ranges of values for the associations in the FSC. See Section V.C for a definition of the parameters named in these tables.

TABLE III.H.1 Band-Independent FSC Extrema*

Parameter	Minimum	Maximum
RA	$00^h00^m00.4^s$	$23^h59^m59.1^s$
DEC	−89°54′47″	89°42′53″
UNCMAJ	3″	55″
UNCMIN	1″	13″
POSANG	0°	179°
MINREL	80	99
CONFUSE	0	12
CIRRUS	0	14
CATNBR	0	7
NID	0	27
IDTYPE	0	15

* No extrema information is given for character data, such as the NAME parameter.

303

TABLE III.H.2 Band-Dependent FSC Extrema

Parameter	FQUAL	12 μm MIN	12 μm MAX	25 μm MIN	25 μm MAX	60 μm MIN	60 μm MAX	100 μm MIN	100 μm MAX
FQUAL	–†	1	3	1	3	1	3	1	2
FNU	=1	0.015	23	0.016	173.9	0.049	2592	0.128	10700
(Jy)	>1	0.031	9941	0.028	6583	0.091	12290	0.345	19190
	=2	0.031	252	0.028	409.9	0.091	12290	0.345	19190
	=3	0.038	9941	0.040	6583	0.119	1089	–¶	–¶
RELUNC	=1	0‡	38	0‡	41	0‡	41	0‡	39
(%)	>1	1	39	1	42	1	32	1	33
SNR	>1	2.6	3.5×10^5	2.4	1.5×10^5	3.1	1.3×10^5	3.1	8500
	=2	2.6	6500	2.4	1.1×10^4	3.1	1.3×10^5	3.1	8500
	=3	4.8	3.5×10^5	6.1	1.5×10^5	4.9	2.5×10^4	–¶	–¶
LOCSNR	>1	3.5	260	3.5	240	3.5	300	3.5	77
	=2	3.5	83	3.5	80	3.5	91	3.5	77
	=3	3.5	260	4.5	240	3.5	300	–¶	–¶
AREA	>1	6	737	6	529	6	272	12	354
NOBS	>1	4	198	4	166	4	202	4	213
XTNBR	–†	0	6	0	6	0	5	0	4
NOISCOR	>1	.97	4.27	.97	4.77	1.05	15.75	1.20	20.12
NOISRAT	>1	1.497	2.723	1.488	4.267	1.463	5.120	1.016	7.529

† Any FQUAL

¶ FQUAL =3 was never assigned to a 100 μm flux density in the Version 2 catalog.

‡ For sources with too little coverage an uncertainty on the upper limit cannot be computed.

D 10015

TABLE III.H.3 Associations Data Extrema¶

Parameter	Minimum	Maximum
RECNO	2	173043
CATNO	1	50
RADIUS	0″	833″
POS	0°	359°
DSTMAJOR	0″	599″
DSTMINOR	0″	600″
FIELD1	−999†	9999‡
FIELD2	−999	9999
FIELD3	−999	9999

¶ No extrema information is given for character fields, such as parameters TYPE or SOURCE.

† −999 is the FIELD1-3 indicator for "no information available".

‡ 9999 is the value given for the FIELD1-3 parameters when the true value has overflowed, i.e. saturated.

305

D 10015

Authors:

Section A	M. Moshir, G. Kopan, G. Rohrbach, and T. Ch ster
Section B	M. Moshir
Section C	M. Moshir, D. Gregorich, G. Kopan, and T. Chester
Section D	M. Moshir
Section E	P. Hacking and M. Moshir
Section F	W. Rice, L. Hermans, T. Conrow, and M. Moshir
Section G	M. Moshir, T. Conrow, L. Fullmer, and D. Gregorich
Section H	T. Conrow

306

D 10015

IV. COMPARISON OF THE FAINT SOURCE CATALOG TO OTHER IRAS PRODUCTS

A. Comparison of the FSC to the PSC

A.1 Introduction

Nearly all PSC sources unaffected by coverage differences between the catalogs are found in the FSC, with the exception of many 100 μm PSC sources, which are likely due to the infrared cirrus. Some areas of the sky covered by the PSC are not covered by the FSC in one or more wavelength bands. These coverage differences must be taken into account when comparing the FSC to the PSC; many PSC sources one might otherwise expect to see in the FSC may be absent if they lie in a region left unsurveyed by the FSC.

With the caveats above in mind, some general numbers are:

- The FSC contains 173,044 sources for $|b| > 10°$, as compared to 102,178 sources in the PSC in the same region. Not appearing in the PSC and lying below its 95% completeness threshold are 98,000 new FSC sources.
- For $|b| > 20°$, which was surveyed by the 60 μm band in the FSC (cf. Section IV.A.4 below), there are 120,236 FSC sources, compared to 59,498 sources in the PSC. Of the $|b| > 20°$ FSC sources, 71,000 are new.
- Nearly 73,000 sources are common to both the PSC and the FSC for $|b| > 10°$. Of these common sources, 45% gained one or more bands in the FSC, 2% lost one or more bands, 51% stayed the same, and the rest both gained and lost bands.

Processing differences between the two catalogs resulted in slightly different positions and flux densities for sources common to both catalogs. The positional accuracy of the FSC is equal or superior to that of the PSC except in the cross-scan direction for bright 12 μm sources, where the PSC is $\sim$ 20% better due to the availability of more information and the use of more sophisticated algorithms.

Flux density estimates of the two catalogs agree (with a dispersion of about 7%) and show no significant differences in a comparison to a stellar predictive model at high SNR. For low SNR values, below SNR $\sim$ 10 in the PSC, the FSC provides more accurate flux densities.

Section IV.A.2 describes in detail the intersection of the PSC and the FSC, including changes in band structure and comparisons of positions and flux densities between the two catalogs.

Section IV.A.3 discusses the FSC sources not found in the PSC. Most, of course,

307

represent new sources in the FSC. About a quarter, however, are present in the PSC Reject file (PSCR) and were excluded from the PSC because they were insufficiently confirmed.

Section IV.A.4 discusses those PSC sources not present in the FSC. Nearly a third (29%) of the $|b| > 10°$ PSC sources are missing from the FSC. Large parts of the $|b| > 10°$ sky were essentially not covered in one or more bands by the processing which produced the FSC. PSC sources detected in the affected bands in such regions of sky were often left out of the FSC. Another large segment of missing PSC sources are 100 μm sources generated by the infrared cirrus. Excluding these two categories, less than 3% of the $|b| > 10°$ PSC sources are missing from the FSC; most of their absences are explained by insufficient coverage, asteroid contamination, resolved sources or confusion.

Figure IV.A.1 is a pictorial summary of this section.

A.2 Sources Common to the FSC and the PSC

A.2.a Changes in Band Structure

Of the FSC sources, 42% are associated to the PSC (Section II.G.3). These are the sources that are readily identifiable as being common to both catalogs. The enhanced sensitivity of the FSC, combined with differences in processing, have often resulted in changes in the band structure of these sources. For example, 45% of the PSC sources common to the FSC have at least one additional flux density measurement in the FSC. A further delineation of the changes in band structure follows. See Figure IV.A.2 for a graphical representation of this section.

Table IV.A.1 shows a spectral decomposition of the PSC sources common to the FSC. The first column lists the possible band combinations, encoded in the following fashion: The presence or absence of a measured flux density (high or moderate flux-density quality) in a given band is denoted by "1" or "0". Measurements at 12, 25, 60, and 100 μm are encoded, from left to right, as the digits of a four-digit number. Thus, a source measured only at 12 μm is represented as "1000", while one measured at 12 and 60 μm is denoted by "1010". The second column gives the percentage of the total PSC associations that are of the specified band type. For example, 39% of the PSC sources common to the FSC are detected only at 12 μm in the PSC.

Table IV.A.1 also gives the corresponding FSC band combinations for each PSC type. Using the same coding scheme as above, all possible FSC band combinations are listed across the top of the table. For a given PSC type, reading across a row gives the resulting band structures in the FSC as a percentage of the PSC sources in that category. Continuing the example from the previous paragraph, Table IV.A.1 shows that 37% of the PSC sources

D 10015

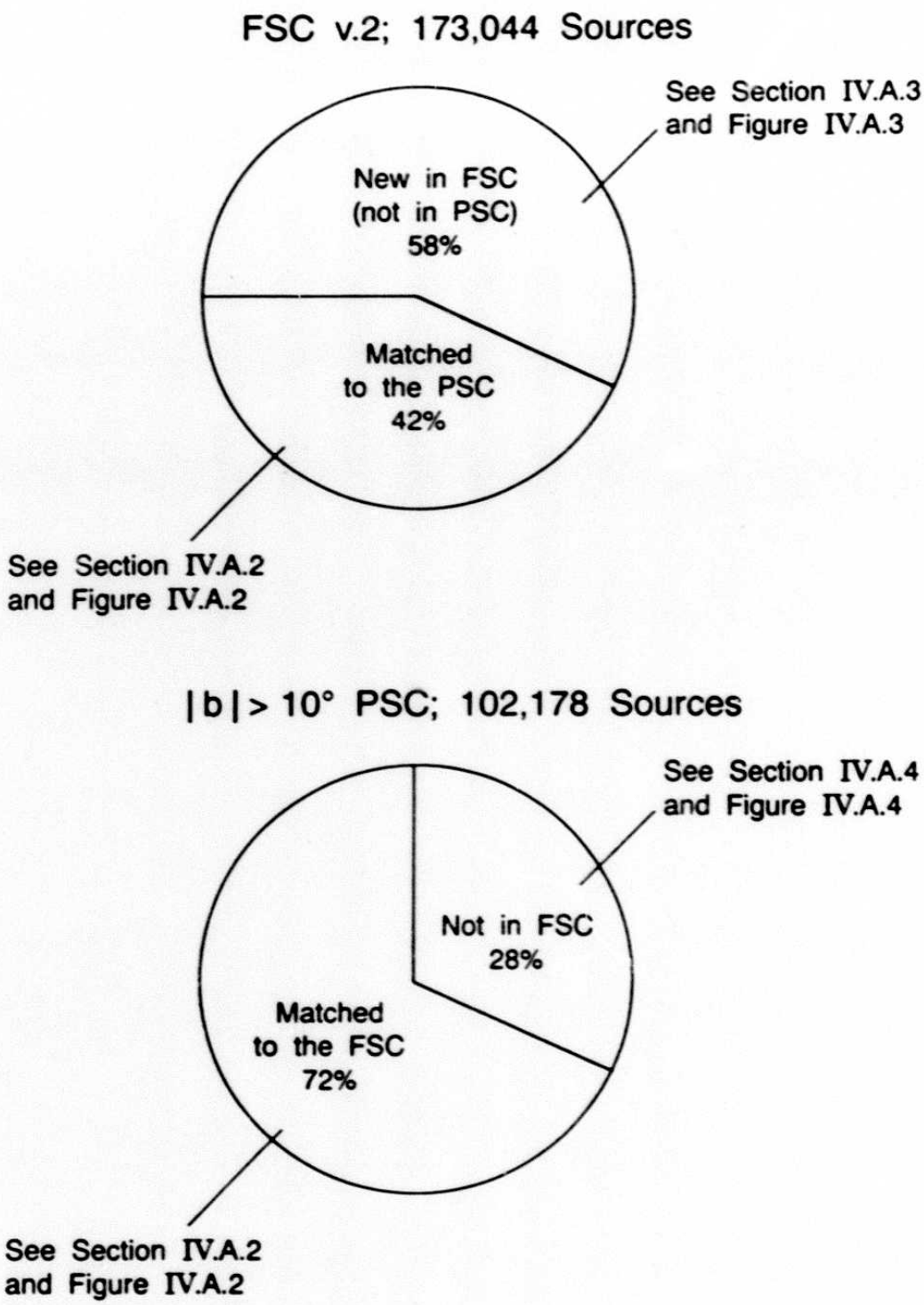

Figure IV.A.1 Pictorial comparison of the FSC and PSC source contents for |b| >10° .

309

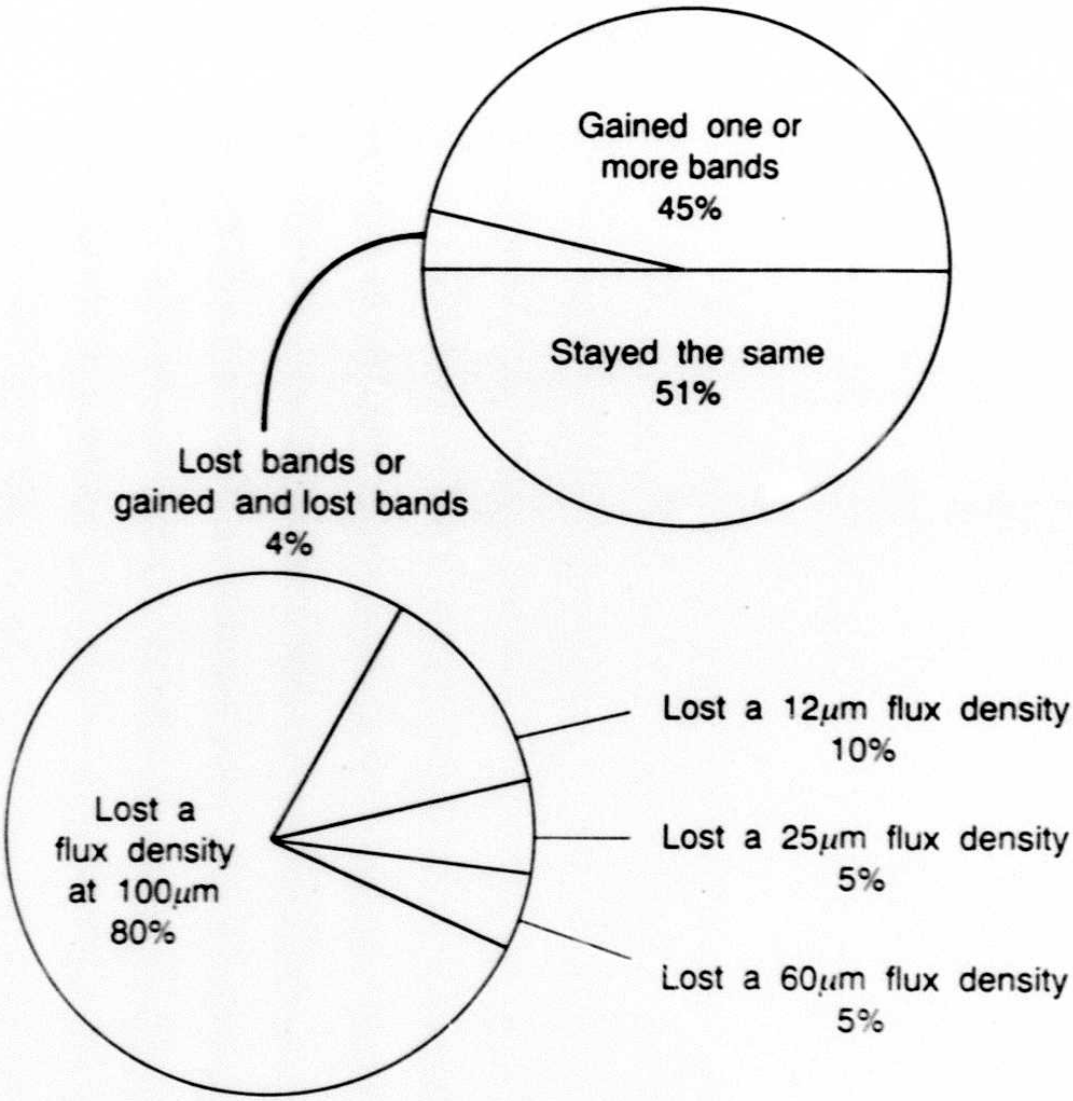

Figure IV.A.2 Changes in band structure for sources common to the FSC and the PSC for $|b| > 10°$.

detected only at 12 μm were also detected only at 12 μm in the FSC, whereas 62% gained a flux density at 25 μm, with the remaining 1% scattered over several columns indicated by a dash in each applicable band combination in the table. Blanks in the table indicate zero percent in the given category.

The table reveals that, in a very few cases, the original bands detected in the PSC are

Table IV.A.1 FSC Spectral Classification vs. PSC Spectral Classification (%)

PSC Band Combination†	% of PSC Sources with this Combin.	FSC Band Combination†														
		1000	1100	1110	1111	0100	0110	0111	0010	0011	0001	1101	1010	1011	1001	0101
1000	39	37	62	-‡	-	-					¶	-	-	-		
1100	24	-	83	15	-	-	-					-	-	-		
1110	4	-	5	89	5	-	-	-					-	-		
1111	2	-	3	19	76	-	-	-		-		-	-	-	-	
0100	-	2	43	18	1	27	9	-								
0110	-	1	7	35	9	6	30	10	-	-		-		-		
0111	3	-	1	5	63	-	3	25	-	1		-		-		
0010	6	-	-	2	-	-	12	10	31	40			1	-		-
0011	15	-	-	-	14	-	2	25	4	47			-	6	-	-
0001	3	3	-	-	1		-	4	16	71		-	-	3	-	
1101	-	1	62	20	11	-	-					4	-			
1010§	-	13	29	37	7		1			1			10	2		
1011§	-	8	15	11	48	1	1	3	1				3	5		
1001	-	24	55	5	3							5	3	2	3	
0101§	-	5	29	14	14	14		10		10		5				

† Example: 1000 = high- or moderate-quality flux density at 12 μm only; 1010 = high- or moderate-quality flux densities at 12 and 60 μm; etc.

‡ - = fewer than 1% of sources in this category.

¶ Sources detected only at 100 μm were not allowed in the FSC.

§ These categories have fewer than 100 associations to the FSC.

completely absent from their FSC associations. (Look, for example, at the row describing PSC 100 μm-only sources, labeled "0001"). Many of these are extended objects of some sort, which are "broken" into 2 or more sources by the FSC or the PSC. Differences in source extraction and bandmerging give these "pieces" different band structures in the two catalogs. In other cases, a PSC flux density, almost always a 100 μm flux density, was eliminated from the FSC for reasons described in Section IV.A.4.

Summarizing the results in Table IV.A.1, 45% of PSC sources in the FSC have at least one additional band in the FSC, 51% have the same band structure in both catalogs, 2% lost one or more bands and 2% both lost and gained bands. Of those 4% of the common sources which either lost bands or both gained and lost bands, 80% included the loss of a flux density at 100 μm. The remaining 20% of missing flux densities (10%, 5% and 5% at 12, 25 and 60 μm, respectively) result from the "clipping" of data associated with known asteroids, differences in extraction of extended objects as mentioned, and, possibly in a few rare cases, removal of radiation hits from detector data prior to coaddition (see Section II.C.2).

A.2.b Comparison of FSC and PSC Positions

The FSC positional accuracies relative to optical and radio catalogs are given in Section III.E. Table IV.A.2 below compares the PSC and FSC position error population σs with respect to stars in the SAO catalog and galaxies with accurately measured positions (Dressel and Condon 1976). The objects are divided into bright and faint subsets. Only objects present in both the FSC and the PSC were used. The FSC positional accuracies are comparable or superior to the PSC in both the in-scan and cross-scan directions in all but one case: the PSC is moderately superior in the cross-scan direction at high SNR at 12 μm.

The improved in-scan pointing in the FSC is due to the improved boresight pointing accuracy, as described in Section II.B. The *IRAS* PSC processing used elaborate models which took advantage of the probability density functions of the individual detections, and remains the best source of cross-scan positional information for bright objects. Cross-scan positions in the PSC for faint objects, however, are sometimes compromised by weak radiation hits pulling the positions to one side. The FSC positions are less susceptible to weak radiation hits due to more robust algorithms.

A.2.c Comparison of FSC and PSC Flux Densities

The FSC processing was designed to provide optimal reliability and flux-density accuracy for low SNR point sources. The *IRAS* PSC used amplitude estimation by template fits to individual detector data streams (see the *Main Supplement*, Section V.C). FSDB

TABLE IV.A.2 FSC and PSC Positional Error Comparison (1 σ) for Sources in Common

FSC Flux Density Cut	Number	Minor Axis(″) FSC	Minor Axis(″) PSC	Major Axis(″) FSC	Major Axis(″) PSC
SAO Stars					
$f_\nu(12\ \mu m) > 1.2$ Jy	7,894	2.0	2.8	14.4	11.8
$f_\nu(12\ \mu m) < 1.2$ Jy	18,108	2.6	4.5	17.5	20.0
Dressel and Condon Galaxies					
$f_\nu(60\ \mu m) > 1.9$ Jy	611	5.6	6.7	13.3	13.4
$f_\nu(60\ \mu m) < 1.9$ Jy	1,231	6.1	7.4	17.4	19.7

sources were extracted from coadded plates binned in pixels, as described in Section II.C. The binning introduces an error on the order of 3-5%, as described in Section III.F.3. The PSC flux density is generally expected to be more accurate at high SNRs due to these processing differences. At low SNRs, the FSS is more accurate, due to the filtering and trimmed-average processing (Section II.B) and the use of all data samples. (At low SNRs for the PSC, only those individual detections exceeding the detection threshold were used.) The flux over-estimation correction (see *Main Supplement* Section XII.A.1) also affected the PSC at lowest flux levels. While this correction was an undoubted benefit to the PSC, the need for it in only the PSC underscores the superiority of the FSC at low PSC SNR values.

Photometrically, the FSC and the PSC are in agreement (with a dispersion of $\sim$ 5–7% at high SNRs). The FSC agrees well at all flux-density levels with a predictive model based on visual magnitudes (see Section III.F). The point at which one should use the PSC flux density in lieu of the FSC flux density has not been determined exactly due to the lack of an absolute reference, but a preliminary recommendation is to use the PSC flux density in cases where the PSC SNR is in excess of 10.

A.3 FSC Sources not Present in the PSC

There are nearly 100,000 FSC sources which do not appear in the PSC. Twenty-three percent of these are in the PSCR, almost all of which were rejected from the PSC either because they lie in the single HCON sky or because other confirmation criteria were not met. These will be examined in more detail in Section IV.A.3.a. Of the remaining sources, found neither in the PSC nor the PSCR, about 0.8% are over the 95% completeness limit

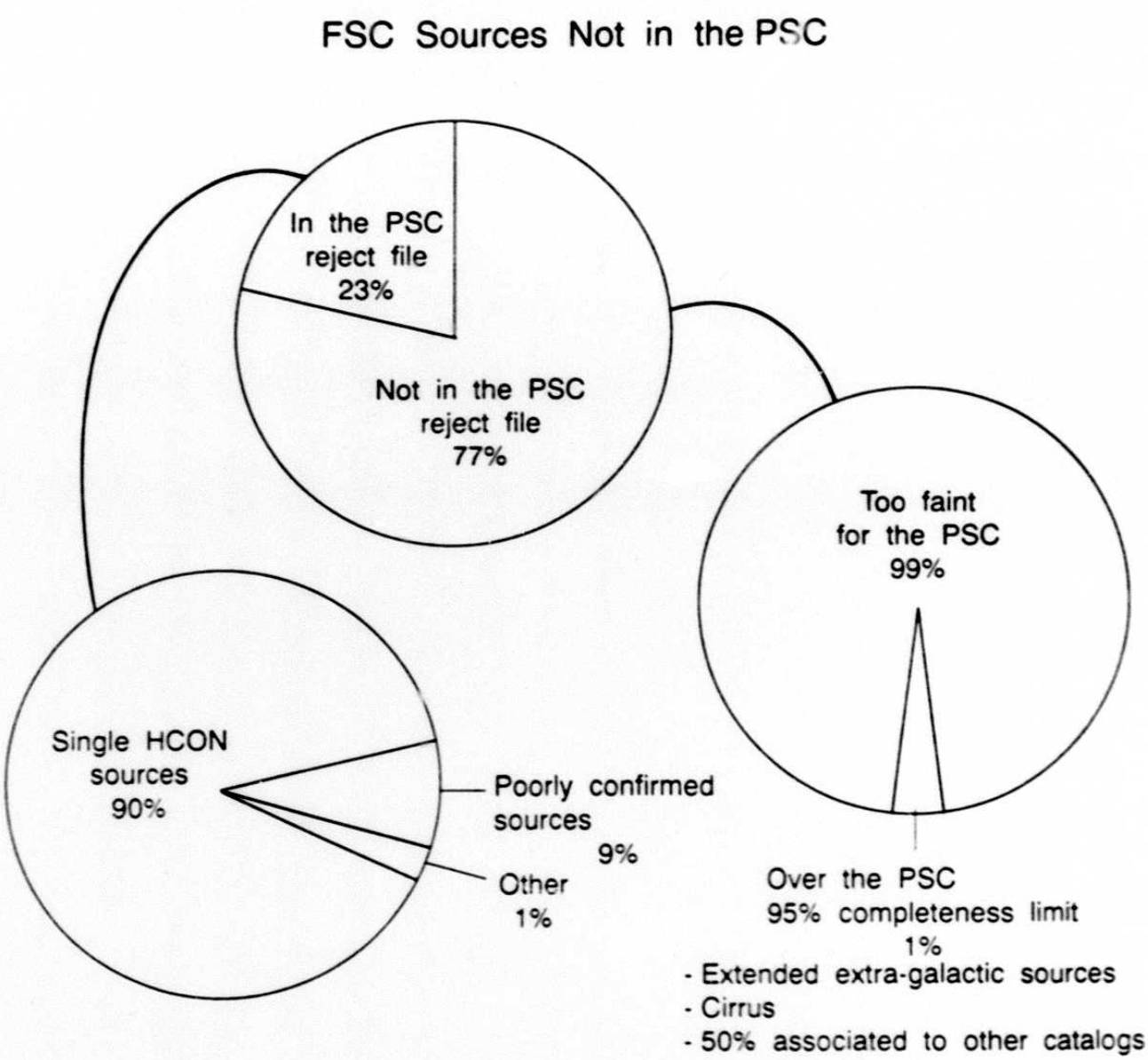

Figure IV.A.3 Pictorial description of the FSC sources not present in the PSC for |b| >10° .

of the PSC. Section IV.A.3.a below examines the reasons for their absence from the PSC. Figure IV.A.3 summarizes the discussion in this section graphically.

A.3.a FSC Sources in the PSCR File

Ninety percent of the FSC sources missing from the PSC but in the PSC Reject file

are single HCON sources and are therefore prevented from entering the PSC (see Chapter V.D in the *Main Supplement* for a full discussion of the PSC confirmation strategy).

About 9% of the FSC sources in the PSCR failed to enter the PSC because, although they successfully months confirmed, they failed to meet other confirmation criteria at the seconds confirmation level. Both of these effects happen when a source is near the PSC detection threshold and therefore is detected only intermittently. It also happens when a source is resolved and is sometimes extracted from the detector data as a point source and sometimes not. This latter characteristic is typical of the infrared cirrus.

The population of sources failing to enter the PSC for this reason appears to be a typical cross-section of FSC sources with a moderate level of cirrus contamination. One can detect cirrus contamination in a population of FSC sources by examining the distribution of cirrus flag values (see Section III.G.7), 60 to 100 μm flux density ratio and other cirrus-affected values within the population.

About 0.5% of the missing FSC sources failed to enter the PSC because they were in regions processed by the High Source Density (HSD) Processor (cf. *Main Supplement* Section V.H.6). The specialized set of rules applied by the HSD to deal with the most dense regions of sky enhances source selection differences between the catalogs. In such regions one should expect substantial differences between the PSC and the FSC. However, since the FSC only descends to $|b| = 10°$, there is very little overlap between the HSD-processed sky and the FSC (cf. Section III.A.7).

The remaining FSC sources missing from the PSC but present in the PSCR (less than 1%) are missing for largely unexplored reasons. The population as a whole, however, appears to be heavily contaminated by sources derived from the infrared cirrus.

A.3.b FSC Sources Over the 95% Completeness Limit of the PSC

About 0.8% of the FSC sources are above the PSC 95% completeness limit but are found neither in the PSC nor the PSCR. Most of these sources appear to be extended. Extended objects, as already mentioned in connection with the infrared cirrus, are treated erratically by PSC and FSC processing.

About half of the sources are associated to catalogs, mostly extragalactic catalogs, and show signs of extent.

Most of the others are cold 60 and 100 μm sources unassociated to a catalog but showing signs of extent and having higher than average values of the cirrus flag. These are indicative of cirrus contamination, a known source of unreliability in the FSC.

315

D 10015

A.3.c Summary

Of the roughly 100,000 sources in the FSC not appearing in the PSC, nearly all represent legitimate, new sources. Of these, 23% are in the PSC Reject File, nearly all of which are missing from the PSC because they are faint and therefore insufficiently confirmed. About 2% of the new sources lie above the 95% completeness limit of the PSC. Most of these show signs of being extended galaxies or infrared cirrus.

A.4 Sources Present in the PSC but Missing from the FSC

Of the $|b| > 10°$ PSC sources, 29% fail to find counterparts in the FSC. Of these 82% are in the FSCR but were excluded from the FSC for a variety of reasons; most were rejected because the FSC source selection rules left areas of the sky "unsurveyed" by the FSC (cf. Section II.G.6), or because the sources were cirrus contaminated. The 18% which failed to find matches either in the FSC or the FSCR result mostly from cirrus contamination.

In the following sections we discuss the missing PSC sources segregated by the reason for their absence. Figure IV.A.4 presents a graphical summary of these results.

A.4.a PSC Sources 'Unsurveyed' by the FSC

The source selection rules affect different bands differently, depending on sky position. Between absolute galactic latitudes of 10° and 20°, the 60 μm band cannot achieve final catalog status but the 12 and 25 μm bands can. In addition, there are areas of sky at 12, 25, and 60 μm where the high sky noise prevents one or more bands from reaching catalog status, no matter how bright the source (see Figures I.A.3 and 4). It is as though these areas were not surveyed in the excluded bands. Detections in other bands must bring such sources into the FSC. If no other bands are bright enough to achieve catalog quality, the source will be left out of the FSC.

Of the missing PSC sources, 23% are missing because either the galactic latitude constraint or the cirrus contamination or sky noise left the 60 μm band unsurveyed by the FSC. Four percent are missing because the 12 or 25 μm bands were left unsurveyed.

Figures IV.A.5 and 6 show Aitoff projection maps of those PSC sources missing because they are unsurveyed by the FSC in 12 μm and 60 μm, respectively. Both figures contain a small number of sources widely scattered over the parts of the high galactic latitude sky which received only four coverage scans (2 HCON sky), as opposed to the normal six scans (3 HCON sky). These sources do *not* delineate a contiguous region of sky left unsurveyed by the FSC at 12 or 60 μm. Instead, they are individual sources victimized by low level random variation in our estimate of the local sky noise, exacerbated

316

D 10015

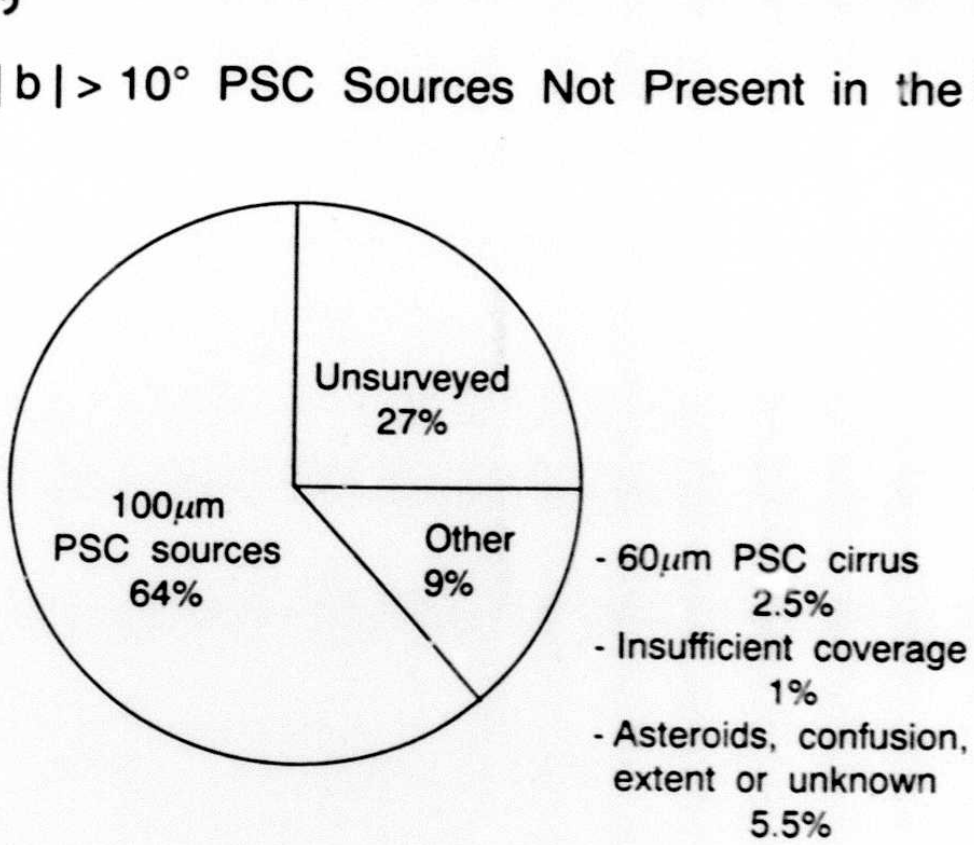

Figure IV.A.4 Pictorial description of the PSC sources not present in the FSC for |b| >10° .

by the low coverage. This effect pushed the sky noise beyond the range which had been analyzed, making an estimate of the sources' reliability impossible. Their flux density qualities were thus downgraded to moderate, making these sources ineligible for the FSC. This is a randomly-occurring result of being in low coverage areas, affecting individual sources, *not* a contiguous region of sky.

A.4.b 100 μm PSC Sources

Since the 100 μm band is severely contaminated by cirrus it was decided that no source would be allowed into the FSC based solely on a 100 μm detection. Detections in other bands could carry such a source into the FSC. Of the absent PSC sources, 23% are in the FSCR and could only get into the FSC based on their 100 μm signal. They were thus excluded.

Another 41% are 100 μm PSC sources which were not detected at all at 100 μm in the

317

D 10015

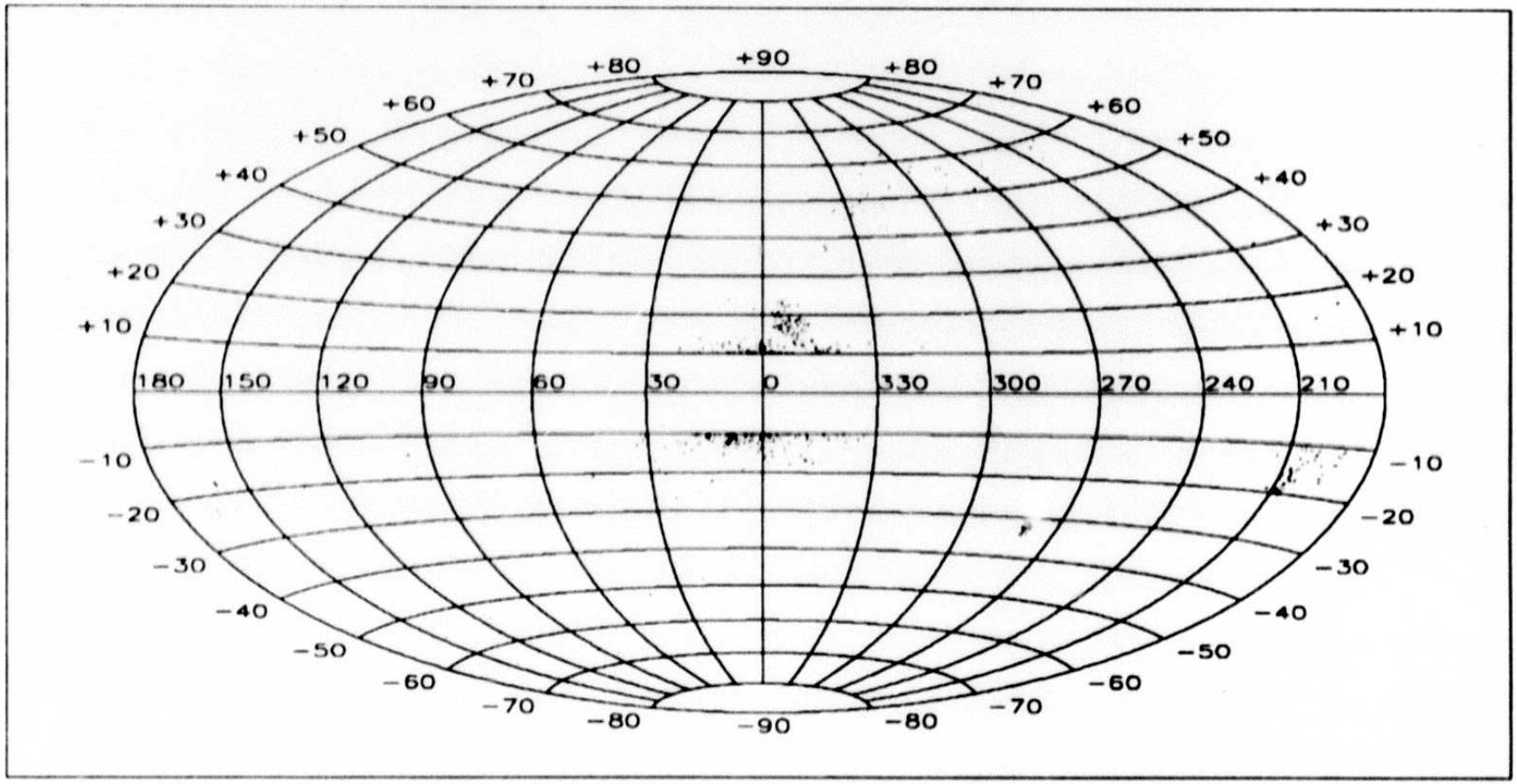

Figure IV.A.5 Aitoff projection map of 1,123 PSC sources 'unsurveyed' by the FSC at 12 μm, the map is in galactic coordinates.

3/9

D 10015

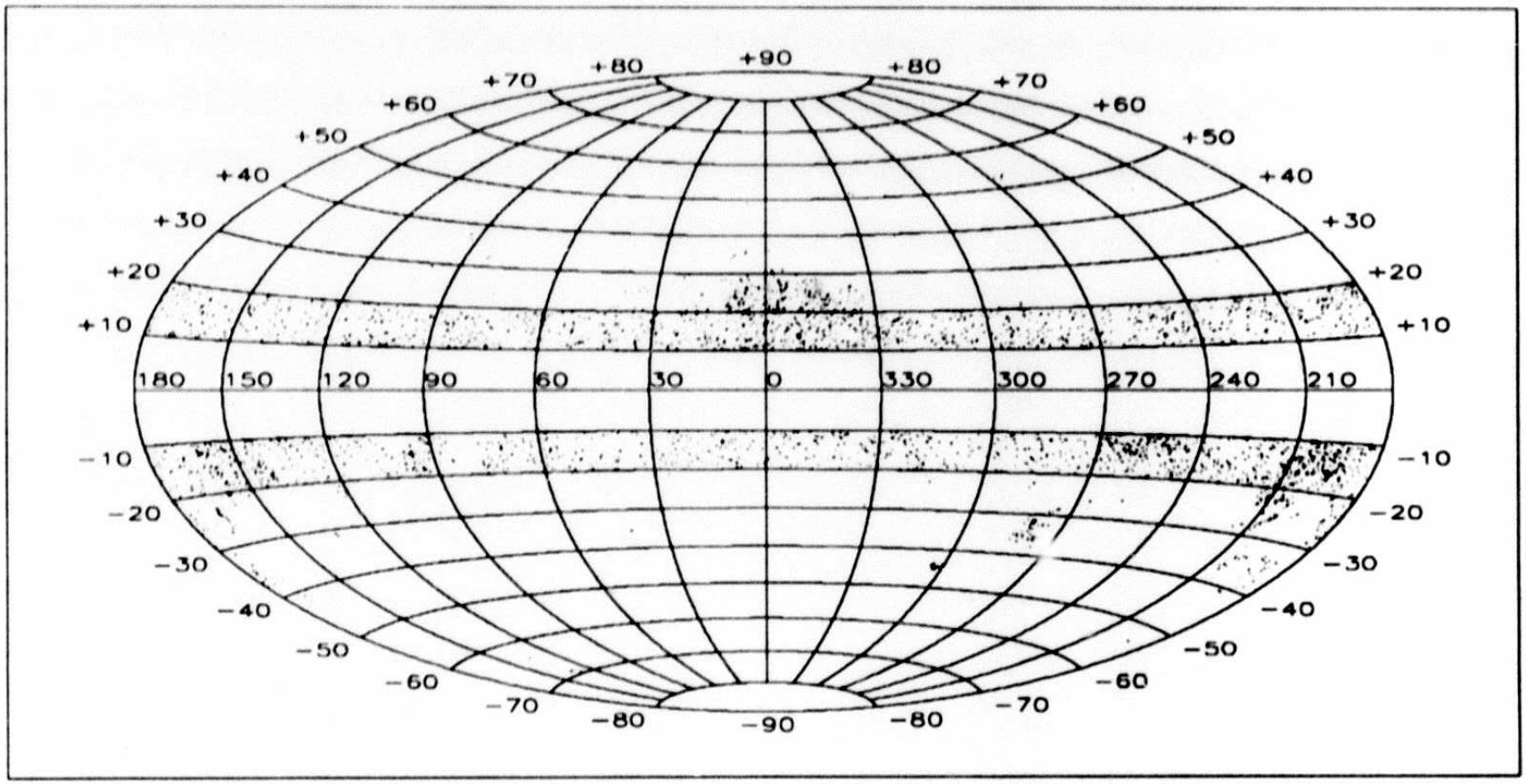

Figure IV.A.6 Aitoff projection map of 6,565 PSC sources 'unsurveyed' by the FSC at 60 μm, the map is in galactic coordinates.

FSC. 100 μm sources may be suppressed from the FSC because they lie in cirrus-infested sky. This could serve to raise the extraction threshold enough to exclude many 100 μm sources bright enough to be in the PSC. Also, the source itself may be cirrus and therefore extended. The different processing schemes involved in making the PSC and the FSC can lead to radically different results for extended objects, sometimes including a source in one catalog excluded from the other.

Thus 91% of the missing PSC sources for $|b| > 10°$ are absent because they are 100 μm cirrus (41%), were unsurveyed by the FSC at 100 μm (23%) or were left unsurveyed in other bands (27%) (cf. Section IV.A.4.a).

A.4.c Miscellaneous Alibis

Of the missing PSC sources, 2.5% are 60 μm PSC sources which found no matches either in the FSC or the FSCR. The vast majority of these appear to be cirrus with their 100 μm component stripped away, most likely because it was too extended.

Another 1% of the missing PSC sources match FSCR sources with too few detector crossings to enter the catalog (the threshold is 6). It is possible to end up with fewer than 6 counts in 2 or 3 HCON sky due to one or more of the following:

- The snipping of data associated with known asteroids.
- The deglitching of radiation hits.
- Smaller detector masks used in FSS processing.
- Detectors 25 and 42 being turned off in FSS processing.
- Dead detectors.

A few sources (15) were tagged as either cross-talk (cf. Section III.G.3) or comet trails (cf. Section III.G.1) and were excluded from the FSC on that basis.

The last 5.5% of the missing PSC sources result from an unknown admixture of several causes. An unusually large number of these PSC objects are 25 μm sources, which are probably false PSC sources (cf. *Main Supplement* page XII-21). Many of them are the result, once again, of extended objects being handled differently by FSC processing than the PSC processing. Many are pairs of stars resolved by the PSC but unresolved in the FSC, resulting in a very different FSC position for the composite object, leaving one or both PSC representations unmatched. Some of the missing PSC objects offer no facile explanation of their absence from the FSC. Time constraints prevented us from further study of these objects. Alibis for those sources are left as an exercise for the reader.

A.4.d Summary

Of the $|b| > 10°$ PSC sources, 29% are absent from the FSC. The absence of about 96% of these missing sources can be explained, mostly because they are extended (almost all cirrus) or were not surveyed by the FSC. Thus, 96% of the sources in the PSC are either in the FSC or have a good reason for not being included.

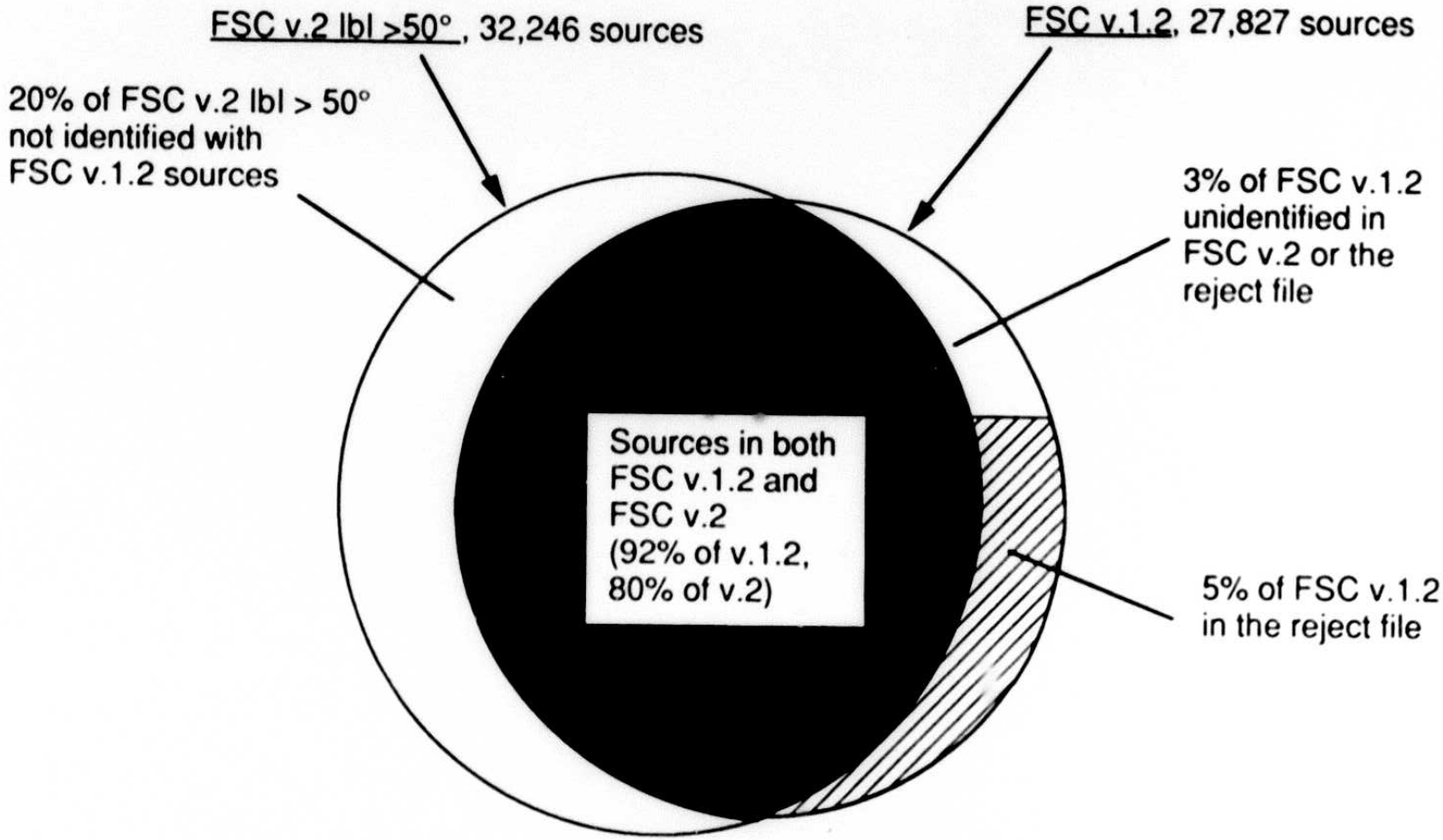

Figure IV.B.1 Comparison of the ($|b| > 50°$) FSC v.2 and FSC v.1.2.

B. Comparison of FSC v.2 to FSC v.1.2

B.1 Overview

In producing version 2 of the FSC, many changes were made in the extraction and bandmerge procedures used to create version 1.2 of the FSC (hereafter FSC v.2 and FSC v.1.2). These changes were designed to produce a deeper, cleaner catalog. For this reason, sources that appeared in version 1.2 may be slightly changed or, in a few rare instances, absent completely from version 2. *The vast majority of FSC* v.1.2 *sources are virtually unchanged in flux, position, and band structure in the version 2 catalog.*

Figure IV.B.1 summarizes the changes for $|b| > 50°$ from version 1.2 to version 2. This section is designed to aid the users of FSC v.1.2 in translating and continuing their work with the version 2 catalog. Section IV.B.2 details the procedure used to identify FSC v.1.2 sources in the version 2 database. For reasons explained there, the identifications were *not* done by performing a simple radial search about the version 1.2 source positions. Instead, more complicated and, in some cases, conservative criteria were used, with the aim of minimizing erroneous matches at the expense of leaving some v.1.2 sources unidentified.

Using these identification methods, 97% of FSC v.1.2 sources were identified in the version 2 FSS; 92% are actually contained in FSC v.2. These sources, and any changes they may have undergone, are discussed in Section IV.B.3. The other 5% are in the FSR. These sources had high-quality fluxes in FSC v.1.2, and for a variety of reasons, lost their high-quality status in version 2, and consequently were excluded from FSC v.2. Subsection IV.B.4b discusses these sources. All version 1.2 sources identified in the version 2 FSC or reject file are flagged (FPFLAG_C = 1) for easy identification.

The remaining 3% of FSC v.1.2 sources were unidentified in version 2. These are sources which are either missing entirely from version 2, or are present but, for a variety of reasons, could not be identified without more in-depth analysis. The majority of unidentified sources fall into the *latter* category. Subsections IV.B.2d-f present the limitations of the identification process. The characteristics of the unidentified sources are discussed in subsection IV.B.4c. In addition, Appendix IV.1 lists the names of all unidentified FSC v.1.2 sources.

Those sources with $|b| > 50°$ which are in the FSC v.2 but are *not* identified with a version 1.2 source form the subject of Section IV.B.5. Approximately 6500 sources fall into this category, constituting 20% of the FSC v.2 for $|b| > 50°$. It is estimated that up to one-tenth of these are actually unidentified FSC v.1.2 sources, as mentioned above. The remaining $\approx$90% are new sources which did not appear in FSC v.1.2. Some of these were sources which narrowly missed inclusion in the version 1.2 catalog and, due to the effects

323

of reprocessing, are now of catalog quality. Others are completely new sources revealed in what were previously confused or obscured regions of sky.

B.2 Identification of FSC v.1.2 Sources in FSC v.2

B.2.a Introduction

The IAU requirement that all sources present in subsequent versions of a released catalog retain their former names necessitates the *identification*, in FSC v.2, of all FSC v.1.2 sources. Processing differences which led to FSC v.2, however, may cause slight, or, in a few cases, substantial changes in the flux, position, and/or band structure of FSC v.1.2 sources appearing in v.2. In addition, FSC v.2 contains sources that were not present in FSC v.1.2, and vice versa.

The procedure used to identify FSC v.1.2 sources in the FSC v.2 involves more than a simple closest-positional-match algorithm. At the very least, the user is encouraged to read subsection IV.B.2.e, which briefly explains how to recognize FSC v.1.2 identifications in v.2 and gives a few caveats as to their use.

Figure IV.B.2 shows a schematic representation of when the identification process occurred in relation to other Faint Source processes (cf. Figure II.A.1). Because it was necessary to retain the FSC v.1.2 names of any FSC v.1.2 sources present in FSC v.2, the identification process was required to be completed before FSC v.2 could be generated. (Source naming does not occur until the catalog generation step, since part of the source name is an identifier signaling final catalog or reject file.) Thus the analysis to identify FSC v.1.2 sources was performed concurrently with the analysis to determine FSC v.2 catalog criteria.

As a consequence the FSC v.1.2 identifications were made, not to FSC v.2 sources (which were not selected yet at that time) but instead to sources in the FSDB. Each FSC v.1.2 source was simply identified with a nearby FSDB source which closely resembled it, if one existed.

Finally, the following should be noted about the nomenclature used in this section. The FSDB is the database of *all* sources extracted by version 2 processing. This database contained sources of different reliabilities, from spurious entries to reliable ones. FSC v.2 was created by selecting sources from this database which met criteria for high reliability. FSDB sources which did not meet v.2 catalog criteria are put in the FSR (Faint Source Reject) file. In this section, the term FSS v.2 will be used to refer to all released products of v.2 processing, namely the union of FSC v.2 and the FSR.

324

D 10015

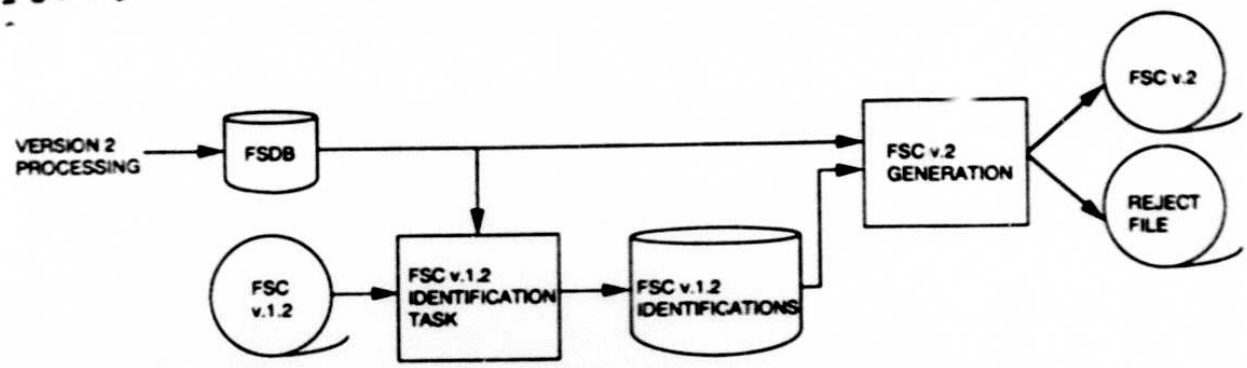

Figure IV.B.2 Relationship of identification processing to other processes.

B.2.b Requirements and Constraints

The IAU naming convention requires that all FSC v.1.2 - v.2 identifications be one-to-one. In other words, a single FSC v.1.2 source cannot be identified with two or more version 2 sources, and two FSC v.1.2 sources cannot be identified with a single version 2 source. Although this might seem an unusual situation, consider the following case: a FSC v.1.2 4-band source which, in version 2, has been resolved into two separate sources, a star (12 and 25 μm detections) and a galaxy (60 and 100 μm detections). Examination of POSS plates indicates that the version 2 rendering is the correct one. Thus the problem arises as to how a *single* FSC v.1.2 name is transferred to two distinct objects.

The FSC v.1.2 naming convention already contains an indicator - letter F designating the catalog, 8 numerals designating the position, and an additional letter - uniquely designating sources which have the same position numbers. Thus, the FSC v.1.2 source in question here could not have its version 2 components labeled with the v.1.2 source name plus an "A" or "B", as these are already legitimate source names and would therefore cause confusion. Instead, the decision was made to make no name transfers in these cases. Thus, the requirement that all v.1.2 - v.2 identifications be one-to-one is solely to enable the transfer of FSC v.1.2 names to their *identified* version 2 counterparts.

It is important to realize that, because in the cases mentioned above, no transfer of FSC v.1.2 name to v.2 source occurs, these sources are officially *unidentified* in FSC v.2. If they were identified, then they would be required to bear their FSC v.1.2 names. Since they have new names in version 2, they are treated as new sources unidentified with FSC v.1.2. The version 2 flag FPFLAG_C, signaling a source present in FSC v.1.2 is set to zero, and the FSC v.1.2 names associated with these sources are listed in the appendix

325

D 10015

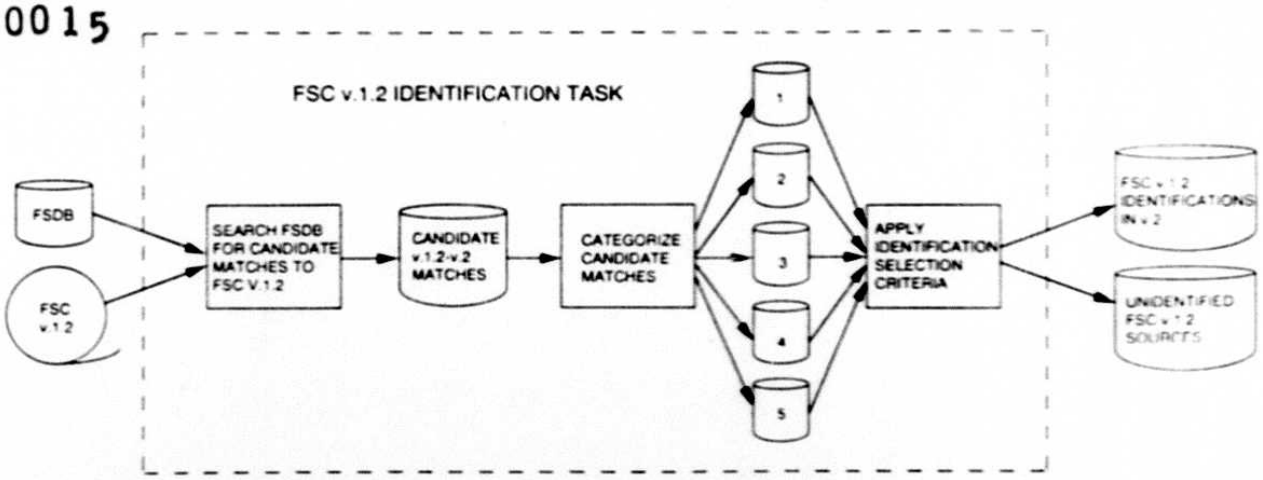

Figure IV.B.3 Steps used in identification processing.

of unidentified FSC v.1.2 sources (Appendix IV.1). For further discussion, see Section IV.B.4.c.

Another fundamental requirement imposed on FSC v.1.2 - FSC v.2 source identifications was that the version 2 source and the version 1.2 source have at least one wavelength detected in common. For example, a 60 μm FSC v.1.2 source cannot be identified with a version 2 source which does not have a 60 μm detection. This requirement was imposed to provide at least one wavelength in which detections could be compared for purposes of identification. In general, if a source is bright enough to be included in FSC v.1.2, then at least one of its bands is expected to be detected in the version 2 FSS, whether or not it qualifies for FSC v.2 catalog inclusion.

Due to time constraints, the resources and methods were prioritized to ensure the identification of a maximum number of sources during the allocated time. Furthermore it should be noted that the identification program was designed to be conservative. In a trade-off between completeness and reliability we opted for high reliability of identifications. ***Therefore, all criteria developed for identification were designed to include almost exclusively highly reliable*** v.1.2 - v.2 ***matches, at the cost of excluding some possibly true identifications of a more uncertain nature.*** Also, in any cases where an unambiguous v.2 identification could not be made for an FSC v.1.2 source, the v.1.2 source was left as unidentified rather than risk making a false identification.

B.2.c Method

Figure IV.B.3 presents a schematic view of the steps outlined in this section.

326

D 10015

The identification of FSC v.1.2 sources in the FSDB was carried out in several steps. First, all possible candidate matches to FSC v.1.2 sources were found by selecting all FSDB sources within a 5′ radius centered on FSC v.1.2 positions. Then for each match the statistics on the similarity in flux density, position, and band structure between the v.1.2 and v.2 sources of a candidate match were calculated. On the basis of these statistics, the candidate match pairs were divided into groups: Those with similar band structure, those with similar flux densities, those with similar band structures and flux densities, etc. Band structure was evaluated in a straightforward fashion: identical, or not. (See below for exclusion of v.1.2 – v.2 matches which had no bands in common.) Flux density was not expected to change from FSC v.1.2 to FSC v.2 (see Section IV.B.3.b). However, due to a change in computer hardware from v.1.2 to v.2, we expected to observe some difference in flux density values due to round-off error. Therefore, fractional differences in flux density less than 0.5% were taken to indicate similar flux densities; values greater than this limit were treated as dissimilar. Radial distance was not used directly to separate candidate matches into categories, but was instead reserved for use in later analysis.

The next step in the identification process resulted in the enumeration of possible match scenarios, and their relative significance. Candidate matches were divided into 5 match quality groups (the same source may at times find matches in more than one category):

i Identical band structures in v.1.2 and v.2, and for *every* wavelength detected, the flux density differences between v.1.2 and v.2 within the specified error limit (22,737 sources)

ii Identical band structure in v.1.2 and v.2, and a flux density difference within the error limit for *at least one* detected wavelength (996 sources)

iii Different band structures, but for *at least one* wavelength detected in v.1.2 and v.2, a flux density difference within the error limit (3,471 sources)

iv Identical band structure, but in *none* of detected wavelengths flux density differences within the error limit (674 sources)

v Different band structures, and for *none* of the bands detected in both v.1.2 and v.2, a flux density difference within the error limit (1,488 sources)

The groups are arranged in the order of the most reliable to the least reliable matches. Note that only group (v) can contain sources which have no common bands in v.1.2 and v.2.

Finally the criteria for selecting a given match as the *identification* were developed. The identification process usually consisted of two parts: (1) selection of a "best candidate

327

match" from among all v.2 candidates for a v.1.2 source, and (2) evaluation of the reliability of the proposed v.1.2–v.2 identification. In practice, the various match categories enumerated in the previous paragraph were arrived at through experimentation. Due to time constraints cases of ambiguity were deferred for later analysis. Eventually the positional difference, in conjunction with the quality of the match (belonging to one of the five categories enumerated earlier), was used to determine the reliability of the proposed identification. Positional difference thresholds depended on the match group.

Due to time limitations, analysis was made in a cost effective manner. The majority of FSC v.1.2 sources had a candidate match in group (i), and because this group was perceived to be the most reliable set of matches, candidates in this group were analyzed first. After group (i), the analysis was organized from the easiest and most reliable groups (*e.g. one* v.2 source within a 5′ radius) to hardest and least reliable (*e.g. multiple* matches, all in the lower reliability match groups). In the following, groups of sources, and the order in which they were analyzed, along with the criteria developed for their analysis will be presented.

1. FSC v.1.2 sources whose closest positional match was in group (i) were all declared to be valid identifications. This identified 82% of FSC v.1.2.
2. Sources which had a match in group (i) but also had a positionally closer match in another group were individually examined and resolved. Normally, this type of analysis would be deferred to later, due to the time involved. However, in this case there were only 13 sources and they were identified in a short time.
3. Sources whose only match was in group (ii) were all found to have small match distances. All were passed as identifications.
4. Sources which had a match in group (ii) and a match in group (v) were all found to be positionally closer to the matches from group (ii). Further analysis indicated that the group (ii) matches were reliable. All were identified with their group (ii) matches.
5. Sources with matches only in group (iii) sometimes had *multiple* matches in that group. Analysis revealed the *closest* positional matches in this group were good identifications.
6. Matches only in group (iv) were selected as identifications if their closest match in the group met the conditions $|\Delta_{in-scan}| \leq 8''$ and $|\Delta_{cross-scan}| \leq 25''$. (These criteria were empirically found to select reliable identifications.)
7. Sources with matches in groups (iv) and (v) were identified with their group (iv) matches if they met the criteria listed in 6.
8. Sources with matches only in group (v) were first thresholded to include only sources

with a band in common (in keeping with the requirements), and, in the case of sources with multiple matches in this group, only the closest positional match was kept. After this, sources were kept as identifications if they met the conditions $|\Delta_{in-scan}| \leq 5.3''$ and $-11'' \leq \Delta_{cross-scan} \leq 8''$. (These conditions were also empirically determined to yield reliable identifications.)

Once the time allotted to the identification process expired, all the identifications which had been made were assembled and searched for any "duplicate" v.2 records. The identification method used insures that all FSC v.1.2 sources are identified with *only one* v.2 source; however, v.2 sources identified with more than one FSC v.1.2 source can only be found once the complete list of identifications is available. In keeping with the one-to-one identification requirement, the compiled list was searched and all cases of *two* v.1.2 sources matching a *single* v.2 source were isolated. A total of 12 v.2 records were found to be matched to more than one v.1.2 source. These were resolved by individual examination, with the better v.1.2 match being retained and the other v.1.2 source being relegated to the list of *unidentified* sources.

This identification process was able to identify 97% of FSC v.1.2 sources during the allotted time. However given more time, other groups of sources could have been correctly identified. In particular, sources in group (iii) are surprisingly reliable identifications in many cases. The only analysis carried out on this group was for FSC v.1.2 sources whose only candidate matches were in group (iii). This still leaves over 600 sources in group (iii), a majority of which would probably have been identified with FSC v.1.2 sources had time permitted. Thus, the body of unidentified FSC v.1.2 sources which are actually present in v.2 products probably belong to the category of sources having a match in group (iii) and a match in another group at a farther distance. This would have been the next category of sources analyzed.

In summary, this contorted method was necessary to ensure that the transfer of FSC v.1.2 names to the v.2 sources occurred as a result of *identifications* and not due to *positional associations*.

B.2.d Results

Ninety-seven percent of the sources in FSC v.1.2 have been formally identified with FSS (i.e., FSC or FSR) v.2 sources. The 3% which were not identified belong to one of two categories:

1- Those sources for which a v.2 match does not exist or cannot be uniquely identified.
2- Those sources which do exist in FSDB v.2 but could not be identified in the time allotted to the identification process

A list of all unidentified FSC v.1.2 sources appears at the end of this chapter in Appendix IV.1.

It is estimated that an additional 1–2% of FSC v.1.2 could have been identified. For further discussion, see Sections IV.B.2.e–f and IV.B.4.c. However it is estimated that still roughly 1% of sources would remain unidentifiable in v.2. In Section IV.B.2.b it was mentioned that some sources cannot be formally identified because they do not correspond in a one-to-one fashion to a single v.2 source. In addition to this, 8 FSC v.1.2 sources found no v.2 sources within the 5′ search radius used to select candidate matches. Subsequent follow-up of these sources revealed no corresponding v.2 sources existed. We believe that still other unidentified FSC v.1.2 sources which do have v.2 sources in their vicinity are unrelated to any of these v.2 sources. These sources would also be truly missing in FSS v.2. Thus, of the FSC v.1.2 sources unidentified in v.2, *some are truly absent*, whereas others cannot be identified due to the logistics of the naming procedure. For an explanation of mechanisms which could result in the complete loss of FSC v.1.2 sources from v.2, see Section IV.B.4.c.

B.2.e Use and Interpretation of FSC v.1.2 Identifications

The flag FPFLAG_C (found in the long form of FSC v.2 and in the FSR) signals a version 2 source which is identified with FSC v.1.2. *The* FPFLAG *is the only pointer for locating an FSC* v.1.2 *source identified in FSC* v.2. When this flag is set to 1, the v.2 source in question has been identified with an FSC v.1.2 source. Furthermore, *the* v.2 *source has the same catalog name as the FSC* v.1.2 *source it has been identified with*, in accordance with IAU requirements.

The user should be aware of the following consequences of the identification process and naming convention:

1) *Identical* v.1.2 *and* v.2 *source names do not always indicate a* v.1.2-v.2 *IDENTIFICATION*. Since source names are determined by position, FSC v.1.2 and FSC v.2 sources may have the same names any time they have similar celestial coordinates. Thus, a v.2 source with the same name as an FSC v.1.2 source is not necessarily an identification; the two sources may just be positionally coincident (However, if the two sources are very close together, there is a good chance that they are the same source; 560 sources were found to have identical names but were *not* categorized as being verified identifications. See Section IV.B.4.c). To identify FSC v.1.2 sources in the version 2 FSS reliably, the user must *always* check the FPFLAG field.
2) *In the FSDB, an "F" in a source name does NOT reliably indicate a CATALOG source*. When an FSC v.1.2 source is identified in the v.2 of FSDB, its entire name

is transferred to the v.2 source. The first character in all FSC v.1.2 names is an "F", signifying a FSC source. All of the FSC v.2 names also have the prefix "F". Thus relying on *name alone* in the FSDB might bring about erroneous conclusions. There are instances where a FSC v.1.2 source is identified with a FSS v.2 source *rejected* from FSC v.2 (this comprises ~5% of FSC v.1.2 sources), however, the rejected source still bears the FSC v.1.2 name. All of the sources in the FSR have the prefix "Z" except when a source in the reject file has been identified with a FSC v.1.2 source, in which case the name prefix is "F"! Proper identification of a *catalog* source is accomplished by noting the value of the FCAT flag in the long form of the FSR and FSC.

3) ***Unidentified FSC*** **v.1.2** ***sources are not necessarily absent from FSS*** **v.2.** It has been mentioned earlier that sources may be listed as unidentified for any of several reasons, only one of which is that they are actually missing from v.2 FSS. The next section discusses how to determine if a FSS v.2 counterpart for an unidentified FSC v.1.2 source really exists.

B.2.f Locating Unidentified FSC v.1.2 Sources in FSS v.2

In Section IV.B.2.d it was stated that a majority of unidentified FSC v.1.2 sources can be found in either FSC v.2 or in the FSR. These sources remain unidentified solely due to lack of time, as the identification process would have required follow-up on an individual basis. In many cases, individual examination can reveal an obvious v.2 analog of a FSC v.1.2 source.

The user wishing to determine whether v.2 counterparts of unidentified FSC v.1.2 sources exist, should perform a search about the FSC v.1.2 position within a radius of 2′–3′ in either the FSC v.2 or the FSR. Comparison of source attributes between the FSC v.1.2 source and any matched v.2 candidates should quickly reveal whether the v.2 source is a true identification or not. The user should bear in mind that an unidentified FSC v.1.2 source could be present in either FSC v.2 or FSR. Ideally, *both* products should be consulted before making a final decision about a v.2 counterpart of an unidentified FSC v.1.2 source.

B.3 Sources in FSC v.1.2 and FSC v.2

Ninety-two percent of FSC v.1.2 sources are identified in FSC v.2. Due to the differences in processing between the two catalogs, however, a version 1.2 source may be changed in band structure, position, or flux density in FSC v.2. With a few rare exceptions, these changes are small, and many sources appear virtually unchanged in FSC v.2. The following subsections detail the differences between the v.1.2 and v.2 representations of all sources identified in both catalogs.

331

D 10015

B.3.a Comparison of Band Structures

In Table IV.B.1 the FSC v.2 band structure of all identified FSC v.1.2 sources can be seen. Column 1 represents the possible band combinations of sources in FSC v.1.2. All other columns are labeled by the band structure of these sources in FSC v.2, and the last column denotes FSC v.1.2 sources which are *completely absent* from FSC v.2.

The band combinations in the table are encoded in the following fashion: The presence or absence of a measured flux density (high- or moderate-quality flux density) in a given band is denoted by a "1" or a "0". Measurements at 12, 25, 60, and 100 μm are represented, from left to right, as the digits in a four-digit number. Thus, in this system, a source measured only at 12 μm is represented as "1000", while one measured at 12 and 60 μm is denoted by "1010".

The numbers in the table give the percentage of sources in a given row which belong in the given column. For example, the first row gives the statistics for sources that were detected only at 12 μm in FSC v.1.2 (labeled "1000" in column 1). Reading across on this row shows that 89% of these remained 12 μm-only detections in FSC v.2, 2% gained a 25 μm detection, and a trace amount (symbolized by dashes) gained only a 60 μm or a 100 μm detection. The remaining 9% of FSC v.1.2 12 μm-only sources were unidentified in FSC v.2, as shown in the last column of the chart. For details on sources in this column, see Section IV.B.4.

Table IV.B.1 reveals that most sources retain the same band structure in FSC v.2 as in FSC v.1.2. This results in part from the criteria used for identification of FSC v.1.2 sources in FSC v.2 (see subsection IV.B.2). The most striking deviation from this pattern is the absence of all FSC v.1.2 100 μm-only sources from FSC v.2. This is a direct result of the exclusion in version 2 of 100 μm detections from high-quality flux status (see Sections I.A, II.G.6, III.D.1, III.D.3.d for further discussions). Under this decision, 100 μm flux densities can only enter FSC v.2 if they bandmerge to a high-quality detection in another band. None of the FSC v.1.2 100 μm-only sources gained a detection in any other band, and thus all were excluded from FSC v.2. Most are, however, found as 100 μm-only sources in the FSR. For further discussion, see Section IV.B.4.

The results presented in Table IV.B.1 can be summarized by Figure IV.B.4. Here, the number of FSC v.1.2 sources which gained or lost a measured flux density in FSC v.2 is displayed graphically as a percentage of the total number of FSC v.1.2 sources identified in FSC v.2. The figure shows that 90% of the sources identified in FSC v.1.2 and FSC v.2 have the same band structure in both catalogs. The remaining 10% are divided into sources which gained detections at new wavelengths in FSC v.2 (2%); sources

332

Table IV.B.1 FSC v.2 Spectral Classification as a Function of FSC v.1.2 Spectral Classification (%)

FSC v.1.2 Band Combination†	FSC v.2 Band Combination†															% not Present in FSC v.2
	1000	1100	1110	1111	0100	0110	0111	0010	0011	0001	1101	1010	1011	1001	0101	
1000	89	2										-‡		-		9
1100	8	87	-													4
1110	1	9	86	1		-		-				1				3
1111		-	2	82		-	6	-	1		-	-	3	-		4
0100§					29											71
0110			1			70	3	14	1							11
0111			-	3		3	70	1	17				-			7
0010						-	-	87	4			-	-			8
0011			-	-		-	1	9	84			-	-			6
0001																100
1101§	8	38									31					23
1010§	13	2	1					15	1			49	2			16
1011	-	-		4			1	2	24			1	57			11
1001§	37	2									5			23		33
0101§																100

† Example: 1000 = high- or moderate-quality flux density at 12 μm only; 1010 = high- or moderate-quality flux densities at 12 and 60 μm; etc.

‡ - = fewer than 1% of sources in this category.

§ These categories have fewer than 100 sources in FSC v.1.2

D 10015

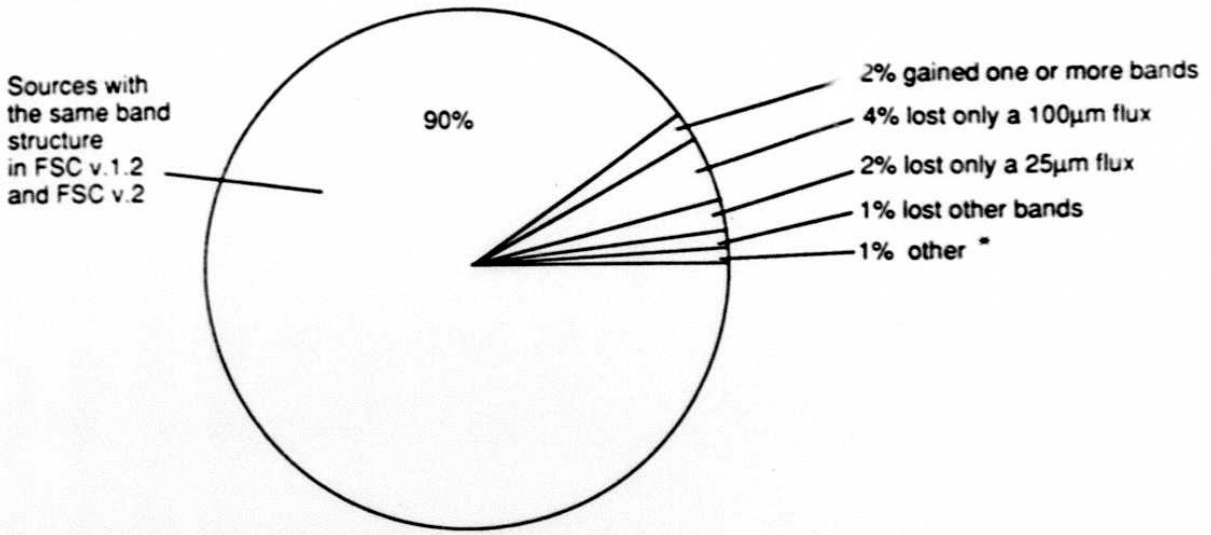

Figure IV.B.4 Changes in band structure of FSC v.1.2 sources which have been identified in FSC v.2. The 1% in the "other" category represents mostly the accumulation of fractional percentages from other categories, with a trace amount of sources which both lost and gained bands (0.1%).

which lost v.1.2 detections at one or more wavelengths (7%); and other sources (1%). The "other" category is mainly for book-keeping and mostly represents round-off from all other categories. However, a small percentage (~0.1%) of FSC v.1.2 sources both lost and gained detections at different wavelengths in FSC v.2 (example: FSC v.1.2 "0011" becomes FSC v.2 "1110" source); these sources are included in the "other" category as well.

In Figure IV.B.4 the FSC v.1.2 sources which lost one or more measured flux densities in FSC v.2 are further divided into categories based on the lost detection wavelength. The figure shows that the majority of sources which lost a detection lost only a 100 μm flux density. This is primarily due to the special changes in processing from version 1.2 to version 2 which were designed to provide a more localized estimate of confusion noise. In version 2, the thresholding noise was computed on scales of $\sim 1°$. This permitted a more accurate determination of confusion noise, with the result that the number of 100 μm extractions in high cirrus regions was appreciably reduced.

Returning to Figure IV.B.4, we see that 2% of FSC v.1.2 sources lose only a 25 μm flux density in FSC v.2. These sources lost their 25 μm flux density in FSC v.2 due to changes made to the v.2 extraction process (see Section II.E.3). In v.1.2 processing, one of

334

the conditions for source extraction was that the signal-to-local-noise ratio of *at least* one pixel in the source be above 4.5. In v.2, this was changed to a requirement that the SNR of the *peak* flux pixel of the source be above 3.5. Applying the v.2 extraction criteria to FSC v.1.2 sources reveals that, compared with 12 μm and 60 μm, roughly twice as many v.1.2 25 μm detections fail to be extracted in v.2. This effect is attributable to the greater variation in noise at 25 μm (resulting from lower coverage) as compared to 12 μm and 60 μm, which makes it relatively more likely for the peak pixel of a 25 μm v.1.2 detection to fall below the local SNR 3.5 threshold of v.2 than for 12 μm or 60 μm detections.

Once the "unusual" loss of FSC v.1.2 bandmerged detections at 25 μm and 100 μm has been accounted for, the percentages given in Figure IV.B.4 show that the number of FSC v.1.2 sources which lose detections in FSC v.2 is roughly equivalent to the number which gain detections. Loss or gain of detections at all wavelengths is attributable to the two processing changes described above (those changes were implemented at all 4 wavelength bands; their effects were most strongly felt at a certain wavelength), and to a host of other minor changes in processing. Differences in the re-thresholding of extracted sources, the slightly increased sensitivity in some areas of sky (due to more localized noise estimates), and changes in the search window sizes for the bandmerger are all things which changed the band structure of a small number of sources. In general, however, most FSC v.1.2 sources have the same band structure in FSC v.2, with the most noticeable exception being the loss of spurious 100 μm detections attributable to cirrus contamination.

B.3.b Comparison of Flux Densities

Version 2 software changes did not affect the coadded FSS plates and thus the pixel flux densities and noises did not change between versions. Software changes affected only the source extractor, bandmerger, and parts of the data base generator (see Section II.H). The flux density of an extraction is simply the value of the flux density in the peak-flux pixel of the extraction region. Thus flux density of a source is not expected to change from FSC v.1.2 to FSC v.2. However, round-off errors due to the storage of FSC v.1.2 data in FITS format (for practical reasons the short form of FSC v.1.2 does not have the full precision of the original data base), and also changes in the selection of a representative source in regions of plate overlap have caused minor differences between the recorded flux densities of FSC v.1.2 sources and FSC v.2.

Figure IV.B.5 shows the distribution of the logarithm of the percent absolute difference in flux density of sources in FSC v.1.2 and FSC v.2 at 12, 25, and 60 μm. Each figure contains only high and moderate quality detections; *no* flux density upper limits have been used.

335

D 10015

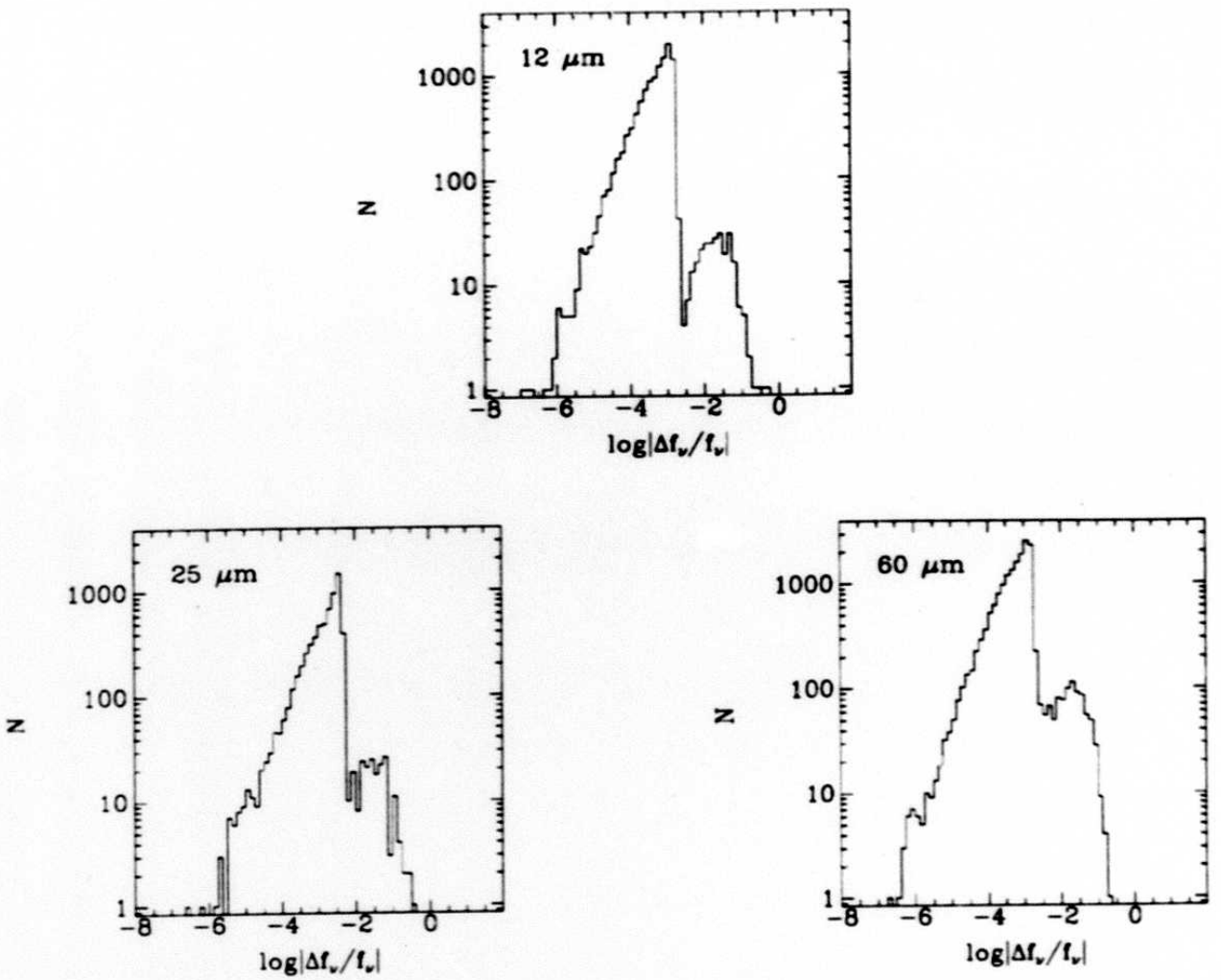

Figure IV.B.5 Flux density differences between FSC v.1.2 and FSC v.2 sources at 12, 25, and 60 μm.

Each of the plots displays the same distinctive behavior: a large, rising population of sources at small percentage flux-density differences, which falls abruptly at higher flux-density difference values. The peak observed at small flux density differences is due to the use of FSC v.1.2 from a FITS format tape (only the short form tape for FSC v.1.2 was made, which of necessity carried less than the full available precision for reported fields). The error expected due to this round-off is $\sim \frac{1}{2}\%$. Thus, differences in flux density of less than $\frac{1}{2}\%$ can be explained by FITS round-off error.

The histograms in figure IV.B.5 indicate the presence of two populations in the identified set. The predominant population has a fractional flux density difference of less than $\frac{1}{2}\%$ (notice the sudden drop near the $\frac{1}{2}\%$ bin, $\log(0.005) = -2.3$). This population is

336

due to the FITS round-off error. The large number of sources found below the $\frac{1}{2}\%$ limit represents the efficiency of the identification process at matching FSC v.1.2 and FSC v.2 sources with close flux densities (notice that the identification process did not *require* a flux density difference of less than $\frac{1}{2}\%$). The much smaller population in the histograms, those sources which have fractional flux density differences greater the expected FITS round-off error, are attributable to the changes in software between versions 1.2 and 2. Although the actual flux density in a given pixel does not change from v.1 to v.2, the procedure for selecting a representative source from among duplicates in regions of plate overlap does (see Section II.G.2). This sometimes results in the FSC v.1.2 and FSC v.2 representations of a source coming from different FSS plates. Differences in binning and scan angle from plate to plate can result in an average 5% difference in flux density at a given position (see Section III.F.3). Thus, those sources whose representations are on a different plate in version 1 than version 2 would be expected to have larger flux-density differences. To verify this hypothesis, several sources with flux-density differences greater than 1% were individually examined. In every case, a FSC v.2 source which differed by more than 1% from its FSC v.1.2 counterpart's flux density had a duplicate source on a different plate which agreed with the FSC v.1.2 source's flux-density to within the expected $\frac{1}{2}\%$. Aside from confirming that "binning error" is responsible for the observed large flux density differences, this underscores the accuracy of the identification procedure!

Thus, all observed flux density differences between FSC v.1.2 sources and their FSC v.2 counterparts can be explained by FITS round-off or binning errors for sources on different plates in the two catalogs. The largest flux density differences are as high as 40% (see Figure IV.B.5). Only a handful of sources have flux density differences this high, and, for such a small number of sources, flux density differences of this magnitude can be attributed to extreme excursions in the difference in flux density due to binning within a plate.

B.3.c Positional Differences

Source positions in FSC v.2 may vary from those of FSC v.1.2 for any of a number of reasons. The vast majority of FSC v.1.2 sources change position by only a few arcseconds in FSC v.2. A very few have a difference in position of 20″ or more, and a handful are greater than 1′ removed from their FSC v.1.2 positions. Despite these changes, FSC v.2 positional accuracy is not diminished compared to FSC v.1.2, and some data indicate it may even be better (see Section III.E).

Several differences in FSC v.2 processing may result in different positions for FSC v.1.2 sources present in FSC v.2. Firstly, sources which are detected at different wavelengths in

337

FSC v.2 than in FSC v.1.2 will have slightly different positions in the two catalogs. This is because the position of a bandmerged source is derived from the flux-weighted centroid positions of the detections making up the source. The addition or subtraction of a wavelength will therefore affect the calculated position of the final bandmerged source. In cases where the FSC v.1.2 source involved a 100 μm detection, the effect is even more pronounced; the version 2 bandmerger does not include 100 μm positions in the bandmerged position calculation, whereas the version 1 bandmerger did (see Section III.F.3).

Another situation in which the FSC v.1.2 and FSC v.2 positions for a source might differ by more than a few arcseconds is in the case of extended sources. An extended source might well be extracted differently in size and shape in v.1.2 than in v.2, causing a change in position. Related to this, differences in how thresholding noise is handled in version 2 may result in a difference in the number of pixels extracted in a source. Since the position of a detection is determined by the flux density-weighted centroid of its pixels, a loss or gain of pixels can affect the final source position. Finally, differences in the process of re-thresholding (see Section II.E.3) may result in new or refined version 2 positions for FSC v.1.2 sources.

Figure IV.B.6 shows the overall distribution of positional differences resulting from these changes. Here, the radial distance, in arcseconds, from the FSC v.1.2 position to its corresponding FSC v.2 source-position is histogrammed. The bins are 2″ wide. As can be seen, the vast majority of sources have little or no change in position. A small tail of sources at larger separation distances results from the more extreme cases of the scenarios given above. It should be noted that any false or incorrect FSC v.1.2–FSC v.2 identifications might be expected to exhibit large changes in position. Partial analysis has not revealed any false identifications, but, if they exist, they might well account for a few of the outliers in Figure IV.B.6.

To ensure that no loss of positional accuracy occurred due to the processing changes that resulted in different positions for FSC v.1.2 sources in FSC v.2, the positions from FSC v.1.2 and FSC v.2 were checked against the positions of SAO stars they are associated with. If one catalog had poorer positional accuracy, the expected result would generally be a larger dispersion in separation distances between the SAO positions and sources in that catalog. Analysis of these data showed almost identical results for the two catalogs. The average standard deviation, median, and mode of the SAO-to-FSC distance distributions were the same, within 2% in the largest case, for FSC v.1.2 and FSC v.2. The FSC v.2 positions are, on the whole, slightly closer to their associated SAO stars than FSC v.1.2

D 10015

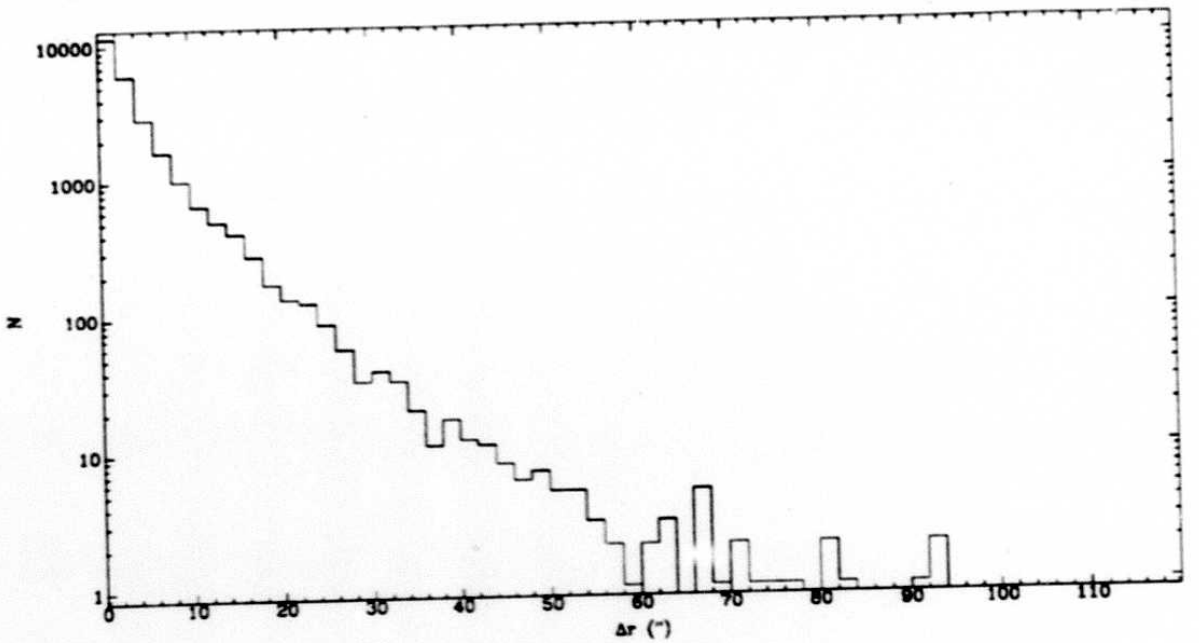

Figure IV.B.6 Radial distances between identified FSC v.1.2 and FSC v.2 sources.

sources. The conclusion is therefore that there is no loss of positional accuracy from FSC v.1.2 to FSC v.2 due to slight changes in the position of sources present in both catalogs.

B.3.d Differences in Signal to Noise Ratio

Since many of the differences between FSC v.1.2 processing and FSC v.2 processing involve calculating and compensating for various types of noise, the v.1.2 and v.2 SNR values for a given source vary significantly and in no regular or easily quantifiable fashion. Because of this, it is difficult to perform a straightforward comparison of v.1.2 and v.2 SNRs. Furthermore, the method of noise calculation was changed so much that little useful information is to be gained by such a comparison. However, in order to characterize the nature of the change in SNR from FSC v.1.2 to FSC v.2 and for the sake of completeness, Figure IV.B.7 gives plots of FSC v.1.2 SNR vs. FSC v.2 SNR for all four wavelengths. As above, a source is only represented at a given wavelength if it is detected at that wavelength in both FSC v.1.2 and FSC v.2. The apparent quantization of FSC v.1.2 values is due to the storage of these data in FITS format, where SNR values were limited to 2 significant figures. For $|b| > 50°$, the improvement in noise computation is most noticeable at 100 μm, where the effects of infrared cirrus are properly taken into account. As a result the SNRs at 100 μm in v.2 are in general smaller than in v.1.2. These figures will give the user a feel for how the SNR of a FSC v.1.2 source might change in FSC v.2.

339

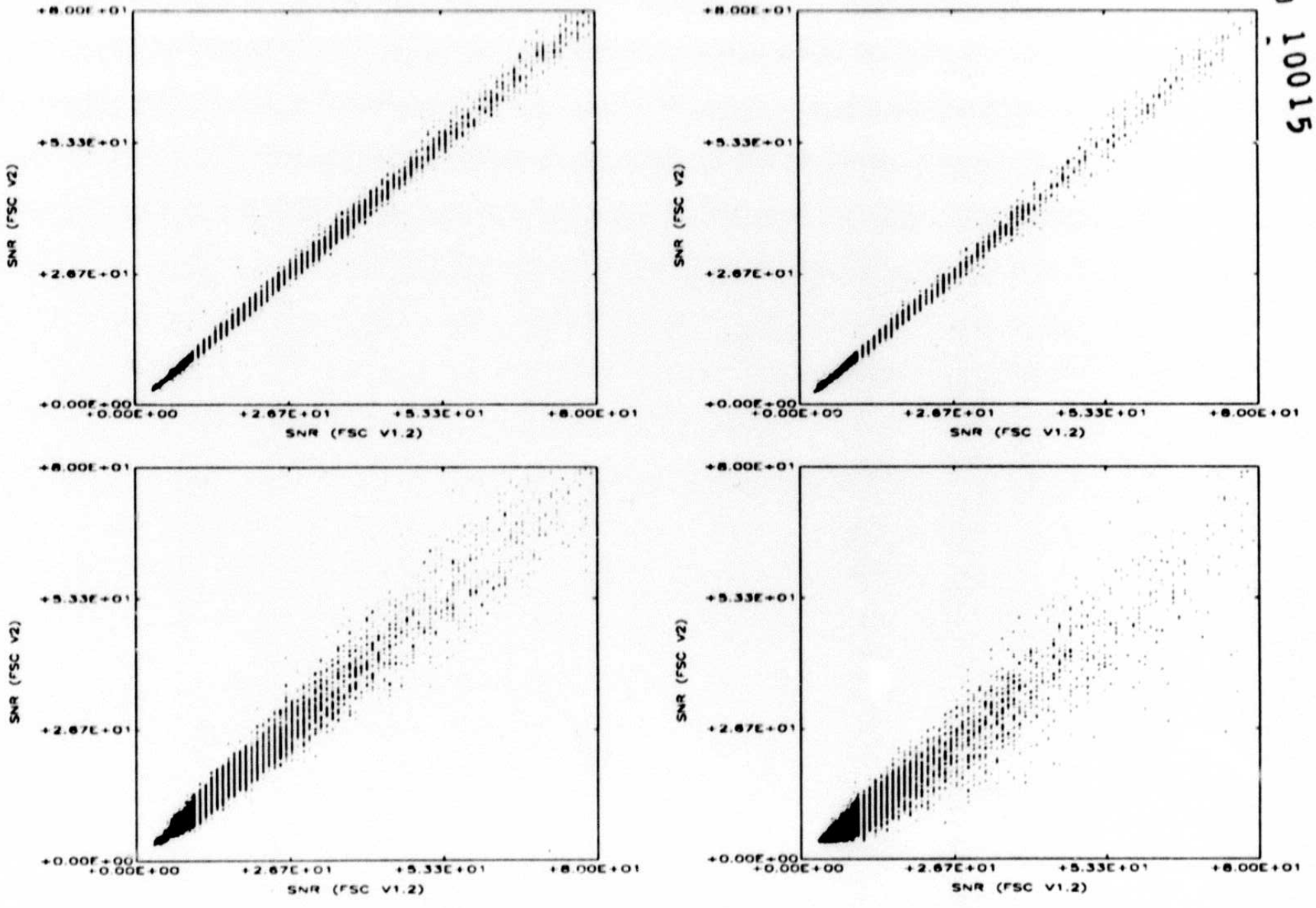

Figure IV.B.7 Comparison of the SNRs for identified FSC v.2 and FSC v.1.2 sources at 12 (upper left), 25 (upper right), 60 (lower left), and 100 μm (lower right).

D 10015

Table IV.B.2 FSC v.1.2 Sources Not Identified in FSC v.2

FSC v.1.2 Band Combination	# in category not identified in FSC v. 2	% of FSC v.1.2 band type	% in category identified in FSR	% in category not identified in FSR*
1000	536	9	8	1
1100	156	4	2	2
1110	20	3	1	2
1111	54	4	1	3
0100	15	71	62	9
0110	30	11	2	9
0111	105	7	1	6
0010	285	8	5	3
0011	614	6	3	3
0001	209	100	90	10
1101	3	23	8	15
1010	14	16	7	9
1011	51	11	3	8
1001	14	33	19	14
0101	2	100	-	100
Total	2108	8	5	3

* Sources in this category are listed in Appendix IV.1. (Names of Unidentified FSC v.1.2 Sources).

B.4 FSC v.1.2 Sources Not Identified in FSC v.2

B.4.a Introduction

Eight percent of FSC v.1.2 sources are not identified in FSC v.2. The majority of these sources, comprising 5% of FSC v.1.2, have been identified in the FSR. These are FSC v.1.2 sources detected by version 2 processing but excluded from FSC v.2 for a variety of reasons. The remaining 3% of FSC v.1.2 sources were not identified in the FSR. These sources are referred to as unidentified in version 2 processing, and are listed in Appendix IV.1. Some sources in this group may actually be present in FSC v.2 or the FSR but remain unidentified for reasons to be discussed. Others are actually undetected by version 2 processing due to differences between this processing and that of version 1.

Table IV.B.2 provides an analysis of the FSC v.1.2 sources not identified in FSC v.2. Column 1 lists the various band combinations of FSC v.1.2 sources. The encoding scheme for band structures is the same as the one used in Table IV.B.1. For each band combination

341

D 10015

listed in column 1, column 2 gives the number of FSC v.1.2 sources of that type which are not identified in FSC v.2. Column 3 expresses this number as a percentage of all FSC v.1.2 sources of the specified type, and columns 4 and 5 show the percentage of FSC v.1.2 sources in the given type which respectively are, or are not, identified in the FSR.

For example, the first row contains data for FSC v.1.2 sources detected only at 12 μm (encoded "1000" in column 1). Column 2 indicates that 536 of the FSC v.1.2 sources detected only at 12 μm are not identified in FSC v.2. This number represents 9% of the total number of FSC v.1.2 12 μm-only sources, as shown in column 3. Finally, columns 4 and 5 show that 8% of FSC v.1.2 sources detected only at 12 μm are identified in the FSR, and 1% are not. It should be obvious that columns 4 and 5 represent a breakdown of the FSC v.1.2 sources not identified in FSC v.2, and, as such, the percentages in these columns should always add to the percentage given in column 3.

B.4.b Sources Identified in the FSR

As stated above, 5% of FSC v.1.2 sources are identified in the FSR. These are sources which met FSC v.1.2 catalog criteria but, as represented by version 2 processing, did not meet the criteria for inclusion in FSC v.2. Some of these sources were rejected from FSC v.2 because of changes in catalog criteria from FSC v.1.2 to FSC v.2. Others had slightly different source attributes in version 2 and therefore fell below the thresholds for version 2 catalog inclusion. Details and examples of both these occurrences are presented below in the analysis of the specific types of FSC v.1.2 sources identified in the FSR.

The data describing the specific FSC v.1.2 band types identified in the FSR are given in column 4 of Table IV.B.2. The largest percentage of a given band type identified in the FSR is 90% of the 100 μm-only sources. This high percentage of 100 μm-only sources rejected from FSC v.2 is a direct consequence of the catalog criteria for FSC v.2 (see Section III.D.3). Under these criteria, 100 μm flux-density detections were all denoted moderate quality; none were given the high-quality designation. To be included in FSC v.2, a source must have at least one high-quality flux-density measurement. Thus, FSC v.1.2 100 μm-only sources which remained 100 μm-only sources in version 2 were excluded from the FSC v.2 by virtue of the fact that they possessed no high-quality detections. This was the case for all identified FSC v.1.2 100 μm-only sources.

The exclusion of 100 μm flux-density measurements from high-quality flux status also caused some multiband FSC v.1.2 sources to be rejected from FSC v.2. These sources contained flux-density measurements in many bands, but, in version 1.2, possessed high-quality flux-density measurements only at 100 μm. In version 2, these 100 μm detections were denoted moderate quality, and, if the source had no other flux-density measurements

342

which achieved high-quality flux status in version 2, the sources were subsequently rejected from FSC v.2. Approximately 50% of the FSC v.1.2 sources detected only at 60 and 100 μm and identified in the FSR were rejected from FSC v.2 for this reason. Of the other multiband FSC v.1.2 sources containing a 100 μm flux density and identified in the FSR, roughly 70% are rejected for the same reason.

In contrast to the rejection of 100 μm-only sources, the rejection of 8% of the FSC v.1.2 12 μm-only sources from FSC v.2 appears much more difficult to explain. However, examination of these sources shows that they all fall into one of three categories. First, roughly 3% of the FSC v.1.2 12 μm-only sources are in regions of sky where the SNR threshold for catalog inclusion is slightly higher in FSC v.2 than for FSC v.1.2. Although FSC v.2 sources were actually determined by reliability thresholds, this translates to an SNR threshold, which can then be compared with values used in creating FSC v.1.2. In FSC v.1.2, a flat SNR threshold was used for the whole $|b| > 50°$ sky. In FSC v.2, this threshold was dependent on noise and galactic latitude. When compared with FSC v.1.2, then, FSC v.2 SNR thresholds for catalog inclusion are sometimes higher and sometimes lower, causing small numbers of sources to cross catalog thresholds they previously fell just above or just below. This results in a gain in FSC v.2 of sources not included in FSC v.1.2 for some regions of sky (see section IV.B.5), and a loss of some known FSC v.1.2 sources in others.

In addition to areas of sky which had higher SNR thresholds for catalog admission in FSC v.2, some areas with $|b| > 50°$ were essentially excluded from catalog consideration due to the level of sky noise in the region (see Sections III.D.3.a, IV.A.4.a). These are areas of high sky noise for which a statistically dependable reliability curve could not be accurately determined. Thus, sources in these regions have no quoted reliability. Because of this, these areas are effectively "unsurveyed" by FSC v.2, and no sources can be admitted to the catalog which lie in these regions (different for each band). Approximately 2% of the FSC v.1.2 12 μm-only sources were in regions with sky noise greater than 36 mJy, the limit for the 12 μm reliability curves, and were therefore rejected from FSC v.2.

Finally, some FSC v.1.2 sources were rejected from FSC v.2 because they had a lower SNR after version 2 reprocessing than they did in FSC v.1.2. Differences in how noise is handled in FSC v.1.2 and FSC v.2 often cause the SNR of sources to be different from one catalog to the other (see section IV.B.3.d). Usually the difference is slight and of no consequence. However, when a FSC v.1.2 source has an SNR near the catalog threshold, a slight change of SNR can cause that source to fall below the catalog threshold for FSC v.2. Approximately 3% of the FSC v.1.2 12 μm-only sources were rejected from FSC v.2

for this reason. In combination with the 5% of FSC v.1.2 12 μm-only sources rejected due to the changes in catalog thresholding criteria described above, these make up the 8% of 12 μm-only FSC v.1.2 sources identified in the FSR.

The three effects just described are not confined to 12 μm detections. All FSC v.1.2 band types experience loss and gain of some detections in FSC v.2 for these reasons. However, the effect is most pronounced in single band sources, where catalog candidacy is determined by the strength of only one detection. If the one detection of a single band FSC v.1.2 source falls just below the catalog thresholds in v.2, there are no other detections which may retain their high-quality flux density status and thereby keep the source in FSC v.2. Instead, the source is rejected from FSC v.2. Thus, FSC v.1.2 12 μm-only and 60 μm-only sources also have a significant percentage of their members identified in the FSR. The relative percentage of 60 μm-only sources identified in the FSR is less than that for 12 μm-only sources; this is because FSC v.2 is slightly deeper at 60 μm than FSC v.1.2, so there are fewer regions of sky where the v.2 catalog thresholds are higher than those for FSC v.1.2. On the other hand, 25 μm-only sources show a much greater percentage identified in the FSR. This is mostly due to small number statistics (there are many fewer 25 μm-only sources than 12 μm-only or 60 μm-only) and the fact that 25 μm is, in general, a much weaker band strongly affected by noise variations.

Finally, some FSC v.1.2 band types associated with highly reliable sources, such as three- and four-band sources, had a small percentage of their members rejected from FSC v.2. Many of these had only one high-quality flux density detection in FSC v.1.2, and so were susceptible to rejection from FSC v.2 if they fell into one of the categories outlined above. For example, the entire 1% of FSC v.1.2 four-band sources that were rejected from FSC v.2 had either: (1) a 100 μm detection as their only high-quality flux density in FSC v.1.2, or (2) only one high-quality flux density detection in another band, which then was rejected from high-quality flux density status in v.2 for one of the above reasons. In addition to this, other reliable FSC v.1.2 sources were excluded from FSC v.2 for being in excluded regions of sky, such as comet trails, etc. Although regions like this also existed in FSC v.1.2, they were recalculated in FSC v.2 due to new information and better methods. Consequently, some FSC v.1.2 sources that were not previously associated with these regions now are, and are therefore rejected from FSC v.2.

Thus, the rejection of, in total, 5% of FSC v.1.2 sources from FSC v.2 can be entirely explained by the mechanisms just presented. Almost 60% of these sources are single band detections rejected from FSC v.2 due either to small changes in catalog thresholds or small changes in source attributes, such as SNR. An additional 30% (roughly) had their only

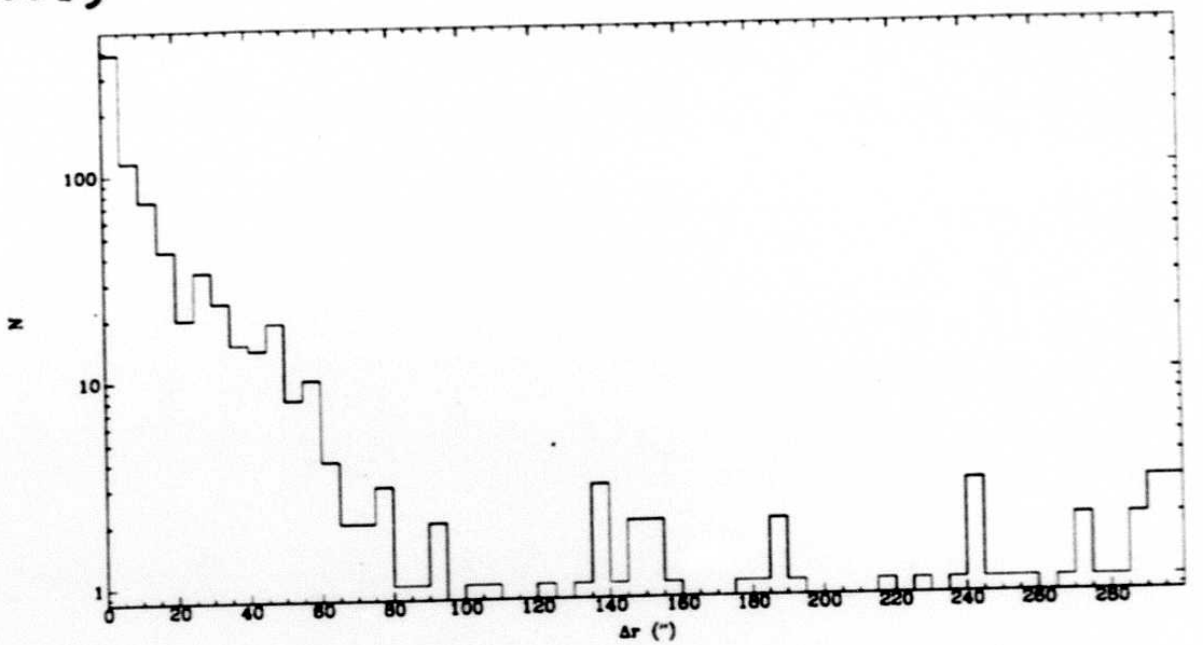

Figure IV.B.8 Radial distances between unidentified FSC v.1.2 sources and their nearest v.2 sources.

high-quality FSC v.1.2 flux-density detection at 100 μm, and were therefore rejected from FSC v.2 when this band was excluded from high-quality flux density status in version 2. The remaining FSC v.1.2 sources identified in the FSR are rejected for miscellaneous reasons, mostly involving recalculation of comet trails and so forth.

B.4.c Unidentified Version 1 Sources

The sources represented in column 5 in Table IV.B.2 are FSC v.1.2 sources which have not been identified in either FSC v.2 or the FSR. These sources are collectively referred to as the unidentified FSC v.1.2 sources, and are listed by name in Appendix IV.1. Some, perhaps a majority, of these sources actually exist in FSC v.2 or the FSR but were not identified in the time allotted to the identification task. Others were located in one of these two products, but could not be formally identified due to lack of resources. Finally, some FSC v.1.2 sources are truly missing from both FSC v.2 and the FSR.

B.4.c.1 Unidentified FSC v.1.2 Sources Present in v.2

Proof that unidentified FSC v.1.2 sources are actually present in v.2 data products is abundant. First of all, many of these sources have nearby version 2 sources, as shown by Figure IV.B.8 (the v.2 sources are different enough in band structure, flux density, etc. that they were not immediately accepted as identifications - see Section IV.B.2.c). In this figure, the distance from FSC v.1.2 unidentified sources to their nearest v.2 neighbors is

histogrammed in 5″ bins. Fully 50% of the FSC v.1.2 unidentified sources have a v.2 source within 5″ of their position; 61% have a version 2 source within 10″. Only 8 unidentified FSC v.1.2 sources are off the scale of this plot, having no v.2 neighbors within a 5′ radius of their positions.

The presence of so many FSC v.1.2 sources with nearby v.2 sources on the unidentified sources list can be explained by the exhaustion of time allocated to this analysis before all eligible FSC v.1.2–v.2 matches had been analyzed. As explained in Section IV.B.2.c, FSC v.1.2 sources and their candidate v.2 matches were segregated into "match quality" groups which were prioritized and analyzed. Unfortunately, before all the groups could be analyzed, time ended on the identification task, leaving at least one moderately reliable group of matches unanalyzed. If most of these sources were, in fact, present in version 2, this would explain the results shown in Figure IV.B.8.

Evidence that this is the case comes from analysis carried out to investigate the presence of "reliable" band types in the unidentified sources shown in Table IV.B.2. As shown in column 5, many reliable band types are among the unidentified FSC v.1.2 sources, such as those detected in 3-consecutive or 4 bands. To understand how 4-band and other bright FSC v.1.2 sources could remain unidentified in version 2, a sample of these sources was individually examined, along with nearby version 2 sources. The sample consisted of all the unidentified 4-band sources, plus the brightest 12 or 60 μm sources. In total, 50 sources of 6 different band types were analyzed individually, plus all the version 2 sources within a 5′ radius of each of these v.1.2 sources (the same search radius used for FSC v.1.2–v.2 identifications).

The search revealed that 62% of the sources in the sample had a definite, single, version 2 representation, not included in the formally identified sources because it belonged to one of the groups of unanalyzed matches. In all cases, the version 2 match was a member of the match quality group slated to be the next analyzed, had analysis continued. (The group contained v.1.2-v.2 matches which had different band structures, but at least one commonly-detected band which agreed within the flux-density limits for identification. See section IV.B.2.c) This, in combination with information about this match quality group given in Section IV.B.2.c, strengthens the assertion that this match group in particular contains many reliable matches that would have been formal identifications had time remained for the identification task. Indeed, with almost 600 unidentified sources in this one group, the majority of unidentified sources probably have a reliable match in this group and are likely present in FSC v.2.

B.4.c.2 FSC v.1.2–v.2 Matches Which Are Not One–to–One

As discussed in section IV.B.2.b, the identification requirements specify that all formal FSC v.1.2–v.2 identifications must be of a one-to-one nature. This is to enable the transfer of the source names of identified sources from one version to the other. For this reason, all FSC v.1.2 sources which have "split" in version 2 to become more than one source, or multiple FSC v.1.2 sources which have merged into a single version 2 source cannot be formally identified. Approximately 22% of the sample of unidentified FSC v.1.2 sources with reliable band types belong to this category.

This does not occur as frequently as might be suggested by the results of the multiband sample given above. Three- and four-band sources are, of course, much more likely to be split than a two-band source, since they simply have more bands. Mergers, on the other hand, are inherently difficult to detect by the processing methods used in the identification task (cases where two FSC v.1.2 sources are combined into one v.2 source). Most mergers would have been removed by hand at the last stage of identification processing, where all v.2 sources matched to two or more v.1.2 sources were individually examined. Only 12 v.2 sources had more than one FSC v.1.2 match, and not all of these were mergers. Thus, the detected incidence of mergers is much less than that for splits, with the result that, when examining 3- and 4-band sources, one probably sees the majority of FSC v.1.2 sources excluded from identification for not having a one-to-one v.2 match.

B.4.c.3 Ambiguous Cases

In contrast to those sources which are present but cannot be identified due to the logistics of source-naming, the presence of some unidentified FSC v.1.2 sources cannot be determined even when individually examined. These are sources which have a v.2 source nearby, but, for example, do not have a band structure or flux density similar to the v.2 source. (For an explanation of how sources may exhibit a "change" in flux density from FSC v.1.2 to FSC v.2, see Section IV.B.3.b.) Or they may have a similar band structure but a large separation distance. In cases like these, much further in-depth analysis would be needed to determine whether or not the FSC v.1.2 source could actually be identified with the nearby v.2 source, and even with this analysis some of these cases probably could not be adequately resolved. Thus, at the level of analysis of the identification task, these sources are ambiguous and their presence or absence in version 2 is undetermined: the FSS plates were not examined due to lack of resources. Twelve percent of the sample of "reliable" source types were in this category, demonstrating that even bright, multiband sources cannot always be declared definitely present or definitely absent in version 2 from a cursory examination of the FSDB.

B.4.c.4 FSC v.1.2 Sources Missing From v.2

Finally, some FSC v.1.2 sources are completely absent from FSC v.2 and the FSR. Evidence comes not only from the multiband source sample where 4% of the sources had no version 2 counterparts in a 5′ radius of their positions, but also from examination of the 8 FSC v.1.2 sources with no version 2 sources at all within 5′. In the case of these latter sources, a further search of the FSDB using a 10′ radius failed to turn up any evidence that these sources were present in v.2 at larger separation distances.

Analysis of both these sets of sources revealed several mechanisms which could cause FSC v.1.2 sources not to be extracted in v.2. Almost all of them involve changes made in the calculation of noise from v.1.2 to v.2. Fortunately, most should affect only a small number of sources, so the total number of FSC v.1.2 sources that are missing from v.2 is probably quite low.

The ways in which changes in the noise computation have been found to affect the extraction of FSC v.1.2 sources are:

1) Cirrus and other sources in regions of high confusion noise are handled more effectively. Previously, small, high confusion-noise regions of a plate were thresholded at too low a noise value. Improvements in the noise calculation and thresholding procedures have allowed these areas to be correctly thresholded, with the result that some sources which were not sufficiently distinguished from the noise around them were not extracted. Most of the sources excluded by this change are probably cirrus or cirrus-contaminated. This explains the presence of, in general, larger percentages of 100 μm band types among the FSC v.1.2 unidentified sources. (As further evidence, all 21 unidentified FSC v.1.2 100 μm-only sources were searched for in the FSDB. Of these, 43% percent were definitely absent, as compared with the 4% missing from the multiband sample.)

2) Sources near, but not in, low coverage areas may sometimes not be extracted. This is because the noise used to calculate SNR for thresholding purposes in version 2 is an interpolation over noise cells in an area $\sim$ 200 – 300 pixels square (see Section II.E.2); a different method and smaller area were used in v.1.2. Extraction of sources in high coverage areas may be adversely affected in version 2 when one or more of the noise cells used in the interpolation has significantly lower coverage than the high-coverage region. In these cases, the much higher noise calculated in the low-coverage areas strongly affects the interpolated noise, with the result that some sources are not extracted that previously were. Only one of the 8 FSC v.1.2 sources with no v.2 sources in a 5′ radius was lost due to this effect.

3) Rethresholding of sources in regions with higher noise in v.2 than v.1.2 may sometimes result in a single source being extracted, where two sources were present in v.1.2. If the two v.1.2 sources separated by rethresholding differ sufficiently in SNR, then the higher calculated noise in version 2 may, upon v.2 rethresholding, cause the fainter source not to be extracted. There is evidence that this is the case for 2 of the 8 FSC v.1.2 sources which had no v.2 neighbors. Both sources were single band, 60 μm detections. In two other cases, an extreme noise spike (SNR=100) took the place of the brighter, nearby source in the above scenario. In these cases, the "noise spike" source which survived rethresholding was then rejected due to a low peak pixel SNR value. Both FSC v.1.2 sources lost in this way were 12 μm-only sources. It should be pointed out that other possible configurations of the re-thresholding algorithm would also have resulted in the loss of some, and probably more, sources from FSC v.1.2 to FSC v.2 processing.

Aside from these three effects due to differences in the calculation of noise from v.1.2 to v.2, one other change has affected the extraction of small numbers of FSC v.1.2 sources. In version 1.2, extraction was based not only on SNR, but also on the condition that the extracted source have *at least one* pixel above another SNR threshold. In version 2, this was changed to the condition that the *peak flux pixel* be above a certain special threshold. For further information on the values used for thresholding, see section II.E; for discussion of the effects on FSC v.1.2 extractions, see section IV.B.3.b.

B.4.c.5 Summary

The majority of FSC v.1.2 unidentified sources are actually present in either FSC v.2 or the FSR, but could not be identified in the time allotted to the identification task. In combination with those unidentified sources which are present but cannot be formally identified for many reasons (one source split into two, cases where the source name cannot be transferred to the v.2 source since the match is not one-to-one, etc.), they probably constitute 60–75% of the unidentified FSC v.1.2 sources. The remaining sources are either definitely absent from version 2 or ambiguous (i.e. data are insufficient to determine whether they are present or not). Taken together, they comprise about 1% of FSC v.1.2 sources. *Thus, the percentage of FSC v.1.2 sources actually lost through version 2 reprocessing is 1% or less of the total sources in FSC v.1.2.*

B.5 FSC v.2 Sources not Identified with FSC v.1.2 Sources

Of the 32,246 sources in FSC v.2 with $|b| > 50°$, 6,528 are not identified with a FSC v.1.2 source (20% of FSC v.2, as shown in Figure IV.B.1). The majority of these sources are totally new 60 μm sources in FSC v.2, a result of the improvements made in noise

calculation in version 2. The rest are either previously-detected sources which did not meet FSC v.1.2 catalog criteria, or actual FSC v.1.2 sources present in FSC v.2 but listed as unidentified. Thus, the set of FSC v.2 sources not identified with FSC v.1.2 can be broken into the following three groups:

1- Sources not previously detected (new sources): Better calculation and finer tracking of noise in the version 2 processing have made it possible to go fainter in some regions of sky than was the case in FSC v.1.2. In these regions, sources which were not even detected during the FSC v.1.2 processing effort have been extracted, and the most reliable of these have entered FSC v.2. Since they are faint, the majority of these sources are detected only in one band (see below). The number of these sources present in the FSC v.2 sources not identified with FSC v.1.2 can be determined by estimating the number of sources in the next two groups.

2- Previously-detected sources which did not meet FSC v.1.2 catalog criteria: During the FSS v.1.2 processing effort, there were many sources, often with detections in multiple bands, which, for a variety of reasons, did not meet the necessary criteria for inclusion in FSC v.1.2. In version 2 re-processing, some of these sources have been able to enter FSC v.2. Some are sources which have slightly higher SNRs in version 2, allowing them to pass catalog thresholds they previously failed to reach. Others are in areas of sky where the catalog SNR thresholds are lower in v.2 than in v.1.2, permitting some lower SNR sources to enter the catalog for the first time. Finally, a few sources which, in version 1.2 were excised for possible contamination by comet trail debris, have, due to version 2 refinements, been declared free of contamination and allowed to enter FSC v.2.

3- Unidentified FSC v.1.2 sources: As was stated in the last subsection (IV.B.4.c), some unidentified FSC v.1.2 sources are undoubtedly present in FSC v.2. The version 2 representations of these sources, when they exist, are, of course, not identified with their FSC v.1.2 counterpart. Thus, they are included in the FSC v.2 sources which are not identified with FSC v.1.2.

The exact number of unidentified FSC v.1.2 sources in FSC v.2 cannot be calculated, since we do not know exactly which sources are present (they are, after all, unidentified). We do know, however, that it cannot be more than the total number of unidentified FSC v.1.2 sources (832). Thus, no more than 13% of the FSC v.2 sources which are not identified with FSC v.1.2 can be unidentified v.1.2 sources; in fact, the actual percentage must be less than this (see section IV.B.4.c) because it is known that some unidentified FSC v.1.2 sources are definitely *not* present in FSC v.2.

D 10015

Table IV.B.3 Band Combinations of FSC v.2 Sources Not Identified with FSC v.1.2 Sources

Band Combination†	Number
1000	283
1100	73
1110	13
1111	16
0100	5
0110	106
0111	70
0010	4099
0011	1791
0001‡	–
1101	3
1010	39
1011	29
1001	1
0101‡	–
Total	6528

† Example: 1000 = high- or moderate-quality flux density at 12 μm only; 1010 = high- or moderate-quality flux densities at 12 and 60 μm; etc.

‡ No sources of this category present in FSC vs. 2.

Evidence of these three types of sources in the FSC v.2 not identified with FSC v.1.2 can be found by examining the various band combinations present in this set of sources. Table IV.B.3 gives the number of sources of each band combination present in the FSC v.2 not identified with FSC v.1.2. The encoding scheme for the band combinations is the same as that used throughout this section (see Section IV.B.3.a). Notice that every band type present in FSC v.2 is represented in the FSC v.2 sources not identified with FSC v.1.2, including 3- and 4-band sources. It would be highly unlikely to "uncover" many sources bright enough to be detected in 3 bands which were not detected at all by version 1.2 processing. Thus sources of the last two types listed above are present in this set.

Individual examination of the four-band sources present in the FSC v.2 sources not identified with FSC v.1.2 confirms that they are, in fact, all members of one of the last two groups of sources given above. Two of the 4-band sources have only one high-quality flux density and relatively low SNRs; these were rejected from FSC v.1.2, probably because their v.1.2 SNRs were below the FSC v.1.2 catalog thresholds. All the other 4-band sources

351

are positionally very close to unidentified FSC v.1.2 4 band sources. Undoubtedly, these are the version 2 counterparts of these FSC v.1.2 sources.

This brings up an interesting point. Through the normal course of analysis of the FSC v.2 sources not identified with FSC v.1.2, we have indisputably identified 14 of the unidentified FSC v.1.2 sources. Why, then, do these sources remain on the list of unidentified v.1.2 sources? As stated in Section IV.B.2.a, the primary purpose of the identification procedure was to transfer FSC v.1.2 source names to their FSC v.2 counterparts. At the stage at which this analysis was completed, it was already too late to go back and change the catalog names of any FSC v.2 sources, or change the FSC v.1.2 flag value to reflect a positive identification. Instead, we had to leave these sources in the list of unidentified FSC v.1.2 sources. See Section IV.B.2.e for further discussion.

In general, analysis of the rest of the sources represented in Table IV.B.3 shows that virtually every band combination contains some FSC v.1.2 unidentified sources. However, comparison of Table IV.B.3 with the data for unidentified sources given in Table IV.B.2 gives an idea of the maximum number of unidentified FSC v.1.2 sources which could be present in the sample. Even if all the unidentified FSC v.1.2 sources were present in FSC v.2, a condition we know to be false, it is still obvious that there are many new sources in FSC v.2. By far, the overwhelming majority of these sources are detections at 60 μm. This is because many of the version 2 refinements in the noise calculation were particularly effective at 60 and 100 μm. Since 100 μm was not independently analyzed for catalog inclusion, only the benefit at 60 μm shows up here.

In summary, unidentified FSC v.1.2 sources make up less than 13% of the FSC v.2 sources not identified with FSC v.1.2. This leaves no fewer than 5700 new sources in FSC v.2, roughly 18% of the catalog. The presence of multiband sources in this set of "new" objects is explained by the fact that changes in processing allowed sources detected by version 1 processing but rejected from FSC v.1.2 to now meet FSC v.2 catalog criteria. Thus, these sources had been previously detected, and were not just pulled, multiple detections and all, out of "thin air." In addition, changes in version 2 processing did reveal many new detections, most of which are single band, and the vast majority of which are detected at 60 μm.

352

D 10015

Authors:

Section A T. Conrow

Section B G. Rohrbach

353/354 ✓

D 10015

APPENDIX IV.1 NAMES OF FSC V.1.2 SOURCES UNIDENTIFIED IN V.2

F00000+0827	F00282+1010	F01022−1235	F01327−1833	F02056−1654
F00007+0820	F00306−3712	F01028−2903	F01344−5240	F02059−3433
F00008+0820	F00308−0522	F01050−6337	F01355−3821	F02070+0252
F00010+0821	F00324+0433	F01050−1610	F01361+0016	F02075−4345
F00020+0239	F00328−4722	F01052+0154	F01364−4016	F02075−4107
F00021+0916	F00339−2137	F01063−6202	F01375+0528	F02094−2939
F00022−0151	F00341−6503	F01064−6202	F01386−6115	F02101−2818
F00025−0405	F00353+0230	F01064+0106	F01387−6129	F02107−1141
F00029−3613	F00360−2432	F01069−0624	F01396−2847	F02110−1407
F00074−2514	F00368−4320	F01076−0910	F01402−4747	F02111−0906
F00084−1305	F00372+0947	F01083−4312	F01432−2640	F02118+0624
F00088+0606	F00382−3728	F01104−3807	F01453−5932	F02119−0653
F00090−0054	F00382+0233	F01119−1447	F01455−3351	F02127−6206
F00095−5905	F00387−6535	F01121−3231	F01459−0904	F02137−1209
F00095−0759	F00389+0921	F01121−0128	F01462−4144	F02142−1536
F00107−2652	F00394+1122	F01128−3736	F01467−2719	F02143−4941
F00107−1850	F00407−0636	F01130−0656	F01474+0842	F02147−3812
F00109−2932	F00412−4752	F01133+0947	F01475−1933	F02156−3917
F00114−5716	F00420−3355	F01157+0305	F01489−5027	F02158−6338
F00118−4042	F00438−3904	F01159−4630	F01490−1354	F02168−6214
F00123−2421	F00461−0648	F01174−5202	F01490+0208	F02210−3305
F00125−0039	F00470−0655	F01196−0528	F01502−1807	F02222−1552
F00131−3931	F00472+0010	F01196+0041	F01502−1258	F02226−4529
F00131+0806	F00474−5008	F01203−3651	F01502−0341	F02232−5652
F00141−3258	F00480−2353	F01204−3651	F01504−1710	F02235−5757
F00146−0134	F00481−0648	F01209−1841	F01511−3647	F02246−3948
F00165−5644	F00483+1143	F01216−2422	F01527+0622	F02251−1023
F00165+1035	F00484−0826	F01225−0458	F01534−0033	F02262−5750
F00167−6009	F00493−0917	F01225−0454	F01551−5406	F02264−1647
F00170−1104	F00519−0647	F01233−3938	F01556−2643	F02264−0550
F00176−5953	F00539−5327	F01246−3648	F01580−5515	F02266−1650
F00178−5758	F00543−6413	F01246−1853	F02000−3250	F02273−4421
F00202−0933	F00544−0525	F01263−5253	F02009+0219	F02274−1148
F00203−6052	F00569+0745	F01273−2552	F02014+0811	F02278−2639
F00211−1700	F00580−0815	F01274−1555	F02015−5252	F02278+0320
F00232−6311	F00581−0815	F01281−0255	F02043−5525	F02282−1057
F00256−0208	F00593−0704	F01282−4335	F02043−0203	F02286−1622
F00272−0031	F00594−2339	F01292−2212	F02047−0612	F02299−2207
F00277−2128	F00594−1133	F01313−1150	F02047−0607	F02302−3515
F00282+1007	F01009−1107	F01327−0446	F02048−5527	F02308−1310

continued

355

APPENDIX IV.1 NAMES OF UNIDENTIFIED FSC V.1.2 SOURCES (Continued)

F02312−2901	F03070−0506	F03375−2535	F10339+3811	F11241+1307
F02312−2659	F03084−0924	F03375−1909	F10345+3809	F11251+1729
F02323+0101	F03092−3712	F03398−2448	F10355+5648	F11255+5120
F02328−6245	F03093−4315	F03407−4918	F10361+4155	F11260+0922
F02333+0256	F03101−1246	F03451−3351	F10371+2525	F11266−0650
F02334−3511	F03101−1033	F03454−3154	F10372+2420	F11267−0407
F02340−5823	F03103−4527	F03513−3425	F10417+1942	F11274+1608
F02352−1541	F03103−1156	F03520−3857	F10419+3826	F11275+3813
F02373−3122	F03106−1243	F03523−3702	F10431+1711	F11289+0620
F02379−1710	F03110−1027	F09441+3459	F10437+1625	F11289+6453
F02380−1744	F03113−1853	F09527+3331	F10448+5913	F11290+6452
F02385−5418	F03118−3753	F09528+3125	F10509+2710	F11296+5621
F02385−3024	F03127−0727	F09583+4117	F10543+5310	F11300−0154
F02390−3245	F03150−1409	F09588+2002	F10547+4421	F11301−0522
F02391−6027	F03151−3245	F10013+3013	F10599+2214	F11306+4717
F02395−1826	F03156−2633	F10016+2741	F11002+4353	F11332+0705
F02399−3451	F03165−2252	F10070+1411	F11007+4436	F11346+6228
F02402−3901	F03178−1216	F10075+3840	F11012+6007	F11348−0237
F02402−3857	F03190−2619	F10090+3629	F11016+3755	F11349−0016
F02415−1501	F03206−5308	F10103+3442	F11027+4347	F11355+1128
F02426−1847	F03217−2142	F10137+4225	F11036+2309	F11371+2012
F02453−2117	F03220−1150	F10144+2321	F11045+0351	F11378−0433
F02462−2731	F03230−1224	F10152+1611	F11057+3006	F11391−0158
F02469−2604	F03233−4204	F10152+4140	F11062+2652	F11391+5430
F02482−5235	F03237−1749	F10159+1729	F11068+5422	F11406+2038
F02521−0131	F03242−5257	F10171+2039	F11089+5222	F11413+2027
F02533−4818	F03246−2843	F10174+2857	F11090+5221	F11422+6459
F02537−1353	F03252−4615	F10176+4514	F11097−0355	F11431−0713
F02569−4004	F03257−4003	F10183+4457	F11111+0012	F11465+2718
F02571−0629	F03258−4000	F10225+0903	F11116+5313	F11468−0313
F02577−5715	F03265−4547	F10232+2151	F11122+6058	F11469−0637
F02578−5622	F03270−4504	F10248+1712	F11132−0213	F11473+5046
F02581−1136	F03271−4315	F10252+0834	F11162+5335	F11474+5044
F02590−5345	F03276−5224	F10256+4919	F11163+3746	F11474+6136
F02593−4145	F03288−1448	F10265+2621	F11174+5422	F11480+1147
F02595−3716	F03319−4907	F10275+2651	F11186+0342	F11482+5524
F03018−0747	F03325−2908	F10296+5350	F11191+3218	F11483+5214
F03028−0943	F03329−5330	F10311+3610	F11195+5939	F11486+5855
F03031−3758	F03333−5143	F10320+1127	F11217+0054	F11507+1110
F03063−1754	F03345−3229	F10321+2158	F11226+0600	F11510+4257

continued

APPENDIX IV.1 NAMES OF UNIDENTIFIED FSC V.1.2 SOURCES (Continued)

F11537+5734	F12196+2533	F12488−0509	F13169+3955	F13457+5702
F11551−0953	F12206+5843	F12505−0256	F13185+4555	F13463+5749
F11551+3233	F12215+4903	F12509+0226	F13187+3008	F13464+2807
F11551+3234	F12229+0755	F12510−1146	F13187+3205	F13474+6013
F11564+0048	F12234+0444	F12511−0621	F13194+3130	F13478−0952
F11573−1025	F12234+1556	F12514−0821	F13195+3900	F13479+2130
F11574+5308	F12239+1253	F12526+0319	F13200+2057	F13489+2456
F11580+2021	F12241+5212	F12528+1307	F13210+3359	F13499+2218
F11587+6124	F12242−0808	F12532+6600	F13215+3117	F13503+0230
F11592+2041	F12244−0810	F12534−0811	F13219−1102	F13506+4726
F12001+0215	F12247+0731	F12544−0643	F13227+1217	F13512+3809
F12002−0816	F12248+0632	F12547−0917	F13233−1058	F13519+5622
F12018+3054	F12251+1321	F12561+2731	F13235−0323	F13524−0919
F12022−0206	F12279+3929	F12585+2803	F13249+0219	F13524−0816
F12022+3246	F12279+4922	F13002+6603	F13259+1142	F13536+0515
F12029+5132	F12282+1240	F13007+6400	F13268+1135	F13539+5959
F12033+5145	F12299+4259	F13010−0640	F13272−1037	F13542+4728
F12035+2052A	F12303+3754	F13011−0451	F13280+3135	F13544+2830
F12057+5850	F12305+1034	F13017+2233	F13300+6651	F13544+3817
F12066+2709	F12311+5055	F13050+4619	F13305+5217	F13545+0950
F12071+0210	F12318+3659	F13064+6143	F13306+5310	F13564+3741
F12075+1642	F12326+1731	F13069+4248	F13318−0407	F13590+0429
F12090+2952	F12363+1648	F13080+3237	F13318+3501	F14002+5203
F12092+2336	F12365+4126	F13080+5818	F13332+3513	F14008−0547
F12102−0555	F12368+6130	F13089−0021	F13335−0814	F14021+5436
F12113+1327	F12401+1434	F13089+4359	F13340−0808	F14034+6038
F12119+6117	F12415+3226	F13093+4712	F13342+5234	F14047+2840
F12125+3328	F12420−0948	F13096+5126	F13358+5906	F14049+5710
F12129−0511	F12421+1804	F13107+2145	F13363+2759	F14056+4310
F12139+0744	F12425+6042	F13108+1339	F13370+2656	F14057+5149
F12141+1433	F12431+6052	F13115+5658	F13375+1154	F14070+2636
F12141+5211	F12441+1314	F13123+3029	F13375+3022	F14071+1945
F12143+4918	F12445+0920	F13127−0749	F13397+4740	F14072+0818
F12144+3954	F12466+4756	F13141+5720	F13413+5302	F14079+4025
F12146+5524	F12470+1404	F13142+6233	F13420+3744	F14098+5358
F12166+1217	F12477+3747	F13143+0315	F13424+3728	F14104+2751
F12178+0927	F12481−0829	F13145+3150	F13429−0704	F14113−0603
F12181−0641	F12486+4756	F13151+3121	F13439+3650	F14118+0002
F12187+1147	F12488−0917	F13154−0002	F13456+0738	F14119+4757
F12188+1146	F12488−0917A	F13166+2850	F13457−0812	F14130+3047

continued

APPENDIX IV.1 NAMES OF UNIDENTIFIED FSC V.1.2 SOURCES (Continued)

F14136+3606	F14386+2306	F14577+0327	F15318+2730	F22349−3223
F14142+2118	F14386+6039	F14581+4941	F15331+2717	F22363−2253
F14160+2132	F14390−0110	F14582+5829	F15367+4658	F22381−5717
F14172+4422	F14390+5403	F14584+4934	F15396+2241	F22396−4425
F14172+4758	F14392−0111	F14589+4815	F15418+4755	F22396−2336
F14175+0413	F14398+5034	F15002+6024	F15426+4115	F22423−4852
F14181+0542	F14408+0748	F15008+2411	F15440+2343	F22437−3732
F14192+3530	F14411+4143	F15009+1050	F15446+3900	F22519−4330
F14198−0009	F14419+0942	F15010+1854	F15463+4131	F22522−4656
F14201+1356	F14431+4844	F15015+0541	F15493+4312	F22530−5839
F14210+2246	F14434+3859	F15023+0822	F21453−3222	F22539−3723
F14211+2246	F14434+4843	F15033+4850	F21469−4340	F22544−2628
F14225+1044	F14436+3353	F15036+1940	F21492−3704	F22551−4622
F14233+2345	F14445+6056	F15047+2245	F21496−2533	F22574−2722
F14248+2714	F14458+3704	F15048+3417	F21500−3501	F22575−5734
F14256+2132	F14460+2734A	F15051+0627	F21511−4606	F22576−5443
F14266+3913	F14462+2733	F15051+1623	F21553−3258	F22576−4157
F14271+0855	F14464+2219	F15069+1808	F21579−2841	F22581−2334
F14284+1411	F14467+5252	F15075+5536	F21584−3404	F22584−3754
F14287+3511	F14471+3801	F15079+4412	F21597−3717	F22589+0208
F14292+3550	F14472+5112	F15081+3219	F22003−3404	F23007−4319
F14304+2429	F14477+3056	F15106+1151	F22047−5257	F23021−3705
F14305+0546	F14485+0429	F15113+4127	F22060−4614	F23026+0216
F14305+3656	F14485+0430	F15121+3156	F22095−2512	F23027−2245
F14307+2220	F14487+0949	F15140+3432	F22102−2357	F23047−2551
F14310+2013	F14488+0949	F15145+5630	F22127−4605	F23063−6323
F14312+2103	F14492+5740	F15152+3133	F22151−3025	F23071−4308
F14318−0253	F14501+5357	F15188+1747	F22215−2151	F23086−2711
F14322+3721	F14503+5127	F15188+1811	F22230−5544	F23112−1339
F14323+2047	F14517+1241	F15190+2630	F22231−5540	F23133−4551
F14323+3111	F14519+0659	F15193+1809	F22233−2816	F23149−0807
F14326−0046	F14523+2413	F15206+3342	F22244−5816	F23166+0043
F14331+1612	F14541+1751	F15232+3317	F22266−2855	F23168−0205
F14335+1704	F14548+1150	F15259+1854	F22268−2109	F23170−3843
F14336+1637	F14550+1952	F15281+1637	F22284−2126	F23187−4510
F14338+5525	F14557+1109	F15283+1452	F22331−4034	F23203+0110
F14344+5845	F14562+1754	F15304+3017	F22333−3628	F23212−4352
F14364−0254	F14566+1635	F15314+2009	F22334−3626A	F23271−0635
F14379+4257	F14566+1731	F15314+2118	F22343−1914	F23278+0510
F14383+5600	F14574+2718	F15316+1443	F22345−1031	F23279−2216

continued

D 10015

V. THE FORMATS OF THE FSS PRODUCTS

A. Introduction

This chapter describes the formats of the Faint Source Survey (FSS) products: the plate tapes, the Faint Source Catalog (FSC), the Faint Source Reject File (FSR), and this Explanatory Supplement. A brief description is given of each entry in the catalogs; tables describe each column of the catalog in more detail and give, for the machine readable versions, the logical type of each variable and its length in bytes. The FITS header for each tape contains the date and version number of the data on the tape.

B. The FSS Plates

The FSS plates present the best available information on the *point-source filtered* flux density, noise and data coverage at any point in the sky covered by the *IRAS* telescope. These maps are 1584×1584 pixels at 12 and 25 μm, and 792×792 pixels at 60 and 100 μm. The FITS format maps are produced from the original FSS plates which are in IPAC's own *DEEPSKY* format in which each pixel is a *REAL*$*4$ variable. The production of the FITS version of the plates was undertaken with the goal of preserving the dynamic range of the original plates subject to a realistic and manageable number of resulting tapes. The conversion of *REAL* $*$ 4 data to the integer form appropriate to the FITS format was performed at a resolution of $0.05 \times$ *plate median noise*. Depending on the dynamic range present in *either* the flux density or noise grid of a given spectral band, the resolution for the FITS grid in that specific band was chosen to be either two or four bytes. In all cases the map of data counts per pixel was produced in the one-byte format. In the most optimal case when all grids are produced in the two-byte format, there can be at most five FSS plates per magnetic tape. They are written at 6250 bpi on 9-track, unlabeled tapes, and occupy 639 magnetic tapes. The data are also available on 40 8-mm tapes. The total data volume amounts to $\sim$ 73 gigabytes. Should the demand warrant, at a later date the data may be made available in CD-ROM form as well.

B.1 The FSS FITS Grids

The standard references on FITS format, along with the header record of each grid, give a complete description of the involved formats (Wells, Greisen, and Harten 1981; Greisen and Harten 1981; Harten, Grosbøl, Greisen and Wells 1988a and b). Each plate is presented as four sets of three files (headers plus grids) for each spectral band. The set of three grids for each band consists of:

1) Map of flux density per pixel.

2) Map of 1-σ noise per pixel.

3600

3) Map of detector coverages per pixel.

The first three records of each file contain the FITS header. The grid commences in the fourth record as a continuous stream of pixel values in 2880 byte records. The unused portion of the final record is padded with zeros. Depending on the dynamic range of each spectral band, either of two- or four-byte integers are used for the flux density and noise grids (as indicated by the FITS keyword BITPIX), and in all cases one-byte integers are used for the data count grids. It should be recalled that the flux-density grid has a value at any pixel for which the number of data counts is non-zero, whereas the noise grid does not report values at any pixel which has fewer than four data counts. In Tables V.B.1 through V.B.3 the sample grid headers for the flux density, noise and count grids are displayed. In Table V.B.4 the explanations for some of the FITS keywords are given.

B.2 Flux Calibration of FSS Plates

The FSS plates being released are an exact copy (within the digitization scale defined in Section V.B.1) of the plates from which the FSDB is generated. Following the release of FSC version 1 for $|b| > 50°$ in December of 1988, further analysis of calibration using a larger sample going below 50° revealed that a *very small* correction factor was required. This correction was applied to the whole FSDB, and all of the released products from the second version of the FSDB incorporate these small adjustments. However this correction occurred after the FITS format copies of the FSS plates had been produced. *Therefore the users of the* FSS *plates should multiply the flux density and noise grids at* 12 *through* 100 μm *by* 1.015, 1.008, 0.9674, 0.9665 *respectively*.

Furthermore, in going from the plates to the FSDB (FSC plus FSR), a flux-density calibration correction was applied to the sources which takes into account the non-linear behavior of load resistors due to different background brightnesses (see Section II.G.5). The user of these plates is therefore warned that if the flux density of a given FSDB source is measured directly from the plates, the FSDB flux density can be different from the plate value by a few percent. *Thus the careful user will compute the appropriate non-linear correction factors and apply them to the values read from the plate*.

C. The Faint Source Catalog

The information about faint infrared point sources is presented in increasing detail, progressing from the short tape version of the catalog to the long tape version containing more detailed information about the parameters of each source. The short catalog tape (Section V.C.1) is intended for astronomers desiring to make statistical studies and to search the catalog for large numbers of sources. The long catalog tape (Section V.C.2) is meant to provide all the available data on any given source such as pointers to duplicate

301

sources from plates which overlap the source, a list of all correction factors applied to each source, and the results of template fits to each source. The long form is meant for more detailed studies of smaller numbers of sources.

TABLE V.B.1 FITS Grid Header for the Flux Map

```
SIMPLE  =                    T / STANDARD FITS FORMAT
BITPIX  =                   16 / 2 BYTE TWOS-COMPL INTEGERS
NAXIS   =                    3 / NUMBER OF AXES
NAXIS1  =                 1584 / NZ = Z  GRID DIMENSION
NAXIS2  =                 1584 / NY = Y  GRID DIMENSION
NAXIS3  =                    1 / 8 WAVELENGTHS
BLOCKED =                    T / TAPE MAY BE BLOCKED
COMMENT                         **********************
COMMENT                         ***  FLUX DENSITY  **
COMMENT                         **********************
BSCALE  =          1.401886E-03 / TRUE=TAPE*BSCALE + BZERO
BZERO   =          0.0
BUNIT   = 'JY       '           / FLUX DENSITY
BLANK   =                -32768 / TAPE VALUE FOR EMPTY CELL
CRVAL1  =          1.815000E+02 / RA AT ORIGIN (DEGREES)
CRPIX1  =                 793.  /        Z-AXIS ORIGIN (CELL) = (NZ/2)+1
CTYPE1  = 'RA---SIN'            / DECREASES IN VALUE AS SAMPLE INDEX
COMMENT                           INCREASES  (ORTHOGRAPHIC PROJECTION)
CDELT1  =         -4.166666E-03 / Z-GRID CELL WIDTH (DEGREES)
CROTA1  =          0.0          / TWIST ANGLE UNDEFINED FOR Z-AXIS
CRVAL2  =          2.499998E+01 / DEC AT ORIGIN (DEGREES)
CRPIX2  =                 793.  /        Y-AXIS ORIGIN (CELL)= (NY/2)+1
CTYPE2  = 'DEC--SIN'            / INCREASES IN VALUE AS LINE INDEX
COMMENT                           INCREASES  (ORTHOGRAPHIC PROJECTION)
CDELT2  =          4.166666E-03 / Y-GRID CELL WIDTH (DEGREES)
CROTA2  =          0.0          / ROTATES +NAXIS2 INTO +DEC AXIS (ANGLE
COMMENT                           MEASURED POSITIVE CCW FROM +NAXIS2 TO
COMMENT                           +DEC)  (DEGREES)
CRVAL3  =              1.2E-05  / WAVELENGTH IN METERS
CRPIX3  =                   1.
CTYPE3  = 'LAMBDA   '
CDELT3  =                   0.
CROTA3  =                   0.
DATAMAX =          5.479973E+00 / JY       (TRUE VALUE)
DATAMIN =         -1.682264E-01 / JY       (TRUE VALUE)
COMMENT                           NO. OF EMPTY CELLS =       0
NCF     =          1.001069E+00 / NOISE CORRECTION FACTOR
EPOCH   =                1950.  /        ERES0
DATE-OBS= ' 0/ 0/83'            / DATE OF OBSERVATION (DD/MM/YY)
DATE    = '21/ 9/88'            / DATE THIS TAPE WRITTEN (DD/MM/YY)
ORIGIN  = 'IPAC     '           / INSTITUTION:INFRARED PROCESSING AND
COMMENT                                       ANALYSIS CENTER;
COMMENT                                       MAIL CODE:100-22 CALTECH
TELESCOP= 'IRAS     '
INSTRUME= 'FSS      '
COMMENT                           FSSID = FSPP
FSSPLATE=                1213.  /        FSS PLATE NO.
DATE-CR = '72800129'            / FSS PLATE FILE CREATION DATE(YDDDHHMM
PLTNOISE=          2.803772E-02 / EST. PLATE MEDIAN NOISE (JY)
```

TABLE V.B.1 FITS Grid Header for the Flux Map (continued)

```
HISTORY                                  CALFAC USED = 0.995 * 7.418E+12
COMMENT                                  GRID TWIST =  1.800000E+02 (DEG) MEAS
COMMENT                                  URED FROM SOUTH TO +Y, CW IS POSITIVE
COMMENT                                  GAIN HORN. USED =   1.400000E+00
COMMENT                                  NFILT =        23
COMMENT                                  KFILT =        -1
OBJECT  = 'MD4F10  '                    / PLATE LABEL
COMMENT                                  CMOON=  2.692879E+01 DEG.; MIN. CONE
COMMENT                                                       ANGLE OF MOON.
COMMENT                                  CJUP =  6.783405E+01 DEG.; MIN. CONE
COMMENT                                                       ANGLE OF JUPITER.
COMMENT                                  CSAT =  3.556181E+01 DEG.; MIN. CONE
COMMENT                                                       ANGLE OF SATURN.
COMMENT                                  CMARS=  8.613010E+01 DEG.; MIN. CONE
COMMENT                                                       ANGLE OF MARS.
COMMENT
COMMENT                                  MAX/MIN UNCERTAINTIES ON IN-SCAN
COMMENT                                  BORESIGHT POSITION =
COMMENT                                    5.786275E+00/  1.998857E+00 ARC SEC
COMMENT
COMMENT                                  MAX/MIN UNCERTAINTIES ON CROSS-SCAN
COMMENT                                  BORESIGHT POSITION =
COMMENT                                    2.617488E+01/  5.968496E+00 ARC SEC
COMMENT
COMMENT                                  PROGRAM VERSION AND COMPILATION DATE
COMMENT                                   (MM/DD/YY): M-P0.99  9/29/87.
COMMENT                                  NUMBER OF IN-TOLERANCE FRAMES = 9119.
COMMENT    REFERENCES:
COMMENT  IRAS SDAS SOFTWARE INTERFACE SPECIFICATION(SIS) #623-94/NO. FS01
COMMENT  EXPLANATORY SUPPLEMENT TO THE IRAS FAINT SOURCE SURVEY (NOV.1988)
COMMENT  ASTRON. ASTROPHYS. SUPPL. SER. 44,(1981) 363-370(RE:FITS)
END
```

TABLE V.B.2 FITS Grid Header for the Noise Map

```
SIMPLE  =                    T          / STANDARD FITS FORMAT
BITPIX  =                   16          / 2 BYTE TWOS-COMPL INTEGERS
NAXIS   =                    3          / NUMBER OF AXES
NAXIS1  =                 1584          / NZ = Z  GRID DIMENSION
NAXIS2  =                 1584          / NY = Y  GRID DIMENSION
NAXIS3  =                    1          / # WAVELENGTHS
BLOCKED =                    T          / TAPE MAY BE BLOCKED
COMMENT                                   **********
COMMENT                                   ******  NOISE  ******
COMMENT                                   **********
BSCALE  =         1.401886E-03          / TRUE=TAPE*BSCALE + BZERO
BZERO   =         0.0
BUNIT   = 'JY      '                    / NOISE (ESTIMATED CELL NOISE)
BLANK   =               -32768          / TAPE VALUE FOR EMPTY CELL
COMMENT                                   CELLS WITH LESS THAN 4 COUNTS HAVE
COMMENT                                   "EMPTY" VALUE FOR COMPUTED NOISE.
CRVAL1  =         1.815000E+02          / RA AT ORIGIN (DEGREES)
CRPIX1  =                793.                    / Z-AXIS ORIGIN (CELL) = (NZ/2)+1
```

D 10015

TABLE V.B.2 FITS Grid Header for the Noise Map (continued)

```
CTYPE1  = 'RA---SIN'                / DECREASES IN VALUE AS S APLE INDEX
COMMENT                               INCREASES  (ORTHOGRAPH.C PROJECTION)
CDELT1  =        -4.166666E-03      / Z-GRID CELL WIDTH (DEGREES)
CROTA1  =         0.0               / TWIST ANGLE UNDEFINED FOR Z-AXIS
CRVAL2  =         2.499998E+01      / DEC AT ORIGIN (DEGREES)
CRPIX2  =                793.               / Y-AXIS ORIGIN (CELL)= (NY/2)+1
CTYPE2  = 'DEC--SIN'                / INCREASES IN VALUE AS LINE INDEX
COMMENT                               INCREASES  (ORTHOGRAPHIC PROJECTION)
CDELT2  =         4.166666E-03      / Y-GRID CELL WIDTH (DEGREES)
CROTA2  =         0.0               / ROTATES +NAXIS2 INTO +DEC AXIS (ANGLE
COMMENT                               MEASURED POSITIVE CCW FROM +NAXIS2 TO
COMMENT                               +DEC)  (DEGREES)
CRVAL3  =              1.2E-05      / WAVELENGTH IN METERS
CRPIX3  =                    1.
CTYPE3  = 'LAMBDA  '
CDELT3  =                    0.
CROTA3  =                    0.
DATAMAX =         1.993482E+00      / JY       (TRUE VALUE)
DATAMIN =         0.0               / JY       (TRUE VALUE)
COMMENT                               NO. OF EMPTY CELLS =    1068
NCF     =         1.001069E+00      / NOISE CORRECTION FACTOR
EPOCH   =                1950.               / EMESO
DATE-OBS= ' 0/ 0/83'                / DATE OF OBSERVATION (DD/MM/YY)
DATE    = '21/ 9/88'                / DATE THIS TAPE WRITTEN (DD/MM/YY)
ORIGIN  = 'IPAC    '                / INSTITUTION:INFRARED PROCESSING AND
COMMENT                                            ANALYSIS CENTER;
COMMENT                                            MAIL CODE:100-22 CALTECH
TELESCOP= 'IRAS    '
INSTRUME= 'FSS     '
COMMENT                               FSSID = FSPP
FSSPLATE=                1213.               / FSS PLATE NO.
DATE-CR = '72800129'                / FSS PLATE FILE CREATION DATE(YDDDHHMM
PLTNOISE=         2.803772E-02      / EST. PLATE MEDIAN NOISE (JY)
HISTORY                               CALFAC USED = 0.995 * 7.418E+12
COMMENT                               GRID TWIST =  1.800000E+02 (DEG) MEAS
COMMENT                               URED FROM SOUTH TO +Y, CW IS POSITIVE
COMMENT                               GAIN NORM. USED =   1.400000E+00
COMMENT                               NFILT =        23
COMMENT                               KFILT =        -1
OBJECT  = 'ND4F10  '                / PLATE LABEL
COMMENT                               CMOON=  2.692879E+01 DEG.; MIN. CONE
COMMENT                                                    ANGLE OF MOON.
COMMENT                               CJUP =  6.783405E+01 DEG.; MIN. CONE
COMMENT                                                    ANGLE OF JUPITER.
COMMENT                               CSAT =  3.556181E+01 DEG.; MIN. CONE
COMMENT                                                    ANGLE OF SATURN.
COMMENT                               CMARS=  8.613010E+01 DEG.; MIN. CONE
COMMENT                                                    ANGLE OF MARS.
COMMENT
COMMENT                               MAX/MIN UNCERTAINTIES ON IN-SCAN
COMMENT                               BORESIGHT POSITION =
COMMENT                                 5.786275E+00/  1.998857E+00 ARC SEC
COMMENT
COMMENT                               MAX/MIN UNCERTAINTIES ON CROSS-SCAN
COMMENT                               BORESIGHT POSITION =
COMMENT                                    2.617488E+01/  5.968496E+00 ARC SEC
COMMENT
```


304

TABLE V.B.2 FITS Grid Header for the Noise Map (continued)

```
COMMENT                                   PROGRAM VERSION AND COMPILATION DATE
COMMENT                                    (MM/DD/YY): M-P  .99  9/29/87.
COMMENT                                   NUMBER OF IN-TOLERANCE FRAMES = 9119.
COMMENT    REFERENCES:
COMMENT  IRAS SDAS SOFTWARE INTERFACE SPECIFICATION(SIS) #623-94/NO. FS01
COMMENT  EXPLANATORY SUPPLEMENT TO THE IRAS FAINT SOURCE SURVEY (NOV.1988)
COMMENT  ASTRON. ASTROPHYS. SUPPL. SER. 44,(1981) 363-370(RE:FITS)
END
```

TABLE V.B.3 FITS Grid Header for the Count Map

```
SIMPLE  =                    T          / STANDARD FITS FORMAT
BITPIX  =                    8          / 1-BYTE UNSIGNED BINARY INTEGERS
NAXIS   =                    3          / NUMBER OF AXES
NAXIS1  =                 1584          / NZ = Z  GRID DIMENSION
NAXIS2  =                 1584          / NY = Y  GRID DIMENSION
NAXIS3  =                    1          / 8 WAVELENGTHS
BLOCKED =                    T          / TAPE MAY BE BLOCKED
COMMENT                                   **********
COMMENT                                   ******  COUNT  ******
COMMENT                                   **********
BSCALE  =                   1.                  / TRUE=TAPE*BSCALE + BZERO
BZERO   =                   0.
BUNIT   = 'COUNT   '                    / COUNT(NO.OF DETECTOR PASSES OVER CELL
BLANK   =                    0          / TAPE VALUE FOR EMPTY CELL
CRVAL1  =         1.815000E+02          / RA AT ORIGIN (DEGREES)
CRPIX1  =                793.                  / Z-AXIS ORIGIN (CELL) = (NZ/2)+1
CTYPE1  = 'RA---SIN'                    / DECREASES IN VALUE AS SAMPLE INDEX
COMMENT                                   INCREASES  (ORTHOGRAPHIC PROJECTION)
CDELT1  =        -4.166666E-03          / Z-GRID CELL WIDTH (DEGREES)
CROTA1  =         0.0                   / TWIST ANGLE UNDEFINED FOR Z-AXIS
CRVAL2  =         2.499998E+01          / DEC AT ORIGIN (DEGREES)
CRPIX2  =                793.                  / Y-AXIS ORIGIN (CELL)= (NY/2)+1
CTYPE2  = 'DEC--SIN'                    / INCREASES IN VALUE AS LINE INDEX
COMMENT                                   INCREASES  (ORTHOGRAPHIC PROJECTION)
CDELT2  =         4.166666E-03          / Y-GRID CELL WIDTH (DEGREES)
CROTA2  =         0.0                   / ROTATES +NAXIS2 INTO +DEC AXIS (ANGLE
COMMENT                                   MEASURED POSITIVE CCW FROM +NAXIS2 TO
COMMENT                                   +DEC)  (DEGREES)
CRVAL3  =              1.2E-05          / WAVELENGTH IN METERS
CRPIX3  =                   1.
CTYPE3  = 'LAMBDA  '
CDELT3  =                   0.
CROTA3  =                   0.
DATAMAX =                  20.                  / COUNT    (TRUE VALUE)
DATAMIN =                   2.                  / COUNT    (TRUE VALUE)
COMMENT                                   NO. OF EMPTY CELLS =       0
EPOCH   =                1950.                  / EME50
DATE-OBS= ' 0/ 0/83'                    / DATE OF OBSERVATION (DD/MM/YY)
DATE    = '21/ 9/88'                    / DATE THIS TAPE WRITTEN (DD/MM/YY)
ORIGIN  = 'IPAC    '                    / INSTITUTION:INFRARED PROCESSING AND
COMMENT                                              ANALYSIS CENTER;
COMMENT                                              MAIL CODE:100-22 CALTECH
TELESCOP= 'IRAS    '
INSTRUME= 'FSS     '
```

TABLE V.B.3 FITS Grid Header for the Count Map (continued)

```
COMMENT                                  FSSID = FSPP
FSSPLATE=                  1213.                 / FSS PLAT. NO.
DATE-CR = '72800129'                   / FSS PLATE FILE CREATION DATE(YDDDHHMM
COMMENT                                  GRID TWIST =  1.800000E+02 (DEG) MEAS
COMMENT                                  URED FROM SOUTH TO +Y, CW IS POSITIVE
COMMENT                                  GAIN NORM. USED =   1.400000E+00
COMMENT                                  NFILT =         23
COMMENT                                  KFILT =         -1
OBJECT  = 'MD4F10  '                   / PLATE LABEL
COMMENT                                  CMOON=  2.692879E+01 DEG.; MIN. CONE
COMMENT                                                       ANGLE OF MOON.
COMMENT                                  CJUP =  6.783405E+01 DEG.; MIN. CONE
COMMENT                                                       ANGLE OF JUPITER.
COMMENT                                  CSAT =  3.556181E+01 DEG.; MIN. CONE
COMMENT                                                       ANGLE OF SATURN.
COMMENT                                  CMARS=  8.613010E+01 DEG.; MIN. CONE
COMMENT                                                       ANGLE OF MARS.
COMMENT
COMMENT                                  MAX/MIN UNCERTAINTIES ON IN-SCAN
COMMENT                                  BORESIGHT POSITION =
COMMENT                                    5.786275E+00/  1.998857E+00 ARC SEC
COMMENT
COMMENT                                  MAX/MIN UNCERTAINTIES ON CROSS-SCAN
COMMENT                                  BORESIGHT POSITION =
COMMENT                                    2.617488E+01/  5.968496E+00 ARC SEC
COMMENT
COMMENT                                  PROGRAM VERSION AND COMPILATION DATE
COMMENT                                   (MM/DD/YY): M-P0.99  9/29/87.
COMMENT                                  NUMBER OF IN-TOLERANCE FRAMES = 9119.
COMMENT    REFERENCES:
COMMENT  IRAS SDAS SOFTWARE INTERFACE SPECIFICATION(SIS) 8623-94/NO. FS01
COMMENT  EXPLANATORY SUPPLEMENT TO THE IRAS FAINT SOURCE SURVEY (NOV.1988)
COMMENT  ASTRON. ASTROPHYS. SUPPL. SER. 44,(1981) 363-370(RE:FITS)
END
```

TABLE V.B.4 FITS Keywords

Keyword	Description
BITPIX	Denotes whether FLUX DENSITY and NOISE grids are 2- or 4-byte integers. COUNT grid is always a 1-byte integer.
BZERO	The baseline is always zero.
BUNIT	The FLUX DENSITY and NOISE grids are in Janskys. The COUNT grid is dimensionless.
CDELT1	This parameter is negative since increasing samples along AXIS1 are in the −RA direction.
NCF†	This parameter is the *noise correction factor* for the whole plate.
DATE-OBS	The UT date of observations, always 0/0/83.
DATE	The PST date that the FITS format version of this plate was processed at IPAC.
FSSPLATE	The Faint Source Survey plate number. This numbering scheme agrees with the ESO plate numbers.
DATE-CR	The date of the initial processing of the FSS plate at IPAC.
OBJECT	The label of FSS plates; always "MD4F10 ".

† Everywhere else in this document, the *noise correction factor* is referred to as NOISCOR.

C.1 The Short Machine-Readable Version of the Faint Source Catalog

The short FSC tape is presented as FITS table data. In order to do this, the associations block has been split out as a separate file. It takes one 6250-bpi tape to hold all of these files for the version 2 catalog.

The FITS table format consists of the following:

- The catalog is split into two files, one for the non-association data (FSC_DATA) and one for the association data (FSC_ASSOC).
- There are two headers, each with 80-byte records, within each file.
- The first header in each file identifies that the tape is written in FITS format.
- The second header constitutes the FITS keyword file giving the format information for the rest of the file.
- The data part (i.e., non-header part) of FSC_DATA has 240-byte records.
- The data part of FSC_ASSOC has 64-byte records.
- The tape is blocked to multiples of 2880 bytes.

D 10015

TABLE V.C.1 Header File for FSC Data Files

```
SIMPLE  =                    T / Standard FITS format
BITPIX  =                    8 / Character data
NAXIS   =                    0 / No image data array presen
EXTEND  =                    T / There may be standard extensions
BLOCKED =                    T / Tape may be blocked to multiples of 2880

END
```

Specifically, the formats of the files are as follows:

FILE 1:

Block 1 – short header file

Blocks 2–10 – FSC_DATA header

Blocks 11–END – FSC_DATA

FILE 2:

Block 1 – short header file

Blocks 2–4 – FSC_ASSOC header

Blocks 5–END – FSC_ASSOC

The short header file is given in Table V.C.1.

Table V.C.2 gives a sample of the header for the non-association data and Table V.C.3 gives a sample of the header for the association data. Tables V.C.4 (FSC data) and V.C.5 (association data) describe each entry in the short catalog tape. All of this information is contained in the actual FITS headers, but is presented here in an easier-to-read format. Each catalog entry required 240 bytes of ASCII data for the non-association data and NID × 64 bytes of ASCII data for the association data (NID refers to the number of positional associations). In these tables the column "Format" refers to the length and type of the (FORTRAN) character field used to read or write each entry.

The tape is written with 240-character (ASCII) logical records for the non-association data and with 64-character records for the association data. The number of logical records per physical record is 36 for the headers, 12 for the non-association data, and 45 for the association data. These numbers apply to unblocked files only and should be multiplied by the blocking factors for blocked files.

In general, for quantities that have a value in each wavelength band, subscripts or array indices range from 1 to 4 and refer, respectively, to 12, 25, 60 and 100 μm. A number of the flags which are discussed below have values in each of the four wavelength

368

D 10015

TABLE V.C.2 Portion of FITS Header for FSC Data File

```
XTENSION= 'TABLE   '                   /  Table extension
BITPIX  =                              8 / Character data
NAXIS   =                              2 / Simple 2-D matrix
NAXIS1  =                            240 / Number of characters per record
NAXIS2  =                         173044 / Number of records in the file
PCOUNT  =                              0 / No "random" parameters
GCOUNT  =                              1 / Only one group
TFIELDS =                             58 / Number of data fields per record
EXTNAME = 'FSC_DATA'                   / IRAS Faint Source Catalog - main data file
AUTHOR  = 'IPAC    '                   / Infrared Processing and Analysis Center
REFERENC= 'Version 2.0'                / Catalog reference
DATE    = '12/09/90'                   / Date file was generated (dd/mm/yy)

COMMENT This FITS header is NOT a complete scientific document for the subject
COMMENT catalog.    It serves only as a minimal description of the general
COMMENT format and structure of the data file.

COMMENT A copy of "Explanatory Supplement to the Faint Source Survey",
COMMENT Version 2, should be used to answer questions about the data
COMMENT in the FSC.

COMMENT Names which refer to each of the four IRAS bands of 12, 25, 60 and
COMMENT 100 microns are suffixed with the numerals 12, 25, 60 and 100.
COMMENT For example FNU_12 is the flux density at 12 microns.

TTYPE1  = 'NAME    '                   / Source name
TBCOL1  =                              1 / Start column
TFORM1  = 'A12     '                   / Fortran format

TTYPE2  = 'RAHR    '                   / Hours RA, equinox 1950.0, epoch 1983.5
TBCOL2  =                             13 / Start column
TFORM2  = 'I2      '                   / Fortran format
TUNIT2  = 'HR      '                   / Units are hours of time
. . .

TTYPE11 = 'POSANG  '                   / Uncertainty ellipse position angle
TBCOL11 =                             33 / Start column
TFORM11 = 'I3      '                   / Fortran format
TUNIT11 = 'DEG     '                   / Units are degrees
COMMENT POSANG (field 11) is measured in degrees east of north between the
COMMENT major axis of the ellipse and the local equatorial meridian.

etc.
```


369

TABLE V.C.3 Portion of FITS Header for FSC Association Data

```
XTENSION= 'TABLE   '                    / Table extension
BITPIX  =                               8 / Character data
NAXIS   =                               2 / Simple 2-D matrix
NAXIS1  =                              64 / Number of characters per record
NAXIS2  =                          235935 / Number of records in the file
PCOUNT  =                               0 / No "random" parameters
GCOUNT  =                               1 / Only one group
TFIELDS =                              12 / Number of data fields per record
EXTNAME = 'FSC_ASSOC'                     / IRAS Faint Source Catalog - associations table
AUTHOR  = 'IPAC    '                      / Infrared Processing and Analysis Center
REFERENC= 'Version 2.0'                   / Catalog reference
DATE    = '12/09/90'                      / Date file was generated (dd/mm/yy)

COMMENT This FITS header is not a complete scientific document for the subject
COMMENT catalog.  It serves only as a minimal description of the general format
COMMENT and structure of the data file.    A copy of the "Faint Source Survey
COMMENT Explanatory Supplement", Version 2, should be used to answer
COMMENT questions about the data in the IRAS Faint Source Catalog.

COMMENT Source catalog reference:  IRAS Faint Source Catalog, Version 2.0,
COMMENT IPAC, 1990 September.

COMMENT This table contains only the point source association fields for each
COMMENT source in the IRAS FSC. The observational data for each source are
COMMENT in table FSC_DATA. Each association is tagged with the IRAS source name
COMMENT with which it is associated, as well as the sequential record number
COMMENT within table FSC_DATA where the observational data can be found.
COMMENT Field names are identical with the field names given in
COMMENT the IRAS Faint Source Survey Explanatory Supplement.

TTYPE1  = 'NAME    '                    / Source name
TBCOL1  =                               1 / Start column
TFORM1  = 'A12     '                    / Fortran format

TTYPE2  = 'RECNO   '                    / Main data table record number for source
TBCOL2  =                              13 / Start column
TFORM2  = 'I6      '                    / Fortran format

TTYPE3  = 'CATNO   '                    / Catalog number
TBCOL3  =                              19 / Start column
TFORM3  = 'I2      '                    / Fortran format

etc.
```

D 10015

TABLE V.C.4 Format of FSC Data File for Short FSC Tape

Start Byte	Name	Description	Units	Format
000	NAME	Source Name	—	12A1
012	RAHR	Right Ascension B1950	Hour of time	I2
014	RAMIN	Right Ascension B1950	Minute of time	I2
016	RASEC	Right Ascension B1950	deci-Second of time	I3
019	DECSGN	Declination Sign	±	A1
020	DECDEG	Declination B1950	Arc Degree	I2
022	DECMIN	Declination B1950	Arc Minute	I2
024	DECSEC	Declination B1950	Arc Second	I2
026	UNCMAJ	Uncertainty ellipse major axis	Arc Second	I3
029	UNCMIN	Uncertainty ellipse minor axis	Arc Second	I3
032	POSANG	Uncertainty ellipse position angle	Degree (East of North)	I3
035	NOBS[1]	Number of times observed in each band	—	4I3
047	FNU[1]	Flux densities (1 value per band, non-color corrected)	Jansky (10^{-26} W m^{-2} Hz^{-1})	4E9.3
083	FQUAL[1]	Flux density quality (1 value per band)	—	4I1
087	RELUNC[1]	Percent relative flux density uncertainties (1 value/band)	—	4I3
099	MINREL	Minimum percent reliability	—	I2
101	SNR[1]	Signal-to-noise ratio in each band	—	4E7.1
129	LOCSNR[1]	Local SNR in each band	—	4E7.1
157	AREA[1]	Number of pixels above threshold in each band	—	4I3
169	CATNBR	No. of nearby catalog sources	—	I2
171	EXTNBR[1]	No. of nearby extractions in each band	—	4I2
179	CIRRUS	No. of nearby 100-μm-only extractions	—	I2
181	CONFUSE	Confusion flag (1 flag/band, bit-encoded)	—	I2
183	NOISCOR[1]	Noise correction factor (1 value per band)	—	4F5.2
203	NID	No. of positional associations	—	I2
205	IDTYPE	Type of object (bit-encoded)	—	I2
207	NOISRAT	Ratio of quantiles at 87% and 68% (1 value per band)	—	4F5.3
227	SPARE	Spare padding	—	A13

371

D 10015

TABLE V.C.4 Format of FSC Data File for Short FSC Tape (continued)

NOTES:

1 In the FITS header, these quantities are suffixed by the wavelength. Example: FNU(4) is given as FNU_12, FNU_25, FNU_60, and FNU_100.

TABLE V.C.5 Format of Association Data for FSC Tape

Start Byte	Name	Description	Units	Format
00	NAME	Source Name	—	A12
12	RECNO	Record No. in main data table	—	I6
18	CATNO	Catalog No.	—	I2
20	SOURCE	Source ID	—	A15
35	TYPE	Source Type/Spectral Class	—	A5
40	RADIUS	Radius vector from *IRAS* source to association	Arc Second	I3
43	POS	Position angle from *IRAS* source to association	Degree (East of North)	I3
46	DSTMAJOR	Distance from *IRAS* source to association along the *IRAS* position error major axis	Arc Second	I3
49	DSTMINOR	Distance from *IRAS* source to association along the *IRAS* position error minor axis	Arc Second	I3
52	FIELD1	Object field #1 (magnitude/other)	Catalog dependent	I4
56	FIELD2	Object field #2 (magnitude/other)	Catalog dependent	I4
60	FIELD3	Object field #3 (magnitude/other)	Catalog dependent	I4

372

D 10015 **TABLE V.C.6 Source Designations for all *IRAS* Catalogs**

Catalog	Source Name
Point Source Catalog	*IRAS* 12345-6789
Point Source Reject File	*IRAS* R12345-6789
Small Scale Structure Catalog	*IRAS* X1234-678
Serendipitous Survey Catalog	*IRAS* S12345-678
Faint Source Catalog	*IRAS* F12345-6789
Faint Source Reject File	*IRAS* Z12345-6789

bands. For compactness these are bit-encoded into a single byte (2 digit integer, values 0–15) in the following manner. The four *highest* bits of the byte are always zero, and the four *lowest* bits of the byte correspond to the four wavelength bands with bit 0 (Least Significant Bit) for 12 μm, bit 1 for 25 μm, bit 2 for 60 μm and bit 3 for 100 μm. The presence of a flag in a band is denoted by setting its bit to 1. Thus a flag set at 12 and 25 μm would have a value of 0011=3 while a flag set at 25, 60 and 100 μm would have a value of 1110=13. A flag encoded in this manner will be referred to as "bit-encoded by band".

The remainder of this section discusses individual entries in the catalog.

Source Name: NAME

The *IRAS* source name is derived from its position by combining the hours, minutes and tenths of minutes of right ascension and the sign, degrees and minutes of the declination. In obtaining the minutes of right ascension and declination for the name, the positions were truncated. This quantity is preceded by the letter 'F' to designate a FSC source, and the letter 'Z' to designate a Reject File source (except for version 1.2 catalog sources now placed in the reject file which retain their 'F' designation, see Section IV.B.2.e). The letters 'A', 'B', 'C', etc., are appended to names of sources so close together that they would otherwise have had identical names. Due to the large number of duplicate sources caused by plate overlap, we have changed the convention used in the PSC and eliminated the 'A' for the first such source with a duplicate name. Names were uniquely assigned to both catalog and reject file sources, including duplicate sources, with catalog sources named first. An example of a reference to a FSC source is *IRAS* F12345-6789. Table V.C.6 collects all the various designations for sources in all *IRAS* catalogs.

Position: RAHR, RAMIN, RASEC, DECSGN, DECDEG, DECMIN, DECSEC

Positions are given for the equinox B1950.0 and epoch 1983.5. Hours (RAHR) and

373

minutes (RAMIN) of right ascension are given as integers while seconds (RASEC) are rounded to integer deci-seconds. The declination is given as a character sign (DECSGN) followed by integer values of degrees (DECDEG), minutes (DECMIN) and seconds (DECSEC).

Positional Uncertainty: UNCMAJ, UNCMIN, POSANG

As discussed in Section II.F.3, the uncertainty in the position for a source depends primarily on its brightness in the various wavelength bands and the number of sightings. The final uncertainty is expressed as an ellipse whose semi-major (UNCMAJ) and semi-minor (UNCMIN) axes are the 1-σ errors given in seconds of arc. The orientation (POSANG) of the ellipse on the sky is expressed in terms of the angle between the major axis of the ellipse and the local equatorial meridian. It is expressed in degrees east of north.

Number of sightings: NOBS(4)

The number of individual detector sightings at the peak-flux pixel is given.

Flux Density: FNU(4)

Each of the four wavelengths has a *non-color-corrected* flux density in units of Janskys (1 Jy = $10^{-26}\ Wm^{-2}Hz^{-1}$). The quality of each flux density is designated by FQUAL (see below).

The flux densities have been calculated assuming an intrinsic source energy distribution such that the flux density f_ν is proportional to ν^{-1}. Corrections to other spectral shapes can be made by consulting Section VI.C in the *Main Supplement* or by the table inside the back cover of this Supplement.

Note that the flux density quoted for some sources could be zero if there were not enough data available to derive a good upper limit (see Sections II.F.4 and III.H).

Flux Density Quality: FQUAL(4)

As described in Section II.F.4, a flux-density measurement can be either high quality (FQUAL=3), moderate quality (FQUAL=2) or an upper limit (FQUAL=1).

Flux Density Uncertainties: RELUNC(4)

Each flux-density measurement (*including upper limit estimates*) has an associated uncertainty expressed as a 1-σ value in units of $100 \times \delta f_\nu / f_\nu$. Uncertainties are computed from a combination of many data, including SNR, LOCSNR, and NOBS. For further information see Section II.F.4.

374

D 10016

Minimum Reliability: MINREL

The minimum reliability for a source is the maximum of the reliability as calculated individually for each band. See Section III.D for more information.

Signal-to-Noise Ratios: SNR(4), LOCSNR(4)

Two signal-to-noise ratios are reported. The parameter called SNR is calculated through the use of a noise (68% quantile) calculated over an area of roughly $79.25' \times 79.25'$ at 12 and 25 μm and an area of $\sim 99.5' \times 99.5'$ at 60 and 100 μm, which is accurate to $\sim 3\%$. This signal-to-noise ratio is the one which is generally referred to as *the* SNR (see Section III.A.4). The local SNR (LOCSNR) is calculated using the noise for the pixel containing the peak flux density of the source (see Section II.C.4).

Area of source: AREA(4)

The area of each source is calculated as the number of contiguous pixels with flux density above three times the noise after possible rethresholding.

Confusion: CONFUSE, CATNBR, EXTNBR(4)

As described in Section II.F.5, the bandmerger attempted to identify sources that were confused with neighboring sources in one or more bands. The CONFUSE flag is set in a given band if any instance of confusion was present in that band.

Other indicators of possible confusion are given by CATNBR and EXTNBR. CATNBR gives the number of nearby catalog sources within a radius of 6′. EXTNBR gives for each band the number of extractions within a radius of 6′.

Cirrus Indicators: CIRRUS, NOISCOR(4), NOISRAT(4)

Over nearly the entire sky, portions of the FSS plates are affected by the infrared cirrus. Cirrus can seriously hamper efforts to extract point sources from the data and can also produce structure on a point source scale that can masquerade as true point sources. The CIRRUS flag gives the number of 100 μm-only sources *or cold* 60 and 100 μm sources (defined by $\log f_\nu(60\ \mu\text{m})/f_\nu(100\ \mu\text{m}) \leq -0.75$) in the extraction database within a radius of 30′. It is a coarse discriminant that warns the user that cirrus which contains structure on a point source scale is present in a given region. Values above 2 usually indicate contamination. The ratio of noise (68% quantile) to the *median instrumental* noise, NOISCOR, is a global measure of cirrus contamination, especially at 100 μm. See Section III.C.4 for more details. Another global measure of cirrus, NOISRAT, is the ratio of the 87% and 68% quantiles of the positive values from the flux density grid (see Section III.G.7).

375

) 10015

Positional Associations: NID, IDTYPE, CATNO, SOURCE, TYPE, RADIUS, DSTMINOR, DSTMAJOR, POS, FIELD1-3

Much of the utility of the FSC comes from the association of infrared objects with sources known to exist from other astronomical catalogs. As described in Section II.G, a large number of catalogs have been searched for positional matches. The total number of matches found is given by NID. Each match results in a 64-character description which is placed in a separate association file in order to conform to the FITS catalog format.

When NID > 0, an association record exists. IDTYPE ranges from 1 to 15 and states whether an association was found in a stellar catalog (bit 0), an extragalactic catalog (bit 1), catalogs with other types of objects (bit 2) or in a catalog with mixed types or derived partially/completely from *IRAS* data (bit 3). Note that this differs from the convention used in previous *IRAS* data products where only the total of the association types was given. For example, if associations were found to both an extragalactic catalog and a stellar catalog the IDTYPE was 'multiple'. We are now preserving the information as to which type of catalogs were matched.

SOURCE is the name of the object in that catalog and TYPE its character or spectral type, if available. A vector is drawn from the *IRAS* position to the associated object. RADIUS is the length of that vector in arcseconds. POS is the angle between the vector and the local equatorial meridian expressed in degrees east of north. DSTMAJOR is the distance from the *IRAS* source to the associated object along the major axis of the positional uncertainty ellipse of the *IRAS* source and DSTMINOR is the similar distance along the minor axis.

Three fields (FIELD1-3) have values depending on the catalog in question (consult Table II.G.5). Typically, FIELD1,2 are magnitudes (in decimag) and FIELD3 a size.

C.2 The Long Machine-Readable Version of the Faint Source Catalog

The long FSC tape is presented as FITS table data. In order to do this, the associations block has been split out as a separate file in the same fashion as the short form. It takes one 8-mm tape to hold all of these files for the version 2 catalog.

The FITS table format consists of the following:

- The catalog is split into two files, one for the non-association data (FSC_DATA) and one for the association data (FSC_ASSOC).
- There are two headers, each with 80-byte records, within each file.
- The first header in each file identifies that the tape is written in FITS format.

376

- The second header constitutes the FITS keyword file giving the format information for the rest of the file.
- The data part (i.e., non-header part) of FSC_DATA has 1440-byte records.
- The data part of FSC_ASSOC has 144-byte records.
- The tape is blocked to multiples of 2880 bytes.

Specifically, the formats of the files are as follows:

FILE 1:

Block 1 – long header file
Blocks 2–50 – FSC_DATA header
Blocks 51–END – FSC_DATA

FILE 2:

Block 1 – long header file
Blocks 2–7 – FSC_ASSOC header
Blocks 8–END – FSC_ASSOC

The long header file is given in Table V.C.1.

Table V.C.7 gives a sample of the header for the long form non-association data and Table V.C.8 gives a sample of the header for the long form association data. Tables V.C.9 (FSC data) and V.C.10 (association data) describe each entry in the long catalog tape. All of this information is contained in the actual FITS headers, but is presented here in an easier-to-read format. Each catalog entry requires 1440 bytes of ASCII data for the non-association data and NID × 144 bytes of ASCII data for the association data (NID refers to the number of positional associations). In these tables the column "Format" refers to the length and type of the (FORTRAN) character field used to read or write each entry.

The tape is written with 1440-character (ASCII) logical records for the non-association data and with 144-character records for the association data. Similarly to the short form, for quantities that have a value in each band, subscripts or array indices range from 1 to 4 and refer, respectively, to 12, 25, 60 and 100 μm. A number of flags are composites of bits. For compactness these are bit-encoded and are referred to as "bit-encoded".

The individual entries in the long form of the catalog will be described in the remainder of this section.

C.2.a Non-association Data

Source Name: NAME

The source name is the same as that described for the short form.

TABLE V.C.7 Portion of FITS Header for Long FSC Data File

```
XTENSION= 'TABLE   '           / Table extension
BITPIX  =                    8 / Character data
NAXIS   =                    2 / Simple 2-D matrix
NAXIS1  =                 1440 / Number of characters per record
NAXIS2  =               173044 / Number of records in the file
PCOUNT  =                    0 / No "random" parameters
GCOUNT  =                    1 / Only one group
TFIELDS =                  328 / Number of data fields per record
EXTNAME = 'FSC_DATA'           / IRAS Faint Source Catalog - main data file
AUTHOR  = 'IPAC    '           / Infrared Processing and Analysis Center
REFERENC= 'Version 2.0'        / Catalog reference
DATE    = '19/05/92'           / Date file was generated (dd/mm/yy)

COMMENT This FITS header is NOT a complete scientific document for the subject
COMMENT catalog.    It serves only as a minimal description of the general
COMMENT format and structure of the data file.

COMMENT A copy of "Explanatory Supplement to the Faint Source Survey",
COMMENT Version 2, should be used to answer questions about the data
COMMENT in the FSC.

COMMENT Names which refer to each of the four IRAS bands of 12, 25, 60 and
COMMENT 100 microns are suffixed with the numerals 12, 25, 60 and 100.
COMMENT For example FNU_12 is the flux density at 12 microns.

TTYPE1  = 'NAME    '           / Source name
TBCOL1  =                    1 / Start column
TFORM1  = 'A12     '           / Fortran format

TTYPE2  = 'FCAT    '           / Final catalog flag
TBCOL2  =                   13 / Start column
TFORM2  = 'A1      '           / Fortran format

TTYPE3  = 'RAH     '           / Hours RA, equinox B1950.0, epoch 1983.5
TBCOL3  =                   14 / Start column
TFORM3  = 'I2      '           / Fortran format
TUNIT3  = 'HR      '           / Units are hours of time

TTYPE4  = 'RAM     '           / Minutes RA, equinox B1950.0, epoch 1983.5
TBCOL4  =                   16 / Start column
TFORM4  = 'I2      '           / Fortran format
TUNIT4  = 'MIN     '           / Units are minutes of time
BCOL13  =                   35 / Start column
. . .

etc.
```

TABLE V.C.8 Portion of FITS Header for Long FSC Association Data

```
XTENSION= 'TABLE   '           / Table extension
BITPIX  =                    8 / Character data
NAXIS   =                    2 / Simple 2-D matrix
NAXIS1  =                  144 / Number of characters per record
NAXIS2  =               235935 / Number of records in the file
PCOUNT  =                    0 / No "random" parameters
GCOUNT  =                    1 / Only one group
TFIELDS =                   29 / Number of data fields per record
EXTNAME = 'FSC_ASSOC'          / IRAS Faint Source Catalog - associations table
AUTHOR  = 'IPAC    '           / Infrared Processing and Analysis Center
REFERENC= 'Version 2.0'        / Catalog reference
DATE    = '19/05/92'           / Date file was generated (dd/mm/yy)

COMMENT This FITS header is NOT a complete scientific document for the subject
COMMENT catalog.  It serves only as a minimal description of the general format
COMMENT and structure of the data file.    A copy of "Faint Source Survey
COMMENT Explanatory Supplement", Version 2, should be used to answer
COMMENT questions about the data in the IRAS Faint Source Catalog.

COMMENT Source Catalog Reference:  IRAS Faint Source Catalog, Version 2.0,
COMMENT IPAC, 1992 May.

COMMENT This table contains only the point source association fields for each
COMMENT source in the IRAS FSC.  The observational data for each source are
COMMENT in table FSC_DATA. Each association is tagged with the IRAS source name
COMMENT with which it is associated, as well as the pointer of the source
COMMENT within table FSC_DATA where the observational data can be found.
COMMENT Field names are identical with the field names given in
COMMENT the IRAS Faint Source Survey Explanatory Supplement.

TTYPE1  = 'NAME    '           / Name of source in FSC
TBCOL1  =                    1 / Start column
TFORM1  = 'A12     '           / Fortran format

TTYPE2  = 'KEYFSS  '           / Pointer of source in FSC
TBCOL2  =                   13 / Start column
TFORM2  = 'I7      '           / Fortran format

TTYPE3  = 'IDRECNO '           / Pointer of this group of associations
TBCOL3  =                   20 / Start column
TFORM3  = 'I7      '           / Fortran format

TTYPE4  = 'NID     '           / Total number of positional associations
TBCOL4  =                   27 / Start column
TFORM4  = 'I2      '           / Fortran format

TTYPE5  = 'IDSEQNO '           / Sequential number of this association
TBCOL5  =                   29 / Start column
TFORM5  = 'I2      '           / Fortran format
. . . .

etc.
```

Catalog Flag: FCAT

A flag is set to 'T' when an entry is a catalog source. This is a redundant parameter for the catalog tape. It is useful when the reject file is used (see Section IV.B.2.e).

Position: RAH, RAM, RAS, DECSIGN, DECD, DECM, DECS

Positions are given for the equinox B1950.0 and epoch 1983.5, similar to the short form.

Position: RAH_2000, RAM_2000, RAS_2000, DECSIGN_2000, DECD_2000, DECM_2000, DECS_2000

Positions are given for the equinox J2000.0 and epoch 1983.5. Hours (RAH_2000) and minutes (RAM_2000) of right ascension are given as integers while seconds (RAS_2000) are rounded to integer deci-seconds. The declination is given as a character sign (DECSIGN_2000) followed by integer values of degrees (DECD_2000), minutes (DECM_2000) and seconds (DECS_2000).

Position: RA, DEC

Positions are given for the equinox B1950.0 and epoch 1983.5. The full precision available is quoted in degrees, for Right Ascension (RA) and Declination (DEC).

Position: L, B

Positions are given for the equinox B1950.0 and epoch 1983.5. The full precision available is quoted in degrees, for galactic longitude l^{II} (L) and galactic latitude b^{II} (B).

Record Pointer: KEYFSS

An integer-valued pointer to each record is provided for those users who may wish to establish a random access data base.

Positional Uncertainty: UNCMAJOR, UNCMINOR, POSANG

Definitions are similar to those for the short form. The semi-major (UNCMAJOR) and semi-minor (UNCMINOR) axes are given in centi-seconds of arc. The orientation (POSANG) of the ellipse on the sky is in deci-degrees east of north.

Number of sightings: NOBS(4)

The number of individual detector sightings at the peak-flux pixel is given.

Flux Density: FNU(4)

Each of the four wavelengths has a *non-color-corrected* flux density in units of Janskys (1 Jy = $10^{-26}\ Wm^{-2}Hz^{-1}$). The quality of each flux density is designated by FQUAL (see below).

TABLE V.C.9 Format of FSC Data File for Long FSC Tape

Start Byte	Name	Description	Units	Format
0000	NAME	Source Name	—	12A1
0012	FCAT	Final catalog flag	—	A1
0013	RAH	Right Ascension B1950	Hour of time	I2
0015	RAM	Right Ascension B1950	Minute of time	I2
0017	RAS	Right Ascension B1950	Second of time	F3.1
0020	DECSIGN	Declination Sign B1950	±	A1
0021	DECD	Declination B1950	Arc Degree	I2
0023	DECM	Declination B1950	Arc Minute	I2
0025	DECS	Declination B1950	Arc Second	I2
0027	RAH_2000	Right Ascension J2000	Hour of time	I2
0029	RAM_2000	Right Ascension J2000	Minute of time	I2
0031	RAS_2000	Right Ascension J2000	Second of time	F3.1
0034	DECSIGN_2000	Declination Sign J2000	±	A1
0035	DECD_2000	Declination J2000	Arc Degree	I2
0037	DECM_2000	Declination J2000	Arc Minute	I2
0039	DECS_2000	Declination J2000	Arc Second	I2
0041	RA	Right Ascension B1950	Degree	F10.6
0051	DEC	Declination B1950	Degree	F10.6
0061	L	Galactic Longitude	Degree	F10.6
0071	B	Galactic Latitude	Degree	F10.6
0081	KEYFSS	Data Base Pointer	—	I7
0088	UNCMAJOR	Uncertainty ellipse major axis	Arc Second	F5.2
0093	UNCMINOR	Uncertainty ellipse minor axis	Arc Second	F5.2
0098	POSANG	Uncertainty ellipse position angle	Degree (East of North)	F4.1
0102	NOBS[1]	Number of times observed in each band	—	4I3
0114	FNU[1]	Flux densities (1 value per band, non-color corrected)	Jansky (10^{-26} W m^{-2} Hz^{-1})	4E10.4
0154	FQUAL[1]	Flux density quality, final product (1 value per band)	—	4I1
0158	RELUNC[1]	Relative flux density uncertainties (1 value/band)	Percent	4F3.1
0170	RELIAB[1]	Percent reliability (1 value per band)	—	4I2
0178	SNR[1]	SNR in each band	—	4E10.4
0218	LOCSNR[1]	Local SNR in each band	—	4E10.4

continued

281

TABLE V.C.9 Format of FSC Data File for Long FSC Tape (Continued)

Start Byte	Name	Description	Units	Format
0258	CATNBR	No. of catalog sources within 6′	—	I2
0260	CATNBR30	No. of catalog sources within 30′	—	I2
0262	EXTNBR	No. of extractions within 6′	—	I2
0264	EXTNBR30	No. of extractions within 30′	—	I2
0266	CATNBR1[1]	No. *same band* catalog sources within 6′ (1 value/band)	—	4I2
0274	CATNBR2[1]	No. *same band* catalog sources within 30′ (1 value/band)	—	4I2
0282	EXTNBR1[1]	No. of *same band* extractions within 6′ (1 value/band)	—	4I2
0290	EXTNBR2[1]	No. of *same band* extractions within 30′ (1 value/band)	—	4I2
0298	CIRRUS1	No. of nearby 100 μm-only *or cold*[2] extractions within 30′	—	I2
0300	CIRRUS2	No. of nearby 100 μm-only *or cold*[2] extractions within 20′	—	I2
0302	CIRRUS3	No. of nearby 100 μm-only *or cold*[2] extractions within 6′	—	I2
0304	C1SIMPLE	No. of nearby 100 μm-only extractions within 30′	—	I2
0306	C2SIMPLE	No. of nearby 100 μm-only extractions within 20′	—	I2
0308	C3SIMPLE	No. of nearby 100 μm-only extractions within 6′	—	I2
0310	FNULIM[1]	Flux density upper-limit (1 value/band, non-color corrected)	Jansky (10^{-26} W m^{-2} Hz^{-1})	4E10.4
0350	FNUPLATE[1]	Flux density from plate (1 value/band, non-color corrected)	Jansky (10^{-26} W m^{-2} Hz^{-1})	4E10.4
0390	SIGPLATE[1]	Flux density rms error from plate (1 value/band, non-color corrected)	Jansky (10^{-26} W m^{-2} Hz^{-1})	4E10.4
0430	NONLCOR[1]	Non-linear flux density correction (1 value/band)	—	4E9.3
0466	PLATE	Plate extracted from	—	I4

continued

D 10015

TABLE V.C.9 Format of FSC Data File for Long FSC Tape (Continued)

Start Byte	Name	Description	Units	Format
0470	AREA[1]	Number of pixels above threshold (1 value/band)	—	4I3
0482	YCNTROID	Flux-weighted centroid along plate y-axis	Pixels	F7.2
0489	ZCNTROID	Flux-weighted centroid along plate z-axis	Pixels	F7.2
0496	BEAMANGY	Beam orientation angle with respect to plate y-axis	Degree (East of Plate y-axis)	F4.1
0500	BEAMMAJ[1]	Beam size along major axis (1 value/band)	Arc Second	4I4
0516	BEAMMIN[1]	Beam size along minor axis (1 value/band)	Arc Second	4I4
0533	YOFFSET[1]	Centroid distance to peak pixel along y-axis (1 value/band)	Arc Second	4I4
0548	ZOFFSET[1]	Centroid distance to peak pixel along z-axis (1 value/band)	Arc Second	4I4
0564	SHAPEMAJ[1]	Pixel distribution semi-major axis (1 value/band)	Arc Second	4I4
0580	SHAPEMIN[1]	Pixel distribution semi-minor axis (1 value/band)	Arc Second	4I4
0596	SHAPANGY[1]	Pixel distribution orientation with respect to plate y-axis (1 value/band)	Degree (East of Plate y-axis)	4F4.1
0612	MAXLSNR[1]	Maximum local SNR over pixel distribution (1 value/band)	—	4E9.3
0648	ISLCOR[1]	Island correction factor (1 value per band)	—	4E9.3
0684	AVENOBS[1]	Average of counts above threshold (1 value/band)	—	4F6.2
0708	SIGNOBS[1]	RMS deviation of counts above threshold (1 value/band)	—	4E8.2
0740	AVN[1]	Regional average coverage (1 value/band)	—	4E9.3
0776	AVINVN[1]	Regional average inverse coverage (1 value/band)	—	4E9.3
0812	AVINVRN[1]	Regional average inverse square root coverage (1 value/band)	—	4E9.3

continued

383

TABLE V.C.9 Format of FSC Data File for Long FSC Tape (Continued)

Start Byte	Name	Description	Units	Format
0848	CCMAX[1]	Maximum value of correlation coefficient (1 value/band)	deci-percent	4I4
0864	CCMAXLOC[1]	Pointer to location of CCMAX (1 value/band)	—	4I1
0868	CNTRDCC[1]	Correlation coefficient at centroid position (1 value/band)	deci-percent	4I4
0884	FRATIO[1]	Ratio of template-fit flux density to peak flux density (1 value/band)	—	4F6.3
0908	NOISRAT[1]	Ratio of quantiles at 87% and 68% (1 value/band)	—	4F6.3
0932	NOISCOR[1]	Noise correction factor (1 value/band)	—	4F6.3
0956	NPARENT[1]	Pre-rethresholding source number (1 value/band)	—	4I4
0972	NCHLDRN[1]	Post-rethresholding number of sources/parent (1 value/band)	—	4I2
0980	PROBLIN[1]	Percent probability of sources lining up at random (1 value/band)	—	4I2
0988	BMSEED	Seed band for bandmerger	—	I1
0989	BMFQUAL[1]	Bandmerger flux density quality index (1 value/band)	—	4I1
0993	NBNONUL	Number of merged bands which are not upper-limits	—	I1
0994	NBDETECT	Number of merged bands which are detections	—	I1
0995	QUALINDX[1]	Bandmerger quality index (1 value/band)	—	4I3
1008	BMFLAG1[1]	Bandmerger warning flag 1 (1 value/band)	—	4I1
1011	BMFLAG2[1]	Bandmerger warning flag 2 (1 value/band)	—	4I1
1015	BMFLAG3[1]	Bandmerger warning flag 3 (1 value/band)	—	4I1
1019	BMFLAG4[1]	Bandmerger warning flag 4 (1 value/band)	—	4I2
1027	BMFLAG5[1]	Bandmerger warning flag 5 (1 value/band)	—	4I1

continued

D 10045

TABLE V.C.9 Format of FSC Data File for Long FSC Tape (Continued)

Start Byte	Name	Description	Units	Format
1031	BMFLAG6[1]	Bandmerger warning flag 6 (1 value/band)	—	4I1
1035	COMPDIST[1]	Centroid to the component-band radial distance (1 value/band)	Arc Second	4F6.2
1035	COMPANGL[1]	Centroid to the component-band position angle (1 value/band)	Degree	4F5.1
1079	NDUPS	Number of source duplicates	—	I2
1081	DUPKEY_A	List of duplicate source pointers	—	I7
.	.	.	.	.
.	.	.	.	.
1193	DUPKEY_Q	.	.	.
1200	NOVRLAP	Number of overlapping plates	—	I1
1201	LST-OVRLP_A	List of overlapping plate numbers	—	I4
.	.	.	.	.
.	.	.	.	.
1217	LST-OVRLP_E	.	.	.
1221	PLAT-NDUP_A	Number of dups for each overlapping plate	—	I1
.	.	.	.	.
.	.	.	.	.
1225	PLAT-NDUP_E	.	.	.
1226	NID	Number of positional associations	—	I2
1228	IDTYPE	Type of associated object (bit-encoded)	—	I2
1230	IDFLAG1	Association flag for the 1st catalog	—	I1
.	.	.	.	.
.	.	.	.	.
1279	IDFLAG50	Association flag for the 50th catalog	—	I1
1280	IDKEY	Pointer to the record in association data base	—	I7
1287	FPFLAG_A	First final product flag	—	I1
.	.	.	.	.
.	.	.	.	.
1291	FPFLAG_E	Fifth final product flag	—	I1

continued

385

D 10015

TABLE V.C.9 Format of FSC Data File for Long FSC Tape (Continued)

Start Byte	Name	Description	Units	Format
1292	MRGMAPN	Merge map number	—	I4
1296	MRGSEQN	Sequential bandmerge number	—	I4
1300	POS-ANG2000	Position uncertainty ellipse position angle (measured East of North, equinox J2000.0)	Degree	F4.1
1304	SPARE		—	A136

NOTES:

1 In the FITS header, these quantities are suffixed by the wavelength. Example: FNU(4) is given as FNU_12, FNU_25, FNU_60, and FNU_100.

2 Cold is defined by $\log(f_\nu(60\ \mu m)/f_\nu(100\ \mu m)) \leq -0.75$.

The flux densities have been calculated assuming an intrinsic source energy distribution such that the flux density f_ν is proportional to ν^{-1}. Corrections to other spectral shapes can be made by consulting Section VI.C in the *Main Supplement* or by the table inside the back cover of this Supplement.

Note that the flux density quoted for some sources could be zero if there were not enough data available to derive a good upper limit (see Sections II.F.4 and III.H).

Final Product Flux Density Quality: FQUAL(4)

A flux-density measurement can be either high quality (FQUAL=3), moderate quality (FQUAL=2) or an upper limit (FQUAL=1). Quality is determined by whether an individual detection qualifies for entry into the catalog on its own merit. This is to be differentiated from BMFQUAL described later.

Flux Density Uncertainties: RELUNC(4)

Flux-density measurement uncertainty, similar to the short form.

Reliability: RELIAB(4)

The reliability in percentage for each individual detection. A value of zero indicates lack of sufficient information for its calculation. See Section III.D.3 for more information.

Signal-to-Noise Ratios: SNR(4), LOCSNR(4)

Description is identical to the short form.

386

D 10015

TABLE V.C.10 Format of Association Data for Long FSC Tape

Start Byte	Name	Description	Units	Format
000	NAME	FSS Source Name	—	A12
012	KEYFSS	FSS pointer in main database	—	I7
019	IDRECNO	Association pointer	—	I7
026	NID	Total number of positional associations	—	I2
028	IDSEQNO	Sequential number of association per FSS source	—	I2
030	CATNO	Catalog number	—	I2
032	SOURCE	Source ID	—	A15
047	TYPE	Source Type/Spectral Class	—	A5
052	A_RA	Association Right Ascension B1950.0	Degree	F9.5
061	A_DEC	Association Declination B1950.0	Degree	F9.5
070	IDTYPE	Type of associated object (bit-encoded)	—	I2
072	WINDOW	Catalog-dependent association window	Arc Second	I3
075	RADIUS	Radius vector from *IRAS* source to association	Arc Second	F4.1
079	POS	Position angle from *IRAS* source to association	Degree (East of North)	F4.1
083	DSTMAJOR	Distance from *IRAS* source to association along the *IRAS* position error major axis	Arc Second	F4.1
087	DSTMINOR	Distance from *IRAS* source to association along the *IRAS* position error minor axis	Arc Second	F4.1
091	FIELD1	Object field #1 (magnitude/other)	Catalog dependent	I4
095	FIELD2	Object field #2 (magnitude/other)	Catalog dependent	I4
099	FIELD3	Object field #3 (magnitude/other)	Catalog dependent	I4
103	FNUPSC[1]	Flux density of PSC association, field is saturated at $\gtrsim$ 32 Jy (1 value/band, non-color corrected)	mJy (10^{-29} W m^{-2} Hz^{-1})	4I5

continued

387

TABLE V.C.10 Format of Association Data for Long FSC Tape (Continued)

Start Byte	Name	Description	Units	Format
123	FNUERR[1]	Relative flux density uncertainty of PSC association (1 value/band)	deci-percent	4I3
135	RECNO	Sequential number of FSS record		I6
141	ASPARE			A3

1 In the FITS header, these quantities are suffixed by the wavelength. Example: FNU(4) is given as FNU_12, FNU_25, FNU_60, and FNU_100.

Catalog Neighbor Counts: CATNBR, CATNBR30, CATNBR1(4), CATNBR2(4)

CATNBR gives the number of nearby catalog sources within a radius of 6′. CATNBR30 gives the same parameter within a radius of 30′. CATNBR1 gives the number of nearby *same band* catalog sources within a 6′ radius. CATNBR2 gives the number of nearby *same band* catalog sources within a radius of 30′.

Database Neighbor Counts: EXTNBR, EXTNBR30, EXTNBR1(4), EXTNBR2(4)

EXTNBR gives the number of nearby database sources within a radius of 6′. The same quantity within a radius of 30′ is given by EXTNBR30. EXTNBR1 gives the number of nearby *same band* database sources within a 6′ radius. EXTNBR2 gives the number of nearby *same band* database sources within a radius of 30′.

Cirrus Indicators: CIRRUS1, CIRRUS2, CIRRUS3, C1SIMPLE, C2SIMPLE, C3SIMPLE

Over nearly the entire sky, portions of the FSS plates are affected by the infrared cirrus. Cirrus can seriously hamper efforts to extract point sources from the data and can also produce structure on a point source scale that can masquerade as true point sources. The flags CIRRUS1, CIRRUS2, and CIRRUS3 give the number of 100 μm-only sources or cold 60 and 100 μm sources (*i.e.* $\log f_\nu(60\ \mu\text{m})/f_\nu(100\ \mu\text{m}) \leq -0.75$) in the extraction database within radii of 30′, 20′, and 6′ respectively. These flags are coarse discriminants that warn the user that cirrus which contains structure on a point source scale is present in a given region. CIRRUS1 values above 2 usually indicate contamination. In the short form of the catalog, CIRRUS1 is labeled CIRRUS.

Flags C1SIMPLE, C2SIMPLE, and C3SIMPLE give the number of 100 μm-only sources in the extraction database within radii of 30′, 20′, and 6′ respectively.

Flux Density Upper Limits: FNULIM(4)

A 90% confidence flux density upper limit has been computed. Consult Section II.F.4. The uncertainty in this estimate is given by RELUNC. FNULIM is given in Janskys. Under some rare conditions there are not enough data to compute an upper limit and in those cases FNULIM is set to zero.

Flux Density and Noise from the Plate: FNUPLATE(4), SIGPLATE(4)

FNUPLATE is the peak flux density within a 5 × 5 pixel region centered on the final source position from the FSS plate. These flux density values do *not* include the non-linear load resistor corrections. SIGPLATE is the median of noise values within a 5 × 5 pixel region centered on the final source position from the FSS noise grid. Consult Section II.F.5 for caveats. FNUPLATE and SIGPLATE are given in Janskys.

Non-Linear Corrections to Flux Density: NONLCOR(4)

To incorporate the non-linear behavior of load resistors to the background brightness and source strength, corrections have been applied to flux densities measured from the FSS *plates*. The flux density values FNU include this correction. For further details consult Section II.G.5.

FSS Plate: PLATE

The plate number corresponding to the representation of the source is given. There may be duplicates of the source on other plates. Consult Section II.G.2 for details.

Area of Source: AREA(4)

Similar to the short form.

Centroid Positions: YCNTROID, ZCNTROID

The source position in pixel units. The positions are in reference to the plate PLATE (see above). They result from flux density-weighted centroids over the re-thresholded source area. The coordinates are along the Y- and Z-axis of FSS plates. Consult Section II.E.3 for details. YCNTROID and ZCNTROID are quoted in terms of an equivalent 1584 × 1584 pixel plate (pixel counts start at 1).

Point Source Beam: BEAMANGY, BEAMMAJ(4), BEAMMIN(4)

The *expected* orientation of a point source with respect to the *plate* Y-axis (measured east of positive Y-axis) has been computed from all of the the spacecraft passes over the region, by taking into account the orientation of each scan. This angle differs from POSANG which is measured east of north. The major and minor FWHMs of the point

source profiles at each band are also reported through BEAMMAJ and BEAMMIN, for more information see Section II.D.5.

Threshold Area Shape: YOFFSET(4), ZOFFSET(4), SHAPEMAJ(4), SHAPEMIN(4), SHAPANGY(4)

The distance between the flux density-weighted centroid of a source and the position of peak flux density pixel along the plate Y- (YOFFSET) and Z-axis (ZOFFSET) is reported for each detection. Furthermore the semi-major and semi-minor principal axes (SHAPEMAJ, SHAPEMIN) and orientation (with respect to plate Y-axis, SHAPANGY) of the pixel distribution at each detected band are computed from the shape matrix

$$\frac{\Sigma_{\rm area} f_{x_i x_j} \times (x_i - x_{i0})(x_j - x_{j0})}{\Sigma_{\rm area} f_{x_i x_j}}.$$

For details see Section II.E.3.

Maximum per Pixel Signal-to-Noise Ratio: MAXLSNR(4)

The maximum observed value of per pixel signal-to-noise ratio over the pixel distribution is reported at every detected band. This is to be differentiated from LOCSNR which is the pixel signal-to-noise ratio at the *peak* flux density pixel.

Island Correction Factor: ISLCOR(4)

The reported signal-to-noise ratio, SNR, already *includes* a correction factor which compensates for the very local variations in coverage. This correction is labeled the island correction factor. The correction has been applied *only* at 12 and 25 μm, and *only when* FPFLAG_D is set to 0. See also description of FPFLAG.

Pixel Coverage Statistics: AVENOBS(4), SIGNOBS(4)

The average (AVENOBS) and standard deviation (SIGNOBS) of the per pixel coverage over the source pixel distribution are reported at every detected band.

Regional Coverage: AVN(4), AVINVN(4), AVINVRN(4)

The coverage statistics $< NOBS >_\Gamma$ (mean coverage, AVN), $< 1/NOBS >_\Gamma$ (mean inverse coverage, AVINVN), and $< 1/\sqrt{NOBS} >_\Gamma$ (mean inverse square root coverage, AVINVRN) are interpolated from a grid of values calculated over areas Γ of roughly $79.25' \times 79.25'$ at 12 and 25 μm and $\sim 99.5' \times 99.5'$ at 60 and 100 μm. See Section II.E.2.

Template Fit Parameters: CCMAX(4), CCMAXLOC(4), CNTRDCC(4), FRATIO(4)

For every detection a two-dimensional point source template is fitted to the thresholded pixels. The value of the resulting correlation coefficient is computed with the template placed at the flux density-weighted centroid (CNTRDCC) and also at four nearest

neighbor locations. The location giving the *maximum* value of the five thus computed correlation coefficients is reported in CCMAXLOC, and the maximum value of the correlation coefficient is CCMAX. The coding for CCMAXLOC is as follows (for units of shift see Section II.E.4):

- A value of 1 refers to the centroid location, denoted (0,0).
- A value of 2 indicates a location given by (+Y,0)
- A value of 3 indicates a location given by (0,−Z)
- A value of 4 indicates a location given by (−Y,0)
- A value of 5 indicates a location given by (0,+Z)

From the resulting template fit a flux density value is also derived. The ratio of this flux density to the peak flux density is reported in FRATIO. See Section II.E.4.

Noise Distribution Parameters: NOISRAT(4), NOISCOR(4)

The 87% and 68% quantiles of the positive flux density distributions have been computed on cells of $\sim 79.25' \times 79.25'$ at 12 and 25 μm and $\sim 99.5' \times 99.5'$ at 60 and 100 μm. The ratio of the 87% to 68% quantile is reported in NOISRAT (a Gaussian distribution will have NOISRAT=1.5). The ratio of the 68% quantile to the median of the noise grid is quoted in NOISCOR (a Gaussian distribution will have NOISCOR $\sim$ 1). For more details consult Sections II.E.2, III.A.1, III.C.4, and III.G.7.

Area Rethreshold Data: NPARENT(4), NCHLDRN(4)

The source extractor marks contiguous regions satisfying the area and SNR thresholds as described in Section II.E.3. The marked region is assigned a unique number, NPARENT. If the thresholded region exceeds 50 pixels (100 pixels at 100 μm) the area is re-examined at a new threshold as described in Section II.E.3. The number of sources from the new rethresholding is reported in NCHLDRN.

Probability of Linear Feature: PROBLIN(4)

Whenever a parent is rethresholded and yields two or more children, a linear fit is made to the spatial distribution of these sources and the correlation coefficient computed. The probability that the same number of points chosen *at random* yield a similar correlation coefficient is computed and returned in PROBLIN. Most often the parent yields only two children and thus the PROBLIN would be 1.0 (given as 99% in the catalog).

Bandmerger Information: BMSEED, BMFQUAL(4), NBNONUL, NBDETECT

The merging of a multiband source can be initiated at either of the 12, 25, or 60 μm bands, BMSEED indicates the band number of the initiating seed (12 μm $\equiv$ 1, 25 μm $\equiv$ 2, 60 μm $\equiv$ 3). A given detection can become a seed only if its *band merge* quality,

BMFQUAL, is high (=3). This is to be differentiated from FQUAL (for details see Section II.F.2).

For a multiband source the number of *non-upperlimit* bands is given by NBNONUL, and the number of *detected* bands (regardless of whether they are flagged as confused) is given by NBDETECT.

Bandmerger Flags: QUALINDX(4), BMFLAG1, BMFLAG2, BMFLAG3, BMFLAG4, BMFLAG5, BMFLAG6

To indicate how a quoted flux density or an upper limit was derived, a quality index, QUALINDX, is reported for every band (for details see Section II.F.4.c).

The bandmerger provides potential problems at each wavelength through six flags. The flags are: same-band confusion (BMFLAG1), >1 merger (BMFLAG2), >1 seed (BMFLAG3), moderate quality merger (BMFLAG4), plate edge (BMFLAG5), and unused merger (BMFLAG6). For detailed definition of these flags see Section II.F.5.

Component-Band Position Information: COMPDIST(4), COMPANGL(4)

A vector is drawn from the centroid position to each component-band's position. The length of this vector (COMPDIST) is in centi-seconds of arc, and the position angle of this vector (COMPANGL) measured east of north is in deci-degrees.

Duplicate Source Information: NDUPS, DUPKEY_A - _Q

Due to plate overlaps, the same source within the overlap regions may have several renditions. The total number of duplicates for the source is reported through NDUPS (a maximum of *seventeen* duplicates exists). The data base pointers to these duplicates are reported through a list, DUPKEY_A through DUPKEY_Q. Only the first NDUPS members of the list are meaningful. For details see Section II.G.2.

Duplicate Plate Information: NOVRLAP, LSTOVRLP_A - _E, PLATNDUP_A - _E

For every source falling within plate overlap regions, the number of overlapping plates is reported through NOVRLAP (at any point in the sky a maximum of *five* plates can overlap). The list of overlapping plate numbers is reported through the list LSTOVRLAP. and the number of duplicates from each overlapping plate is reported through the list PLATNDUP_A through PLATNDUP_E. Only the first NOVRLP members of the list are meaningful. For details consult Section II.G.2.

Positional Association Pointers: NID, IDTYPE, IDFLAG1-50, IDKEY

As described in Section II.G, a large number of catalogs have been searched for positional matches to FSS sources. The total number of matches found is given by NID. Each

match results in a 144-character description which is placed in a separate association file in order to conform to the FITS catalog format.

When NID > 0, an association record exists. IDTYPE ranges from 1 to 15 and states whether an association was found in a stellar catalog (bit 0), an extragalactic catalog (bit 1), catalogs with other types of objects (bit 2) or in a catalog with mixed types or derived partially/completely from *IRAS* data (bit 3). Both of these parameters are as defined in the short form catalog.

Catalogs searched were given an integer identification number ranging from 1 to 50. Catalog names and their identifying number are in Table II.G.4. To indicate which catalogs have associations to the FSS source, fifty flags have been created. IDFLAG×× (where ×× is the numerical index of the catalog, see Table II.G.4) has been set to 1 when an association has occured. For example, IDFLAG1 corresponds to catalog 1 (General Catalogue of Variable Stars), IDFLAG25 corresponds to catalog 25 (Catalog of Dwarf Galaxies) and so forth. Note that these flags complement IDTYPE by identifying the constituent associated catalogs.

The association records are reported in a separate file to conform to the FITS catalog convention. A data base pointer, IDKEY, for the corresponding record has been provided to help users establish random access to the association file.

Final Product Flags: FPFLAG_A - _E

Five integer valued flags are provided which give the adjustments to source status during final product generation.

Sources identified as being due to optical cross-talk were deleted from the catalog and FPFLAG_A was set to 1 (for details see Section III.G.4). Sources falling on a comet trail were removed from the catalog, and FPFLAG_B was set to 1 (consult Section III.G.2 for details). A source which has been identified with FSC version 1.2 has FPFLAG_C set to 1 (for details consult Section IV.B.1).

At approximately $|b| \sim 5°$, the application of the island correction factor to the SNR at 12 and 25 μm was stopped. To indicate that *no* island correction factor has been applied, FPLFLAG_D is set to 1 (consult Section II.E.2). At approximately $|b| \sim 5°$ the source extraction thresholds were raised also. To indicate that extraction thresholds were raised, FPFLAG_E has been set to 1 (for more details see Section II.E.3).

Band Merger Pointers: MRGMAPN, MRGSEQN

For each source the bandmerger produces a book-keeping record of detections in each band which were merged with other bands. Pointers to the corresponding tables are

recorded in MRGMAPN and MRGSEQN. These two parameters are of value only in conjunction with the FSS raw data archived at IPAC.

Position Uncertainty Ellipse J2000 : POSANG2000

The orientation of the positional uncertainty ellipse is given for the equinox J2000.0.

C.2.b Association Data

Source Name: NAME

The name of FSS source having this association.

Record Pointer: KEYFSS

Integer-valued pointer refers to the FSS source having this association.

Association Record Pointer: IDRECNO, NID

The association records are indexed separately from the non-associated data. For each association a pointer is supplied to help users establish random access to the data. The total number of associations for each FSS source is NID. The association records are variable length, thus the record with pointer IDRECNO will have a length given by NID × 144 bytes.

Record Identifiers: IDSEQNO

The association records for these NID associations are stored sequentially, with the pointer to the sequential order being IDSEQNO (which ranges from 1 to NID).

Association Name and Type: CATNO, SOURCE, TYPE

The catalog number, CATNO (see Table II.G.4 for a list) and the source name in that catalog, SOURCE, are given. For catalogs 40 and 48 the spectral type/luminosity class or object classification are reported in TYPE. For details see Table II.G.5.

Association Position: A_RA, A_DEC

Position is given for the equinox B1950.0. The full available precision is quoted in degrees, for right ascension (A_RA) and declination (A_DEC).

Association Type: IDTYPE

IDTYPE is a bit encoded parameter, ranging in value from 1 to 15. It identifies the association catalog as being a purely stellar catalog (bit 0 is set), a purely extragalactic catalog (bit 1 is set), a catalog with other types of objects (bit 2 is set), or a catalog derived partially/completely from the *IRAS* data (bit 3 is set).

Association Window: WINDOW

Associations are made within rectangular windows of at least half widths 26″ × 165″. If the positional uncertainty of the associated catalog is not small or the catalog contains a size information, then the window is expanded until it contains the size or positional uncertainty of the catalog. The window size used is reported in seconds of arc (WINDOW). See also Section II.G.3.

Association Match Vector: RADIUS, POS, DSTMAJOR, DSTMINOR

A vector is drawn *from* the FSS position *to* the association. The length of this vector (RADIUS) is in deci-seconds of arc, and the position angle of this vector (POS) measured East of North is in deci-degrees.

Projections of this vector along the major and minor axes of the FSS uncertainty ellipse are given by DSTMAJOR and DSTMINOR, respectively, in deci-seconds of arc.

Association Information: FIELD1, FIELD2, FIELD3

Three fields (FIELD1-3) have values depending on the catalog in question (consult Table II.G.5). Typically FIELD1,2 are magnitudes (in decimag) and FIELD3 is a size.

Association from PSC: FNUPSC(4), FNUERR(4)

When the associated catalog is the PSC, the flux density of the associated PSC source is reported for each band (FNUPSC) in mJy. These flux densities are non-color-corrected. Furthermore, the fields become saturated at any band where the PSC source has a flux density $\gtrsim$ 32 Jy.

The relative flux density uncertainty of FNUPSC is given by FNUERR in deci-percent.

Counter: RECNO

Sequential number of the FSS record.

C.3 The Machine-Readable Version of the Reject File

The Reject File tape is presented as FITS table data. Its format is identical to the long form of the FSC.

395

D 10019

D. The Explanatory Supplement

This Explanatory Supplement is available as a set of ASCII files in TEX format on floppy disks, with each chapter or section, depending on length, in a separate file. At a later date this Supplement may be made available on a CD-ROM as well.

Authors:

M. Moshir and T. Chester

396

D 10015

VI. REFERENCES

Altenhoff, W.J., Downes, D., Pauls, T., and Schraml, J., 1979, *Astron. Astrophys.* [*Suppl.*], **35**, 23.

Alter, G., Balasz, B., and Ruprecht, J., 1970, *Catalogue of Star Clusters and Associations*, Budapest: Akademiai Kiado.

Arp, H., 1966, *Ap. J.* [*Suppl.*], **14**, 1.

Bingelli, B., Sandage, A., and Tamman, G.A., 1985, *Astron. J.*, **90**, 9.

Blitz, L., Fich, M., and Stark, A.A., 1982, *Ap.J.* [*Suppl.*], **49**, 183.

Cederblad, S., 1946, *Lund Annals*, Ser. 2, No. 119.

Chester, T.J., 1986, in *Light on Dark Matter*, editor F.P. Israel, Reidel:Dordrecht, p. 3.

Condon, J.J., 1974, *Ap. J.*, **188**, 279.

de Vaucouleurs, G., de Vaucouleurs, A., and Corwin, Jr., H.G., 1976, *Second Reference Catalogue of Bright Galaxies*. Austin: University of Texas Press.

Dorschner, V.J., and Gurtler, J., 1964, *Ast. Nachr.*, **287**, 257.

Dressel, L.L., and Condon, J.J., 1976, *Ap. J.* [*Suppl.*], **31**,187.

Explanatory Supplement to IRAS Catalogs and Atlases, 1988, Pasadena: California Institute of Technology.

Fowler, J.W., and Rolfe, E.G., 1982, *J. of Astr. Sci.*, **30**, 385.

Gliese, W., 1969, *Veroffentl. Astron. Rechen-Instituts Heidelberg*, No. 22.

Griesen, E.W., and Harten, R.H., 1981, *Astron. Astrophys.* [*Suppl.*], **44**, 371.

Harten, R.H., Grosbøl, P., Griesen, E.W., and Wells, D.C., 1988a, *Astron. Astrophys.* [*Suppl.*], **73**, 359.

Harten, R.H., Grosbøl, P., Griesen, E.W., and Wells, D.C., 1988b, *Astron. Astrophys.* [*Suppl.*], **73**, 365.

Haynes, R.F., Caswell, J.L., and Simons, L.W.J., 1979, *Aust. J. Phys. Astrophys.* [*Suppl.*], No. 48.

Hoffleit, D., 1982, *The Bright Star Catalogue, Fourth Revised Edition*. New Haven: Yale University Observatory.

Kalman, R.E., 1960, *ASME Trans.*, **82D**, 35.

Kleinmann, S.G., and Joyce, R.R., 1984, private communication.

Kuhr, H., Witzel, A., Pauliny-Toth, I.I.K., and Nauber, U., 1981, *Astron. Astrophys.* [*Suppl.*], **45**, 367.

397

D 10015

Kukarkin, B.V., Kholopov, P.N., Artirukhina, N.M., Fedorovich, V.P., Frolov, M.S., Goranskij, V.P., Gorynya, N.A., Karitskaya, E.A., Kireeva, N.N., Kukarkina, N.P., Kurochkin, N.E., Medvedeva, G.M., Perova, N.B., Ponomareva, G. A., Samus, N.N., and Shugarov, S.Yu, 1981, *New Catalog of Suspected Variable Stars* (on magnetic tape), Sternberg Inst., Moscow State University.

Kukarkin, B.V., Kholopov, P.N., Efremov, Yu.N., Kukarkina, N.P., Kurochkin, N.E., Medvedeva, G.I., Perova N.B., Fedorovich, V.P., and Frolov, M.S., 1970, *General Catalog of Variable Stars, 3rd Edition*, Vol. II, Sternberg Inst., Moscow State University.

Kukarkin, B.V., Kholopov, P.N., Pskovsky, Yu.P., Efremov, Yu.N., Kukarkina, N.P., Kurochkin, N.E., Medvedeva, G.I., Perova, N.B., Fedorovich, V.P., and Frolov, M.S., 1971, *General Catalogue of Variable Stars*, Vol. III, Sternberg Inst., Moscow State University.

Lauberts, A., 1982, *The ESO/Uppsala Survey of the ESO(B) Atlas*. Munich: European Southern Observatory.

Lee, O.J., Baldwin, R.J., and Hamlin, D.W., 1943, *Annals of the Dearborn Observatory*, **V**, Part 1A.

Lee, O.J., and Bartlett, T.J., 1944, *Annals of the Dearborn Observatory*, **V**, Part 1B.

Lee, O.J., Gore, G.D., and Bartlett, T.J., 1947, *Annals of the Dearborn Observatory*, **V**, Part 1C.

Lonsdale, C.J., Hacking, P.B., Conrow, T.P., Rowan-Robinson, M., 1990, *Ap.J.*, **358**, 60.

Lynds, B.T., 1962, *Ap. J. [Suppl.]*, **7**, 1.

Markarian, B.E., 1967, *Astrofizika*, **3**, 55.

Markarian, B.E., 1969a, *Astrofizika*, **5**, 443.

Markarian, B.E., 1969b, *Astrofizika*, **5**, 581.

Markarian, B.E., and Lipovetskii, V.A., 1971, *Astrofizika*, **7**, 511.

Markarian, B.E., and Lipovetskii, V.A., 1972, *Astrofizika*, **8**, 155.

Markarian, B.E., and Lipovetskii, V.A., 1973, *Astrofizika*, **9**, 487.

Markarian, B.E., and Lipovetskii, V.A., 1974, *Astrofizika*, **10**, 307.

Markarian, B.E., and Lipovetskii, V.A., 1976a, *Astrofizika*, **12**, 389.

Markarian, B.E., and Lipovetskii, V.A., 1976b, *Astrofizika*, **12**, 657.

Markarian, B.E., Lipovetskii, V.A., and Stepanyan, D.A., 1977a *Astrofizika*, **13**, 225.

398

D 10015

Markarian, B.E., Lipovetskii, V.A., and Stepanyan, D.A., 1977b, *Astrofizika*, **13**, 397.

Markarian, B.E., Lipovetskii, V.A., and Stepanyan, D.A., 197[illegible] *Astofizika*, **15**, 201.

Markarian, B.E., Lipovetskii, V.A., and Stepanyan, D.A., 1979b, *Astrofizika*, **15**, 363.

Markarian, B.E., Lipovetskii, V.A., and Stepanyan, D.A., 1979c, *Astrofizika*, **15**, 549.

Markarian, B.E., Lipovetskii, V.A., and Stepanyan, D.A., 1981, *Astrofizika*, **17**, 619.

Marsalkova, P., 1974, *Astrophys. Sp. Sci.*, **27**, 3.

Melnyk, M., 1986, *Noise Estimation for Mid-average Data Processing*, IPAC IOM 240-86-146.

Moshir, M., 1986, *2-Dimensional Detector Response Functions and Their New Solid Angles*, IPAC IOM 240-86-83.

Moshir, M., 1989, *B.A.A.S.*, **21**, 768.

Murdock, H.S., Crawford, D.F. and Jauncey, D.L., 1973, *Ap. J.*, **183**, 1.

Neugebauer, G., and Leighton, R.B., 1969, *Two-Micron Sky Survey*, NASA SP-3047. Washington, D.C.: National Aeronautics and Space Administration.

Nilson, P., 1973, Uppsala General Catalogue of Galaxies, Nova Acta Regiæ Societatis Scientiarium Upsaliensis, Ser. V:A, **1**.

Price, S.D., and Murdock, T.L., 1983, *The Revised Air Force Geophysics Laboratory Infrared Sky Survey*, AFGL-TR-83-0161. Hanscom Air Force Base, Massachusetts: Air Force Geophysics Laboratory.

Review of Particle Properties, 1990, Phys. Lett. B, **239**, III.35.

Rowan-Robinson, M., Walker, D., Chester, T., Soifer, T., Fairclough, A.C., 1986, *M.N.R.A.S.*, **219**, 483.

Rowan-Robinson, M., Hughes, J., Jones, M., Leech, K., Vedi, K., Walker, D.W., 1991, *M.N.R.A.S.*, **249**, 729.

Smithsonian Astrophysical Observatory Star Catalog, (4 vols.) 1966, Pub. 4652. Washington, D.C.: Smithsonian Institution.

Stephenson, C.B., 1973, *Publications of the Warner and Swasey Observatory*, **1**, No. 4, Case Western Reserve University.

Stephenson, C.B., 1976, *Publications of the Warner and Swasey Observatory*, **2**, No. 2, Case Western Reserve University.

399

D 10015

Sykes, M.V., Lebofsky, L.A., Hunten, D.M., and Low, F., 1986, *Science*, **232**, 115.

Tukey, J.W., 1962, *Annals of Mathematical Statistics*, **33**, 1.

van den Bergh, S., 1966a, *A. J.*, **71**, 922.

van den Bergh, S., 1966b, *A. J.*, **71**, 990.

van den Bergh, S., and Herbst, W., 1975, *A. J.*, **80**, 208.

Véron-Cetty, M.P., and Véron, P., 1984, *A Catalogue of Quasars and Active Nuclei, 2nd Edition*. ESO Report No. 5 (Munich: European Southern Observatory).

Vorontsov-Velyaminov, B.A., 1959, *Atlas and Catalog of Interacting Galaxies*, Sternberg Inst., Moscow State University.

Vorontsov-Velyaminov, B.A., and Arhipova, V.P., 1963, *Morphological Catalog of Galaxies*, **Part III**. Moscow State University.

Vorontsov-Velyaminov, B.A., and Arhipova, V.P., 1964, *Morpological Catalog of Galaxies*, **Part II**. Moscow State University.

Vorontsov-Velyaminov, B.A., and Arhipova V.P. 1968, *Morphological Catalog of Galaxies*, **Part IV**. Moscow State University.

Vorontsov-Velyaminov, B.A., and Arhipova, V.P., 1974, *Morphological Catalog of Galaxies*, **Part V**. Moscow State University.

Vorontsov-Velyaminov, B.A., and Krasnogorskaja, A.A., 1962, *Morphological Catalog of Galaxies*, **Part I**. Moscow State University.

Wackerling, L.R., 1970, *Mem. R.A.S.*, **73**, 153.

Waters, L.B.F.M., Coté, J., and Aumann, H.H. 1987. *Astron. Astrophy.*, **172**, 225.

Wells, D.C., Griesen, E.W., and Harten, R.H., 1981, *Astr. Ap. [Suppl.]*, **44**, 363.

Wesselius, P.R., 1979, unpublished.

Wright, Edward, 1984, (private communication).

Young, E.T., Neugebauer, G., Kopan, E.L., Benson, R.D., Conrow, T.P., Rice, W.L., and Gregorich, D.T., 1985, *User's Guide to IRAS Pointed Observation Products*, Pasadena: Jet Propulsion Laboratory.

Zwicky, F., and Herzog, E., 1963, *Catalogue of Galaxies and of Clusters of Galaxies*, Vol. II. Pasadena: California Institute of Technology.

Zwicky, F., and Herzog, E., 1966, *Catalogue of Galaxies and of Clusters of Galaxies*, Vol. III. Pasadena: California Institute of Technology.

401

D 10015

Zwicky, F., and Herzog, E., 1968, *Catalogue of Galaxies and of Clusters of Galaxies*, Vol. IV. Pasadena: Calfornia Institute of Technology.

Zwicky, F., Herzog, E., and Wild P., 1961, *Catalogue of Galaxies and of Clusters of Galaxies*, Vol. I. Pasadena: California Institute of Technology.

Zwicky, F., Karpowicz, M., and Kowal, C.T., 1965, *Catalogue of Galaxies and of Clusters of Galaxies*, Vol. V. Pasadena: California Institute of Technology.

Zwicky, F. and Kowal, C.T., 1968, *Catalogue of Galaxies and of Clusters of Galaxies*, Vol. VI. Pasadena: California Institute of Technology.

Zwicky, F., Sargent, W.L.W., and Kowal, C.T., 1975, *A. J.*, **80**, 545.

Zwicky, F., and Zwicky, M.A., 1971, *Catalogue of Selected Compact Galaxies and of Post-eruptive Galaxies*. Zurich: Offsetdruk L. Speich.

402

D 10015

VII. ACKNOWLEDGEMENTS

The creation of a Faint Source Survey from the *IRAS* data was conceived of by the U.S. *IRAS* Science Team. We further acknowledge their guidance throughout this project, as well as their direct efforts in helping in specific aspects. The U.S. *IRAS* Science Team consists of G. Neugebauer, chairman, H.H. Aumann, C.A. Beichman, T.J. Chester, T.N. Gautier, F.C. Gillett, M.G. Hauser, J.R. Houck, F.J. Low, B.T. Soifer, R.G. Walker, and E.T. Young.

The *IRAS* Faint Source Survey is one of the many products of the *IRAS* Extended Mission funded by NASA. We thank N. Boggess, F.C. Gillett, C. Hartman, C. Pellerin, and G. Riegler of NASA for their support over the last seven years.

The Faint Source Survey would never have been produced in a timely manner and with such high quality without the efforts of the Data Management Team at IPAC. The Data Management Team consists of G. Smith (former supervisor), G. Lairmore, current supervisor, R. Beck, R. Abihai, R. Bailey, E. Erwin, R. Frayre, H. Hanson, G. Johnson, J. Lampley, Leslie Lloyd, P. Lynn, G. Pate, and R. Urban. We thank also the staff at the computer facility, especially our tape librarians D. Rayman and J. Suchner.

Other members of the IPAC staff provided important support. J. Bennett created the software to place the plates in FITS format and developed the software to convert B1950 to J2000 coordinates. R. Scholey leading the library staff, C. Bennett, Larry Lloyd, and D. Wilcher, organized and kept track of the voluminous outputs. R. Benson and J. Fowler contributed useful encouragement and advice. Many members of staff at IPAC gave valuable comments on the draft of this document. C. Oken combined her artistic and technical talents to draw illustrations for this document and also designed the IPAC logo.

This Supplement was typed in TEX by J. Chacon and D. Milton, who also helped to ensure that consistency of style and grammar was maintained. Their competence was a significant factor in producing this Supplement. Their devotion and efforts resulted in a high quality document. We thank K. Young for recommending the ArborText, Inc. *dvips* which greatly facilitated the production of this Supplement.

E.L. Wright first suggested using the trimmed-average algorithm, and we acknowledge useful discussions with him.

We benefitted from the work of those who used the FSS before publication (according to the pre-release criteria advertised in the IPAC Newsletter) and gave feedback to us.

We thank M. Rowan-Robinson and W. Saunders for their comments on the manuscript.

403

IPAC is funded by NASA as part of the *IRAS* extended mission program under contract to JPL.

D 10015

VIII. GLOSSARY OF ABBREVIATIONS AND TERMS

α	Equatorial longitude
A_DEC	Declination of associated source (Equinox B1950.0)
Anomalies	Artifacts discovered in the *IRAS* data such as off-axis reflections from bright sources, reflections from dust particles, paint flakes, etc.
AOs	Additional Observations conducted by the *IRAS* satellite pointed at a specific target (also called Pointed Observations)
A_RA	Right ascension of associated source (Equinox B1950.0)
AREA	Number of pixels above threshold in each band of a source
Associations	Positional coincidences of a source with sources from other catalogs. No identification is guaranteed.
AVENOBS	Average of observed counts over a source's pixel distribution
AVINVN	Average of *inverse* of counts per pixel computed on an extended *region* Γ
AVINVRN	Average of *inverse square root* of counts per pixel computed on an extended *region* Γ
b, B	Galactic latitude b^{II}
Bandmerging	For a given source, the process of combining detections at different wavelengths and upper limits at non-detected wavelengths
Band Structure	The set of bands which have detections
Beam	A two-dimensional map of variable shape, depending on sky location; gives the in-scan, cross-scan extent of an *IRAS* point source in each band
BEAMMAJ	Full width at half maximum extent of the beam along the major axis
BEAMMIN	Full width at half maximum extent of the beam along the minor axis

405

BEAMANGY	Orientation of the beam with respect to the plate y-axis
β	Ecliptic latitude
Binning	The operation of placing individual detector measurements into a fixed grid covering the sky
Bit-encoded	Flags which have a value at all four wavelength bands are encoded into a byte, with the lowest 4 bits representing on/off status of the flag at each of four bands
BMFLAG1	Bandmerger flag 1, shows same band confusion
BMFLAG2	Bandmerger flag 2, shows whether more than one merger was found by the seed
BMFLAG3	Bandmerger flag 3, shows whether more than one seed selected the merger
BMFLAG4	Bandmerger flag 4, shows how many seeds could have selected the merger
BMFLAG5	Bandmerger flag 5, shows proximity to plate edges
BMFLAG6	Bandmerger flag 6, shows whether the merger was used
BMFQUAL	Flux quality flag as used by the bandmerger
BMSEED	Band number for a source which initiated the bandmerging process
Boresight	A fiducial point on the IRAS focal plane used for position reconstruction
C1SIMPLE	Number of nearby 100 μm-only extractions within 30′
C2SIMPLE	Number of nearby 100 μm-only extractions within 20′
C3SIMPLE	Number of nearby 100 μm-only extractions within 6′
CATNBR	Number of catalog sources within a radius of 6′
CATNBR1	Number of *same band* catalog sources within a radius of 6′
CATNBR2	Number of *same band* catalog sources within a radius of 30′

CATNBR30	Number of catalog sources within a radius of 30′
CATNO	Catalog number used for associations
CCMAX	Maximum value of correlation coefficient for a source
CCMAXLOC	Pointer to location giving maximum value for correlation coefficient
CDJ	Critical Daily Job, the software used for the original *IRAS* data processing
CGU	Convolved-Gaussian-Uniform Distribution, the position probability density of *IRAS* sources along the major axis (cross-scan)
Chaining	The process by which duplicate representations of a source are flagged outside the nominal window of 45″
Cirrus	(see Infrared Cirrus)
Cirrus Flag (CIRRUS)	The number of sources detected only at 100 μm *or cold* sources within a radius of 30′ about each source (*short* form of the FSC)
CIRRUS1	In the Point Source Catalog, the number of sources detected only at 100 μm in a one square degree box centered on each source. In the *long* form of the FSC it is the number of sources detected only at 100 μm *or cold* sources within a radius of 30′ about each source
CIRRUS2	The number of sources detected only at 100 μm *or cold* sources within a radius of 20′ about each source
CIRRUS3	The number of sources detected only at 100 μm *or cold* sources within a radius of 6′ about each source
CNTRDCC	The correlation coefficient of the fit of the two-dimensional point source template (positioned at the centroid position) to the data
Coadd	The process of averaging all *IRAS* survey data within a pixel
Cometary Debris	Particles along the orbit of comets producing infrared emission
COMPANGL	Position angle of the vector pointing from the centroid position to the component band position

COMPDIST	Length of the vector pointing from the centroid to the component band position
Completeness	Estimate of probability that a catalog contains a source of given flux density, expressed in percent
Confirmation	For the PSC, the detections of each source had to agree in flux and position within each HCON to be considered "hours-confirmed". Two HCONs had to agree in position (no flux test) to be weeks-confirmed and enter the PSC. For the FSC, individual data points (after trimming) must agree well enough so that the local SNR is higher than the band-dependent thresholds for the FSC.
CONFUSE	Confusion flag (1 flag per band, hex encoded), set if any instance of confusion was detected by the Bandmerger
Confusion	The state that occurs when the density of sources exceeds the resolution of the instrument, so that measurements no longer apply to individual sources
Counts	Number of times scanned with an individual detector or summed over all detectors in each band (number of times observed in each band)
CPS	Connected Polynomial Segment Fit used in the Pointing Reconstruction improvement
CRDD	Calibrated Raw Detector Data, the input detector data for the FSS
Cross-Scan	Direction perpendicular to the scanning direction of the *IRAS* satellite or along the resultant maximum positional uncertainty axis resulting from a combination of several scans
Cross-Talk, electronic	Low level 1-Hz noise present in detector data from temperature sensors in the focal plane
Cross-Talk, optical	Spreading of bright IR images in the focal plane due to diffraction pattern of secondary support spider
CSTAT	Confusion status reported in the PSC
Data Conditioning	Removal of radiation hits, anomalies, and moving sources such as asteroids and comets from the input data to the FSS

D 10015

DEC	Declination, rendered in full precision (in degrees) in the *long* form FSC (Equinox B1950.0)
DECD	Declination degrees (Equinox B1950.0) (*long* form FSC)
DECD_2000	Declination degrees (Equinox J2000.0)
DECDEG	Declination degrees (Equinox B1950.0) (*short* form FSC)
DECM	Declination minutes (Equinox B1950.0) (*long* form FSC)
DECM_2000	Declination minutes (Equinox J2000.0)
DECMIN	Declination minutes (Equinox B1950.0) (*short* form FSC)
DECS	Declination seconds (Equinox B1950.0) (*long* form FSC)
DECS_2000	Declination seconds (Equinox J2000.0)
DECSEC	Declination seconds (Equinox B1950.0) (*short* form FSC)
DECSGN	Declination sign (Equinox B1950.0) (*short* form FSC)
DECSIGN	Declination sign (Equinox B1950.0) (*long* form FSC)
DECSIGN_2000	Declination sign (Equinox J2000.0)
Deglitching	Removal of (bright) radiation hits
δ	Equatorial latitude
Detector Masks	The defined physical sizes of the infrared detectors
Detector Response Function	The two-dimensional map of the expected response of a detector to a point source
DSTMAJOR	Distance from an *IRAS* source to an associated source along the major axis of the *IRAS* position error ellipse
DSTMINOR	Distance from an *IRAS* source to an associated source along the minor axis of the *IRAS* position error ellipse
Dup	Duplicate source extracted from overlapping plates

409

D 10015

DUPKEYS_A ... DUPKEYS_Q	List of pointers for duplicate sources
Duplicate Source (Dup)	Duplicate source extracted from overlapping plates
ESO/SERC /POSS	The optical sky surveys. The European Southern Observatory Sky Survey covers the Southern Hemisphere and the Palomar Observatory Sky Survey covers the Northern Hemisphere
EXTNBR	Number of nearby extractions within a radius of 6′
EXTNBR1	Number of nearby *same band* extractions within a radius of 6′
EXTNBR2	Number of nearby *same band* extractions within a radius of 30′
EXTNBR30	Number of nearby extractions within a radius of 30′
Extraction	A region of the FSS plates satisfying SNR and area thresholds
Extractor	The software that extracts sources from the FSS plates
FAC	Fine Attitude Calibration performed on board the *IRAS* satellite to tune the *IRAS* pointing
FCAT	Flag set to 'T' when a source is in the FSC
FIELD1,2,3	Field number 1, 2, and 3 given in the association data. These fields contain data which are catalog dependent
Filtering	(See Median Filtering)
FITS	Flexible Image Transport System, a standard tape format for astronomical image data
FNU	Flux density (1 value per band) with units of Jansky $10^{-26} W m^{-2} Hz^{-1}$
FNULIM	Ninety percent confidence flux density upper limit
FNUERR	Relative flux density uncertainty of PSC association
FNUPLATE	Flux density measured directly from the plate

410

D 10015

FNUPSC	Flux density of the PSC association
Focal Plane	The set of 62 infrared detectors at the focus of the *IRAS* telescope
FPFLAG_A ... FPFLAG_E	Flags from final product generation
FQUAL	Flux density quality (1 value per band)
FRATIO	Ratio of flux density of template-fit to the peak flux density
FSC	Faint Source Catalog
FSDB	Faint Source DataBase, consisting of all plate extractions (after bandmerging) above approximately 3 σ
FSDB Generator	The software that collects the extracted and bandmerged sources and places them in the Faint Source Database
FSR	The Faint Source Reject File consisting of all FSDB sources not selected for inclusion in the FSC
FSS	Faint Source Survey
FSTAT	Flux status reported in the PSC
FWHM	Full-Width of signal at Half Maximum
'galaxies'	Sources defined for illustrative purposes using the criterion of $f_\nu(60\ \mu\text{m}) > f_\nu(12\ \mu\text{m})$ for sources which exceed the FSC threshold at 60 μm
Γ	A sub-region of a plate over which noise and coverage statistics are computed, varies from (79.25′) to $(99.5')^2$ at 12 to 100 μm
Gyros	Gyroscopes used for pointing reconstruction. Also delicious sandwiches!
HCON	Hours-Confirming Coverage, consisting typically of 2 scans of the sky separated by 1-36 hours, usually resulting in coverage by 4 separate detectors

4/11

High-Quality Flux Density	A flux density that exceeds the catalog thresholds
IDFLAG1-50	Flags denote whether associations to a given catalog were found
IDKEY	Pointer to the record in the association database
IDRECNO	Association record pointer
IDSEQN	Sequential number of association within a given record
IDTYPE	Bit-encoded parameter indicating type of associated catalogs
In-Scan	Direction along the scanning direction of the *IRAS* satellite or along the resultant minimum positional uncertainty axis resulting from a combination of several scans
Infrared Cirrus	Filamentary sources that have structure comparable to the IRAS resolution in one dimension but that are often degrees long in the other dimension
Instrumental Noise	The noise measured at a given pixel in the FSS plates; it includes all noise sources except that due to source and structure confusion
Instrumental SNR	Signal-to-noise ratio formed from signal at a pixel and the signal-to-median of instrumental noise coming from the noise grid
IPAC	Infrared Processing and Analysis Center at Caltech
IR	Infrared
IRAS	Infrared Astronomical Satellite
Island Effect Correction	A correction made for inhomogeneous coverage over a given area. For example, when the noise is computed over an area whose average number of counts is 8, for an individual pixel within that area with only 6 counts, the noise must be corrected by the Island Effect Correction
ISLCOR	Island effect correction
Jansky	Unit of flux density equal to $10^{-26} W m^{-2} Hz^{-1}$
Kalman Filter	Algorithm which processes measurements which can be direct or

	indirect and of varying quality, to update the coefficients and associated uncertainties of a mathematical model
KEYFSS	Integer valued pointer for database sources
KIR	Known Infrared Sources, a set of sources used to monitor/improve the *IRAS* pointing
KIR Type	Number assigned to different classes of known infrared sources
Known Infrared Sources	Known Infrared Source, a set of sources used to monitor/improve the *IRAS* pointing
ℓ, L	Galactic longitude ℓ^{II}
λ	Ecliptic longitude
Local SNR	LOCSNR
LOCSNR	Signal-to-Noise Ratio at a given pixel
LSTOVRLP_A ... LSTOVRLP_E	List of plates which overlap the plate in question
Main Supplement	Explanatory Supplement to the *IRAS* Catalogs and Atlases
MAXLSNR	Maximum observed LOCSNR over a source's pixel distribution
Measured Infrared Error	Measured InfraRed Error File containing the seconds-confirmed position error histories of the Known Infrared Sources
Median Filtering	Removal of low frequencies from the baseline of the input data for the FSS via a median filter
MINREL	Estimate of the lowest bound to reliability of a given source, in percent
MIRE	Measured InfraRed Error File containing the position error histories of the Known Infrared Sources
Moderate-Quality Flux Density	Flux densities that have SNR > 3 but that do not meet catalog thresholds by themselves

Momentum Coils	Electromagnetic coils used to create torques via interaction with the Earth's magnetic field, used periodically to spin down the attitude-control reaction wheels (instead of using reaction jets)
MRGMAPN	Numerical identifier within the merge-map file
MRGSEQN	Sequential band merge number
N	Number of detectors covering a given pixel
N	In Section III.C.6 and 7 and Section III.D.3 only, the number of sources with flux density greater than a given value
NAME	Source name formed from the coordinates
NBDETECT	The number of merged bands which are detections
NBNONUL	The number of merged bands which are not upper limits
NCHLDRN	The number of source which result from area rethresholding of a given source
NDUPS	Number of source duplicates
Neighbor	A nearby source in any of a number of contexts
NID	Number of positional associations
NOBS	Number of times observed in each band
NOISCOR	Noise Correction Factor
Noise Correction Factor	The ratio of the 68% quantile of positive flux densities to the median value of the whole noise grid
NOISRAT	Ratio of the 87% quantile to the 68% quantile of positive flux densities
NONLCOR	Nonlinear flux correction
Nonlinear Flux Correction	A final flux correction applied after source extraction from the Faint Source Plates prior to placing sources in the FSDB

D 10015

Nonlinear Load Resistor	The source of the nonlinear flux correction
NOVRLAP	Number of overlapping plates
NPARENT	Numerical identifier of a source prior to area rethresholding
OBS	A single *IRAS* observation, usually a single scan of the sky
Observation	The basic planning unit for *IRAS* operations. A survey observation (the only kind used for FSS) consisted of a single scan ($\leq$50 min) at constant sun angle and constant scan rate
Optical Crosstalk	Spurious sources introduced by spider-arm reflections from the mirror supports
'other'	Sources defined for illustrative purposes as those sources which are not 'stars' or 'galaxies'
Pixel	Fundamental building block of plates, $0.25' \times 0.25'$ in size at 12 and 25 μm, $0.5' \times 0.5'$ at 60 and 100 μm
Pixel Noise	One-σ estimate of data dispersion in one pixel
PLATE	Gives number of the plate from which the source was extracted
Plates	Faint Source Survey Plates
PLATNDUP_A ... PLATNDUP_E	Number of dups from each overlapping plate
Pointed Observations	Non-survey observations conducted by the *IRAS* satellite pointed at a specific target (also called Additional Observations)
Pointing Reconstruction	Reconstruction of pointing direction of boresight
Point Source Filtering	Median filtering of the input data to the FSS in order to remove low-frequency structure
Point Spread Function	The resulting two-dimensional signal distribution in a plate after the coaddition of all survey scans

4/5

D 10015

POS	Positional angle from an *IRAS* source to an associated source in degrees East of North
POSANG	The position angle of the major axis of the positional uncertainty ellipse in degrees East of North (Equinox B1950.0)
POSANG2000	The position angle of the major axis of the positional uncertainty ellipse in degrees East of North (Equinox J2000.0)
Position Reconstruction	Reconstruction of sky positions of detected IR sources
PROBLIN	Probability that sources line up at random, in percent
PSC	Point Source Catalog
Pseudo-Detector Width	Width of overlap region between multiple detectors treated as a simple detector for cross-scan pointing refinement
QUALINDX	Bandmerger quality index, indicating the manner in which a quoted flux density or upper limit was derived
Quantile	Percentile in colloquial language
R	Reliability of a source at a given spectral band; computed from log N – log S arguments
RA	Right Ascension, rendered in full precision (in degrees) in the *long* form FSC (Equinox B1950.0)
Radiation hit	Detector signal produced when a charged particle impacted a detector
RADIUS	Radius vector from an *IRAS* source to an associated source
RAH	Right Ascension hour of time (Equinox B1950.0) (*long* form FSC)
RAH_2000	Right Ascension hour of time (Equinox J2000.0)
RAHR	Right Ascension hour of time (Equinox B1950.0) (*short* form FSC)
RAM	Right Ascension minute of time (Equinox B1950.0) (*long* form FSC)

4/16

D 10015

RAM_2000	Right Ascension minute of time (Equinox J2000.0)
RAMIN	Right Ascension minute of time (Equinox B1950.0) (*short* form FSC)
RAS	Right Ascension deci-second of time (Equinox B1950.0) (*long* form FSC)
RAS_2000	Right Ascension deci-second of time (Equinox J2000.0)
RASEC	Right Ascension deci-second of time (Equinox B1950.0) (*short* form FSC)
RECNO	Record number in main data table, given in the Association Data Table
Reject File	The Faint Source Reject File, consisting of all extractions from the Plates above approximately 3 σ
RELIAB	Reliability of a source in percent
Reliability	Estimate of probability that a detection of given SNR, coverage, etc., is a genuine IR source, in percent
RELUNC	Percent relative flux density uncertainties (1 value per band)
Rep	The Representative selected from the different extractions of an individual source from different Plates
Representative	The Representative selected from the different extractions of an individual source from different plates
S/C, s/c	Spacecraft
SAO	Smithsonian Astrophysical Observatory Star Catalog
Seconds-Confirmed	Detected on the correct combination of detectors with the correct time difference to be consistent with a true fixed source
SHAPANGY	Orientation of the pixel distribution with respect to the plate y-axis
SHAPEMAJ	Semi-major axis of the pixel distribution
SHAPEMIN	Semi-minor axis of the pixel distribution
SIGNOBS	RMS deviation of the counts measured over the pixel distribution

417

D 10015

SIGPLATE	Flux density rms error measured in the noise grid
SNR	Signal-to-Noise Ratio, signal divided by thr sholding noise
Solid Angle	The effective solid angle of the sky observed by each *IRAS* detector
SOP	Satellite operation plan, roughly a half-day of *IRAS* data
Source Counts	The number of sources with flux densities greater than a given value
Spider	Telescope secondary mirror support structure
SOURCE	Source ID, name of the object in the catalog association to *IRAS* source
Source	A source of IR radiation
SSC	Serendipitous Survey Catalog
'stars'	Sources defined for illustrative purposes using the criterion of $f_\nu(12\ \mu m) > f_\nu(60\ \mu m)$ for sources above the catalog threshold at 12 μm
Symmetrization	The act of making all dup lists of a set of duplicate sources identical
Template	The theoretical two-dimensional point spread function at a given point after coaddition
Thresholding Noise	Noise, estimated by the 68% quantile of positive flux density values measured on areas Γ
Trimmed Average	The arithmetic average of data points remaining after excluding points falling into a given top and bottom percentage of all points
TYPE	Source type or spectral class given for a catalog entry that associates to an *IRAS* source
Type, KIR	(See KIR Type)
UNCMAJ	UNCMAJOR

418

UNCMAJOR	Uncertainty ellipse major axis in arc seconds
UNCMIN	UNCMINOR
UNCMINOR	Uncertainty ellipse minor axis in arc seconds
Upper Limit Flux Density	A measure of the maximum flux density in the vicinity of a source for a wavelength at which the source is not detected. The confidence level of the upper limit is 90%.
UTCS	Seconds past 1981, January 1.0 UT
WINDOW	Catalog dependent association window, used in source association processing
Working Survey Data Base	A file containing all the hours-confirmed sources from the Point Source Catalog processing
WSDB	Working Survey Data Base, containing all the hours-confirmed sources from the Point Source Catalog processing
YCNTROID	Flux weighted centroid of an extraction along the plate y-axis
YOFFSET	Distance of centroid position from the peak flux pixel along the plate y-axis
ζ	A measure of large-scale/small-scale coverage variation over a sub-region of a plate, Γ
ZCNTROID	Flux weighted centroid of an extraction along the plate z-axis
ZOFFSET	Distance of centroid position from the peak flux pixel along the plate z-axis
'100 μm only'	Sources defined for illustrative purposes using the criterion of flux detection only at 100 μm
36-Hour File	A file from the PSC Processing that contains all seconds-confirmed bandmerged sources prior to hours confirmation

D 10015

INDEX

A

B

4/20

C

V21

) 10015

1/22

D

D 10015

E

F

425

426

K

L

M

N

) 10015

429

D 10015

O

P

430

D 10015

Q

R

431

D 10015

S

432

D 10015

433

D 10015

U

V

W

Y

Z

434

RANDOM *IRAS* INFORMATION

DATA CHARACTERISTICS

Survey Scan Rate: 3.85′/sec
SOPs: 1-600 (~ half-day units of data)
Useful Survey Data: ~ 5,800 scans; 9.7×10^6 seconds
Useful AO Data: ~ 9,000 observations; ~ 5×10^6 seconds
Survey + AO Data: 60% of total time. (Rest spent in calibration observations, slewing, telescope problems, etc.)

Product	Data Volume (Gbytes)
Compressed raw data	27
Uncompressed raw data	53
Calibrated Raw Detector Data	29
Boresight Pointing Data	2
Faint Source Plates	73
IRAS Sky Survey Atlas (HCONs1-3)	3.4
Sky Brightness Images	2
AO images	2
IRAS Sky Survey Atlas (HCON0)	1.1
FS Reject File	0.9
PSC Reject File	0.4
FSC	0.3
Galactic Plane Images	0.3
PSC	0.2
Zodiacal History File	0.1
Cataloged Galaxies	0.06
Small Scale Structure	0.06
CPC Images	0.03
SSC	0.01
LRS catalog	0.005
Asteroids and Comets	0.005

D 10015

RANDOM *IRAS* INFORMATION

Color-Corrected Flux Density Corresponding to 0.0 *mag*

Wavelength (μm)	Flux Density (Jy)
12	28.3
25	6.73
60	1.19
100	0.43

Flux-to-Flux Density Conversion Factors

Nominal Wavelength (μm)	Band Pass (μm)	K*
12	7.5 – 15.5	13.48
25	16 – 31	5.16
60	30 – 84	2.58
100	70 – 140	1.00

$$^{*}f_{\nu} = \frac{F \times 10^{14}}{K}$$

Conversion to Row 10 Crossing Times

Detectors	Δt (sec)
1 – 3	– 7.1
4 – 7	– 6.0
8 – 11	– 4.5
12 – 15	– 3.9
16 – 18	– 3.1
19 – 22	– 2.6
23 – 26	– 1.9
27 – 30	– 1.5
31 – 34	– 0.6
35 – 38	0.0
39 – 42	0.8
43 – 46	1.3
47 – 50	2.0
51 – 54	2.4
55 – 58	3.4
59 – 62	4.6

437

D 10015

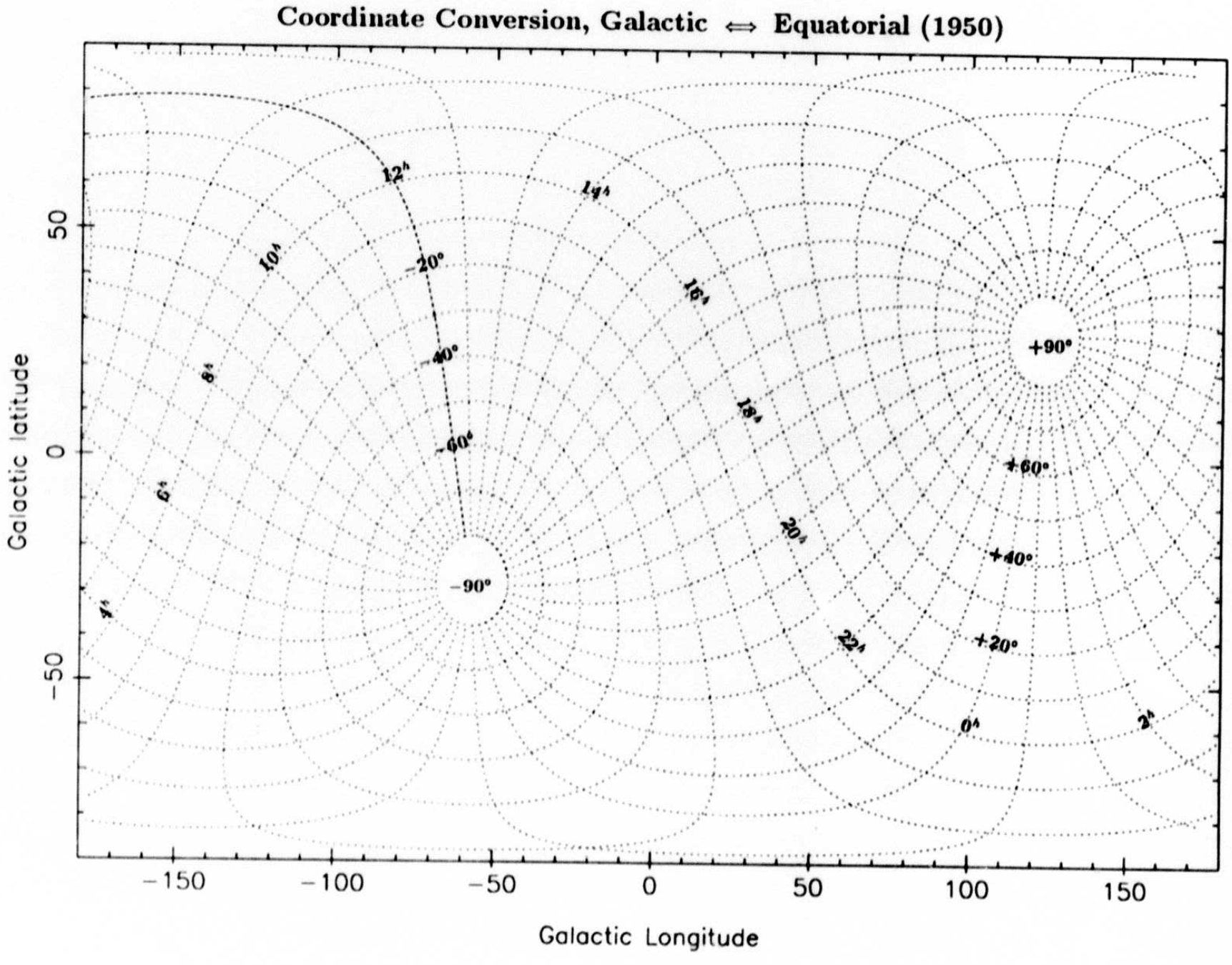
Coordinate Conversion, Galactic ⟺ Equatorial (1950)
Galactic latitude
Galactic Longitude
50
0
−50
−150
−100
−50
0
50
100
150
12h
14h
10h
16h
8h
18h
6h
20h
4h
22h
2h
0h
−20°
−40°
−60°
−90°
+90°
+60°
+40°
+20°

TABLE Suppl. VI.C.6 Color Correction Factors, K[1]

INTRINSIC POWER LAW[2]	RATIO OF FLUX DENSITIES BEFORE COLOR-CORRECTION			CORRECTION FACTOR			
α	$\frac{f_\nu(12\mu m)}{f_\nu(25\mu m)}$	$\frac{f_\nu(25\mu m)}{f_\nu(60\mu m)}$	$\frac{f_\nu(60\mu m)}{f_\nu(100\mu m)}$	K(12 μm)	K(25 μm)	K(60 μm)	K(100 μm)
-3.0	0.113	0.063	0.21	0.91	0.89	1.02	1.02
-2.5	0.162	0.102	0.275	0.92	0.91	1.00	1.01
-2.0	0.232	0.164	0.355	0.94	0.93	0.99	1.00
-1.5	0.333	0.262	0.460	0.97	0.96	0.99	1.00
-1.0	0.480	0.417	0.600	1.00	1.00	1.00	1.00
-0.5	0.694	0.662	0.786	1.04	1.04	1.02	1.00
0.0	1.005	1.045	1.037	1.10	1.10	1.05	1.01
0.5	1.459	1.642	1.378	1.17	1.16	1.09	1.02
1.0	2.123	2.567	1.843	1.25	1.23	1.15	1.04
1.5	3.094	3.992	2.484	1.35	1.32	1.23	1.06
2.0	4.519	6.170	3.373	1.47	1.41	1.32	1.09
2.5	6.610	9.480	4.617	1.61	1.53	1.44	1.12
3.0	9.681	14.475	6.370	1.78	1.67	1.59	1.16

INTRINSIC	RATIO OF FLUX DENSITIES BEFORE COLOR-CORRECTION			CORRECTION FACTOR			
TEMP(°K)	$\frac{f_\nu(12\mu m)}{f_\nu(25\mu m)}$	$\frac{f_\nu(25\mu m)}{f_\nu(60\mu m)}$	$\frac{f_\nu(60\mu m)}{f_\nu(100\mu m)}$	K(12 μm)	K(25 μm)	K(60 μm)	K(100 μm)
10000	4.345	6.050	3.350	1.45	1.41	1.32	1.09
5000	4.172	5.931	3.327	1.43	1.40	1.32	1.09
4000	4.086	5.872	3.316	1.42	1.40	1.31	1.09
3000	3.944	5.773	3.297	1.41	1.39	1.31	1.09
2000	3.666	5.578	3.259	1.38	1.38	1.31	1.09
1000	2.891	5.005	3.145	1.27	1.34	1.29	1.08
800	2.545	4.730	3.088	1.22	1.32	1.28	1.08
600	2.036	4.287	2.995	1.15	1.29	1.27	1.08
500	1.692	3.950	2.920	1.09	1.26	1.26	1.08
400	1.272	3.478	2.810	1.01	1.22	1.24	1.08
300	0.785	2.780	2.630	0.92	1.15	1.21	1.07
290	0.734	2.693	2.606	0.91	1.15	1.21	1.07
280	0.684	2.602	2.580	0.90	1.14	1.20	1.07
270	0.633	2.506	2.553	0.89	1.13	1.20	1.07
260	0.583	2.407	2.523	0.88	1.12	1.19	1.07
250	0.534	2.304	2.491	0.87	1.11	1.19	1.07
240	0.486	2.196	2.457	0.86	1.09	1.18	1.07
230	0.438	2.084	2.420	0.85	1.08	1.18	1.07
220	0.392	1.967	2.381	0.85	1.07	1.17	1.07
210	0.347	1.845	2.338	0.84	1.06	1.16	1.06
200	0.304	1.719	2.291	0.83	1.04	1.16	1.06
190	0.263	1.589	2.240	0.83	1.02	1.15	1.06
180	0.224	1.455	2.184	0.83	1.01	1.14	1.06
170	0.188	1.317	2.124	0.83	0.99	1.13	1.06
160	0.154	1.176	2.057	0.84	0.97	1.12	1.06
150	0.124	1.034	1.983	0.85	0.95	1.11	1.05
140	0.097	0.892	1.901	0.87	0.93	1.09	1.05
130	0.073	0.751	1.810	0.90	0.91	1.08	1.05
120	0.053	0.614	1.709	0.94	0.89	1.06	1.04
110	0.036	0.484	1.595	1.01	0.86	1.04	1.04
100	0.023	0.363	1.468	1.12	0.84	1.02	1.04
95	0.018	0.307	1.400	1.19	0.83	1.01	1.03
90	0.014	0.256	1.326	1.28	0.83	1.00	1.03
85	0.010	0.208	1.249	1.39	0.82	0.99	1.03
80	0.007	0.165	1.168	1.54	0.81	0.97	1.02
75	0.005	0.127	1.082	1.74	0.81	0.96	1.02
70	0.003	0.095	0.993	2.01	0.81	0.95	1.01
65	0.002	0.067	0.898	2.40	0.82	0.94	1.01
60	0.001	0.045	0.801	2.97	0.83	0.93	1.00
55	—	0.028	0.700	3.86	0.86	0.92	1.00
50	—	0.016	0.597	5.35	0.90	0.91	0.99
45	—	0.008	0.493	8.09	0.97	0.92	0.98
40	—	0.003	0.391	13.79	1.08	0.93	0.98

[1] f_{ν_0} [actual] = f_{ν_0} [quoted]/K (See Suppl. VI.C.3); spectral response given in Table Suppl. II.C.5.

[2] $f_\nu = \nu^\alpha$.

D 10015